CFD Analysis of Transonic Turbulent Cavity Flows

by

Punit Nayyar MEng

Thesis submitted to the Faculty of Engineering,
University of Glasgow, for the degree of Doctor of Philosophy

University of Glasgow
Aerospace Engineering

August 2005

Abstract

This thesis presents the study of transonic cavity flows using CFD. The main focus of the thesis is on the turbulence modelling and simulation of cavity flows. The thesis aims to show the range of applicability of turbulence modelling for cavity flows. Aspects of cavity flow control are also addressed.

The cavity models a weapons bay with a length-to-depth (L/D) ratio of 5 and length-to-width (L/W) ratio of 1. The flow is set to transonic speeds (M=0.85) and the Reynolds number based on the cavity length is in the turbulent regime (Re=6.783 million). At these flow conditions, very high noise levels are encountered inside the cavity combined with intense acoustic and turbulent interactions. Unsteady Reynolds-Averaged Navier-Stokes (URANS) was initially applied and the effectiveness of various two-equation turbulence models such as the Wilcox $k-\omega$ and Menter's Baseline $k-\omega$ and SST turbulence models was assessed. Computations were first performed with the 2D clean cavity to minimise the computational cost, where the 2D cavity was a reasonable representation of the full 3D cavity with doors-on. Results demonstrated that linear statistical turbulence models generally gave reasonable qualitative predictions of the cavity flow-field but on coarse grids only. The amplitudes of the noise levels and frequencies were however less well predicted and the level of agreement deteriorated with grid refinement for the L/D=5 cavity. Nonetheless, out of the models employed, the SST model proved to be the most robust and provided the best agreement with experimental pressure and PIV measurements. The velocity distributions and the turbulent and acoustic spectra at the cavity floor were also analysed and compared with experiments (where possible) and in doing so the influence of turbulent processes in the cavity highlighted.

With the higher acoustic frequencies and the broadband noise less well predicted with linear statistical two-equation turbulence models, attention was diverted towards simulation methods such as Large-Eddy Simulation (LES) and Detached-Eddy Simulation (DES). Numerical results for the 3D L/D=5 cavity with a width-to-depth ratio (W/D) of 1 in both doors-on and doors-off configurations were compared with experiments. Even for coarse grid simulations, better agreement was found between the LES/DES results and experimental pressure and PIV measurements for various grid levels and time-steps than URANS. Results revealed better prediction of higher frequencies in particular with LES and DES. Flow-field analysis showed that URANS predicted a coherent shear layer that spanned the cavity length while both DES and LES clearly captured its breakdown. PIV comparisons revealed good agreement at all stations analysed except at the cavity rear, where the resolution of the experiment was poorer. Resolution near the cavity walls for the PIV experiment was also poor and it was concluded that high-resolution experimental data are required. Good qualitative and quantitative predictions of the cavity flow-field were obtained with low to moderate grid resolutions for LES/DES computations.

The URANS method was then revisited to ascertain why it provided poorer predictions of the cavity flow-field than LES/DES. The range of applicability of URANS was also de-

termined by investigating cavities of different dimensions. Two-dimensional deep, open cavities (L/D=2), transitional cavities (L/D=10) and closed cavities (L/D=16) were studied using the SST turbulence model. Parametric studies in time and space revealed that URANS gave more consistent predictions of the cavity flow-field for higher cavity L/D ratios. This was attributed to the presence of lower frequencies and a lower level of unsteadiness and turbulence in closed cavities. It was concluded that for cavities with $L/D \geq 16$ (at these flow conditions) URANS could be used with good accuracy while for cavities with $L/D < 16$, LES/DES would be required.

With the cavity flow physics better understood, investigations into palliative methods to alleviate the cavity noise in the L/D=5 cavity were conducted. Passive control methods such as the spoiler and slanted cavity walls and active open-loop methods such as continuous mass injection were applied. The spoiler deflected the shear layer away from the cavity opening and prevented impingement at the downstream corner. Reductions of about 25 dB were achieved with the spoiler but this was found to be strongly dependent on the spoiler's position. Additional noise was however produced from the spoiler protruding into the external stream. Slanting the cavity walls increased flow entrainment into the cavity but was effective only when the rear wall was slanted and that too at high angles. Steady jet blowing generally controlled the momentum supplied to the shear layer and was found to be the most effective method. Reductions of about 30 dB were obtained and the frequency content was completely eliminated.

In the final section, the L/D=5 cavity with a store was studied and the effect of a generic missile on the cavity flow-field analysed. The missile was placed at the shear layer plane and numerical simulations of half-body and full-body cavities performed. Results with the half-body geometry were similar to the full-body geometry suggesting that the symmetry condition was a good approximation. The flow was more organised in the cavity indicating that a missile placed at the shear layer reduces the flow asymmetry. Noise levels were also lower and lower frequencies were dominant.

Declaration

The author hereby declares that this dissertation is a record of the work carried out in the Department of Aerospace Engineering at the University of Glasgow during the period from October 2001 to August 2005. The dissertation is original in content except where otherwise indicated.

August 2005

Punit Nayyar

Acknowledgements

First and foremost, I would like to thank my supervisors Drs. George Barakos, Ken Badcock and Prof. Bryan Richards for their continuous support and advice throughout the project. In particular, I would like to thank Dr. George Barakos with whom I have had most contact during this project. His enthusiasm, guidance, hard work and, most importantly, his belief and patience in me, has been tremendous help.

As always, my sincerest and humblest thanks go to my family. They have provided me a unique sort of motivation and support over the last few years.

I would also like to thank the members of the CFD Lab both past and present. I have been fortunate enough to get to know most of them and have made some good friends in the process. Getting to know them, work with them and just interact with them through sports or other social activities have all contributed to making this PhD a memorable experience. My thanks go to Dr. David Lawrie, a former member of the CFD Lab, who helped me a great deal in the beginning of the project.

I would also like to thank the secretaries for taking care of all the little but important administrative tasks. Thanks also go to the 'aerosupport' technical staff members, in particular Kenny Stevenson, for sorting out the many computer-related problems that I pestered them with.

And finally, I would like to graciously acknowledge the financial support of BAE SYSTEMS and EPSRC for funding this project through Award 01800565. I would like to thank Drs. David Kirkham and Mike Henshaw of BAE SYSTEMS for their support and supervision over the course of this project. A special thanks go to Drs. Graham Foster and John Ross of DERA (Bedford) for providing the experimental data. Thanks also go to Drs. Richard Ashworth and Tony Hutton of QinetiQ (Farnborough) for the discussions on cavity flows.

Publications

Journal Papers

P. Nayyar, G. N. Barakos, D. Lawrie, K. J. Badcock, B. E. Richards, J. A. Ross, G. W. Foster, D. A. Kirkham, M. J. Henshaw. **Numerical Study of Transonic Cavity Flows. Part 1: URANS Computations**. *Submitted to the AIAA Journal.*

P. Nayyar, G. N. Barakos, D. Lawrie, K. J. Badcock, B. E. Richards, J. A. Ross, G. W. Foster, D. A. Kirkham, M. J. Henshaw. **Numerical Study of Transonic Cavity Flows. Part 2: Large-Eddy and Detached-Eddy Computations**. *Submitted to the AIAA Journal.*

Papers in Refereed Conference Proceedings

P. Nayyar, G. N. Barakos, K. J. Badcock, B. E. Richards. **Noise Suppression Methods for Transonic Cavity Flows**. *CEAS/KATnet Conference on Key Aerodynamic Technologies to Meet the Challenges of the European 2020 Vision*, Bremen, Germany, 20–22 June 2005.

P. Nayyar, D. Lawrie, G. N. Barakos, K. J. Barakos, B. E. Richards. **Numerical Study of Transonic Cavity Flows Using Large-Eddy and Detached-Eddy Simulations**. *RAeS Aerospace Aerodynamics Research Conference* London, UK, 14–16 September 2004.

D. Lawrie, P. Nayyar, K. J. Badcock, G. N. Barakos, B. E. Richards. **CFD Study of Cavity Flows**. *RAeS Aerospace Aerodynamics Research Conference*, London, UK, 10–12 June 2003.

Papers in Non-Refereed Conference Proceedings

P. Nayyar, G. N. Barakos, K. J. Badcock. **Numerical and Experimental Analysis of Transonic Cavity Flows**. *2nd International Symposium on Integrating CFD and Experiments in Aerodynamics*, Cranfield, UK, 5–6 September 2005.

P. Nayyar, G. N. Barakos, K. J. Badcock. **CFD Analysis of Transonic Cavity Flow using DES and LES**. *FOI/Desider Symposium on Hybrid RANS-LES Methods*, Stockholm, Sweden, 14–15 July 2005.

P. Nayyar, G. N. Barakos, K. J. Badcock, D. A. Kirkham. **Analysis and Control of Transonic Cavity Flow Using DES and LES**. *35th AIAA Fluid Dynamics Conference*, Toronto, Canada, 6–9 June 2005.

R. Steijl, P. Nayyar, M. A. Woodgate, K. J. Badcock, G. N. Barakos. **Application of an Implicit Dual-Time Stepping Multi-Block Solver to 3D Unsteady Flows**. *International Conference on Parallel Computational Fluid Dynamics*, Washington DC, USA, 24–27 May 2005.

P. Nayyar, G. N. Barakos, K. J. Badcock. **Analysis and Control of Weapon Bay Flows**. *RTO/AVT Symposium on Flow-Induced Unsteady Loads and the Impact on Military Applications*, Budapest, Hungary, 25–28 April 2005.

P. Nayyar. **Treatment of Turbulence for Cavity For Problems**. *3rd Osborne Reynolds Seminar and Research Student Award*, Manchester, UK, 5 April 2005.

Technical Aero Reports

P. Nayyar and G. N. Barakos. **A Summary of Turbulence Modelling Approaches in CFD**. *Internal technical report: Aerospace Engineering Report 0206*, University of Glasgow, UK, September 2002.

Contents

Abstract ii

Declaration iv

Acknowledgements v

Publications vii

Table of Contents xi

List of Figures xx

List of Tables xxii

Nomenclature xxiii

1 Introduction 1

1.1 Motivation . . . 1
1.2 Objectives . . . 2
1.3 Types of Cavity Flows . . . 3
1.3.1 Open Cavity Flows . . . 3
1.3.2 Closed Cavity Flows . . . 5
1.3.3 Transitional Cavity Flows . . . 6
1.3.4 Backward- and Forward-Facing Steps . . . 7
1.3.5 Fluid-Dynamic, Fluid-Resonant and Fluid-Elastic Cavity Flows . . . 10
1.4 A Literature Review on Cavity Flows . . . 10
1.4.1 Experimental Studies . . . 13
1.4.2 Theoretical Studies . . . 17
1.4.2.1 Plumblee *et al.* Method (1962) . . . 18
1.4.2.2 Rossiter's Semi-Empirical Formula (1962) . . . 18
1.4.2.3 Bilanin and Covert Model (1973) . . . 19
1.4.2.4 Tam and Block Model (1978) . . . 19
1.4.2.5 Bauer and Dix Model (1991) . . . 20
1.4.2.6 Kerschen *et al.* Model (2005) . . . 21
1.4.3 Numerical Studies . . . 21
1.4.3.1 Direct Numerical Simulation (DNS) . . . 21

1.4.3.2 Unsteady Reynolds-Averaged Navier-Stokes (URANS) . . 23
1.4.3.3 Large-Eddy Simulation (LES) 25
1.4.3.4 Detached-Eddy Simulation (DES) 26
1.4.3.5 Other Numerical Methods 27
1.4.4 Flow Control Studies 28
1.4.4.1 Passive Control 29
1.4.4.2 Active Control - Closed-Loop 30
1.4.4.3 Active Control - Open-Loop 30
1.5 Thesis Outline 30

2 Mathematical Model **40**
2.1 CFD Solver 40
2.2 General Description of Turbulence and its Modelling 43
2.3 Reynolds Averaging 44
2.3.1 Time Averaging 44
2.3.2 Spatial Averaging 45
2.3.3 Ensemble Averaging 45
2.4 Boussinesq-Based Models 46
2.5 Viscosity-Dependent Parameters 47
2.6 One-Equation Models 47
2.6.1 Spalart-Allmaras Model 48
2.6.2 Model Coefficients 49
2.7 Two-Equation Models 49
2.7.1 Model Equations: Linear $k-\omega$ Model 51
2.8 Wall Functions 52
2.9 Large-Eddy Simulation (LES) 54
2.10 Detached-Eddy Simulation (DES) 55

3 Description of Experiment **57**
3.1 Generic Cavity Rig Model 57
3.2 Pressure Measurements 60
3.3 Data Analysis 60
3.4 Experimental Analysis: Doors-On 63
3.5 Experimental Analysis: Doors-Off 64
3.6 Particle Image Velocimetry (PIV) Measurements 64

4 L/D=5 Cavity: URANS Results **70**
4.1 Description of Computational Domain 71
4.2 Coarse and Fine Grid Results 73
4.2.1 Acoustic Spectrum Analysis 73
4.2.2 Band-Limited Frequency Analysis 78
4.2.3 Observations from Acoustic Spectrum Analyses 82
4.2.4 Boundary Layer Characteristics 82

4.2.5 Flow-field Visualisation 87
4.2.6 Turbulent Spectrum Analysis 94
4.3 Very Fine and Ultra Fine Grid Results 97
4.3.1 Velocity Distribution Analysis 97
4.3.2 Flow-field Visualisation 99
4.3.3 Turbulent Spectrum Analysis 102
4.3.4 Observations from Turbulent Spectrum Analyses 102
4.4 Concluding Remarks 104

5 L/D=5 Cavity: LES & DES Computations 106
5.1 Description of Computational Domain 107
5.2 Doors-Off Results 111
5.2.1 Band-Limited Frequency Analysis 113
5.2.2 Flow-field Visualisation 116
5.3 Doors-On Results 123
5.3.1 Band-Limited Frequency Analysis 124
5.3.2 Turbulence Decay Characteristics 127
5.3.3 Broadband Spectrum Analysis 132
5.3.4 Flow-field Visualisation 133
5.4 PIV Comparisons 135
5.5 Concluding Remarks 136

6 Different Aspect Ratio Cavity Flows 140
6.1 Description of Computational Domains 140
6.2 L/D=2 Open Cavity 142
6.2.1 Band-Limited Frequency Analysis 143
6.2.2 Flow-field Visualisation 148
6.3 L/D=10, Transitional Cavity 148
6.3.1 Band-Limited Frequency Analysis 148
6.3.2 Flow-field Visualisation 154
6.4 L/D=16 Closed Cavity 155
6.4.1 Band-Limited Frequency Analysis 155
6.4.2 Flow-field Visualisation 160
6.5 Concluding Remarks 162

7 Flow Control: L/D=5 Cavity 163
7.1 Description of Computational Domain 164
7.2 Acoustic Spectrum Analysis 167
7.3 Band-Limited Frequency Analysis 167
7.4 Flow-field Visualisation 170
7.5 Conclusions 174

8 Cavity with Stores 175
8.1 Description of Computational Domain . . . 176
8.2 Acoustic Spectrum Analysis . . . 177
8.2.1 Band-Limited Frequency Analysis . . . 177
8.2.2 Flow-field Visualisation . . . 180
8.3 Concluding Remarks . . . 183

9 Conclusions 186
9.1 Conclusions from the Present Work . . . 186
9.2 Further Work . . . 190

A Flow Control: Detailed Results for the L/D=5 Cavity 191
A.1 Passive Control: Spoiler . . . 192
A.1.1 Effects of Spoiler Position . . . 192
A.1.1.1 Band-Limited Frequency Analysis . . . 193
A.1.1.2 Flow-field Visualisation . . . 198
A.1.2 Effects of Spoiler Height . . . 202
A.1.2.1 Band-Limited Frequency Analysis . . . 203
A.1.2.2 Flow-field Visualisation . . . 203
A.2 Passive Control: Slanted Cavity Walls . . . 209
A.2.1 Effects of Slant Position . . . 209
A.2.1.1 Band-Limited Frequency Analysis . . . 209
A.2.1.2 Flow-field Visualisation . . . 214
A.2.2 Effects of Slant Angle . . . 216
A.2.2.1 Band-Limited Frequency Analysis . . . 216
A.2.2.2 Flow-field Visualisation . . . 222
A.3 Active Open-Loop Control: Steady Jet Blowing . . . 222
A.3.1 Effects of Jet Position . . . 224
A.3.1.1 Band-Limited Frequency Analysis . . . 224
A.3.1.2 Flow-field Visualisation . . . 227
A.3.2 Effects of Jet Exit Velocity . . . 230
A.3.2.1 Band-Limited Frequency Analysis . . . 232
A.3.2.2 Flow-field Visualisation . . . 232
A.4 Concluding Remarks . . . 237

References 238

List of Figures

1.1 A schematic of the flow-field in the open cavity at subsonic and supersonic speeds. Extracted from the ESDU data sheet [1]. 4

1.2 A schematic of the flow-field in the closed cavity at subsonic and supersonic speeds. Extracted from the ESDU data sheet [1]. 5

1.3 A schematic of the flow-field in a transitional-open and transitional-closed cavity at supersonic speeds. Extracted from the ESDU data sheet [1]. . . . 7

1.4 Typical C_p distributions in the cavity with increasing L/D ratio at subsonic and supersonic speeds. Extracted from the ESDU data sheet [1]. 8

1.5 A schematic of the flow-field in backward-facing and forward-facing steps. Reproduced from Taborda *et al.* [2]. 9

1.6 Illustrations of the bomb bays in manned combat aircraft and Uninhabited Combat Aerial Vehicles (UCAVs). 12

1.7 Typical noise spectrum inside the cavity. The acoustical signature is composed of narrowband noise superimposed on top of broadband noise. Narrowband noise consists of discrete acoustic tones, which are also referred to as Rossiter modes [3]. 15

1.8 A schematic of the acoustic wave patterns inside and outside a rectangular cavity as proposed by Tam and Block [4] in the development of their theoretical model. Reproduced from the article by Tam and Block [4]. 20

3.1 The generic cavity rig model with a sting-mounted store in the ARA 9 ft. by 8 ft. transonic wind tunnel and a schematic of the plan and side views of the cavity model. 58

3.2 Cavity model with doors inclined at 90^o to flow. 59

3.3 Positions of the pressure transducers located inside and outside the cavity in the doors-off configuration. 61

3.4 Positions of the pressure transducers located inside and outside the cavity in the doors-on configuration. 62

3.5 Sound Pressure Levels (SPLs) and spectral analysis (at $x/L = 0.95$) of the 6 kHz sampling rate experimental signal for three signal durations - 3 seconds, 0.1 seconds and 0.2 seconds - for the L/D=5, clean cavity with doors-on. 65

3.6 Sound Pressure Levels (SPLs) and spectral analysis (at $x/L = 0.95$) of the 31.25 kHz sampling rate experimental signal for three signal durations - 3 seconds, 0.1 seconds and 0.2 seconds - for the L/D=5, clean cavity with doors-on. 66

3.7 Sound Pressure Levels (SPLs) and spectral analysis (at $x/L = 0.95$) of the 6 kHz sampling rate experimental signal for three signal durations - 3 seconds, 0.1 seconds and 0.2 seconds - for the L/D=5, clean cavity with doors-off. 67
3.8 Equipment for spraying water droplets for seeding of the cavity (above) used in the PIV experiment by firing the laser (with a width of 5.5 inches) across 4 sections (below) to cover the entire cavity length of 20 inches. . . 68
3.9 Water droplets sprayed into the settling chamber for seeding of the cavity in the PIV experiment. 69

4.1 Schematic of the 2D (L/D=5) cavity grid illustrating all dimensions and boundary conditions applied and the finite width applied with no resolution in the spanwise direction for use with the 3D PMB flow solver [5]. 72
4.2 SPLs and PSD (at $x/L = 0.05$, $x/L = 0.55$ and $x/L = 0.95$) along the cavity floor for the 2D, L/D=5 cavity grid with the $k-\omega$ turbulence model for: coarse grid, $\Delta t = 0.01$ ($\equiv 1.814 \times 10^{-5}$s) [blue (plus markers)]; coarse grid, $\Delta t = 0.005$ ($\equiv 9.07 \times 10^{-6}$s) [red (circular markers)]; fine grid, $\Delta t = 0.01$ ($\equiv 1.814 \times 10^{-5}$s) [green (cross markers)]; fine grid, $\Delta t = 0.005$ ($\equiv 9.07 \times 10^{-6}$s) [magenta (square markers)]. 75
4.3 SPLs and PSD (at $x/L = 0.05$, $x/L = 0.55$ and $x/L = 0.95$) for the 2D, L/D=5 cavity grid with the Baseline $k-\omega$ turbulence model for: coarse grid, $\Delta t = 0.01$ ($\equiv 1.814 \times 10^{-5}$s) [blue (plus markers)]; coarse grid, $\Delta t = 0.005$ ($\equiv 9.07 \times 10^{-6}$s) [red (circular markers)]; fine grid, $\Delta t = 0.01$ ($\equiv 1.814 \times 10^{-5}$s) [green (cross markers)]; fine grid, $\Delta t = 0.005$ ($\equiv 9.07 \times 10^{-6}$s) [magenta (square markers)]. 77
4.4 SPLs and PSD (at $x/L = 0.05$, $x/L = 0.55$ and $x/L = 0.95$) along the cavity floor for the 2D, L/D=5 cavity grid with the SST turbulence model for: coarse grid, $\Delta t = 0.01$ ($\equiv 1.814 \times 10^{-5}$s) [blue (plus markers)]; coarse grid, $\Delta t = 0.005$ ($\equiv 9.07 \times 10^{-6}$s) [red (circular markers)]; fine grid, $\Delta t = 0.01$ ($\equiv 1.814 \times 10^{-5}$s) [green (cross markers)]; fine grid, $\Delta t = 0.005$ ($\equiv 9.07 \times 10^{-6}$s) [magenta (square markers)]. 79
4.5 Band-limited SPL plots along the cavity floor for the 2D, L/D=5 cavity grid with the $k-\omega$ turbulence model for: coarse grid, $\Delta t = 0.01$ ($\equiv 1.814 \times 10^{-5}$s) [blue (plus markers)]; coarse grid, $\Delta t = 0.005$ ($\equiv 9.07 \times 10^{-6}$s) [red (circular markers)]; fine grid, $\Delta t = 0.01$ ($\equiv 1.814 \times 10^{-5}$s) [green (cross markers)]; fine grid, $\Delta t = 0.005$ ($\equiv 9.07 \times 10^{-6}$s) [magenta (square markers)]. 81
4.6 Band-limited SPL plots along the cavity floor for the 2D, L/D=5 cavity grid with the Baseline $k-\omega$ turbulence model for: coarse grid, $\Delta t = 0.01$ ($\equiv 1.814 \times 10^{-5}$s) [blue (plus markers)]; coarse grid, $\Delta t = 0.005$ ($\equiv 9.07 \times 10^{-6}$s) [red (circular markers)]; fine grid, $\Delta t = 0.01$ ($\equiv 1.814 \times 10^{-5}$s) [green (cross markers)]; fine grid, $\Delta t = 0.005$ ($\equiv 9.07 \times 10^{-6}$s) [magenta (square markers)]. 84
4.7 Band-limited SPL plots along the cavity floor for the 2D, L/D=5 cavity grid with the SST turbulence model for: coarse grid, $\Delta t = 0.01$ ($\equiv 1.814 \times 10^{-5}$s) [blue (plus markers)]; coarse grid, $\Delta t = 0.005$ ($\equiv 9.07 \times 10^{-6}$s) [red (circular markers)]; fine grid, $\Delta t = 0.01$ ($\equiv 1.814 \times 10^{-5}$s) [green (cross markers)]; fine grid, $\Delta t = 0.005$ ($\equiv 9.07 \times 10^{-6}$s) [magenta (square markers)]. 86

4.8 Boundary layer profiles at x/L=-0.05 for the 2D, L/D=5, cavity grid with the $k-\omega$ turbulence model for: coarse grid, $\Delta t = 0.01$ ($\equiv 1.814 \times 10^{-5}$s) [green (solid) lines]; coarse grid, $\Delta t = 0.005$ ($\equiv 9.07 \times 10^{-6}$s) [red (dashed) lines]; fine grid, $\Delta t = 0.01$ ($\equiv 1.814 \times 10^{-5}$s) [blue (dash-dot) lines]; fine grid, $\Delta t = 0.005$ ($\equiv 9.07 \times 10^{-6}$s) [magenta (long-dashed) lines]. 88

4.9 Boundary layer profiles at x/L=-0.05 for the 2D, L/D=5, cavity grid with the Baseline $k-\omega$ turbulence model for: coarse grid, $\Delta t = 0.01$ ($\equiv 1.814 \times 10^{-5}$s) [green (solid) lines]; coarse grid, $\Delta t = 0.005$ ($\equiv 9.07 \times 10^{-6}$s) [red (dashed) lines]; fine grid, $\Delta t = 0.01$ ($\equiv 1.814 \times 10^{-5}$s) [blue (dash-dot) lines]; fine grid, $\Delta t = 0.005$ ($\equiv 9.07 \times 10^{-6}$s) [magenta (long-dashed) lines]. 89

4.10 Boundary layer profiles at x/L=-0.05 for the 2D, L/D=5, cavity grid with the SST turbulence model for: coarse grid, $\Delta t = 0.01$ ($\equiv 1.814 \times 10^{-5}$s) [green (solid) lines]; coarse grid, $\Delta t = 0.005$ ($\equiv 9.07 \times 10^{-6}$s) [red (dashed) lines]; fine grid, $\Delta t = 0.01$ ($\equiv 1.814 \times 10^{-5}$s) [blue (dash-dot) lines]; fine grid, $\Delta t = 0.005$ ($\equiv 9.07 \times 10^{-6}$s) [magenta (long-dashed) lines]. 90

4.11 Time-averaged flow-field plots using normalised Mach contours and streamlines for the 2D, L/D=5, cavity with the $k-\omega$ turbulence model for: coarse grid, $\Delta t = 0.01$ ($\equiv 1.814 \times 10^{-5}$s); coarse grid, $\Delta t = 0.005$ ($\equiv 9.07 \times 10^{-6}$s); fine grid, $\Delta t = 0.01$ ($\equiv 1.814 \times 10^{-5}$s); fine grid, $\Delta t = 0.005$ ($\equiv 9.07 \times 10^{-6}$s). . 92

4.12 Time-averaged flow-field plots using normalised Mach contours and streamlines for the 2D, L/D=5, cavity with the Baseline $k-\omega$ turbulence model for the coarse grid, $\Delta t = 0.01$ ($\equiv 1.814 \times 10^{-5}$s); coarse grid, $\Delta t = 0.005$ ($\equiv 9.07 \times 10^{-6}$s); fine grid, $\Delta t = 0.01$ ($\equiv 1.814 \times 10^{-5}$s); fine grid, $\Delta t = 0.005$ ($\equiv 9.07 \times 10^{-6}$s). 93

4.13 Time-averaged flow-field plots using normalised Mach contours and streamlines for the 2D, L/D=5, cavity with the SST turbulence model for the coarse grid, $\Delta t = 0.01$ ($\equiv 1.814 \times 10^{-5}$s); coarse grid, $\Delta t = 0.005$ ($\equiv 9.07 \times 10^{-6}$s); fine grid, $\Delta t = 0.01$ ($\equiv 1.814 \times 10^{-5}$s); fine grid, $\Delta t = 0.005$ ($\equiv 9.07 \times 10^{-6}$s). . 95

4.14 Time-averaged plots of eddy viscosity ($\frac{\mu_t}{\mu_\infty}$) for the 2D, L/D=5 cavity with the $k-\omega$ model (left column) and Baseline $k-\omega$ model (right column) for: coarse grid, $\Delta t = 0.01$ ($\equiv 1.814 \times 10^{-5}$s); coarse grid, $\Delta t = 0.005$ ($\equiv 9.07 \times 10^{-6}$s); fine grid, $\Delta t = 0.01$ ($\equiv 1.814 \times 10^{-5}$s); fine grid, $\Delta t = 0.005$ ($\equiv 9.07 \times 10^{-6}$s). 96

4.15 Time-averaged streamwise ($\frac{U}{U_\infty}$) and transverse ($\frac{V}{V_\infty}$) velocity profiles for the 2D, open, rectangular L/D=5 cavity along the cavity floor using the SST turbulence model. Results correspond to 4 grid levels with a fixed Δt of 0.01 ($\equiv 1.814 \times 10^{-5}$s): coarse grid (solid green lines), fine grid (dashed red lines), very fine grid (dash-dot blue lines) and ultra-fine grid (long-dashed magenta lines). Long dash-dot black line represents PIV measurements. . 98

4.16 PIV streamwise and transverse velocity traces at a distance equal to the depth of the cavity above the cavity lip. 100

4.17 Time-averaged Mach contours with streamlines inside the 2D L/D=5 cavity using the SST turbulence model. Plots correspond to 4 grid levels with $\Delta t = 0.01$ ($\equiv 1.814 \times 10^{-5}$s): coarse grid 4.17(a), fine grid 4.17(b), very fine grid 4.17(c) and ultra-fine grid 4.17(d). All plots drawn to the same scale with Mach number normalised with reference to the free-stream Mach number, $M_\infty = 0.85$. 101

4.18 Time-averaged turbulent kinetic-energy (k) and shear stress (τ_{xy}) profiles for the 2D, open, rectangular L/D=5 cavity using the SST turbulence model. Results correspond to 4 grid levels with $\Delta t = 0.01$ ($\equiv 1.814 \times 10^{-5}$s): coarse grid (solid green lines), fine grid (dashed red lines), very fine grid (dash-dot blue lines) and ultra-fine grid (long-dashed magenta lines). Long dash-dot black line represents PIV measurements. 103

5.1 A schematic of the 3D, L/D=5, W/D=1 cavity (with doors-on) illustrating the positions of the pressure taps at which experimental and numerical results were compared. 107

5.2 Reynolds number effects on the SPLs and PSD (at $x/L = 0.95$) for the 3D, L/D=5, W/D=1 clean cavity (with doors-off) using LES (Smagorinsky SGS). 108

5.3 Reynolds number effects on the band-limited RMS pressure for the 3D, L/D=5, W/D=1 clean cavity (with doors-off) using LES (Smagorinsky SGS). 110

5.4 Different views of the meshing distribution for the very fine (8.5m), doors-off grid. 112

5.5 Different views of the meshing distribution for the fine (4.5m) doors-on grid. 113

5.6 SPLs and PSD plots (at $x/L = 0.05$, $x/L = 0.55$ and $x/L = 0.95$) for the 3D, L/D=5, W/D=1, clean cavity with doors-off using URANS (Menter's Baseline $k-\omega$), DES (Spalart-Allmaras) and LES (Smagorinsky SGS). Plots taken at z/W=0.25 and along the cavity floor (y/D=1). 115

5.7 Band-limited SPLs for the 3D, L/D=5, W/D=1, clean cavity with doors-off comparing URANS (Menter's Baseline $k-\omega$), DES-SA and LES (Smagorinsky SGS) results with experiment. Plots taken at z/W=0.25 and along the cavity floor (y/D=1). 118

5.8 Instantaneous Mach number contours with streamlines for the clean cavity with doors-off at for 4 different time-steps during flow cycle for the URANS (Menter's Baseline $k-\omega$) and DES-SA computations. Plots taken along the cavity centreline (z/W = 0.5). 119

5.9 Three-dimensional perspective of the flow field inside the 3D L/D=5 clean cavity with doors-off using URANS (Menter's Baseline $k-\omega$), DES-SA and LES (Smagorinsky SGS). Plots show instantaneous Mach number contours normalised by the free-stream Mach number of 0.85. 120

5.10 Close-up of the 'vortical spillages' (in the y-z plane) observed near the downstream corner of the 3D, L/D=5, W/D=1 clean cavity with doors-off for the DES-SA with the fine grid for 8 time-steps illustrating their flow cycle. Contours are of Mach number normalised by the free-stream Mach number of 0.85. 121

5.11 SPLs inside the 3D L/D=5, W/D=1 clean cavity with doors-off using LES (Smagorinsky SGS) with the 1m, 2m, 4.5m and 8.5m grids. 123

5.12 SPLs and PSD (at $x/L = 0.05$, $x/L = 0.55$ and $x/L = 0.95$) along cavity floor for the L/D=5, W/D=1, clean cavity with doors-on at 90° vertically comparing 2D URANS (SST), 3D URANS (Baseline $k-\omega$), DES-SA and LES (Smagorinsky SGS) results with experiment. Plots taken at z/W=0.25 and along the cavity floor (y/D=1). 126

5.13 Band-limited SPLs for the 3D, L/D=5, W/D=1, clean cavity with doors-on at 90° vertically comparing 2D URANS (SST), 3D URANS (Baseline $k-\omega$), DES-SA and LES (Smagorinsky SGS) results with experiment. Plots taken at z/W=0.25 and along the cavity floor (y/D=1). 129

5.14 Turbulence decay plots (at $x/L = 0.05$, $x/L = 0.55$ and $x/L = 0.95$) for the 3D, L/D=5, W/D=1 clean cavity with doors-on at comparing 2D URANS (SST), 3D URANS (Baseline $k-\omega$), DES-SA and LES (Smagorinsky SGS) results with experiment. Plots taken at z/W=0.25 and along the cavity floor (y/D=1). 132

5.15 SPLs against Strouhal number (at $x/L = 0.05$, $x/L = 0.55$ and $x/L = 0.95$) for the 3D, L/D=5, W/D=1 clean cavity with doors-on comparing 2D URANS (SST), 3D URANS (Baseline $k-\omega$), DES-SA and LES (Smagorinsky SGS) results with experiment. Plots taken at z/W=0.25 and along the cavity floor (y/D=1). 135

5.16 Instantaneous Mach number contours with streamlines for the clean cavity with doors-on at for 4 different time-steps during flow cycle for the URANS (Menter's Baseline $k-\omega$) and DES (Spalart-Allmaras) computations. Plots taken along the cavity centreline (z/W = 0.5). 136

5.17 SPLs along the cavity floor for the L/D=5, W/D=1, clean cavity with doors-on at 90° vertically comparing DES-SA, DES (with $k-\omega$) and LES (Smagorinsky SGS) results with experiment. Plots taken at z/W=0.25 and along the cavity floor (y/D=1). 137

5.18 Time-averaged streamwise ($\frac{U}{U_\infty}$) and transverse ($\frac{V}{V_\infty}$) velocity profiles for the clean cavity with doors-on along cavity floor at $x/L = 0.05$, $x/L = 0.55$ and $x/L = 0.95$ using 2D URANS coarse grid (with SST model (solid, green line)), fine DES grid (with Spalart-Allmaras (dashed, red line)) and medium LES grid (dashed-dot, blue line). Black line corresponds to experimental PIV data (provided by Ross [6]). 138

6.1 Meshing in and near the cavity for the L/D=5 and L/D=2 coarse grids. . . . 141

6.2 Meshing in and near the cavity for the L/D=10 and L/D=16 coarse grids. . . 142

6.3 SPL and PSD plots (at $x/L = 0.05$, $x/L = 0.55$ and $x/L = 0.95$) for the 2D open, rectangular L/D=2 cavity along the cavity floor using the SST turbulence model for: coarse grid, coarse time-step (solid blue with plus signs); coarse grid, fine time-step (solid red with circular markers); fine grid, coarse time-step (solid green with crosses) and fine grid, fine time-step (solid magenta with square symbols). DES results (with $k-\omega$) for the 3D L/D=2 cavity are shown in black (with triangles). 145

6.4 Band-limited SPLs for the 2D open, rectangular L/D=2 cavity along the cavity floor using the SST turbulence model for: coarse grid, coarse time-step (solid blue with plus signs); coarse grid, fine time-step (solid red with circular markers); fine grid, coarse time-step (solid green with crosses) and fine grid, fine time-step (solid magenta with square symbols). DES results (with $k-\omega$) for the 3D L/D=2 cavity are shown in black (with triangles). . . 147

6.5 Time-averaged Mach number contours with streamlines for the 2D L/D=2, open, deep cavity using the SST turbulence model for coarse and fine grids and time-steps and DES (with $k-\omega$) for the 3D L/D=2 cavity. Plots show Mach number normalised with respect to the free-stream Mach number, $M_\infty = 0.85$. 149

6.6 SPL and PSD plots (at $x/L = 0.05$, $x/L = 0.55$ and $x/L = 0.95$) for the 2D transitional, rectangular L/D=10 cavity along the cavity floor using the SST turbulence model for: coarse grid, coarse time-step (solid blue with plus signs); coarse grid, fine time-step (solid red with circular markers); fine grid, coarse time-step (solid green with crosses) and fine grid, fine time-step (solid magenta with square symbols). DES results (with $k-\omega$) for the 3D L/D=10 cavity are shown in black (with triangles). 151

6.7 Band-limited SPLs for the 2D transitional, rectangular L/D=10 cavity along the cavity floor using the SST turbulence model for: coarse grid, coarse time-step (solid blue with plus signs); coarse grid, fine time-step (solid red with circular markers); fine grid, coarse time-step (solid green with crosses) and fine grid, fine time-step (solid magenta with square symbols). DES results (with $k-\omega$) for the 3D L/D=10 cavity are shown in black (with triangles). 153

6.8 Time-averaged Mach number contours with streamlines for the 2D L/D=10, open, deep cavity using the SST turbulence model for coarse and fine grids and time-steps and DES (with $k-\omega$) for the 3D L/D=10 cavity. Plots show Mach number normalised with respect to the free-stream Mach number, $M_\infty = 0.85$. 154

6.9 SPL and PSD plots (at $x/L = 0.05$, $x/L = 0.55$ and $x/L = 0.95$) for the 2D closed, rectangular L/D=16 cavity at $x/L = 0.55$ and $x/L = 0.95$ along the cavity floor using the SST turbulence model for: coarse grid, coarse time-step (solid blue with plus signs); coarse grid, fine time-step (solid red with circular markers); fine grid, coarse time-step (solid green with crosses) and fine grid, fine time-step (solid magenta with square symbols). 157

6.10 Band-limited SPLs for the 2D closed, rectangular L/D=16 cavity along the cavity floor using the SST turbulence model for: coarse grid, coarse time-step (solid blue with plus signs); coarse grid, fine time-step (solid red with circular markers); fine grid, coarse time-step (solid green with crosses) and fine grid, fine time-step (solid magenta with square symbols). 159

6.11 Time-averaged Mach number contours with streamlines for the 2D, L/D=16, closed cavity using the SST turbulence model for coarse and fine grids and time-steps. Plots show Mach number normalised with reference to the free-stream Mach number, $M_\infty = 0.85$. 161

7.1 Schematics illustrating the different positions and heights of the spoiler, different positions and angles of slanted for shaped cavity walls and different positions and exit jet velocities investigated for the flow control study. 165

7.2 Full schematics (on left column) of grids used for the coarse L/D=5 cavity (7.2(a)), LE spoiler (7.2(c)), slanted TE at 45° (7.2(e)) and jet at front cavity wall (7.2(g)). Close-up of the cavity corner for each of the grids is shown on the right column. 166

7.3 SPLs and pressure traces (at $x/L = 0.05$, $x/L = 0.55$ and $x/L = 0.95$) along the cavity floor of the 2D, L/D=5 cavity using the SST turbulence model with and without control. 169

7.4 Band-limited SPLs within four frequency ranges along the cavity floor of the 2D, L/D=5 cavity using the SST turbulence model with and without control. 172

7.5 Time-averaged Mach contours with streamlines inside the 2D, L/D=5 cavity using the SST turbulence model with and without control. 173

8.1 Mesh distribution on and around the half-body missile without fins. 176

8.2 SPLs and pressure traces (at $x/L = 0.05$, $x/L = 0.55$ and $x/L = 0.95$) along the cavity floor for the 3D, L/D=5, W/D=1 cavity (without doors) with missile without fins using LES for the coarse half-body missile grids and the full-body missile (at two spanwise positions). 179

8.3 Band-limited SPLs along the cavity floor for the 3D, L/D=5, W/D=1 cavity (without doors) with missile without fins using LES for the half-body missile grid and the full-body missile (at two spanwise positions). 182

8.4 Band-limited SPLs within $0\ Hz \leq f \leq 50\ Hz$ along the cavity floor for the 3D, L/D=5, W/D=1 cavity (without doors) with a missile without fins using LES for the coarse and medium half-body missile grids and the fine full-body missile. 183

8.5 Instantaneous pressure contours for the clean cavity (without doors) with and without missile (without fins), where the missile is positioned at the shear layer plane of the cavity. Clean cavity results without missile obtained using 8.5 million LES grid. 184

A.1 SPLs and pressure traces (at $x/L = 0.05$, $x/L = 0.55$ and $x/L = 0.95$) along the cavity floor of the 2D, L/D=5 cavity using the SST turbulence model with: LE Spoiler (Case 1), LE Spoiler (Case 2a), TE Spoiler (Case 3). CFD and experimental results with no spoiler also included. Case 1: $x_{sp}/L = -0.2$, $y_{sp}/L = 0$; Case 2a: $x_{sp}/L = -0.1$, $y_{sp}/L = 0$; Case 3: $x_{sp}/L = 1$, $y_{sp}/L = 0$. Height (h_{sp}) and width (w_{sp}) kept fixed to $1\delta = 0.021L$ and $0.0125L$, respectively. 195

A.2 Band-limited SPLs for the 2D, L/D=5 cavity using the SST model with: LE Spoiler (Case 1), LE Spoiler (Case 2a), TE Spoiler (Case 3). Case 1: $x_{sp}/L = -0.2$, $y_{sp}/L = 0$; Case 2a: $x_{sp}/L = -0.1$, $y_{sp}/L = 0$; Case 3: $x_{sp}/L = 1$, $y_{sp}/L = 0$. Height (h_{sp}) and width (w_{sp}) kept fixed to $1\delta = 0.021L$ and $0.0125L$, respectively. 197

A.3 Time-averaged Mach number contours with streamlines for the 2D, L/D=5 cavity using the SST model with: LE Spoiler (Case 1), LE Spoiler (Case 2a), TE Spoiler (Case 3). Case 1: $x_{sp}/L = -0.2$, $y_{sp}/L = 0$; Case 2a: $x_{sp}/L = -0.1$, $y_{sp}/L = 0$; Case 3: $x_{sp}/L = 1$, $y_{sp}/L = 0$. Height (h_{sp}) and width (w_{sp}) kept fixed to $1\delta = 0.021L$ and $0.0125L$, respectively. All plots are drawn to the same scale with the Mach number normalised with reference to the free-stream Mach number, $M_\infty = 0.85$. 199

A.4 Close-up of the time-averaged flow-field near the vicinity of the two LE spoilers. Case 1: $x_{sp}/L = -0.2$, $y_{sp}/L = 0$; Case 2a: $x_{sp}/L = -0.1$, $y_{sp}/L = 0$. Height (h_{sp}) and width (w_{sp}) kept fixed to $1\delta = 0.021L$ and $0.0125L$, respectively. Mach number contours normalised with reference to the free-stream Mach number, $M_\infty = 0.85$. 201

A.5 SPLs upstream of cavity near the vicinity of the case 2a LE spoiler: $x_{sp}/L = -0.1$, $y_{sp}/L = 0$, $h_{sp} = 1\delta = 0.021L$, $w_{sp}/L = 0.0125$. 202

A.6 SPLs and pressure traces (at $x/L = 0.05$, $x/L = 0.55$ and $x/L = 0.95$) along the cavity floor of the 2D, L/D=5 cavity using the SST turbulence model with: LE Spoiler (Case 2a) and LE Spoiler (Case 2b). Case 2a: $x_{sp}/L = -0.1$, $y_{sp}/L = 0$, $h_{sp}/L = 1\delta$; Case 2b: $x_{sp}/L = -0.1$, $y_{sp}/L = 0$, $h_{sp}/L = 2\delta$. Width (w_{sp}) of spoiler kept fixed at $0.0125L$. 205

A.7 Band-limited SPLs for the 2D, L/D=5 cavity using the SST model with: LE Spoiler (Case 2a) and LE Spoiler (Case 2b). Case 2a: $x_{sp}/L = -0.1$, $y_{sp}/L = 0$, $h_{sp}/L = 1\delta$; Case 2b: $x_{sp}/L = -0.1$, $y_{sp}/L = 0$, $h_{sp}/L = 2\delta$. Width (w_{sp}) of spoiler kept fixed at $0.0125L$. 207

A.8 Time-averaged Mach number contours with streamlines for the 2D, L/D=5 cavity using the SST model with: LE Spoiler (Case 2a) and LE Spoiler (Case 2b). Case 2a: $x_{sp}/L = -0.1$, $y_{sp}/L = 0$, $h_{sp}/L = 1\delta$; Case 2b: $x_{sp}/L = -0.1$, $y_{sp}/L = 0$, $h_{sp}/L = 2\delta$. Width (w_{sp}) of spoiler kept fixed at $0.0125L$. . . 208

A.9 SPLs and pressure traces (at $x/L = 0.05$, $x/L = 0.55$ and $x/L = 0.95$) and SPLs along the cavity floor for the 2D, L/D=5 cavity using the SST turbulence model for a slanted front wall, slanted rear wall and both walls slanted. Slant angle fixed at 45°. 211

A.10 Band-limited SPLs for the 2D, L/D=5 cavity using the SST model with a: slanted front wall, slanted rear wall and both walls slanted. Angle of slant kept fixed at 45°. 213

A.11 Time-averaged Mach number contours with streamlines for the 2D, L/D=5 cavity using the SST model with a: slanted front wall, slanted rear wall and both walls slanted. For reference, results from no-slant case also included. Angle of slant kept fixed at 45°. 215

A.12 Time-averaged streamwise velocity profiles ($\frac{U}{U_\infty}$) using the SST model for the 2D, L/D=5 cavity showing: effects of position with a slanted front wall, slanted rear wall and both walls slanted at 45° ; effects of angle with a rear wall slanted at 30° , 45° and 60° . For reference, numerical results and PIV measurements from no-slant case also included. 217

A.13 SPLs and pressure traces (at $x/L = 0.05$, $x/L = 0.55$ and $x/L = 0.95$) along the cavity floor for the 2D, L/D=5 cavity using the SST turbulence model for the slanted rear wall at angles of 30°, 45° and 60°. 219

A.14 Band-limited SPLs for the 2D, L/D=5 cavity using the SST model for the slanted rear wall at 30°, 45° and 60°. 221

A.15 Time-averaged Mach number contours with streamlines using the SST model for the 2D, L/D=5 cavity with the rear wall slanted at 30°, 45° and 60°. 223

A.16 SPLs and pressure traces (at $x/L = 0.05$, $x/L = 0.55$ and $x/L = 0.95$) along the cavity floor for the 2D, L/D=5 cavity using the SST turbulence model with steady jet blowing applied upstream of cavity, at front wall and at rear wall. Upstream jet: $x_j/L = -0.02$, $y_j/L = 0$; front wall jet: $x_j/L = 0$, $y_j/L = -0.02$; rear wall jet: $x_j/L = 1$, $y_j/L = -0.02$. Jet exit Mach number (M_j), jet slot width (w_j) and blowing co-efficient (C_μ) kept fixed at $0.1M_\infty$, 0.02L and 0.01, respectively. 226

A.17 A close-up of the pressure trace (at $x/L = 0.95$) along the cavity floor for the 2D, L/D=5 cavity using the SST turbulence model with steady jet blowing applied upstream of cavity, at front wall and at rear wall. Upstream jet: $x_j/L = -0.02$, $y_j/L = 0$; front wall jet: $x_j/L = 0$, $y_j/L = -0.02$; rear wall jet: $x_j/L = 1$, $y_j/L = -0.02$. Jet exit Mach number (M_j), jet slot width (w_j) and blowing co-efficient (C_μ) kept fixed at $0.1M_\infty$, 0.02L and 0.01, respectively. . 227

A.18 Band-limited SPLs along the cavity floor for the 2D, L/D=5 cavity using the SST turbulence model with steady jet blowing applied upstream of cavity, at front wall and at rear wall. Upstream jet: $x_j/L = -0.02$, $y_j/L = 0$; front wall jet: $x_j/L = 0$, $y_j/L = -0.02$; rear wall jet: $x_j/L = 1$, $y_j/L = -0.02$. Jet exit Mach number (M_j), jet slot width (w_j) and blowing co-efficient (C_μ) kept fixed at $0.1M_\infty$, 0.02L and 0.01, respectively. 229

A.19 Time-averaged Mach number contours with streamlines inside the 2D, L/D=5 cavity using the SST turbulence model with steady jet blowing applied upstream of cavity, at front wall and at rear wall. For reference, flow-field for the no-jet case also included. Upstream jet: $x_j/L = -0.02$, $y_j/L = 0$; front wall jet: $x_j/L = 0$, $y_j/L = -0.02$; rear wall jet: $x_j/L = 1$, $y_j/L = -0.02$. Jet exit Mach number (M_j), jet slot width (w_j) and blowing co-efficient (C_μ) kept fixed at $0.1M_\infty$, 0.02L and 0.01, respectively. 231

A.20 SPLs and pressure traces (at $x/L = 0.05$, $x/L = 0.55$ and $x/L = 0.95$) along the cavity floor for the 2D, L/D=5 cavity using the SST turbulence model with steady jet blowing applied at the front wall for an exit jet Mach of 0.1 and 0.2. Front wall jet: $x_j/L = 0$, $y_j/L = -0.02$, $w_j/L = 0.02$. Blowing co-efficient (C_μ) varied from 0.01 to 0.02. 234

A.21 Band-limited SPLs along the cavity floor for the 2D, L/D=5 cavity using the SST turbulence model with steady jet blowing applied at the front wall with an exit jet Mach of 0.1 and 0.2. Front wall jet: $x_j/L = 0$, $y_j/L = -0.02$, $w_j/L = 0.02$. Blowing co-efficient (C_μ) varied from 0.01 to 0.02. 236

A.22 Time-averaged Mach number contours with streamlines inside the 2D, L/D=5 cavity using the SST turbulence model with steady jet blowing applied at front wall wfor exit jet Mach numbers of 0.1 and 0.2. Front wall jet: $x_j/L = 0$, $y_j/L = -0.02$, $w_j/L = 0.02$. Blowing co-efficient (C_μ) varied from 0.01 to 0.02. 237

List of Tables

1.1 Developments in experimental studies of weapon bay cavity flows (continued). . . . 32
1.2 Developments in experimental studies of weapon bay cavity flows (concluded). . . . 33
1.3 Developments in analytical studies of weapon bay cavity flows (continued). 34
1.4 Developments in analytical studies of weapon bay cavity flows (concluded). 35
1.5 Developments in numerical studies of weapon bay cavity flows— URANS method. . . . 36
1.6 Developments in numerical studies of weapon bay cavity flows— DNS, LES, Hybrid RANS/LES and other numerical methods. (In last column, number of points in the cavity given as percentage of total amount in parenthesis, where available. For more than one calculation, only the maximum number of points are given.) . . . 37
1.7 Developments in flow control studies of weapon bay cavity flows — Passive control methods. . . . 38
1.8 Developments in flow control studies of weapon bay cavity flows — Active (open-loop and closed-loop) control methods. . . . 39

2.1 Closure coefficients for the Spalart-Allmaras model . . . 49
2.2 Different types of two-equation turbulence models and the corresponding second variable used . . . 50
2.3 Different types of linear $k-\omega$ turbulence models . . . 51
2.4 Values of constants used in linear $k-\omega$ models (continued) . . . 52
2.5 Values of constants used in linear $k-\omega$ models (concluded) . . . 52

4.1 Information about the grids of different densities used for the 2D clean cavity with L/D=5. . . . 71

5.1 Information on grids used for the 3D, L/D=5, clean cavity in the doors-off and the doors-on at 90° configurations. . . . 111
5.2 Comparisons of (approximate) frequencies and their amplitudes predicted between LES, DES, URANS (Menter's Baseline $k-\omega$) for the doors-off clean cavity (at the cavity rear i.e. at $x/L=0.95$), Rossiter's semi-empirical formula [3] and experiment. . . . 116
5.3 Comparisons of (approximate) frequencies and their amplitudes predicted between LES (Smagorinsky SGS for medium grid), DES (Spalart-Allmaras for fine grid), URANS (Baseline $k-\omega$ for coarse grid) for the doors-on clean cavity (at $x/L=0.95$), Rossiter's semi-empirical formula [3] and experiment. 127
5.4 URANS, DES and LES calculation details. . . . 139

6.1 Information about the 2D cavity grids with L/D ratios of 2, 10 and 16. 143
6.2 The range of applicability of the URANS method for transonic, turbulent cavity flows ($M_\infty = 0.85$, $\mathrm{Re}_L = 6.783 \times 10^6$). 162

7.1 Information about the grids used for the 2D, L/D=5, clean cavity control study. 167

8.1 Information on grids used for the missile (without fins) placed at the shear layer plane of the L/D=5, W/D=1 cavity in the doors-off configuration. 175

A.1 Information about the grids used for the 2D, L/D=5, clean cavity control study. 192
A.2 Jet exit conditions for the front wall jet. Values calculated using total reservoir pressure and temperature of 2 atmospheres and 298 K respectively. The jet slot width, w_j, was kept fixed at 0.02L. 232

Nomenclature

Symbols	Definition
α	Rossiter's formula constant
$\frac{D}{Dt}$	Lagrangian derivative
κ_v	Rossiter's formula constant
$\mathbf{F}$	Flux vector in the x-direction
$\mathbf{G}$	Flux vector in the y-direction
$\mathbf{H}$	Flux vector in the z-direction
$\mathbf{W}$	Vector of conserved variables
$\arg_1$,$\arg_2$	Arguments to blending functions F_1 and F_2
Re_δ	Reynolds Number Based on Boundary Layer Thickness
Re_θ	Reynolds Number Based on Boundary Layer Momentum Thickness
a,b	Arbitrary parameters
$B()$	Notation for blending function
C_μ	Closure coefficient for one-equation models
C_μ	$k-\varepsilon$ model coefficient
C_p	Pressure coefficient
C_s	Smagorinsky constant
C_{DES}	DES constant
D	Cavity depth
d	Distance to wall
d_t	Distance from the field point to the trip for the Spalart-Allmaras model
dB	Decibels
dt	CFD time-step

E	Total energy of fluid
e	Specific internal energy
F_1,F_2	Blending functions used in the Baseline $k-\omega$ and SST models
f_i	Body force vector
F_{ij}	Favre-averaged viscous flux
G	Grid filtering function
G_{ij}	Favre-averaged stress tensor
J	Jacobian
k	Heat transfer coefficient
k	Specific turbulent kinetic energy
k_v	Turbulent kinetic energy at the top of the viscous sublayer
L	Cavity length
L/θ	Cavity Length-to-Boundary Layer Momentum Thickness Ratio
LE	Leading-edge
M	Mach number
m	Rossiter mode number; an integer
N	Number of samples/measurements
p	Pressure
P_ω	Dissipation rate specific to k
Pr	Prandtl's number
Pr_t	Turbulent Prandtl number
q_i	(Favre-averaged) Heat flux vector
Q_i	Sub-grid heat flux vector
R_ω	Turbulent Reynolds number for $k-\omega$ model
R_t	Turbulent Reynolds number for $k-\varepsilon$ model
Re	Reynolds number, $R_e = \frac{UL}{\nu}$
S	Vorticity magnitude
S_{ij}	Strain rate tensor of mean flow
T	Integration time
T	Temperature
t	Time

TE	Trailing-edge
u	Velocity in x-direction
U_∞	Free-stream velocity
u_τ	Frictional velocity
u_i	Velocity vector
u_{ijx}	X-component of the velocity vector at position i,j used in the Stochastic Estimation method
V	Volume
v	Velocity in y-direction
W	Cavity width
w	Velocity in z-direction
x,y,z	X-, y- and z- coordinates
x_i	Position vector
y	Distance
y_n	Distance to the nearest wall
$\mathcal{V}_{i,j,k}$	Cell volume
$R_{i,j,k}$	Flux residual
$c_{b1},c_{b2},c_{v1},c_{w2},c_{w3},$ $c_{t1},c_{t2},c_{t3},c_{t4}$	Constants for the Spalart-Allmaras model
$f_{v1},f_{v2},f_w,g,r,f_{t2},f_{t1},$ g_t,χ,c_{w1}	Spalart-Allmaras model functions
L/D	Cavity Length-to-Depth Ratio
L/W	Cavity Length-to-Width Ratio
W/D	Cavity Width-to-Depth Ratio

Greek Symbols Definition

δU	Difference between velocity at the field point and at the trip
δx	Grid spacing along the wall at the trip
Δ	Metric of grid size
δ	Cell height
δ_{ij}	Kronecker delta
μ	Molecular viscosity

μ_t	Dynamic eddy viscosity
ν	Kinematic molecular viscosity
ω_t	Wall vorticity at the trip
$\overline{\phi}$	Mean part of a quantity
ϕ	Arbitrary flow quantity
ρ	Density
σ	Turbulent Prandtl number
τ_w	Dynamic wall shear stress
τ_w	Wall shear stress
τ_{ij}	Sub-grid stress tensor
τ_{ij}	Viscous stress tensor
$\tilde{\nu}$	Working variable
ε	Dissipation rate of k per unit mass of fluid
$alpha^*, \beta^*, \alpha, \beta, \sigma_k, \sigma_\omega, S_l$	Model coefficients for $k-\omega$ model

Acronyms	**Definition**
ADI	Alternating Direction Implicit
B-L	Baldwin-Lomax Turbulence Model
BILU	Block Incomplete Lower-Upper decomposition
C-S	Cebeci-Smith Turbulence Model
CAA	Computational AeroAcoustics
CFD	Computational Fluid Dynamics
CSAR	Computer Services for Academic Research
DES	Detached Eddy Simulation
DES-SA	Detached-Eddy Simulation (with one-equation Spalart-Allmaras model)
DNC	Direct Numerical Computation
DNS	Direct Numerical Simulation
DRP	Dispersion-Relation-Preserving
DS	Direct Simulation
DSM	Dynamic Smagorinsky Sub-Grid Scale Model

DVM	Discrete Vortex Method
FFT	Fast Fourier Transform
FT	Fourier Transform
GCG	Generalised Conjugate Gradient
HWA	Hot-Wire Anemometry
LBM	Lattice-Boltzmann Method
LDA	Laser Doppler Anemometry
LDV	Laser Doppler Velocimetry
LES	Large-Eddy Simulation
LSE	Linear Stochastic Estimation
MILES	Monotone-Integrated Large-Eddy Simulation
MM	Mixed Sub-Grid Scale Model
MPI	Message Passing Interface
MUSCL	Monotone-Upwind Spatial
PDE	Partial Differential Equations
PIV	Particle Image Velocimetry
PMB	Parallel Multi-Block
POD	Proper Orthogonal Decomposition
PSD	Power Spectral Density
QSE	Quadratic Stochastic Estimation
RANS	Reynolds-Averaged Navier-Stokes
RHS	Right-Hand Side
RMS	Root Mean Square
S-A	Spalart-Allmaras Turbulence Model
SE	Stochastic Estimation
SGS	Sub-Grid Scale model
SM	Standard Smagorinsky Sub-Grid Scale Model
SMM	Selective Mixed Sub-Grid Scale Model
SPL	Sound Pressure Level
SST	Shear Stress Transport
UCAV	Uninhabited Combat Aerial Vehicles

URANS	Unsteady Reynolds-Averaged Navier-Stokes
WEM	Wave Extrapolation Method

Subscripts	Definition
τ	Frictional component
av	Cell-averaged
b	Basic
i	Index i=1,2,3...
i	Inviscid component
j	Index j=1,2,3...
k	Index k=1,2,3...
n	Current time-step
n	Nearest
$n+1$	Next time-step
sg	Sub-grid part
t	Trip
t	Turbulent
v	Viscous component
w	Wall

Superscripts	Definition
$'$	Fluctuating part
$+$	Non-dimensionalised wall distance
∞	Free-stream
R	Reynolds stress

Chapter 1

Introduction

1.1 Motivation

Weapon bays have been used in aircraft since the late 1940s and 1950s and they provide many advantages. For the aircraft of that time, for instance, weapon bays provided the advantage of reducing the aircraft drag. As the physics of supersonic flight began to be better understood and planes began to fly faster, weapon bays were again exploited as they enhanced the manœuvrability of the aircraft and also reduced the aerodynamic heating experienced by a store. In the recent years, stealth has become an important concern in the design of aircraft and this will remain a critical design criterion for future aircraft such as Uninhabited Combat Aerial Vehicles (UCAVs). In these circumstances, housing the stores inside the aircraft has the evident advantage of reducing its radar cross-section.

There are however many problems associated with weapon bay flows and these typically arise when the bomb bay doors are opened to release the store. In cavities of low aspect ratio, for instance, the noise inside the cavity has been found to approach 170 dB [7, 8]. This has serious implications on the safety of the store or other sensitive equipment that may be housed inside the cavity. On the other hand, cavities with higher aspect ratio exert large pitching moments on stores causing potentially catastrophic situations. In fact, in some cases, the store has been observed to pitch-up nose-into-the-cavity and collide with other stores in the process.

Cavity flow aerodynamics is also important for many other problems. Undercarriage bays and sunroofs in the automobile industry are also important examples of cavity flows where mitigation of the noise levels is of great significance. Other applications of cavity flows involve supersonic combustion (e.g. flameholders) and there are many other instances of cavity flows in gas turbines and even urban studies, where the ventilation and pollution dispersion characteristics of cavity flows are of interest. The need to understand cavity flow physics is therefore not just confined to weapon bays but is of relevance to multiple disciplines.

One other motivation for the study of cavity flows is to ascertain the role of turbulence in driving these flows. Weapon bay flows, for instance, are usually associated with high Reynolds number flows where the flow is very much in the turbulent regime. In such circumstances, a broad range of turbulent length scales are likely to exist making the role

of turbulence a significant one but one that has not really been addressed in previous works. In doing so, a better understanding of the physical mechanisms of cavity flows can be obtained, which will then enable development of future control strategies to alleviate the harsh aeroacoustic and turbulent cavity environment.

1.2 Objectives

The main objective of this project is to perform numerical analysis of cavity flows via Computational Fluid Dynamics (CFD) with the aim of better understanding the physics of cavity flows especially from the perspective of understanding the role turbulence has to play in driving the flow mechanisms. Most research conducted on cavity flows thus far has focused on the use of linear statistical turbulence models in conjunction with the Unsteady Reynolds-Averaging Navier-Stokes (URANS) approach. Extensive development of turbulence modelling has enabled more versatility and success in predicting a large number of flows in different applications. Although some degree of success has been reported, this has been documented predominantly for supersonic cavity flows. Transonic cavity flows have received little attention but some recent work [9, 10] revealed that CFD results are sensitive to the treatment of turbulence. These studies demonstrated that turbulence models provided inconsistent results in transonic cavity flow problems making it difficult to obtain an accurate picture of the physical mechanisms driving the flow. The project therefore endeavours to explain why turbulence models fail to give accurate and consistent solutions for transonic cavity flows.

Use of simulation techniques such as Large-Eddy Simulation (LES), which rely less on modelling the flow and more on explicitly resolving it, is at the core of this project. LES resolves most of the spatial and temporal scales encountered in a flow making it more attractive and better suited to highly unsteady and turbulent flows like cavity flows. LES is however still expensive when resolving the near-wall properties so alternative methods have looked at using hybrids of URANS and LES to alleviate this problem. Detached-Eddy Simulation (DES) is one such example and for high Reynolds flows should have potential for cavity flows.

The aim is to enhance the knowledge of using all these approaches (URANS, LES and DES) by applying them initially to standard cavity test cases. Numerical analysis of these standard test cases should then provide useful insights into the best options for simulating cavities as well as highlighting the important physical mechanisms involved with cavity flows, including the role of turbulence. The latter point will provide essential input into future flow control efforts into improving the aerodynamic and aeroacoustic environment within weapon bays.

Cavities with a length-to-depth ratio (L/D) of 5 are used as the benchmark test case as this has been extensively studied experimentally by Ross [7, 8, 11–13] at DERA. Designated as the M219 cavity, experimental data for this 3D cavity (where the width-to-depth (W/D) ratio is 1) in both doors-on and doors-off configurations, details of which are provided in Chapter 3, corresponded to a free-stream Mach number of 0.85 and a Reynolds number of 6.783 million based on the cavity length. At these flow conditions, the flow inside the cavity is extremely unsteady and turbulent and therefore extremely challenging for turbulence models.

1.3 Types of Cavity Flows

Cavity flows can be described in many ways. One method looks to describe them using a combination of backward-facing and forward-facing steps with the flow occurring between the cavity dependent on the distance between the two steps and the dimensions of the steps as well as other flow conditions. Perhaps the most common way of categorising cavity flows is however directly based on the flow characteristics that occur in the cavity. In this case, different notations have been used by different researchers. One method describes the flow in the cavity into one of three categories: **fluid-dynamic**, **fluid-resonant** or **fluid-elastic** and was introduced by Rockwell and Naudascher [14]. Another description involves classifying the cavity as one of the following: **open**, **closed** or **transitional**. Which flow is triggered in the cavity is strongly dependent on the cavity L/D ratio, free-stream Mach number and oncoming boundary layer thickness. The terminology of closed and open flow cavities was first introduced by Rossiter [3] and Charwat *et al.* [15], as mentioned previously. One possible hypothesis connects the origin of this notation to the engineering example of a heat engine with a closed cycle, although the exact etymological root is unknown. In this thesis, the latter terminology will be used to describe the cavity.

Open flow usually occurs for deep cavities while the closed flow type occurs for shallow cavities. Defining the boundary between deep and shallow cavities is however not easy. Early investigations in cavity flows [3, 14–16], for instance, defined deep cavities as having $L/D \leq 1$ and shallow cavities as having $L/D > 1$. This was convenient as it also segregated the different modes of acoustic resonance into separate categories. For deep cavities with $L/D \leq 1$, for instance, the acoustic modes in the transverse cavity direction were excited while those in the longitudinal direction were excited for shallow cavities with $L/D > 1$. Since then, different values of L/D ratios were given by researchers to mark the boundaries of deep and closed cavities. The reason for this was realised to be the sensitivity of the type of flow that is generated in the cavity to the free-stream Mach number. Recently, however, especially with the realisation of transitional cavity flow types, more defined limits between deep and shallow cavities have been described. Plentovich *et al.* (1992) [17] defined the open cavity for $L/D \leq 6-8$, transitional for $7 \leq L/D \leq 14$ and closed for $L/D \geq 9-15$. The broad ranges considered accounted for the dependence of the shear layer deflection to the Mach number.

1.3.1 Open Cavity Flows

Open flow occurs for deep cavities (defined to exist for cavities with L/D ratio $\leq$ 10), as found in bays typical of the F-111 aircraft. In this situation, the flow separates at the cavity lip and a shear layer forms across the cavity opening (Figure 1.1). This shear layer impinges on the cavity downstream wall generating acoustical disturbances that propagate upstream as pressure waves (Figure 1.1(a)). On approaching the front cavity wall, these pressure waves further disturb the shear layer, which produces more vortical structures that then enter the cavity and convect downstream. In this manner, a self-sustained pressure oscillation flow cycle persists in the open cavity. The flow in the open, deep cavity tends to be extremely unsteady and turbulent. Coupling between the shear layer, vortical structures, acoustics and turbulence makes it difficult to ascertain what really drives the flow. Flow unsteadiness and the strength of coupling is found to increase

at transonic speeds. In the supersonic flow regime, expansion waves at the cavity lip and compression waves at the cavity trailing-edge (Figure 1.1(b)) also form. Gharib and Roshko [18] also described the open cavity flow as the **shear layer mode**.

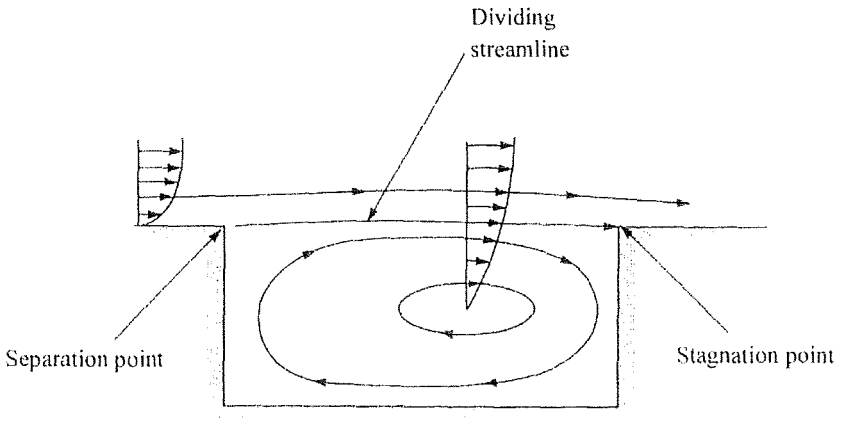

(a) Subsonic Speeds

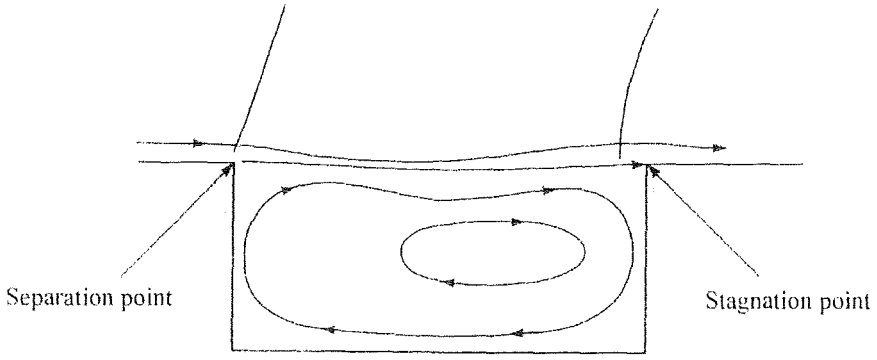

(b) Supersonic Speeds

Figure 1.1: A schematic of the flow-field in the open cavity at subsonic and supersonic speeds. Extracted from the ESDU data sheet [1].

Shear layer deflection can be quite pronounced in the open cavity due to the unsteadiness in the flow. The flapping motion of the shear layer allows mass to enter and leave the cavity and this is responsible for the generation of high noise levels and frequencies in the open cavity. Noise levels as high as 170-180 dB have been observed at the rear of the open cavity. These can cause vibrations in the surrounding structure, including the store or perhaps sensitive avionics equipment, and could cause premature structural fatigue.

In open cavity flow (or in shear layer mode), the flow is nearly parallel and so can alternatively be defined in terms of the notion of absolute or convective instability. The flow is defined as being **convectively unstable** if the energy from the disturbance grows in time but travels only downstream. In this situation, self-sustained oscillations cannot happen since the oscillations would merely convect away if the disturbance is removed. In contrast, if the energy from the disturbance grows and travels upstream, self-excitation is possible and the flow is said to be **absolutely unstable**. Flows that exhibit self-sustained oscillations are then called **globally unstable**. In the shear layer mode, the Kelvin-Helmholtz

instability develops into a global instability via pressure feedback from acoustic waves generated from the cavity trailing-edge.

1.3.2 Closed Cavity Flows

When the cavity L/D ratio is increased, the shear layer has less energy and momentum to span across the cavity opening and ends up dipping into it. When the cavity L/D ratio is sufficiently large, as is the case for closed (shallow) cavities, which occur for $L/D \geq 13$ and are typical of the bomb bays in the B1 bomber, the shear layer actually re-attaches at some point on the cavity floor before separating again on approach to the cavity rear bulkhead (Figure 1.2(a)). A region of low pressure forms at the cavity front and a region of high pressure at the cavity rear. The drag coefficients and transfer properties are also typically higher than in open cavities [19]. Charwat *et al.* [15] alternatively referred the separated region ahead of the reattachment point as a **separation wake** and the separated region behind the reattachment point as a **recompression wake**.

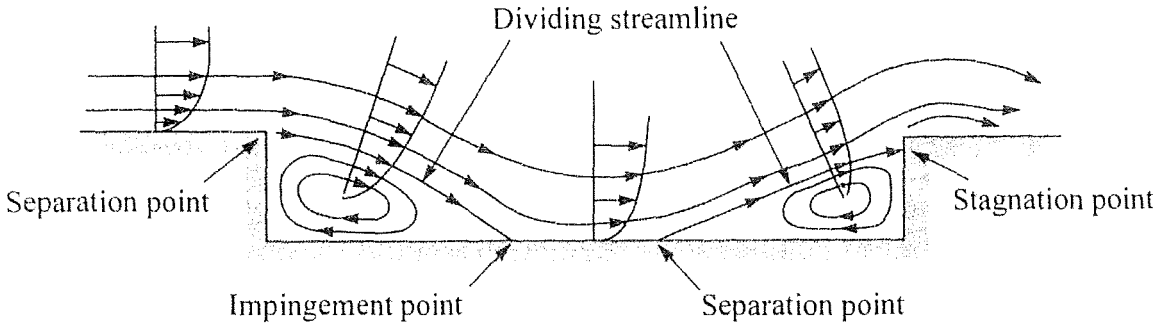

(a) Subsonic Speeds

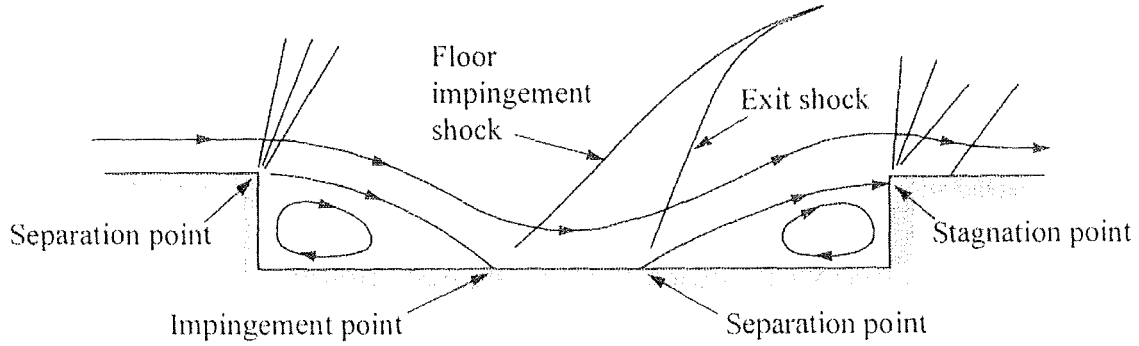

(b) Supersonic Speeds

Figure 1.2: A schematic of the flow-field in the closed cavity at subsonic and supersonic speeds. Extracted from the ESDU data sheet [1].

For supersonic speeds, expansion and compression waves still form at the cavity leading- and trailing-edges as for the open cavity (Figure 1.2(b)). In addition, impingement shocks

form where the shear layer re-attaches at the cavity floor and exit shocks form where the shear layer changes angle and re-separates due to the adverse pressure gradient at the cavity rear. Shear layer deflection is less significant for the closed cavity resulting in lower frequencies being dominant and noise levels somewhat lower than open cavities. This is more beneficial for the safety of equipment that may be stored in the cavity.

Under certain conditions, a variant of closed cavity flow exists. The two recirculation regions existing for the closed cavity and the reattachment point is still observed but the flow is more unsteady and violent. Large-scale vortical shedding from the cavity leading-edge now prevails and the size of the shed vortex typically equals or exceeds the cavity dimensions. The shedding at the cavity front is combined with violent ejection of fluid at the cavity trailing-edge where the large vortex interacts with the downstream cavity wall. The large-scale nature of the vortical structures in this flow causes massive separation upstream of the cavity lip as well as in the boundary layer downstream of the cavity as the vortex convects away. Gharib and Roshko [18] termed this type of flow as the **wake mode** due to its resemblance to a bluff body wake. This cavity flow mode has however only been associated with low Reynolds number flows where the state of the upstream boundary layer is laminar. At higher Reynolds and Mach numbers, this mode has not been observed in experiments and is likely that the wake mode will become the closed cavity mode for higher Reynolds numbers if the cavity L/D ratio is large enough.

1.3.3 Transitional Cavity Flows

Such cavity flow types occur where the cavity L/D ratio falls between the boundaries of open and closed cavity types, i.e. $10 \leq L/D \leq 13$. For supersonic speeds, this transitional region is further segregated into the transitional-open and transitional-closed flow types [1]. A description of these intermediate stages is given as follows.

Starting from a closed cavity flow configuration at supersonic speeds, if the length is gradually reduced, the impingement and exit shocks begin to move closer together. At some L/D ratio, these shocks will merge signifying a decrease in the proportion of the shear laying touching the cavity floor. At this point, the flow is regarded as being **transitional-closed** (Figure 1.3(b)). If the cavity length is decreased further still, the shear layer will begin to detach from the cavity floor. There will then be some L/D ratio at which the shear layer detaches completely from the floor and a transfer of flow from the higher-pressure region at the rear of the cavity to the lower-pressure region at the front begins to occur. This change in flow-field is also marked by the replacement of the single shock wave with a series of expansion and compression waves (Figure 1.3(a)). At this stage, the flow is said to be **transitional-open**. For subsonic speeds, this region between open and cavity flows is collectively referred to as **transitional flow** and characteristics from a combination of transitional-open or transitional-closed cavities in supersonic speeds may dominate. Note that further reductions in the cavity length would result in the flow reverting to the open cavity flow configuration.

The effect of the flow type and hence the L/D ratio for a given Mach number on the pressure distribution along the cavity floor is illustrated in Figure 1.4, which is extracted from the ESDU data sheet [1]. At supersonic speeds, four cavity flow types exist while only three are defined at subsonic speeds. The effect of the shock appears to have the strongest influence on the extent of the transitional flow region causing dramatic changes in the flow, which now exhibits patterns not observed at subsonic speeds [1].

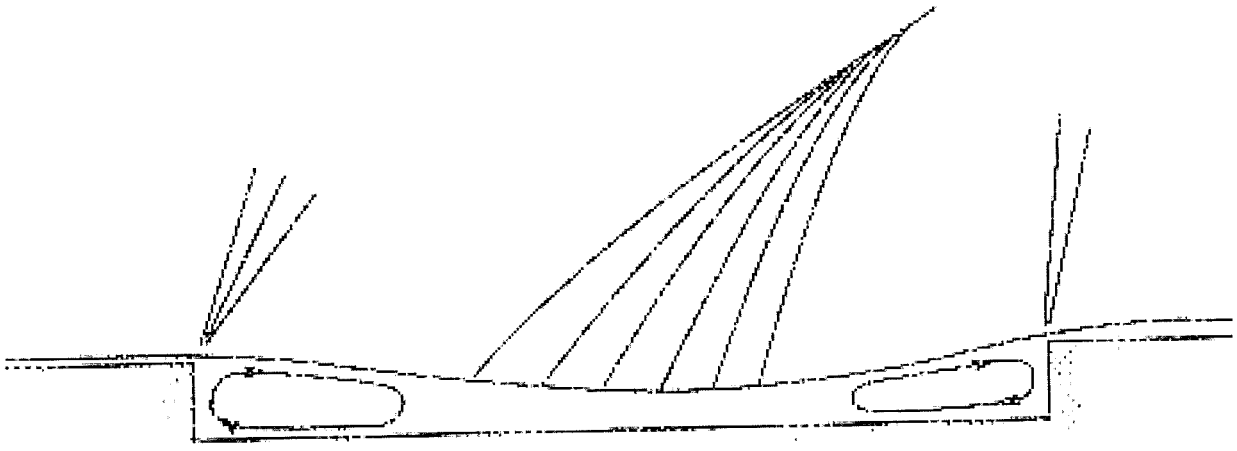

(a) Transitional-Open Cavity Flow

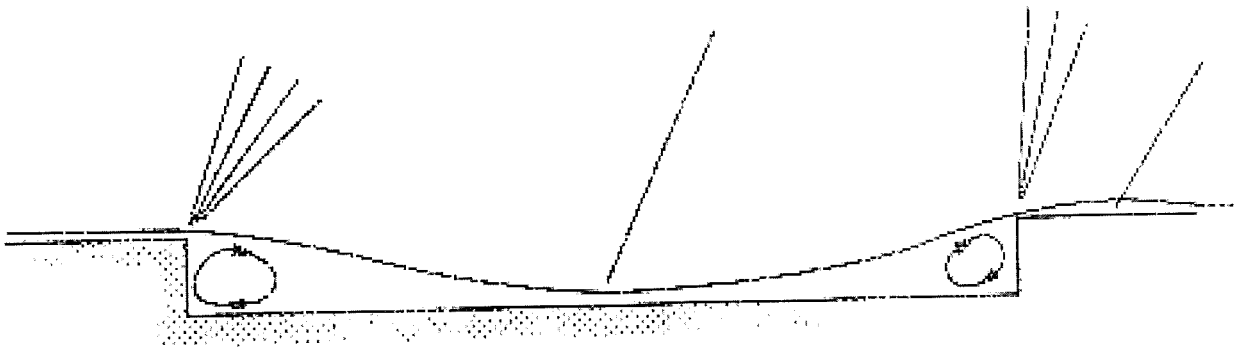

(b) Transitional-Closed Cavity Flow

Figure 1.3: A schematic of the flow-field in a transitional-open and transitional-closed cavity at supersonic speeds. Extracted from the ESDU data sheet [1].

In this figure it can be observed that despite the complex nature of the open cavity flow, the longitudinal static pressure distribution (C_p) is typically uniform for most of the cavity length except a rise toward the cavity rear (depicted as (a) in Figure 1.4(a)). This is desirable from a store separation perspective as it provides a favourable pressure gradient (with low pitching moments) resulting in a good store release. As the L/D ratio is increased, a change in sign is observed in the C_p distribution ((b)-(d) in Figure 1.4(a)). For the closed cavity, large variations in the C_p distribution are observed due to the differential pressure caused by the lower and higher pressure regions at the cavity front and rear, respectively. From a store separation perspective, the closed cavity configuration should be avoided. Large pitching moments are exerted on the store and in some cases it has been observed that the store pitches back into the cavity.

1.3.4 Backward- and Forward-Facing Steps

The cavity flow phenomenon can also be conveniently addressed as flow over a backward-facing step proceeded by flow over a forward-facing step. The backward-facing step comprises a region of separation and expansion at its corner followed by reattachment at the

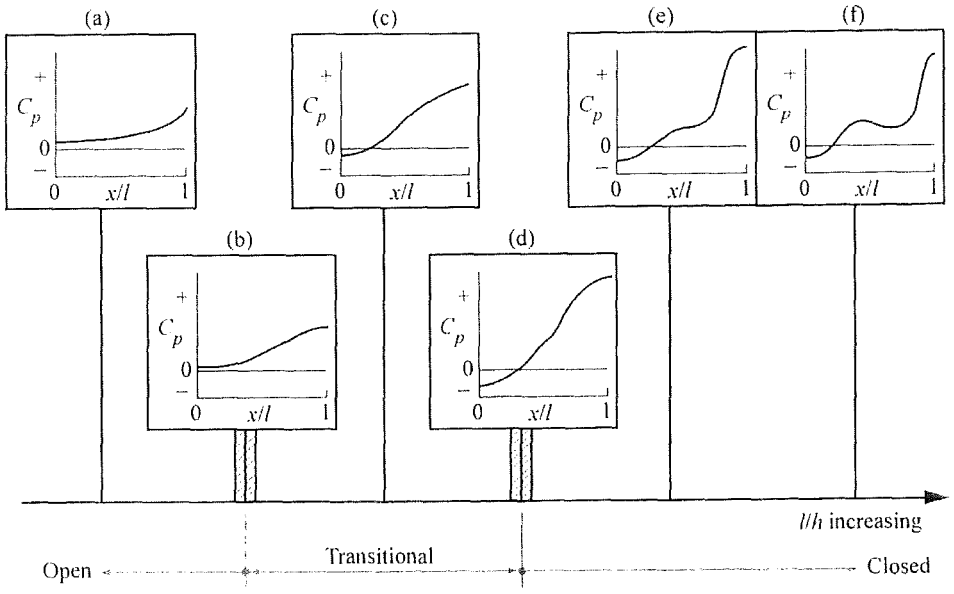

(a) Subsonic Speeds

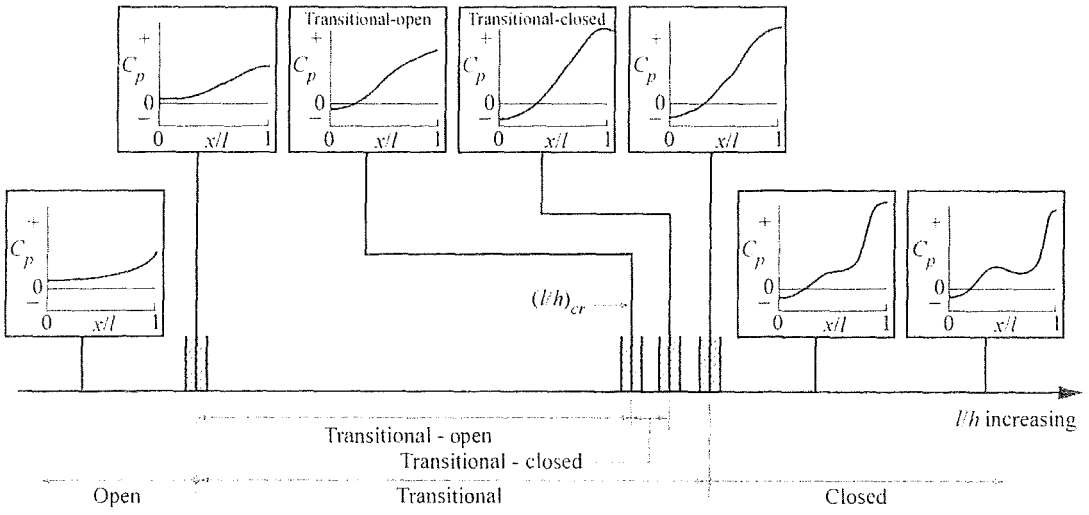

(b) Supersonic Speeds

Figure 1.4: Typical C_p distributions in the cavity with increasing L/D ratio at subsonic and supersonic speeds. Extracted from the ESDU data sheet [1].

floor and a recovery region as indicated in Figure 1.5(a). In contrast, the forward-facing step contains a region of separation and compression at its corner followed by large separation downstream of the corner (Figure 1.5(b)). Taborda *et al.* [2] highlighted that the reattachment point after the backward-facing step occurs approximately after the midpoint of the cavity length, more specifically between the normalised streamwise positions (delineated as the ratio of the distance from the cavity leading edge to the cavity length, x/L) of 0.6 and 0.9. If the forward-facing step is located before this reattachment point, an open cavity forms, otherwise a closed cavity is generated. Transitional cavity types are therefore generated where the reattachment points lie anywhere between 0.6 and 0.9 [2].

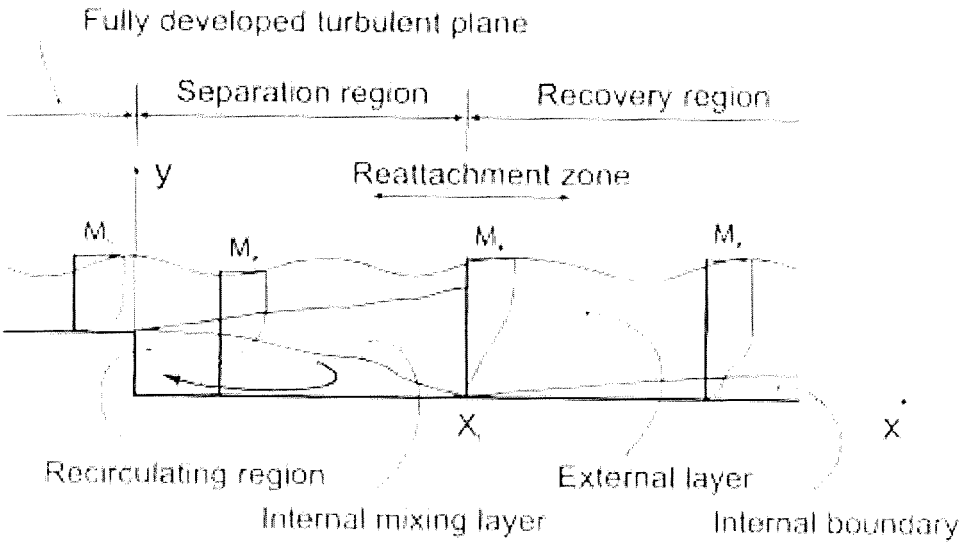

(a) Backward-Facing Step

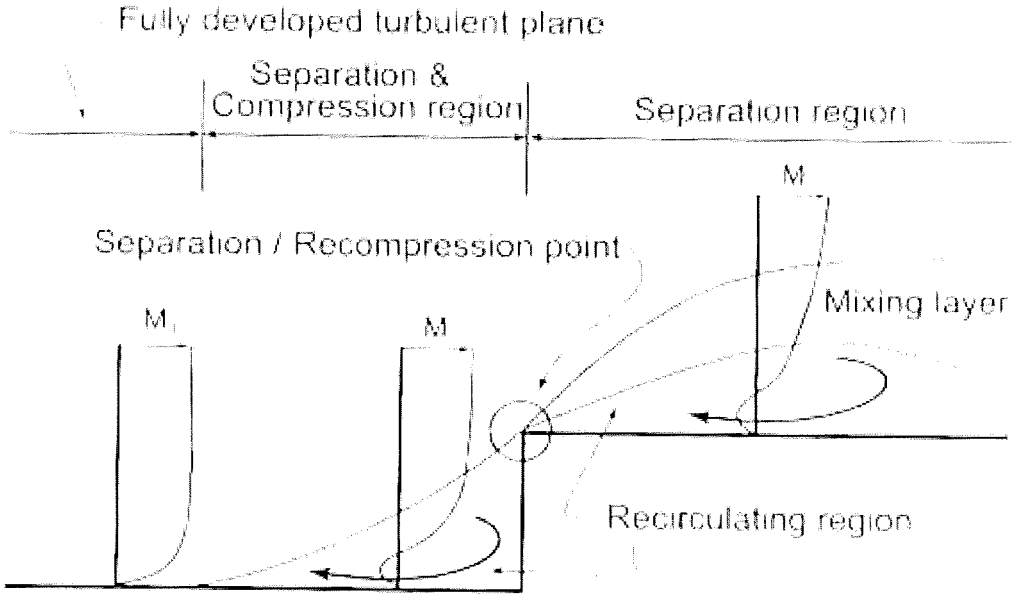

(b) Forward-Facing Step

Figure 1.5: A schematic of the flow-field in backward-facing and forward-facing steps. Reproduced from Taborda *et al.* [2].

This issue of the cavity flow being represented as flow down and then up a step was also addressed by Rossiter [3].

1.3.5 Fluid-Dynamic, Fluid-Resonant and Fluid-Elastic Cavity Flows

In 1978, Rockwell and Naudascher [14] categorised the flow of a fluid over a cavity into three groups: **fluid-dynamic**, **fluid-resonant** and **fluid-elastic**. In the fluid-dynamic cavity, oscillations are driven by the instabilities in the shear layer and vortex shedding, with a strong coupling between the shear layer and flow inside the cavity. No acoustic modes are involved and neither high Mach numbers nor compressibility effects are required [20]. Oscillating flows at low speeds over shallow cavities typically fall in this category. Rockwell and Naudascher compare the fluid-dynamic cavity to the jet-edge type oscillation where the jet impinges on the edge. They further highlight that the Reynolds number, ratio of boundary layer thickness to the cavity length (δ/l), ratio of boundary layer momentum thickness to cavity length (θ/L) as well as the L/D ratio are all important physical parameters in fluid-dynamic cavities.

For the fluid-resonant cavity, oscillations are governed by compressibility effects or free-surface wave phenomena (e.g. standing waves). Self-sustained oscillations which are strongly coupled with resonant wave effects can be classified as fluid-resonant. The acoustic wavelength in this case is of the same order or smaller than the characteristic length, L. In flow-resonant cavities, the resulting wave motion occurs in the transverse direction for deep cavities ($L/D \leq 1$) whereas it occurs in the longitudinal direction for shallow cavities ($L/D > 1$). Important parameters in fluid-resonant cavities are similar to those stated above for fluid-dynamic cavities.

In the fluid-elastic cavity, oscillations in the flow are coupled with the motion of the solid boundary. In this case, the shear layer perturbations are excited if one or more of the cavity walls undergo large displacements. Amplification of the perturbed shear layer flow in the fluid-elastic cavity is enhanced through a resonance-type process. This type of cavity flow is complicated especially for an analytical description to be made due to the interaction of structural and fluid dynamics. Inertia, elastic and damping characteristics of the structure are all important physical parameters in fluid-elastic cavities. Komerath *et al.* [20] mentions loudspeakers used to drive cavity flow oscillations as an example of fluid-elastic cavities.

In some cases, it can be difficult to isolate which fluid flow type presides, as they may all co-exist. With reference to the rectangular L/D=5 cavity investigated in this project, the cavity is representative of both fluid-dynamic and fluid-resonant cavity oscillations.

1.4 A Literature Review on Cavity Flows

For about half a century, research studies have been conducted in an attempt to better understand cavity flows. Their complexity typically derive from the strong coupling with a multitude of processes occurring simultaneously. For instance, boundary layer separation, shear layer instability, vortical flow, acoustic radiation and even shock/expansion wave interaction in supersonic flows are all key processes in cavity flows. All are closely

correlated with the other making it difficult to identify the exact nature and source of cavity flow mechanisms. Such intricate flow phenomena in cavities can modify the acoustic and convective heat transfer environments and further complicate the computation of reliable and accurate measurements. Combined with an increase in total drag and the generation of flow-induced oscillations (albeit in specific configurations), which in turn affects the stability of the aircraft and the contents of the cavity, such undesirable flow features of cavities emphasise why the need to comprehend the physics of such flows has held such research significance for so long.

By definition, any region of separation, groove or cut-out can be regarded as a cavity. Examples of systems being modelled as single or a series of cavities can be found in many engineering disciplines including experimental fluid mechanics, vehicle aerodynamics, industrial aerodynamics and gas dynamics amongst others. Slotted wind tunnels are common examples pertinent to experimental fluid mechanics where the unsteadiness caused by the cavity can affect the quality of test results [21, 22]. Open windows, sunroofs and doors are important cavity flow examples in the automobile industry where the elimination of noise generated by the movement of flow of air over the open cavity offers a commercial advantage from the perspective of producing a more comfortable and environmentally-friendly vehicle. Ricot *et al.* [23], for example, analysed the coupling between vortex shedding over the automotive sunroof and acoustic resonance of the passenger compartment in generating large noise levels from self-sustained flow oscillations. Industrial aerodynamics investigations of urban street canyons represented by models of cavities have been thoroughly investigated with a view to comprehending and controlling the ventilation [24] and pollution dispersion qualities [25, 26] in cities. Slots in fluid measuring instruments have also been explored in gas dynamics applications where understanding the influence of vortical structures created inside cavities on the accuracy of measurements by the instrument [27] has held some interest. An elaborate list of other examples of cavity flows is provided by Komerath *et al.* [20].

The majority of research performed on cavity flows has however focused on cavities found in aerospace-related applications such as weapon bays, open cockpits, under-carriage wheel wells, aerodynamic windows, turbomachinery and propulsion. Other less common examples include in-flight refuelling ports and pressure vents in the space shuttle's cargo bay [28]. Effects of compressor aerodynamics due to the shrouded stator and rotating cavities found in gas turbines are typical examples of turbomachinery applications of cavity flows [29, 30]. Propulsion analyses in cavity flow research have been emerging more recently since the introduction of cavity-based flameholders where studies are devoted to fuel injection and flameholding problems in high-speed engine designs such as scramjets and ramjets [31–34]. From the perspective of aerodynamic windows, research has been undertaken into analysing the optical distortion effects caused by the unsteady flow-field in the cavity [35, 36].

Under-carriage wheel wells have also received some attention from the point of view of cavity noise over the past years [4, 37]. Wheel bays are considered the primary source of noise because of landing gear deployment during the landing approach and touchdown. In fact, during the landing phase, the airframe noise may well exceed the engine noise. Airframe noise, in turn, is the main constituent of passenger cabin noise as the noise is either radiated through the air to the cabin wall or is propagated as vibrations through the structure. This excessive noise therefore poses a threat in disturbing the surrounding populated area and has fuelled some research into finding ways to alleviate this problem and simultaneously meet the future generation aerospace technology standards, which

include a reduction in the noise pollution level associated with the increasing air traffic [38].

However, within aerospace applications, the bulk of cavity flow research has been dominated by the studies of weapon bays of manned combat aircraft such as the F-111 (shown in Figure 1.6(a)). With Uninhabited Combat Aerial Vehicles (UCAVs) such as the X-45 (shown in Figure 1.6(b)) also likely to exploit weapon bays to enhance the stealth properties of the aircraft, weapon bay cavity flow research is likely to hold significant interest in the future. Since the mid 1950s, numerous experimental and numerical investigations have been performed toward improving the understanding of cavity flows, especially from the perspective of bomb bays. Some key developments in the experimental, theoretical

(a) Manned Combat Aircraft (F-111)

(b) UCAV (X-45)

Figure 1.6: Illustrations of the bomb bays in manned combat aircraft and Uninhabited Combat Aerial Vehicles (UCAVs).

and numerical studies of weapon bay cavity flows are presented in the following sections and are summarised later in Tables 1.1-1.2, 1.3-1.4, 1.5 and 1.6. A more comprehensive account of the prediction and experimental investigations before 1987 is provided by Komerath *et al.* [20] and after 1987 by Grace [39]. Shaw and Shimovetz [40], Colo-

nius [41] and Takeda and Shieh [42] also provide good reviews describing the different methods used for measuring and predicting cavity flows.

1.4.1 Experimental Studies

The first experimental works on cavity flows investigated the phenomenon only as a part of other major studies. Wieghardt (1942) [43] measured the drag coefficients on many surface irregularities, including cavities. In Wieghardt's studies, the drag coefficients for the cavity were obtained by subtracting the measured drag values of an aerodynamic surface with and without the cavity. With aluminium powder pictures of the flow in a water tank, Wieghardt also provided a first view of the flow-field inside the cavity and illustrated the existence of a single vortex or system of vortices. Tillman (1944) [44] then extended the work of Wieghardt to more surface irregularities and also performed further studies on circular and grooved cavities. His studies on grooved cavities were conducted over a wider range of L/D ratios and demonstrated that the values of drag coefficients varied depending on the L/D ratio. Tillman also noted that the maximum drag value varied with the ratio of the cavity length to the boundary thickness, δ. This is likely to be the first reference to the importance of the L/D ratio and the oncoming boundary layer thickness in cavities.

No further studies were performed to explain the drag variations or to obtain a greater understanding of the flow until the early 1950s when bomb bays of aircraft of that time exhibited signs of buffet [45, 46], which is described as the response of the aircraft to the unsteady pressure field in cavities. These highlighted the need for understanding weapon bay flows and instigated a trend of experiments devoted specifically to the investigation of cavity flows. Karamcheti [47, 48] and Roshko [49] in 1955 were among the first to investigate cavity flows, especially in relation to flow aeroacoustics. Karamcheti [47, 48] used schlieren, interferometry and Hot-Wire Anemometry (HWA) techniques to study the subsonic and supersonic flow past cavities cut into a flat plate. He found the acoustic field to be dependent on three parameters: cavity dimensions, type of oncoming boundary layer and free-stream Mach number. He also described that for deep cavities, the shear layer bridges the cavity opening and highlighted the existence of a minimum cavity length at which the shear layer no longer spans the cavity opening and therefore no longer impinges on the cavity's downstream wall thereby resulting in no acoustic resonance. This observation effectively forms the basis of flow control methods to suppress the harsh acoustic environment within cavities. Based on his analyses of the acoustic fields, he also postulated that the measured frequency (f) was inversely proportional to the cavity length (L), and can be expressed as

$$f = \alpha(M)\frac{1}{L} \tag{1.1}$$

where α was the constant of proportionality. It was a function of the free-stream Mach number and varied for laminar and turbulent flows. This was the first attempt to analytically calculate the frequencies and was a precursor to Rossiter's famous formula.

Roshko [49] presented pressure and velocity measurements of the flow in a rectangular cavity, where the cavity was represented by a slot in the floor of a wind tunnel. By performing experiments over a broad range of geometries and at different speeds (details of which are provided in Table 1.1), Roshko managed to provide the first insights of cavity flow mechanisms. He elucidated that the drag in the cavity was almost completely due to

the pressures exerted on the walls with friction playing a small role. He also demonstrated the differences in the flow for shallow and deep cavities and postulated that the formation of the vortex in the cavity is due to the deflection of the shear layer. For shallow cavities, for instance, he identified that the shear layer re-attached on the cavity floor, an observation that was important due to the need at that time for shallow cavities to accommodate longer missiles of smaller diameter. Since then, Roshko's observations for shallow cavities have been successfully validated by more recent studies. His schlieren experiments showed propagation of sound waves and highlighted that the downstream edge of the cavity is a source of significant noise for deep cavities.

The works of Karamcheti and Roshko then paved the way to a large volume of experimental studies over the next few decades. Tables 1.1 and 1.2 summarise some key developments over the years. In 1962, Plumblee *et al.* [50] conducted numerous wind tunnel investigations on cavities across a broad range of Mach numbers extending from the subsonic to the very high supersonic regime. He highlighted that the acoustic levels were more pronounced at the cavity rear and the cavity width had little effect on the acoustic levels. Plumblee *et al.* also mentioned that there existed a minimum Mach number below which cavity tones are not excited. According to their theory, Plumblee *et al.* concluded that the turbulent shear layer is the source of the broadband noise which drives the cavity oscillations and that the response of the cavity to the broadband noise is key to the amplification of certain narrowband tones. This was later refuted as experiments revealed that even the presence of laminar boundary layers at the point of separation at the mouth of the cavity produced louder tones despite the fact that broadband excitation was absent.

The most significant contribution towards the understanding of cavity flows was however provided by Rossiter *et al.* at the Royal Aircraft Establishment in the early 1960s. In the first of many technical reports, Rossiter re-addressed the problem of buffet in the armament bay of the T.S.R. 2 from 1960 [51, 52]. In 1962, Rossiter [3] (as well as Charwat *et al.* [15]) classified cavities as open, closed or intermediate and gave pictorial representations of the different flow-fields that developed in each case. Both Rossiter and Charwat suggested that the flow pattern occurring in and around the cavity depended strongly on the cavity L/D ratio and coined the term **critical L/D ratio**, which defines the L/D ratio at which the flow approximately changes from open to closed. Rossiter also provided significant theories on the differences between the flows in deep and shallow cavities, postulated that the possible cause of the acoustic tones were due to the instabilities in the shear layer that spans the open cavities, provided a preliminary analysis of the differences between 2D and 3D cavity flows and suggested that the critical L/D ratio was dependent on the oncoming boundary layer thickness, the aircraft's attitude and the presence of external bomb bay doors [3].

In 1962, Rossiter highlighted that bomb bay buffet was observed to occur more readily in bomb bays that had a L/D ratio close to the critical value. His findings suggested that the design of bomb bays near the critical L/D ratio should be avoided entirely because during certain manœuvres, for instance, the flow in the bomb bay may revert to an open flow type, which has the strongest pressure fluctuations [3]. Rossiter specifically looked at bomb bay buffet for the Canberra B7 (L/D=8) [53] and the T.S.R. 2 (L/D=7) [54] and realised that the pressure fluctuations are most intense in the vicinity of the rear bulkhead and on the ceiling of the bomb bay. He found that a significant reduction in the magnitudes of the fluctuations is achieved with increasing incidence of the aircraft and pointed out that the intensity of these pressure fluctuations decrease rapidly behind the bomb bay. Rossiter further applied statistical methods to analyse the random nature of the unsteady

pressure field and discovered that the disturbances travel along the roof of the bomb bay at approximately half the free-stream velocity [53].

From the extensive measurements on cavities over various dimensions for various Mach numbers, Rossiter further provided insights into the cavity flow acoustics mechanisms by analysis of the unsteady pressure field. His results revealed that the unsteady pressure field contained both random (broadband noise spectrum) and periodic (narrowband noise spectrum) components [55]. In shallow cavities, Rossiter identified the existence of a broad band of frequencies, predominantly originating from random pressure fluctuations. For deeper cavities, on the other hand, a series of periodic, discrete acoustic tones were also generated in conjunction with the broadband spectrum (Figure 1.7). These acoustic tones were attributed to acoustic resonance in the cavity and were excited by a phenomenon similar to that causing edge tones. For very deep cavities, Rossiter mentioned that noise was governed by the periodic acoustic tones with the random broadband component becoming less dominant. A Mach number increase was also observed to result in an increase in the magnitude of the periodic component [3, 55].

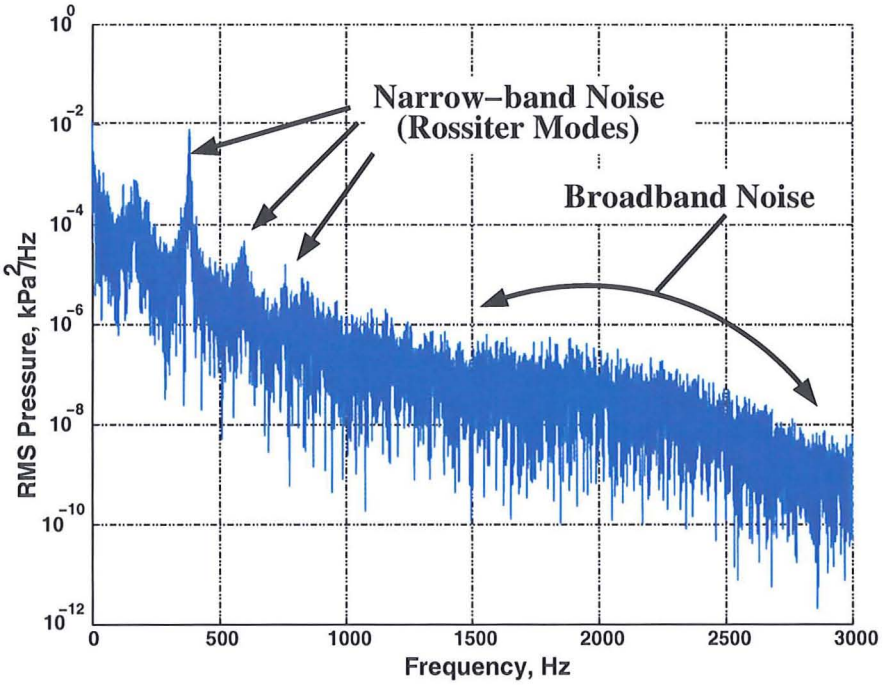

Figure 1.7: Typical noise spectrum inside the cavity. The acoustical signature is composed of narrowband noise superimposed on top of broadband noise. Narrowband noise consists of discrete acoustic tones, which are also referred to as Rossiter modes [3].

Based on his numerous experiments, Rossiter developed a semi-empirical formula to predict the acoustic frequencies created in the cavity [3]. Rossiter's model was derived from an edge-tone analogy and relied on the assumption that the acoustic radiation results from the vortices, which are shed and convected downstream from the cavity's lip, impinging on the cavity rear bulkhead. These acoustic pulses propagate upstream inside the cavity and, on reaching the front cavity wall, cause the shear layer to separate upstream of the cavity lip. This instigates the shedding of new vortices and leads to the formation of a feedback loop, thereby completing Rossiter's description of the cavity flow cycle, which is sometimes referred to as the **vortex-wave interaction model**. Visualisation of these vortices being shed into the cavity and the acoustical pressure waves existing outside the

cavity were apparent from his experiments. However, the standing waves existing inside the cavity were not shown as well. Nonetheless, this work laid the foundations for more comprehensive theories regarding cavity resonance put forth by Heller and Bliss [56] and Rockwell and Naudascher [57].

For about a decade, much of the work on cavity flows came to a halt until the mid 1970s. During this period, several experiments describing the cavity flow mechanisms were performed. Heller and Bliss [56] in 1975 conducted the famous water table visualisation experiment, which highlighted the pressure waves travelling in the cavity. Their wind tunnel tests yielded mode shapes, temperature data and suppression effectiveness. Heller and Bliss determined the first three modes for a range of L/D ratios (see Table 1.1) and acknowledged that the front wall of the cavity acted as a 'reflecting' wall while the back wall produced the maximum pressure amplitude suggesting that it was the source of the acoustics. Poor comparisons between their experiments and flight tests were however obtained because the positions where the mode shapes were analysed for the two were different, leading them to the conclusion that the mode shape may depend on the vertical position [40].

Based on the concept of unsteady planar compression waves, Heller and Bliss [56] explained the cavity flow phenomena using the shear layer oscillation cycle, sometimes called the **wave interaction mechanism**. They proposed that acoustical disturbances generated at the cavity rear propagate outward as compression waves. The upstream compression wave approaches the front cavity wall, reflects back and then travels downstream. Unsteadiness in the shear layer then originates from the wave pattern that results from these pressure waves. Heller and Bliss also put forward the **mass breathing** philosophy whereby mass is expelled and injected into the cavity through the flapping motion of the shear layer.

In 1978, Rockwell and Naudascher (1978) [14, 57] described the shear layer motion in the cavity resonance cycle to be driven primarily by the transient vortex motions inside the cavity, in what is called the **vortex interaction mechanism**. They suggested that the vortices that were generated from the oscillating shear layer sometimes impinged on the rear cavity wall and mixed with other vortices inside the cavity. Interaction of the shear layer and vortices with the cavity rear edge then led to a mass-breathing process as described by Heller and Bliss [56]. However, unlike the Heller and Bliss theory, Rockwell and Naudascher put forward the notion that this captured shear layer vortex interacted with internal cavity vortices, displacing them and causing pressure oscillations inside the cavity. These fluctuations then propagated upstream and disturbed the shear layer at the cavity lip leading to an external excitation of the shear layer that instigated further vortex shedding, thereby completing the feedback loop.

In the same year, Tam and Block [4] also conducted experiments on wheel well bays with the aim of understanding the mechanism of noise generation within them. Based on the shear layer oscillations and mass breathing process, Tam and Block described that the unsteadiness in the flow and the acoustics was generated when the shear layer dipped into the cavity and external fluid was drawn into the cavity. The resulting transient high pressure region then led to the formation and emission of a compression wave. Pressure waves were propagated in all directions, with the internal wavefront reflecting off the front cavity wall and cavity floor as well. These primary and secondary waves interacted with the shear layer to produce further instabilities within the shear layer adding to the unsteadiness and acoustics of the flow. These reflections are considered in their theoretical model, which is described later on.

Towards the beginning of the 1980s, the requirement for faster, more manœvrable and stealthier aircraft was becoming more paramount. This initiated a slightly different type of cavity flow research: one with a perspective of store release and separation characteristics. Stallings Jr. *et al.* (1983-89) [58, 59] conducted experimental investigations into the store separation characteristics at supersonic speeds and identified the presence of poor separation characteristics for shallow cavities and more favourable conditions for deep cavities. A review of the experimental analyses undertaken on cavity store separation is presented by Wilcox Jr. [60].

Other notable works in the late 1980s include the experiments by Gharib and Roshko (1987) [18, 61]. Their experiments were conducted for an axisymmetric cavity in an incompressible (water) flow at very low speeds. Their analyses revealed that the self-sustained flow oscillation cycle became highly asymmetric in the azimuthal direction and that the shear layer was no longer observed to impinge on the downstream cavity corner as the cavity L/D ratio was progressively increased. The flow now fluctuated violently and Gharib and Roshko called this phase of the cavity flow-field the **wake mode** due to its resemblance to the wake of a bluff body. They also noted a remarkable increase in drag.

With the internal storage of missiles to reduce the radar signature and the drag of the aircraft being more exercised, research into cavity flows in conjunction with store release and separation analysis progressed into the 1990s. A significant contribution was made by Foster, Ross *et al.* (1992-2005) at DERA, Bedford, who conducted various wind tunnel experiments to study the loads exerted on stores before and during release (i.e. while the store traversed the shear layer) [7, 8]. Effects of different methods for alleviating the intense acoustics generated within the cavity via cavity shaping, spoilers and mass injection were also addressed by Ross [11, 12]. Parametric studies of cavity flows with Mach and Reynolds number sweeps and different cavity aspect ratios also constituted a part of the cavity flow research conducted by Ross *et al.* [13].

Research into consecutive cavities, alternatively referred to as tandem cavities, have also emerged recently. Taborda, Bray and Knowles [2] investigated the effect of the upstream cavity on the downstream cavity for different cavity geometries and spacings between the cavities. Their results demonstrate lower pressures exhibited in the downstream cavity suggesting difficulties in store deployment. This was found to increase as the cavity L/D ratio increased.

The introduction of advanced experimental techniques like Particle Image Velocimetry (PIV) [6, 62–65] and Laser-Doppler Velocimetry (LDV) [66] have been useful in providing further understanding of the cavity flow phenomenon. Information on the velocity and turbulent distribution can be obtained from these methods, which allow for better validation of numerical results. However, for highly unsteady and turbulent flows, as is the case with cavity flows, even higher resolution PIV experiments may be required (especially near the walls) to obtain an accurate picture of the cavity flow-field [6, 65]. In most cases, such new experimental methods are either still expensive, data from them are not readily available or their reliability/accuracy still leaves much to be desired [67].

1.4.2 Theoretical Studies

In conjunction with experimental studies, some analytical studies have also been undertaken. These include efforts made in developing theoretical methods and semi-empirical

formulae to predict the resonant frequencies and/or amplitudes in cavities. Most notable of these is Rossiter's semi-empirical formula [3] and Tam and Block's theoretical model [4] to predict the acoustic field. Tables 1.3 and 1.4 summarise the key developments in the analytical studies of cavity flows.

1.4.2.1 Plumblee *et al.* Method (1962)

Plumblee *et al.* [50] developed an analytical method to predict the resonant frequencies and amplitudes of the acoustic tones of a rectangular cavity of arbitrary dimensions. Their method involved the calculation of the radiation impedance of a cavity opening at all Mach numbers using retarded potential theory and then solving the wave equation with all the other five sides of the cavity having infinite impedance. The fluid within the cavity was assumed to be at rest by Plumblee *et al.* while the fluid outside the cavity moved at constant velocity. For cavity resonance to occur, Plumblee *et al.* said that the normalised pressure amplitude at the cavity floor must reach a maximum, where the normalised pressure was taken as the forcing pressure at the mouth of the cavity.

A table of radiation resistance and reactance was also provided by Plumblee *et al.* in the usage of their method, which was based on an iterative approach. Plumblee *et al.* compared their theoretical method's frequency and amplitude response with their corresponding experimental results, concluding that the theoretical model provided a good definition of the problem.

1.4.2.2 Rossiter's Semi-Empirical Formula (1962)

Using dimensional and empirical analysis, Rossiter postulated a semi-empirical formula to calculate the cavity resonance frequencies [3]. His formula was based on an edge-tone analogy and assumed that acoustic radiation resulted from the vortices. In his original formulation, the resonant frequency f_m corresponding to the mth mode was given by

$$f_m = \frac{U_\infty}{L} \frac{(m-\alpha)}{\left[\left(\frac{1}{\kappa_v}\right)+M_\infty\right]} \tag{1.2}$$

where U_∞ is the free-stream velocity, L is the cavity length, M_∞ is the free-stream Mach number and m is an integer that is eponymously referred to as the Rossiter mode. The terms α and κ_v are constants and are determined from experiments to be 0.25 and 0.57 respectively for a L/D=4 cavity.

Rossiter's equation assumes that the total time for the flow cycle is a sum of the time taken for the vortices to convect downstream and the time taken for the acoustic waves to propagate upstream. The phase lag between the two is represented by the parameter α while κ_v depicts the proportion of the free-stream velocity at which the vortices in the cavity convect downstream. In actual fact, Rossiter showed that the phase lag term varied with the L/D ratio and this was later confirmed by Shaw and Shimovetz [40], who compared Rossiter's formula with flight test and wind tunnel data for Mach numbers ranging from 0.6 to 3 and L/D ratios ranging from 4 to 7. Their results indicated that the agreement between the three sets of data were acceptable but could be ameliorated at the lowest frequency if alternative phase lag values, as proposed by Rossiter [3], were used. Shaw

and Shimovetz however described that the dependence of Rossiter's formula to the phase lag term diminished for higher mode numbers, m.

Rossiter based this formula on experiments conducted on cavities of various aspect ratios over a Mach number ranging from 0.4 to 1.4. Within this range, it predicts the frequencies generated in the self-sustained pressure oscillation cycle in cavity flows to good accuracy, especially the dominant tone. Beyond this Mach range, Rossiter's accuracy deteriorates and several modifications have been implemented by various researchers to compensate for this [71]. An updated version of the Rossiter's original formula is as follows

$$f_m = \frac{U_\infty}{L} \frac{m - \alpha}{\frac{M_\infty}{\sqrt{1+\frac{(\gamma-1)}{2}M_\infty^2}} + \frac{1}{k_v}} \tag{1.3}$$

where γ is the ratio of specific heats. As far as prediction of the cavity resonant frequencies is concerned, Rossiter's formula still remains the most referenced and popular by far.

1.4.2.3 Bilanin and Covert Model (1973)

Bilanin and Covert (1973) [98] proposed an improvement to Rossiter's model by relating the flow cycle in terms of the instabilities in the shear layer. This improvement accounted for the lack of explanation provided in Rossiter's model for the generation of the acoustical disturbances at the cavity's downstream wall and how the feedback acoustic waves at the cavity front excite the shear layer. Bilanin and Covert reported that the shear layer is periodically perturbed at the mouth of the cavity and this leads to the growth of instabilities in the shear layer that convect downstream. The resulting fluctuating shear layer motion induces a periodic inflow of external fluid into the cavity and a discharge of cavity fluid into the external flow some time later. It was this process of mass inflow and outflow that was attributed to be the source of acoustic radiation at the cavity rear. Bilanin and Covert then described that acoustic waves propagate upstream inside the cavity without disturbing the shear layer, as was described by Rossiter. The difference with Rossiter's model was however that Bilanin and Covert attributed the excitation of the shear layer at the cavity front to the accumulation of localised pressure from the impact of the acoustic wave with the front wall.

1.4.2.4 Tam and Block Model (1978)

Tam and Block [4] developed a mathematical model (based on Bilanin and Covert's model [98]) to calculate the acoustics generated inside the cavity. Their model takes into consideration the effect of many parameters not addressed in previous models such as shear layer thickness, cavity L/D ratio, effects of reflection of acoustic waves from bottom wall and effects of external acoustic waves. The cavity was assumed to behave two-dimensionally and was based on experimental results by East [99], which showed that the acoustic and the mean flow behaviour were not correlated. Tam and Block also ignored effects of the mean flow inside the cavity and assumed that the acoustic waves were produced by a line source located at the cavity trailing-edge and considered only the convection effect of the mean flow and propagation velocity of sound. In this manner, they were able to theoretically re-construct the wavefronts emitted by the line source and

extended the wave patterns to outside the cavity (as shown in Figure 1.8) to simulate the cavity acoustic field.

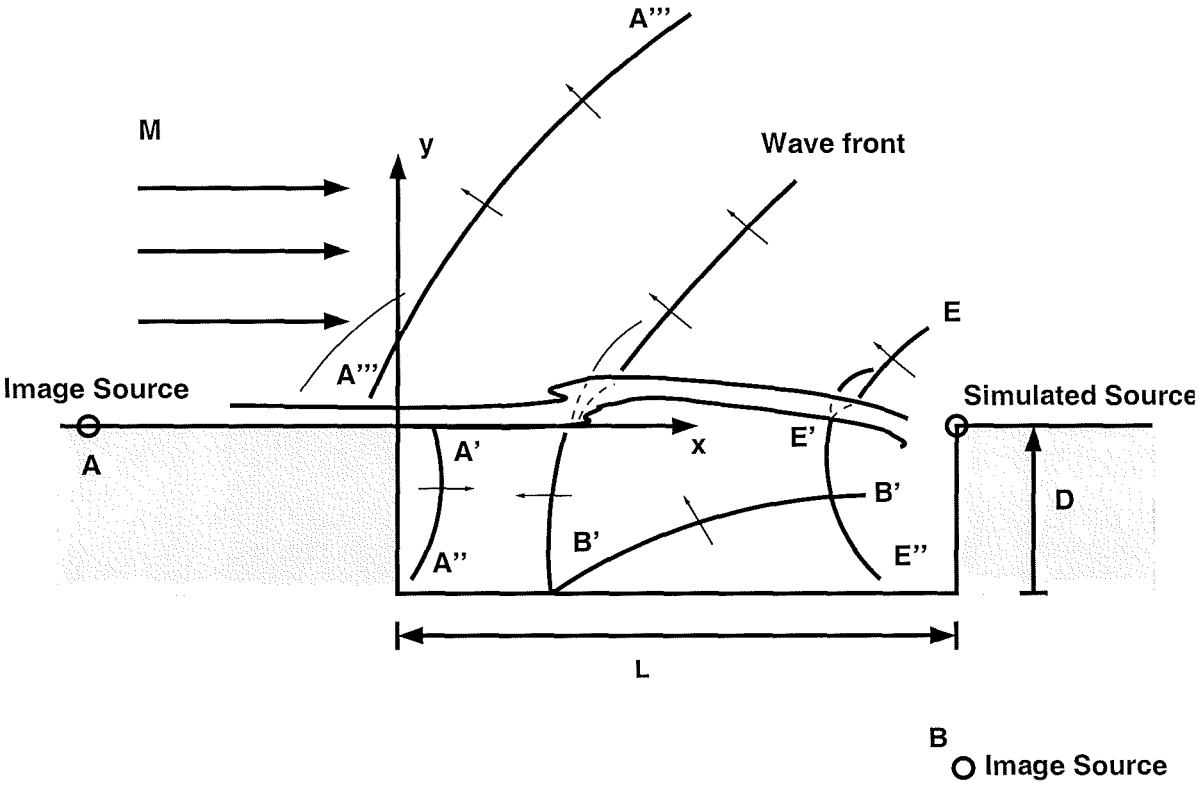

Figure 1.8: A schematic of the acoustic wave patterns inside and outside a rectangular cavity as proposed by Tam and Block [4] in the development of their theoretical model. Reproduced from the article by Tam and Block [4].

Comparisons with experiment and Rossiter's formula revealed favourable agreement especially since no adjustable constants were used in the model by Tam and Block. The fact that their mathematical model also predicted the correct change in Strouhal number for the acoustic tones with a change in the shear layer thickness, suggested that their model contained the essential physics of the cavity flow phenomenon. Comparisons with their experiments and results from their mathematical model for low subsonic Mach numbers (i.e. $M_\infty \leq 0.2$) revealed that the flow was governed by resonance from the transverse acoustic modes. They highlighted that the transition from normal mode resonance to feedback resonance was gradual and that a unified theory based on their mathematical model could be developed to describe this.

1.4.2.5 Bauer and Dix Model (1991)

Bauer and Dix [100] developed a semi-empirical formula to predict the resonant frequencies and their amplitudes. For the prediction of the frequencies, Rossiter's formula was modified by introducing a new convection term. For the prediction of the amplitudes, a response coefficient for each mode was derived, which in turn was dependent on the viscous and wave damping. Unfortunately, the model did not agree well with experimental data in terms of amplitudes with the predicted overall acoustic level falling below the level of the resonant modes [40].

1.4.2.6 Kerschen *et al.* Model (2005)

The theoretical model recently proposed by Kerschen *et al.* [101] does not require any empirical constants or other heuristic assumptions that were typically employed in previous analytical prediction models. Kerschen *et al.* predict the scattering processes occurring at the cavity corners and combine it with a method to account for the propagation of the disturbances in the central region of the cavity. A global description of the acoustic field in the cavity could thus be obtained.

The prediction of the scattering coefficients is fundamental to this model. The phases of the scattering coefficients are used to calculate the resonant frequencies while their amplitudes are used to compute the temporal growth or decay of the acoustic modes. Treatment of the cavity corner geometry for studying the scattering processes is performed and the scattering coefficients then calculated with the shear layer modelled as a vortex sheet. Propagation analyses involved using the triple decomposition method to compute the evolution of the instability wave in the shear layer and the evolution of the acoustic modes. The triple decomposition method assumes that the flow-field consists of three components: a mean (time-averaged) part, a coherent (phase-averaged) part and a fluctuating (turbulent) part. Influence of the random turbulent fluctuations on the large-scale motions is then approximated using an eddy viscosity model. A combination of the scattering and propagation analyses then results in an eigenvalue problem, the real part of which determines the oscillation frequency while the imaginary part determines the growth or decay rate of the mode. Unlike previous models, this model also determines whether an acoustic mode is stable or unstable.

The general consensus on the capability of theoretical models is that they can predict the frequencies relatively well but fail to accurately predict the amplitudes. Another limitation with these models is that important physics can often be lost due to the simplifying assumptions made. In spite of this, efforts are still continuously being made in the developments of theoretical models. More details of some key developments made in this area in the past are given in Tables 1.3 and 1.4.

1.4.3 Numerical Studies

Combined with rising wind tunnel costs and the relatively limited success of theoretical models, efforts in the last decade have therefore looked toward alternative methods such as Computational Fluid Dynamics (CFD) to analysing cavity flows. The main aim of CFD is to numerically solve the Navier-Stokes equations and involves solving the linked partial differential equations on complex shaped domains. Tables 1.5 and 1.6 summarise the key developments made in the analyses of cavity flows using numerical methods.

1.4.3.1 Direct Numerical Simulation (DNS)

The most straightforward way to solve the Navier-Stokes equations involves discretising the domain using a computational grid and explicitly resolving all the flow properties, i.e. **Direct Numerical Simulation (DNS)**. The advantage of DNS is that it can be used to calculate and visualise many quantities that are difficult to measure experimentally. DNS

however typically requires highly accurate high-order schemes to restrict the dissipation and dispersive errors. This gives it little versatility in coping with complex geometries or general boundary conditions. Furthermore, in high Reynolds number flows, where the flow falls in the turbulent regime, the number of turbulent scales can be very large. To use DNS in such flows would require extremely fine computational grids so that eddies to the very smallest scales can be resolved. The computational overhead associated with such a technique is far beyond the scope of even today's computational resources. Consequently, DNS applications are currently confined to low Reynolds number flows over simple geometries. Despite this, DNS has been applied to a wide range of applications in the research of turbulence, in providing deeper understanding of the processes involved with turbulence and contributing to the improvement of existing turbulence models. A critical part of numerical simulations is the application of proper boundary conditions. For DNS, Colonius *et al.* (1993) [107] as well as Bogey and Bailly (2002) [108] have addressed this.

From the perspective of cavity flows, DNS investigations have begun to appear a few years ago with the aim of improving the current understanding of the flow physics so as to lead to more efficient and effective control methodologies. Colonius (1999-2002) [109–111] conducted DNS on 2D cavities of various cavity planforms from low subsonic to high subsonic speeds for low Reynolds numbers (based on the boundary layer momentum thickness, θ). They employed a sixth-order finite-differencing compact scheme with a fourth-order Runge-Kutta method for time integration and discussed the differences between the shear layer and wake modes and defined the transition between the two to occur with increasing L/D ratio and Mach number with other parameters being held constant. Colonius *et al.* [109–111] also mentioned that mode-switching occurred whereby both wake and shear modes were present at different times. One important point they raised was that the wake mode was triggered at lower Reynolds numbers where the oncoming boundary layer was laminar. Colonius *et al.* compared their DNS results with experiments by Karamcheti and demonstrated good agreement. Hamed *et al.* (2001) [112, 113] performed DNS on a 2D L/D=2 cavity at Reynolds number based on the cavity length, Re_L, of 3000 at some transonic and supersonic speeds. Their simulations demonstrated an increase in the size of the primary vortex in the cavity with increasing Mach number and was generally successful in capturing the main physical mechanisms of the flow, including vortex shedding, shock waves and coupling of acoustic and velocity fields.

Recently, DNS has become attractive in the context of **Computational AeroAcoustics (CAA)**. When DNS (or even Large-Eddy Simulation (LES)) is used with CAA, it is generally referred to as **Direct Simulation (DS)** or **Direct Noise Computations (DNC)** of the flow. Combined with the strong acoustic field produced, the geometrical simplicity of the cavity makes it an attractive test case for CAA studies. Although it has been acknowledged that prediction of the sound generation process was fundamental to determining accurately the amplitude of the oscillations and the magnitude of the frequencies, problems such as the poor resolution of the acoustic waves and spurious flow oscillations marred any progress in CAA research of cavity flows [114]. The reason for the former was attributed to excessive dispersion and dissipation from low-order and upwind finite-difference schemes and finite volume discretisations as well as poor grid resolution while excessive reflections of acoustical disturbances from artificial boundary conditions was the cause of the latter [41].

The introduction of compact high-order finite-difference schemes by Lele (1992) [115] and optimised compact and explicit finite-difference schemes such as Dispersion-Relation-Preserving (DRP) schemes by Tam and Webb (1993) [116] have however proved to be efficient in resolving the acoustic fields. Together with high-order-accurate Runge-Kutta

schemes for time advancement, such as those used by Colonius *et al.* [109–111], these have proved to be good for DNS computations as they minimise the numerical dissipation and dispersion errors of acoustic waves. As far as the boundary conditions are concerned, Colonius *et al.* (1993) [107] have demonstrated that repeated reflections of acoustic waves due to artificial boundary conditions can lead to self-forcing of the flow making it difficult to distinguish real from numerical instabilities [41]. Boundary conditions remain a challenge in resonant flows such as cavity flows to allow for free movement of acoustic and vortical waves with minimal reflection [41]. Some examples of DNS in CAA analyses of cavity flows include the works by Gloerfelt *et al.* (2002) [117–119].

1.4.3.2 Unsteady Reynolds-Averaged Navier-Stokes (URANS)

The impracticability of DNS for most flows salient to engineering applications necessitated the use of models for some aspects of the flow. One commonly employed technique involves segregating the turbulent flow so that it is composed of a mean flow component with a random flow component superimposed on it. Such an approach therefore permits the averaging of the flow and enables the construction of a set of partial differential equations based on the Navier-Stokes equations, that describe the mean flow. These mean terms are known but the fluctuating terms are not and so a model is needed to account for their effect. This approach is called the **Reynolds-Averaged Navier-Stokes** method. For unsteady flows, **Unsteady Reynolds-Averaged Navier-Stokes (URANS)**, or **Very Large-Eddy Simulation (VLES)** is used. URANS describes the flow based on the assumption of a slowly varying mean flowfield with a superimposed field of random fluctuations. All the flow properties using URANS are however modelled using a turbulence model and it is here that the bulk of the research in cavity flows has concentrated on since the 1990s.

Developments in the turbulence modelling side of CFD has seen many different types of turbulence models being used over the last three decades for RANS computations. The vast majority of turbulence models employed for engineering calculations are based on the **eddy-viscosity concept** and the **Boussinesq approximation**. The eddy viscosity can be described as the turbulent Reynolds number and therefore requires knowledge of the density, velocity, a reference length and viscosity. Variations in density and viscosity tend to be not as significant for most applications so the eddy viscosity concept relies on formulations for a turbulent velocity and length scale. Where both the turbulent velocity and length scales are based on empirical values, the turbulence model is classified as a **zero-equation model**. If the velocity scale is solved using a transport equation and the length scale based on an empirical constant then the turbulence model is classed as a **one-equation model**. Where both the velocity and length scales are solved using transport equations, the turbulence model is classified as a **two-equation model**.

Historically, one of the first attempts to numerically solve cavity flows was for inviscid flow and no turbulence model was employed. Borland (1977) [120] solved the 2D Euler equations for time-dependent inviscid compressible flow in high subsonic flows over open cavities. His results showed promise as he achieved the overall noise levels and the values of the frequencies to be of the same order of magnitude as experiment.

The majority of the numerical computations using URANS have however focused on the use of zero-equation turbulence models with application to mostly supersonic cavity flows. At supersonic speeds, the acoustic waves that are typically observed for open cavities no

longer propagate upstream outside the cavity thereby simplifying the problem. In these conditions, the zero-equation turbulence model has been exploited by many researchers with varying degree of success. Hankey and Shang (1980) [121] solved the compressible Navier-Stokes equations for a 2D supersonic open cavity using the Cebeci-Smith [122] zero-equation turbulence model with both frequencies and their magnitudes successfully predicted. Since then through to the late 1990s most URANS computations of cavity flows predominantly exploited the Baldwin-Lomax [123] zero-equation turbulence model. Significant contributions were made by Baysal *et al.* (1987-89) [124–128] and Tam, Orkwis and Disimile (1995-1998) [19, 129–131]. Tam, Orkwis and Disimile however reported limited success with the Baldwin-Lomax model from their numerous simulations of 2D supersonic cavity flows. To improve the predictions, many modifications to the standard Baldwin-Lomax model were proposed. These included the relaxation modification to eliminate the abrupt change in eddy viscosity levels from the boundary layer on the flat plate upstream of the cavity to the free shear layers across the cavity opening. Other corrections made to the Baldwin-Lomax model include multiple-wall corrections and the Degani-Schiff first peak modification [129].

Despite the many modifications to the standard Baldwin-Lomax model, however, no model performed significantly better than the others [19]. Consequently, more complicated two-equation turbulence models have started to be applied in cavity flows. Shih *et al.* (1994) [132], for instance, have applied the $k-\varepsilon$ [133] turbulence model to supersonic cavities while Zhang *et al.* (1988-99) [67, 81, 134–137] have conducted extensive simulations of supersonic cavities using the $k-\omega$ [138] turbulence model.

Since the early 1990s, several works regarding the numerical computation of store separation from a cavity at supersonic free-stream speeds have been performed with the aim of understanding the interference effects between store and cavity. Baysal *et al.* (1992) [139] conducted numerical simulations for stores placed outside and inside the cavity and concluded that the interference effects were stronger for stores placed inside. Atwood (1994) [140] looked at the separation of a canard-controlled store from an open rectangular cavity. Mesh generation was simplified using a Chimera overset meshing process, in which separate, overlapping domains were used to define the cavity and store. The movement of the store was achieved by moving the entire domain around it and the influence of the unsteady field in the cavity on the store and vice versa obtained by exchanging and interpolating information across the separate domains. Suhs (1995) [141] also employed the Chimera grid methodology for a deep weapons bay through moderate subsonic to low supersonic speeds. Suhs analysed the effect of the store at three positions— inside the cavity, at the shear layer and outside the cavity— using the Baldwin-Lomax model with a relaxation modification and obtained the best agreement with experiment when the store was placed outside the cavity.

Research into hypersonic cavities has also been undertaken by Morgenstern and Chokani (1994) [142]. Hypersonic cavity flows are even simpler than supersonic cavities in that the flow can be treated as laminar thereby avoiding the need of a turbulence model altogether. Perhaps the most complicated and computationally intensive cavity flows however occur at transonic regimes. Unlike the supersonic regime, acoustical waves do propagate upstream inside and outside of the cavity at transonic speeds. What complicates the problem further is the strong coupling between the motion of the shear layer, the vortical structures, turbulence and indeed the acoustical field. Although transonic cavity flow investigations are still limited some have begun to appear towards the late 1990s and the beginning of this century. Henderson *et al.* (2000-01) [9, 143] and Lawrie *et al.* (2003-04) [10, 144], for instance, analysed open, deep cavities over a broad range of moderate

to high subsonic and low supersonic speeds using a variety of two-equation turbulence models. Their research identified the inabilities of even two-equation models to predict cavity flows, a point also confirmed by Sinha *et al.* [145].

1.4.3.3 Large-Eddy Simulation (LES)

Although URANS is typically well-suited to unsteady flows, there is increasing evidence suggesting that it is not appropriate for cavity flow applications. In the recent years, therefore, attention has diverted from purely statistical turbulence models to simulation techniques such as **Large-Eddy Simulation (LES)**. LES involves dividing the turbulent flow by scale rather than by statistical properties. The smaller, more isotropic scale eddies are modelled using a sub-grid scale (SGS) model while the larger scale eddies are explicitly resolved. This restricts the amount of modelling used. Furthermore, as LES only resolves the larger eddies, coarser grids than those used in DNS can be used. Near walls, however, the resolution of the computational domain still approaches DNS standards. To overcome this, wall modelling was proposed by Deardorff in 1970 [158] and Schumann in 1975 [159] for the purpose of LES computations. These wall modelling methods were originally commonly used in RANS computations [160].

Recently, instances of LES applied to cavity flows have emerged in literature. Smith (2001) [161, 162] presents preliminary results of LES on supersonic weapon bay flows using unstructured grids. Larchevêque *et al.* (2003) [160, 163] use LES for the understanding of deep cavities representative of aeronautical optical cavities with a L/D and L/W ratio of 0.42 at high subsonic speeds over wind tunnel Reynolds numbers (details are provided in Table 1.6). They reported good agreement with experiments and further used their simulation results to introduce a new empirical equation to compute the phase lag term (γ) used in Rossiter's semi-empirical formula.

Arguably the most well-known work on LES of cavity flows is by Rizzetta and Visbal (2003) [164]. They conducted large-eddy simulations on a very fine grid of over 20 million points on a L/D=5 cavity at supersonic speeds. Rizzetta and Visbal highlighted that it would not have been possible to resolve the fine-scale turbulent structures at the same Reynolds number as used in experiments due to the requirement of even finer computational domains and so performed their numerical simulations at Reynolds number an order of magnitude lower. To reduce the computational run-time yet further, they performed separate flat plate simulations, averaged the data to make it periodic in time and recycled it into the cavity. Comprehensive works on cavity flows using LES have also recently been undertaken by Gloerfelt (2004) [165]. His investigations looked at the mode-switching phenomenon (investigated in previous works by the same author [118, 119, 166–169]) where acoustic modes can alternate in time. This is believed to be characteristic of high Reynolds number flows where intermittency effects in the shear layer cause multiple modes to co-exist. Due to the large number of turbulent scales and the apparent non-linear interactions between the modes, DNS becomes too expensive and URANS (especially with linear statistical turbulence models) inappropriate. Combined with little experimental evidence (Kegerise *et al.* (2004) [83] is one exception), this study gives another illustration of the potential of LES for cavity flows. Their preliminary results used a very coarse mesh but captured the main features of the experiment by Kegerise *et al.* [83] even though mode-switching was not observed.

LES however suffers largely from problems similar to DNS in that accurate boundary conditions are required to prevent any spurious acoustic wave reflections and CAA methods

such as Wave Extrapolation Methods (WEM) are perhaps needed to reduce the cost of computing the far-field acoustics. Other difficulties with LES include the use of proper numerical algorithms to preserve the nature of the acoustic field and ensure proper separation between the resolved and unresolved scales [165]. Modelling the latter also has instigated research into sub-grid scale modelling. Advances in LES are extensively addressed by Lesieur and Métais (1995) [170], Moin (1997) [171] and Piomelli (1999) [172]. One progress was the introduction of the **Monotone-Integrated LES (MILES)** method by Boris *et al.* (1992) [173] in which no sub-grid scale model is used and the inherent dissipation of the upwind scheme is used to describe the dissipative behaviour of the unresolved turbulent scales. Larchevêque *et al.* (2003) [160] also applied MILES to the same cavity (i.e. with a L/D and L/W ratio of 0.42) to which he applied conventional LES. He obtained similar results to the conventional LES approach although the level of turbulence was found to be slightly higher with MILES.

1.4.3.4 Detached-Eddy Simulation (DES)

In conjunction with a sub-grid scale (SGS) model to predict the small scale eddies in LES computations, however, a turbulence model is used to account for the energy transfer between large and small scales. Usual eddy viscosity models were however developed in the framework of homogeneous isotropic turbulence so in high Reynolds number flows fine grids (although not as fine as DNS) are required for the resolution of near-wall properties. Consequently, LES is still expensive. In light of this, recent endeavours have looked at adopting hybrid methods of URANS and LES. One such method is called **Detached-Eddy Simulation (DES)** and was introduced by Spalart [191].

Spalart's DES formulation (1997) [191] proposed to use the one-equation Spalart-Allmaras turbulence model [192] as both a turbulence model for the RANS part and a sub-grid scale model for the LES part. In this manner, DES combined the RANS method in the attached boundary layer near the wall with the superior capability of LES in the regions away from the wall. As a result, DES promises to solve the 3D unsteady Navier-Stokes equations at high Reynolds numbers with reasonable computational run-times. Advances in the DES technology came in the form of using more advanced turbulence models rather than the Spalart-Allmaras model. Batten *et al.* (2001) introduced the **Limited Numerical Scales (LNS)** approach which is similar to DES but used the two-equation $k-\omega$ model. Strelets (2001) [193] and Bush *et al.* (2001) [194] introduced a DES version of the SST model while Travin *et al.* (2002) [195] described the use of the $k-\varepsilon$ model in DES formulations.

Since the last few years, DES investigations of cavity flows have begun to appear in literature. Shieh and Morris (2000-01) [180, 196] employed the original formulation of DES with the Spalart-Allmaras model and investigated the physics of subsonic 2D and 3D cavity flows at different aspect ratios with a turbulent oncoming boundary layer. Their results confirmed the presence of a wake mode flow cycle in the 2D cavity and a shear layer mode in the 3D cavity. Hamed *et al.* (2003) [183, 184] reported on the effects of Reynolds number on a L/D=5 cavity at supersonic regimes using DES with the SST model. Other notable hybrid RANS/LES works have used the $k-\varepsilon$ turbulence model. Mendonça *et al.* (2003) [185], for instance, applied DES with the $k-\varepsilon$ model to the L/D=5 cavity and compared with the RANS $k-\varepsilon$ computations highlighting the superior capability of DES to predict the broadband noise spectrum. Details of these DES computations are provided in Table 1.6.

1.4.3.5 Other Numerical Methods

In the recent years, various numerical methods have been devised and applied to cavity flows. One aspect of these novel numerical techniques involve developing acceleration algorithms to reduce the cost and run-time of numerical simulations. One such approach looks at describing the cavity flow using a type of low-order model called **Proper Orthogonal Decomposition (POD)** introduced by Lumley [197]. Due to the large number of frequencies that may exist in the cavity, the idea behind the POD technique is to use a few modes to model the flow. For a dataset that has been discretised in space and time, the POD modes are most easily computed using the **method of snapshots**, in which the vector of dependent variables, $u(x,t)$, is given by

$$u(x,t) = \sum_{j=1}^{N} a_j(t)\phi_j(x) \tag{1.4}$$

where x is the vector of discretised spatial points, $a_j(t)$ are the coefficients and $\phi_j(x)$ are the **POD modes** (alternatively referred to as the **Karhunen-Loève eigenfunctions** or **empirical eigenfunctions**. A detailed theoretical description of the POD method is provided by Colonius [41]. A flow-field can be well defined by a POD decomposition if the coefficients $a_j(t)$ decay rapidly for large j. In this situation, the percentage of energy that is captured in the first few modes becomes significant. The data that are required by POD (so that it can extract the coherent features) is typically obtained from some other numerical simulation or experiments. Sinha *et al.* (2000) [175] used POD for analysing a supersonic deep cavity. Their investigations demonstrated that POD was efficient in predicting the fundamental phenomenology underlying the flow oscillations of the weapons bay and mentioned that POD would also be suitable for flow control studies. Rowley *et al.* (2000-01) [188, 189] used POD and Galerkin projection to obtain a lower-model that captures the dynamics of the cavity with data from DNS results as input. Their recent publications showed that POD accurately predicted the dynamical response of the cavity over short and long periods of time.

Other methods applied to cavity flows include the **Discrete Vortex Method (DVM)**. Cain *et al.* (1999) [187] used this as a fast and economical method for the prediction of the nonlinear dynamics of the shear layer in an open rectangular cavity. The DVM is based on a discretised model of the free shear layer vorticity field and employs a Lagrangian method to compute the temporal and spatial evolution of the discrete field. Cain *et al.* however reported limited success and stressed the need for refinements of the model. The **Lattice Boltzmann Method (LBM)** has also recently been applied by Ricot *et al.* (2002) [190] to open rectangular cavities at very low Mach numbers. Treatments to account for high Reynolds number effects were made to their 2D model, which was found to give good agreement with experiment.

Another relatively novel approach to cavity flows uses **Stochastic Estimation (SE)** to estimate the velocities in the shear layer given the surface pressure measurements. This method has appeared from the realisation that time-resolved measurements are needed, for example, in the optimisation of active control strategies for a wide range of flow conditions. Stochastic estimation overcomes the difficulties experienced during experiments in inserting probes in the flow for many complicated geometries and enables an image of the time-resolved flow-field to be constructed, something that cannot be readily obtained from current experiment methods. Stochastic Estimation was originally introduced by Adrian in 1977 [198] as a method for estimating the coherent structures in turbulent flows [199].

The velocity field could then be approximated by performing an ensemble averaging using the time-dependent wall pressure as the condition

$$\tilde{u}_{ijx} = \langle u_{ijx}(t) | p(t) \rangle \tag{1.5}$$

where the subscripts denote the position i and j while the x denotes the component of the velocity to be estimated. Angle brackets are used to represent ensemble averaging while the velocities $(u_{ijx}(t))$ and pressures $(p(t))$ correspond to fluctuating values. The conditional average could then be approximated by a power series to obtain a stochastic estimate, the order of which was determined by the the number of terms that were retained in the power series. A **Linear Stochastic Estimate (LSE)** therefore used one term while a **Quadratic Stochastic Estimate (QSE)** used two. The coefficients in the power series could then be determined by minimising the error between the conditional average and the estimate [200]. Murray and Ukeiley (2003) [201] used LSE and QSE to predict the flow-field characteristics using LES results over a L/D=6 at supersonic speeds. Comparisons among the three methods showed good agreement, with QSE providing more accurate description of the turbulent energy and the finer details of the vorticity.

1.4.4 Flow Control Studies

Prediction and understanding of cavity flow mechanisms is driven by the need to design flow control methodologies to mitigate the acoustic loads. Attempts to suppress the harsh aeroacoustic cavity environment have been made since the 1950s. Perhaps the first flow control endeavours can be credited to Norton (1952) [45] and later Rossiter (1962) [3]. Both Norton and Rossiter proposed the use of spoilers ahead of the cavity to attenuate bomb bay buffet. While Rossiter deduced that the spoiler increased the boundary layer thickness, Norton presumed that spoilers may also be effective in reducing the frequency content in cavities by modifying the shear layer properties. Tests with the T.S.R. 2 by Rossiter [54] revealed that a small spoiler placed ahead of the bomb bay can produce reductions of the pressure fluctuations in the cavity.

As the physics of cavity flows began to be better understood, it was realised that the cavity in the shear layer and wake modes experienced significant noise levels due to the interaction of the flow primarily at the downstream cavity corner. The noise levels and the acoustic radiation generated were then maintained and continuously nurtured by a feedback loop that was instigated at the upstream cavity corner. In the open cavity shear layer mode, for instance, the source of the acoustics was the shear layer impinging the cavity's downstream wall with the feedback loop created from the perturbation of the shear layer by the acoustic waves at the cavity upstream wall. On the other hand, for the wake mode, high noise levels were produced from the impact of large-scale vortical structures on the cavity downstream wall with the feedback loop created from massive separation ahead of the cavity due to large displacements of the shear layer at the cavity upstream wall. Efforts in controlling this highly unsteady flow therefore focused on reducing (or preventing altogether) the noise levels at the cavity rear and thereby breaking the feedback loop.

The bulk of the flow control studies have focused on developing methods to suppressing the high noise levels generated in the shear mode open cavity. Shaw and Shimovetz [40] suggested that if the shear layer can be forced to extend across the cavity opening or re-attach at some stable stagnation point, no feedback process would be established

and therefore no acoustic resonance will be produced. This strategy has been adopted as the basis of much of the flow control work. Two flow control approaches have been researched and implemented: **passive** and **active** control. Active control methods can be further divided into **open-loop control** and **closed-loop control**. These are briefly described in the following sections. For a comprehensive review of different passive and active control strategies, the reader is directed to excellent reviews by Cattafesta [202] and Takeda [42]. Cattafesta [202] in particular gives a very comprehensive description (in tabular format) of the geometrical specifications and the flow conditions used in the different investigations of control methods.

Classification of flow control methods into passive and active categories is open to conjecture. Steady jet blowing, for instance, can also be perceived as a form of passive control as the jet acts as a permanent device that continuously blows air into the cavity without adapting to the flow conditions, as active control methods should do. Here, however, only permanently fixed **physical** devices are classified as passive control methods. Steady or time-varying acoustical and vortical methods and moving physical devices with no feedback loop are classified as open-loop active control while methods where a feedback loop is used are classified as closed-loop active control.

1.4.4.1 Passive Control

Passive control methods involve manipulation of the existing cavity geometry or addition of external and permanent physical devices. Out of all the methods involving insertion of physical devices to alter the flow in the cavity, spoilers or fences of various shapes and sizes (positioned primarily upstream of the cavity lip) are by far the most popular. The capability of the leading-edge (LE) spoiler in reducing the aeroacoustic noise and enhancing weapon separation characteristics has proved to be extremely effective. So much so that since the F-111 combat aircraft all modern USAF fighters and bombers with internal bomb bays were fitted with leading edge spoilers [203]. Research investigating the effectiveness of spoilers and other devices studied in this category are classified as 'additive' in Table 1.7.

Passive control methods exploiting modification of the cavity geometry to suppress the unsteady pressure field include predominantly slanting of cavity walls. Since the source of the acoustic field is the downstream cavity wall for the open cavity in shear layer mode, most experimental and numerical investigations have looked at shaping the rear cavity wall to minimise the magnitude of the radiated sound. A ramped, wedged or slanted rear wall has been found to be quite effective as it forces a change in the direction of acoustic waves as they reflect off the sloped rear wall thereby modifying the way they interact with the shear layer. Passive venting via porous or slotted floors/walls has also been investigated. These have been applied mostly to shallow cavities where a closed-type flow exists and aim to equalise the pressure in the cavity along the longitudinal axis by extracting higher pressure at the cavity rear to the lower pressure region at the front of the cavity. A brief summary of the different contributions made in the understanding of the different devices in this category, which are classified as 'manipulative', are given in Table 1.7.

1.4.4.2 Active Control - Closed-Loop

The main advantage of passive control over active control is its low cost and simplicity. Although such methods are effective in improving the aeroacoustic ambiance within the cavity, they are only designed for specific flight configurations and their performance deteriorates at off-design or time-varying situations. In such scenarios, the performance of permanent devices used in passive control methods may be much worse than without the passive control device present. Active control therefore becomes more attractive as it can be optimal over a wider range of operating conditions. Active flow control approaches can either be open-loop or closed-loop and involve the introduction of additional energy to the flow via an actuator.

Closed-loop methods represent the most recent and complicated techniques but have gained popularity over the years. In such strategies, a flow state parameter such as pressure or velocity is modified by some control algorithm to produce a feedback signal that is fed into the actuator. Research into closed-loop control has proved effective in reducing the magnitudes of the acoustic tones with some indications that it might be effective in reducing the broadband noise spectrum as well. Furthermore, where both open-loop and closed-loop strategies have been compared, it has been identified that closed-loop methods are more economical, requiring an order of magnitude less power than open-loop counterparts [218]. Contributions to closed-loop strategies for flow control of cavity flows are summarised in Table 1.8, which groups the research efforts based on the actuator used.

1.4.4.3 Active Control - Open-Loop

In open-loop active control strategies, no feedback loop is implemented. Open-loop controllers can alternatively be described as those in which the energy added to the flow through some actuator is not coupled with a flow state parameter. Vortical passive devices, i.e. devices that inject air into the cavity, are classified here as open-loop control methods. Physical devices that move are also included into this category.

Perhaps the most common open-loop active control mechanism involves pulsed mass injection. This requires installation of injection nozzles at different positions in the cavity and has the advantage of attenuating cavity flow oscillations even when the weapon bay doors are opening and closing [219]. The concept of pulsed injection was first investigated by Shaw, who injected air normal to freestream through slots just upstream of the cavity leading edge to disturb the incoming boundary layer. Since then, the effectiveness of pulsed mass injection has also been studied by many others. Other active methods have also been adopted and are summarised in Table 1.8.

1.5 Thesis Outline

Chapter 2 details the various different turbulence models and simulation methods such as LES and DES used in this thesis. A description of the experimental set-up used by Ross *et al.* at DERA Bedford to obtain pressure and PIV measurements is then provided in Chapter 3.

The objective of Chapter 4 is to establish the best turbulence modelling option for the numerical analysis of cavity flows. URANS is initially applied on 2D cavities (which are good representations of full 3D cavities with doors on) with a L/D ratio of 5. URANS gives reasonable qualitative descriptions of the 2D cavity flow features but only for coarse grids. Simulation of the full 3D L/D=5 cavity (with a width-to-depth ratio of 1) is then performed (Chapter 5) in both doors-on and doors-off configurations using both LES and DES. Results are compared with experimental unsteady pressure and PIV measurements as well as 3D URANS results for the same case. Although LES and DES provide a more accurate and consistent description of the cavity flow-field, computations are more expensive.

To further assess the applicability of URANS for cavity flows, URANS is applied to cavities of different dimensions in Chapter 6. Flows over very deep cavities (L/D=2), transitional cavities (L/D=10) and closed cavities (L/D=16) at the same flow conditions as for the L/D=5 are discussed. Results show where URANS can be used for these L/D ratios and where LES and DES have to be used for better and more consistent predictions of the cavity flow-field.

With the understanding of the cavity flow mechanisms gained from such numerical investigations, methods for controlling the high noise levels and frequencies produced in the L/D=5 cavity are addressed in Chapter 7. URANS is applied to the coarse 2D cavity here because many control devices are studied and URANS gives reasonable prediction for 2D cavities. Passive control techniques including the spoiler and slanted cavity walls and active open-loop methods including steady jet blowing are applied.

Finally, numerical simulations of a cavity with a store are undertaken in Chapter 8. A missile is placed inside the cavity and its effect on the flow-field inside the cavity are assessed. Since LES gives consistently good predictions of the cavity flow-field it was used here since the influence of the missile is relatively unknown.

Table 1.1: Developments in experimental studies of weapon bay cavity flows (continued).

Study	Geometry Specifications	Flow Conditions	Method Details
Karamcheti (1955) [47, 48]	$2 \leq L/D \leq 10$ (2D)	$0.25 \leq M_\infty \leq 1.5$ $0.75 \times 10^6 \leq \mathrm{Re}_L \leq 1.1 \times 10^6$	Schlieren; Interferometry; HWA; Shadowgraphs; Phasemeters; Magnetic Tape Recordings
Roshko (1955) [49]	$1 \leq L/D \leq 62.5$ (2D)	$22.86m/s < U_\infty < 64m/s$	Static Orifices; Pitot Probes; Schlieren Pictures;
McDearmon (1960) [68]	$2.19 \leq L/D \leq 23.8$; $0.5 \leq L/W \leq 7.69$	$M_\infty = 3.55$	Schlieren Photographs; Shadowgraphs; Pressure Orifices; Manometers
Rossiter (1960-66) [3, 51–55]	$1 \leq L/D \leq 10$ (2D & 3D cavities)	$0.4 \leq M_\infty \leq 1.2$ $0.75 \times 10^6 \leq \mathrm{Re}_L \leq 2.2 \times 10^6$	Manometers; Pressure Transducers; Magnetic Tape Recordings; Vapour Screen Technique
Charwat *et al.* (1961) [15]	2D cavities	$2 \leq M_\infty \leq 4$	Micro-Manometers; Schlieren Pictures
Plumblee *et al.* (1962) [50]	2D & 3D cavities	$0.2 \leq M_\infty \leq 5$	Pressure Transducers
Rockwell and Knisely (1970-80) [57, 69]	$71 < L/\theta < 144$	$106 \leq \mathrm{Re}_\theta < 324$	Hydrogen Bubble Visualisation; LDA
Heller and Bliss (1975) [56, 70]	$2.3 \leq L/D \leq 5.5$	$0.8 \leq M_\infty \leq 2$ $12 \times 10^6 \leq \mathrm{Re}/m < 15 \times 10^6$	Water Table Visualisation
Sarohia (1976) [16]	$0 \leq L/D \leq 50$ (axisymmetric)	$0m/s < U_\infty < 27m/s$ $\mathrm{Re}_\delta = 1,040$	HWA; Spark Shadowgraphs
Tam and Block (1978) [4][a]	$0.783 \leq L/D \leq 2.348$	$0.05 \leq M_\infty \leq 0.4$	Microphones
Kaufman *et al.* (1983) [71]	$5.1 \leq L/D \leq 9.9$	$0.6 \leq M_\infty \leq 3$ $6.7 \times 10^6 \leq \mathrm{Re}/m < 9.3 \times 10^6$	Pressure Taps/Transducers; Thermocouples; Schlieren Images; Oil Flow Visualisation
Stallings *et al.* (1983-89) [58, 59]	$4.44 \leq L/D \leq 14$	$1.7 \leq M_\infty \leq 2.86$ $5.61 \times 10^6 \mathrm{Re} < 6.27 \times 10^6$	Strain Gauges; Static Pressure Orifices; Oil Flow Visualisation
Gharib and Roshko (1983-87) [18, 61, 72]	$80 < L/\theta < 150$	$16m/s < U_\infty < 27m/s$	Water Tunnel; Pressure Taps; LDA; Diluted Colouring and Fluorescein Dye
Ross *et al.* (1992-2005) [6–8, 11–13, 65]	$3.33 \leq L/D \leq 13.33$; $2.6 \leq L/W \leq 10.664$	$0.4 \leq M_\infty \leq 1.6$ $0.833 \times 10^6 \leq \mathrm{Re}_L \leq 16.67 \times 10^6$	5-Component Balance; Static, Unsteady Pressure Transducers; PIV
Plentovich *et al.* (1992-97) [17, 73, 74]	$1 \leq L/D \leq 17.5$ $0.0626 \leq L/W \leq 17.5$	$0.2 \leq M_\infty \leq 0.95$ $6.67 \times 10^6 \leq \mathrm{Re}/m < 330 \times 10^6$	Pressure Transducers; 6-Component Strain-Gauge Balance; Pressure Orifices
Squire and Nasser (1993) [75]	$19 \leq L/D \leq 57$	$0.9 \leq M_\infty \leq 1.3$ $21.4 \times 10^6 \leq \mathrm{Re}/m < 28.6 \times 10^6$	Pressure Tappings; Schlieren Images
Rahman and Nasser (1996) [76]	$L/D = 3.3$; $L/W = 2$	$U_\infty = 0.3m/s$; $\mathrm{Re}_L = 0.35 \times 10^6$	LDV; Dye Path Tracing

[a] Undercarriage Bays

Table 1.2: Developments in experimental studies of weapon bay cavity flows (concluded).

Study	Geometry Specifications	Flow Conditions	Method Details
Disimile *et al.* (1997-2000) [77, 78]	$1 \leq L/D \leq 2$ $0.085 \leq L/W \leq 0.682$	$M_\infty = 2$([77]; $U_\infty = 12.16m/s$ $10,500 \leq \mathrm{Re}_\theta = 73,400$	Pressure Transducers; HWA; Microphones
Cattafesta *et al.* (1998-2001) [79, 80]	$2 \leq L/D \leq 4$	$0.4 \leq M_\infty \leq 0.6$ $2.5 \times 10^6 \leq \mathrm{Re}_L \leq 3 \times 10^6$	Unsteady Pressure Transducers; (Quantitative) Schlieren Images; HWA
Zhang *et al.* (1998) [81]	$L/D = 3$	$M_\infty = 1.5$; $\mathrm{Re}_L = 1.35 \times 10^6$	Spark Schlieren
Kegerise *et al.* (1999-2004) [82, 83]	$2 \leq L/D \leq 4$ $L/W = 3$	$0.4 \leq M_\infty \leq 0.6$ $\mathrm{Re}_L = 1.524 \times 10^6$	Optical Deflectometry; Pressure Transducers; Schlieren Images
Ahuja and Mendoza (1995) [84]	$0.03125 \leq L/D \leq 3.75$ $0.4685 \leq L/W \leq 3.748$	$0.065 \leq M_\infty \leq 1$ $0.045 \times 10^6 \leq \mathrm{Re}_L \leq 12 \times 10^6$	Tufts; Water Table Visualisation; Pitot Probe; HWA; Microphones
Czech *et al.* (2000) [85]	$1 \leq L/D \leq 3$ $2.67 \leq L/W \leq 9.54$	$U_\infty = 16m/s$ $\mathrm{Re}_\theta < 1400$	HWA; Microphones
Esteve *et al.* (2000) [66]	$L/D = 10$ $L/W = 10$	$12m/s < U_\infty < 20m/s$ $1.2 \times 10^6 \leq \mathrm{Re}_L \leq 2.1 \times 10^6$	LDV; Pressure Orifices; Pressure Transducers
Chung (2001-03) [86, 87]	$2.43 \leq L/D \leq 43$ $0.5 \leq L/W \leq 2$	$0.33 \leq M_\infty \leq 1.28$	Pressure Taps; Pitot Probe; Pressure Transducers
Knowles *et al.* (2001-04) [2, 64, 88, 89]	$4 \leq L/D \leq 16$ $2 \leq L/W \leq 4.16$	$0.82 \leq M_\infty \leq 0.92$	PIV; Pressure Transducers; Oil Flow Visualisation
Martel *et al.* (2001) [90]	$4 \leq L/D \leq 8$ $L/W = 0.5$	$M_\infty = 0.8$ $\mathrm{Re}_L \leq 0.28 \times 10^6$	Shack-Hartman Sensor
Murray and Elliot (2001) [91]	$L/D = 3$	$1.8 \leq M_\infty \leq 3.5$ $1.4 \times 10^6 \leq \mathrm{Re}_L \leq 2.6 \times 10^6$	Schlieren Photography; Planar Laser Imaging
Ünalmis *et al.* (2001-04) [92, 93]	$3 \leq L/D \leq 7$ $L/W = 2$	$2 \leq M_\infty \leq 5$ $5.08 \times 10^6 \leq \mathrm{Re}_L \leq 8.89 \times 10^6$	Pressure Transducers; Planar Laser Imaging; PIV
Meganathan and Vakili (2002) [63]	$2 \leq L/D \leq 4.5$ $0.8 \leq L/W \leq 1.8$	$18.33m/s < U_\infty < 70m/s$ $1222 \leq \mathrm{Re}_\theta < 2752$	PIV; Unsteady Pressure Transducers; Microphones
Radhakrishnan *et al.* (2002) [94]	$2 \leq L/D \leq 4.5$ $0.6 \leq L/W \leq 1.4$	$0.3 \leq M_\infty \leq 0.6$	PIV; Pressure Transducers
Raman *et al.* (2002) [95]	$3 \leq L/D \leq 8$	$0.6 \leq M_\infty \leq 1.19$	Microphones; Spark-Schlieren; Photoluminescent Pressure Sensitive Paint
Chattelier *et al.* (2004) [96]	$0.33 \leq L/D \leq 3$ $0.0625 \leq L/W \leq 3$	$M_\infty = 0.11$ $0.1 \times 10^6 \leq \mathrm{Re}_L \leq 0.3 \times 10^6$	Microphones; Pitot Tubes; PIV
Ashcroft and Zhang (2005) [97]	$2 \leq L/D \leq 4$ $0.1111 \leq L/W \leq 0.2222$	$32m/s < U_\infty < 42m/s$ $0.22 \times 10^6 \leq \mathrm{Re}_L \leq 0.56 \times 10^6$	Pressure Transducers; Microphones; PIV; LDA; Oil Flow Visualisation

Table 1.3: Developments in analytical studies of weapon bay cavity flows (continued).

Study	Predictive Capability	Description	Remarks
Plumblee *et al.* (1962) [50]	Frequencies; Amplitudes	Uses Retarded potential theory to calculate radiation impedance for cavity opening then applies wave equation with infinite impedance assumed for other five cavity walls. Iterative. Provides look-up table for resistance and reactance.	Difficult to use. Does not readily converge. Not very accurate.
Rossiter (1962) [3]	Frequencies	Semi-empirical. Edge-tone analogy. Calculates phase lag between vortex convection time and acoustic wave propagation time. Good accuracy between $0.4 < M_\infty < 1.4$. Most popular.	Accuracy deteriorates outside Mach range; sensitive to phase lag term, α, esp. for lower mode numbers.
McGregor and White (1970) [102]	Drag	Uses cubic polynomial to derive velocity profile in shear layer. Includes compressibility, boundary layer and resonance effects. Reasonable agreement with experiment.	
Bilanin and Covert (1973) [98]	Frequencies	Similar to Rossiter's formula but uses no empirical constants. Idealised shear layer as thin vortex sheet. Used line source as noise source and line pressure force to simulate excitation of shear layer by acoustic waves at cavity front. Good comparison at high supersonic Mach number.	Poor comparison at low supersonic and high subsonic Mach numbers. Vortex sheet model not appropriate for high Mach number flows.
Heller and Bliss (1975) [70]	Frequencies	Modified Rossiter's formula. Static temperature in cavity assumed to be stagnation temperature of free-stream.	
Smith and Shaw (1975) [103]	Frequencies Amplitudes	Empirical method based on flight test data. Easy to use. Good first order prediction of flow-induced environment. Also predicts longitudinal distribution of energy in cavity	

Table 1.4: Developments in analytical studies of weapon bay cavity flows (concluded).

Study	Predictive Capability	Description	Remarks
Tam and Block (1978) [4][a]	Frequencies	Improves Bilanin and Covert mathematical model [98]. Includes effects of shear layer thickness. Removes assumption of point force excitation. Considers reflection of acoustic waves from bottom wall. Favourable agreement reported.	
Bartel and McAvoy (1981) [104]	Frequencies	Employs acoustic eigenmodes of cavity assuming radiation loss of cavity opening is very low.	Not very accurate.
Kaufman *et al.* (1983) [71]	Frequencies	Modification of Rossiter's formula. Derived table of values for convective term from their data and compared with Rossiter's data to calculate phase lag term and compared predicted values with measured values.	Minor improvement to Rossiter's formula noted, so suffers from similar problems.
Bauer and Dix (1991) [100]	Frequencies Amplitudes	Extension to Rossiter's formula. Proposed new convection term in Rossiter's formula to compute frequencies. Amplitudes predicted based on response coefficient of each mode which was a function of viscous and wave damping.	Not accurate predictions of amplitudes.
Yu *et al.* (1994) [105]	Frequencies	Similar to Bartel and McAvoy's method [104]. Solves 2D wave equation and uses longitudinal and transverse modes.	Not very accurate.
Golliard and Bruggeman (1998) [106]	Broadband Noise	Based on response of first acoustic modes of cavity to pressure fluctuations below turbulent boundary layer, which is modelled by a wavenumber-frequency spectrum. Reasonable agreement.	Amplitudes lower than experiment at higher frequencies.
Kerschen *et al.* (2005) [101]	Frequencies; Mode Growthor Decay Rate; Mode Stability	Propagation and scattering models. Formula to predict frequencies similar to Rossiter's formula without empirical constants. Shear layer modelled as vortex sheet. Good agreement with experiment.	Slight over-prediction of first mode frequency.

[a] Undercarriage Bays

Table 1.5: Developments in numerical studies of weapon bay cavity flows— URANS method.

Study	Geometry Specifications	Flow Conditions	Turbulence Model
Borland (1977) [120]	$\leq L/D \leq$; $\leq L/W \leq$	$\leq M_\infty \leq$; $\times 10^6 \leq \mathrm{Re}_L \leq \times 10^6$	None (Euler)
Hankey and Shang (1980) [121]	$L/D = 2.25$; $L/W = 4$	$M = 1.5$; $\mathrm{Re}_L = 1.17 \times 10^6$	C-S
Gorski *et al.* (1987) [146]	$L/D = 6.2$ (3D)	$M = 2.36$; $\mathrm{Re}/m = 6.6 \times 10^6$	B-L
Suhs (1987-95) [141, 147–149]	$4.5 \leq L/D = 5.6$; $L/W = 3$	$0.6 \leq M_\infty \leq 1.5$; $1.61 \times 10^6 \leq \mathrm{Re}_L \leq 3.9 \times 10^6$	B-L (modified)
Baysal *et al.* (1988-1994) [124, 125, 127, 139, 150]	$3 \leq L/D \leq 16$; $1.3 \leq L/W \leq 5$	$1.5 \leq M_\infty \leq 2.75$; $0.25 \times 10^6 \leq \mathrm{Re}_L \leq 4.5 \times 10^6$	B-L (modified)
Rizzetta (1988) [151]	$L/D = 5.07$; $L/W = 1.9$	$M = 1.5$; $\mathrm{Re}_L = 1.09 \times 10^6$	B-L (modified; half-cavity)
Srinivasan *et al.* (1988-91) [126, 128]	$4.4 \leq L/D \leq 11.7$; $L/W = 4.4$	$0.58 \leq M_\infty \leq 0.9$; $5.32 \times 10^6 \leq \mathrm{Re}_L \leq 5.6 \times 10^6$	B-L (modified)
Zhang *et al.* (1988-99) [67, 81, 134–137, 152]	$1 \leq L/D \leq 5$	$1.5 \leq M_\infty \leq 2.5$; $\times 10^6 \leq \mathrm{Re}_L \leq \times 10^6$	$k-\omega$
Dougherty *et al.* (1990) [153]	$L/D = 2$ (2D)	$0.6 \leq M_\infty \leq 1.2$; $\mathrm{Re}_L = 1.65 \times 10^6$	B-L
Fuglsang and Cain (1992) [154]	$L/D = 4.5$ (2D)	$M = 0.85$; $\mathrm{Re}/m = 6.9 \times 10^6$	B-L upstream of cavity & laminar elsewhere
Tu (1992) [155]	$L/D = 4.5$	$M = 1.2$; $\mathrm{Re}_L = 2.5 \times 10^6$	B-L (modified)
Atwood (1992-94) [35, 36, 140][a]	$2 \leq L/D = 4.5$	$0.9 \leq M_\infty \leq 1.2$; $1.47 \times 10^6 \leq \mathrm{Re}_L \leq 3.8 \times 10^6$	B-L
Shih *et al.* (1994) [132]	$L/D = 5.07$ (2D)	$M_\infty = 1.5$; $\mathrm{Re}_L = 1.09 \times 10^6$	$k-\varepsilon$
Morgenstern and Chokani (1994) [142]	$5.33 \leq L/D \leq 10.67$	$M = 6.3$; $1.033 \times 10^6 \leq \mathrm{Re}/m < 4.085 \times 10^6$	None (Laminar)
Orkwis and Disimile (1995-98) [129, 131]	$L/D = 2$; $L/W = 0.083$	$M = 2$; $\mathrm{Re}_\theta = 36{,}900$	B-L (modified) & Laminar
Rahman and Naser (1996) [76]	$L/D = 3.3$; $L/W = 2$	$U_\infty = 0.3m/s$; $\mathrm{Re}_L = 0.35 \times 10^6$	$k-\varepsilon$
Tam *et al.* (1996) [19, 130]	$L/D = 2$ (2D)	$M = 2$; $\mathrm{Re}_\theta = 36{,}900$	B-L
Tracey and Richards (1996) [156]	$4.4 \leq L/D \leq 20$ (2D)	$0.6 \leq M_\infty \leq 0.9$; $\mathrm{Re}_L \leq 28.1 \times 10^6$	B-L (modified)
Sinha *et al.* (1998) [145]	$L/D = 4.5$ (2D)	$M = 2$; $4.5\mathrm{Re}_L \leq \times 10^6$	B-L, $k-\varepsilon$, $k-\omega$
Shieh and Morris (1999) [38]	$L/D = 4$ (2D)	$M = 0.5$; $\mathrm{Re}_L = 0.02 \times 10^6$	None (Laminar)
Rona and Dieudonné (2000) [157]	$L/D = 3$ (2D)	$M = 1.5$	None (Laminar)
Henderson *et al.* (2000-01) [9, 143]	$5 \leq L/D \leq$; $L/W = 1$	$0.85 \leq M_\infty \leq 1.19$; $6.783 \times 10^6 \leq \mathrm{Re}_L \leq 7.348 \times 10^6$	$k-\omega$
Radhakrishnan *et al.* (2002) [94]	$L/D = 2.5$ (2D)	$0.3 \leq M_\infty \leq 0.6$	$k-\varepsilon$
Lawrie *et al.* (2003-2004) [10, 144]	$L/D = 5$; $L/W = 5$	$0.3 \leq M_\infty \leq 1$; $0.005 \times 10^6 \leq \mathrm{Re}_L \leq 6.783 \times 10^6$	$k-\omega$, Baseline $k-\omega$, SST

[a] Optical Cavities

Table 1.6: Developments in numerical studies of weapon bay cavity flows— DNS, LES, Hybrid RANS/LES and other numerical methods. (In last column, number of points in the cavity given as percentage of total amount in parenthesis, where available. For more than one calculation, only the maximum number of points are given.)

Study	Geometry Specifications	Flow Conditions	Method	Grid Size
Colonius *et al.* (1999) [109, 110]	$1 \leq L/D \leq 5$; $20.3 < L/\theta < 123.1$	$0.2 \leq M_\infty \leq 0.8$; $56.8 \leq \mathrm{Re}_\theta < 73.9$	DNS	
Hamed *et al.* (2001) [112, 113]	$L/D = 2$ (2D)	$0.6 \leq M_\infty \leq 1.1$; $\mathrm{Re}_L = 3000$	DNS	
Gloerfelt *et al.* (2001-02) [117–119]	$L/D = 2$ (2D)	$M = 0.7$; $\mathrm{Re}_D = 41000$	DNS	0.244×10^6 (10%)
Rowley *et al.* (2002) [111]	$1 \leq L/D \leq 5$ (2D)	$0.2 \leq M_\infty \leq 0.8$; $56.8 \leq \mathrm{Re}_\theta < 73.9$	DNS	
Larsson *et al.* (2004) [174]	$L/D = 4$ (2D)	$M = 0.15$; $\mathrm{Re}_L = 0.006 \times 10^6$	DS (CAA)	1.12×10^6
Sinha *et al.* (1998-2000) [145, 175]	$4.5 \leq L/D = 6$	$1.5 \leq M_\infty \leq 2$	LES (1-eqn. SGS)	
Smith (2001) [161, 162]	$L/D = 4.5$; $L/W = 4.5$	$M = 1.2$; $\mathrm{Re}_L \leq 1.5 \times 10^6$	LES (SM)	0.614×10^6
Yao *et al.* (2001) [176]	$L/D = 4$; $L/W = 0.33$	Incompressible; $5000 \leq \mathrm{Re}_L \leq 50000$	LES (DSM)	
Gloerfelt *et al.* (2002-03) [119, 167, 168, 177]	$1 \leq L/D \leq 3$; $0.5 \leq L/W \leq 1.28$	$0.6 \leq M_\infty \leq 0.8$; $28700 \leq \mathrm{Re}_D < 48600$	LES (SM)	5.4×10^6 (16.5%)
Larchevêque *et al.* (2003) [160, 163][a]	$L/D = 0.42$; $L/W = 0.42$	$M = 0.8$; $\mathrm{Re}_L = 0.86 \times 10^6$	LES (SMM) & MILES	1.627×10^6
Rizzetta (2003) [164]	$L/D = 5$; $L/W = 5$	$M = 1.19$; $\mathrm{Re}_L \leq 0.2 \times 10^6$	LES (DSM)	20.6×10^6
Gloerfelt (2004) [165]	$L/D = 2$	$M = 0.4$; $\mathrm{Re}_L \leq 1.52 \times 10^6$	LES (DSM & selective filter)	0.354×10^6 (37.8%)
Dubief and Delcayre (2000) [178]	$L/D = 4$; $L/W = 4$	$M = 0.95$; $\mathrm{Re}_L \leq 1.25 \times 10^6$	LES	Coarse
Lillberg and Fureby (2000) [179]	$L/D = 2$; $L/W = 2$	$M = 1.5$; $\mathrm{Re}_L = 60 \times 10^6$	LES (SM) & MILES	0.7×10^6
Shieh and Morris (2000) [180]	$2 \leq L/D \leq 4.4$; $L/W = 1$	$0.4 \leq M_\infty \leq 0.6$; $\mathrm{Re}_L = 0.88 \times 10^6$	DES (S-A)	1.7×10^6 (22.6%)
Sinha *et al.* (2000) [175]	$L/D = 6$	$M = 1.5$	DES ($k-\varepsilon$)	
Nichols and Nelson (2001) [181]	$L/D = 4.5$; $L/W = 4.5$	$M = 0.95$; $\mathrm{Re}_L \leq 3.75 \times 10^6$	DES (SST)	1.133×10^6
Arunajatesan *et al.* (2002) [182]	$L/D = 5.6$; $L/W = 5.6$	$M = 0.6$; $\mathrm{Re}_L = 1.45 \times 10^7$	DES ($k-\varepsilon$)	1.375×10^6 (half-model)
Hamed *et al.* (2003) [183, 184]	$L/D = 5$; $L/W = 10$	$M = 1.19$; $0.12 \times 10^6 \leq \mathrm{Re}_L \leq 1 \times 10^6$	DES (SST)	2.27×10^6 (17.5%)
Mendonça *et al.* (2003) [185]	$L/D = 5$; $L/W = 5$	$M = 0.85$; $\mathrm{Re}_L \leq 6.783 \times 10^6$	DES ($k-\varepsilon$)	1.1×10^6
Viswanathan *et al.* (2003) [186]	$L/D = 5$ (Axisymmetric)	$M = 0.4$; $\mathrm{Re}_L \leq 0.18 \times 10^6$	DES (S-A)	5.9×10^6
Cain *et al.* (1999) [187]	$L/D = 5$ (2D)	$M = 0.6$	DVM	
Sinha *et al.* (2000) [175]	$L/D = 6$	$M = 1.5$	POD	
Rowley *et al.* (2000-01) [188, 189]	$2 \leq L/D \leq 4$; $\leq L/W \leq$	$M = 0.6$; $56.8 \leq \mathrm{Re}_\theta < 68.5$	POD	
Ricot *et al.* (2002) [190]	$L/D = 1$ (2D)	$M = 0.044$	LBM	0.625×10^6 (0.004%)

[a] Optical Cavities

Table 1.7: Developments in flow control studies of weapon bay cavity flows — Passive control methods.

Method	Additive/ Manipulative	Geometry Specifications	Flow Conditions	Study
Boundary Layer Divertor	Additive	$0.056 \leq L/D \leq 0.727$	$3m/s \leq U_\infty \leq 30m/s$	Zoccola (2000) [204]
Ducts	Manipulative	$L/D = 4$ (2D)	$\mathrm{Re}_L = 0.03 \times 10^6$	Forristal and Cooper (2000) [205]
Multiple Pins	Additive	$0.2 \leq L/D \leq 8.3$; $0.71 \leq L/W \leq 16.6$	$1.8 \leq M_\infty \leq 2.6$	Smith *et al.* (1992) [206]
Porous or Slotted Walls for Passive Venting	Manipulative	$4.4 \leq L/D \leq 17.5$; $\leq L/W \leq$	$1.7 \leq M_\infty \leq 2.65$	Wilcox (c.1990s) [207]
		$6.7 \leq L/D \leq 17.5$	$0.2 \leq M_\infty \leq 0.95$	Stallings *et al.* (1994) [208]
		$3.35 \leq L/W \leq 4.375$	$5.36 \times 10^6 \leq \mathrm{Re}_L \leq 11.55 \times 10^6$	
		$L/D = 3$ (2D)	$M_\infty = 2.5$; $\mathrm{Re}_L = 1.35 \times 10^6$	Jeng and Payne (1995) [209]
		$3 \leq L/D \leq 5$; $1 \leq L/W \leq 1.67$	$M_\infty = 5$; $\mathrm{Re}/m \leq 50 \times 10^6$	Perng and Dolling (2001) [210]
Slanted/Shaped Downstream Cavity Wall	Manipulative	1/15th scale of F-111 bay	$0.95 \leq M_\infty \leq 1.3$	Clark (1979) [211]
		$L/D = 2$; $L/W = 0.24$	$\mathrm{Re}_L = 0.00672 \times 10^6$	Pereira and Sousa (1993) [212]
		$L/D = 4.5$ (2D)	$M_\infty = 0.95$; $\mathrm{Re}/m = 8 \times 10^6$	Baysal *et al.* (1994) [150]
		$5 \leq L/D \leq 10$	$0.6 \leq M_\infty \leq 1.6$	Ross and Peto (1997-98) [11, 12]
		$L/D = 5$; $L/W = 1$	$0.85 \leq M_\infty \leq 1.19$	Henderson (2000-01) [9, 143]
			$6.783 \times 10^6 \leq \mathrm{Re}_L \leq 7.348 \times 10^6$	
		$3 \leq L/D \leq 5$; $1 \leq L/W \leq 1.67$	$M_\infty = 5$; $\mathrm{Re}/m = 50 \times 10^6$	Perng and Dolling (1998-2001) [210, 213]
Slanted/Shaped Upstream Cavity Wall	Manipulative	$5 \leq L/D \leq 10$	$0.6 \leq M_\infty \leq 1.6$	Ross and Peto (1997) [11]
		$3 \leq L/D \leq 5$; $1 \leq L/W \leq 1.67$	$M_\infty = 5$; $\mathrm{Re}_L = 50 \times 10^6$	Dolling *et al.* (1998) [213]
Static Spoiler/Fences	Additive	1/15th scale of T.S.R.2 bay	$0.4 \leq M_\infty \leq 2$	Rossiter and Kurn (1963) [54]
		1/15th scale of F-111 bay	$0.95 \leq M_\infty \leq 1.3$	Clark (1979) [211]
		$L/D = 4.5$ (2D)	$M_\infty = 0.95$; $\mathrm{Re}/m = 8 \times 10^6$	Baysal *et al.* (1994) [150]
		$L/D = 2$; $L/W = 6.4$	$0.6 \leq M_\infty \leq 1.5$	Sarno and Franke (1994) [214]
		$5 \leq L/D \leq 10$	$0.6 \leq M_\infty \leq 1.6$	Ross and Peto (1997-98) [11, 12]
		$5.6 \leq L/D \leq 9$; $2.8 \leq L/W \leq 4.5$	$0.6 \leq M_\infty \leq 1.4$	Ukeiley *et al.* (2004) [215]
Unpowered Resonance Tube	Additive	$L/D = 5$; $L/W = 5$	$0.6 \leq M_\infty \leq 1.35$; $\leq \mathrm{Re}_L = 5.5 \times 10^6$	Stanek *et al.* (2000) [216]
Vortex/Cylindrical Rods or Generators	Additive	1/15th scale of F-111 bay	$0.95 \leq M_\infty \leq 1.3$	Clark (1979) [211]
		1/15th scale of F-111 bay	$0.9 \leq M_\infty \leq 1.5$	Smith *et al.* (2002) [217]
		$5.6 \leq L/D \leq 9$; $2.8 \leq L/W \leq 4.5$	$0.6 \leq M_\infty \leq 1.4$	Ukeiley *et al.* (2004) [215]

Table 1.8: Developments in flow control studies of weapon bay cavity flows — Active (open-loop and closed-loop) control methods.

Actuator	Open- or Closed-Loop?	Geometry Specifications	Flow Conditions	Study
Leading-Edge Oscillating Flaps/Spoilers	Open	$L/D = 2$; $L/W = 6.4$	$0.6 \leq M_\infty \leq 1.5$	Sarno and Franke (1994) [214]
		$8.25 \leq L/D \leq 13.49$	$0.6 \leq M_\infty \leq 1.5$	Shaw (1998) [220]
Miniature Fluidic Oscillators	Open	$L/D = 6$; $L/W = 1.71$	$0.4 \leq M_\infty \leq 0.7$	Raman *et al.* (1999) [221]
Oscillating Spoilers	Closed	$L/D = 10$	$13.9m/s \leq U_\infty \leq 45.73m/s$	Mongeau *et al.* (1998) [222]
Piezoceramic Wedge	Open	$L/D = 5$; $L/W = 5$	$0.6 \leq M_\infty \leq 1.35$; $\mathrm{Re}_L = 5.5 \times 10^6$	Stanek *et al.* (2000) [216]
Piezoelectric Flaps	Closed	$0.5 \leq L/D \leq 5$; $0.5 \leq L/W \leq 5$	$40m/s \leq U_\infty \leq 45m/s$	Cattafesta *et al.* (1997-99) [218, 223]
		$L/D = 5$; $L/W = 3$	$0.275 \leq M_\infty \leq 0.85$	Kegerise *et al.* (2002-04) [224, 225]
			$8 \times 10^6 \leq \mathrm{Re}/m = 11.4 \times 10^6$	
Pulsed Mass Injection	Open	$L/D = 2$; $L/W = 6.4$	$0.6 \leq M_\infty \leq 1.5$	Sarno and Franke (1994) [214]
		$L/D = 4.33$ (2D)	$M_\infty = 1.5$; $\mathrm{Re}_L = 55.8 \times 10^6$	Lamp and Chokani (1997) [226]
		$3 \leq L/D \leq 9$; $2.25 \leq L/W \leq 6.77$	$0.85 \leq M_\infty \leq 1.46$	Shaw (2000) [227]
		$L/D = 4.5$; $L/W = 4.5$	$M_\infty = 1.5$	Smith *et al.* (2000) [219]
		$5 \leq L/D \leq 9$; $1.67 \leq L/W \leq 3$	$M_\infty = 2$; $3.83 \times 10^6 \leq \mathrm{Re}_L \leq 6.9 \times 10^6$	Bueno *et al.* (2002) [228]
Steady Jet Blowing or Continuous Mass Injection	Open	$L/D = 2$; $L/W = 6.4$	$0.6 \leq M_\infty \leq 1.5$	Sarno and Franke (1994) [214]
		$L/D = 4.33$; $L/W = 4.33$	$0.5 \leq M_\infty \leq 1.8$; $\mathrm{Re}_L \leq 9.21 \times 10^6$	Vakili *et al.* (1995) [229]
		$4 \leq L/D \leq 4.33$; $L/W = 3$	$0.15 \leq M_\infty \leq 1.5$	Lamp and Chokani (1997-99)
			$5.9 \times 10^6 \leq \mathrm{Re}/m \leq 55.8 \times 10^6$	[37, 226]
		1/5th scale of F-111 Bay	$0.95 \leq M_\infty \leq 1.3$	Grove *et al.* (2000) [203]
		$L/D = 5$ (2D)	$M_\infty = 0.85$; $\mathrm{Re}_L = 6.783 \times 10^6$	Festzy *et al.* (2000) [230]
		$5 \leq L/D \leq 9$; $1.67 \leq L/W \leq 3$	$M_\infty = 2$; $3.83 \times 10^6 \leq \mathrm{Re}_L \leq 6.9 \times 10^6$	Bueno *et al.* (2002) [228]
Synthetic Jets	Closed	$L/D = 5$; $L/W = 3$	$0.275 \leq M_\infty \leq 0.45$	Cabell *et al.* (2002) [231]
		$2 \leq L/D \leq 5$	$0.1 \leq M_\infty \leq 0.55$	Williams (2000-03) [232–236]
		$L/D = 4$; $L/W = 1$	$0.25 \leq M_\infty \leq 0.5$	Samimy *et al.* (2004) [237]
Thermal Excitation	Open	Axiysmmetric Cavities	$16m/s < U_\infty < 27m/s$	Gharib (1983-87) [61, 72]
Unsteady Jet Blowing	Open	$L/D = 4$; $L/W = 3$	$M_\infty = 0.15$; $\mathrm{Re}_L = 0.906 \times 10^6$	Lamp and Chokani (1999) [37]
		$L/D = 5$ (2D)	$M_\infty = 0.85$; $\mathrm{Re}_L \leq 6.783 \times 10^6$	Festzy *et al.* (2000) [230]

Chapter 2

Mathematical Model

2.1 CFD Solver

All computations were performed using the Parallel Multi-Block (PMB) flow solver [5] developed at the University of Glasgow. The flow solver has been continually revised and updated over a number of years and has been successfully applied to a variety of problems including cavity flows, hypersonic film cooling, spiked bodies, flutter and delta wing flows amongst others. The PMB code is a 3D multi-block structured solver which solves the Navier-Stokes equations in the 3D Cartesian frame of reference. The Navier-Stokes equations consist of Partial Differential Equations (PDEs) describing the laws of conservation for:

- Mass (continuity equation).
- Momentum (Newton's 2nd Law).
- Energy (1st Law of Thermodynamics).

The continuity equation simply states that the mass must be conserved. In Cartesian coordinates, x_i, this is written as

$$\frac{\partial \rho}{\partial t} + \frac{\partial (\rho u_i)}{\partial x_i} = 0 \tag{2.1}$$

where ρ is the density of the fluid, t is the time and u_i is the velocity vector. In the above, tensor notation is used, which implies summation for repeated indices.

The second conservation principle states that momentum must be conserved. It is written in Cartesian coordinates as

$$\frac{\partial (\rho u_i)}{\partial t} + \frac{\partial (\rho u_i u_j)}{\partial x_j} = \rho f_i - \frac{\partial p}{\partial x_i} + \frac{\partial \tau_{ij}}{\partial x_j} \tag{2.2}$$

where f_i represents the body forces, p the pressure and τ_{ij} the viscous stress tensor, which is defined as

$$\tau_{ij} = \mu \left[\left(\frac{\partial u_i}{\partial x_j} + \frac{\partial u_j}{\partial x_i} \right) - \frac{2}{3} \delta_{ij} \frac{\partial u_k}{\partial x_k} \right] \tag{2.3}$$

μ is the molecular viscosity and δ_{ij} represents the Kronecker delta, which is defined as

$$\delta_{ij} = \begin{cases} 1 & \text{if i=j} \\ 0 & \text{otherwise} \end{cases} \tag{2.4}$$

The third principle can be written in Cartesian coordinates as

$$\frac{\partial \rho E}{\partial t} + \frac{\partial}{\partial x_j}\left[u_i(\rho E + p)\right] - \frac{\partial}{\partial x_j}\left(u_i \tau_{ij} - q_j\right) = 0. \tag{2.5}$$

where E is the total energy of the fluid, defined as

$$E = \rho\left[e + \frac{1}{2}u_i u_i\right] \tag{2.6}$$

and e is the specific internal energy with $u_i u_i$ representing the kinetic energy.

The heat flux vector, q_i, is calculated using Fourier's Law

$$q_i = -k\frac{\partial T}{\partial x_i} \tag{2.7}$$

where k is the heat transfer coefficient and T is the temperature of the fluid.

These three laws of conservation can be combined and written in Equation 2.8, which is referred to as the Navier-Stokes equation of viscous flow. For brevity, vector notation is used

$$\frac{\partial \mathbf{W}}{\partial t} + \frac{\partial\left(\mathbf{F}^i + \mathbf{F}^v\right)}{\partial x} + \frac{\partial\left(\mathbf{G}^i + \mathbf{G}^v\right)}{\partial y} + \frac{\partial\left(\mathbf{H}^i + \mathbf{H}^v\right)}{\partial z} = 0 \tag{2.8}$$

where $\mathbf{W}$ is the vector of conserved variables and is defined by

$$\mathbf{W} = (\rho, \rho u, \rho v, \rho w, \rho E)^T \tag{2.9}$$

with the variables ρ, u, v, w, p and E having their usual meaning of density, the three components of velocity, pressure and total energy, respectively. The superscripts i and v in Equation 2.8 denote the inviscid and viscid components of the flux vectors $\mathbf{F}$ (in the x-direction), $\mathbf{G}$ (in the y-direction) and $\mathbf{H}$ (in the z-direction). The inviscid flux vectors, $\mathbf{F}^i$, $\mathbf{G}^i$ and $\mathbf{H}^i$, are given by

$$\begin{aligned} \mathbf{F}^i &= \left(\rho u, \rho u^2 + p, \rho uv, \rho uw, u(\rho E + p)\right)^T, \\ \mathbf{G}^i &= \left(\rho v, \rho uv, \rho v^2 + p, \rho vw, v(\rho E + p)\right)^T, \\ \mathbf{H}^i &= \left(\rho w, \rho uw, \rho vw, \rho w^2 + p, w(\rho E + p)\right)^T. \end{aligned} \tag{2.10}$$

while the viscous flux vectors, $\mathbf{F}^v$, $\mathbf{G}^v$ and $\mathbf{H}^v$, contain terms for the heat flux and viscous forces exerted on the body and can be represented by

$$\begin{aligned} \mathbf{F}^v &= \frac{1}{\mathrm{Re}}\left(0, \tau_{xx}, \tau_{xy}, \tau_{xz}, u\tau_{xx} + v\tau_{xy} + w\tau_{xz} + q_x\right)^T, \\ \mathbf{G}^v &= \frac{1}{\mathrm{Re}}\left(0, \tau_{xy}, \tau_{yy}, \tau_{yz}, u\tau_{xy} + v\tau_{yy} + w\tau_{yz} + q_y\right)^T, \\ \mathbf{H}^v &= \frac{1}{\mathrm{Re}}\left(0, \tau_{xz}, \tau_{yz}, \tau_{zz}, u\tau_{xz} + v\tau_{yz} + w\tau_{zz} + q_z\right)^T. \end{aligned} \tag{2.11}$$

where the term τ_{ij} represents the viscous stress tensor and q_i the heat flux vector.

Although the Navier-Stokes equations completely describe turbulent flows, the large number of temporal and spatial turbulent scales associated with high Reynolds numbers make it difficult to resolve all the turbulent scales computationally. In such circumstances, the number of turbulent scales are reduced by time averaging the Navier-Stokes equations to give the Reynolds-Averaged Navier-Stokes equations (RANS). This results in additional unknowns (called Reynolds stresses) which must be modelled. The viscous stress tensor mentioned in Equation 2.11 is then approximated by the Boussinesq hypothesis, more description of which is provided in the following sections.

The PMB flow solver uses a cell-centred finite volume approach combined with an implicit dual-time method. In this manner, the solution marches in pseudo-time for each real time-step to achieve fast convergence. According to the finite volume method, the RANS equations can be discretised for each cell by

$$\frac{d}{dt}\left(\mathbf{W}_{i,j,k}\mathscr{V}_{i,j,k}\right)+\mathbf{R}_{i,j,k}=0. \tag{2.12}$$

where $\mathscr{V}_{i,j,k}$ denotes the cell volume and $\mathbf{R}_{i,j,k}$ represents the flux residual.

The implicit dual-time method proposed by Jameson [238] is used for time-accurate calculations. The residual is redefined to obtain a steady state equation which can be solved using acceleration techniques. The following system of equations are solved in the implicit scheme during the time integration process

$$\frac{\Delta V\mathbf{W}^{m+1}_{i,j,k}-\Delta V\mathbf{W}^{m}_{i,j,k}}{\Delta V\Delta\tau}\frac{\Delta V\mathbf{W}^{n+1}_{i,j,k}-\Delta V\mathbf{W}^{n}_{i,j,k}}{\Delta V\Delta t}=\mathbf{R}^{n+1}_{i,j,k} \tag{2.13}$$

where ΔV is the change in cell volume, $\Delta\tau$ is the pseudo time-step increment and Δt is the real time-step increment. The flux residual $\mathbf{R}^{n+1}_{i,j,k}$ is approximately defined by

$$\mathbf{R}^{n+1}_{i,j,k}\approx\mathbf{R}^{n}_{i,j,k}+\frac{\partial\mathbf{R}^{n}_{i,j,k}}{\partial\mathbf{W}^{n}_{i,j,k}}\left(\mathbf{W}^{n+1}_{i,j,k}-\mathbf{W}^{n}_{i,j,k}\right) \tag{2.14}$$

By substituting Equation 2.14 into Equation 2.13, the linear system can be approximated to

$$\left(\frac{1}{\Delta t}+\frac{\partial\mathbf{R}^{n}}{\partial\mathbf{W}}\right)\Delta\mathbf{W}=-\mathbf{R}^{n} \tag{2.15}$$

where the subscripts i,j,k have been dropped for clarity and ΔW is used for $\left(\mathbf{W}^{n+1}_{i,j,k}-\mathbf{W}^{n}_{i,j,k}\right)$.

Osher's upwind scheme [239] is used to resolve the convective fluxes although Roe's flux-splitting scheme [240] is also available. The MUSCL variable extrapolation method is employed in conjunction to formally provide second-order accuracy. The van Albada limiter is also applied to remove any spurious oscillations across shock waves. The central differencing spatial discretisation method is used to solve the viscous terms. The non-linear system of equations that is generated as a result of the linearisation is then solved by integration in pseudo-time using a first-order backward difference. A Generalised Conjugate Gradient (GCG) method is then used in conjunction with a Block Incomplete Lower-Upper (BILU) factorisation as a pre-conditioner to solve the linear system of equations, which is obtained from a linearisation in pseudo-time.

The flow solver can be used in serial or parallel mode. To obtain an efficient parallel method based on domain decomposition, different methods are applied to the flow

solver [241]. An approximate form of the flux Jacobians resulting from the linearisation in pseudo-time is used which reduces the overall size of the linear system by reducing the number of non-zero entries. Between the blocks of the grid, the BILU factorisation is also decoupled thereby reducing the communication between processors. Each processor is also allocated a vector that contains all the halo cells for all the blocks in the grid. Message Passing Interface (MPI) is used for the communication between the processors in parallel. Most computations undertaken for the cavity flow analysis have been performed on the Beowulf Pentium 4 100-processor workstations of the CFD Laboratory at the University of Glasgow. For very large grids, however, calculations were conducted on different supercomputing clusters such as Computer Services for Academic Research (CSAR) [242] in Manchester, UK and HPCx [243] in Edinburgh, UK, and the necessary porting of the PMB code onto these facilities performed. The CSAR system comprises five primary resources which consist of a combination of SGI Origin and Altix systems with MIPS R12000 and Itanium 2 processors, respectively, providing a total of 1168 processors. The HPCx system is based on IBM's AIX operating system and comprises 50 IBM POWER4+ Regatta nodes, i.e. 1600 processors, delivering a peak performance of 10.8 TeraFlops.

A number of linear and non-linear statistical turbulence models have been implemented into PMB. Large-Eddy Simulation (LES) and Detached-Eddy Simulation (DES) formulations were originally implemented into the code for this project [244]. Both methods have since then been used for various other applications. At the moment, the standard Smagorinsky sub-grid scale (SGS) model is used for LES while the one-equation Spalart-Allmaras [192] turbulence model is used to realise the turbulent properties for DES computations. Options for DES with two-equation Wilcox $k-\omega$ [138] and Menter's Shear-Stress Transport (SST) [245] turbulence models are also available. All these turbulence models and indeed the simulation techniques are described in greater detail in the following sections.

2.2 General Description of Turbulence and its Modelling

Turbulent flows are irregular in the sense that they contain structures which show rapid fluctuations in time and space. A broad range of scales are observed to exist at high Reynolds numbers where turbulence develops as an instability of the laminar flow. Starting with the laminar flow, fluid layers slide smoothly past each other and the molecular viscosity dampens any high-frequency small-scale instability. At high Reynolds number, the flow reaches a periodic state. The character of the flow also changes and becomes more diffusive and dissipative. This flow has increased mixing friction, heat transfer rate and spreading rate. Boundary layers consequently become thicker and less susceptible to separation.

The non-linearity of the Navier-Stokes equations leads to various interactions between the turbulent fluctuations of different wavelengths and directions. Wavelengths extend from a maximum comparable to the width of the flow to a minimum fixed by viscous dissipation of energy. A key process that spreads the motion over wide range of wavelengths is called vortex stretching. Turbulent structures in the flow gain energy if the vortex elements are primarily orientated in a direction which allow the mean velocity gradients to stretch them. This mechanism is called **production of turbulence**. The kinetic energy of the turbulent structures is then convected, diffused and dissipated.

Most of the energy is carried by the large scale structures, the orientation of which is sensitive to the mean flow. The large eddies cascade energy to the smaller ones via stretching. Small eddies have less pronounced preference in their orientation and statistically appear to be isotropic. For the shortest wavelengths, energy is dissipated by viscosity. This description corresponds to what is known as **isotropic turbulence**. For this flow, the ratio of the largest to smaller scale increases with Reynolds number.

If the unsteady Navier-Stokes equations are used to calculate the flow, a vast range of length and time scales would have to be computed. This would require a very fine grid and a very high resolution in time. This approach known as **Direct Numerical Simulation of turbulence (DNS)** is by today's computing speeds applicable only to flows at very low Reynolds number. One technique called **Large-Eddy Simulation** explicitly resolves the scales away from the wall and exploits modelling in the near-wall regions. A sub-grid scale (SGS) model is used to model the smaller scales which are assumed to be more isotropic. Although less computationally intensive than DNS, this is still expensive, especially for higher Reynolds number flows.

A turbulence model therefore needs to account for some part of the fluctuating motion in order to keep the computing cost down. The optimum model should therefore be simple to implement, general and derived out of the flow physics. It is equally important that the model is computationally stable and co-ordinate invariant. These statistical turbulence models are applied to a special form of the equations of motion called the Reynolds-Averaged Navier-Stokes (RANS) equations. These are obtained by Reynolds averaging the Navier-Stokes equations.

2.3 Reynolds Averaging

In a turbulent flow, the fields of pressure, velocity, temperature and density vary randomly in time. Reynold's approach involves separating the flow quantities into stationary and random parts. The quantities are then presented as a sum of the mean flow value and the fluctuating part

$$\phi = \overline{\phi} + \phi' \tag{2.16}$$

This formulation is then inserted into the conservation equations and a process known as **Reynolds averaging** is performed. Three averaging methods are possible:

- Time averaging.
- Spatial averaging.
- Ensemble averaging.

2.3.1 Time Averaging

Time averaging is the most common averaging method. It can be used only for statistically stationary turbulent flows, i.e. flows not varying with time on the average. For such flows, the mean flow value is defined as

$$\overline{u_i} = \lim_{T\to\infty} \frac{1}{T} \int_i^{i+T} u_i(t)\,\mathrm{d}t \tag{2.17}$$

In practice, $T \to \infty$ means that the integration time T needs to be long enough relative to the maximum period of the assumed fluctuations.

2.3.2 Spatial Averaging

Spatial averaging can be applied to homogeneous turbulence, which is a type of turbulent flow that is uniform in all directions, on average. In this case, a parameter is averaged over all the spatial directions by performing a volume integral. The mean flow value is then defined as

$$\overline{u_i} = \lim_{V\to\infty} \frac{1}{V} \int\int\int_V u_i(x,t)\,\mathrm{d}t \tag{2.18}$$

where V represents the volume of the domain.

2.3.3 Ensemble Averaging

The most general type of averaging is called ensemble averaging and is applicable to flows that decay in time, for instance. This method of averaging is similar to time-averaging but rather than dividing by the integration time, T, the mean flow value is obtained by taking a sum over all the measurements or samples, N, and is defined by

$$\overline{u_i} = \lim_{N\to\infty} \frac{1}{N} \sum_{n=1}^{N} u_i(x,t) \tag{2.19}$$

For turbulent flows that are both stationary and homogeneous, all the three types of averages mentioned above are assumed to be equal. This assumption is referred to as the **ergodic hypothesis**.

By time-averaging the mass, momentum and energy equations, the Reynolds-Averaged Navier-Stokes (RANS) equations are obtained. The continuity equation remains the same since it is linear with respect to velocity. However, extra terms appear in the momentum and energy equations due to the non-linearity of the convection term. These extra terms are called the **Reynolds Stresses**, τ_{ij}^R, and are defined in tensor notation as being equivalent to $-\rho\overline{u_i'u_j'}$. The time-averaged momentum equation then takes the form

$$\frac{\partial(\rho u_i)}{\partial t} + \frac{\partial(\rho u_i u_j)}{\partial x_i} = \rho f_i - \frac{\partial p}{\partial x_i} + \frac{\partial}{\partial x_j}\left(\tau_{ij} + \tau_{ij}^R\right) \tag{2.20}$$

where the overbar has been dropped from the mean values for clarity. A similar result is obtained for the energy equation (Equation 2.5). The main problem in turbulence modelling involves calculating the Reynolds stresses from the known mean quantities. One common approach is based on Boussinesq's approximation.

2.4 Boussinesq-Based Models

The Boussinesq approximation is based on an analogy between viscous and Reynolds stresses and expresses the Reynolds stresses as a product of the eddy viscosity (μ_t) and the velocity gradient. The Boussinesq's eddy viscosity hypothesis states that

$$-\rho\overline{u_i'u_j'} = \mu_t\left[\left(\frac{\partial u_i}{\partial x_j}+\frac{\partial u_j}{\partial x_i}\right)-\frac{2}{3}\delta_{ij}\frac{\partial u_k}{\partial x_k}\right]-\frac{2}{3}\rho\delta_{ij}k \tag{2.21}$$

where k represents the specific kinetic energy of the fluctuations and is given by

$$k \equiv \frac{u_i'u_i'}{2} \tag{2.22}$$

The key idea behind Boussinesq's hypothesis is that the Reynolds stresses can be calculated as a product of the dynamic eddy-viscosity, μ_t, and the strain-rate tensor of the mean flow, i.e.

$$-\rho\overline{u_i'u_j'} = 2\mu_t S_{ij} - \frac{2}{3}\delta_{ij}k \tag{2.23}$$

where

$$S_{ij} = \frac{1}{2}\left(\frac{\partial u_i}{\partial x_j}+\frac{\partial u_j}{\partial x_i}-\frac{2}{3}\delta_{ij}\frac{\partial u_k}{\partial x_k}\right) \tag{2.24}$$

Eddy viscosity, μ_t, is a scalar and consequently the Reynolds stress components are linearly proportional to the mean strain-rate tensor. What is implied here is that compressibility plans a secondary rate in the development of the turbulent flow-field. According to Morkovin's hypothesis [246], compressibility affects turbulence only at hypersonic speeds.

To compute μ_t, further modelling is required and it is at this point that turbulence models come into play. Turbulence models are classified into categories based on the number of transport equations required to calculate μ_t. According to the number of transport equations needed for the calculation of the eddy viscosity, the Boussinesq-based models are classified as:

- **Algebraic** or **zero-equation** models, such as the Cebeci-Smith [122] and Baldwin-Lomax [123] models.
- **One-equation** models, such as the Spalart-Allmaras [192] and Baldwin-Barth [247] models.
- **Two-equation** models, such as the $k-\omega$ [138], $k-\varepsilon$ [133], SST [245] and $k-g$ [248] models.
- **Multi-equation** models: three-equation [249–251], four-equation [252], five-equation [253, 254] and multiple time-scale [255–257] models.

An additional family of models solves equations for all components of the Reynolds stress tensor. These are also known as **Reynolds Stress Models (RSM)**, **second-order closures** or **second-moment closures**.

2.5 Viscosity-Dependent Parameters

Non-dimensionalised wall distances for turbulent flow, y^*, and non-turbulent flow, y^+, are defined by the following

$$y^* \equiv \frac{y_n k^{1/2}}{\nu}, \qquad y^+ \equiv \frac{y_n u_\tau}{\nu}, \tag{2.25}$$

where y_n is the distance from the nearest wall, $u_\tau \equiv \sqrt{\tau_w/\rho}$ is the frictional velocity and τ_w represents the dynamic wall shear stress. Turbulent Reynolds numbers for the $k-\varepsilon$ model (denoted by R_t) and for the $k-\omega$ model (denoted by R_ω) are given by the following equation

$$R_t \equiv \frac{k^2}{\nu\varepsilon}, \qquad R_\omega \equiv \frac{k}{\nu\omega}. \tag{2.26}$$

2.6 One-Equation Models

This type of turbulence model was designed to improve the ability of algebraic models to account for the convection and diffusion of turbulence. This was accomplished by employing an additional transport equation, usually for the realisation of the kinetic energy of turbulence, k . The general form of this transport equation takes the following form

$$\frac{\partial k}{\partial t} + u_j \frac{\partial k}{\partial x_j} = \tau_{ij}\frac{\partial u_i}{\partial x_j} - \varepsilon + \frac{\partial}{\partial x_j}\left[\frac{\mu}{\rho}\frac{\partial k}{\partial x_j} - \frac{1}{2}\overline{u_i' u_i' u_j'} - \frac{1}{\rho}\overline{p' u_j'}\right] \tag{2.27}$$

The first term in Right-Hand Side (RHS) ($\tau_{ij}\frac{\partial u_i}{\partial x_j}$) represents the **production of turbulence**. From the terms in the square brackets, the first ($\frac{\mu}{\rho}\frac{\partial k}{\partial x_j}$) is the **molecular diffusion** term, the second ($\overline{u_i' u_i' u_j'}$) is the **turbulent flux of the turbulent kinetic energy** and the third ($\frac{1}{\rho}\overline{p' u_j'}$) is the **pressure diffusion** term, which is usually neglected due to its small contribution. The term ε is the **dissipation rate** of k per unit mass of fluid, and is usually defined by

$$\varepsilon = \frac{\mu}{\rho}\overline{\frac{\partial u_i'}{\partial x_k}\frac{\partial u_i'}{\partial x_k}} \tag{2.28}$$

Eddy viscosity for one-equation turbulence models is usually calculated by

$$\mu_t = \rho C_\mu l_{mix}\sqrt{k} \tag{2.29}$$

where C_μ is a coefficient specific to the model.

Baldwin-Barth [247] and Spalart-Allmaras [192] are the most common one-equation models. History effects of turbulent kinetic energy are better accounted for in one-equation models than algebraic models due to the additional differential equation, which can be particularly important in non-equilibrium flows. Although one-equation models are tuned for aerodynamic flows with adverse pressure gradients and transonic flow conditions, they also work well for flow regions where the mean velocity gradient is zero. Due to their modular design, one-equation models are also very easy to manipulate. For instance, in the case of the Spalart-Allmaras model described in the next section, better prediction of near-wall effects and transition is obtained by adding the third and fourth terms in Equation 2.32. This modular design of one-equation models has added to their popularity in

aerospace applications. The disadvantage of such models is that they include no mechanism for the omputation of the length scale, l. Thus, highly turbulent flows are difficult to predict. In that respect, one-equation models are still similar to algebraic models.

Many modifications have been undertaken to one-equation turbulence models, especially to the Spalart-Allmaras model, with the view of extending their range of applications. Extensions to compressible supersonic flows over complex configurations have been addressed by Deck [258] while rotational and curvature effects to account for the change on turbulent shear stress have been addressed by Spalart and Shur [259]. The Spalart-Allmaras model has also been modified to be used in DES computations [191].

2.6.1 Spalart-Allmaras Model

The one-equation Spalart-Allmaras turbulence model [192] solves a transport equation for the eddy viscosity directly. The kinematic eddy viscosity, (ν_t), in the Spalart-Allmaras model is calculated by

$$\nu_t = \tilde{\nu} \cdot f_{v1} \tag{2.30}$$

where

$$f_{v1} = \frac{\chi^3}{\chi^3 + c_{v1}^3} \qquad \text{and} \qquad \chi = \frac{\tilde{\nu}}{\nu} \tag{2.31}$$

In the above equations, and hereafter, the term f refers to a function, c refers to a constant, ν is the molecular viscosity and $\tilde{\nu}$ is the undamped eddy viscosity that obeys the following transport equation

$$\begin{aligned} \frac{D\tilde{\nu}}{Dt} &= c_{b1}(1-f_{t2})\tilde{S}\tilde{\nu} + \frac{1}{\sigma}\left(\nabla\cdot((\nu+\tilde{\nu})\nabla\tilde{\nu}) + c_{b2}(\nabla\tilde{\nu})^2\right) \\ &\quad - \left(c_{w1}f_w - \frac{c_{b1}}{\kappa^2}f_{t2}\right)\left(\frac{\tilde{\nu}}{d}\right)^2 + f_{t1}\Delta U^2 \end{aligned} \tag{2.32}$$

The first term on the right-hand side is the production term, the second is the diffusion term and the third is the near-wall term. The last term models transition downstream of tripping. The subscript b stands for *basic*, w for *wall* and t for *trip*. The parameter σ represents the turbulent Prandtl number and d is the wall-distance.

The term $\tilde{S}$ in Equation (2.32) is defined by the following equation, where S is the magnitude of vorticity

$$\tilde{S} = S + \frac{\tilde{\nu}}{k^2 d^2} f_{v2}, \qquad f_{v2} = 1 - \frac{\chi}{1+\chi f_{v1}} \tag{2.33}$$

The function f_w in Equation (2.32) is given by

$$f_w = g\left(\frac{1+c_{w3}^6}{g^6+c_{w3}^6}\right)^{1/6}, \qquad g = r + c_{w2}\left(r^6 - r\right), \qquad r = \frac{\tilde{\nu}}{\tilde{S}k^2d^2} \tag{2.34}$$

For large r, the function f_w approaches a constant value. Values for r where this occurs can be truncated to approximately 10. The wall boundary condition is satisfied where $\tilde{\nu} = 0$. In the free-stream, 0 is the best value to use for the working variable $(\tilde{\nu})$, provided that numerical errors do not push $\tilde{\nu}$ to negative values near the edge of the boundary

layer (the exact solution cannot go negative). Values below $\nu/10$ are also acceptable. The same applies to the initial condition. The f_{t2} function is defined by

$$f_{t2} = c_{t3} \cdot e^{-c_{t4} \cdot \chi^2} \tag{2.35}$$

The trip function f_{t1} is defined as

$$f_{t1} = c_{t1} g_t \cdot e^{-c_{t2} \frac{\omega_t^2}{\Delta U^2} \left(d^2 + g_t^2 d_t^2 \right)}. \tag{2.36}$$

where d_t is the distance from the field point to the trip, ω_t is the wall vorticity at the trip, ΔU is the difference between the velocity at the field point and that at the trip and $g_t = \min(0.1, \Delta U / \omega_t \Delta x)$, in which Δx is the grid spacing along the wall at the trip.

2.6.2 Model Coefficients

Values used in PMB for the Spalart-Allmaras turbulence model constants are given in Table 2.1.

Table 2.1: Closure coefficients for the Spalart-Allmaras model

Coefficient	c_{b1}	σ	c_{b2}	κ	c_{w2}	c_{w3}	c_{v1}	c_{t1}	c_{t2}	c_{t3}	c_{t4}
Value	0.1355	2/3	0.622	0.41	0.3	2	7.1	1	2	1.1	2

The constant c_{w1} is defined as

$$c_{w1} = \frac{c_{b1}}{k^2} + \frac{(1 + c_{b2})}{\sigma} = 3.2391. \tag{2.37}$$

A value of 2/3 has been used for the turbulent Prandtl number, σ.

2.7 Two-Equation Models

By far the most popular type of turbulence model used is of the two-equation type. Two-equation models are 'complete', i.e. can be used to predict properties of a given flow with no prior knowledge of the turbulence structure or flow geometry. Two transport equations are used for the calculation of the turbulent kinetic energy, k , and turbulence length scale, l, or a function of it. The choice of the 2nd variable is arbitrary and many proposals have been presented. The most popular involves using:

- ε — dissipation rate of turbulence.
- ω — k-specific dissipation rate.
- τ — turbulent time-scale.

Table 2.2: Different types of two-equation turbulence models and the corresponding second variable used

Two-Equation Model	Equation 2nd Variable Used	
Kolmogorov (c. 1942) [260]	$k^{1/2}l^{-1}$	ω (Frequency Length Scale)
Rotta (c. 1950)	l	
Harlow-Nakayama (1968) [261]	$k^{3/2}l^{-1}$	ε (Energy Dissipation Rate)
Spalding (1969) [262]	kl^{-2}	ω'^2 (Vorticity fluctuations squared)
Speziale (1992) [263]	$lk^{-1/2}$	τ (Time-Scale)
Nee	kl	kl (k times length scale)
Harlow-Nakayama	$lk^{-1/2}$	ν_t (Eddy viscosity)

A description of the different types of two-equation models is provided in Table 2.2. As well as indicating the variable used for the second transport equation, Table 2.2 includes the equation used to calculate the eddy viscosity.

One of the most widely used two-equation turbulence models is the $k-\varepsilon$ model. One of the original versions of this model was developed by Jones and Launder [133] in 1972. The turbulent scale in the $k-\varepsilon$ model is calculated using a second transport equation for the turbulent dissipation rate, ε. The eddy viscosity for the $k-\varepsilon$ model is typically derived from

$$\mu_T = C_\mu \rho \frac{k^2}{\varepsilon} \tag{2.38}$$

where C_μ is the model coefficient. The advantage of the $k-\varepsilon$ model is that it performs well for attached flows with thin shear layers and jets but fails to predict the correct flow behaviour in many flows with adverse pressure gradients, extended separated flow regions, swirl, buoyancy, curvature secondary flows and unsteady flows.

The other class of two-equation turbulence models that is widely used is the $k-\omega$ model. In 1988, Wilcox [138] developed the famous $k-\omega$ model originally conceived by Kolmogorov. The $k-\omega$ model is similar to the $k-\varepsilon$ model but instead uses the k -specific dissipation rate as a second variable to compute the turbulent length scale. The eddy viscosity is obtained by

$$\mu_T = \rho \frac{k}{\omega} \tag{2.39}$$

Although the $k-\omega$ model provides better performance in adverse pressure gradient flows, it suffers largely from the same problems as the $k-\varepsilon$ model. Hybrid versions of the $k-\omega$ and $k-\varepsilon$ models called the Baseline $k-\omega$ and SST models were later introduced by Menter [245]. These, in particular the SST version, perform well in separated flows. The idea behind the Baseline $k-\omega$ model is to exploit the robust and accurate formulation of the $k-\omega$ model near the wall but to also take advantage of the lack of sensitivity to free-stream values of the $k-\varepsilon$ model away from the wall. Menter [245] achieved this by transforming the $k-\varepsilon$ model into the same format as the $k-\omega$ formulation. This process generated an additional cross-diffusion parameter in the ω transport equation. For the SST model [245], the idea was to improve the Baseline $k-\omega$ model by including terms to account for the transport of the principal shear stress. This term is incorporated in Reynolds Stress Models (RSM) and was also applied in the Johnson-King model [264]. Its importance was realised based on the significantly improved results for adverse pressure gradient flows [245].

2.7.1 Model Equations: Linear $k-\omega$ Model

Mathematical formulations of the different types of the linear $k-\omega$ two-equation turbulence models discussed in the previous sections are described here. More information on the $k-\varepsilon$ and $k-g$ models can be obtained from Ref. [244].

Since the introduction of the linear $k-\omega$ model by Wilcox in 1988 [138], the other notable modification to the $k-\omega$ model came from Menter in 1994 [245] who proposed the hybridisation of the $k-\omega$ model with the $k-\varepsilon$ model, as described previously. Table 2.3 lists the four notable versions of the $k-\omega$ models and further describes if they include parameters to compute the low Reynolds number properties.

Table 2.3: Different types of linear $k-\omega$ turbulence models

Type of Model	Low-Re
Wilcox (1988) [138]	Yes
Wilcox (1994) [265]	Yes
Menter (1994) [245] — (i) Baseline Model	Yes
Menter (1994) [245] — (ii) SST Model	Yes

Turbulence transport equations used in the formulation of the $k-\omega$ models are given by the following.

$$\frac{\partial}{\partial t}(\rho k)+\frac{\partial}{\partial x_j}(\rho U_j k)=\frac{\partial}{\partial x_j}\left[\left(\mu+\frac{\mu_t}{\sigma_k}\right)\frac{\partial k}{\partial x_j}\right]+\rho\left(P-\beta^*\omega k\right) \tag{2.40}$$

$$\frac{\partial}{\partial t}(\rho\omega)+\frac{\partial}{\partial x_j}(\rho U_j\omega)=\frac{\partial}{\partial x_j}\left[\left(\mu+\frac{\mu_t}{\sigma_\omega}\right)\frac{\partial\omega}{\partial x_j}\right]+\rho\left(\frac{\alpha}{\nu_t}P-\frac{\beta}{\beta^*\omega^2}\right)+\rho S_l \tag{2.41}$$

In the transport equation for k and ω above, the production of turbulence, P, and the dissipation rate specific to k , P_ω, is defined by

$$P_k=\tau_{ij}^R\frac{\partial u_i}{\partial x_j}, \qquad P_\omega=\rho\frac{\alpha}{\nu_t}P_k. \tag{2.42}$$

Values for the coefficients used in all the four types of linear $k-\omega$ models discussed here are given in the Tables 2.4 and 2.5.

Menter's models [245] are constructed as a 'blend' of the $k-\omega$ and $k-\varepsilon$ models. Here the $k-\varepsilon$ model is phrased in the same form as the $k-\omega$ model so as to exploit its independence of free-stream values. Blending of the $k-\varepsilon$ and $k-\omega$ model values for α, β, σ_k^{-1} and σ_ω^{-1} is (in this notation) given by the following equation

$$B\begin{pmatrix}a\\b\end{pmatrix}\equiv F_1 a+(1-F_1)b. \tag{2.43}$$

The blending function is defined by

$$F_1=\tanh\left(\arg_1^4\right), \tag{2.44}$$

Table 2.4: Values of constants used in linear $k-\omega$ models (continued)

Type of Model	α^*	β^*	α	β
Wilcox (1988) [138]	1	$\frac{9}{100}$	$\frac{5}{9}$	$\frac{3}{40}$
Wilcox (1994) [265]	$\frac{\frac{1}{40}+\frac{R_\omega}{6}}{1+\frac{R_\omega}{6}}$	$\frac{9}{100}\frac{\frac{5}{18}+\left(\frac{R_\omega}{8}\right)^4}{1+\left(\frac{R_\omega}{8}\right)^4}$	$\frac{5}{9}\frac{\frac{1}{10}+\frac{R_\omega}{2.7}}{1+\frac{R_\omega}{2.7}}$	$\frac{3}{40}$
Menter (1994) [245] *(Baseline)*	1	0.09	$B\begin{pmatrix}0.553\\0.440\end{pmatrix}$	$B\begin{pmatrix}0.075\\0.083\end{pmatrix}$
Menter (1994) [245] *(SST)*	$\min\left(1,\frac{0.31}{F_2}\frac{\omega}{w}\right)$	0.09	$B\begin{pmatrix}0.553\\0.440\end{pmatrix}$	$B\begin{pmatrix}0.075\\0.083\end{pmatrix}$

Table 2.5: Values of constants used in linear $k-\omega$ models (concluded)

Type of Model	σ_k	σ_ω	S_l
Wilcox (1988) [138]	2	2	0
Wilcox (1994) [265]	2	2	0
Menter (1994) [245]*(Baseline)*	$\frac{1}{B\begin{pmatrix}0.5\\1.0\end{pmatrix}}$	$\frac{1}{B\begin{pmatrix}0.5\\0.856\end{pmatrix}}$	$B\begin{pmatrix}0\\\frac{1.71}{\omega}\nabla k\cdot\nabla\omega\end{pmatrix}$
Menter (1994) [245]*(SST)*	$\frac{1}{B\begin{pmatrix}0.85\\1.0\end{pmatrix}}$	$\frac{1}{B\begin{pmatrix}0.5\\0.856\end{pmatrix}}$	$B\begin{pmatrix}0\\\frac{1.71}{\omega}\nabla k\cdot\nabla\omega\end{pmatrix}$

where

$$arg_1 = min\left[\max\left(\frac{k^{1/2}}{\beta^*\omega y},\frac{500\nu}{y_n^2\omega}\right),\frac{2k\omega}{y_n^2\max\left(\nabla k\cdot\nabla\omega,0.0\right)}\right]. \tag{2.45}$$

The SST model places an additional vorticity-dependent limiter on the shear stress

$$F_2 = \tanh\left(arg_2^2\right), \qquad arg_2 = \max\left(\frac{2k^{1/2}}{\beta^*\omega y},\frac{500\nu}{y^2\omega}\right). \tag{2.46}$$

Note that this model also uses a slightly different value of σ_k.

For low-Reynolds number versions of the $k-\omega$ model and Menter's Baseline $k-\omega$ and SST models, the following boundary conditions are assumed for a direct integration to the wall

$$\text{For } k: \quad k_w = 0, \qquad flux(k)_w = 0. \tag{2.47}$$

$$\text{For } \omega: \quad \omega = \infty, \qquad flux(\omega)_w = -\nu\nabla\omega. \tag{2.48}$$

where the subscript w denotes the value *at* the wall.

2.8 Wall Functions

In the finite-volume approach, wall functions supply the following quantities when the near-wall cell is too large to resolve the flow structure close to the wall:

- Wall shear stress (and heat flux) for the mean-flow equations,
- Volume-averaged production and dissipation terms for the k equation;
- Near-wall values of ε (and, in principle, ω) and structure functions $\overline{u_\alpha u_\beta}/k$.

In equilibrium shear flows, a universal law of the wall is assumed such that the mean velocity profile (for a smooth wall) takes the following form

$$\frac{U}{u_\tau} = \begin{cases} \frac{1}{k}\ln(Ey^+) & , \quad y^+ \geq y_v^+ \\ y^+ & , \quad y^+ \leq y_v^+ \end{cases} \tag{2.49}$$

where $y^+ = y_n u_\tau/\nu$ and k, E and y_v^+ are constants. Continuity requires $E = \exp(ky_v^+)/y_v^+$. A typical dimensionless sublayer height is $y_v^+ = 11.2$. Kinematic shear stress $\tau_w = u\tau^2$ would be calculated from U at the near-wall node. However, this leads to an eddy viscosity $\nu_t = ku_\tau y$ which vanishes at impingement points, where U vanishes, at variance with the observed maximum heat transfer at such points.

The solution (by Chieng and Launder [266]) is to adopt a turbulent velocity scale based on the turbulent kinetic energy, $u_0 \sim C_\mu^{1/4} k_P^{1/2}$, and corresponding eddy viscosity, so that the (constant) shear stress in the fully turbulent layer is

$$\tau = ku_0 y \frac{\partial U}{\partial y}, \tag{2.50}$$

with the solution at the near-wall node (assumed to lie in the fully turbulent layer) given by

$$U = \frac{\tau_w}{ku_0} \ln\left(E\frac{yu_0}{\nu}\right). \tag{2.51}$$

Thus, the wall shear stress is deduced from

$$\tau_w = \frac{k\left(C_\mu^{1/4} k_p^{1/2}\right) U_p}{\ln\left(E^* y_p^*\right)}, \tag{2.52}$$

where a subscript 'p' denotes a value at the near-wall node and k, E^* and $y_n^* u$ take the values 0.41, 5.4 and 20.4, respectively. Strictly speaking, the use of wall functions requires the near-wall node to lie within the fully turbulent region; say, $y^+ \geq 30$ or $y^+ \geq 55$. If, for any reason, $y^* \leq y_n^* u$, then τ_w should be set equal to the viscous stress $\nu U_p/y_p$. To implement the scheme in the momentum equations, the co-ordinate projections of τ_w are used to replace the diffusive fluxes on cell faces abutting the boundary through the source terms.

To establish turbulence quantities, universal profiles must be adopted for production and dissipation. It is assumed that

$$P = 0, \qquad \varepsilon \sim \frac{2\nu k}{y^2}, \qquad (y \leq y_n u) \tag{2.53}$$

$$P = \tau_w \frac{\partial U}{\partial x}, \qquad \varepsilon \sim \frac{u_0^3}{ky}, \qquad (y \geq y_n u) \tag{2.54}$$

where $y_v = y_n u^* \nu/k_v^{1/2}$ and k_v is the turbulent kinetic energy at the top of the viscous sublayer, taken to be equal to k_p (although more complex algorithms may be constructed). In the dissipation equation the value of ε at the near-wall node is set equal to that defined

above. In the k equation, k and its flux are set to zero at the wall and *cell-averaged* values of dissipation used in the near-wall cell. Integrating the profiles above then gives the following

$$P_{av} = \frac{\tau_w^2}{C_\mu^{1/4} k_p^{1/2} k\delta} \ln(\delta/y_v) \tag{2.55}$$

$$\varepsilon_{av} = \frac{2\nu k_v}{y_v \delta} + \frac{C_\mu^{3/4} k_p^{3/2}}{k\delta} \ln(\delta/y_v) \tag{2.56}$$

where $\delta\,(=2y_p)$ is the cell height.

2.9 Large-Eddy Simulation (LES)

Although most of the LES work has been carried out for incompressible cases, compressible flow investigations with LES have started to appear. Starting from the application of spatial filtering

$$\overline{f} = \int_V G f \mathrm{d}v \tag{2.57}$$

where G represents a grid filtering function. Each variable of f is decomposed as

$$f = \overline{f} + f_{sg} \tag{2.58}$$

with $\overline{f}$ denoting the filtered part and f_{sg} denoting the sub-grid part.

The different treatment of the compressible cases starts here where the filtered part is replaced with its Favre-averaged [267] component

$$\tilde{f} = \frac{\overline{\rho f}}{\overline{\rho}} \tag{2.59}$$

The above formulation in conjunction with the filtering results in several additional terms to the Navier-Stokes equations. All of these new terms are concentrated in the viscous flux vectors.

In the transformed co-ordinate system, for instance, for the ξ-direction, the viscous flux reads

$$F = \frac{1}{J} \begin{bmatrix} \xi_{xi}(G_{i1} + \tau_{i1}) \\ \xi_{xi}(G_{i2} + \tau_{i2}) \\ \xi_{xi}(G_{i3} + \tau_{i3}) \\ \xi_{xi}\left[u_j(G_{ij} + \tau_{ij}) - q_i - Q_i\right] \end{bmatrix} \tag{2.60}$$

where G_{ij} is the Favre-averaged stress tensor and is defined as

$$G_{ij} = \mu\left(\frac{\partial u_i}{\partial \xi_k}\frac{\partial \xi_k}{\partial x_j} + \frac{\partial u_j}{\partial \xi_k}\frac{\partial \xi_k}{\partial x_i} - \frac{2}{3}\delta_{ij}\frac{\partial u_k}{\partial \xi_l}\frac{\partial \xi_l}{\partial x_k}\right) \tag{2.61}$$

q_i is the Favre-averaged heat flux vector

$$q_i = -\left[\frac{1}{[(\gamma-1)M_a^2]}\left(\frac{\mu}{P_r}\right)\frac{\partial \tau}{\partial \xi_j}\frac{\partial \xi_j}{\partial x_i}\right] \tag{2.62}$$

τ_{ij} is the sub-grid stress and is defined as

$$\tau_{ij} = -Re\ \rho\left(u_i\tilde{u}_j - \tilde{u}_i\tilde{u}_j\right) \tag{2.63}$$

and Q_i is the sub-grid heat flux, which is defined as

$$Q_i = Re\ \rho\left(\widetilde{u_i T} - \tilde{u}_i\tilde{T}\right) \tag{2.64}$$

Note that both τ_{ij} and Q_i need to be modelled. The simplest approach is based on Smagorinsky's suggestion of a sub-grid turbulent viscosity

$$\mu_t = Re\ C_s\ J^{-\frac{2}{3}}\rho S_m \tag{2.65}$$

$$S_m = \sqrt{2S_{ij}S_{ij}} \tag{2.66}$$

$$S_{ij} = \frac{1}{2}\left(\frac{\partial u_i}{\partial\xi_k}\frac{\partial\xi_k}{\partial x_j} + \frac{\partial u_j}{\partial\xi_k}\frac{\partial\xi_k}{\partial x_i}\right) \tag{2.67}$$

The term $J^{-\frac{2}{3}}$ arises from the transformation and the grid-filter and C_s is the Smagorinsky 'constant'. Also,

$$\tau_{ij} = 2\mu_t\left(S_{ij} - \frac{1}{3}S_{kk}\delta_{ij}\right) + \frac{1}{3}\tau_{kk}\delta_{ij} \tag{2.68}$$

where $\frac{1}{3}\tau_{kk}\delta_{ij}$ is the isotropic part and is usually small for incompressible flows compared to the pressure.

For compressible flow, the sub-grid stress tensor τ_{ij} and the sub-grid heat flux tensor Q_i is given by

$$\tau_{kk} = -2\mathrm{Re}\ C_I\ J^{-\frac{2}{3}}\rho S_m^2 \tag{2.69}$$

$$Q_i = \left(\frac{\mu_t}{P_{rt}}\right)\frac{\partial\tilde{T}}{\partial\xi_j}\frac{\partial\xi_j}{\partial x_i} \tag{2.70}$$

where C_I is a parameter.

2.10 Detached-Eddy Simulation (DES)

Despite the potential of LES, there are problems in resolving the near-wall turbulent stresses since the required resources approach those of Direct Numerical Simulation (DNS). Overall, pure LES just gives 10 times higher Reynolds numbers than DNS so it is of limited practical application. Alternatives to this include RANS, in which a turbulence model is required to solve all flow properties and LES with a Sub-Grid Scale (SGS) model, which solves the near-wall properties while the grid explicitly resolves the flow properties elsewhere. Another alternative that has gained popularity over the years involves hybrids of LES and RANS such as Detached-Eddy Simulation (DES).

The original idea of DES was postulated by Spalart *et al.* [191]. Its underlying principle involved using RANS for the near-wall and boundary layer and LES everywhere outside. It is this concept that is called **DES: Detached-Eddy Simulation**.

Spalart *et al.* [191] modified the S-A model to achieve a DES equivalent. The only modification is in the dissipation term of the transport equation of $\tilde{\nu}$

$$-C_{w1}f_{w1}\left(\frac{\tilde{\nu}}{\tilde{d}}\right)^2 \tag{2.71}$$

In the pure one-equation Spalart-Allmaras turbulence model [192], the terms $\tilde{d}$ and d, which represent the distance to the wall, were identical, i.e.

$$\tilde{d} = d = \text{distance of the nearest wall} \tag{2.72}$$

In the DES formulation of the Spalart-Allmaras model, however, these terms are different and $\tilde{d}$ is given by

$$\tilde{d} = C_{DES}\Delta \tag{2.73}$$

where C_{DES} is a constant and Δ is the metric of the grid size.

In practice, the distance to the wall in the DES formulation of the one-equation Spalart-Allmaras model is expressed as a comparison between the actual distance to the wall and that calculated by $C_{DES}\Delta$, which essentially computes the size of the maximum cell length

$$\tilde{d} = \min\left(d, C_{DES}\Delta\right) \tag{2.74}$$

$$\Delta = \max\left(\Delta_x, \Delta_y, \Delta_z\right) \qquad \forall \quad \text{cell.} \tag{2.75}$$

When the cell length (i.e. $C_{DES}\Delta$) is less than the actual distance to the nearest wall (d), LES is triggered. RANS is activated when the converse occurs. This boundary between LES and RANS is therefore completely dependent on the geometry and on the density of the computational domain. For stretched meshing, the actual distance to the wall d is likely to be always smaller than the actual cell length near the wall so RANS will remain active there. Note that other metric relations are also possible.

For closures other than S-A (e.g. two-equation models), the corresponding DES formulation was proposed by Strelets [193]. A similar idea put forward by Batten *et al.* [268] is called **LNS: Limited Numerical Scales** and has several advantages compared to the original DES. For instance, LNS claims to be 'automatic' by detecting the areas of application of the RANS and LES without *a priori* knowledge of the location of walls or wall-distances. Furthermore, LNS approaches DNS as $\Delta \to 0$ and reverts back to RANS at the far-field of the flow if the grid there is coarse. Ref. [244] describes how to implement LNS.

For DES with the two-equation $k-\omega$ model, the only modification, as with the one-equation Spalart-Allmaras DES variant, is in the dissipation term

$$-\beta^* \rho \omega k \tag{2.76}$$

The turbulent length scale is defined by

$$l = \frac{k^{1/2}}{\beta^* \omega} \tag{2.77}$$

Re-arranging for $\beta^*\omega$ and substituting into equation 2.76 gives

$$-\rho \frac{k^{3/2}}{l} \tag{2.78}$$

where l is given by

$$l = \min\left(l, C_{DES}\Delta\right). \tag{2.79}$$

C_{DES} is set to 0.78 and Δ is as before.

Chapter 3

Description of Experiment

The experimental data used to validate the numerical results in this thesis were provided by Ross, Foster *et al.* [7, 8, 13, 65, 269], who performed numerous experiments on cavities of different configurations and various flow conditions at DERA Bedford, UK. The wind tunnel experiments, which comprised mostly unsteady pressure measurements, were predominantly conducted in the wind tunnel facility of Aircraft Research Association (ARA) Ltd. at Bedford. The ARA wind tunnel is a 9 ft. by 8 ft. (2.74m by 2.44m) continuous flow, transonic wind tunnel (TWT) with ventilated roof, floor and side walls. The main objective of the earliest studies [7, 8] was to investigate the effect of the unsteady pressure field and the acoustic variation in the weapons bay on the stores. Toward the late 1990s, tests were also carried out with the aim of assessing the effectiveness of various palliative devices in controlling the unsteady and harsh aeroacoustic environment in the weapons bay [11, 12]. Recently, analysis of the variations of the acoustic levels in weapon bays [13] and use of non-intrusive experimental methods such as PIV as well as numerical methods such as CFD have also been applied with the aim of gaining a better understanding of the cavity flow environment [6, 65, 269].

3.1 Generic Cavity Rig Model

The generic cavity rig model is shown inside the wind tunnel in Figure 3.1. The basic geometry of the cavity was designed to be sting-mounted in the wind tunnel and the model was capable of representing a broad range of cavity geometries of varying dimensions. A remote drive mechanism was also installed and this enabled sting-mounted store analysis to be performed, as illustrated in Figure 3.1(a). This facility allowed the store to be traversed across the cavity depth up to a distance approaching several diameters outside the cavity.

For the purposes of this project, experimental results from the L/D=5, clean cavity configuration were employed. In this configuration, the cavity length was specified to be 20 inches with a depth and width of 4 inches. The entire cavity was embedded into the surface of a flat plate, which extended to a length of 31 inches ahead of the cavity as depicted in Figure 3.1(b). Immediately behind the cavity, a second cavity, which housed the driving mechanism for the normal motion system, was present. This second cavity was closed with a cover plate so that it was flush with the flat plate surface. The sting mounting

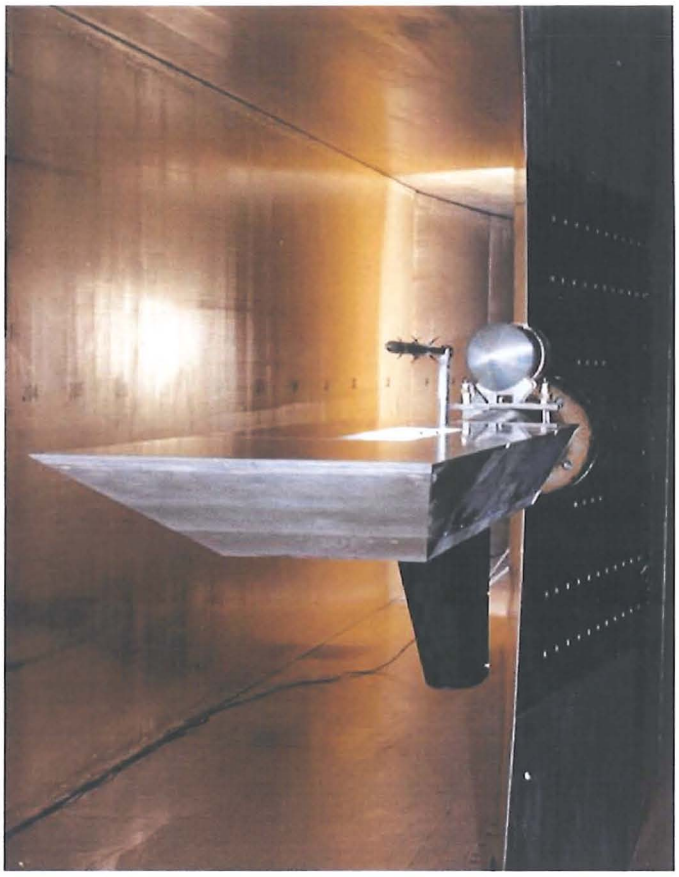

(a) Wind tunnel with sting-mounted store

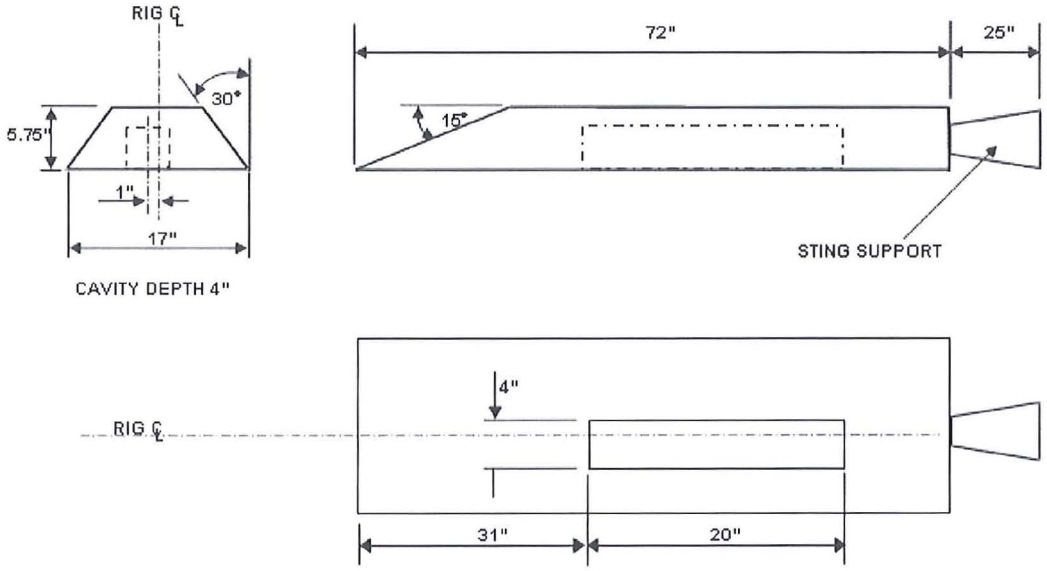

(b) Cavity Rig Model

Figure 3.1: The generic cavity rig model with a sting-mounted store in the ARA 9 ft. by 8 ft. transonic wind tunnel and a schematic of the plan and side views of the cavity model.

extended to a distance of 25 inches aft of the flat plate behind the actual cavity model. The complete cavity assembly was boxed in and provided sufficient room for mounting pressure switches. The front end of the assembly was wedged at an angle of 15° to the oncoming flow, as shown in Figure 3.1(b).

The generic cavity rig model was positioned at zero incidence, sideslip and yaw and the wind tunnel was operated at a Mach number of 0.85 with atmospheric pressure and temperature. The Reynolds number of the flow was approximately 13.4×10^6 per metre, which was equivalent to a value of 6.783×10^6 based on the cavity length. The wind tunnel was operated at a total pressure and temperature of approximately 14.5 psi and 310 K, respectively [270].

Weapon bay doors could also be attached to the cavity model as illustrated in Figure 3.2 to analyse the effect of the doors on the unsteady flow-field in the bay. The height of the bay doors was half the cavity depth, i.e. 2 inches, and slots were provided to hold the bay door brackets. Bay door junctions were inclined at 45° to facilitate opening and closing of doors. Comparison of the experimental results with doors open vertically at 90° with 2D CFD results revealed that the doors prevented any leakage at the cavity edges in the spanwise direction forcing the flow to channel into the cavity. In the doors-on configuration, the flow therefore may behave as if it was two-dimensional and the cavity may be modelled as 2D.

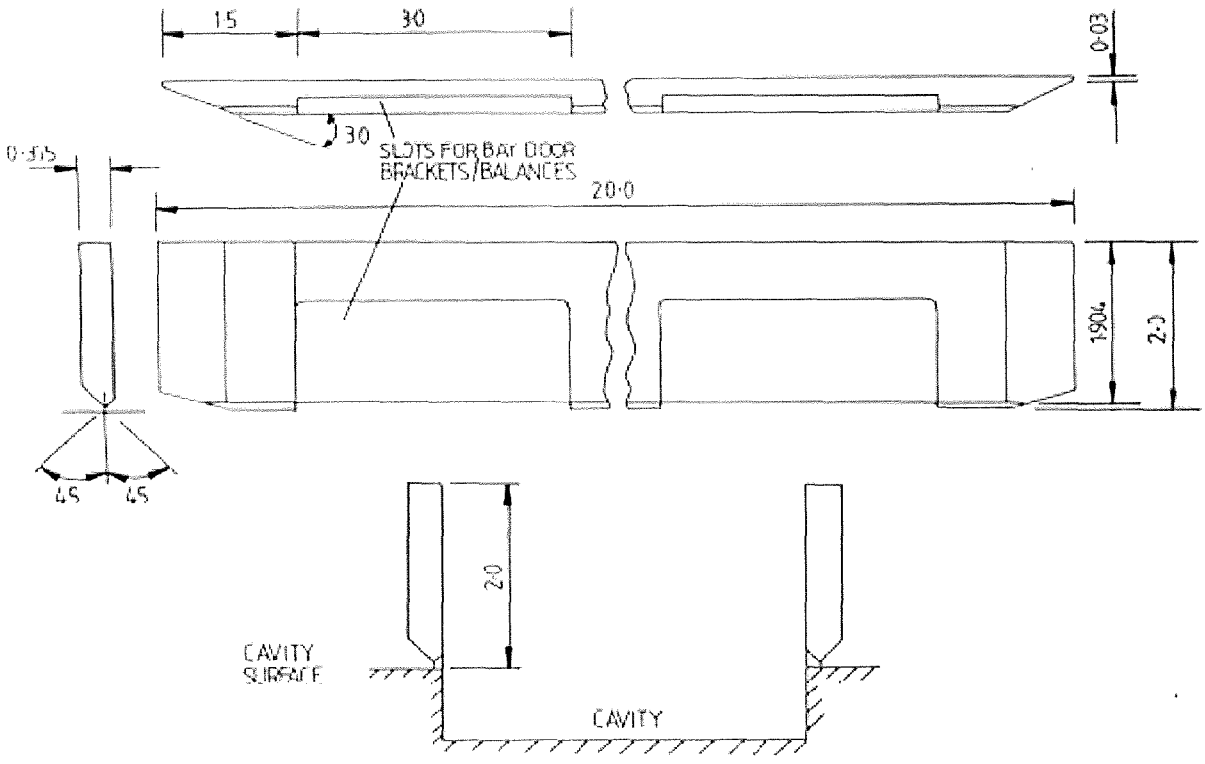

Figure 3.2: Cavity model with doors inclined at 90° to flow.

3.2 Pressure Measurements

Unsteady pressure measurements were registered inside and outside the cavity via Kulite pressure transducers for both the doors-off and doors-on configurations. For the empty cavity with doors-off, ten pressure transducers were aligned along the centreline of the floor of the cavity rig as shown in Figure 3.3. The centreline of the cavity rig was not coincident with the centreline of the actual cavity model. These ten pressure transducers were thus offset from the cavity rig model centreline by 1 inch as shown in Figure 3.1. Two pressure transducers were also positioned on the flat plate ahead of the cavity, one on the flat plate aft of the cavity and two on the front wall [270].

Aside from the standard ten pressure transducers at the cavity floor, two more pressure transducers were used on the front plate, rear plate and rear walls in the doors-on configuration, as indicated in Figure 3.4. Three additional transducers were placed on the inside section of the bay door and one on its outside. Four transducers were positioned on the port side cavity wall as well. In both doors-on and doors-off configurations, one pressure transducer was situated on the port side working section of the wind tunnel.

The data were sampled at 6 kHz using a high-speed digital data acquisition system for doors-on and doors-off. In addition to this, a higher sampling rate of 31.25 kHz was also employed for the deep, L/D=5 cavity with doors-on [270]. of the experimental data signal was approximately 3 seconds for most cases although some longer record lengths of 30 and 60 seconds were also obtained.

3.3 Data Analysis

The experimental pressure measurements were then post-processed and presented in terms of Sound Pressure Levels (SPLs) and Power Spectral Density (PSD). The SPLs are an indication of the intensity of noise generated inside the cavity and can be obtained from the measurements using the equation

$$\mathrm{SPL\,(dB)} = 20\log_{10}\left(\frac{\mathrm{p_{rms}}}{2\times10^{-5}}\right) \tag{3.1}$$

where the p_{rms} is the RMS pressure and is defined by

$$p_{rms} = \sqrt{\frac{\sum_{i=1}^{N}(p_i - p_{mean})^2}{N}} \tag{3.2}$$

with N denoting the number of samples, p_i denoting the instantaneous pressure at every measurement and p_{mean} representing the mean pressure, which is given by

$$p_{mean} = \frac{\sum_{i=1}^{N} p_i}{N} \tag{3.3}$$

In Equation 3.1, the RMS pressure is normalised by the International Standard for the minimum audible sound of 2×10^{-5} Pa. Spectral analysis was performed using Fast Fourier

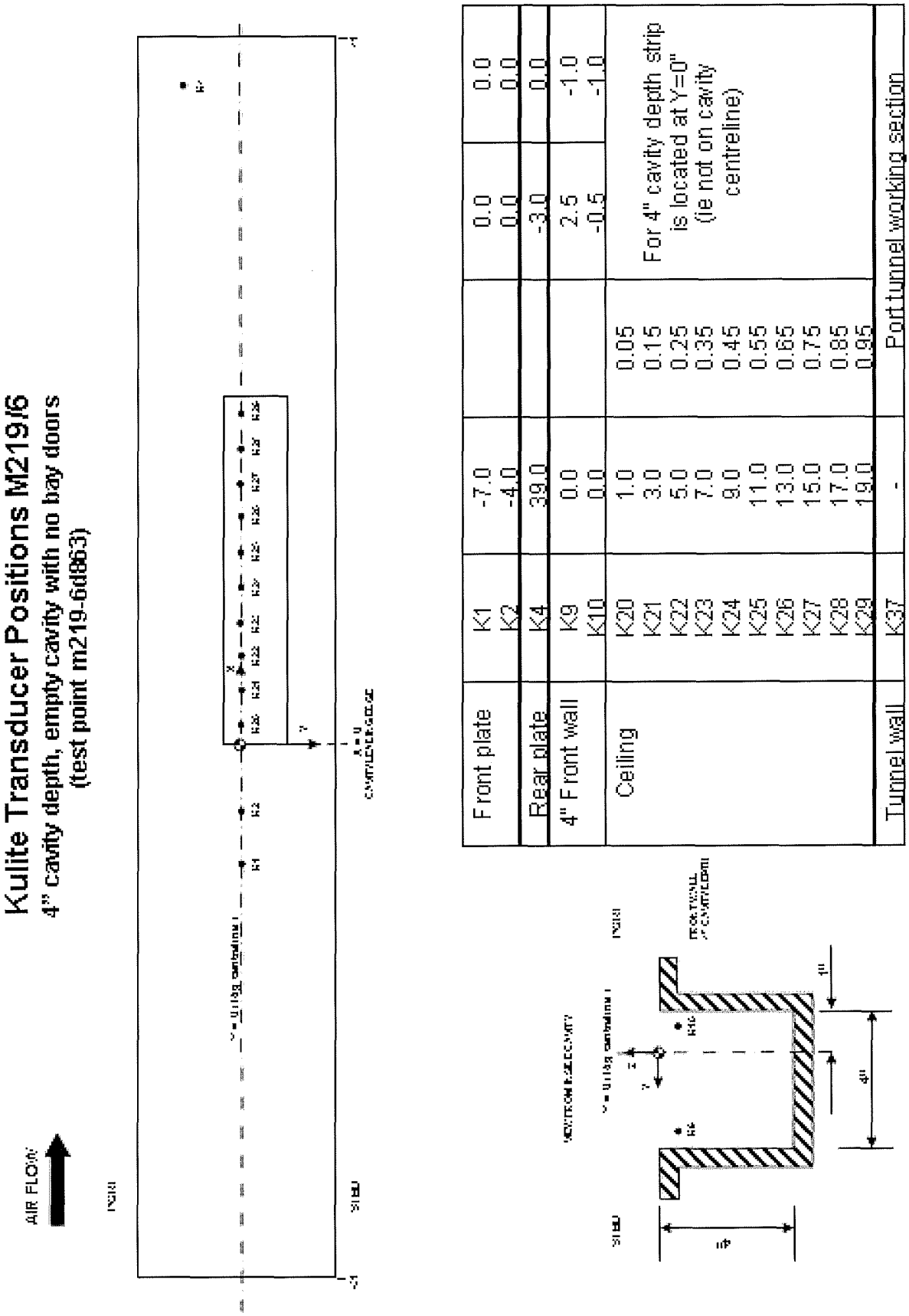

Front plate	K1	-7.0		0.0	0.0
	K2	-4.0		0.0	0.0
Rear plate	K4	39.0		-3.0	0.0
4" Front wall	K9	0.0		2.5	-1.0
	K10	0.0		-0.5	-1.0
Ceiling	K20	1.0	0.05	For 4" cavity depth strip is located at Y=0" (ie not on cavity centreline)	
	K21	3.0	0.15		
	K22	5.0	0.25		
	K23	7.0	0.35		
	K24	9.0	0.45		
	K25	11.0	0.55		
	K26	13.0	0.65		
	K27	15.0	0.75		
	K28	17.0	0.85		
	K29	19.0	0.95		
Tunnel wall	K37	-	Port tunnel working section		

Figure 3.3: Positions of the pressure transducers located inside and outside the cavity in the doors-off configuration.

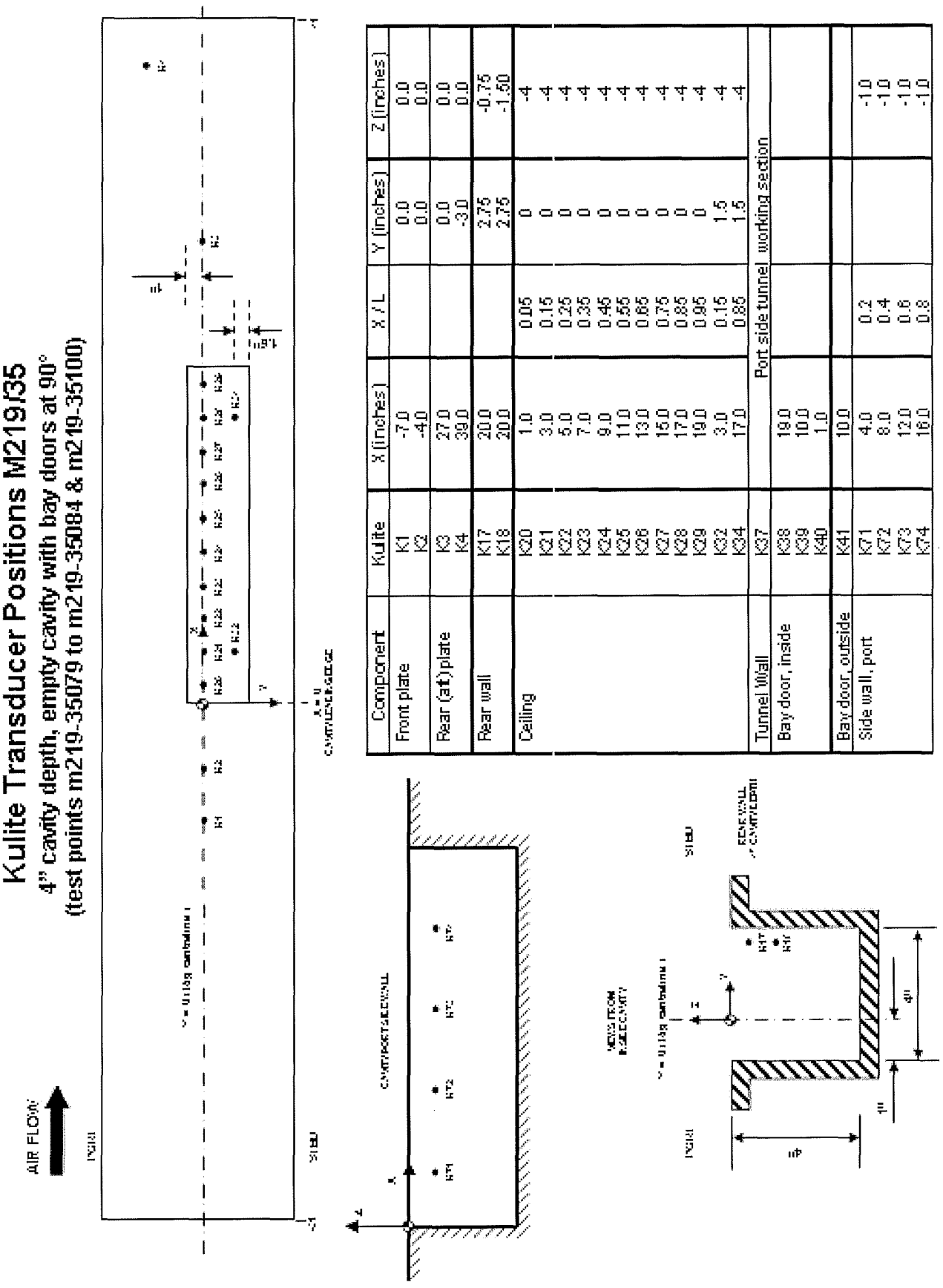

Component	Kulite	X (inches)	X / L	Y (inches)	Z (inches)
Front plate	K1	-7.0		0.0	0.0
	K2	-4.0		0.0	0.0
Rear (aft) plate	K3	27.0		0.0	0.0
	K4	39.0		-3.0	0.0
Rear wall	K17	20.0		2.75	-0.75
	K18	20.0		2.75	-1.50
Ceiling	K20	1.0	0.05	0	-4
	K21	3.0	0.15	0	-4
	K22	5.0	0.25	0	-4
	K23	7.0	0.35	0	-4
	K24	9.0	0.45	0	-4
	K25	11.0	0.55	0	-4
	K26	13.0	0.65	0	-4
	K27	15.0	0.75	0	-4
	K28	17.0	0.85	0	-4
	K29	19.0	0.95	0	-4
	K32	3.0	0.15	1.5	-4
	K34	17.0	0.85	1.5	-4
Tunnel Wall	K37	Port side tunnel working section			
Bay door, inside	K38	19.0			
	K39	10.0			
	K40	1.0			
Bay door, outside	K41	10.0			
Side wall, port	K71	4.0	0.2		-1.0
	K72	8.0	0.4		-1.0
	K73	12.0	0.6		-1.0
	K74	16.0	0.8		-1.0

Figure 3.4: Positions of the pressure transducers located inside and outside the cavity in the doors-on configuration.

Transform (FFT) to obtain the Power Spectral Density (PSD), which presents the RMS pressure versus frequency and provides a measure of the frequency content inside the cavity. To compute the FFT of the data signal, Welch's method was employed where the Hanning function is used as the apodization function, which is already integrated in the MATLAB software package.

A more in-depth study of the frequency content of the signals was then undertaken by performing band-limited frequency analysis. In this case, the resultant signal in the frequency domain (after FFT) was filtered using four frequency bands and then averaged to give a mean pressure variation for each frequency band. This was performed for each of the ten pressure transducers situated on the cavity floor, as indicated in Figures 3.3 and 3.4. Sound Pressure Levels were then calculated using Equation 3.1 and plotted with respect to the cavity length. Each of the four frequency ranges used in this analysis contain at least one of the Rossiter modes calculated using the formula given by Equation 1.3 of Chapter 1. For the L/D=5 cavity, the first frequency band ($50\ Hz \leq f \leq 250\ Hz$) straddles the first Rossiter mode ($\approx 160\ Hz$), the second band ($350\ Hz \leq f \leq 450\ Hz$) contains the second mode ($\approx 380\ Hz$), the third band ($500\ Hz \leq f \leq 700\ Hz$) includes the third mode ($\approx 600\ Hz$) and the fourth band ($750\ Hz \leq f \leq 850\ Hz$) comprises the fourth mode ($\approx 820\ Hz$). Band-limited frequency analysis is useful in understanding which mode plays the most significant role and therefore helps to identify the physical processes driving the flow. When making comparisons with different methods, as will be discussed later, analysing the data in this way can also be effective in illustrating the differences between the methods.

3.4 Experimental Analysis: Doors-On

The noise level and frequencies generated inside the L/D=5, W/D=1 cavity with doors-on based on experimental measurements are presented in Figure 3.5 for the 6 kHz sampling rate signal and in Figure 3.6 for the 31.25 kHz sampling rate signal. In both cases, plots for different experimental signal durations of 3s (blue lines with plus symbols), 0.2s (red lines with circular markers) and 0.1s (green lines with crosses) are superimposed for SPLs and PSD at the cavity rear, i.e. at $x/L = 0.95$ where the most sensitive pressure transducer ('Kulite 29') is located. On the same figures, approximate values of the Rossiter modes as calculated by Rossiter's formula discussed in Chapter 1 are denoted as dotted black lines.

Variations in noise level are negligible among experimental signal lengths of 3 seconds (which is the actual experiment duration) and truncated signal lengths of 0.1 and 0.2 seconds for both sampling rates, as indicated in Figures 3.5(a) and 3.6(a). Variations in spectral plots are however more pronounced and this is demonstrated in Figures 3.5(b) and 3.6(b), which correspond to the 6 kHz and 31.25 kHz sampled signals respectively.

Longer experiment signal lengths increase the number of samples, denoted by N in Equation 3.2, proportionally and therefore reduce the RMS pressure values. The frequency magnitudes are therefore much lower and because of the larger number of samples, the resolution, for the longer duration signal, is much sharper with thin sidelobes at the main acoustic tone locations. SPLs are calculated using logarithms so effects of experiment signal duration are less evident. All CFD computations were run to an approximate real-time of 0.1 or 0.2 seconds. When comparing the numerical results with experiment, it was

therefore ensured that the computational results were sampled at the same rate as experiment and that the experimental signal length corresponded to the same final run-time as CFD.

From Figures 3.5 and 3.6, it is evident that the second Rossiter mode ($\approx$ 380 Hz) is the dominant acoustic tone and that the SPL curve has a 'W' shape with a maximum SPL value of 168 dB at the cavity rear.

3.5 Experimental Analysis: Doors-Off

SPL variation and spectral analysis of the entire experimental signal for the L/D=5 cavity with doors-off are presented in Figure 3.7. Unlike for the doors-on case, the SPL shape takes the form of a 'tick'-shape and the third Rossiter mode ($\approx$ 600 Hz) has a higher magnitude. More frequencies exist with doors not included with no single tone being dominant and this is typically manifested in the form of a SPL curve with fewer kinks.

3.6 Particle Image Velocimetry (PIV) Measurements

Measurements of the cavity flowfield were provided by PIV experiments conducted by Ross [6, 65]. A stereoscopic two-camera system accompanied with a two-head Nd-YaG laser was employed for measurements of all three velocity components. Each laser pulse was fired within time intervals of 1μs. Four data acquisitions were taken with each acquisition comprising 2 photographic images taken at 1μs intervals. The width of the laser sheet was limited to approximately 5.5 inches so the total cavity length of 20 inches was captured in 4 sections using the motorised camera/laser traverse gear shown in Figure 3.8.

Seeding was originally provided by various combinations of water droplets sprayed in the settling chamber (as indicated in Figure 3.9) and vegetable oil mist diffusion from small holes in the cavity floor. Vegetable oil mist diffusion was however later not used because the oil particles were found to adhere to the surface.

Analysis of data signals was performed by phase-locking onto each peak of signal and introducing a series of delays to synchronise image acquisitions at a particular part of the cycle. A number of acquisitions were then taken and averaged to define the flowfield at that part of the cycle. For highly unsteady flows with multiple cyclic components it was recognised that phase-locking on any one component does not 'freeze' the flowfield. As highlighted by Ross [6], the highly turbulent flow in cavities makes it difficult to account for all aspects of the flow-field. For complete definition of the flowfield with time-dependency, very high-speed image acquisition equipment would be required.

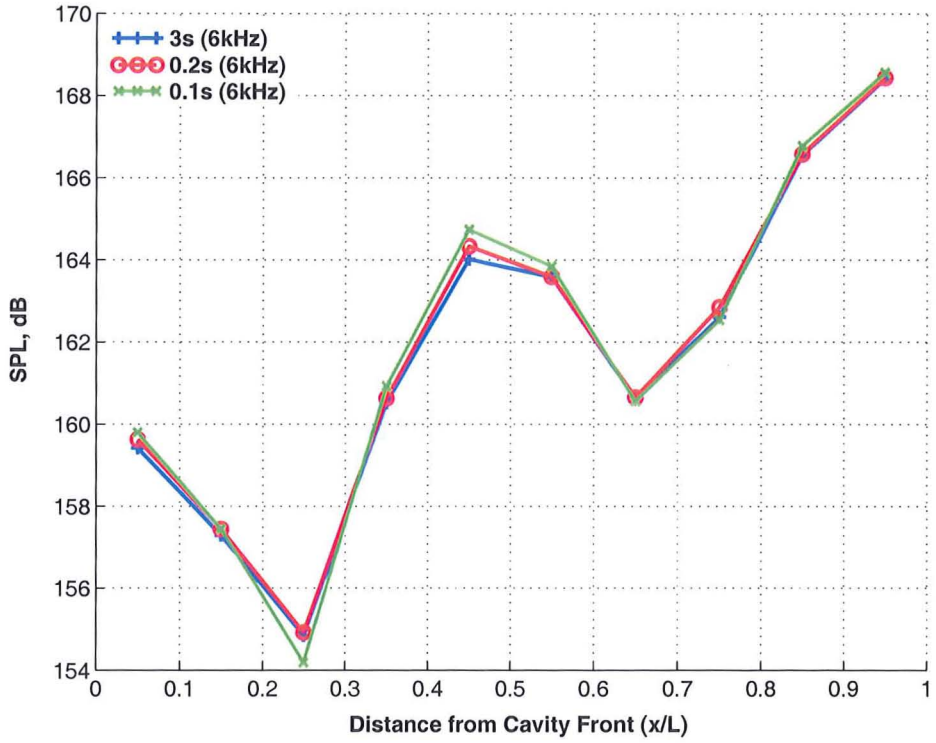

(a) SPLs

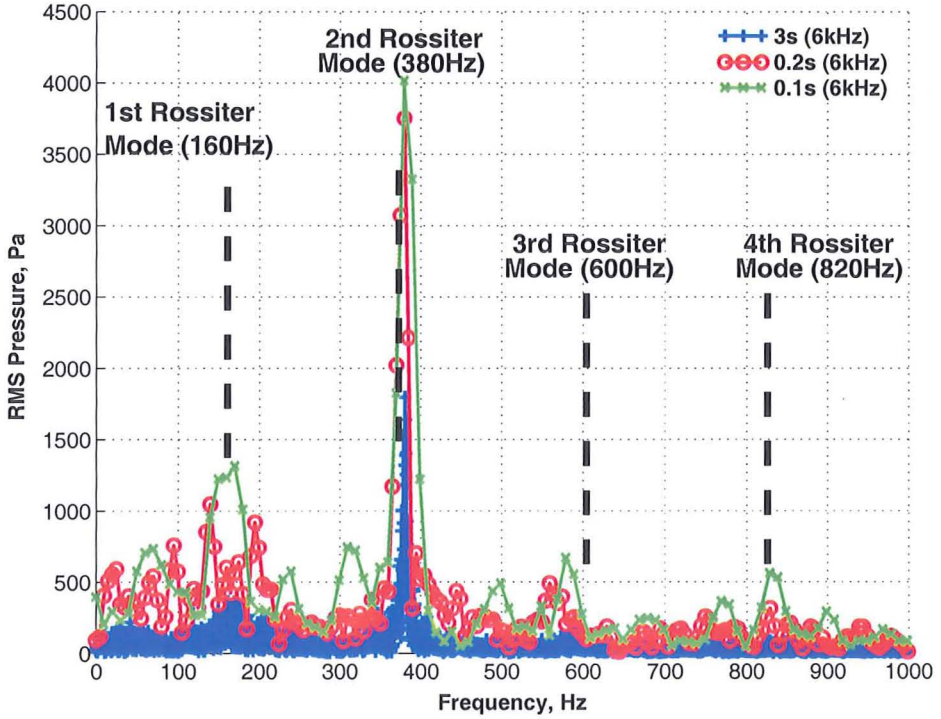

(b) PSD ($x/L = 0.95$)

Figure 3.5: Sound Pressure Levels (SPLs) and spectral analysis (at $x/L = 0.95$) of the 6 kHz sampling rate experimental signal for three signal durations - 3 seconds, 0.1 seconds and 0.2 seconds - for the L/D=5, clean cavity with doors-on.

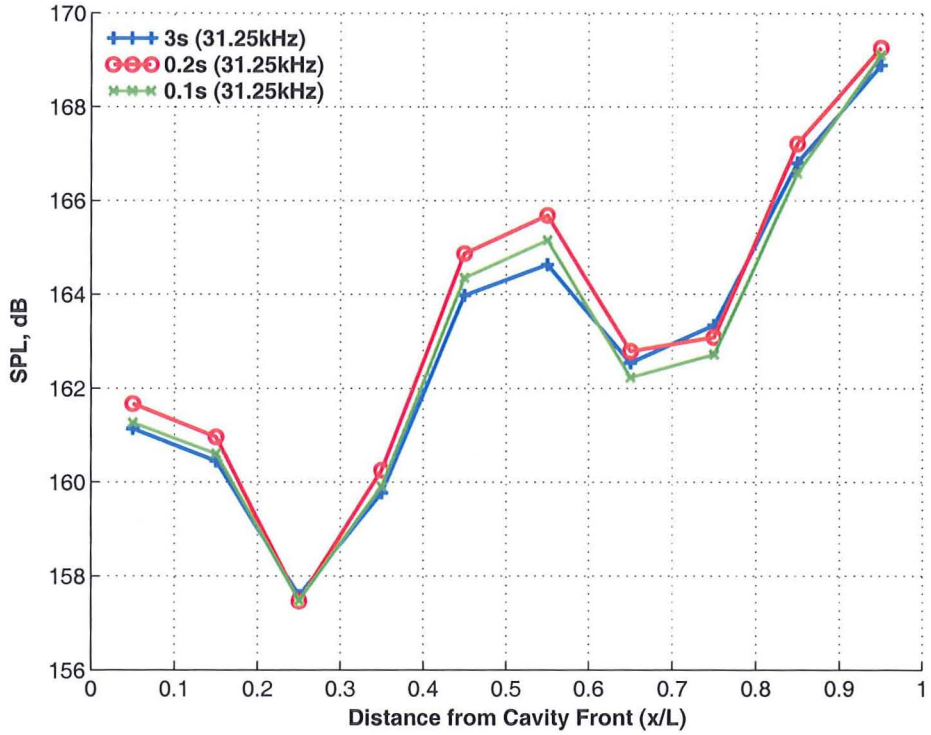

(a) SPLs

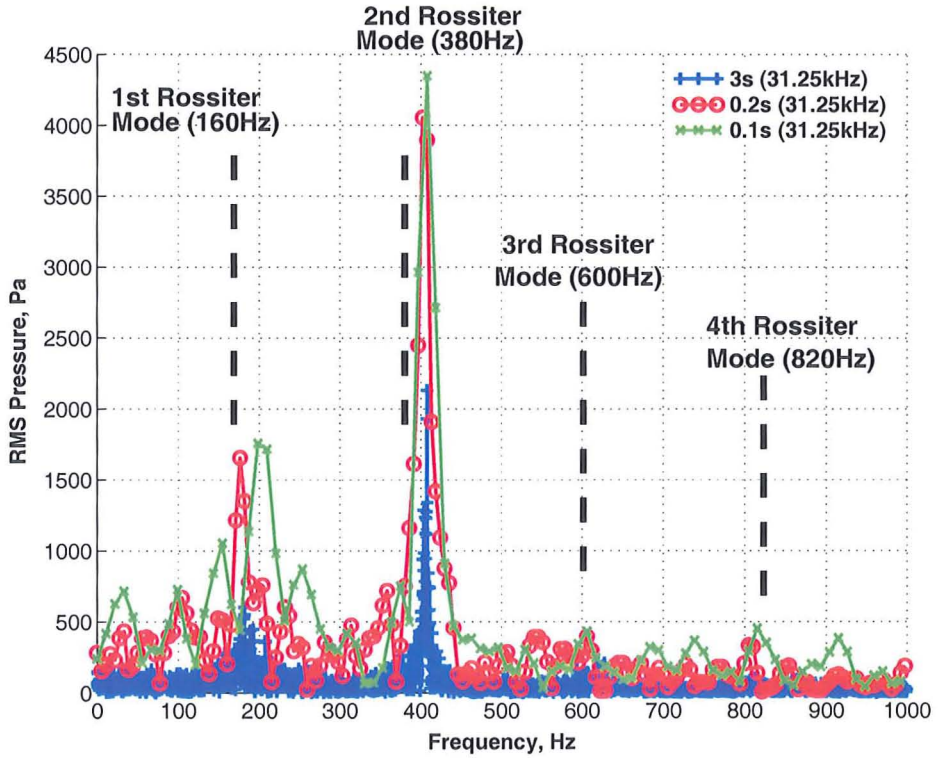

(b) PSD ($x/L = 0.95$)

Figure 3.6: Sound Pressure Levels (SPLs) and spectral analysis (at $x/L = 0.95$) of the 31.25 kHz sampling rate experimental signal for three signal durations - 3 seconds, 0.1 seconds and 0.2 seconds - for the L/D=5, clean cavity with doors-on.

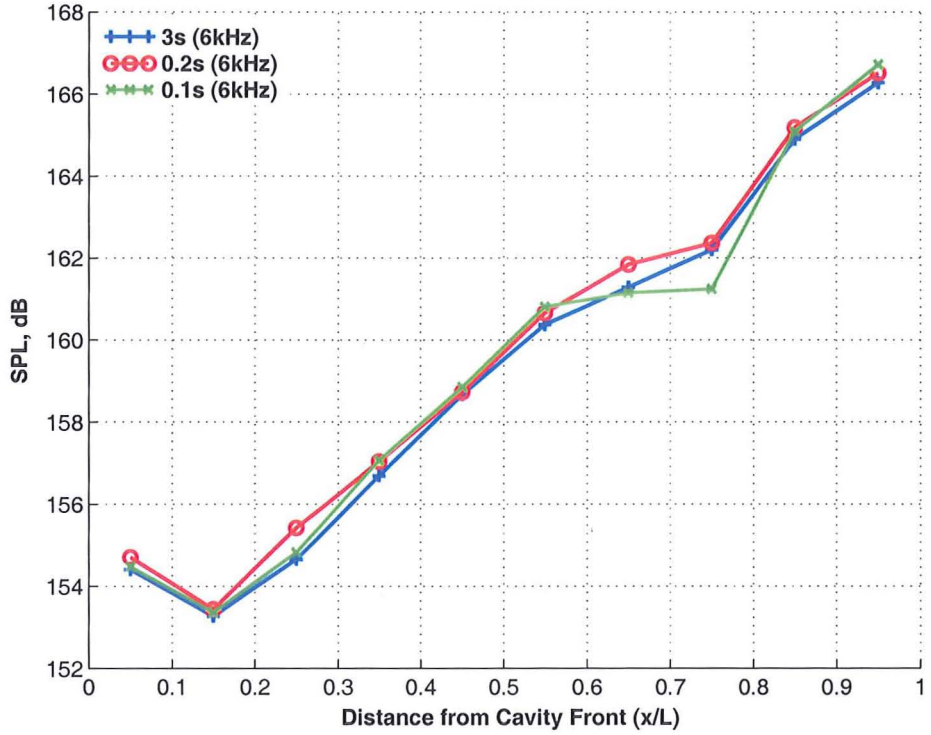

(a) SPLs

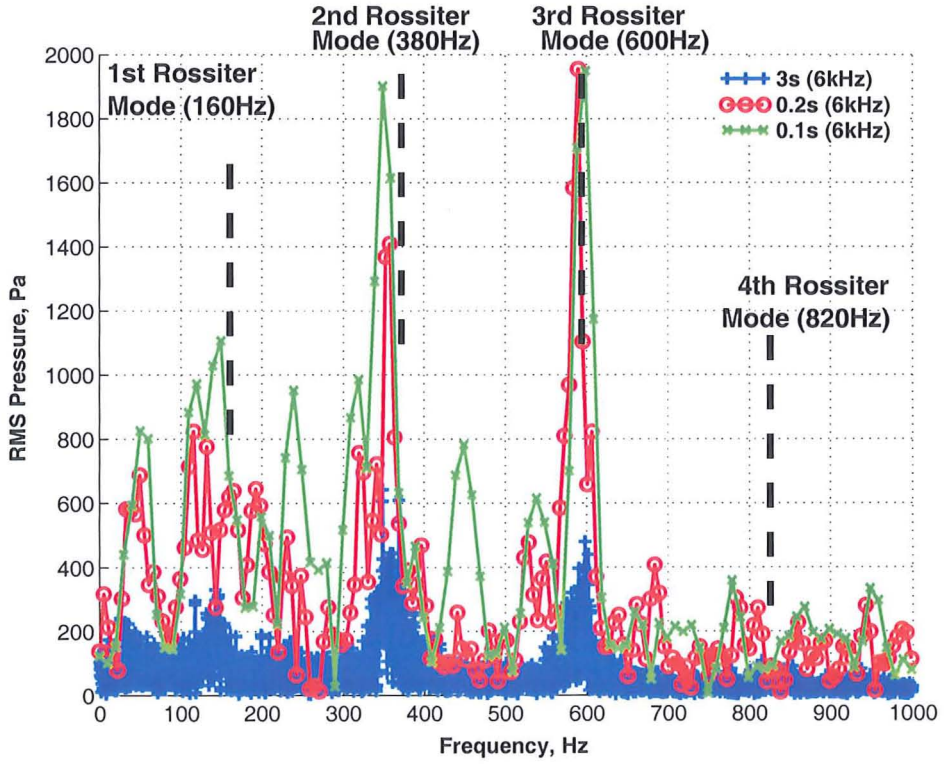

(b) PSD ($x/L = 0.95$)

Figure 3.7: Sound Pressure Levels (SPLs) and spectral analysis (at $x/L = 0.95$) of the 6 kHz sampling rate experimental signal for three signal durations - 3 seconds, 0.1 seconds and 0.2 seconds - for the L/D=5, clean cavity with doors-off.

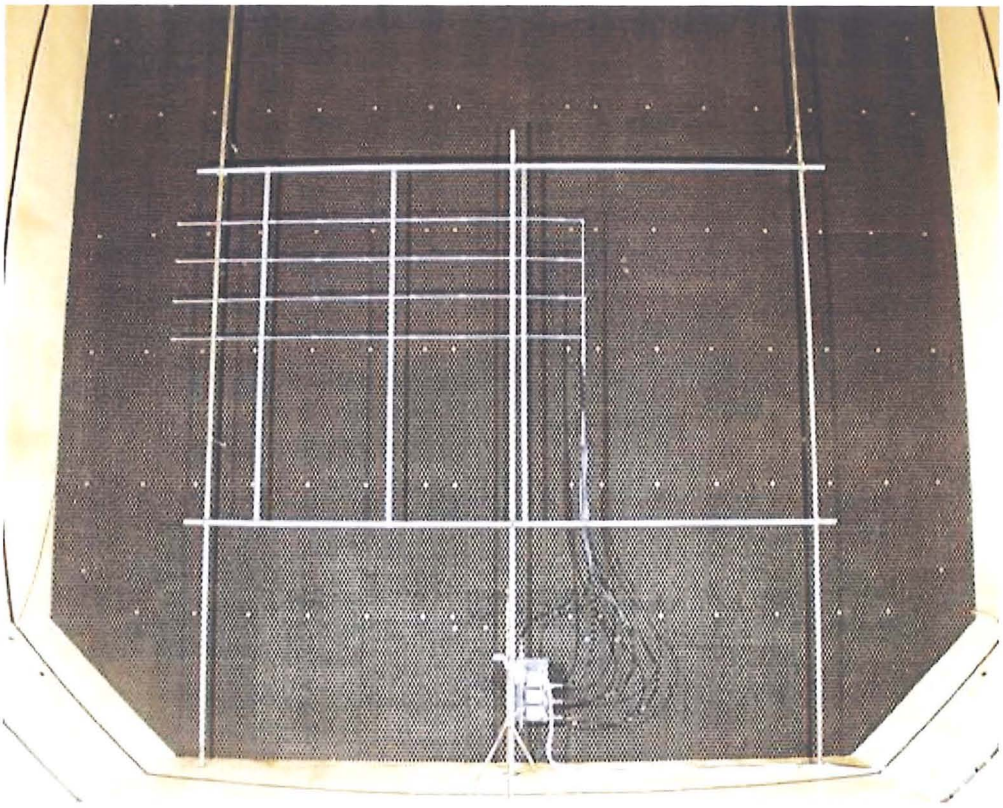

(a) Equipment for seeding the cavity

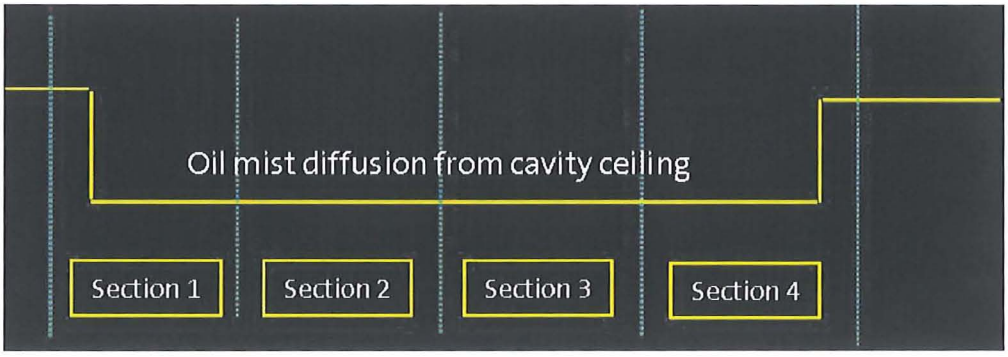

(b) Four cavity sections

Figure 3.8: Equipment for spraying water droplets for seeding of the cavity (above) used in the PIV experiment by firing the laser (with a width of 5.5 inches) across 4 sections (below) to cover the entire cavity length of 20 inches.

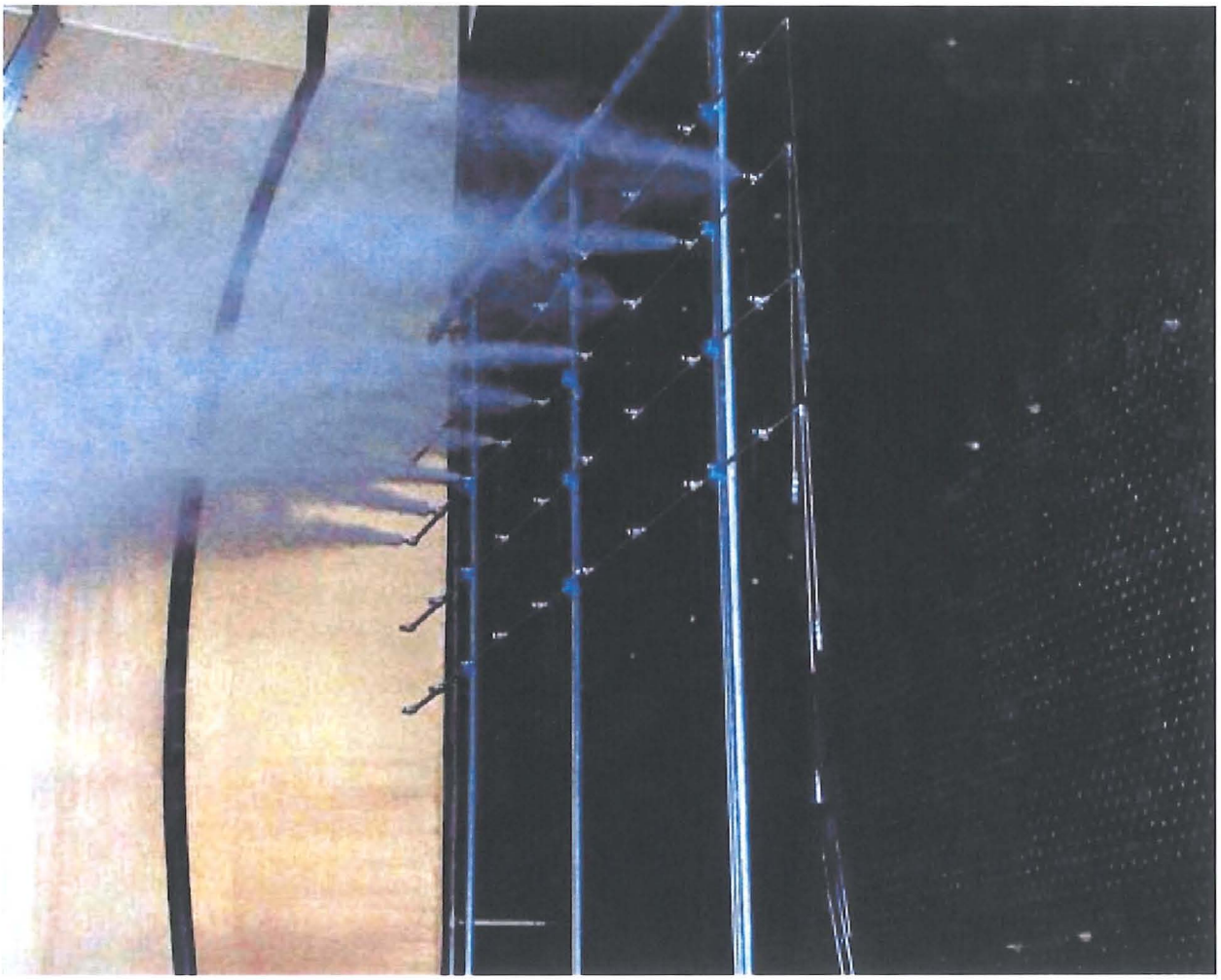

Figure 3.9: Water droplets sprayed into the settling chamber for seeding of the cavity in the PIV experiment.

Chapter 4

L/D=5 Cavity: URANS Results

Previous research in cavity flows at the University of Glasgow by Henderson [9] and Lawrie [10] applied the URANS method to the study of 2D and 3D cavity flows. Henderson [9] focused primarily on understanding the physics of open, transitional and closed 2D cavity flows using the $k-\omega$ turbulence model by Wilcox [138]. Results obtained on coarse grids demonstrated good agreement with experiment but this deteriorated with finer grids. Grid independence was not achieved for the 2D open cavity flow case considered and it was suggested that URANS was not appropriate for this type of flow due to mean flow and turbulence interactions. Lawrie [10] researched predominantly with 3D cavity flows, although some 2D cavity flow investigations were also carried out, over a wide range of Mach and Reynolds numbers for both the wake and the shear layer modes. Lawrie [10] utilised both the $k-\omega$ model by Wilcox [138] and the Baseline $k-\omega$ model by Menter [245]. For 2D cavities in the shear layer mode, Lawrie [10] concluded that the Baseline $k-\omega$ turbulence model was more robust than the $k-\omega$ model, with the latter being very sensitive to grid refinement. For the 3D cavity, Lawrie suggested using other methods apart from URANS.

Neither Henderson [9] nor Lawrie [10] however elucidated why the turbulence model was sensitive to the type of computational domain employed and why grid convergence was difficult to achieve. A thorough investigation into 2D cavity flows with the URANS method was therefore performed in order to explain this. Three-dimensional cavities were not analysed initially because the presence of three-dimensional effects would have complicated the problem further.

The effects of grid density and computational time-step were addressed here for three two-equation turbulence models: standard $k-\omega$ [138], Baseline $k-\omega$ [245] and the SST [245] turbulence models. Description of these models was given in Chapter 2. Analysis of the acoustic and the turbulent spectra as well as the velocity distribution was conducted at the cavity floor. Such analyses allowed an understanding of the influence of turbulent processes on the cavity flow-field to be obtained. The performance of the turbulence models is also highlighted via comparisons of the predicted turbulent and velocity profiles inside the cavity against experiments. All the numerical results of 2D cavity computations were compared with the experimental 3D cavity data in the doors-on configuration, as was explained previously in Chapter 3.

4.1 Description of Computational Domain

Four different grids were used for the 2D L/D=5 cavity, as detailed in Table 4.1.

Table 4.1: Information about the grids of different densities used for the 2D clean cavity with L/D=5.

Name	Overall Points	Points in Cavity	Wallspacing	Blocks in Cavity (Overall)
Coarse	33,250	10,302	$y = 1.05 \times 10^{-5}$	1 (6)
Fine	90,570	52,118	$y = 1.05 \times 10^{-5}$	1 (6)
Very Fine	362,286	208,472	$y = 1.05 \times 10^{-5}$	1 (6)
Ultra Fine	1,449,150	833,888	$y = 1.05 \times 10^{-5}$	4 (12)

The coarse L/D=5 cavity grid consists of approximately 33,000 grid points and comprises six blocks with the cavity completely contained within one block, as shown in Figure 4.1, which also indicates the boundary conditions applied. While constructing the grid, all dimensions were scaled with respect to the cavity length, L. The blocks immediately ahead and aft of the cavity contained flat plates 1.55 and 1.05 times the cavity length, respectively, as in the experiment (Figure 3.1(b)). The length of the far-field domain was specified to be 1.5 times the cavity length and was based on previous studies where the effects of various far-field lengths were investigated for the L/D=5 cavity. Results revealed that this was the minimum length at which acoustic wave reflections from the far-field boundary were minimised.

Furthermost upstream and downstream of the cavity are two blocks (denoted as blocks 2 and 6 respectively in Figure 4.1(a)) with a y-symmetry boundary condition applied at the surface. The purpose of the furthermost upstream block was to negate numerical errors arising from the 'slip-stick' condition that can occur when the free-stream suddenly encounters and interacts with a solid surface. Similarly, the furthermost downstream block (denoted as block 6 in Figure 4.1(a)) compromises the numerical errors arising from the 'stick-slip' condition, which occurs when a solid surface where the no-slip condition is applied suddenly meets the free-stream. A wall-spacing of $y = 1 \times 10^{-5}$ was applied throughout the computational domain with a combination of bi-geometric and hyperbolic mesh distributions. This wall-spacing has been applied to the cavity in previous computations [9, 10] and has been found to give reasonable resolution of the boundary layer. Since the 3D PMB flow solver is based on a finite volume discretisation method, the 2D cavity grid consisted of unit width in the third dimension as illustrated in Figure 4.1(b). Inevitably no grid points were specified in the spanwise direction and a 2D boundary condition was applied on both z=0 and z=1 planes.

This basic topology of the coarse cavity grid was applied to all the others. The fine L/D=5 grid was constructed from the coarse grid by increasing the number of points inside the cavity with the objective of improving the aspect ratio of cells inside the cavity. All subsequent grids were then constructed from the fine grid by doubling the number of points in each direction apart from the z-direction. The number of blocks for all the finer grids except for the ultra fine grid remained the same. The ultra fine grid was too large to run on a single processor so more blocks were added to allow for better parallelisation. In all

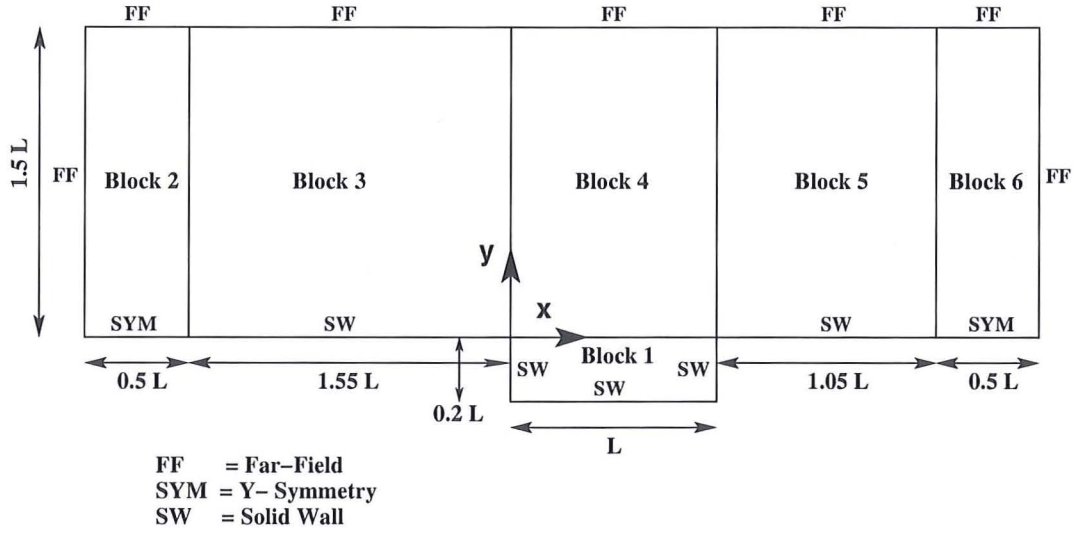

(a) 2D Grid Dimensions and Boundary Conditions

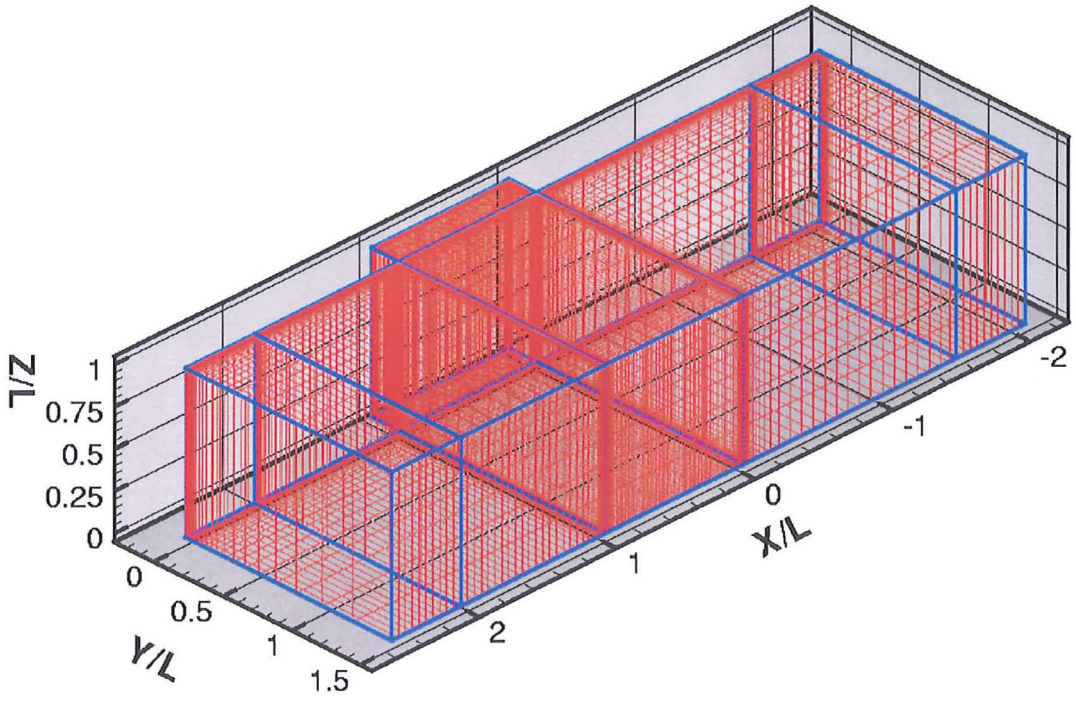

(b) 2D Volume Grid

Figure 4.1: Schematic of the 2D (L/D=5) cavity grid illustrating all dimensions and boundary conditions applied and the finite width applied with no resolution in the spanwise direction for use with the 3D PMB flow solver [5].

finer grids, the wall-spacing was kept fixed to $y = 1 \times 10^{-5}$. Free-stream boundary conditions were applied outside the cavity as illustrated in Figure 4.1(a). Zero velocity was imposed inside the cavity for the initialisation of the solution while free-stream conditions were used elsewhere. The free-stream Mach number was set to 0.85 and the Reynolds number based on the cavity length was specified to be 6.783 million, as was used in the experiment.

4.2 Spatial and Temporal Refinement Effects: Comparison Between Coarse and Fine Grids

Results for the 2D, L/D=5 cavity using the $k-\omega$, Baseline $k-\omega$ and SST turbulence models are first presented for the coarse and fine grids with time-steps of 0.01 ($\equiv 1.814\times 10^{-5}$s) and 0.005 ($\equiv 9.07\times 10^{-6}$s). Based on Nyquist's sampling theorem, time-steps of 0.01 and 0.005 correspond to sampling frequencies of 55.127kHz and 110.25kHz, respectively. Numerical results were sampled at 31.25kHz but were compared with both the 6kHz and 31.25kHz experimental signals.

4.2.1 Acoustic Spectrum Analysis

Noise levels and frequencies generated inside the cavity with the $k-\omega$ model for the coarse and fine grids and time-steps are indicated in Figure 4.2. The SPLs do not change substantially when a lower time-step is used for the coarse grid. The phase and dominance of the discrete tones did however change with a lower time-step. At the front of the cavity, i.e. $x/L=0.05$, both the first and second Rossiter modes were shifted to the right with the second mode's location agreeing much better with experiment when a lower time-step was used (Figure 4.2(b)). Similar observations were made at the cavity middle (i.e. $x/L=0.55$) and rear (i.e. $x/L=0.95$) although at the cavity middle a lower time-step for the coarse grid predicted a greater magnitude of the first Rossiter mode compared to the second mode (Figure 4.2(c)). This increase in the amplitude of the first mode for the coarse grid with fine time-step is compensated for by a decrease in the second mode amplitude resulting in overall SPLs of similar magnitude to the coarse grid with coarse time-step (Figure 4.2(a)). The lower time-step for the coarse did however offer significant improvement for the higher frequencies as shown in the zoomed views inset in Figures 4.2(b) to 4.2(d).

Such effects of temporal refinement are anticipated simply because the lower time-step allows for the resolution of smaller structures of short lifetime. Where the flow changes significantly is when the grid is refined in space. The shape of the SPL curve changes from a 'W' shape for the coarse grid to a 'V'-shape for the fine grid accompanied with an increase of the overall SPLs by a couple of decibels at the cavity front and rear (Figure 4.2(a)). This change of the SPL shape corresponds to a change in the frequency distribution. Dominance also has shifted from the second Rossiter mode to the first for all three stations shown in (Figures 4.2(b)-4.2(d)) suggesting that a 'W' SPL shape corresponds to the second mode being dominant while a 'V' shape suggests a dominant first mode. Time-refined results on the fine grid have the same effect as for the coarse grid, with frequencies being shifted to the right. One observation from these results is that the higher frequencies, which are predominantly evident at the cavity rear (Figure 4.2(d)), are completely eliminated for the fine grids. Numerical dissipation tends to be less with finer grids so the reason for the absence of these higher frequencies in the finer grids may be due to the employed turbulence modelling strategy. Another observation is the over-prediction of the first Rossiter mode in all cases with the $k-\omega$ model.

For the Baseline $k-\omega$ turbulence model, the SPL and PSD produced for the same four computations are shown in Figure 4.3. As with the $k-\omega$ model, the effect of the lower time-step with the coarse grid on SPLs was negligible but shifted the location of the frequencies to the right when analysed in the Fourier domain. Refining the grid in space

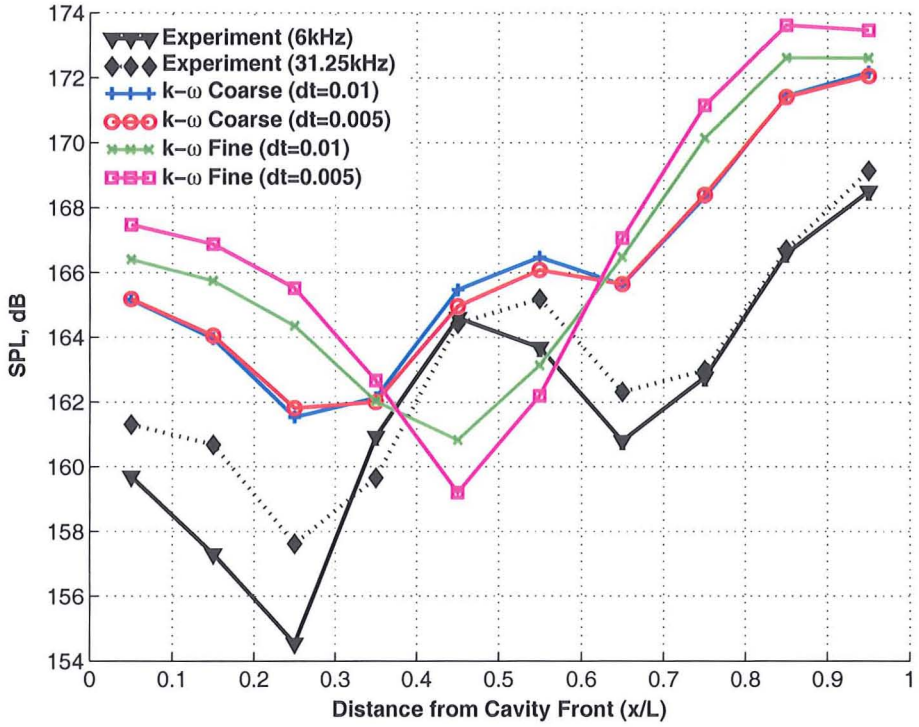

(a) SPLs

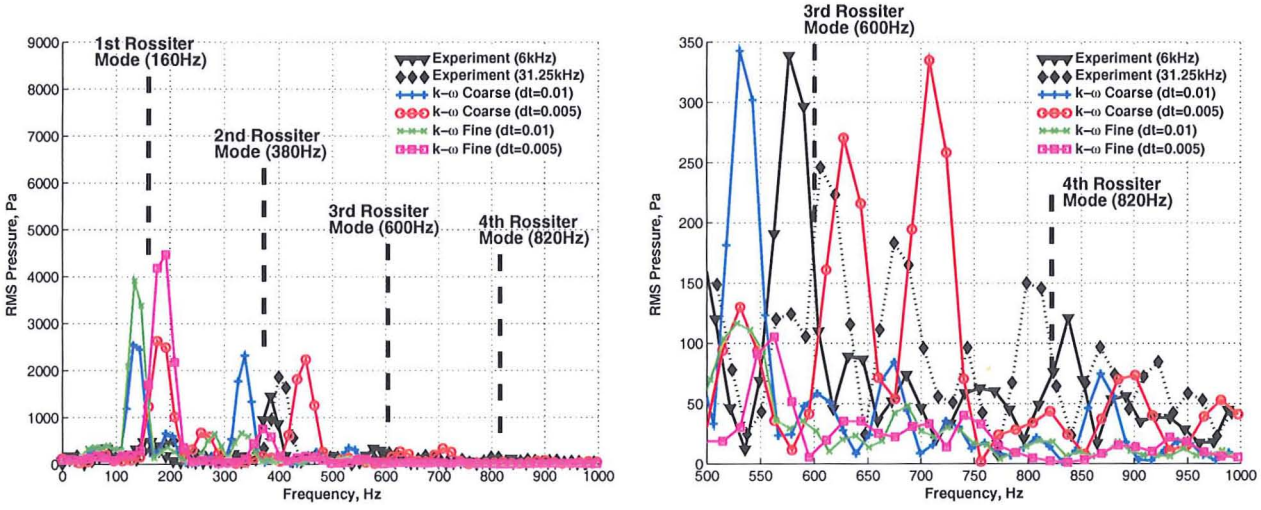

(b) PSD ($x/L = 0.05$): Full Spectrum (left), Zoomed View (right)

Figure 4.2: (continued)

however changed the shape of the SPL curve and hence shifted the dominance from the second mode to the lower frequencies.

Noise levels generated inside the cavity with the Baseline $k-\omega$ model were however far greater when compared to experiment and indeed the $k-\omega$ model results (Figure 4.3(a)). SPLs were slightly higher at the cavity front for the coarse grid with the Baseline $k-\omega$ model than for the $k-\omega$ model suggesting that noise resulting from flow separation at the lip of the cavity is more pronounced with the Baseline $k-\omega$ model.

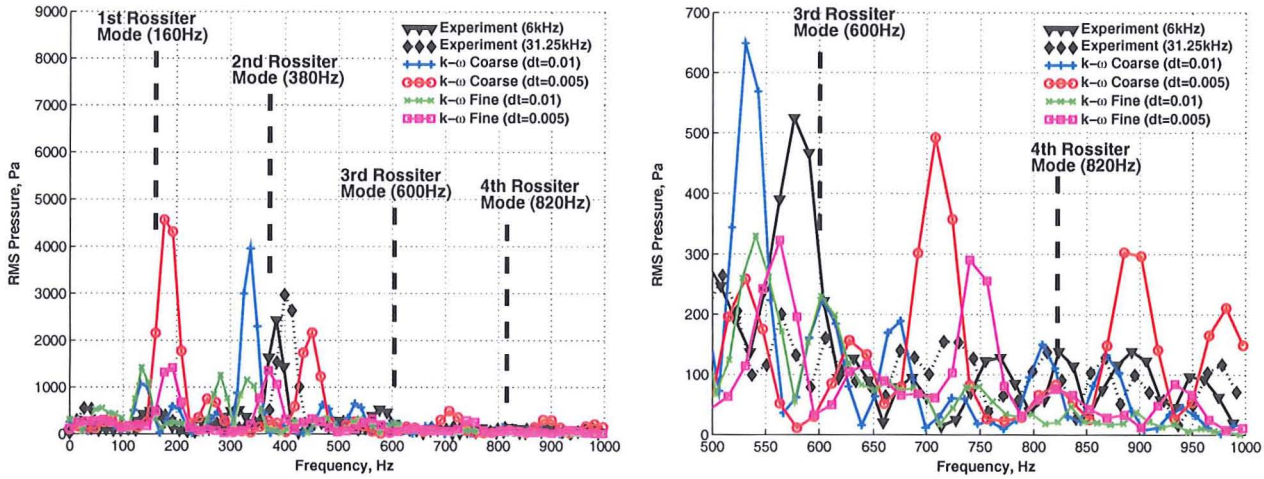

(c) PSD ($x/L = 0.55$): Full Spectrum (left), Zoomed View (right)

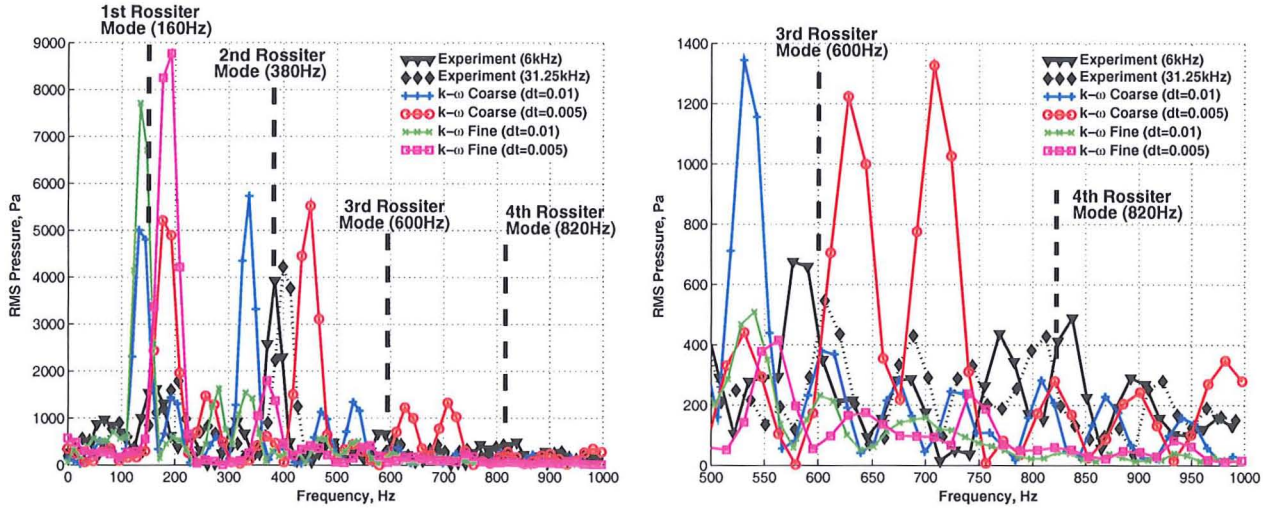

(d) PSD ($x/L = 0.95$): Full Spectrum (left), Zoomed View (right)

Figure 4.2: SPLs and PSD (at $x/L = 0.05$, $x/L = 0.55$ and $x/L = 0.95$) along the cavity floor for the 2D, L/D=5 cavity grid with the $k-\omega$ turbulence model for: coarse grid, $\Delta t = 0.01$ ($\equiv 1.814 \times 10^{-5}$s) [blue (plus markers)]; coarse grid, $\Delta t = 0.005$ ($\equiv 9.07 \times 10^{-6}$s) [red (circular markers)]; fine grid, $\Delta t = 0.01$ ($\equiv 1.814 \times 10^{-5}$s) [green (cross markers)]; fine grid, $\Delta t = 0.005$ ($\equiv 9.07 \times 10^{-6}$s) [magenta (square markers)].

Another difference between the Baseline $k-\omega$ and the standard $k-\omega$ models is the extremely high SPLs of about 180 dB generated at the cavity rear with the fine grids for the Baseline $k-\omega$ model compared to 173 dB for the $k-\omega$ model. Dominant frequencies for the Baseline $k-\omega$ model with the fine grid no longer coincide with any Rossiter mode positions and suggest that the flow has changed from the shear mode to the wake mode. Higher frequencies were also eliminated with the finer grids in a similar manner to the $k-\omega$ model. One other discernible difference between the Baseline $k-\omega$ and $k-\omega$ model results was the less significant dominance of the first mode in the Baseline $k-\omega$ model computations, especially with the coarse grid (Figures 4.3(b)-4.3(d)).

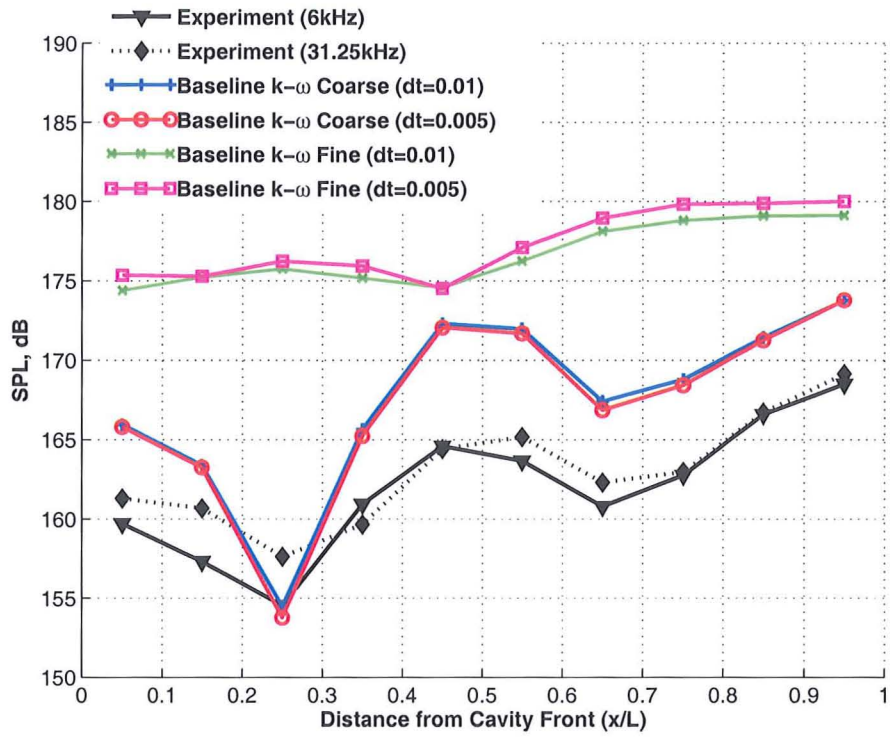

(a) SPLs

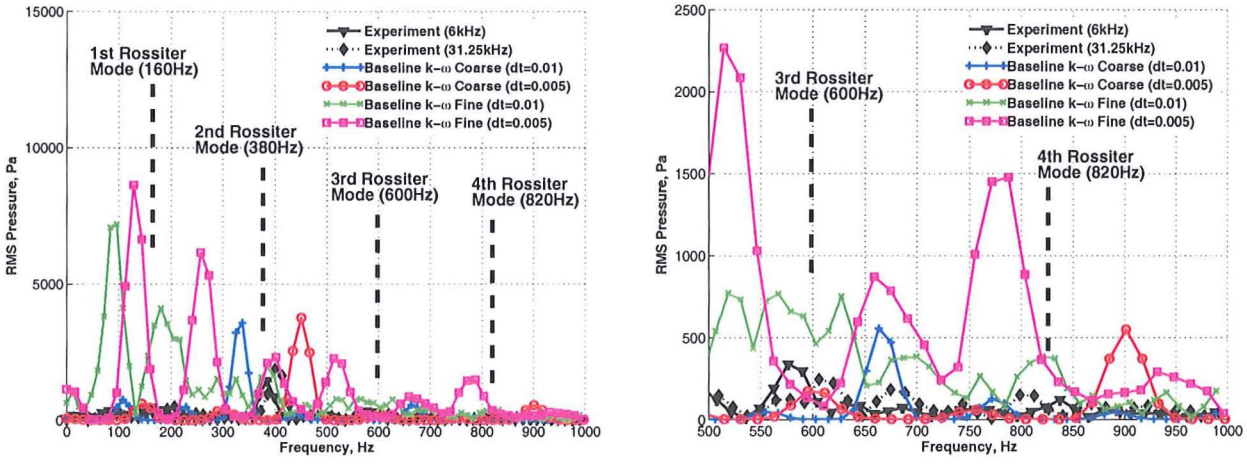

(b) PSD ($x/L = 0.05$): Full Spectrum (left), Zoomed View (right)

Figure 4.3: (continued)

SPL variations and spectral analyses for the coarse and fine grids at different time-steps for the SST model are illustrated in Figure 4.4. Noise levels produced inside the cavity with the SST model are much greater than experiment and $k-\omega$ results, especially at the cavity middle and rear (Figure 4.4(a)). In fact, the SPL distribution is very similar for the Baseline $k-\omega$ and SST models and this is related to the fact that both are zonal models formulated in a similar manner. Spectral analysis reveals a trend that is therefore also similar with the Baseline $k-\omega$ model results.

A change from the 'W' to a 'V'-shaped SPL curve with refinement of the grid in space

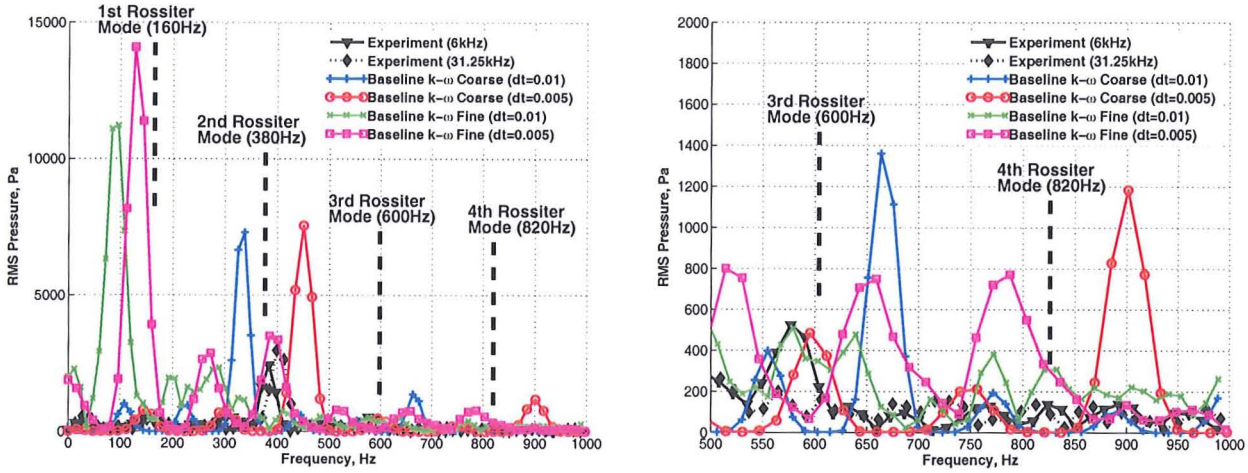

(c) PSD ($x/L = 0.55$): Full Spectrum (left), Zoomed View (right)

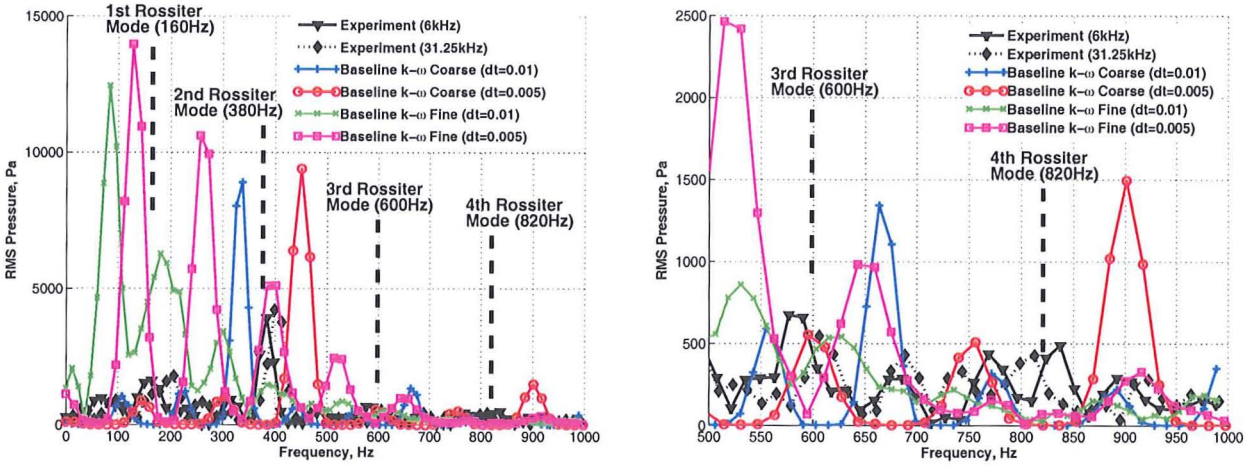

(d) PSD ($x/L = 0.95$): Full Spectrum (left), Zoomed View (right)

Figure 4.3: SPLs and PSD (at $x/L = 0.05$, $x/L = 0.55$ and $x/L = 0.95$) for the 2D, L/D=5 cavity grid with the Baseline $k-\omega$ turbulence model for: coarse grid, $\Delta t = 0.01$ ($\equiv 1.814 \times 10^{-5}$s) [blue (plus markers)]; coarse grid, $\Delta t = 0.005$ ($\equiv 9.07 \times 10^{-6}$s) [red (circular markers)]; fine grid, $\Delta t = 0.01$ ($\equiv 1.814 \times 10^{-5}$s) [green (cross markers)]; fine grid, $\Delta t = 0.005$ ($\equiv 9.07 \times 10^{-6}$s) [magenta (square markers)].

seems to be a common factor between all two-equation models tested. The SPL curve no longer has the characteristic 'double dip' and becomes almost flat with the Baseline $k-\omega$ and SST models. In this case, the overall noise levels are augmented by about 10 dB at the cavity rear compared to experiment. This change in shape of the SPL curve for the fine grid reflects changes in the flow physics inside the cavity (and vice versa). For the Baseline $k-\omega$ and SST models, spectral analysis revealed that frequencies appeared to resemble harmonics of a lower frequency of about 100 Hz. This is much lower than the first Rossiter mode ($\approx$ 160 Hz), as calculated by Rossiter's formula in Equation 1.3 in Chapter 1, that typically exists for the L/D=5 cavity at these flow conditions.

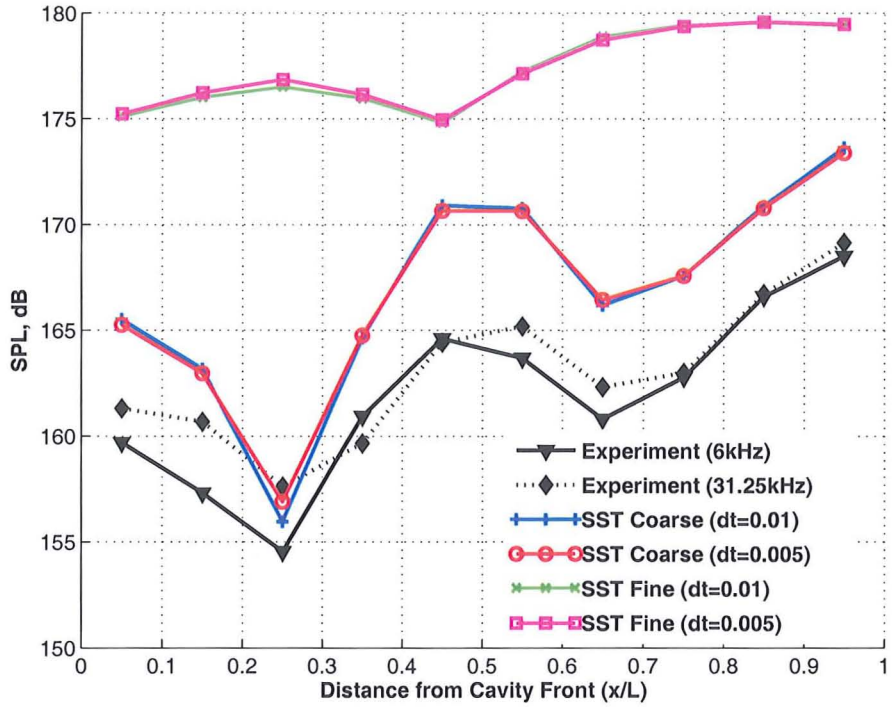

(a) SPLs

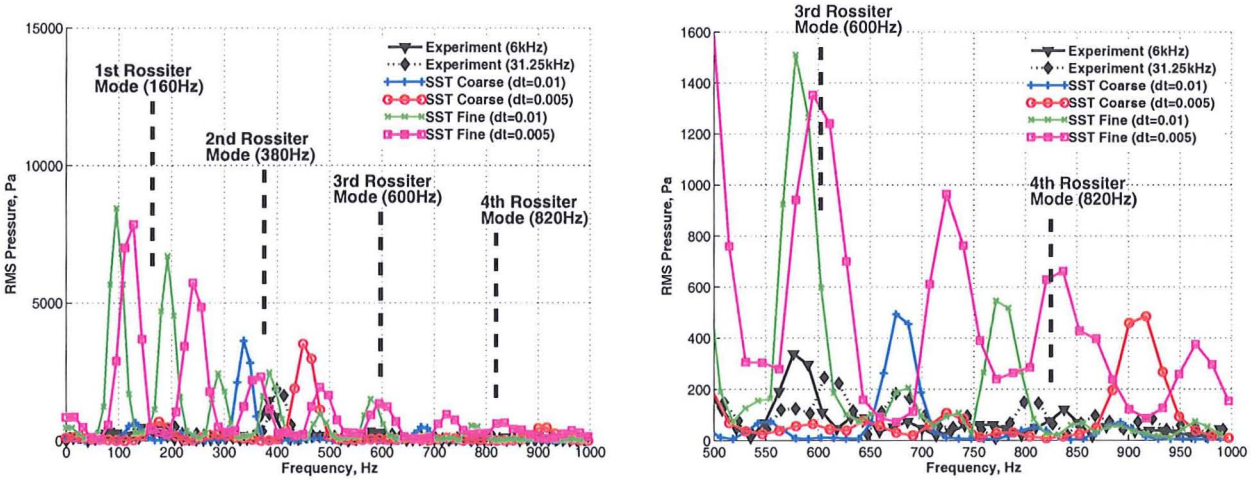

(b) PSD ($x/L = 0.05$): Full Spectrum (left), Zoomed View (right)

Figure 4.4: (continued)

4.2.2 Band-Limited Frequency Analysis

A closer inspection of the results is provided in Figures 4.5 to 4.7, which displays the band-limited noise level variations for 4 frequency ranges for the standard $k-\omega$, Baseline $k-\omega$ and SST models. These plots are useful as they clearly illustrate which modes are influenced by changes in spatial and temporal resolutions. Furthermore, it helps to highlight which frequencies are more dominant for the L/D=5 cavity and therefore can be used to identify the flow mechanisms occurring in the cavity.

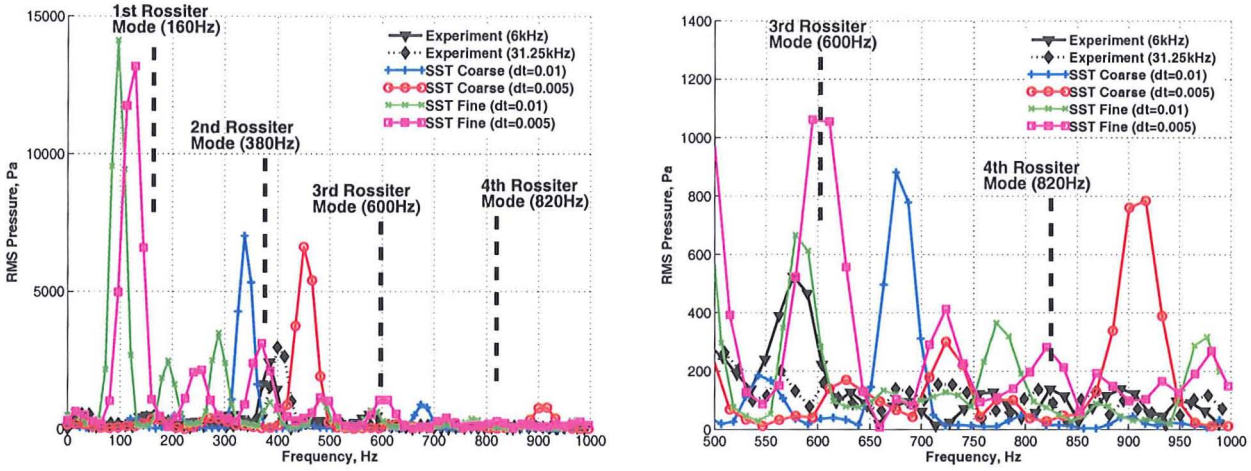

(c) PSD ($x/L = 0.55$): Full Spectrum (left), Zoomed View (right)

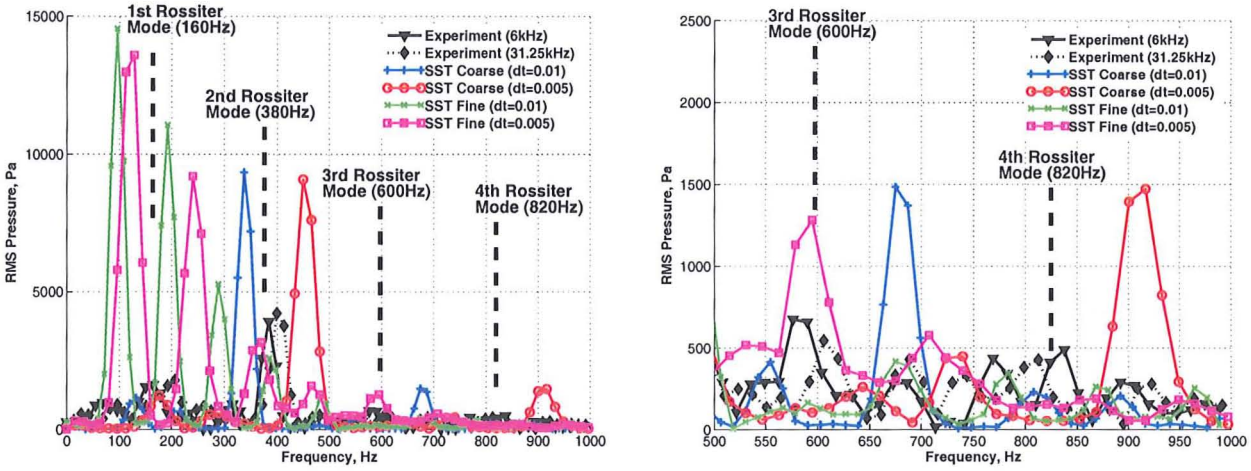

(d) PSD ($x/L = 0.95$): Full Spectrum (left), Zoomed View (right)

Figure 4.4: SPLs and PSD (at $x/L = 0.05$, $x/L = 0.55$ and $x/L = 0.95$) along the cavity floor for the 2D, L/D=5 cavity grid with the SST turbulence model for: coarse grid, $\Delta t = 0.01$ ($\equiv 1.814 \times 10^{-5}$s) [blue (plus markers)]; coarse grid, $\Delta t = 0.005$ ($\equiv 9.07 \times 10^{-6}$s) [red (circular markers)]; fine grid, $\Delta t = 0.01$ ($\equiv 1.814 \times 10^{-5}$s) [green (cross markers)]; fine grid, $\Delta t = 0.005$ ($\equiv 9.07 \times 10^{-6}$s) [magenta (square markers)].

The first ($\approx 160\ Hz$) and fourth ($\approx 820\ Hz$) Rossiter modes always appear to be over-predicted and under-predicted, respectively, by the $k-\omega$ model for both coarse and fine grids and time-steps. In contrast, the accuracy of the predictions of the second ($\approx 380\ Hz$) and third ($\approx 600\ Hz$) modes varies. For the first and third modes, time refinement has little effect on both coarse and fine grids whereas its effect is more evident on the second and fourth modes (Figure 4.5).

For the Baseline $k-\omega$ turbulence model, the trend was similar to that obtained with the $k-\omega$ model. Spatial refinement of the cavity grid increased the magnitudes of the first Rossiter mode significantly with values over-predicting experiment by $\approx$ 25–27 dB. The second mode was relatively well predicted and agreement between the turbulence model

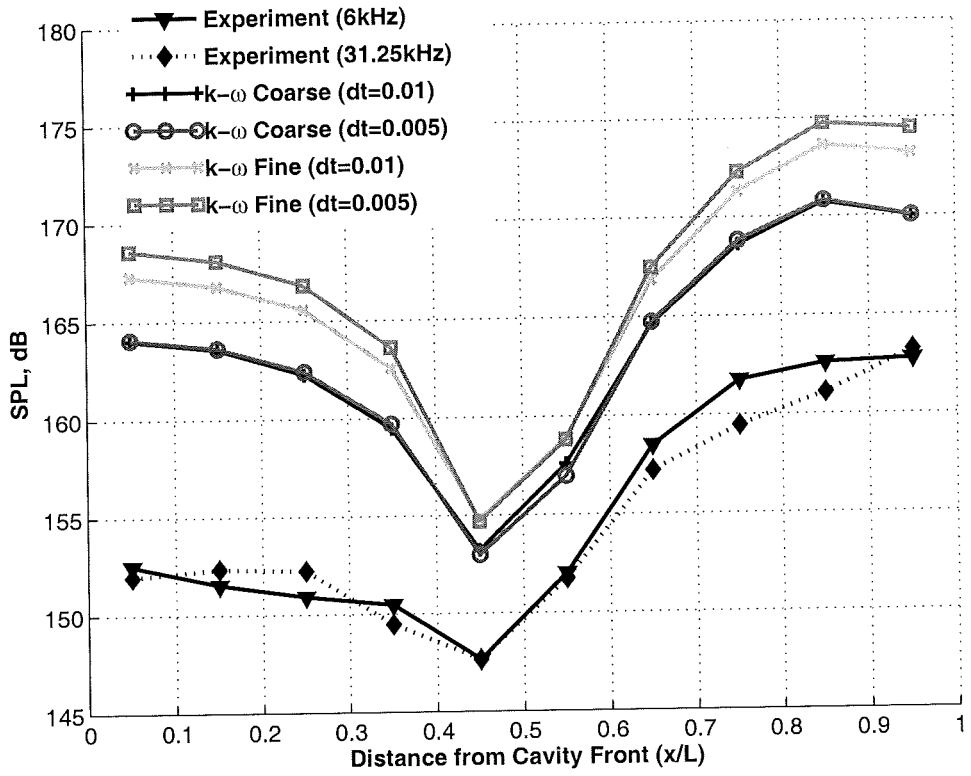

(a) $50\ Hz \leq f \leq 250\ Hz$

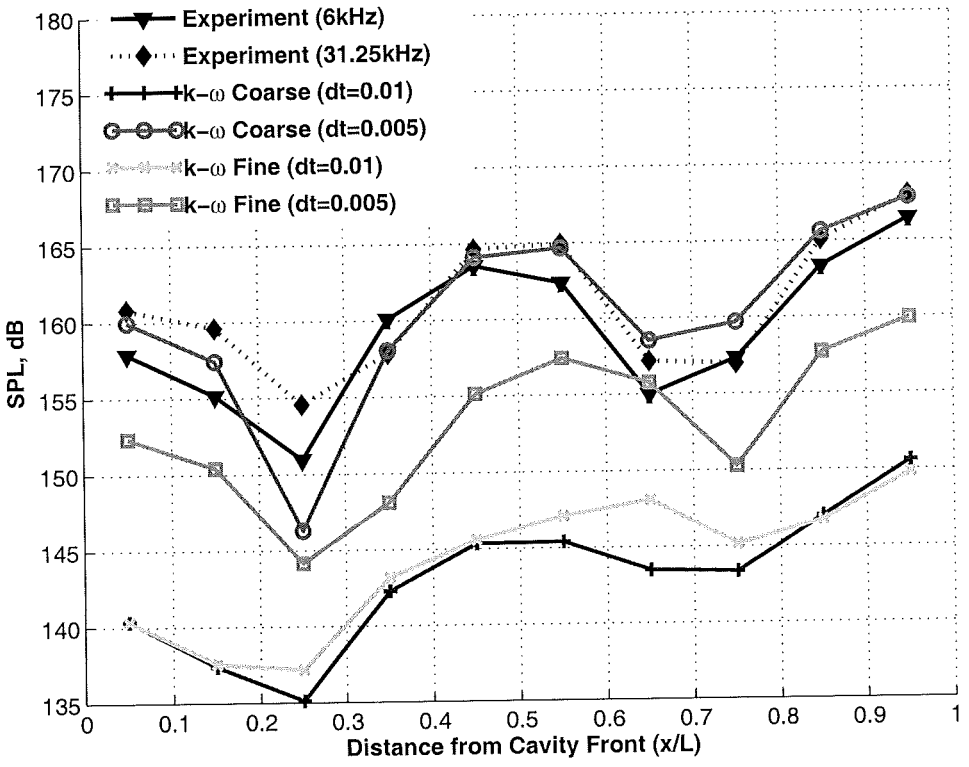

(b) $350\ Hz \leq f \leq 450\ Hz$

Figure 4.5: (continued)

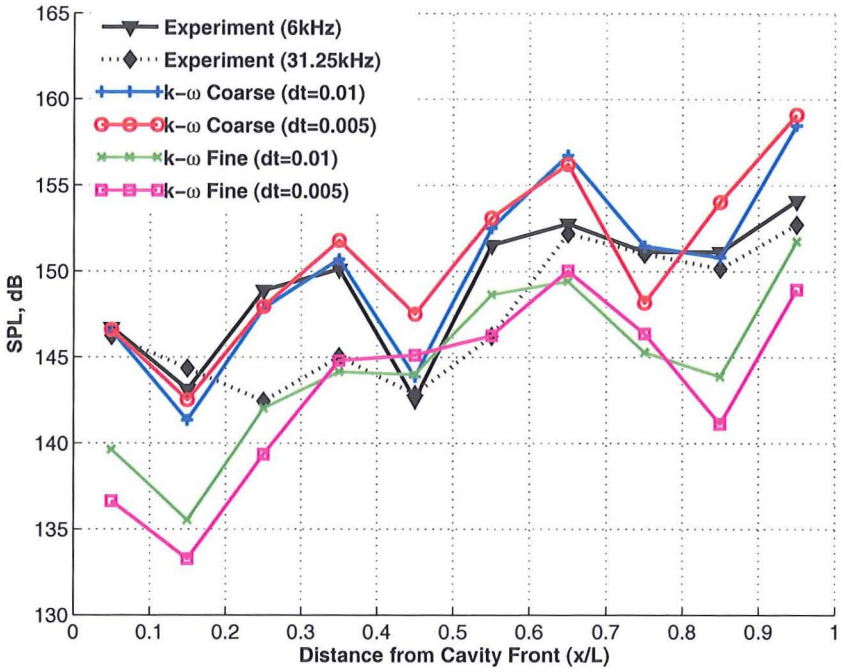

(c) $500\ Hz \leq f \leq 700\ Hz$

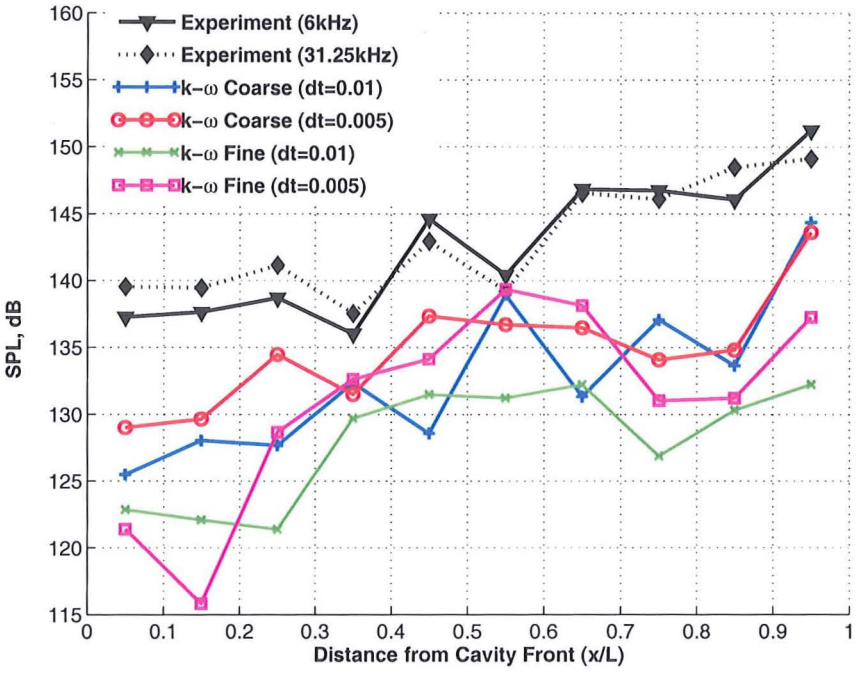

(d) $750\ Hz \leq f \leq 850\ Hz$

Figure 4.5: Band-limited SPL plots along the cavity floor for the 2D, L/D=5 cavity grid with the $k-\omega$ turbulence model for: coarse grid, $\Delta t = 0.01$ ($\equiv 1.814 \times 10^{-5}$s) [blue (plus markers)]; coarse grid, $\Delta t = 0.005$ ($\equiv 9.07 \times 10^{-6}$s) [red (circular markers)]; fine grid, $\Delta t = 0.01$ ($\equiv 1.814 \times 10^{-5}$s) [green (cross markers)]; fine grid, $\Delta t = 0.005$ ($\equiv 9.07 \times 10^{-6}$s) [magenta (square markers)].

and experiment improved with time refinement. Like for the $k-\omega$ results, the third mode was also over-predicted with the fourth mode comparing well with experiment at the cavity rear but deteriorating at the cavity front for finer grids (Figure 4.6).

Results from the coarse grid with the coarse time-step showed good comparison with experiment when the SST turbulence model was employed (Figure 4.7). With finer time-steps, agreement with experiment generally tended to improve especially at the higher frequency end. For the fine grid for coarse and fine time-steps, the first mode is again over-predicted by the SST model, similarly to the $k-\omega$ and Baseline $k-\omega$ model results. Agreement with experiment generally improved with the second Rossiter mode ($\approx 380\ Hz$) with the SST model when the grid was refined in space, as indicated in Figure 4.7(b). With coarse time-steps, the shape of the SPL curve for the second frequency band seemed slightly out of phase with experiment. This was however ameliorated with temporal refinement. Predictions for both the third and fourth Rossiter modes agreed well with experiment at the cavity rear when the grid is refined in space and time but this deteriorated at the cavity front.

4.2.3 Observations from Acoustic Spectrum Analyses

A few observations can be made in light of the results obtained so far. First, the first Rossiter mode is always over-predicted for the fine grid irrespective of the model used. This is particularly the case with the $k-\omega$ model, which also over-predicts the first mode amplitude regardless of grid and time-step (Figure 4.5(a)). Since spatial refinement has the effect of increasing the overall noise levels produced inside the cavity and the first mode exhibits the largest increase, this increase in SPLs is attributed to an increase in the amplitude of the first mode. Clearly, the first mode is highly sensitive to grid refinement. All models, for all grids, show negligible change in the first mode shape and amplitude with a lower time-step.

The second Rossiter mode ($\approx$ 380 Hz) is generally not as sensitive to grid refinement for the Baseline $k-\omega$ (Figures 4.6(b)) and SST (Figure 4.7(b)) models but appears to be sensitive to temporal refinement with agreement with experiment improving with lower time-steps. With the $k-\omega$ model, however, the second mode is still sensitive to the grid: large variations are observed between coarse and fine grids with both coarse and fine time-steps (Figure 4.5(b)). Higher frequencies are generally more sensitive to the time-step used but this is anticipated as the smaller flow scales are better captured with a lower time-step. Sensitivity to temporal refinement is however less pronounced with the $k-\omega$ model for higher frequencies (Figures 4.5(c)-4.5(d)) suggesting that the $k-\omega$ model is particularly sensitive to spatial refinement and less so with time refinement. Similarities with the Baseline $k-\omega$ and SST model results are likely to be due to their similar formulations.

4.2.4 Boundary Layer Characteristics

To understand why a change in the shape of the SPL curve from a 'W' to a 'V' occurs for the $k-\omega$, Baseline $k-\omega$ and SST models with grid refinement, the properties of the boundary layer were investigated. Boundary layer profiles for the flow just upstream of the

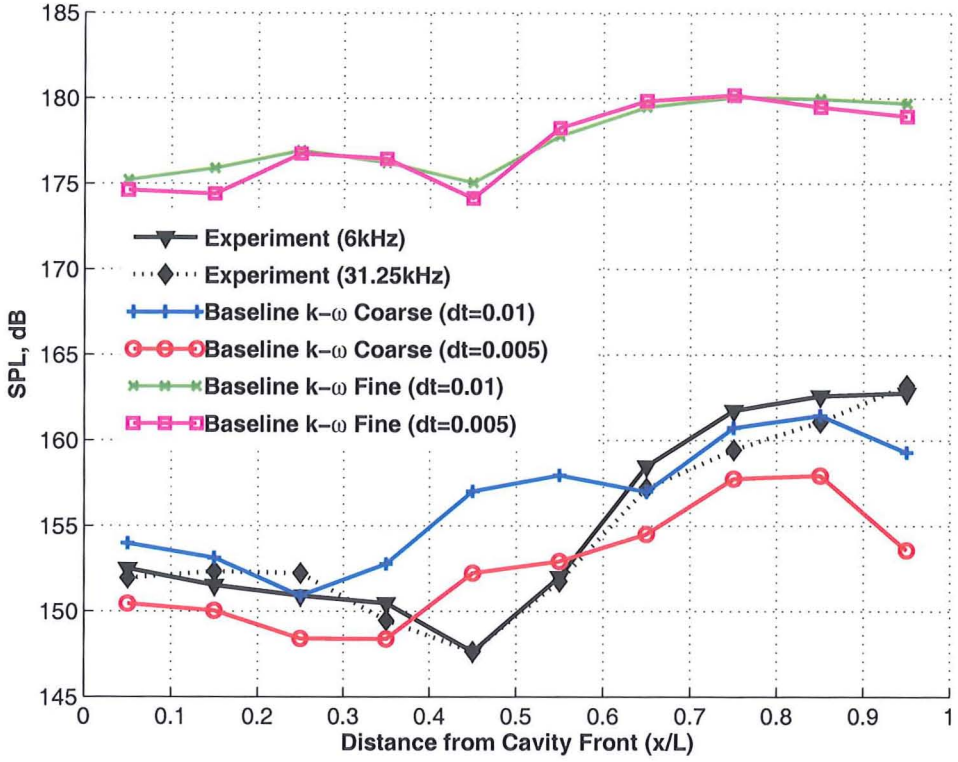

(a) $50\ Hz \leq f \leq 250\ Hz$

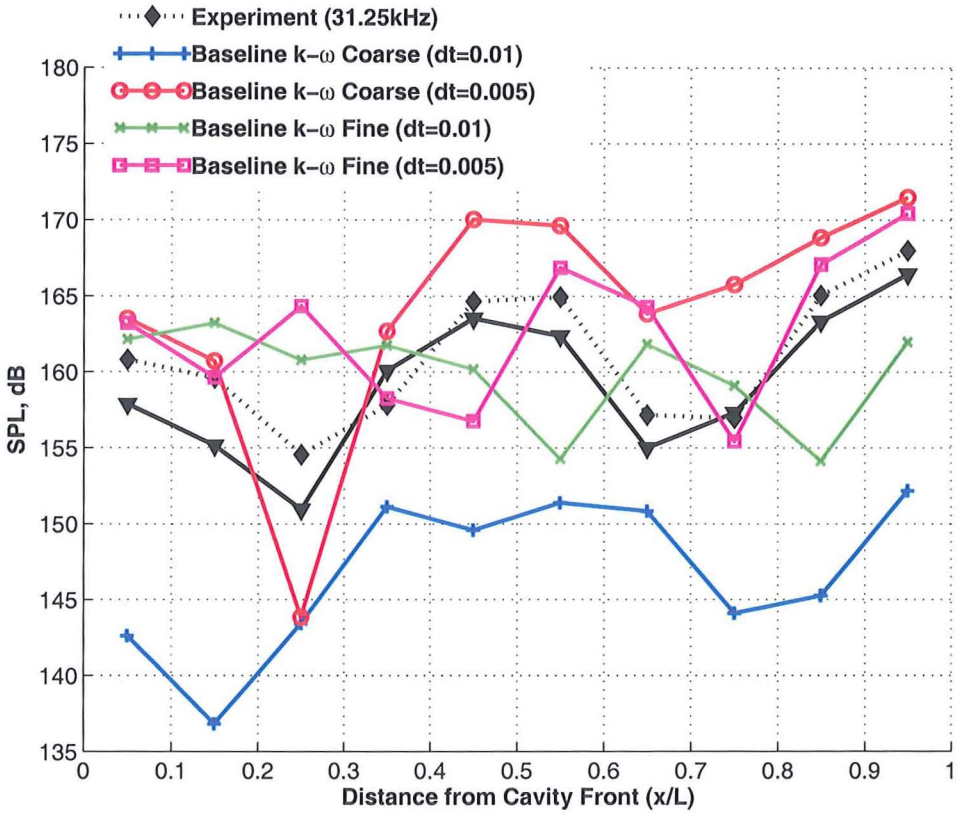

(b) $350\ Hz \leq f \leq 450\ Hz$

Figure 4.6: (continued)

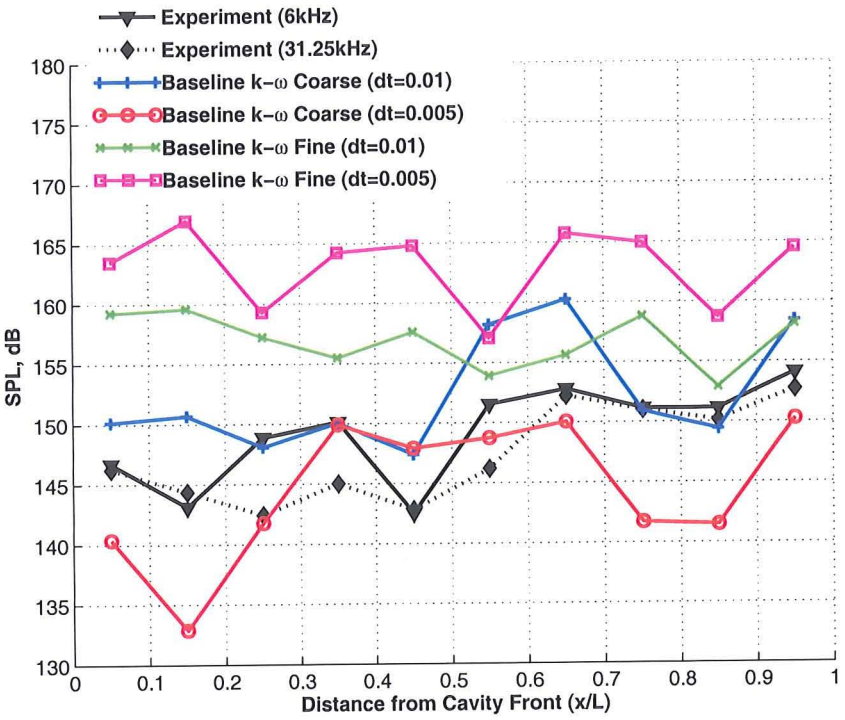

(c) $500\ Hz \leq f \leq 700\ Hz$

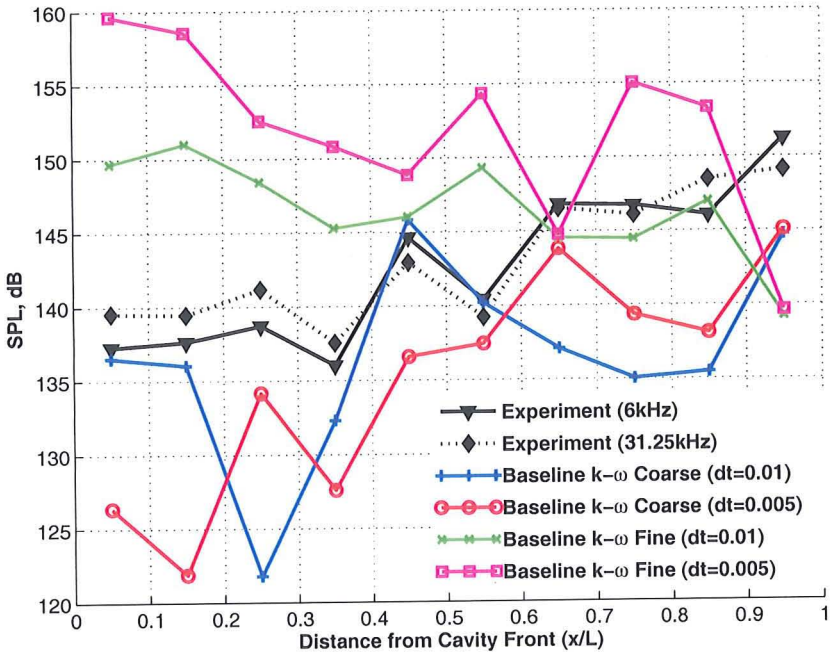

(d) $750\ Hz \leq f \leq 850\ Hz$

Figure 4.6: Band-limited SPL plots along the cavity floor for the 2D, L/D=5 cavity grid with the Baseline $k-\omega$ turbulence model for: coarse grid, $\Delta t = 0.01$ ($\equiv 1.814 \times 10^{-5}$s) [blue (plus markers)]; coarse grid, $\Delta t = 0.005$ ($\equiv 9.07 \times 10^{-6}$s) [red (circular markers)]; fine grid, $\Delta t = 0.01$ ($\equiv 1.814 \times 10^{-5}$s) [green (cross markers)]; fine grid, $\Delta t = 0.005$ ($\equiv 9.07 \times 10^{-6}$s) [magenta (square markers)].

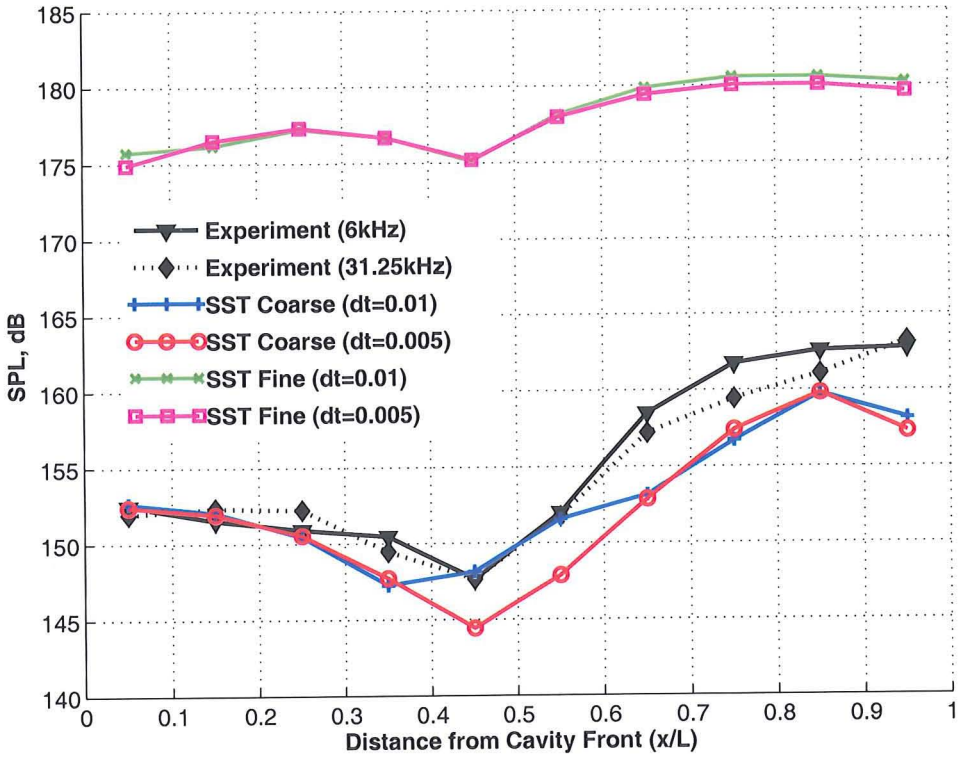

(a) $50\ Hz \leq f \leq 250\ Hz$

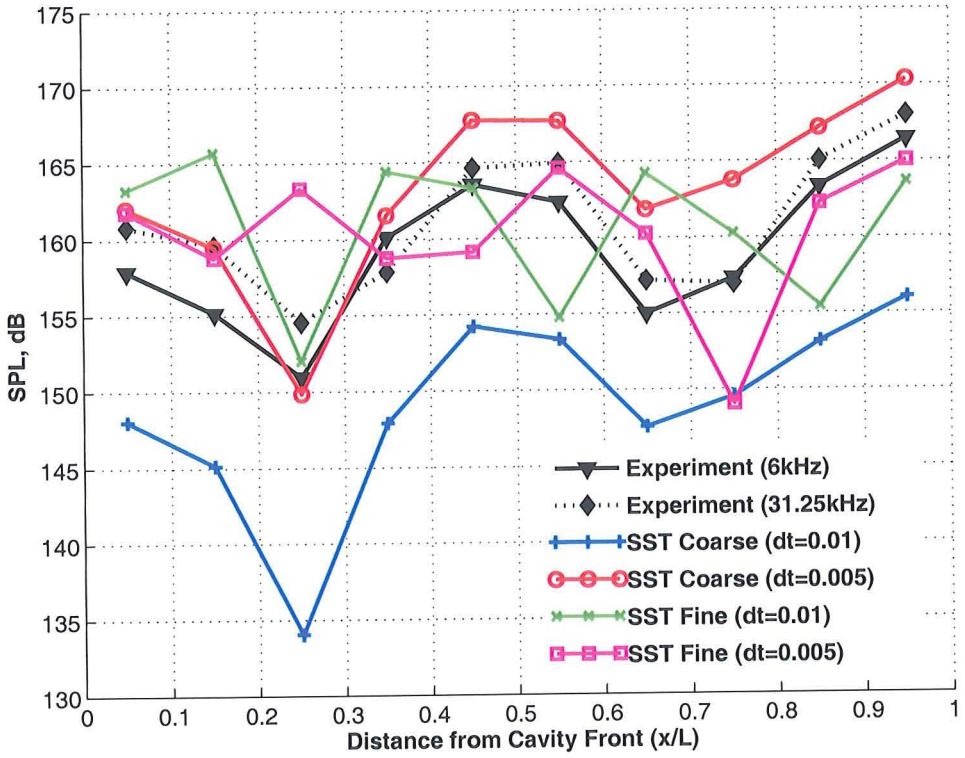

(b) $350\ Hz \leq f \leq 450\ Hz$

Figure 4.7: (continued)

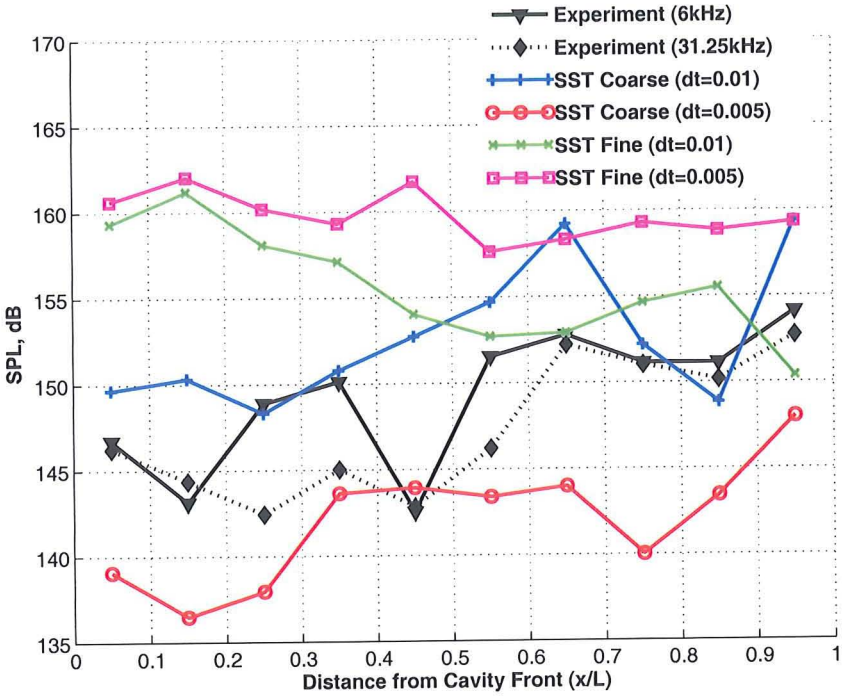

(c) $500\ Hz \leq f \leq 700\ Hz$

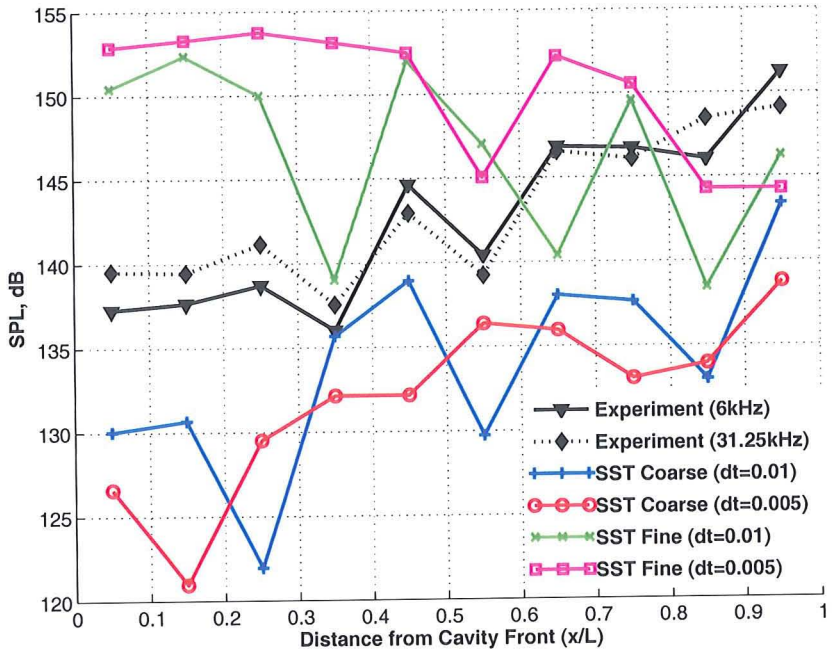

(d) $750\ Hz \leq f \leq 850\ Hz$

Figure 4.7: Band-limited SPL plots along the cavity floor for the 2D, L/D=5 cavity grid with the SST turbulence model for: coarse grid, $\Delta t = 0.01$ ($\equiv 1.814 \times 10^{-5}$s) [blue (plus markers)]; coarse grid, $\Delta t = 0.005$ ($\equiv 9.07 \times 10^{-6}$s) [red (circular markers)]; fine grid, $\Delta t = 0.01$ ($\equiv 1.814 \times 10^{-5}$s) [green (cross markers)]; fine grid, $\Delta t = 0.005$ ($\equiv 9.07 \times 10^{-6}$s) [magenta (square markers)].

mouth of the cavity (at $x/L = -0.05$) for coarse and fine grids and time-steps are illustrated in Figures 4.8, 4.9 and 4.10 corresponding to the $k-\omega$, Baseline $k-\omega$ and SST models, respectively. Thicknesses of the boundary layer are clearly annotated for comparison purposes. Prior to any refinement in space or time, the boundary layer is the thickest for the $k-\omega$ model for the coarse grid at a coarse time-step, $\delta = 0.035L$ (Figure 4.8(a)). Changes in the transverse velocity in space and time for the $k-\omega$ model are minimal. The increase in boundary layer thickness and the slight increase in the transverse velocity for the fine grids suggest that the flow becomes slightly more turbulent as the grid density is increased with the $k-\omega$ model (Figure 4.8(b)).

Temporal refinement has little effect on the shape and intensity of the streamwise and transverse velocity components in the oncoming boundary layer for all models. Refinement in space however has a more obvious change in the characteristics of the boundary layer. Typically, the boundary layer is observed to become thicker as the grid is refined. Compared to the coarse grid, the boundary layer thickness for the fine grid was twice as large for the Baseline $k-\omega$ model and 1.5 times larger for the SST model. Transverse velocity components also exhibit large increases for the Baseline $k-\omega$ (Figure 4.9(b)) and SST (Figure 4.10(b)) models. The profile of the streamwise velocity suggests that a more laminar-like boundary layer exists for the fine grids.

Since these velocity profiles are extracted near the lip of the cavity, where the flow separates, most, if not all, of the energy and momentum contained within the boundary layer is likely to be imparted into the shear layer. For the $k-\omega$ model, the boundary layer characteristics demonstrate a thickening of the boundary layer with finer grids. Consequently, the shear layer predicted by the $k-\omega$ model with finer grids will be thicker and more turbulent, which is less susceptible to deflections from the vortical structures existing inside the cavity. The lack of shear layer fluctuations suppress any higher frequencies from being generated. Lower-frequency motion become the prominent source of noise and the SPL curve exhibits a change in shape from a 'W' to a 'V' shape (Figure 4.2(a)).

In contrast, the large change in transverse velocity component with fine grids for the Baseline $k-\omega$ and SST models demonstrate that the flow has become less turbulent. The lower turbulent levels mean that the vortices are less viscous and freer to move. In fact, the vortices are stronger with the fine grids for the Baseline $k-\omega$ and SST models and evidence of this is provided in the flow-field plots in the next section. The shear layer is also less turbulent and is more prone to fluctuations. The stronger vortices push the weaker shear layer outwards and prevent it from extending across the cavity opening. Since the shear layer does not impinge on the rear wall in this situation, higher frequencies are not generated. Lower frequencies again prevail and the SPL curve changes from a 'W' to a flatter curve with fewer kinks (Figures 4.3(a) and 4.4(a)). This flatter SPL curve for the Baseline $k-\omega$ and SST models is attributed to the shear layer not extending across the cavity.

4.2.5 Flow-field Visualisation

Verification of the results and explanations provided in the previous sections is presented via flow-field visualisation for the $k-\omega$, Baseline $k-\omega$ and SST turbulence models. Time-averaged plots using Mach contours normalised by the free-stream Mach number of 0.85 superimposed with streamlines are employed to illustrate the differences in the cavity

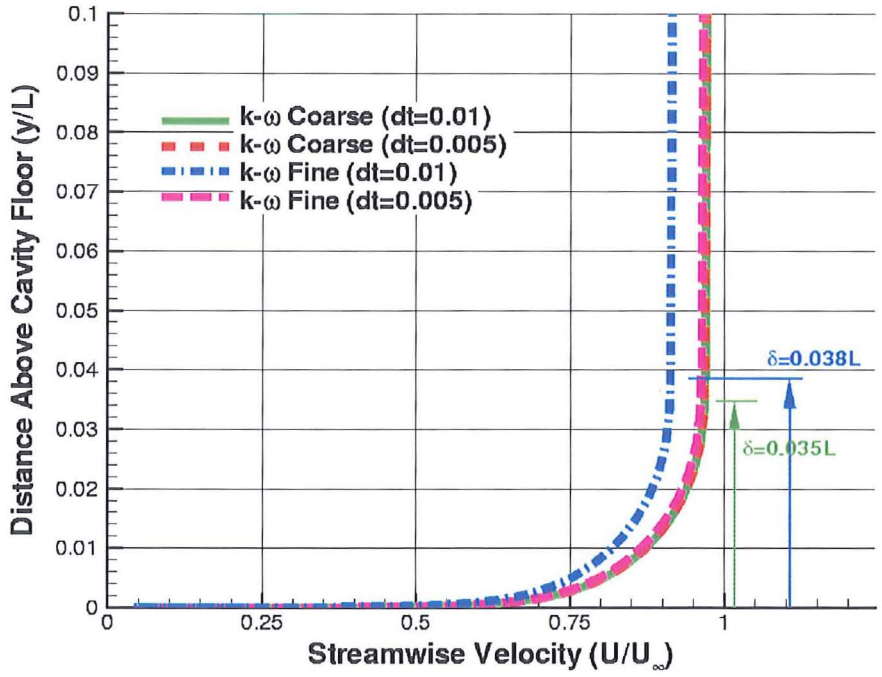

(a) Streamwise Velocity ($\frac{U}{U_\infty}$)

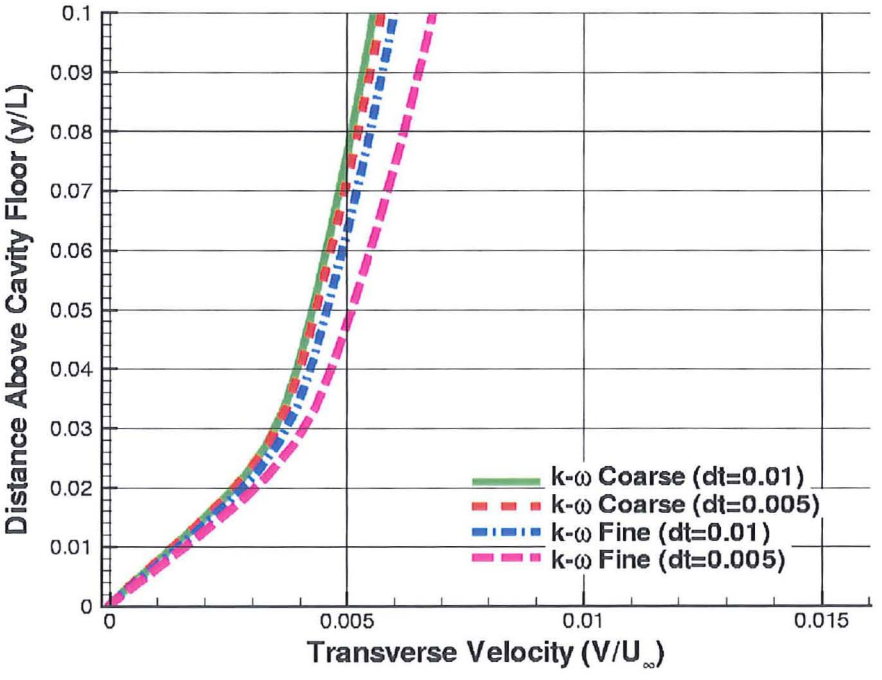

(b) Transverse Velocity ($\frac{V}{V_\infty}$)

Figure 4.8: Boundary layer profiles at x/L=-0.05 for the 2D, L/D=5, cavity grid with the $k-\omega$ turbulence model for: coarse grid, $\Delta t = 0.01$ ($\equiv 1.814 \times 10^{-5}$s) [green (solid) lines]; coarse grid, $\Delta t = 0.005$ ($\equiv 9.07 \times 10^{-6}$s) [red (dashed) lines]; fine grid, $\Delta t = 0.01$ ($\equiv 1.814 \times 10^{-5}$s) [blue (dash-dot) lines]; fine grid, $\Delta t = 0.005$ ($\equiv 9.07 \times 10^{-6}$s) [magenta (long-dashed) lines].

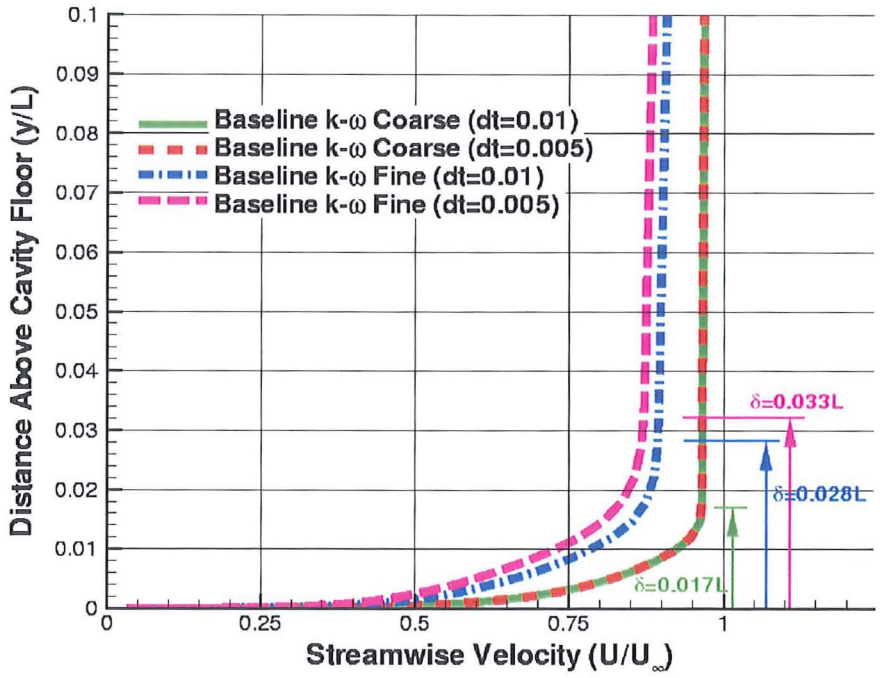

(a) Streamwise Velocity ($\frac{U}{U_\infty}$)

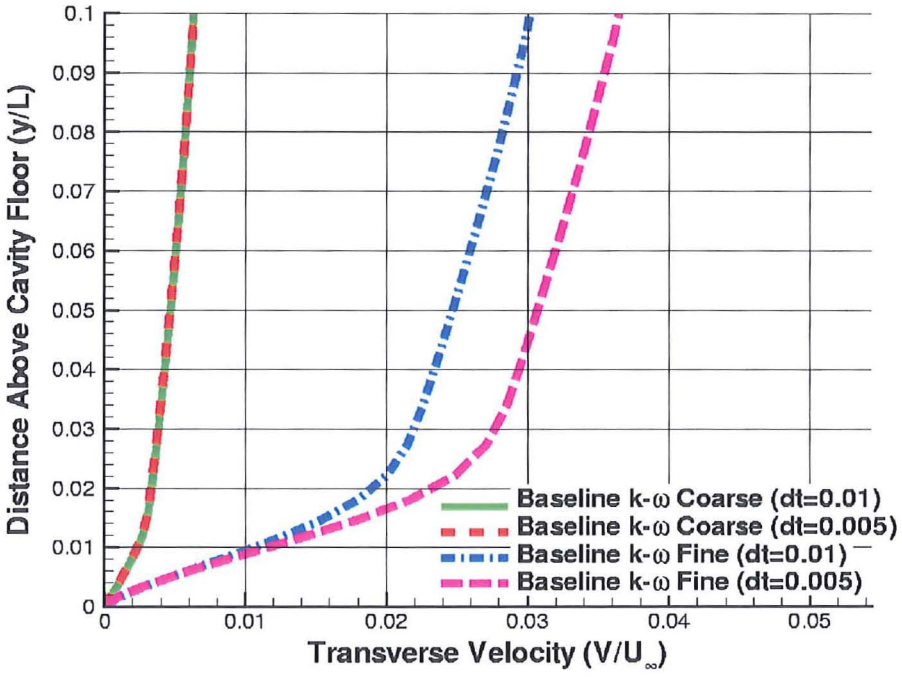

(b) Transverse Velocity ($\frac{V}{V_\infty}$)

Figure 4.9: Boundary layer profiles at x/L=-0.05 for the 2D, L/D=5, cavity grid with the Baseline $k-\omega$ turbulence model for: coarse grid, $\Delta t = 0.01$ ($\equiv 1.814 \times 10^{-5}$s) [green (solid) lines]; coarse grid, $\Delta t = 0.005$ ($\equiv 9.07 \times 10^{-6}$s) [red (dashed) lines]; fine grid, $\Delta t = 0.01$ ($\equiv 1.814 \times 10^{-5}$s) [blue (dash-dot) lines]; fine grid, $\Delta t = 0.005$ ($\equiv 9.07 \times 10^{-6}$s) [magenta (long-dashed) lines].

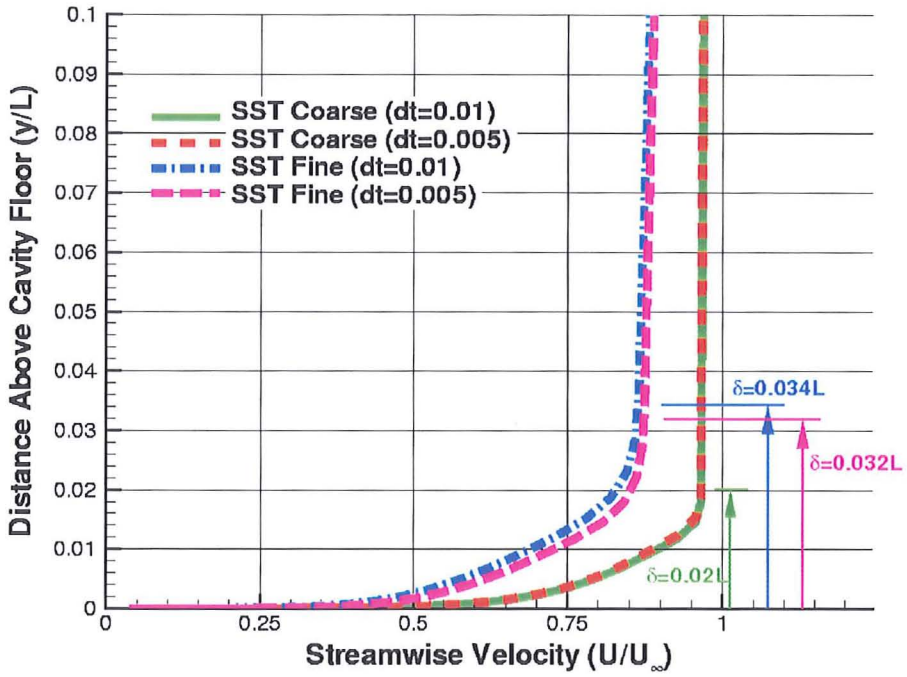

(a) Streamwise Velocity ($\frac{U}{U_\infty}$)

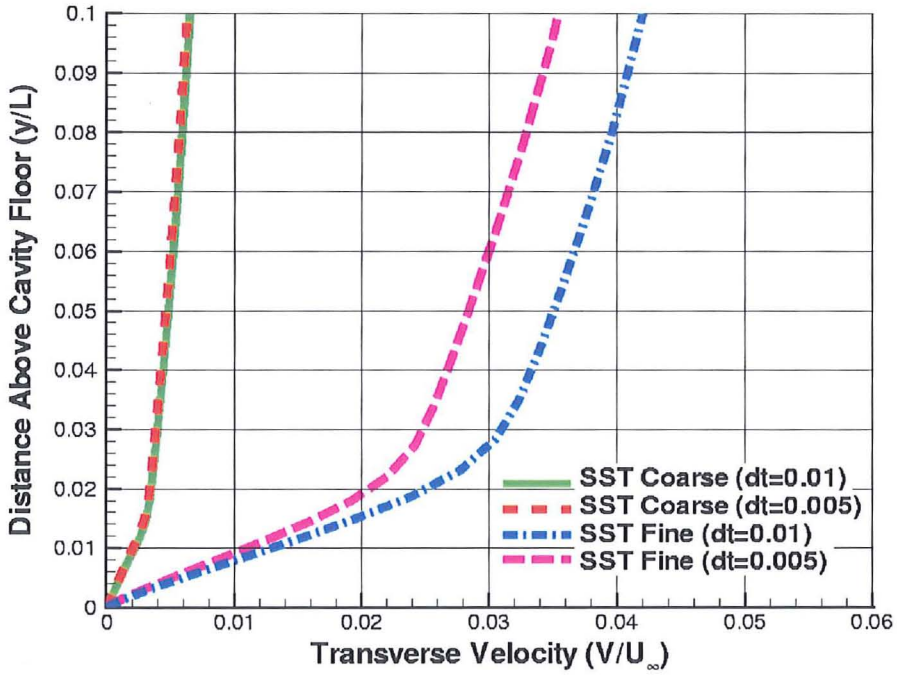

(b) Transverse Velocity ($\frac{V}{V_\infty}$)

Figure 4.10: Boundary layer profiles at x/L=-0.05 for the 2D, L/D=5, cavity grid with the SST turbulence model for: coarse grid, $\Delta t = 0.01$ ($\equiv 1.814 \times 10^{-5}$s) [green (solid) lines]; coarse grid, $\Delta t = 0.005$ ($\equiv 9.07 \times 10^{-6}$s) [red (dashed) lines]; fine grid, $\Delta t = 0.01$ ($\equiv 1.814 \times 10^{-5}$s) [blue (dash-dot) lines]; fine grid, $\Delta t = 0.005$ ($\equiv 9.07 \times 10^{-6}$s) [magenta (long-dashed) lines].

flow mechanisms for the spatial and temporal refinements. Mach contours are used to highlight both shear and boundary layers.

A single primary vortex exists inside the cavity with the $k-\omega$ model and this scenario is sustained irrespective of grid density and time-step as demonstrated in Figure 4.11. The positions of vortex cores have not been affected significantly although the vortex cores appear to be a little more stretched and span a greater proportion of the cavity length in the fine grid computations.

The boundary layer is slightly thicker for the fine grid computations and this results in a thicker shear layer. The shear layer also appears to be more diffused in the fine grid computations at the cavity front and middle (Figure 4.11(c)). Spreading of the shear layer adds more momentum to the vortex inside the cavity increasing its vorticity. Regions of higher Mach number (depicted by the lighter (green) colours) at the cavity floor for the fine grid results (Figures 4.11(c) and 4.11(d)) compared to the coarse grid results (Figures 4.11(a) and 4.11(b)) are a testament to this. The higher noise levels observed at the front of the cavity with the finer grids in Figure 4.2(a) therefore result from this thicker shear layer separating at the lip of the cavity. Similarly, more noise is produced at the rear of the cavity with the finer grids due to the impingement of a thicker shear layer on the downstream wall. For each grid density, lowering the time-step has little effect on the properties of the shear layer and the vortex.

Figure 4.12 displays the flow-field plots for the same four computations with the Baseline $k-\omega$ model. As shown, a large vortex is now predicted at the front of the cavity. Combined with the vortex that spans the rest of the cavity domain, a dual vortex cycle exists for the Baseline $k-\omega$ model on average with the coarse grid. The core of the primary vortex situated near the rear of the cavity is more stretched (Figure 4.12(a)) than that of the $k-\omega$ vortex core (Figure 4.11(a)). Mach values are also higher near the cavity floor and extend over a greater proportion of the cavity length (with the Baseline $k-\omega$ model than with the $k-\omega$ model). Peripheral velocities of the vortex must therefore be predicted to be higher with the Baseline $k-\omega$ model. This is likely to be due to the Baseline $k-\omega$ model being formulated as a blend of the $k-\omega$ and $k-\varepsilon$ models with the $k-\omega$ model activated near the wall and the $k-\varepsilon$ model triggered at a distance away from the wall. The Baseline $k-\omega$ model produces lower levels of eddy viscosity so the vortex exhibits more laminar properties leading to stronger vortices and hence more noise being generated from the interaction with the cavity walls.

On refinement of the grids in space, the time-averaged plots confirm that the flow physics inside the cavity changes completely for the fine grids. Rather than a large vortex located toward the downstream wall of the cavity, a large vortex exists near the front of the cavity (Figure 4.12(c)). This vortex is significantly larger in size and extends out of the cavity depth deflecting the flow around it upwards. This pushes the separation point from the cavity lip to further upstream. Boundary layer height is increased as a result and this enables more energy to be imparted into the vortices adding to their momentum. A shear layer does not form across the cavity opening because of the large vortex at the cavity front and a vortex shedding cycle takes place. A small region of recirculation situated at the upstream wall corner in Figure 4.12(c) is created as the large vortex detaches from the cavity floor. Absorption of energy from the larger vortex ensures growth of this smaller vortex. Negative vorticity accumulates as this smaller vortex grows and pushes the larger vortex away from the walls, which subsequently convects downstream and dissipates away. Energy from the premature separation of the boundary layer is fed into this smaller vortex allowing it to grow further. A flow cycle is thereby maintained and the

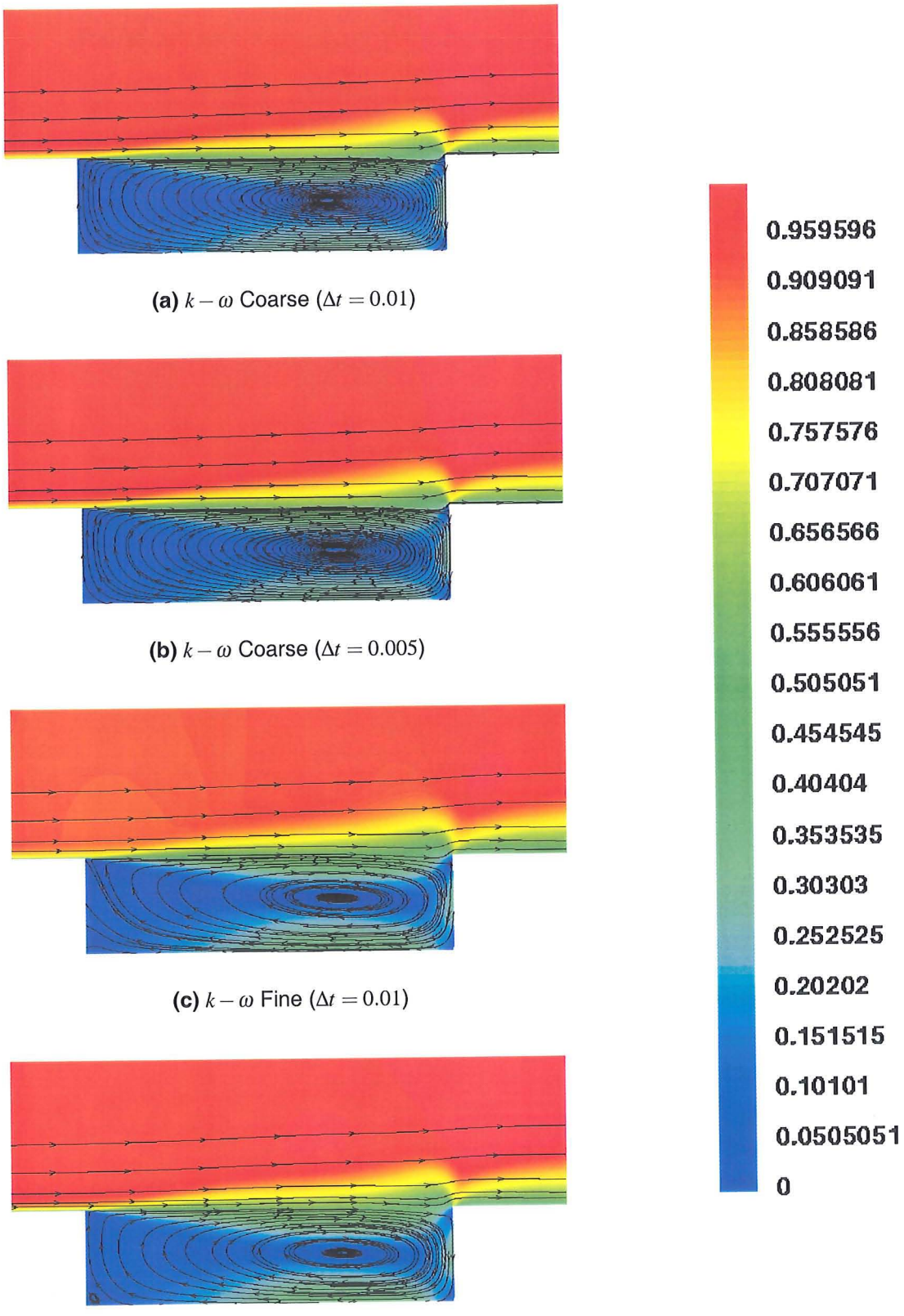

(a) $k-\omega$ Coarse ($\Delta t = 0.01$)

(b) $k-\omega$ Coarse ($\Delta t = 0.005$)

(c) $k-\omega$ Fine ($\Delta t = 0.01$)

(d) $k-\omega$ Fine ($\Delta t = 0.005$)

Figure 4.11: Time-averaged flow-field plots using normalised Mach contours and streamlines for the 2D, L/D=5, cavity with the $k-\omega$ turbulence model for: coarse grid, $\Delta t = 0.01$ ($\equiv 1.814 \times 10^{-5}$s); coarse grid, $\Delta t = 0.005$ ($\equiv 9.07 \times 10^{-6}$s); fine grid, $\Delta t = 0.01$ ($\equiv 1.814 \times 10^{-5}$s); fine grid, $\Delta t = 0.005$ ($\equiv 9.07 \times 10^{-6}$s).

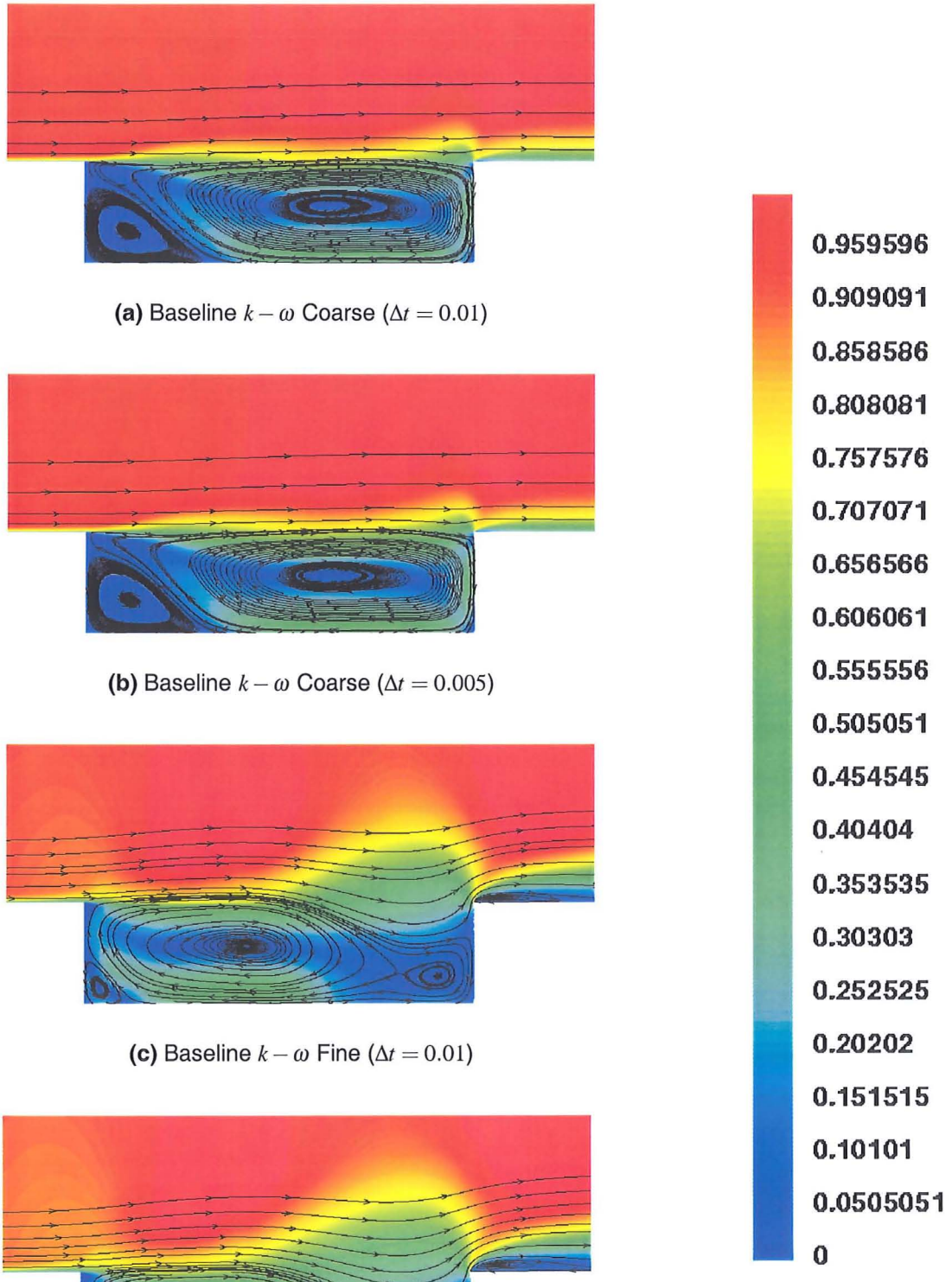

(a) Baseline $k-\omega$ Coarse ($\Delta t = 0.01$)

(b) Baseline $k-\omega$ Coarse ($\Delta t = 0.005$)

(c) Baseline $k-\omega$ Fine ($\Delta t = 0.01$)

(d) Baseline $k-\omega$ Fine ($\Delta t = 0.005$)

Figure 4.12: Time-averaged flow-field plots using normalised Mach contours and streamlines for the 2D, L/D=5, cavity with the Baseline $k-\omega$ turbulence model for the coarse grid, $\Delta t = 0.01$ ($\equiv 1.814 \times 10^{-5}$s); coarse grid, $\Delta t = 0.005$ ($\equiv 9.07 \times 10^{-6}$s); fine grid, $\Delta t = 0.01$ ($\equiv 1.814 \times 10^{-5}$s); fine grid, $\Delta t = 0.005$ ($\equiv 9.07 \times 10^{-6}$s).

vortex shedding cycle continues. High peripheral velocities of the vortices generate high quantities of noise as they interact with the shear layer and the cavity walls and clarifies why the fine grids produce such high SPLs with the Baseline $k-\omega$ model (Figure 4.3(a)).

By refining the fine grid in time, the smaller vortex located at the cavity rear is observed to grow in size (Figure 4.12(d)). Although much smaller in dimension than the primary vortex, its increased vorticity magnitude (identified by a slightly greater region of lighter-coloured Mach contours) creates more noise as it interacts with the cavity floor and back wall supplementing the overall SPLs generated at the cavity floor. A larger number of vortices are also present in the fine grid computations for the Baseline $k-\omega$ model than were noticed with the $k-\omega$ model.

Results from the SST model for the same four computations are presented in Figure 4.13. The differences between the Baseline $k-\omega$ and SST model results are minimal because their formulations are similar.

The fact that the time-averaged flow-field plots of the $k-\omega$ and Baseline $k-\omega$ models are so different from each other suggests that the different formulation far from the wall incorporated in the Baseline $k-\omega$ model is responsible. Greatest dissipation occurs near the cavity walls or at the surfaces of the flat plate upstream and downstream of the cavity. Away from the walls, toward the centre of the cavity and in the shear layer, for instance, the $k-\omega$ model does not introduce additional dissipation to model the decay of turbulence. The flow therefore remains turbulent. Originally designed for free shear flows, the $k-\varepsilon$ model adds more dissipation in regions that are far from the wall. Levels of turbulence inside the cavity with the $k-\varepsilon$ (and hence Baseline $k-\omega$) model should therefore be somewhat lower than with the $k-\omega$ model alone.

4.2.6 Turbulent Spectrum Analysis

Figure 4.14 illustrates the level of turbulence predicted by the $k-\omega$ and Baseline $k-\omega$ models by depicting the variations in eddy viscosity levels across the cavity depth for three stations inside the cavity (namely $x/L=0.05$, $x/L=0.55$ and $x/L=0.95$). The SST model gives results similar to the Baseline $k-\omega$ model and so its results are not described here. Near the wall, the Baseline $k-\omega$ model is identical to the $k-\omega$ model so the predicted boundary layer on the flat plate upstream of the cavity is expected to be the same for both models. Since most energy from the boundary layer is expected to be imparted into the shear layer, at the front of the cavity (i.e. $x/L=0.05$), eddy viscosity levels should be reasonably similar for both models (Figures 4.14(a) and 4.14(b)). And this is observed for the coarse grid at coarse and fine time-steps. Differences however become more evident when the grid is refined in space. At the front of the cavity, this difference is reflected by the greater eddy viscosity levels above the shear layer plane (i.e. y/L=0) across a greater proportion of the cavity for the Baseline $k-\omega$ model. This signifies greater flow activity outside the cavity.

Further downstream and away from the wall where the $k-\varepsilon$ model is active for the Baseline $k-\omega$ model, eddy viscosity levels are less than half for the coarse grid computations with the Baseline $k-\omega$ model ($(\mu_t/\mu_\infty)_{max}\sim 5500$) compared to the $k-\omega$ model ($(\mu_t/\mu_\infty)_{max}\sim 15000$). As the grids are refined in space, eddy viscosity levels remain unchanged for the $k-\omega$ model (Figures 4.14(c) and 4.14(e)) whereas they decrease for the Baseline $k-\omega$ model (Figure 4.14(d) and 4.14(f)).

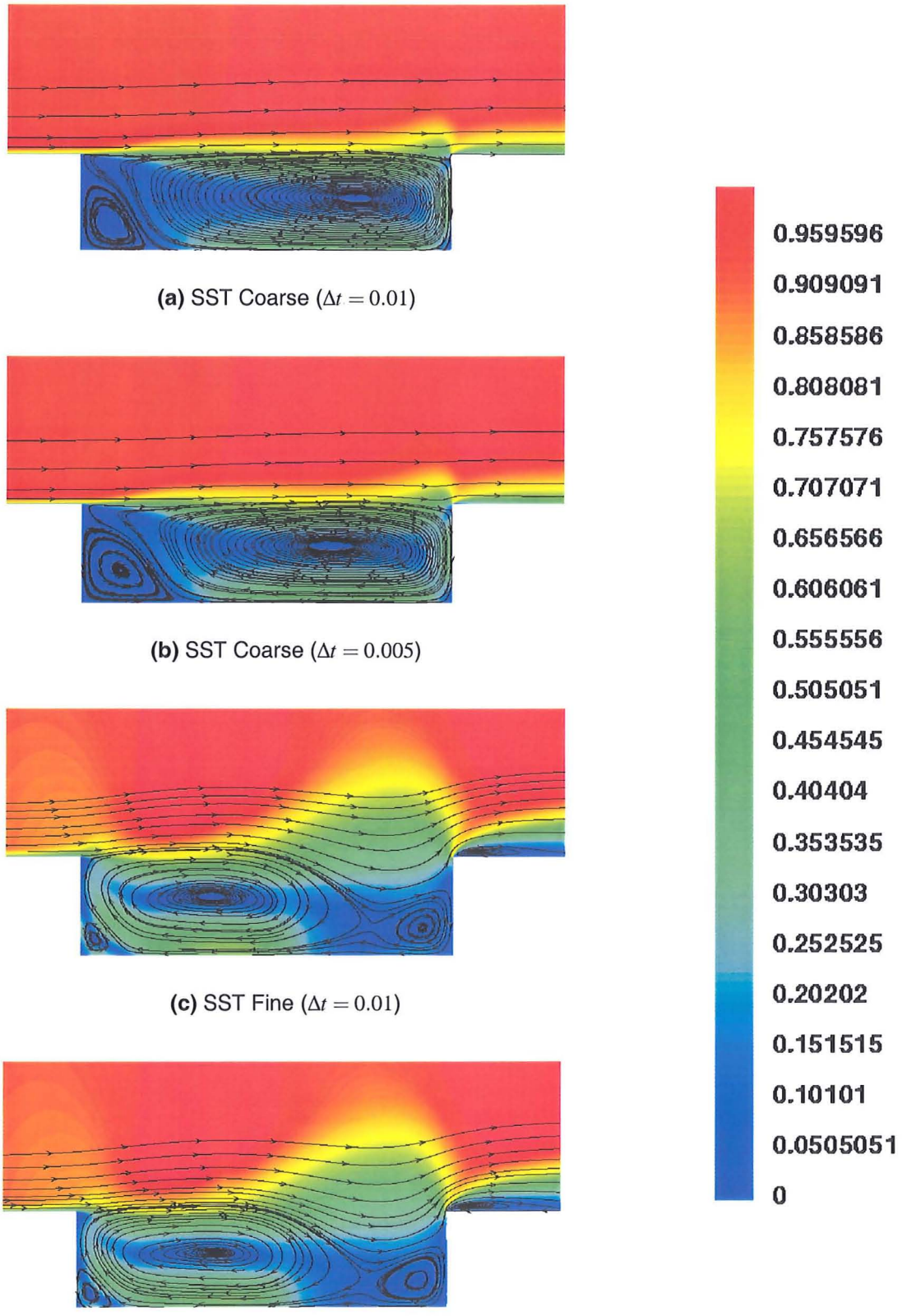

(a) SST Coarse ($\Delta t = 0.01$)

(b) SST Coarse ($\Delta t = 0.005$)

(c) SST Fine ($\Delta t = 0.01$)

(d) SST Fine ($\Delta t = 0.005$)

Figure 4.13: Time-averaged flow-field plots using normalised Mach contours and streamlines for the 2D, L/D=5, cavity with the SST turbulence model for the coarse grid, $\Delta t = 0.01$ ($\equiv 1.814 \times 10^{-5}$s); coarse grid, $\Delta t = 0.005$ ($\equiv 9.07 \times 10^{-6}$s); fine grid, $\Delta t = 0.01$ ($\equiv 1.814 \times 10^{-5}$s); fine grid, $\Delta t = 0.005$ ($\equiv 9.07 \times 10^{-6}$s).

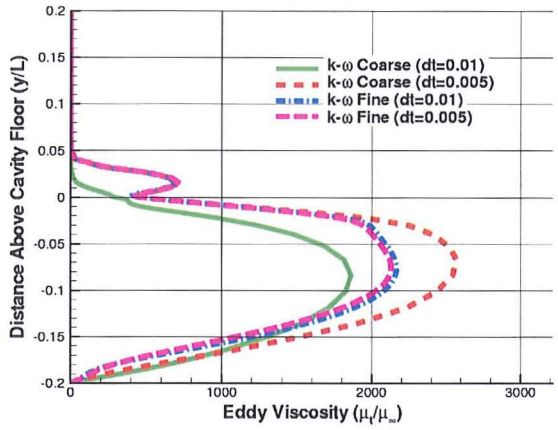

(a) $k-\omega$ $(x/L=0.05)$

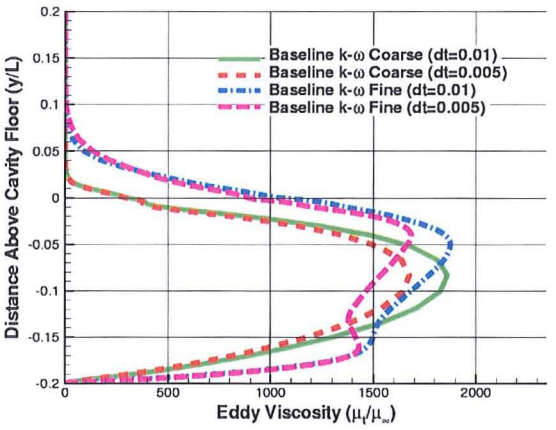

(b) Baseline $k-\omega$ $(x/L=0.05)$

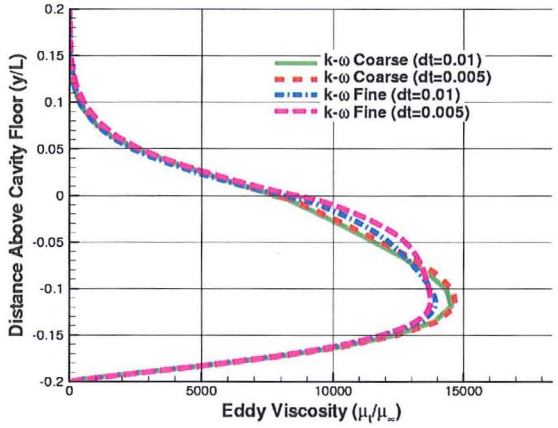

(c) $k-\omega$ $(x/L=0.55)$

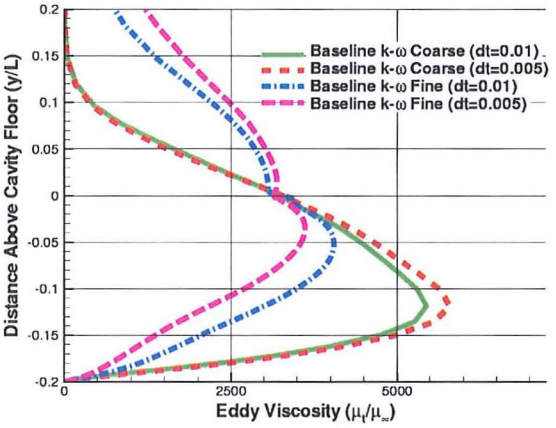

(d) Baseline $k-\omega$ $(x/L=0.55)$

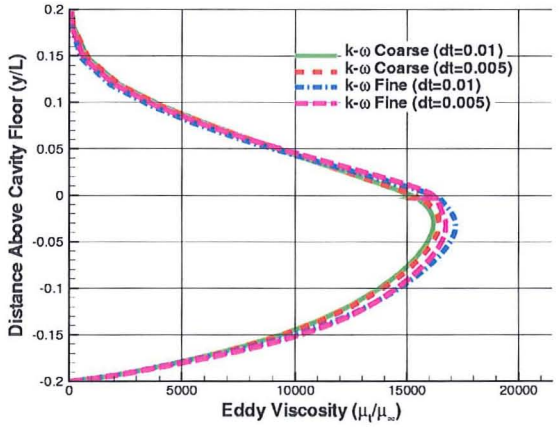

(e) $k-\omega$ $(x/L=0.95)$

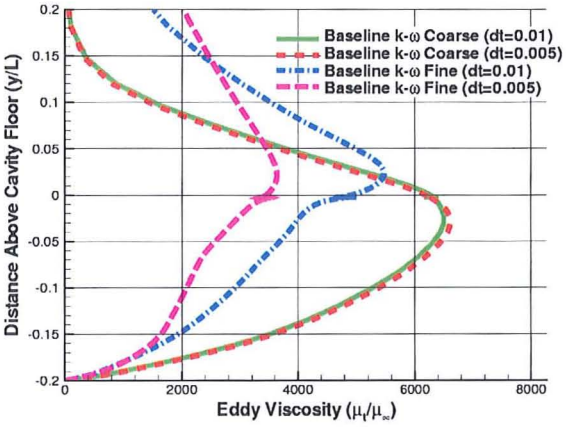

(f) Baseline $k-\omega$ $(x/L=0.95)$

Figure 4.14: Time-averaged plots of eddy viscosity ($\frac{\mu_t}{\mu_\infty}$) for the 2D, L/D=5 cavity with the $k-\omega$ model (left column) and Baseline $k-\omega$ model (right column) for: coarse grid, $\Delta t = 0.01$ ($\equiv 1.814\times10^{-5}$s); coarse grid, $\Delta t = 0.005$ ($\equiv 9.07\times10^{-6}$s); fine grid, $\Delta t = 0.01$ ($\equiv 1.814\times10^{-5}$s); fine grid, $\Delta t = 0.005$ ($\equiv 9.07\times10^{-6}$s).

The general consensus therefore is that the standard $k-\omega$ model is more turbulent than the baseline one. Dissipation with the $k-\omega$ model accounts for the decay of the turbulence at the walls only but fails to do so in the regions away from the walls making the shear layer too turbulent and the vortices too viscous. In contrast, the Baseline $k-\omega$ model predicts lower eddy viscosity away from the walls ensuring that the vortices remain less viscous. With spatial refinement, however, too much dissipation appears to be applied by the $k-\varepsilon$ model within the cavity. Although the vortices exhibit more laminar properties, the much lower turbulence levels allow them to expand in size preventing any shear layer from forming across the cavity opening. Since the SST model is similar in formulation to the Baseline $k-\omega$ model, results between the two models are similar as is reflected by the similar frequency decomposition patterns and noise level distributions presented earlier.

4.3 Spatial & Temporal Refinement Effects: Very Fine and Ultra Fine Grids

From the above results, it would appear that refinement in time only begins to have some sort of effect for the fine grid and that too at higher frequencies as the smaller time-step captures more of the smaller temporal turbulent scales. Improvements in agreement with experiment for higher frequencies with the fine grid with a finer time-step are therefore anticipated. Subsequent sections therefore focus on results with even finer grid densities with a fixed time-step of 0.01 ($\equiv 1.814\times10^{-5}$s). Due to the large run-times and cost associated with running these finer grids, only results with the SST turbulence model were performed. Details of the grids used in this study are given in Table 4.1. Analysis of the acoustic spectrum is not presented here as it has been given for coarser grids in the previous sections. The focus of the analysis performed here will look at studying the velocity distribution and the turbulent spectrum inside the cavity with further refinement in space.

4.3.1 Velocity Distribution Analysis

Figure 4.15 illustrates the time-averaged streamwise and transverse velocity profiles with the SST model for three stations ($x/L=0.05$, $x/L=0.55$ and $x/L=0.95$) along the floor of the cavity. PIV measurements are superimposed. Plots correspond to four different grid levels, details of which are provided in Table 4.1.

For the first two stations ($x/L=0.05$ and $x/L=0.55$), the coarse grid gave the best agreement with PIV for both the streamwise and transverse velocity profiles. At the cavity rear, however, agreement between PIV and numerical results deteriorated significantly. This may however be due to the poor resolution of the PIV experiment at this location. Evidence of this is provided in Figure 4.16, which displays the variations in the streamwise (Figure 4.16(a)) and transverse (Figure 4.16(b)) velocity components for the PIV experiment at a distance equal to the depth of the cavity above the cavity lip. Stations $x/L=0.05$ and $x/L=0.55$ lie within sections 1 and 3 as designated in Figure 4.16. At these points, PIV resolution was good and both velocity components corresponded to their expected values, i.e. the streamwise component equalled the freestream velocity and the transverse

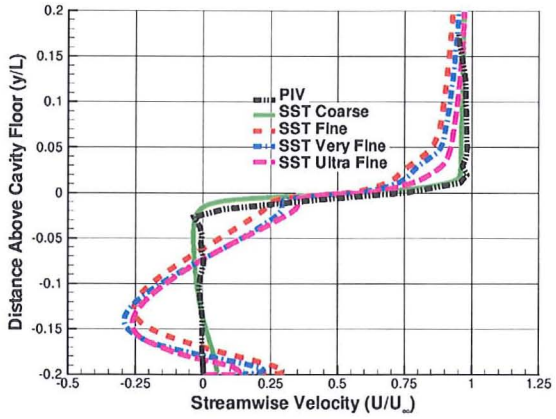

(a) U ($x/L = 0.05$)

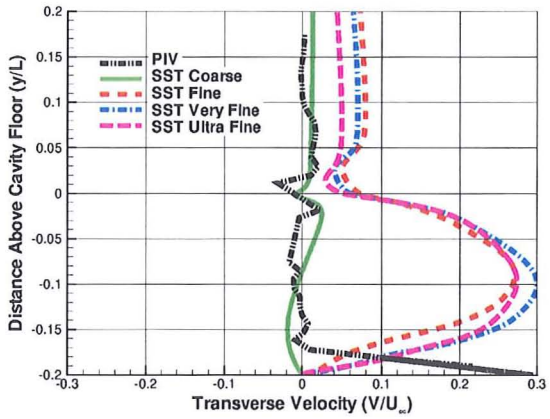

(b) V ($x/L = 0.05$)

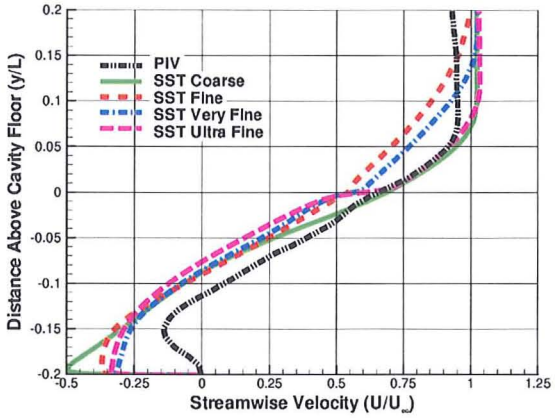

(c) U ($x/L = 0.55$)

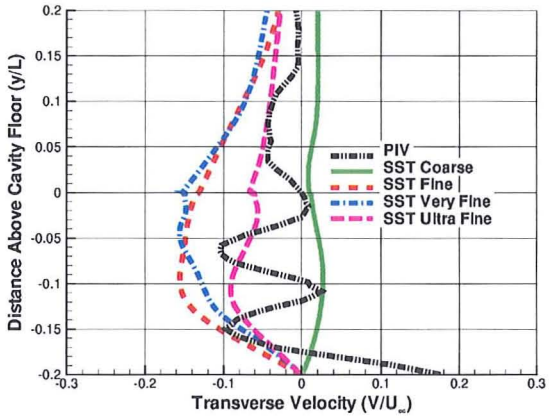

(d) V ($x/L = 0.55$)

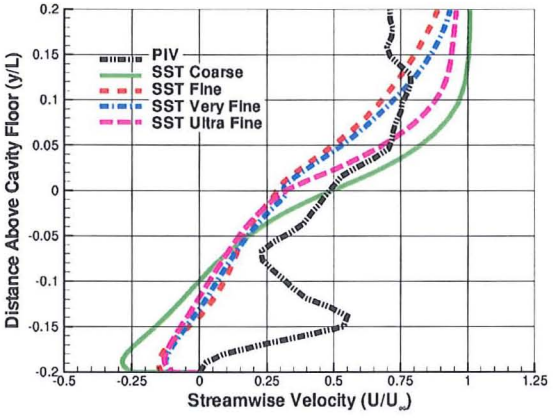

(e) U ($x/L = 0.95$)

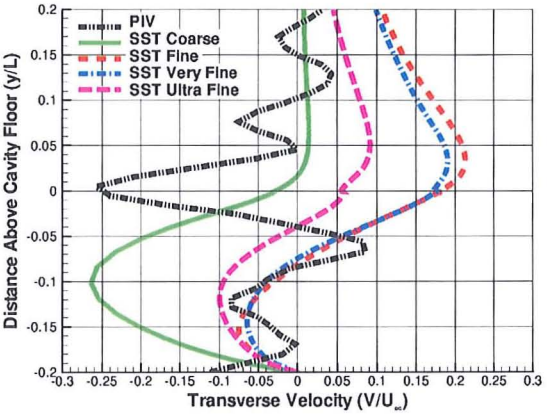

(f) V ($x/L = 0.95$)

Figure 4.15: Time-averaged streamwise ($\frac{U}{U_\infty}$) and transverse ($\frac{V}{V_\infty}$) velocity profiles for the 2D, open, rectangular L/D=5 cavity along the cavity floor using the SST turbulence model. Results correspond to 4 grid levels with a fixed Δt of 0.01 ($\equiv 1.814 \times 10^{-5}$s): coarse grid (solid green lines), fine grid (dashed red lines), very fine grid (dash-dot blue lines) and ultra-fine grid (long-dashed magenta lines). Long dash-dot black line represents PIV measurements.

component equalled zero. At the cavity rear, however, resolution of the PIV experiment diminished so much so that the streamwise velocity component no longer matched the free-stream value and exhibited erratic fluctuations (Figure 4.16(a)). For this reason, the non-dimensionalised value of the streamwise velocity ($\frac{U}{U_\infty}$) above the cavity lip for the PIV trace, depicted by the black line in Figure 4.15(e), does not equal 1. The PIV resolution is also poor at/near the cavity walls and so agreement with the numerical results is also significantly worse at these positions.

Differences between the coarse and fine grid levels are most evident at the cavity front ($x/L = 0.05$). Flows captured by the finer grids appear to have a stronger transverse velocity component compared to the coarse grid (Figure 4.15(b)). In a typical open, rectangular cavity, as is the case here, a shear layer forms across the cavity and flow unsteadiness develops in the cavity as momentum from the shear layer is transferred into the cavity via turbulent stresses. This effect occurs almost immediately after the shear layer forms at the lip of the cavity. This can be elucidated using the time-averaged flow-field plots shown earlier where the shear layer can be observed to thicken. The free-stream velocity however drives the shear layer downstream and hence any vortical structures generated due to this transfer of momentum from the shear layer are also convected downstream. Consequently, little flow activity occurs near the front of the cavity for the shear layer mode. This can be illustrated in Figure 4.15 where the transverse and streamwise velocity profiles for the coarse grid (solid green lines) register little change across the cavity depth near the front wall (Figures 4.15(b) and 4.15(a)). Variations in both streamwise and transverse velocities are, however, more pronounced for the fine grids stressing that there is more activity at the front of the cavity. A large negative streamwise velocity component occurs for all fine grids at the cavity front (Figure 4.15(a)) and this is representative of a large region of recirculation with strong negative (i.e. against the oncoming flow direction) vorticity. This feeds flow from the bottom of the cavity back to the top (and vice versa) near the separation point at the front corner thereby leading to positive transverse velocities as depicted in Figure 4.15(b).

4.3.2 Flow-field Visualisation

Changes in cavity flow behaviour are attributed to the large increase in the transverse velocity component at the cavity front. This transfer of momentum displaces the shear layer upwards and the deflected shear layer forces the separation point to move further upstream. Massive separation is created as a result and strong vortices are shed from the cavity lip rather than being convected downstream within the shear layer. Vortices produced upstream of the mouth of the cavity 'roll-off' into the cavity and form a very large vortical structure that spans a large proportion of the cavity length (Figure 4.17). Driven by the oncoming flow and the premature separation upstream of the cavity, this vortex convects downstream, decelerating and deflecting more flow around it thereby generating high SPLs (Figure 4.4(a)). The flow cycle is termed the wake mode and is no longer driven by self-sustained pressure oscillations and a feedback loop as was originally the case with the shear layer mode for the coarse grid (Figure 4.17(a)). This flow behaviour is observed inside all the finer grid cavities as illustrated in Figures 4.17(b) to 4.17(d).

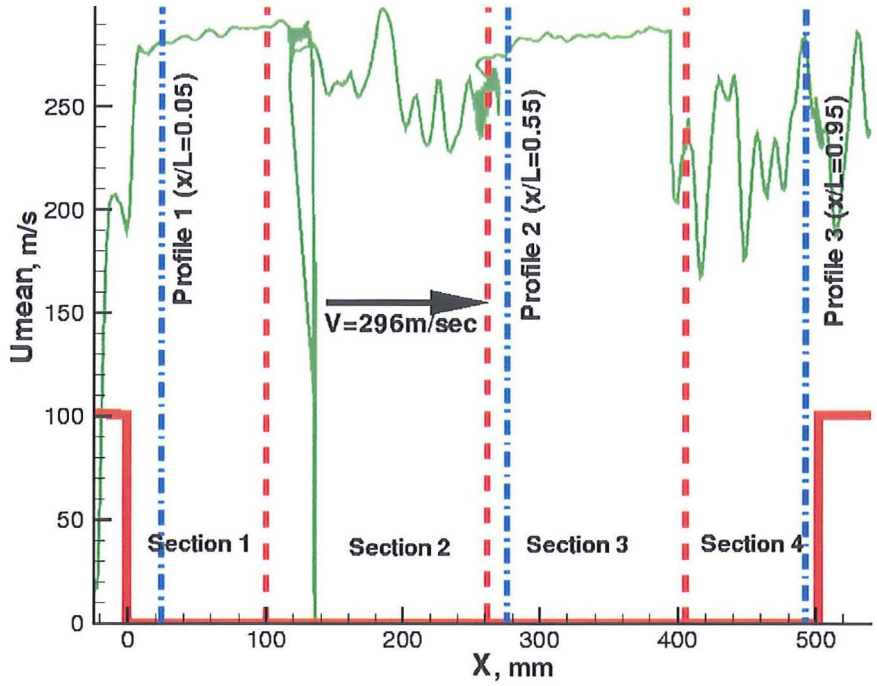

(a) PIV Streamwise (U) Velocity

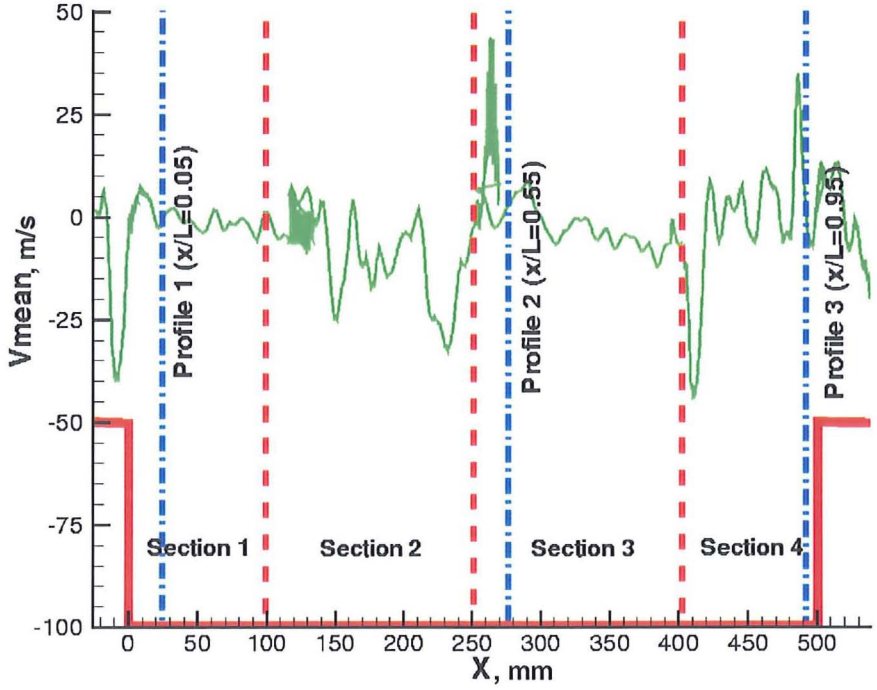

(b) PIV Transverse (V) Velocity

Figure 4.16: PIV streamwise and transverse velocity traces at a distance equal to the depth of the cavity above the cavity lip.

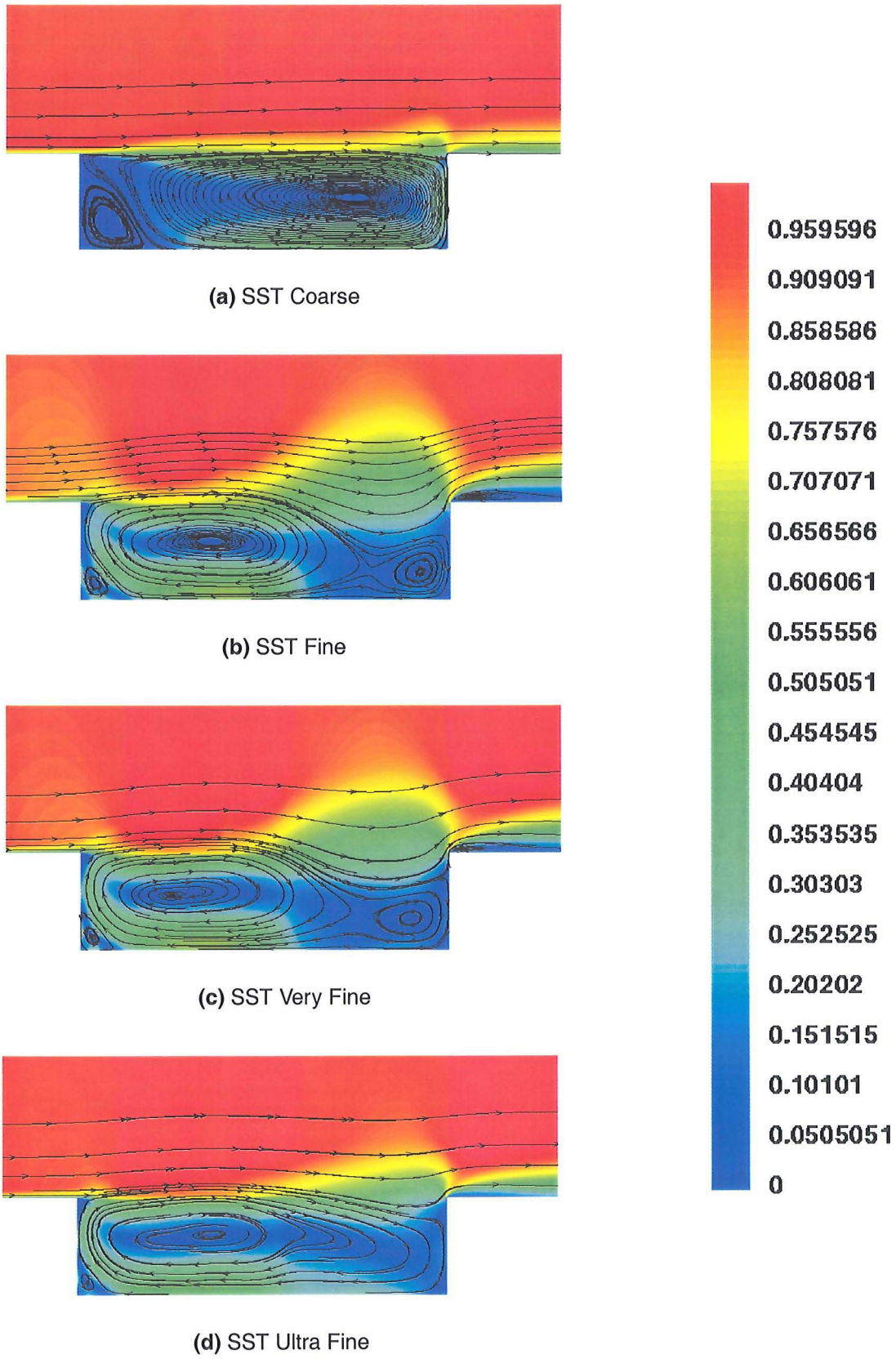

(a) SST Coarse

(b) SST Fine

(c) SST Very Fine

(d) SST Ultra Fine

Figure 4.17: Time-averaged Mach contours with streamlines inside the 2D L/D=5 cavity using the SST turbulence model. Plots correspond to 4 grid levels with $\Delta t = 0.01$ ($\equiv 1.814 \times 10^{-5}$s): coarse grid 4.17(a), fine grid 4.17(b), very fine grid 4.17(c) and ultra-fine grid 4.17(d). All plots drawn to the same scale with Mach number normalised with reference to the free-stream Mach number, $M_\infty = 0.85$.

4.3.3 Turbulent Spectrum Analysis

Further confirmation of this change in flow behaviour between the coarse and fine grids can be obtained by analysing the turbulent kinetic energy and shear stress profiles indicated in Figure 4.18. Greater variations in turbulent kinetic energy and shear stresses are observed for the finer grids at the front of the cavity (Figures 4.18(a) and 4.18(b)). This is due to the stronger vortices that exist in the finer grids. The comparatively little variation in turbulent kinetic energy and shear stress for the coarse grid is again testament to the fact that there is little flow activity at the cavity front with most energy concentrated in the shear layer. Further downstream of the cavity, the shear layer in the coarse grid computation decelerates and the shear stresses gradually transfer energy and momentum into the cavity. An increase in shear stress levels at the cavity middle for the coarse grid in Figure 4.18(d) supports this. The shear stress peak near $y/L = 0$ is still present for the finer grids at the cavity middle (Figure 4.18(d)) and is representative of a stronger primary vortex (with higher peripheral velocities) interacting with the external fluid at this location. At the cavity rear, the shear layer impinges just below the cavity's downstream corner for the shear layer mode. The flow above the dividing streamline is ejected downstream while the flow below it is circulated back into the cavity and a 'deflated' vortex forms at the cavity rear. This mass-breathing process leads to high shear layer deflection and is the source of the pressure waves that propagate upstream externally and internally. Large stresses therefore develop across the cavity depth for the coarse grid as a result of this and is clearly identified by the high shear stress values at the cavity rear in Figure 4.18(f).

For the fine grids, the shear layer does not extend across the cavity as shown in the flow-field plots. In fact, the wake mode prevails and large-scale vortices exist the cavity. These vortices are not confined by the shear layer and so extend outside the cavity. On approaching the downstream wall, more flow is therefore ejected downstream during the wake mode in the fine grid computations than during the shear layer mode in the coarse grid results. The size of the region of ejected flow downstream of the cavity can be identified using the turbulent kinetic energy and, in particular, the shear stress plots at the cavity rear in Figure 4.18. For the coarse grid, for instance, the shear stress levels rise to a maximum value at the shear layer (i.e. $y/L = 0$) and fall to zero at approximately $y/L = 0.1$. In contrast, for the fine grids, the shear stress approach a maximum just above the shear layer plane (at $y/L \approx 0.02$) and fall to zero at $y/L \approx 0.2$. This suggests that the vortex is significantly larger in the cavity in the fine grids and hence the region of separation downstream of the cavity is also larger.

4.3.4 Observations from Turbulent Spectrum Analyses

Despite the strong coupling between the shear layer and the flow structures inside the cavity, some observations on the role of turbulence in cavity flows can be made based on the analysis of the turbulent spectrum. The turbulent kinetic energy was found to control the amount of energy and momentum inserted into the cavity. The eddy viscosity levels, which described the level of turbulence in the flow, combined with the turbulent kinetic energy both tend to have a strong influence on the shear layer thickness. High eddy viscosity (and low turbulent kinetic energy) levels led to more viscous (and slower) vortices and turbulent shear layers that were less free to move. Noise levels produced were still high due to the interaction of the vortices and shear layer with each other and cavity walls.

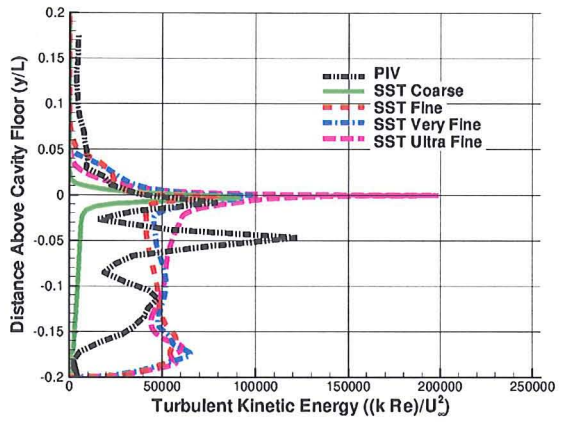

(a) k $(x/L = 0.05)$

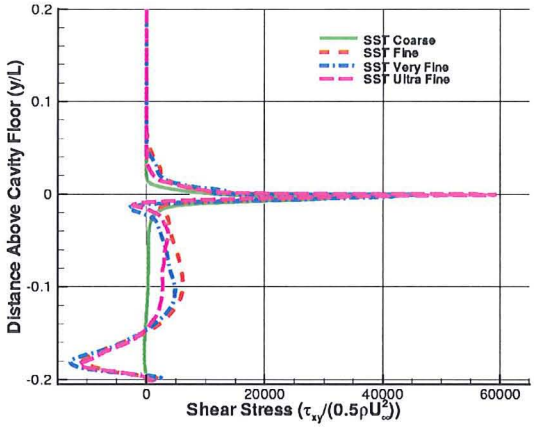

(b) τ_{xy} $(x/L = 0.05)$

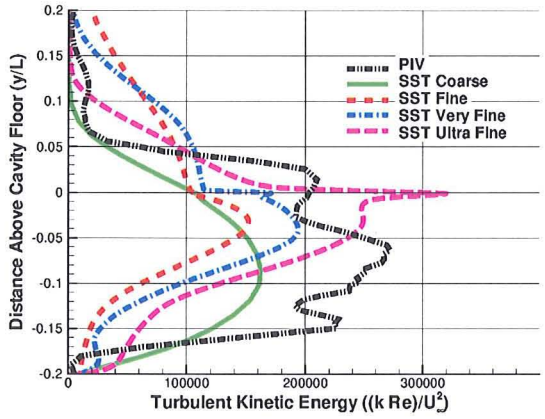

(c) k $(x/L = 0.55)$

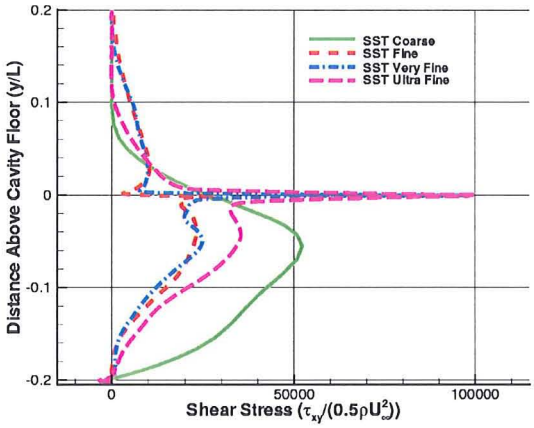

(d) τ_{xy} $(x/L = 0.55)$

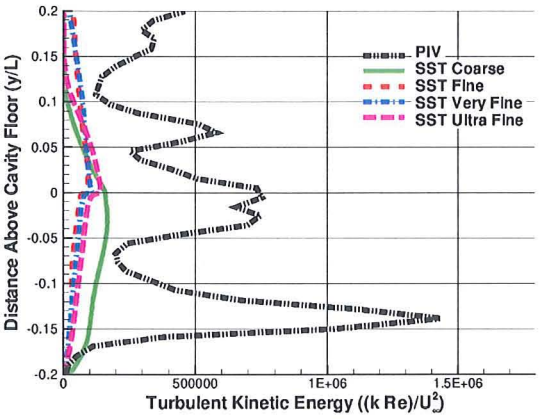

(e) k $(x/L = 0.95)$

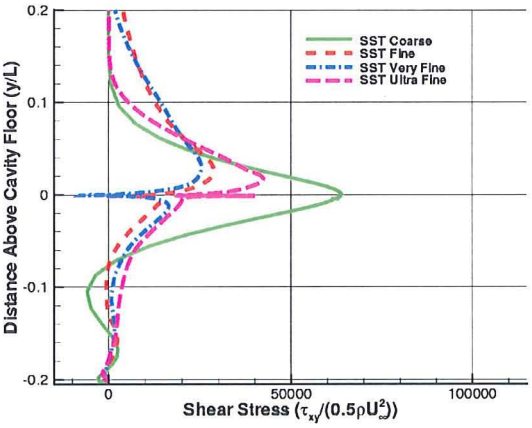

(f) τ_{xy} $(x/L = 0.95)$

Figure 4.18: Time-averaged turbulent kinetic-energy (k) and shear stress (τ_{xy}) profiles for the 2D, open, rectangular L/D=5 cavity using the SST turbulence model. Results correspond to 4 grid levels with $\Delta t = 0.01$ ($\equiv 1.814 \times 10^{-5}$s): coarse grid (solid green lines), fine grid (dashed red lines), very fine grid (dash-dot blue lines) and ultra-fine grid (long-dashed magenta lines). Long dash-dot black line represents PIV measurements.

The thicker, turbulent shear layer was however less prone to deflections and higher frequencies (associated with the interaction of the shear layer with the downstream wall and the movement of the shear layer above and below the downstream corner) were reduced. The effect of the turbulent stresses is difficult to isolate as it is strongly coupled with the turbulent kinetic energy. Nonetheless the turbulent shear stress was found to affect the redistribution rate of momentum from the shear layer into the cavity and therefore controls the unsteadiness in the flow. The lower shear stresses observed with the Baseline $k-\omega$ and SST models resulted in the flow inside the cavity to be more violent and unsteady, especially with finer grids. Higher shear stresses in the $k-\omega$ model appeared to minimise the fluctuations of the shear layer probably by making it less prone to movement from the vortical structures in the cavity. In contrast, normal stresses were found to stretch the vortical structures, altering their physical dimensions, and therefore may affect the breakdown of the shear layer.

Despite the difficulties with the turbulence models predicting the cavity flow features of the L/D=5 cavity with finer grids, a good qualitative description of the flow could be obtained on coarse grids.

4.4 Concluding Remarks

Previous research [9, 10] highlighted the sensitivity of the URANS method to grid refinement and therefore mentioned the difficulty in obtaining an accurate picture of the flowfield produced inside the cavity. Use of turbulence models to numerically model cavity flows and provide consistent and accurate results was therefore also uncertain. In order to assess this, different turbulence models of varying complexity were initially applied here to the 2D, L/D=5 cavity at a free-stream Mach number of 0.85 and a Reynolds number based on the cavity length of 6.783 million. Effects of spatial and temporal refinement were investigated for different two-equation turbulence models. Comparisons were made with experimental pressure and PIV measurements to ascertain the validity of the CFD results.

Spatial and temporal refinement studies were conducted with the $k-\omega$ model by Wilcox [138], the Baseline $k-\omega$ and SST models by Menter [245] with coarse and fine grids at coarse and fine time-steps. Temporal refinement improved the prediction of the higher frequencies as the more intermittent scales were better resolved. Influence of grid refinement was more profound and different for different turbulence models. For the $k-\omega$ model, the SPL curve changed from a 'W' shape to a 'V' shape for the fine grids and the dominant tone shifted from the second Rossiter mode ($\approx$ 380 Hz) to the first mode ($\approx$ 160 Hz). This was attributed to a more turbulent and thicker oncoming boundary layer resulting in a thicker shear layer that was less prone to fluctuations. For the Baseline $k-\omega$ model, the SPL curve became flatter in shape with finer grids and approached amplitudes of 180 dB near the cavity rear, approximately 12 dB higher than experiment. This increase in SPLs was attributed to a reduction in the eddy viscosity levels and more laminar-like boundary layer characteristics. This enabled the vortex to grow and extend outside the cavity forcing the separation point further upstream of the cavity, thereby instigating the formation of the wake mode. The SST model is similar in formulation to the Baseline $k-\omega$ model so produced similar results to the Baseline $k-\omega$ model. All models over-predicted the intensity of the acoustic tones relative to experiment. With spatial refinement, the

largest increase in the frequency magnitudes was associated with the first mode. As the grids were refined, the higher frequencies were suppressed for all models.

Further refinement in space was investigated with the SST model only. It was realised that results for the very fine and ultra fine grids resembled that of the fine grid suggesting that the first refinement in space triggered the change in results. Since the fine grid was created from refining the mesh inside the cavity only with a view to improving the aspect ratio of cells in the shear layer and cavity, the manner in which the grid is refined is highlighted to be important.

Higher resolution experimentation was also realised to be imperative for proper validation of CFD results. Comparisons with PIV measurements was found to be poor at the cavity rear where the resolution of the experiment was not as high.

The $k-\omega$ model was found to over-predict the level of turbulence in the cavity causing a suppression of the higher frequencies. The Baseline $k-\omega$ and SST models limited the production of turbulence but over-predicted the strength of the laminar vortices and caused a change in the flow from a shear layer mode to a wake mode. In terms of turbulence effects, eddy viscosity defined the level of turbulence in the flow while the turbulent kinetic energy controlled the amount of energy and momentum in it. High levels of eddy viscosity in particular led to the development of a thicker, more turbulent shear layer. The shear stress was observed to influence the amount of energy and momentum that is transferred and redistributed from the shear layer into the cavity. Normal stresses were observed to stretch and alter the physical dimensions of the vortical structures and therefore could influence the breakdown of the shear layer.

Chapter 5

L/D=5 Cavity: LES & DES Computations

The requirement for better resolution of the turbulent flow-field and the acoustical signature in cavity flows has diverted attention from the use of purely statistical models towards simulation methods such as Large-Eddy Simulation (LES) [164]. LES works by filtering the flow structures in terms of their scale size, as described in Chapter 2. Any turbulent length scale greater than the grid filter length is therefore explicitly resolved. Due to the turbulent nature of the cavity flow problem, however, the filter length size approaches DNS scales if the small dissipative boundary layer turbulent scales are to be resolved. This becomes very expensive for high Reynolds number flows so hybrid methods of LES and URANS (such as DES) were also applied to cavity flows here.

LES and DES computations are required to be 3D and unsteady so all numerical simulations presented in this chapter were performed in 3D. Calculations were conducted for the clean, open, rectangular cavity with and without doors. Wind tunnel pressure measurements were compared with the relevant computational results in terms of noise levels and frequency content at the locations specified in Chapter 3, a schematic of which is re-iterated in Figure 5.1 for convenience. Numerical results were also compared with PIV measurements to assess the difference in velocity distributions between experiment and simulation.

The cavity considered here again has a L/D ratio of 5 and a width-to-depth ratio (W/D) of 1. The free-stream Mach and Reynolds (based on the cavity length)numbers are 0.85 and 1 million, respectively. In an attempt to minimise the computational overhead in running LES, the Reynolds number was reduced from the experimental Reynolds number of 6.783 million to 1 million. Preliminary studies into the effects of the Reynolds number were conducted for the 3D, L/D=5, clean cavity (with doors-off) using LES on a coarse grid of 1 million points. Two calculations were run: one with the normal Reynolds number of 6.783 million and another with a reduced value of 1 million. SPLs and PSD (at $x/L = 0.95$) are shown in Figure 5.2. Little variation in noise levels and frequency content (at $x/L = 0.95$) was observed between the two Reynolds numbers.

Further evidence of the effect of Reynolds number is provided in Figure 5.3, which depict the variations in RMS pressure for four frequency ranges: $50\ Hz \leq f \leq 250\ Hz$ (which includes the first mode ($\approx 160\ Hz$)), $350\ Hz \leq f \leq 450\ Hz$ (which straddles the second mode ($\approx 380\ Hz$)), $500\ Hz \leq f \leq 700\ Hz$ (which straddles the third mode ($\approx 600\ Hz$)) and $750\ Hz \leq f \leq 850\ Hz$ (which contains the fourth mode ($\approx 820\ Hz$)). RMS pressure variations are more sensitive than SPLs (which are plotted on a logarithmic scale) and hence

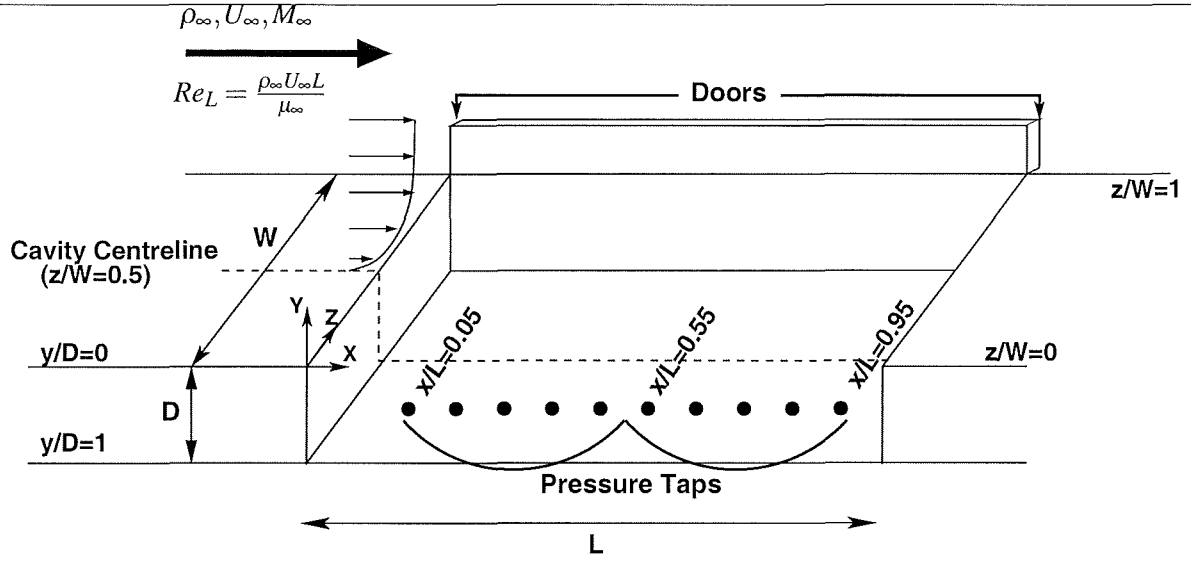

Figure 5.1: A schematic of the 3D, L/D=5, W/D=1 cavity (with doors-on) illustrating the positions of the pressure taps at which experimental and numerical results were compared.

any influence of Reynolds number should be more pronounced. As can be seen in Figure 5.3, however, the curves and the corresponding pressure magnitudes between the 1m and 6.783m Reynolds numbers are close.

Rizzetta [164] also conducted his numerical simulations at a lower Reynolds number and still compared his results with experiments using the actual Reynolds number. Furthermore, the effect of Reynolds number on cavity flows was also studied by Ross[13]. Although Ross conducted the study at higher Mach numbers, his experiments revealed the effects of Reynolds number to be negligible. Based on these results, all numerical simulations using LES and DES were run at a lower Reynolds number of 1 million but still compared with the 6.783 million Reynolds number experimental results.

5.1 Description of Computational Domain

For the grids discussed in Table 5.1, all dimensions were scaled with respect to the cavity length. For the DES and LES grids, the far-field length was set to 3.5 times the cavity length so as to minimise any spurious results from acoustic wave reflections. A flat plate 1.5 times the cavity length was used ahead of the cavity (as was specified in experiment) to allow the oncoming boundary layer to develop naturally. Some attempts were made to run separate LES flat plate computations and then insert the resulting velocity profile at the beginning of the cavity. One of the main reasons for doing so was to allow for quicker cavity calculation run-times and accurate inflow to the cavity. Even with the complete cavity domain, however, run-times were reasonably low and so additional flat plate calculations were not conducted.

The height of the doors was set to half the cavity width, i.e. 0.1 L, while their width was set to 0.375 inches (i.e. 0.01875 L) as in the wind tunnel experiment (Chapter 3). Effects of stores in the cavity are addressed later in Chapter 8.

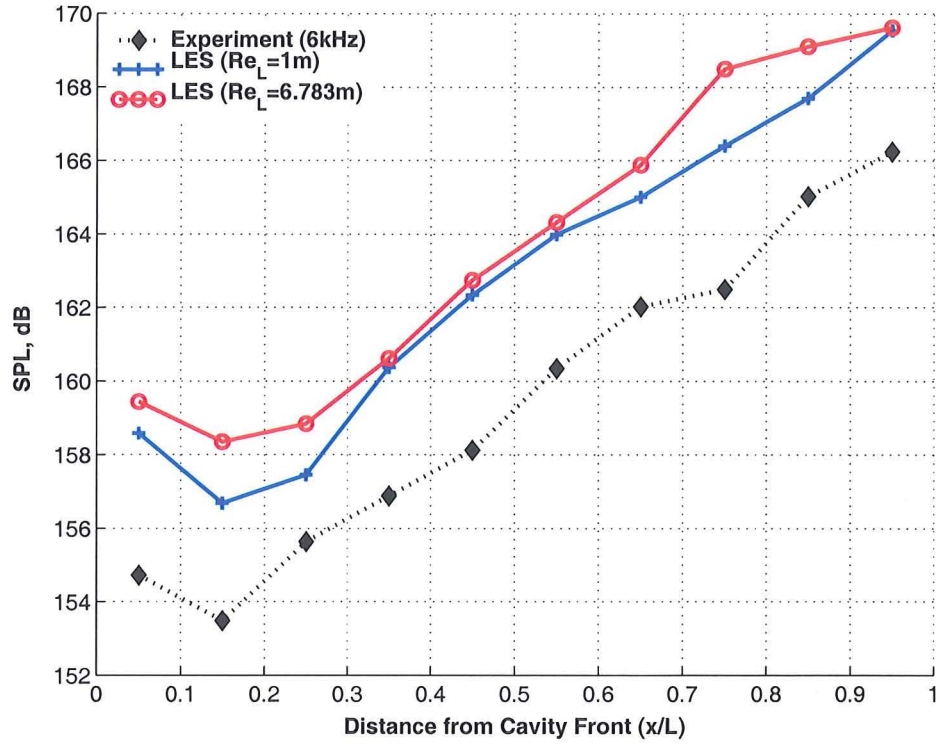

(a) SPLs

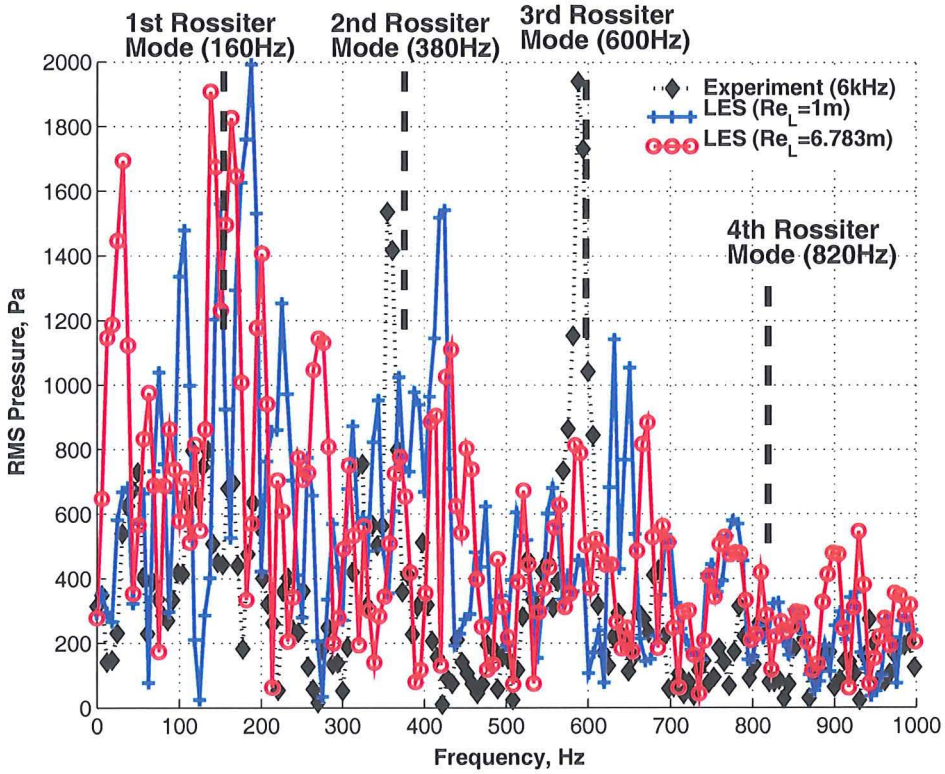

(b) PSD ($x/L = 0.95$)

Figure 5.2: Reynolds number effects on the SPLs and PSD (at $x/L = 0.95$) for the 3D, L/D=5, W/D=1 clean cavity (with doors-off) using LES (Smagorinsky SGS).

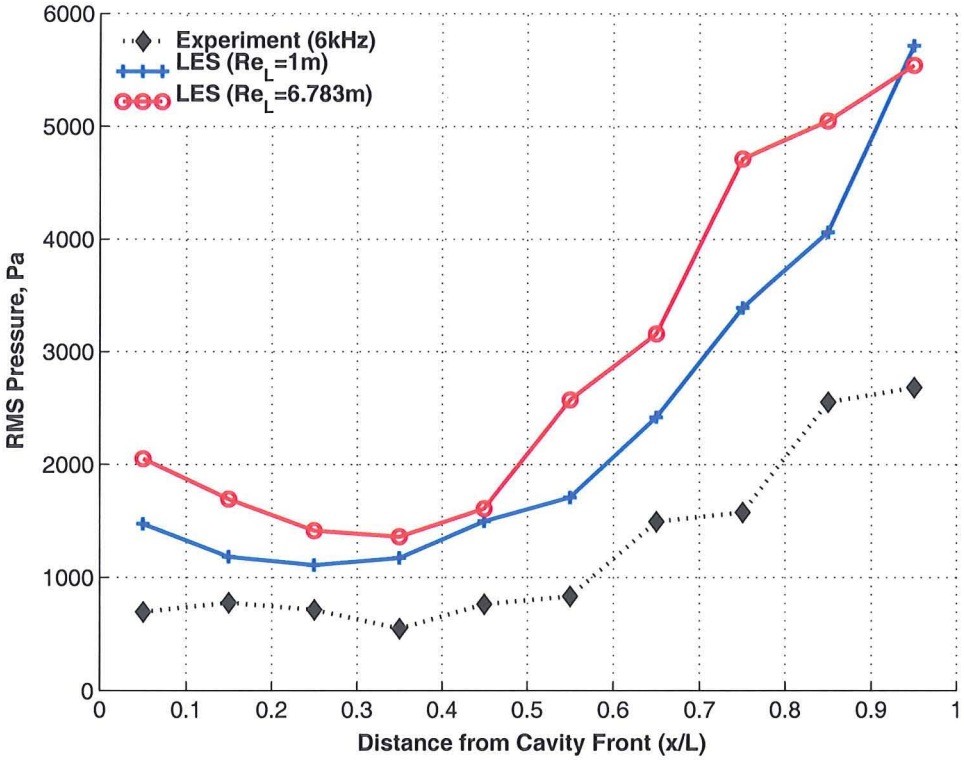

(a) $50\ Hz \leq f \leq 250\ Hz$

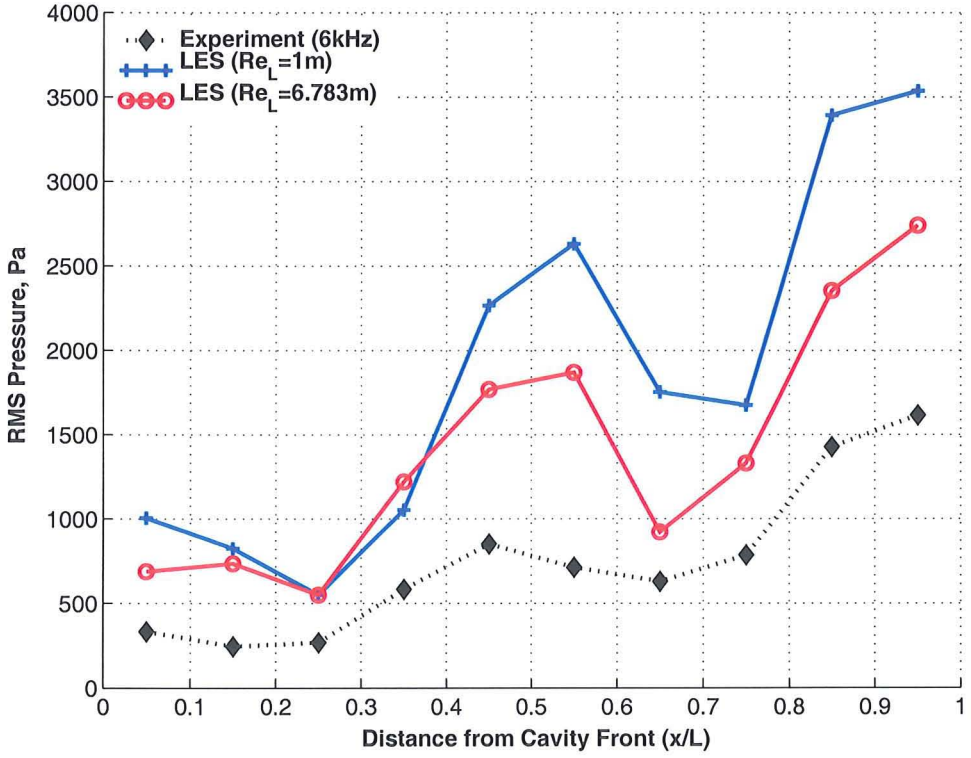

(b) $350\ Hz \leq f \leq 450\ Hz$

Figure 5.3: (continued)

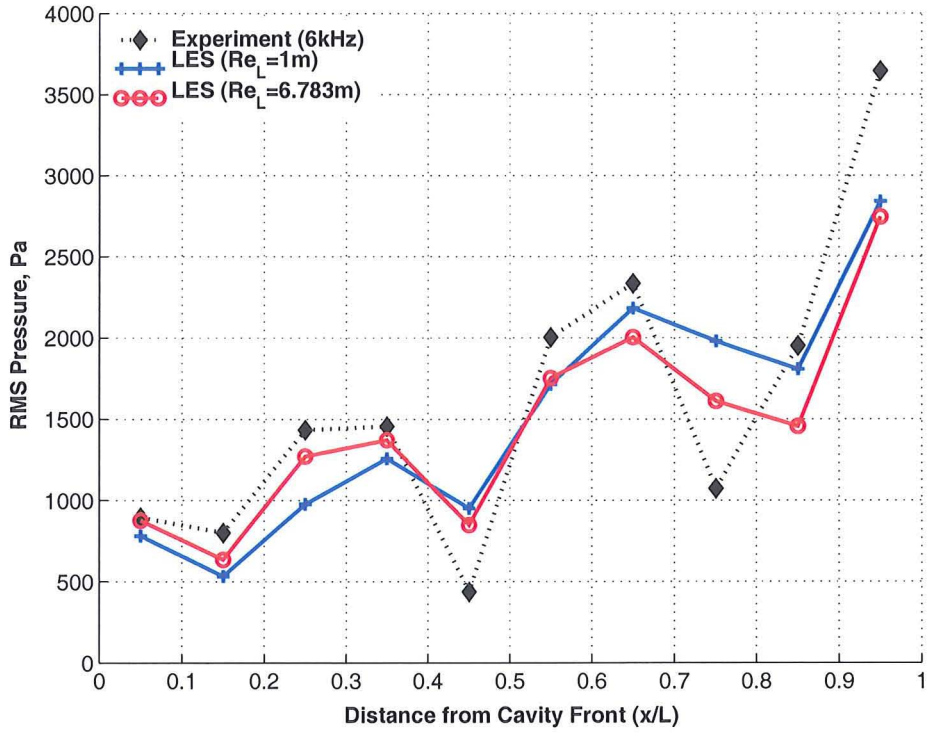

(c) $500\ Hz \leq f \leq 700\ Hz$

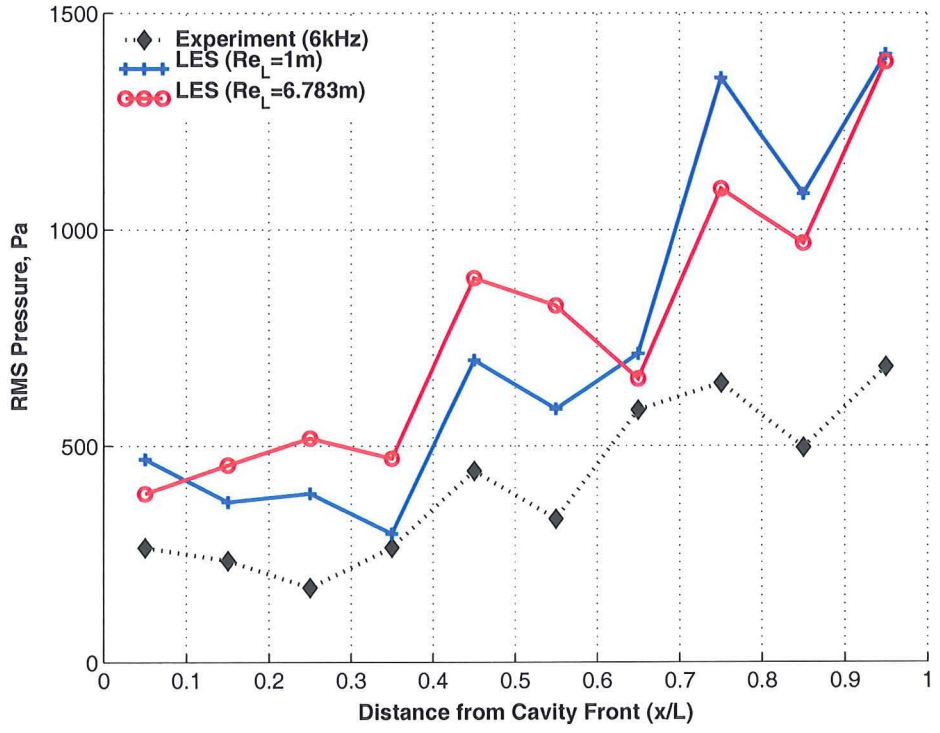

(d) $750\ Hz \leq f \leq 850\ Hz$

Figure 5.3: Reynolds number effects on the band-limited RMS pressure for the 3D, L/D=5, W/D=1 clean cavity (with doors-off) using LES (Smagorinsky SGS).

Table 5.1: Information on grids used for the 3D, L/D=5, clean cavity in the doors-off and the doors-on at 90° configurations.

Grid	Overall Points	Points in Cavity	Wallspacing	Blocks in Cavity (Overall)
Clean cavity with doors-on (at 90°)				
URANS	1,483,173	446,824	$y = 1 \times 10^{-5}$	20 (110)
LES/DES (Coarse)	1,248,544	179,520	$y = 3.125 \times 10^{-3}$	64 (240)
LES/DES (Medium)	2,218,854	493,679	$y = 3.125 \times 10^{-3}$	64 (240)
LES/DES (Fine)	4,783,162	1,177,646	$y = 7.1825 \times 10^{-4}$	64 (240)
Clean cavity with doors-off				
URANS	1,174,824	305,424	$y = 2.214 \times 10^{-5}$	20 (110)
LES/DES (Coarse)	1,225,824	179,520	$y = 3.125 \times 10^{-3}$	64 (256)
LES/DES (Medium)	2,178,480	493,679	$y = 3.125 \times 10^{-3}$	64 (256)
LES/DES (Fine)	4,696,128	1,177,646	$y = 7.1825 \times 10^{-4}$	64 (256)
LES/DES (Very Fine)	8,388,608	2,097,152	$y = 5 \times 10^{-5}$	64 (256)

The finest grid used for the doors-on configuration contained approximately 4.5 million points while the finest grid (denoted as 'very fine' in Table 5.1) for the doors-off case approached 8.5 million points. Figures 5.4 and 5.5 provide views of the mesh distribution employed for the finest grids in the doors-on and doors-off configurations, respectively. In Figure 5.4, the top picture shows the meshing along the cavity centreline (i.e. z/W=0.5) in the xy plane (i.e. streamwise direction). A close-up of the mesh near the corners of the cavity (where uniform mesh distribution with cell aspect ratios as close to one as possible were enforced) is also provided in this view. The other view illustrates the resolution in the spanwise direction. The inclusion of doors has little difference on the mesh distribution in the streamwise plane and so is not shown in Figure 5.5. Instead, the meshing in the xz and yz planes as well as in the regions closest to the corners of the doors are illustrated.

5.2 Doors-Off Results

Results for the clean, doors-off 3D L/D=5, W/D=1 cavity are presented in Figures 5.6 to 5.10. The URANS results were obtained with Menter's Baseline $k-\omega$ turbulence model [245] while LES results were obtained with the standard Smagorinsky SGS model [271]. For DES computations, the Spalart-Allmaras model [192] was used to realise the near-wall properties because it was the simplest model to implement into the code, although the $k-\omega$ model has also been used for DES and results from this are presented in later

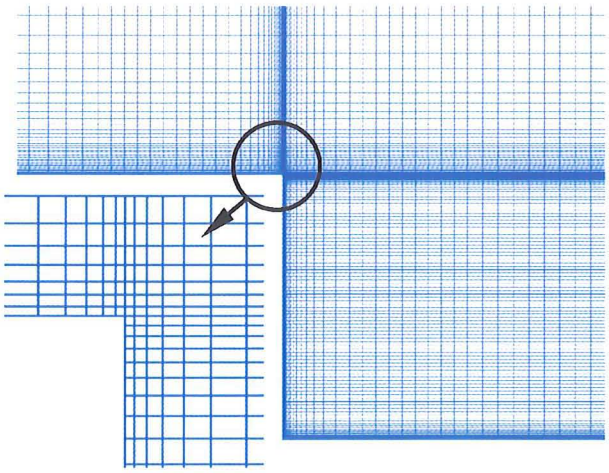

(a) XY Plane (doors-off)

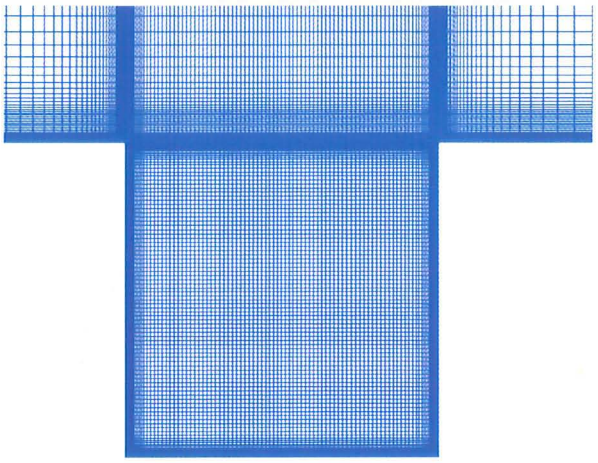

(b) YZ Plane (doors-off)

Figure 5.4: Different views of the meshing distribution for the very fine (8.5m), doors-off grid.

chapters. For the Baseline $k-\omega$ results, a time-step of 0.01 ($\equiv 1.814 \times 10^{-5}$s) was used compared to 0.001 ($\equiv 1.814 \times 10^{-6}$s) for the fine grid DES and very fine grid LES calculations. All numerical data were sampled at 6 kHz in the same manner as experiment.

Unsteady pressure comparisons with experiment reveal best agreement with DES and LES. The shape of the SPL curve for Menter's Baseline $k-\omega$ model is completely different and, as will be explained later, resembles the shape characteristic of the doors-on case, and 2D results discussed previously. LES results with the very fine grid compare best with experiment, with noise levels approaching within 1 dB of experiment at the cavity rear as shown in Figure 5.6(a).

When the doors are excluded, redistribution of momentum in the spanwise direction is possible. In contrast, in the doors-on configuration, the flow tends to be channelled into the cavity and the flow behaves more in a two-dimensional manner. Unlike LES and DES, The fact that Menter's Baseline $k-\omega$ model predicts a completely incorrect SPL shape (Figure 5.6(a)) suggests that it has difficulty in resolving flow effects on the spanwise

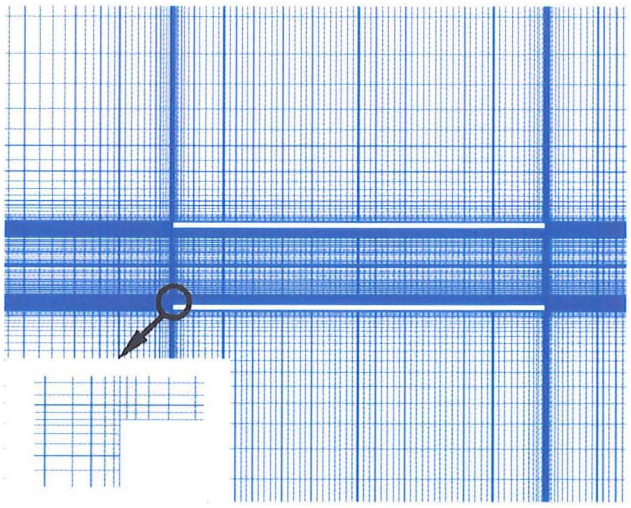

(a) XZ Plane (doors-on)

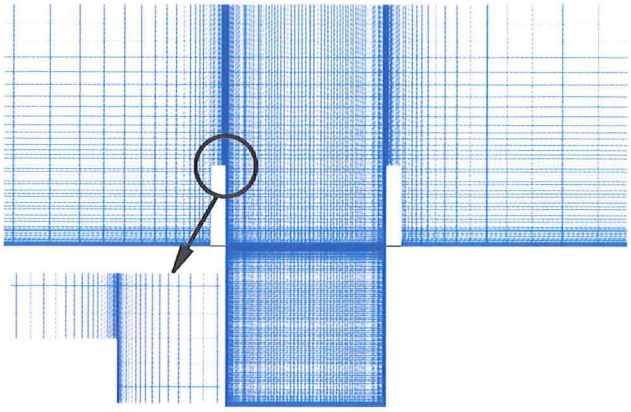

(b) YZ Plane (doors-on)

Figure 5.5: Different views of the meshing distribution for the fine (4.5m) doors-on grid.

dimension. In fact, the shape of the URANS SPL curve was found to resemble the doors-on SPL curve, as will be discussed in more detail later. The difference in frequencies without doors is clearly represented by the spectral analysis in Figures 5.6(b) to 5.6(d). Although Menter's Baseline $k-\omega$ model predicts the 3rd mode relatively well it fails to account for any of the lower or higher frequencies as shown in Table 5.2, which includes approximate values for the amplitudes and locations of the first four Rossiter modes as calculated by Rossiter's formula (Equation 1.3).

5.2.1 Band-Limited Frequency Analysis

Closer inspection of the results is provided by taking windowed SPL plots over four frequency ranges: $50\ Hz \leq f \leq 250\ Hz$, $350\ Hz \leq f \leq 450\ Hz$, $500\ Hz \leq f \leq 700\ Hz$ and $750\ Hz \leq f \leq 850\ Hz$. Figure 5.7 clearly emphasises the better agreement between experiment and simulation techniques than with URANS. As with the 2D computations, URANS manages to capture only the strongest frequency which is the third Rossiter mode ($\approx 600\ Hz$) in the doors-off case. For frequencies other than this dominant tone, URANS results are generally under-predicted. Both DES and LES fare much better across the

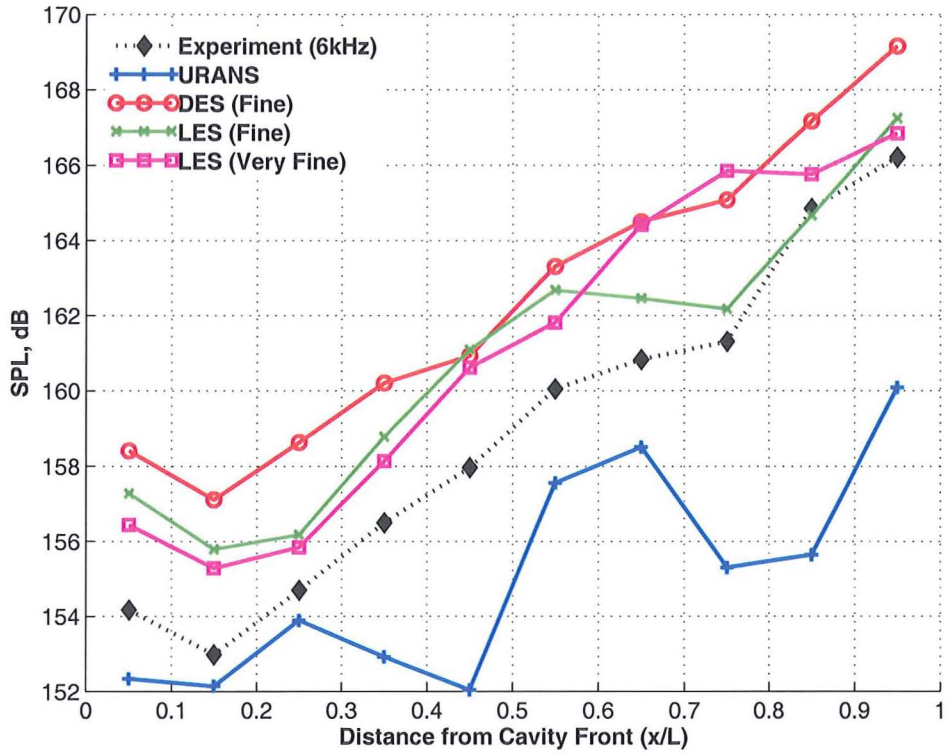

(a) SPLs

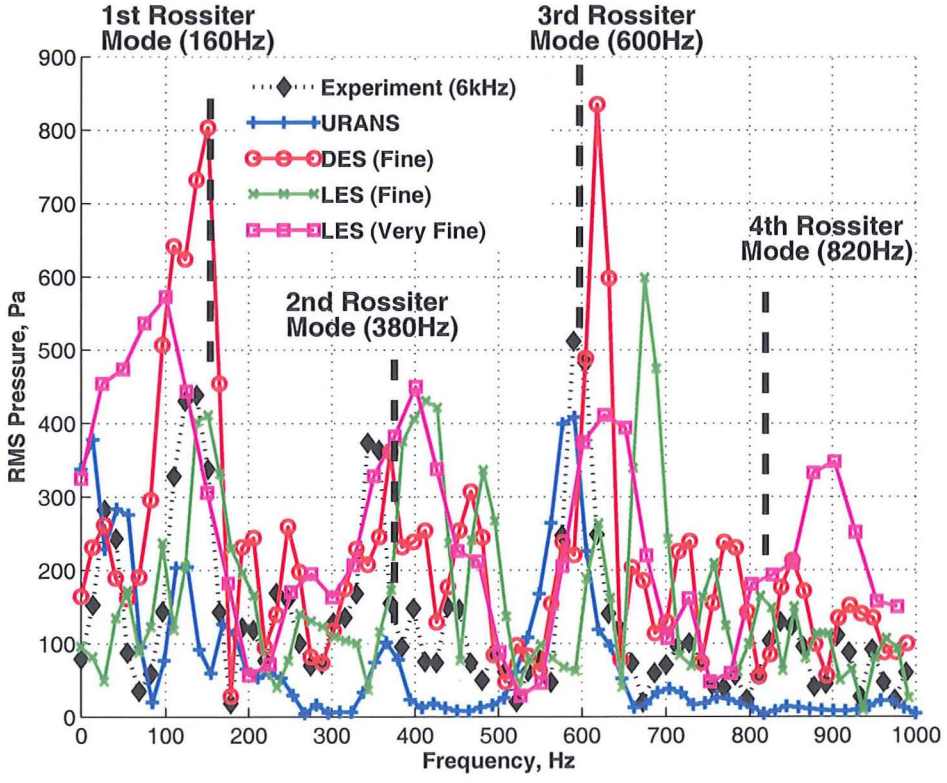

(b) PSD ($x/L = 0.05$)

Figure 5.6: (continued)

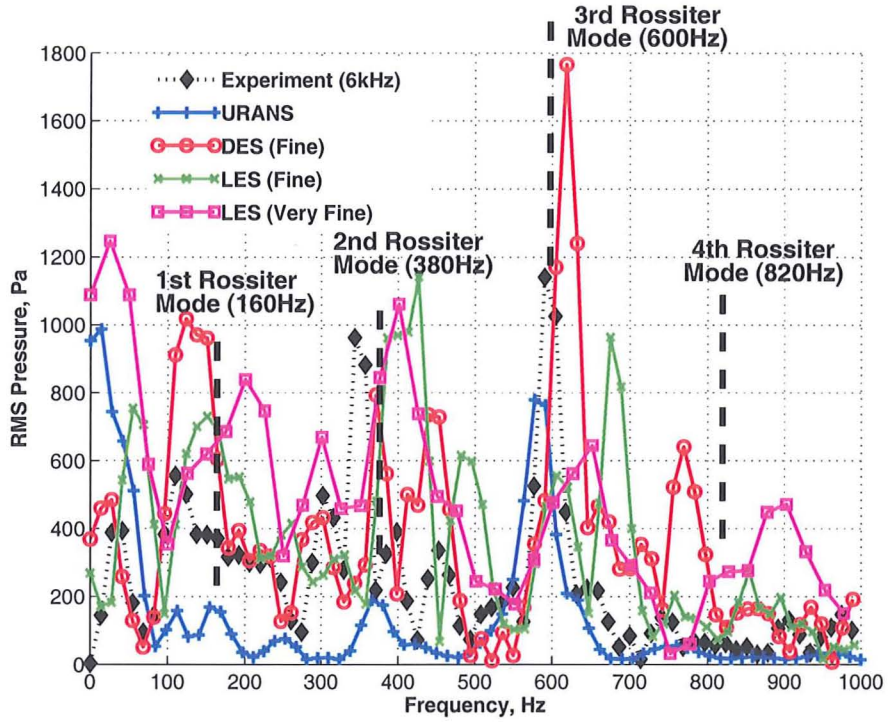

(c) PSD ($x/L = 0.55$)

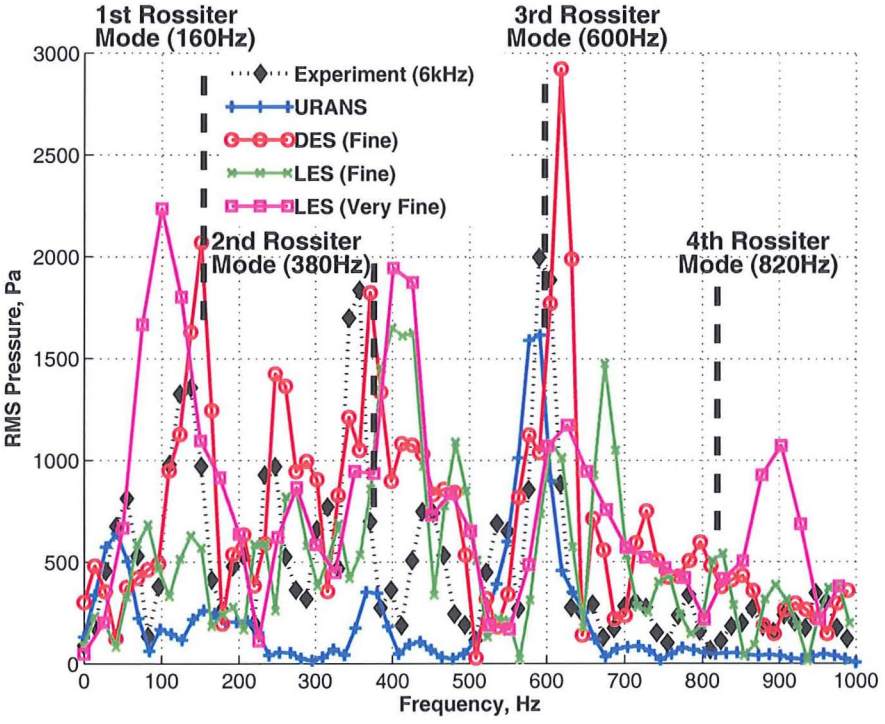

(d) PSD ($x/L = 0.95$)

Figure 5.6: SPLs and PSD plots (at $x/L = 0.05$, $x/L = 0.55$ and $x/L = 0.95$) for the 3D, L/D=5, W/D=1, clean cavity with doors-off using URANS (Menter's Baseline $k-\omega$), DES (Spalart-Allmaras) and LES (Smagorinsky SGS). Plots taken at z/W=0.25 and along the cavity floor (y/D=1).

Table 5.2: Comparisons of (approximate) frequencies and their amplitudes predicted between LES, DES, URANS (Menter's Baseline $k-\omega$) for the doors-off clean cavity (at the cavity rear i.e. at $x/L = 0.95$), Rossiter's semi-empirical formula [3] and experiment.

Method	1st Mode		2nd Mode		3rd Mode		4th Mode	
	Freq. (Hz)	Ampl. (Pa)	Freq. (Hz)	Ampl. (Pa)	Freq. (Hz)	Ampl. (Pa)	Freq. (Hz)	Ampl. (Pa)
Rossiter's Formula	162	-	378	-	594	-	811	-
Experiment (6kHz)	137	1355	358	1834	590	1995	784	329
Baseline $k-\omega$	156	261	382	346	591	1613	-	-
DES (Fine)	150	2065	372	1821	620	2927	796	585
LES (Fine)	140	650	400	1650	670	1500	820	550
LES (Very Fine)	100	2233	401	1942	628	1174	904	1064

entire frequency spectrum analysed. Results are however slightly more favourable with LES at higher frequencies (Figures 5.7(c) and 5.7(d)).

5.2.2 Flow-field Visualisation

Instantaneous Mach number contours for both Menter's Baseline $k-\omega$ model and DES-SA along the cavity centreline are illustrated in Figure 5.8. The Mach number plots distinctly demarcate the lower-velocity, dark-coloured (blue) regions inside the cavity from the transonic, lighter-coloured (yellow) regions outside the cavity. These two regions meet at the shear layer. Menter's Baseline $k-\omega$ model always predicts a larger single primary vortex structure at the cavity rear with some combination of two or more counter-rotating vortices at the cavity front. The shear layer is also consistently found to span the cavity with distinct deflection at the cavity rear (Figure 5.8). It is this dual-vortex cycle inside the cavity that results in the 'W'-shaped SPL curve in Figure 5.6(a). The DES, however, portrays a different picture and is something that is perhaps more intuitively correct for the clean, doors-off cavity. The crucial difference between the DES and URANS results lies in the behaviour of the shear layer and this is evident in Figure 5.8. At no point for the DES computations does the shear layer extend across the entire length of the cavity. At the most, the shear layer can be observed to be coherent up to the middle of the cavity at which point, if not earlier, it breaks down. What follows is intensive mixing and spreading of the energy from the shear layer and the free-stream with the lower-velocity flow region inside the cavity.

With the shear layer detached, the flow is no longer confined inside the cavity. The vortical structures that form (which are typically smaller in size than compared to when the shear layer remains attached across the cavity opening) interact with the cavity walls to create regions of higher pressure and more flow activity. Not confined by the shear layer, the flow can, in some cases, be observed to 'spill' over the cavity. Indications of these 'spillages' can distinctly be seen in both DES and LES computations in Figure 5.9, which provides a three-dimensional perspective of the instantaneous flow-field (using Mach number contours normalised by the free-stream Mach number of 0.85) inside the cavity with doors-off. As the breakdown of the shear layer is not predicted in the URANS computations, these vortical 'spillages' are also not observed (Figure 5.9(a)). A close-up of these vortical

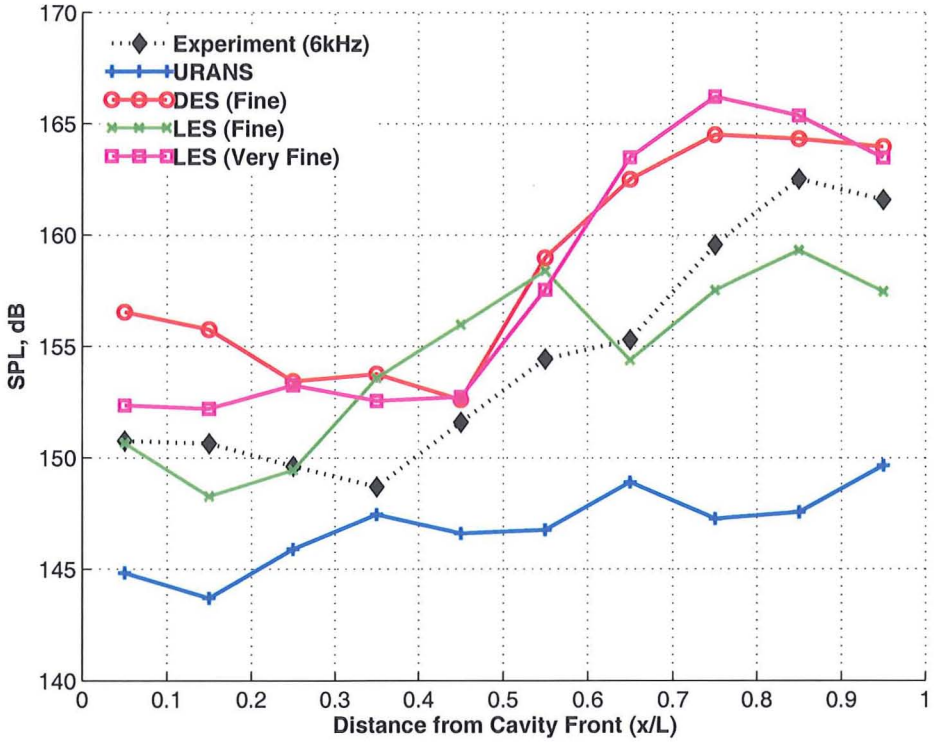

(a) $50\ Hz \leq f \leq 250\ Hz$

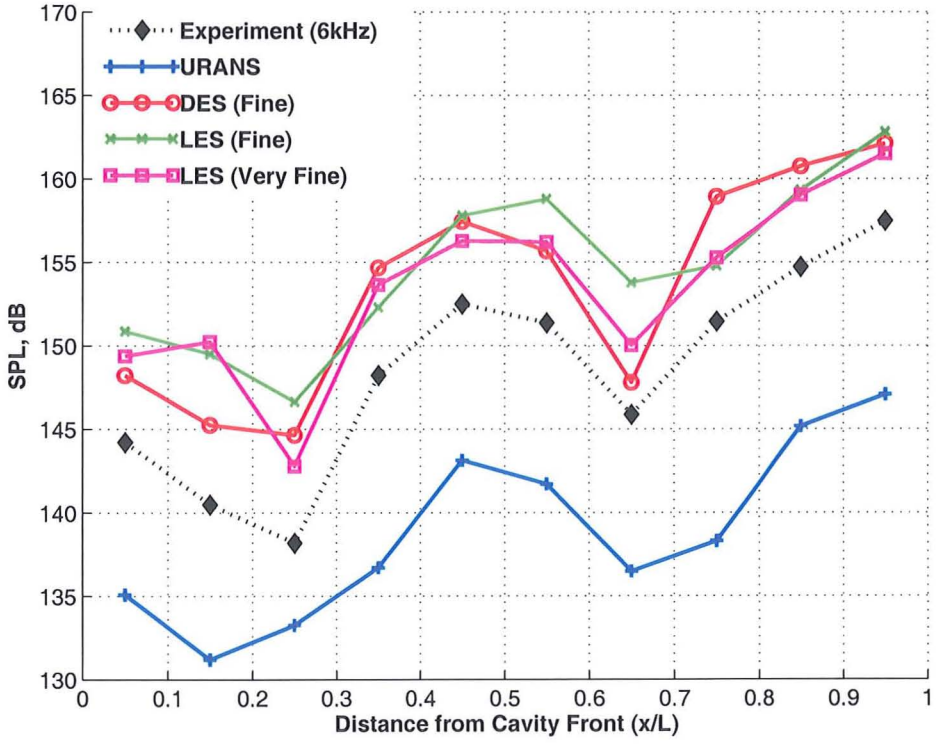

(b) $350\ Hz \leq f \leq 450\ Hz$

Figure 5.7: (continued)

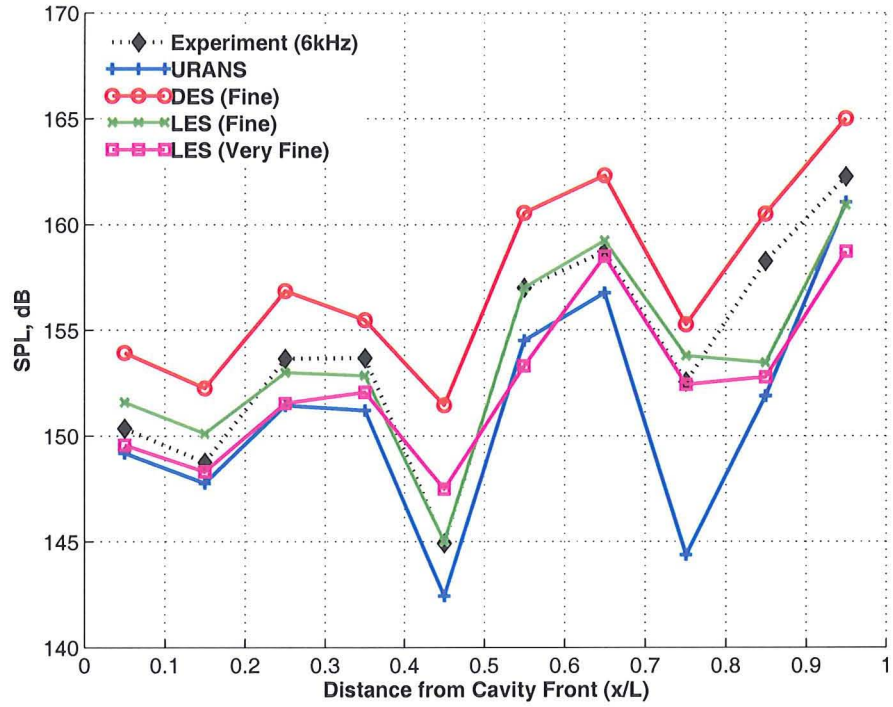

(c) $500\ Hz \leq f \leq 700\ Hz$

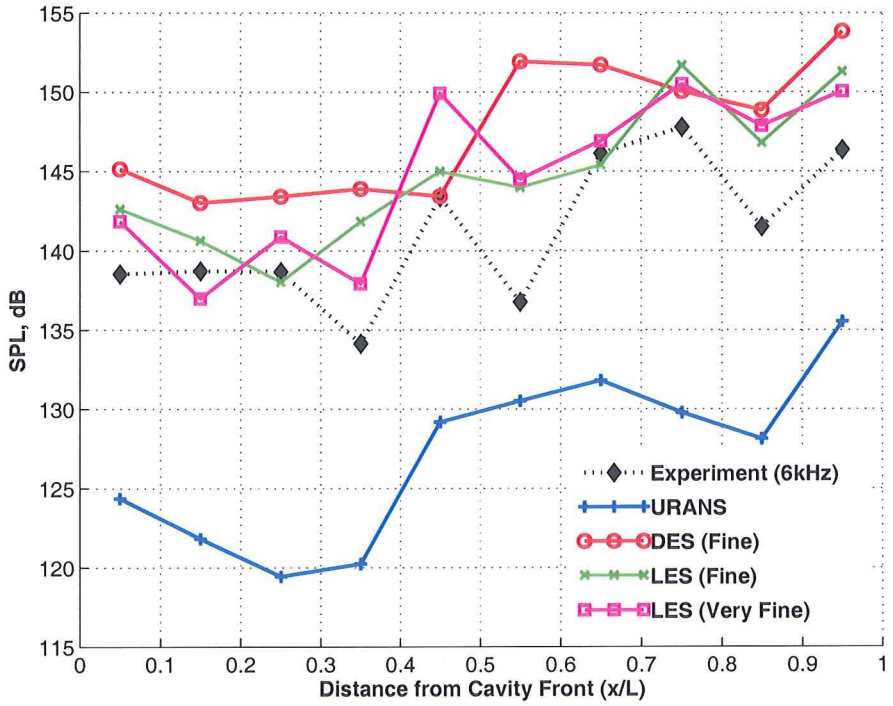

(d) $750\ Hz \leq f \leq 850\ Hz$

Figure 5.7: Band-limited SPLs for the 3D, L/D=5, W/D=1, clean cavity with doors-off comparing URANS (Menter's Baseline $k-\omega$), DES-SA and LES (Smagorinsky SGS) results with experiment. Plots taken at z/W=0.25 and along the cavity floor (y/D=1).

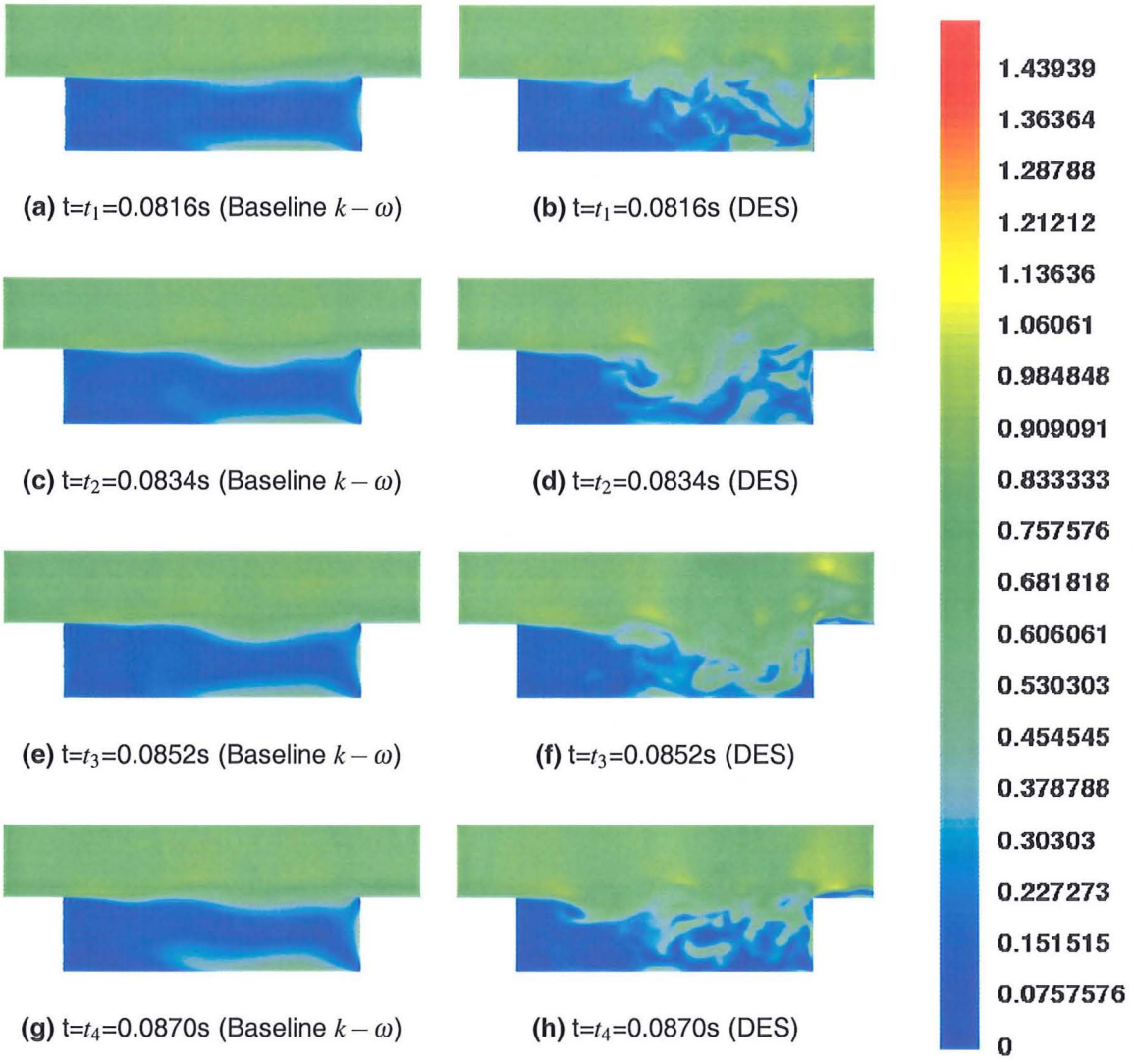

(a) t=t_1=0.0816s (Baseline $k-\omega$) **(b)** t=t_1=0.0816s (DES)

(c) t=t_2=0.0834s (Baseline $k-\omega$) **(d)** t=t_2=0.0834s (DES)

(e) t=t_3=0.0852s (Baseline $k-\omega$) **(f)** t=t_3=0.0852s (DES)

(g) t=t_4=0.0870s (Baseline $k-\omega$) **(h)** t=t_4=0.0870s (DES)

Figure 5.8: Instantaneous Mach number contours with streamlines for the clean cavity with doors-off at for 4 different time-steps during flow cycle for the URANS (Menter's Baseline $k-\omega$) and DES-SA computations. Plots taken along the cavity centreline (z/W = 0.5).

'spillages' for the DES computation are depicted in Figure 5.10. Their production, detachment from the shear layer and dissipation into the surroundings is clearly shown in this figure, which illustrates their flow cycle for eight time-steps during the computation. Analysis of the flow cycle of the vortical 'spillages' reveals that more activity occurs toward the port wall of the cavity (i.e. at z/W=0.2). All computations were conducted without any sideslip or yaw.

Note also the sharp boundary between the regions of higher Mach flow (green) and lower Mach flow (blue) inside the cavity for the LES case in Figure 5.9. DES and URANS results show a less distinct boundary. This is thought to be due to the higher dissipation levels in the turbulence models used in the URANS computations.

These 3D views comprise 3 slices taken very close to the cavity floor, cavity port wall and the cavity downstream wall. The similarity between DES and URANS results is attributed to the fact that DES behaves like URANS near the wall. For the LES computations, the sub-grid scale (SGS) model adds less dissipation than the turbulence model used in

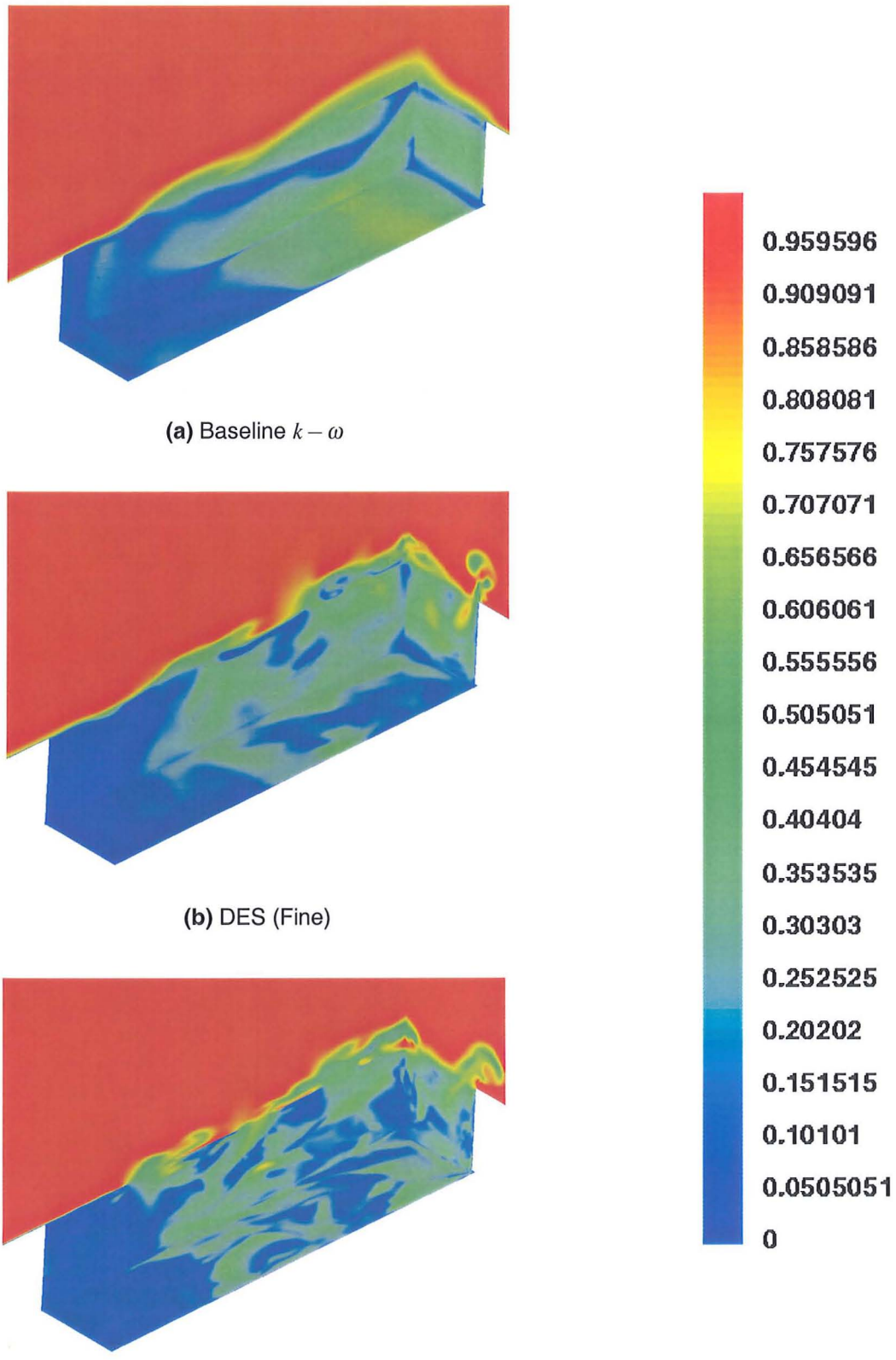

(a) Baseline $k-\omega$

(b) DES (Fine)

(c) LES (Very Fine)

Figure 5.9: Three-dimensional perspective of the flow field inside the 3D L/D=5 clean cavity with doors-off using URANS (Menter's Baseline $k-\omega$), DES-SA and LES (Smagorinsky SGS). Plots show instantaneous Mach number contours normalised by the free-stream Mach number of 0.85.

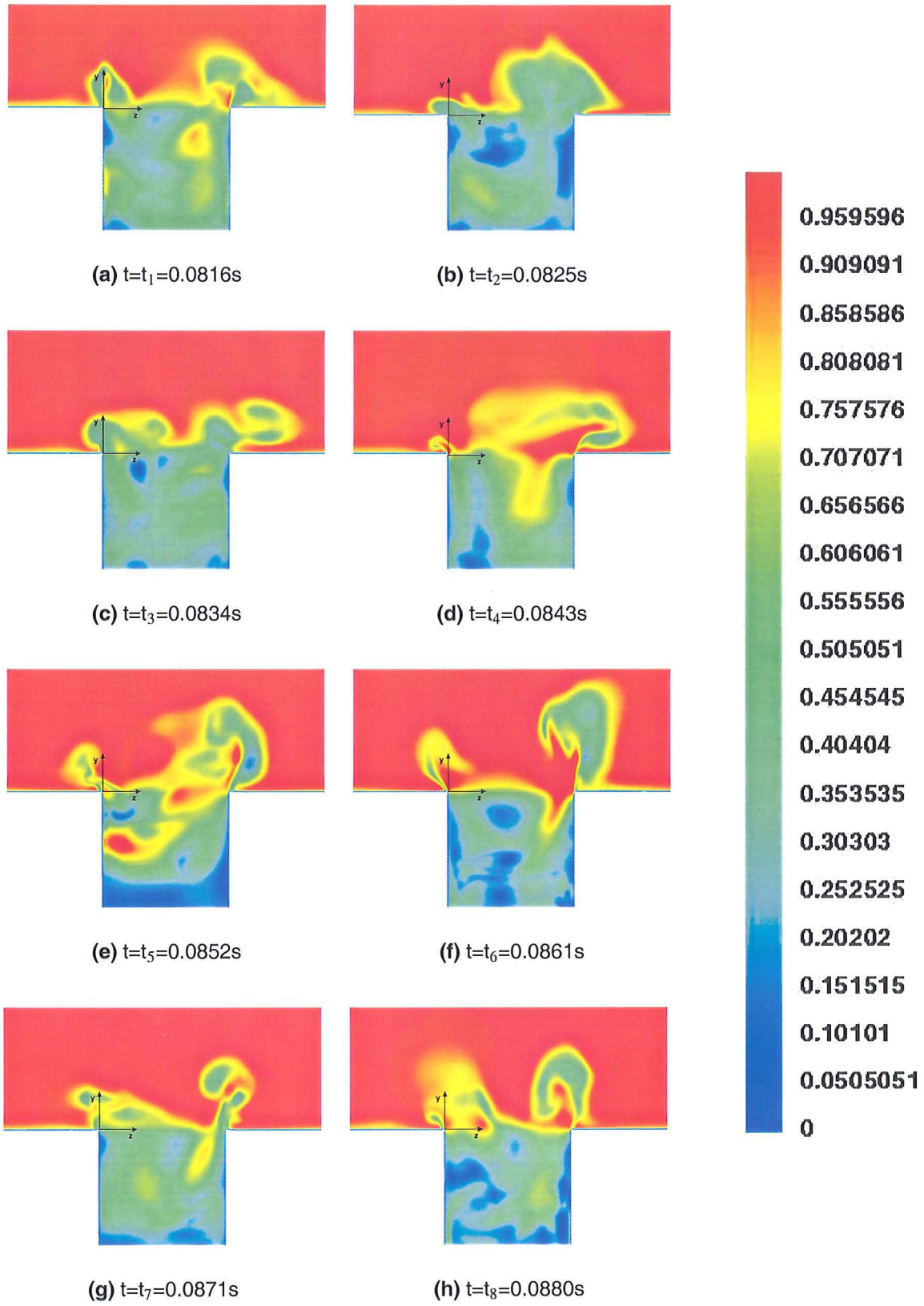

(a) t=t_1=0.0816s **(b)** t=t_2=0.0825s

(c) t=t_3=0.0834s **(d)** t=t_4=0.0843s

(e) t=t_5=0.0852s **(f)** t=t_6=0.0861s

(g) t=t_7=0.0871s **(h)** t=t_8=0.0880s

Figure 5.10: Close-up of the 'vortical spillages' (in the y-z plane) observed near the downstream corner of the 3D, L/D=5, W/D=1 clean cavity with doors-off for the DES-SA with the fine grid for 8 time-steps illustrating their flow cycle. Contours are of Mach number normalised by the free-stream Mach number of 0.85.

URANS and in the near-wall treatment of DES computations. The higher dissipation levels of URANS are indicative of more energy being injected into the more energetic larger vortical structures, which leads to a stronger cascade process. From visual inspection, the shear layer in the URANS computations therefore appears to be very thick, making its breakdown more difficult. Despite the use of a turbulence model in the near-wall region for the DES computations, the shear layer is clearly observed to break down.

The turbulent flow predicted by URANS and in the near-wall regions by DES, also means that the flow is more diffusive. Consequently, smaller scales that occur near the walls are also likely to be spread over a larger area. These smaller, energetic scales have higher vorticity levels and are depicted as lighter (blue) regions in the Mach contour plots in Figure 5.9. The boundary between the lower and higher Mach regions inside the cavity in Figure 5.9 therefore appears to be less defined in the URANS and DES computations.

Since both the doors-on and doors-off cases were run at identical flow conditions, the mean flow energy imparted from the free-stream and the turbulent flow energy imparted from the oncoming boundary layer (the height of which is also identical in both cases) is identical. The doors channel the flow into the cavity and prevent any leakage into the spanwise direction. All the energy from the oncoming boundary layer is therefore concentrated into the shear layer, which maintains its flow path predominantly in the streamwise and transverse plane. The confining presence of the doors precludes large transfer of energy along the spanwise direction outside the cavity. Even inside the cavity, little transport and/or redistribution of energy along the width of the cavity occurs and this is indicative of insignificant three-dimensionality effects at the cavity floor. For the clean cavity case, however, there is a means for energy to be redistributed along the spanwise direction both outside and consequently inside the cavity. Energy is therefore extracted from the shear layer and spread into the surroundings. The pressure at the cavity rear rises due to this mixing process and is manifested in the form of a rising SPL curve (refer to Figure 5.6(a)). This breakdown of the shear layer is, however, not observed at all in Menter's Baseline $k-\omega$ model (Figure 5.8) and is probably why it (and indeed URANS) fail to correctly predict the noise level and frequencies inside the cavity.

One important point to note is the relatively good accuracy of the LES results with experiment for comparatively low-resolution computational domains. To resolve the entire frequency spectrum in the cavity, more spatial and temporal resolution would be required, especially since the frequency of the highest tone approaches 1 kHz in the cavity. However, previous computations with 1m, 2m, 4.5m and 8.5 million at various time-steps have revealed that high density grids are not necessary for reasonably good prediction of the cavity flow-field even at the high Reynolds number of 1 million at which this cavity is run and at transonic conditions. Evidence of this is provided in Figure 5.11, which compares the SPLs for each of the four grids mentioned in the doors-off section in Table 5.1 using LES. Coarse grid results ($\approx$ 1m points) used a time-step of 0.01 ($\equiv 1.814 \times 10^{-5}$s), the medium grid used a time-step of 0.005 ($\equiv 9.07 \times 10^{-6}$s) while a time-step of 0.001 ($\equiv 1.814 \times 10^{-6}$s) was used for the fine and very fine computations. The general shape of the SPL curve as well as amplitudes can clearly be observed to consistently match with each other with spatial and temporal refinement.

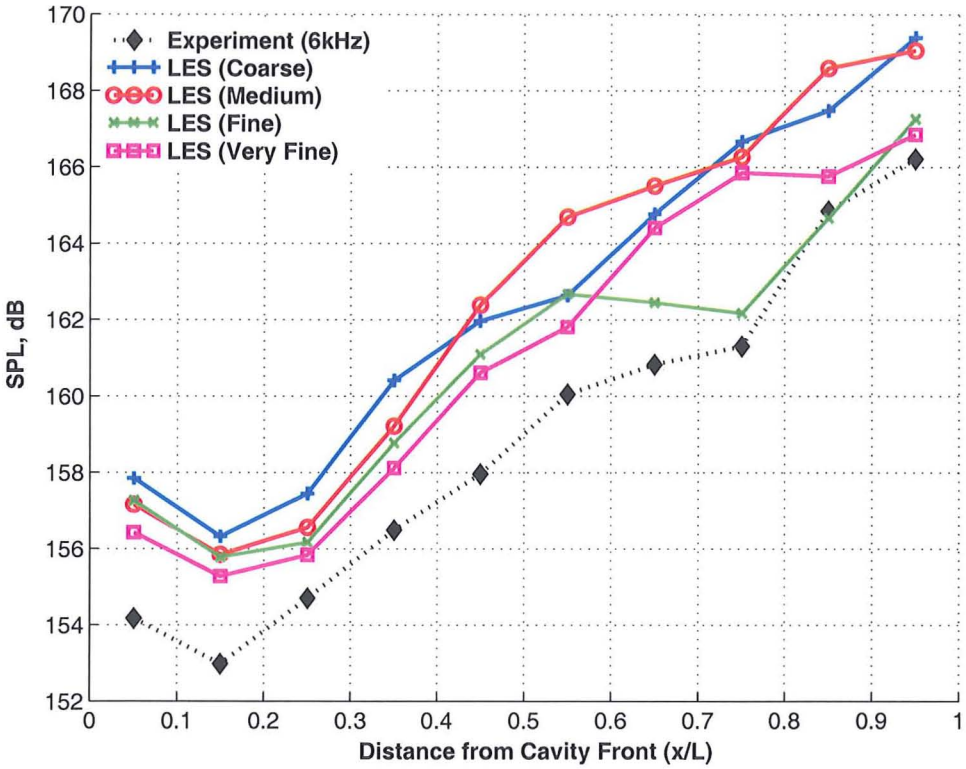

Figure 5.11: SPLs inside the 3D L/D=5, W/D=1 clean cavity with doors-off using LES (Smagorinsky SGS) with the 1m, 2m, 4.5m and 8.5m grids.

5.3 Doors-On Results

Doors-on results for the 3D, L/D=5, W/D=1 cavity based on DES, LES and URANS methods are presented in Figures 5.12 to 5.15. Since DES gave good results for the doors-off case it was decided to run a fine grid DES computation for the doors-on configuration. The one-equation Spalart-Allmaras model [192] was used to realise the near-wall properties in DES computations. This allowed the use of coarser grids than would have been required for LES. For comparison purposes, however, a medium grid LES computation with the doors-on was also conducted. For consistency, Menter's Baseline $k-\omega$ model [245] was used for the URANS calculations of the 3D, L/D=5, W/D=1 cavity with doors-on, as was the case with doors-off. With the 2D cavity thought to be a good representation of the full 3D cavity, results from the 2D cavity are also included. Results from the coarse grid (details of which were provided earlier in Table 4.1 in Chapter 4) were used for the 2D cavity.

Two sets of experimental data were provided in the doors-on configuration, as was mentioned previously in Chapter 3. Normally all wind tunnel measurements for the cavity were conducted with a sampling rate of 6 kHz with the exception of the doors-on case for which an additional experiment with a higher sampling rate of 31.25 kHz was also performed. Experimental results corresponding to both sets of sampled data are included when comparing SPLs, spectrals and band-limited frequency results with computations. Changes in results between the 6 kHz and 31.25 kHz experimental data sets are deliberately highlighted to emphasise the requirement of higher resolution experimental data for high Reynolds number cavity flows. All numerical results were sampled at the 31.25

kHz sampling rate. Overall, about 3 dB of of difference was observed between the two experimental data sets.

Figure 5.12 show the difference between DES, LES and URANS methods in the prediction of noise levels and frequency content at $x/L = 0.05$, $x/L = 0.55$ and $x/L = 0.95$ along the cavity floor. Results for both LES, 2D URANS (SST model) and 3D URANS (Baseline $k-\omega$ model) agree well with experiment. In fact, near the front of the cavity, the shape of the SPL curve for Menter's Baseline $k-\omega$ model [245] follows the experiment better than the LES results. Fourier transform of the numerical signal indicates the frequencies generated inside the cavity as shown in Figures 5.12(b)-5.12(d). These plots illustrate a less promising agreement between Menter's Baseline $k-\omega$ model and experiment. Neither the 1st nor the 3rd Rossiter modes were captured. Table 5.3 presents the comparison between the frequencies and amplitudes predicted by the numerical computations and experiment. The 2nd Rossiter mode ($\approx 380\ Hz$) is well captured in the 3D URANS computations but is over-predicted by about 1 kPa. This over-prediction was found to be a common occurrence for most URANS comparisons with experiment. Even for very coarse grids, however, LES and even DES predict the amplitudes of the frequencies very well.

A distinct difference between the amplitudes of the acoustic tones and the overall SPLs can be observed in the 2D and 3D URANS results in the spectral and noise level distribution in Figure 5.12. Although the 2D results over-predict the magnitude of the 2nd Rossiter mode by as much as approximately 4 kPa at the cavity rear ($x/L = 0.95$) relative to 3D URANS and by about 5 kPa relative to experiment (Figure 5.12(d)), it fares better than the 3D URANS results in predicting the less dominant 1st ($\approx 160\ Hz$) and, to a lesser extent, the 3rd ($\approx 600\ Hz$) Rossiter modes. The full 3D cavity will however have different boundary layer characteristics compared to the 2D cavity due to spanwise effects. In fact, the boundary layer height at the lip of the cavity is typically greater than for the full 3D cavity. It is probable that the significant over-prediction of the frequency amplitudes for the 2D cavity is attributed to this.

Another observation from the SPL and PSD plots is the difference between the 6 kHz and 31.25 kHz experimental signals. Shape of the SPL curves are different for almost all positions along the cavity floor (Figure 5.12(a)). In the frequency domain, a phase shift is observed between the two experimental signals with the higher sampled signal typically shifted to the right for the three stations analysed (Figures 5.12(b)-5.12(d)). Amplitudes of the modes can also differ between the two signals with a difference of about 0.5 kPa noted at the cavity middle ($x/L = 0.55$).

5.3.1 Band-Limited Frequency Analysis

A more in-depth analysis of the numerical results is provided in Figure 5.13, which present the fluctuations in the noise level within four different frequency bandwidths. The first bandwidth ($50\ Hz \leq f \leq 250\ Hz$) straddles the first Rossiter mode ($\approx 160\ Hz$), the second bandwidth ($350\ Hz \leq f \leq 450\ Hz$) contains the second mode ($\approx 380\ Hz$), the third bandwidth ($500\ Hz \leq f \leq 700\ Hz$) includes the third mode ($\approx 600\ Hz$) and the fourth bandwidth ($750\ Hz \leq f \leq 850\ Hz$) includes the fourth mode ($\approx 820\ Hz$).

It can be clearly observed in Figure 5.13 that both DES and LES generally provide better agreement with experiment across all four frequency bandwidths. The best agreement for

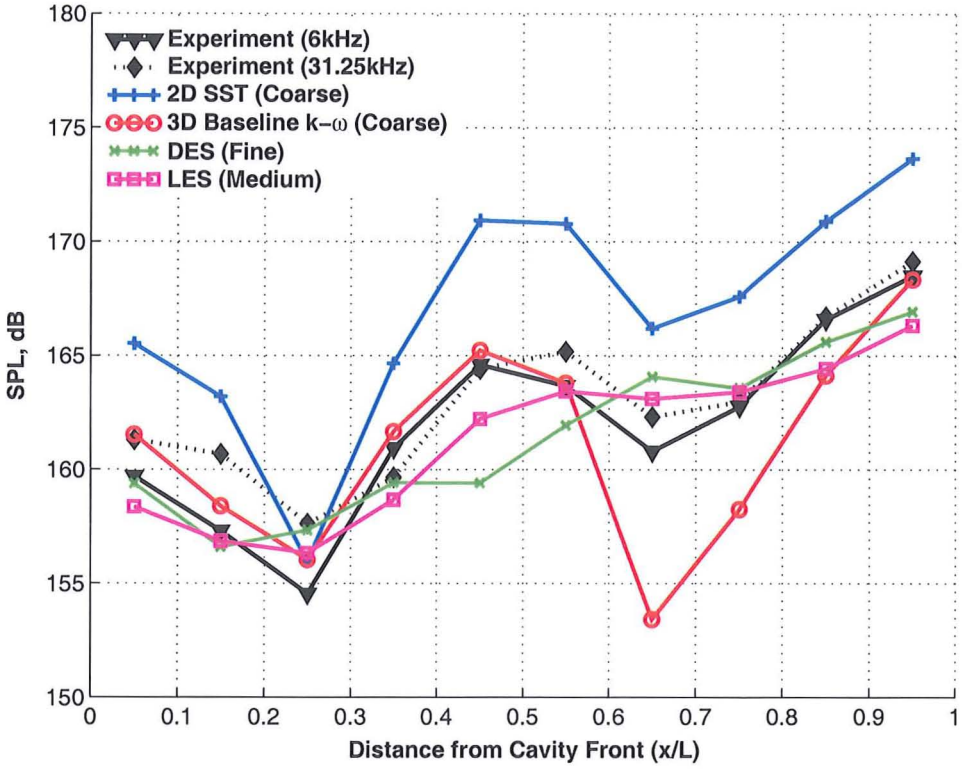

(a) SPLs

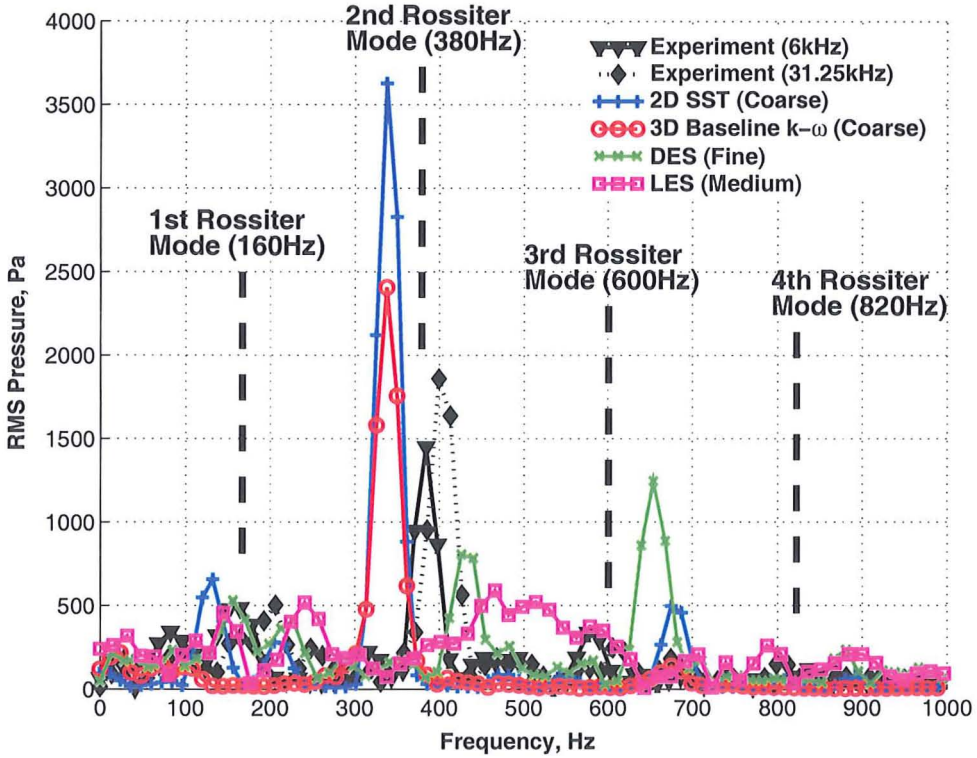

(b) PSD $(x/L = 0.05)$

Figure 5.12: (continued)

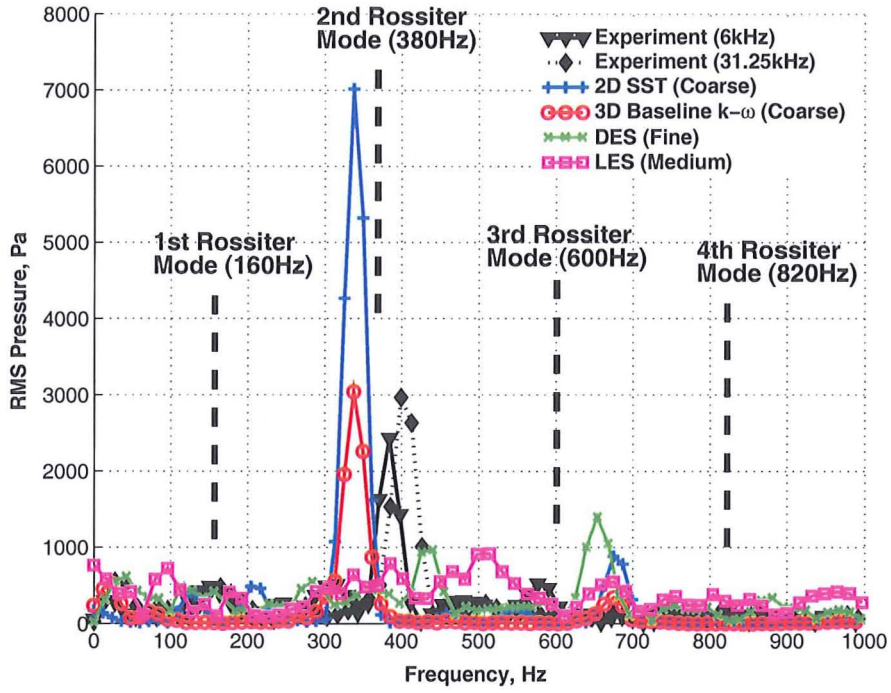

(c) PSD ($x/L = 0.55$)

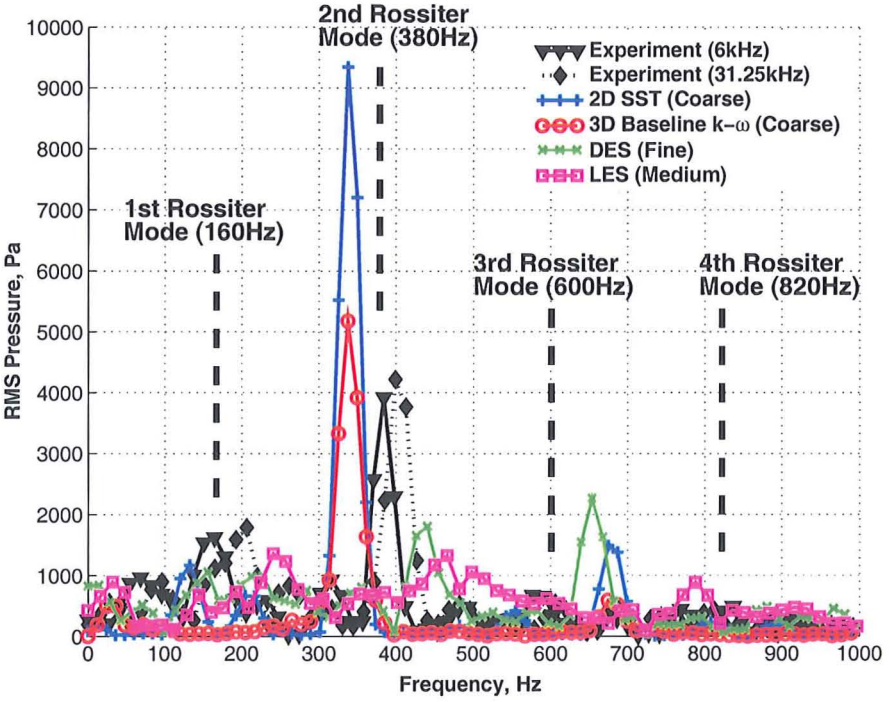

(d) PSD ($x/L = 0.95$)

Figure 5.12: SPLs and PSD (at $x/L = 0.05$, $x/L = 0.55$ and $x/L = 0.95$) along cavity floor for the L/D=5, W/D=1, clean cavity with doors-on at 90° vertically comparing 2D URANS (SST), 3D URANS (Baseline $k-\omega$), DES-SA and LES (Smagorinsky SGS) results with experiment. Plots taken at z/W=0.25 and along the cavity floor (y/D=1).

Table 5.3: Comparisons of (approximate) frequencies and their amplitudes predicted between LES (Smagorinsky SGS for medium grid), DES (Spalart-Allmaras for fine grid), URANS (Baseline $k-\omega$ for coarse grid) for the doors-on clean cavity (at $x/L=0.95$), Rossiter's semi-empirical formula [3] and experiment.

Method	1st Mode		2nd Mode		3rd Mode		4th Mode	
	Freq. Hz	Ampl. Pa	Freq. Hz	Ampl. Pa	Freq. Hz	Ampl. Pa	Freq. Hz	Ampl. Pa
Rossiter's Formula	162	-	378	-	594	-	811	-
Experiment (6kHz)	166	1631	385	3927	577	688	839	493
Experiment (31.25kHz)	207	1786	401	4225	605	539	813	429
2D URANS (SST)	130	1200	340	9500	680	1500	1200	500
3D URANS (Baseline $k-\omega$)	-	-	339	5174	675	594	-	-
DES (Fine)	157	1057	442	1796	654	2263	883	478
LES (Medium)	241	1360	465	1328	-	-	789	886

Menter's Baseline $k-\omega$ model with experiment exists for the 2nd Rossiter mode ($\approx$ 380 Hz) as portrayed in Figure 5.13(b): both the shape and amplitude are well predicted. Since this second Rossiter mode is the dominant mode (Figure 5.12(d)), it has the greatest contribution in the overall noise levels produced in the cavity, especially since the amplitudes of the other modes are significantly smaller. Consequently, the URANS results appear good at a first glance but a closer inspection of other frequency bandwidths in Figure 5.13 reveal that a significantly better comparison exists between LES, DES and experiment. In general, LES/DES capture the higher frequencies much better than URANS.

Better agreement is also achieved between the 2D cavity case and experiment than with the 3D cavity case. This is especially the case for the first Rossiter mode (Figure 5.13(a)). In general, the 2D URANS results tend to predict much higher magnitudes than the 3D URANS results across the entire frequency spectrum analysed. Since DES and LES add less dissipation to the flow, URANS results should predict amplitudes lower than DES and LES results, especially since the broadband spectrum is not accounted for by URANS. This is the case with the 3D URANS but not so with 2D URANS suggesting that the 2D approximation may not be valid. The over-prediction of overtones in this 2D results may be attributed to the oncoming boundary layer profile. For the same initial conditions, the oncoming boundary layer is generally twice as thick in the 2D cavity than for 3D. Consequently more energy is fed into the shear layer and this may explain the augmented 2nd Rossiter mode magnitude and hence overall noise levels.

5.3.2 Turbulence Decay Characteristics

With LES performing better than URANS in predicting the narrowband acoustics inside the cavity, its effectiveness in capturing the turbulent characteristics was assessed. As mentioned previously, at such high Reynolds numbers for the cavity flow, a broad range of turbulence scales exist. Proper prediction of turbulence would therefore depend on

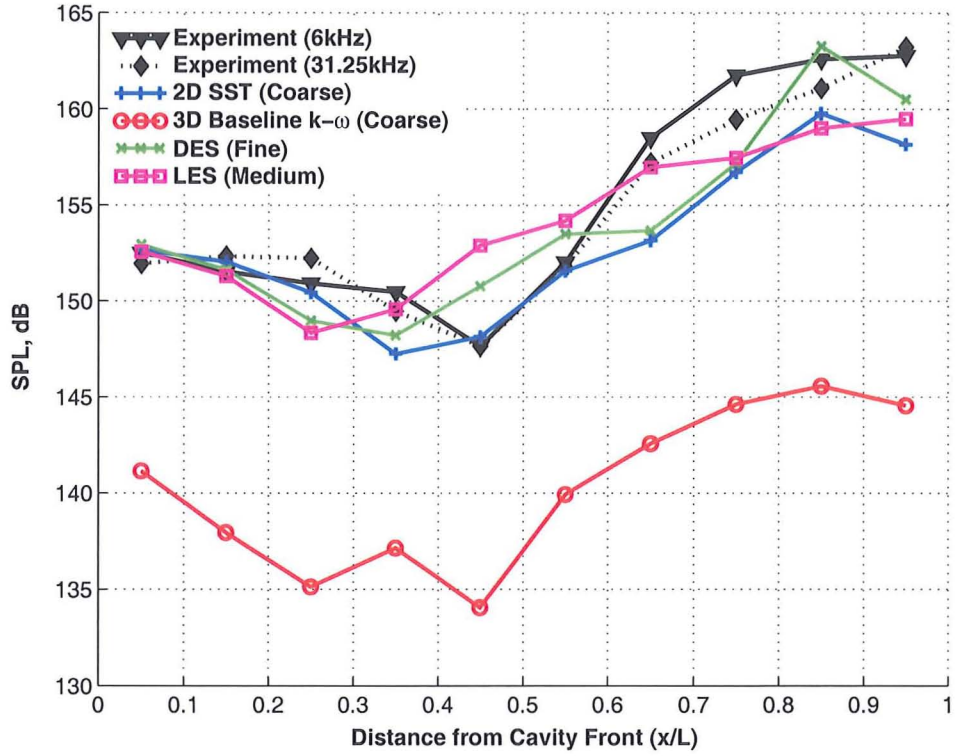

(a) $50\ Hz \leq f \leq 250\ Hz$

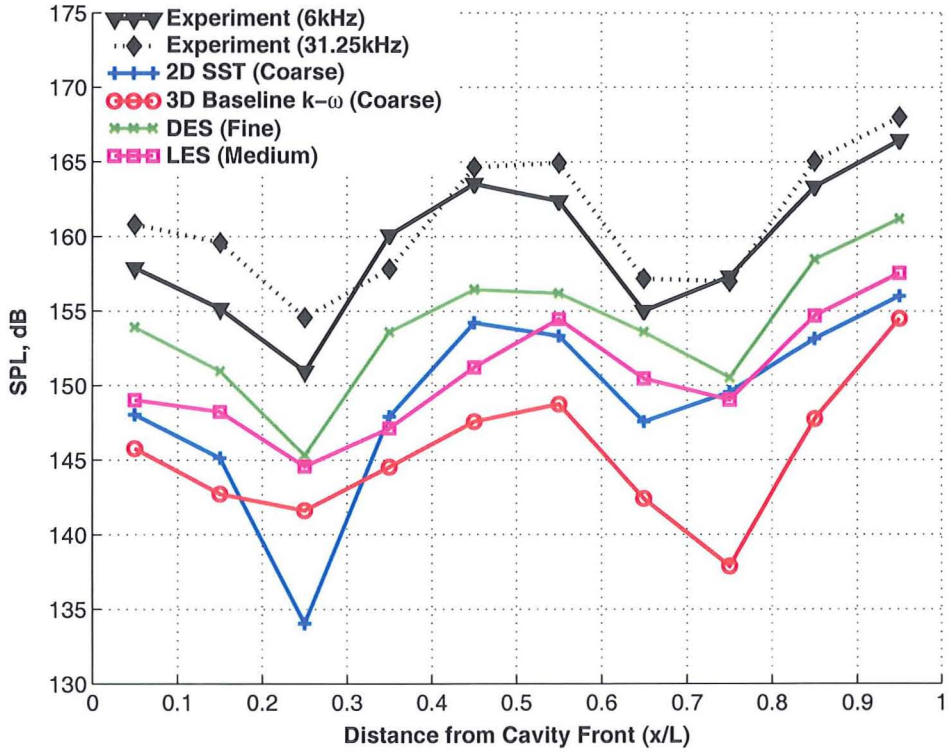

(b) $350\ Hz \leq f \leq 450\ Hz$

Figure 5.13: (continued)

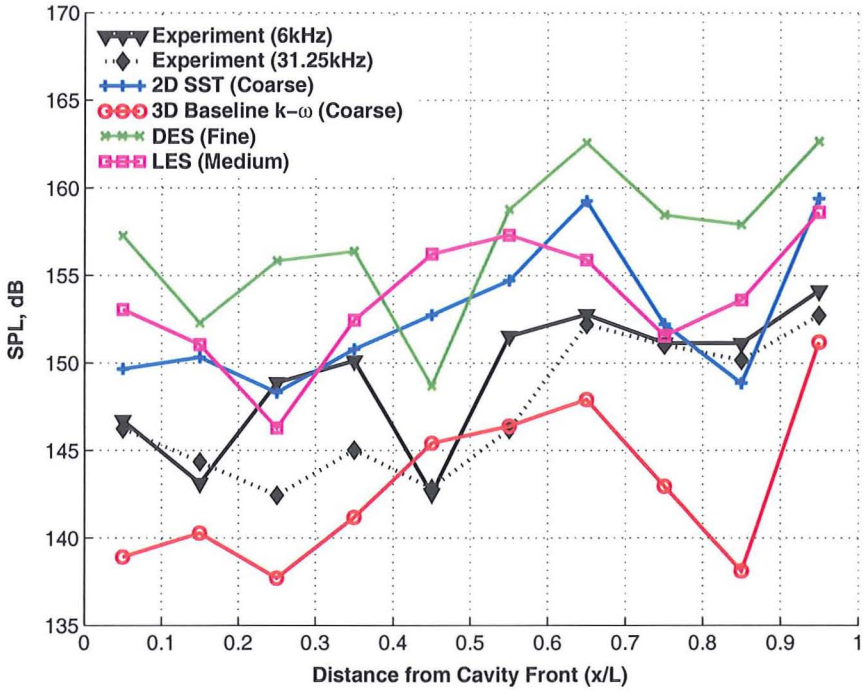

(c) $500\ Hz \leq f \leq 700\ Hz$

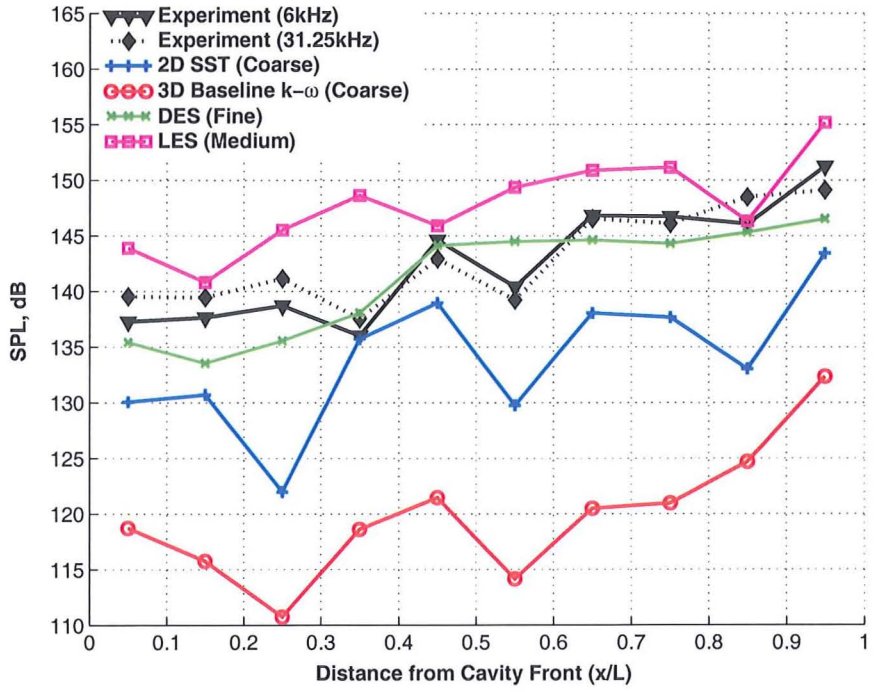

(d) $750\ Hz \leq f \leq 850\ Hz$

Figure 5.13: Band-limited SPLs for the 3D, L/D=5, W/D=1, clean cavity with doors-on at 90° vertically comparing 2D URANS (SST), 3D URANS (Baseline $k-\omega$), DES-SA and LES (Smagorinsky SGS) results with experiment. Plots taken at z/W=0.25 and along the cavity floor (y/D=1).

resolving correctly not only the larger, more-energetic scales, the smaller, more isotropic scales and their interactions between them. Turbulence cascade is therefore important and an illustration of it can be obtained by analysing the turbulence decay spectrum of the cavity flow and comparing it with the theoretical -5/3 Kolmogorov slope. Figure 5.14 illustrate the turbulence decay for DES, LES and Menter's Baseline $k-\omega$ model with experiment for three stations along the cavity floor: cavity front ($x/L = 0.05$), cavity middle ($x/L = 0.55$) and cavity rear ($x/L = 0.95$). The 6 kHz sampling rate experimental signal was inappropriate for analysing the experimental turbulence decay characteristics and as such only the decay spectrum for the 31.25 kHz experimental signal was superimposed here. The solid magenta line in Figure 5.14 represents the -5/3 Kolmogorov slope. Turbulence decay spectrum for DES and (even under-resolved) LES is much closer to experiment than URANS in terms of amplitudes. The decay slope is generally in better agreement with the Kolmogorov -5/3 slope with DES and LES computations. Based on these results, it would seem feasible to use low-resolution grids for LES computations for high-Reynolds number cavity flows.

A couple of observations can be made based on the decay plots in Figure 5.14. Note the distinct peak located between 4-7 kHz in the experimental signal as well as the less clear double peaks at about 7 kHz in the DES, LES and, to a lesser extent, URANS signals, occurring predominantly at the cavity front (Figure 5.14(a)) and towards the end of the shown signal. These peaks in the numerical signals appear to be more evident in the coarser grids and disappear as the grids are refined. These frequencies are too high to be narrowband but may be attributed to the Kelvin-Helmholtz instability in the shear layer. A recent publication by Larchevêque *et al.* (2004) [272] also supports this fact. Larchevêque *et al.* (2004) [272] conducted LES on the same L/D=5, W/D=1 cavity but at a slightly higher Reynolds number and showed that the Kelvin-Helmholtz instability occurred within the 3-6 kHz frequency range.

The Kelvin-Helmholtz instability arises when there are large changes in, for instance, the streamwise velocity component across two parallel streams of different velocities adjacent to each other, i.e. during shear. The flow in these circumstances can become unstable to perturbations of infinitesimal size. At high Reynolds number, a shear layer mode exists in the L/D=5 cavity, where a shear layer forms and extends across the cavity opening. In this situation, Kelvin-Helmholtz instabilities are likely to have a significant effect on the flow.

Variations in velocity gradients across the shear layer will vary from position to position across the cavity opening. Wavenumbers produced by the Kelvin-Helmholtz instability are typically associated with the inverse of the velocity difference across the shear layer interface. Normally, the shear layer becomes thicker further downstream because it loses energy and diffuses and so the velocity gradient across it is more uniform. Velocity difference across the shear layer is therefore much less and hence wavenumbers produced by an instability are much larger. Frequencies generated in this case are therefore higher. At the cavity front (i.e. $x/L = 0.05$), the shear layer is thin and all the energy from the boundary layer is concentrated within it. A much larger velocity gradient exists across the shear layer at this point and hence frequencies generated are somewhat lower than at the cavity middle or rear. This may explain why the peak occurs at a slightly lower frequency of 4 kHz at the front (i.e. $x/L = 0.05$) compared to the 7 kHz at the cavity middle (i.e. $x/L = 0.55$) and rear (i.e. $x/L = 0.95$) in Figure 5.14.

Whether these peaks are definitely due to the Kelvin-Helmholtz instability is uncertain and requires further investigation. Nonetheless, one further piece of evidence that supports the fact that these peaks may be related to the Kelvin-Helmholtz instability (which is a

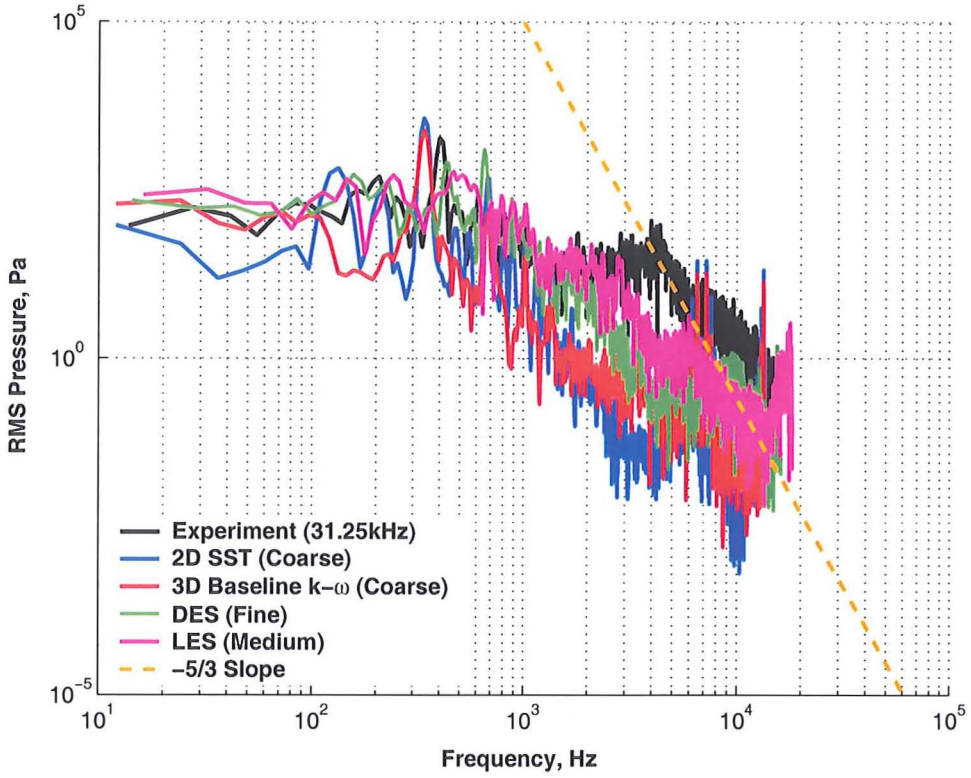

(a) Decay ($x/L = 0.05$)

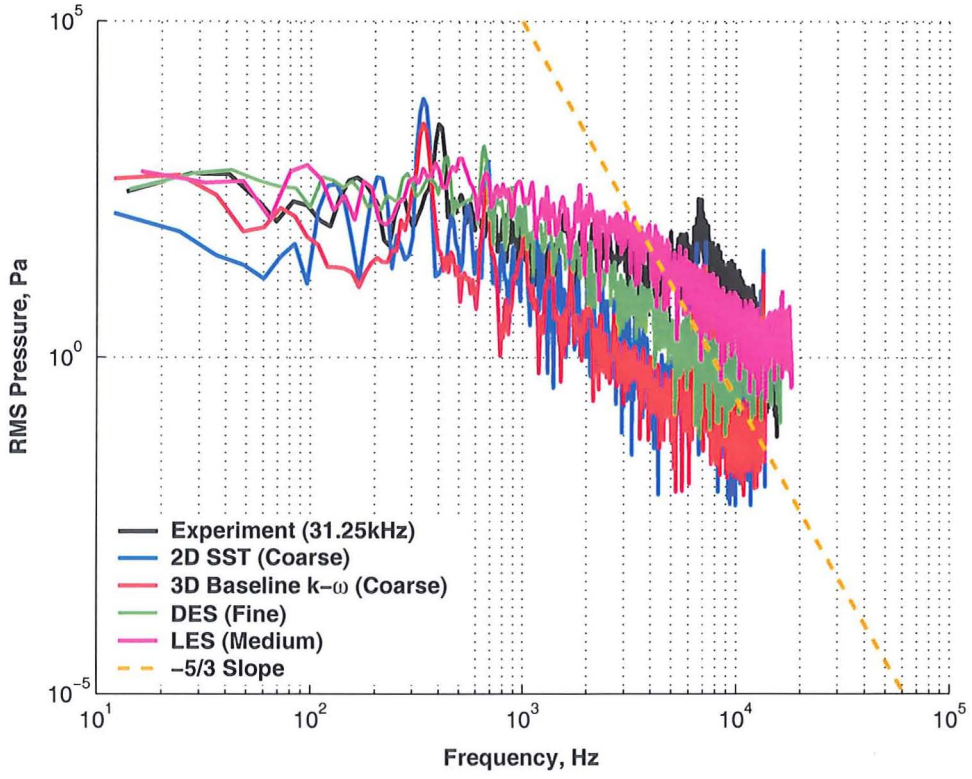

(b) Decay ($x/L = 0.55$)

Figure 5.14: (continued)

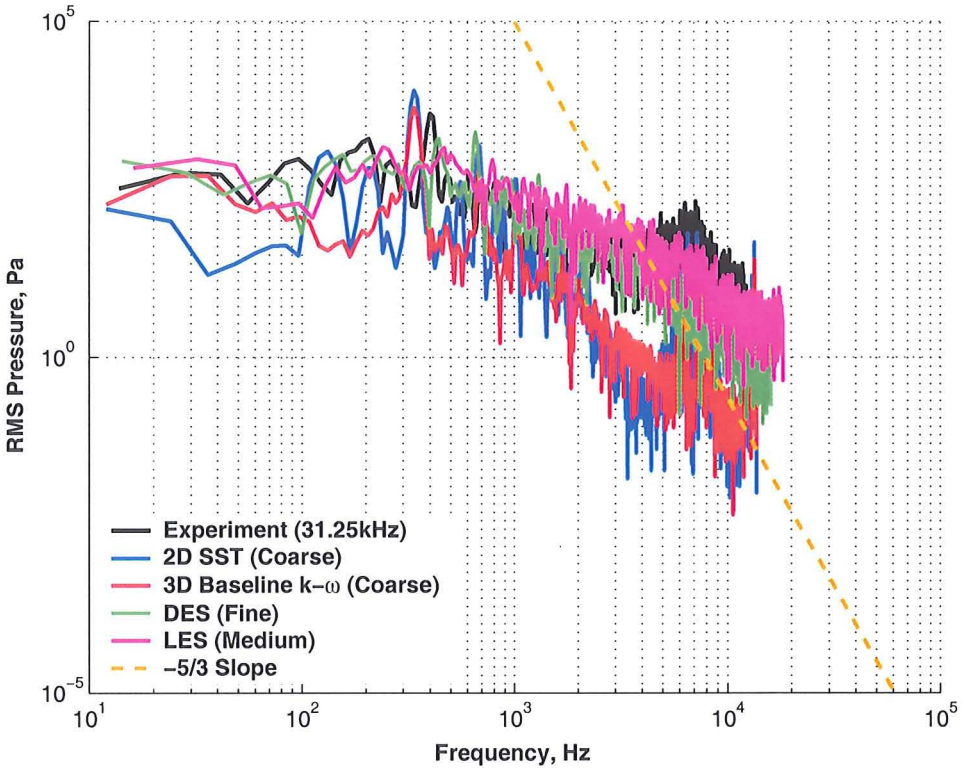

(c) Decay ($x/L = 0.95$)

Figure 5.14: Turbulence decay plots (at $x/L = 0.05$, $x/L = 0.55$ and $x/L = 0.95$) for the 3D, L/D=5, W/D=1 clean cavity with doors-on at comparing 2D URANS (SST), 3D URANS (Baseline $k-\omega$), DES-SA and LES (Smagorinsky SGS) results with experiment. Plots taken at z/W=0.25 and along the cavity floor (y/D=1).

two-dimensional phenomenon) is that these peaks are also observed in 2D cavity flows. It must also be highlighted that the decay plots in Figure 5.14 depict the turbulent decay spectrum at the cavity floor and not at the shear layer, which is where the Kelvin-Helmholtz instability will have the strongest effect. Peaks observed at the cavity floor can however still be indirectly related to the effect of the Kelvin-Helmholtz instability in the same way that pressure waves of a particular frequency existing outside the cavity can interact with the shear layer to provide 'footprints' of the same frequency on the cavity floor.

The second observation is based on the fact that even with a higher sampling rate of 31.25 kHz, the experimental signal is not long enough to analyse the 'roll-off' characteristics at the very high frequency end. Experimental data with a yet higher sampling rate are therefore required for better validation of computations. For comparison purposes, the LES results correspond to a sampling rate of approximately 55 kHz.

5.3.3 Broadband Spectrum Analysis

Aside from the prediction of narrowband noise, analysis of the broadband spectrum was also conducted. Broadband noise may be important in situations where the cavity is

exposed to the free-stream for longer periods of time. In this situation, the structure of the cavity along with its contents can exhibit fatigue failure. The broadband can be analysed by plotting the variation in noise level over a large frequency range. At higher frequencies (or Strouhal numbers), the discrete, acoustic tones are no longer present and the source of all noise becomes broadband, as shown in Figure 5.15. DES and LES results are noted to be closer to experiment in terms of amplitudes. Lower SPLs for Menter's Baseline $k-\omega$ model for the 3D cavity and the SST model for the 2D cavity is a clear representation of the inability of URANS to capture broadband noise.

5.3.4 Flow-field Visualisation

Instantaneous flow-field for the doors-on cavity using the DES (fine) results are presented in Figure 5.16. Comparisons are made with the 2D SST results rather than the 3D Baseline $k-\omega$ results due to the much better agreement provided by the 2D case, as has been demonstrated earlier. Development of the flow cycle is illustrated over four time-steps and compared for both cases. Plots shown in Figure 5.16 correspond to Mach number contours at a slice taken at the centre of the cavity (i.e. z/W=0.5).

Although results from the DES with the Spalart-Allmaras turbulence model provided good agreement with experiment in the doors-off configuration, its accuracy deteriorated when doors were included. This is likely to be attributed to the inadequacy of the one-equation Spalart-Allmaras turbulence model to correctly model the near-wall properties. With only one transport equation to model the kinetic energy of turbulence, it provides no mechanism for calculating the turbulent dissipation and hence turbulent length scales.

Previous studies revealed that the effect of the wall inside the cavity was insignificant to the overall physics of the flow inside the cavity. With doors-off, the turbulence model is active only very close to the cavity walls with LES active elsewhere for DES computations. With little influence of the cavity walls, whether the model can or cannot correctly predict the near-wall characteristics makes little difference. In the doors-on case, however, the turbulence model is forced to be active near the region of the doors as well, which do play a more significant role in channelling the flow in and out of the cavity. Dissipation of turbulence is not properly predicted by the Spalart-Allmaras model perhaps because a transport equation is not included to calculate it, unlike the $k-\omega$ model. This may lead to an inaccurate production of the smaller turbulent scales, thereby providing a comparatively poorer prediction of the acoustic levels and frequencies. This can be demonstrated by analysing the SPLs predicted by DES (Figure 5.12(a)), where the high-pressure plateau at the cavity middle is less well predicted. Menter's Baseline $k-\omega$ model and indeed the SST model used in the 2D cavity computation performed much better in predicting the SPL shape in the doors-on configuration, indicating its superior capability in predicting the near-wall properties. Since both the Baseline $k-\omega$ and SST are zonal models and use the standard $k-\omega$ model near the wall, DES in conjunction with the Wilcox $k-\omega$ model or LES with higher resolution grids should provide better accuracy and agreement with experiment. Evidence of this is given in Figure 5.17, which compares the SPLs for the doors-on L/D=5 cavity using the DES-SA (fine grid) and DES with the $k-\omega$ model (coarse grid) and LES (medium grid). Even for a coarse grid, DES with $k-\omega$ provides better agreement with experiment than DES-SA.

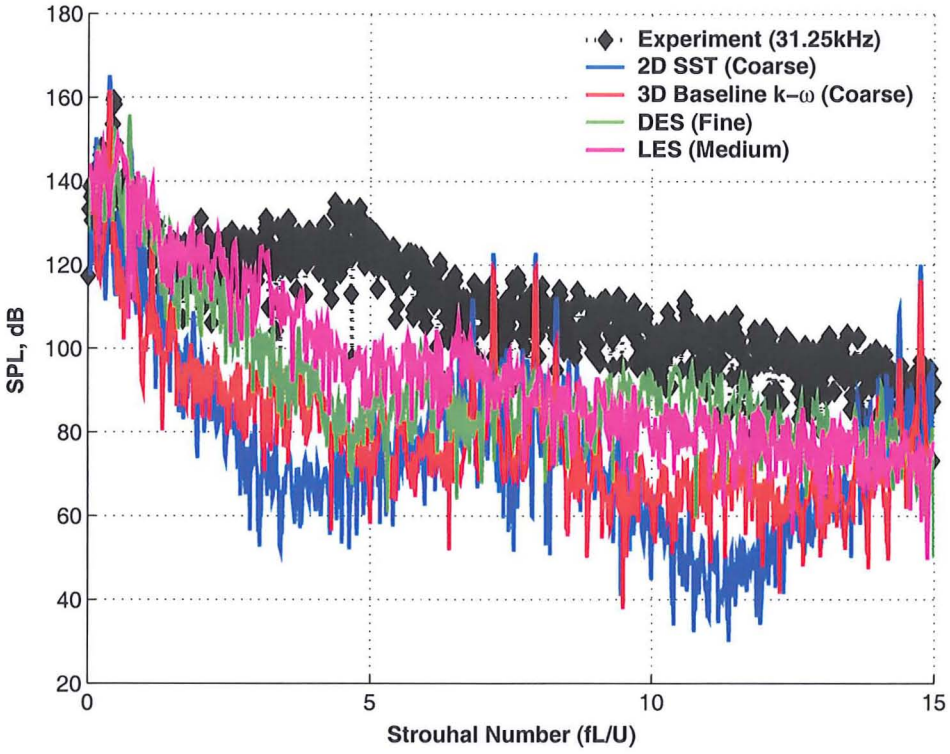

(a) SPL vs Strouhal ($x/L = 0.05$)

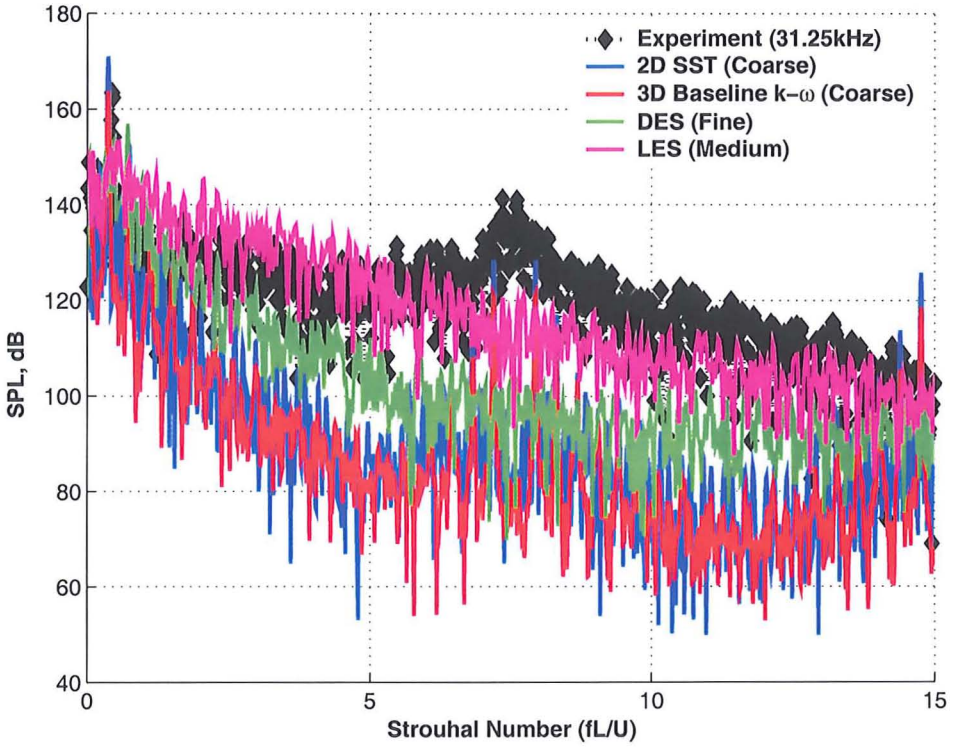

(b) SPL vs Strouhal ($x/L = 0.55$)

Figure 5.15: (continued)

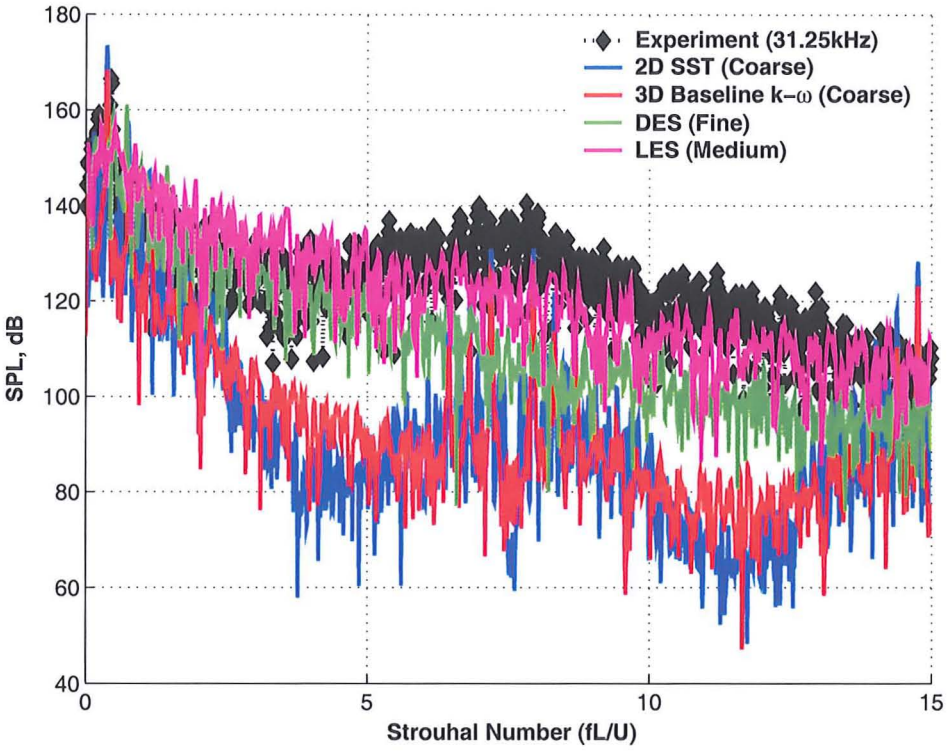

(c) SPL vs Strouhal ($x/L = 0.95$)

Figure 5.15: SPLs against Strouhal number (at $x/L = 0.05$, $x/L = 0.55$ and $x/L = 0.95$) for the 3D, L/D=5, W/D=1 clean cavity with doors-on comparing 2D URANS (SST), 3D URANS (Baseline $k-\omega$), DES-SA and LES (Smagorinsky SGS) results with experiment. Plots taken at z/W=0.25 and along the cavity floor (y/D=1).

5.4 PIV Comparisons

Description of the PIV experiment was given by Ross [6] and Foster [65] and is discussed in detail in Chapter 3. The PIV experiment was conducted for the 3D cavity in the doors-on configuration only and so results from the corresponding doors-on computations are only compared with it.

Streamwise and transverse velocity profiles for three different stations inside the cavity (x/L=0.05, x/L=0.55 and x/L=0.95) for URANS, DES and LES computations are illustrated in Figure 5.18. The black line denotes the PIV measurements. URANS results correspond to time-averaged 2D cavity results using the SST turbulence model. The time-averaged fine-grid DES results using the one-equation Spalart-Allmaras model are also shown along with the medium-grid LES results using the standard Smagorinsky sub-grid scale model. Details of the grids used are presented in Table 5.1. A dimensionless time-step of 0.01 ($\equiv 1.814 \times 10^{-5}$s) was used for the 2D computation, 0.001 ($\equiv 1.814 \times 10^{-6}$s) for the DES computation and 0.005 ($\equiv 9.07 \times 10^{-6}$s) for the LES calculation.

Agreement with PIV is good with all methods at the front of the cavity (Figures 5.18(a) and 5.18(b)) where the flow activity is minimal. Toward the middle of the cavity, better agreement was obtained between DES, LES and PIV. The greater differences at this

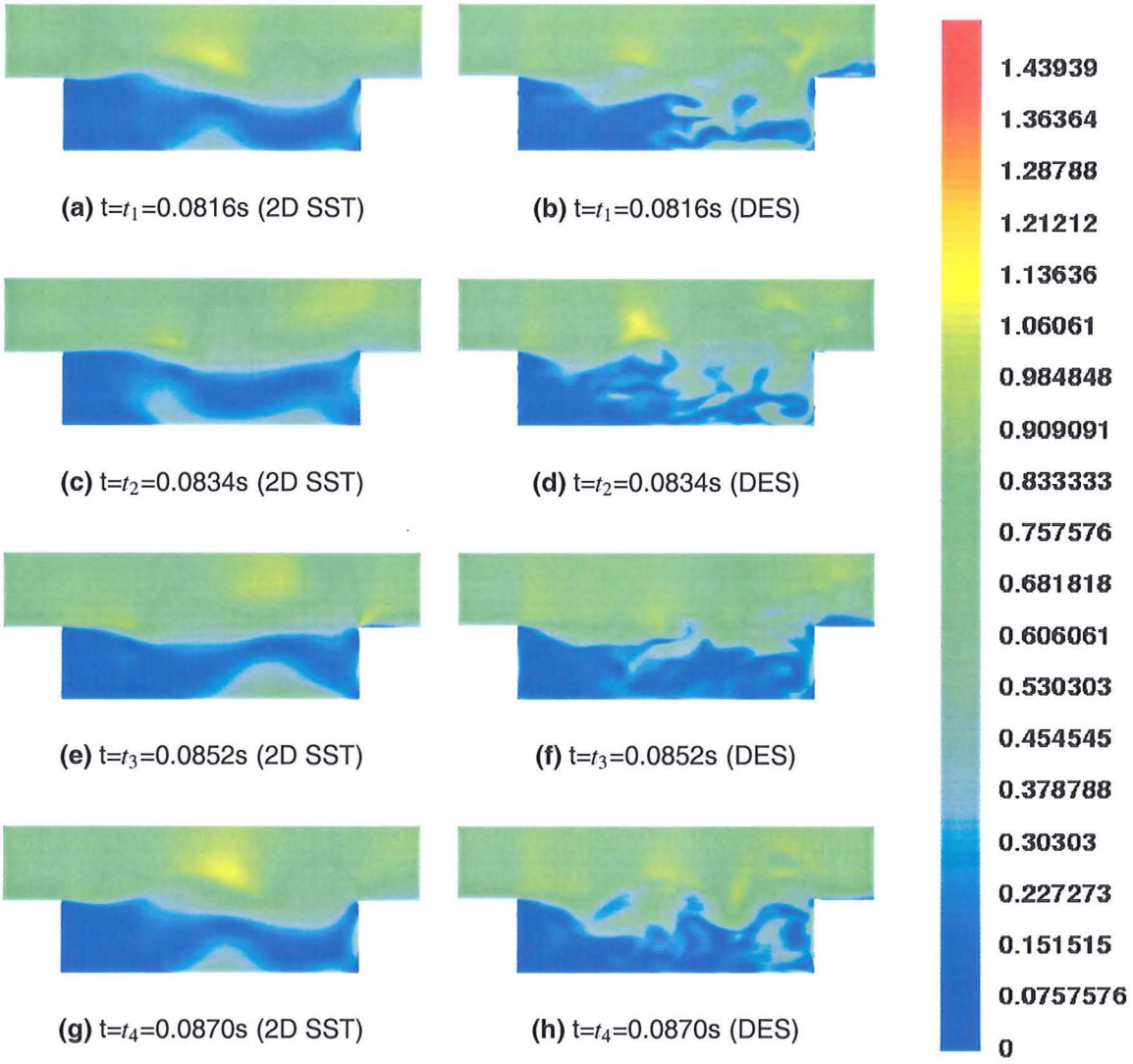

(a) t=t_1=0.0816s (2D SST) **(b)** t=t_1=0.0816s (DES)

(c) t=t_2=0.0834s (2D SST) **(d)** t=t_2=0.0834s (DES)

(e) t=t_3=0.0852s (2D SST) **(f)** t=t_3=0.0852s (DES)

(g) t=t_4=0.0870s (2D SST) **(h)** t=t_4=0.0870s (DES)

Figure 5.16: Instantaneous Mach number contours with streamlines for the clean cavity with doors-on at for 4 different time-steps during flow cycle for the URANS (Menter's Baseline $k-\omega$) and DES (Spalart-Allmaras) computations. Plots taken along the cavity centreline (z/W = 0.5).

location between the 2D URANS results and PIV were attributed to an over-prediction in the strength of the primary vortex inside the cavity. At the rear of the cavity, however, agreement between DES, LES and PIV deteriorated. This may be explained by the poorer resolution of the PIV experiment at this location, which was discussed in detail in the previous chapter (Chapter 4).

5.5 Concluding Remarks

Large-Eddy and Detached-Eddy Simulations of a 3D, L/D=5, W/D=1 clean cavity with and without doors at a Mach number of 0.85 and a Reynolds number of 1 million (based on the cavity length) were performed. Analysis of unsteady pressure measurements with experiment revealed that both DES (in conjunction with the one-equation Spalart-Allmaras model) and LES (Smagorinsky SGS) consistently gave better agreement than URANS in

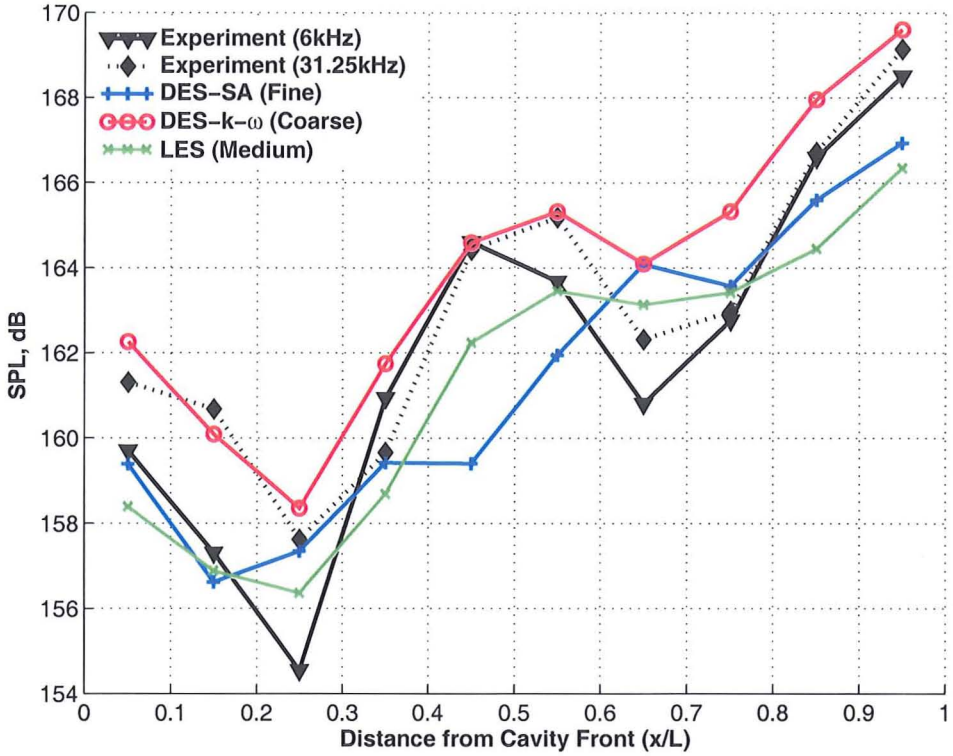

Figure 5.17: SPLs along the cavity floor for the L/D=5, W/D=1, clean cavity with doors-on at 90° vertically comparing DES-SA, DES (with $k-\omega$) and LES (Smagorinsky SGS) results with experiment. Plots taken at z/W=0.25 and along the cavity floor (y/D=1).

terms of frequency content, phase and noise levels for both the doors-on and doors-off configurations. Menter's Baseline $k-\omega$ model was used for the 3D URANS computations.

With doors-off, the 3rd Rossiter mode ($\approx 600\ Hz$) was found to be the dominant mode. Menter's Baseline $k-\omega$ model still predicted a 'W'-shaped SPL curve as it did for the doors-on case unlike LES and DES, which correctly predicted the 'tick'-shape. Windowed SPL plots indicated that both LES and DES fared much better than URANS in predicting the shapes of the SPL curves across four specific frequency bands that contain the first four Rossiter modes found in the cavity for this flow regime. While URANS predicted the dominant 3rd Rossiter mode quite well it was observed that it failed to provide the same level of accuracy for any of the frequencies higher or lower than this dominant mode. Analysis of flow-field plots for the doors-off cavity with Menter's Baseline $k-\omega$ model and DES revealed that DES predicted a breakdown of the shear layer while Menter's baseline $k-\omega$ model consistently illustrated a coherent shear layer that spanned the cavity. It was concluded that URANS had difficulty in accounting for the larger transport and/or diffusion of energy and momentum present in the doors-off case.

With doors-on, the SPL curve takes the form of a 'W' shape, the flow is typically governed by a dual-vortex cycle and the 2nd Rossiter mode ($\approx 380\ Hz$) is dominant. Since the 2D cavity was thought to be a good representation of the full 3D cavity with doors-on, results from the SST model were also compared with the 3D doors-on results. Initial analysis of the doors-on results revealed that better prediction was obtained with 3D URANS than with DES and LES. Band-limited frequency analysis, however, revealed that 3D URANS predicted the dominant (2nd Rossiter) mode well but had difficulty in capturing most of the higher (and in some cases, some of the lower) frequencies as well, as was observed

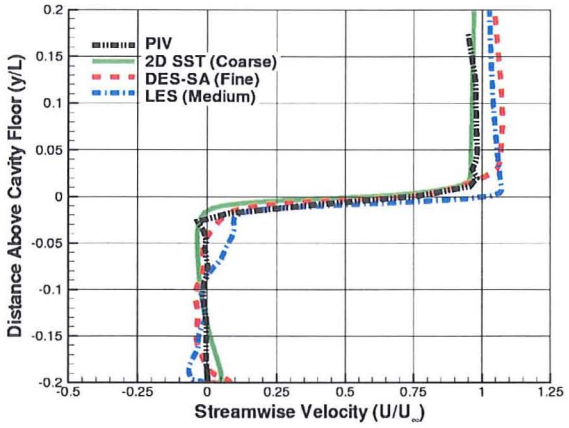

(a) U-Velocity ($x/L = 0.05$)

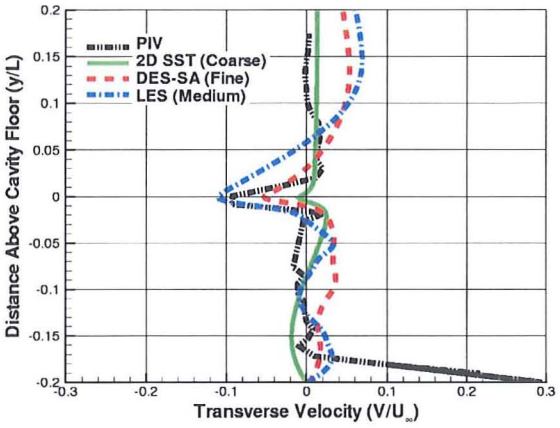

(b) V-Velocity ($x/L = 0.05$)

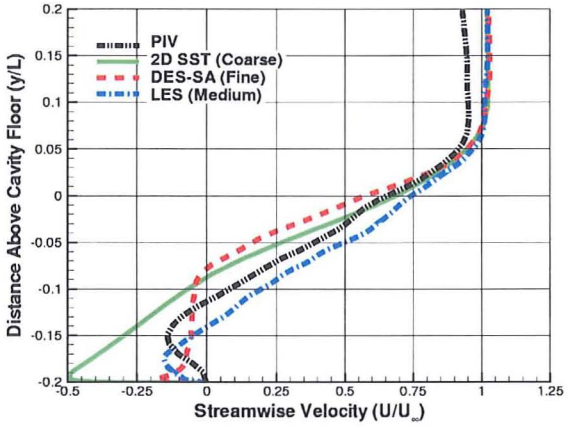

(c) U-Velocity ($x/L = 0.55$)

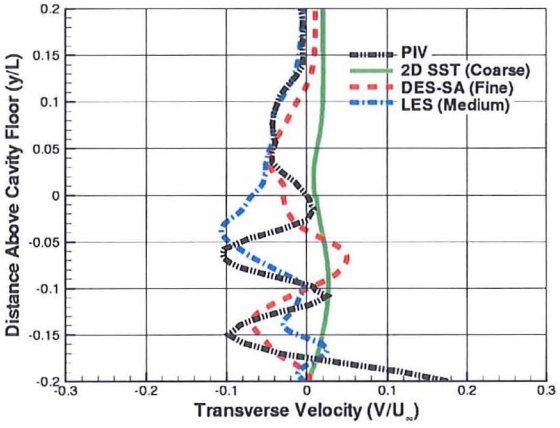

(d) V-Velocity ($x/L = 0.55$)

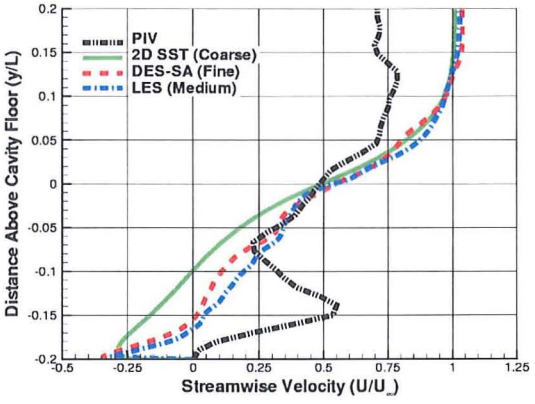

(e) U-Velocity ($x/L = 0.95$)

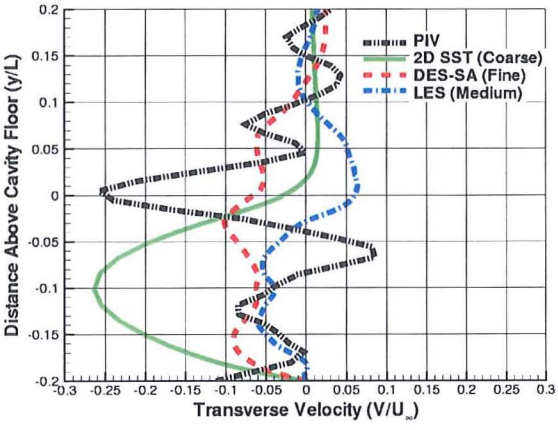

(f) V-Velocity ($x/L = 0.95$)

Figure 5.18: Time-averaged streamwise ($\frac{U}{U_\infty}$) and transverse ($\frac{V}{V_\infty}$) velocity profiles for the clean cavity with doors-on along cavity floor at $x/L = 0.05$, $x/L = 0.55$ and $x/L = 0.95$ using 2D URANS coarse grid (with SST model (solid, green line)), fine DES grid (with Spalart-Allmaras (dashed, red line)) and medium LES grid (dashed-dot, blue line). Black line corresponds to experimental PIV data (provided by Ross [6]).

in the doors-off configuration. In contrast, both DES and LES fared much better in predicting correctly the shapes of the SPL curves and the intensity of the frequency tones. Furthermore, URANS was typically found to consistently over-predict the acoustic tone magnitudes in the doors-on cavity. Results using the 2D cavity with the SST model over-predicted the dominant 2nd Rossiter mode in the doors-on cavity by almost double the experimental values. This was attributed to a much thicker oncoming boundary layer in the 2D cavity and may suggest that the 2D approximation is incorrect for the doors-on cavity. Differences were observed with the two sets of experimental data available for the doors-on cavity. It was concluded that high resolution experimental data are just as much required as high resolution numerical results to obtain an accurate understanding of cavity flow physics.

Analysis of the turbulent decay characteristics revealed a peak at around 4-7 kHz in the experimental and numerical results. Since this is too high to be narrowband, its source may be attributed to the Kelvin-Helmholtz instability. Investigation of the broadband spectrum emphasised the inadequacy of URANS to account for broadband noise.

Streamwise and transverse velocity plots were compared for the doors-on case with PIV measurements and showed consistently good agreement at the cavity front and middle for different DES variants and LES. Comparisons with the best 2D results revealed that the flow is far too energetic and leading to a stronger primary vortex causing significantly more shear layer fluctuations. At the cavity rear, the agreement with PIV deteriorated between LES and DES and these discrepancies may be attributed to poor resolution in the PIV experiment at this position.

The grids used for LES computations were found to provide good agreement with experiment in both doors-on and doors-off configurations. Despite the high Reynolds number of cavity flow under investigation here, it was observed that accurate predictions of the cavity flow-field can be provided by reasonably low-resolution grids by LES standards. However, unlike URANS, LES/DES computations can only be performed in 3D and low time-steps are required for accurate resolution of the cavity flow-field. This is described in Table 5.4, which gives the calculation details for two of the finest LES/DES calculations performed in this project and compares with a 3D URANS calculation. This table shows that although LES/DES is cheaper per time-step, it requires more CPU hours and hence is overall more expensive.

Table 5.4: URANS, DES and LES calculation details.

Calculation Details	**3D URANS**	**DES-SA**	**LES**
Cavity Configuration	Doors-On	Doors-On	Doors-Off
Grid Size	1.5×10^6	4.5×10^6	8.5×10^6
Processors	19	320	256
CFD Time-Step	1.81×10^{-5}	1.81×10^{-6}	1.81×10^{-6}
Unsteady Tolerance	0.005	0.001	0.001
Pseudo-Steps/CFD Time-step	39	6	7
CFD Time-Steps/min.	0.425	9.72	2.57
Total CFD Time-Steps	5,506	50,200	18,546
Total CPU Hours	3,121	28,100	39,936
Signal Duration	0.1 s	0.1 s	0.034 s
Total Run-time	9 days	3.46 days	6 days

Chapter 6

Different Aspect Ratio Cavity Flows

With LES and DES consistently producing good results for the L/D=5 cavity, the URANS method was revisited in an attempt to explain its poor predictions. To assess this, different cavity aspect ratios were investigated and parametric studies in time and space performed to analyse whether more consistent results were obtained with URANS for other cavity geometries. The main objective of this study is to ascertain the range of applicability of the URANS method and is not meant to be a definitive study on different cavity L/D ratios.

Two-dimensional deep, open cavities (L/D=2), transitional cavities (L/D=10) and closed cavities (L/D=16) were studied. All computations were conducted using Menter's SST turbulence model [245], which proved to be the most robust based on the L/D=5 calculations. No experimental data were however available to validate the CFD data so the 2D URANS results were compared to DES (with $k-\omega$) results for the 3D cavity with doors-on. A medium-sized grid of about 2 million points was used for the DES computation.

6.1 Description of Computational Domains

Computational domains for the 2D L/D=2, L/D=10 and L/D=16 calculations were all based on the L/D=5 grid. As for the L/D=5 case, the coarse grids for the L/D=2, L/D=10 and L/D=16 cavities comprised six blocks with the cavity completely contained within one block. Two blocks were used ahead and aft of the cavity while the far-field was maintained at 1.5 times the cavity length. With respect to the L/D=5 grid, only the block containing the cavity and the block above the cavity were modified to account for the different cavity geometries. The other blocks therefore remained unchanged. Figures 6.1 and 6.2 show the mesh distributions for the L/D=2, L/D=10 and L/D16 coarse grids in and near the vicinity of the cavity. For reference, the L/D=5 mesh is also shown.

Finer grids were then constructed from the coarse grid by doubling the number of points in each direction apart from the z-direction. Free-stream conditions were applied outside the cavity and zero-velocity was imposed inside the cavity for the initialisation of the solution. Each grid section was scaled relative to the cavity length, L. For the L/D=2 and L/D=10 grids, the cavity length was fixed and normalised to 1 unit and the depth varied to 0.5 and 0.1, respectively, as shown in Figures 6.1(b) and 6.2(a). In the case of the L/D=16 cavity, the cavity length was increased to 1.6 times its original length and the depth specified to

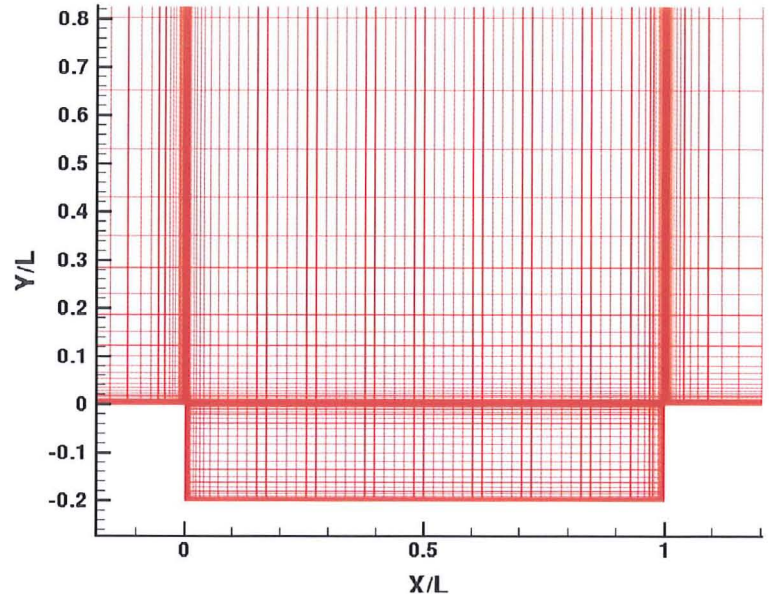

(a) L/D=5 Grid

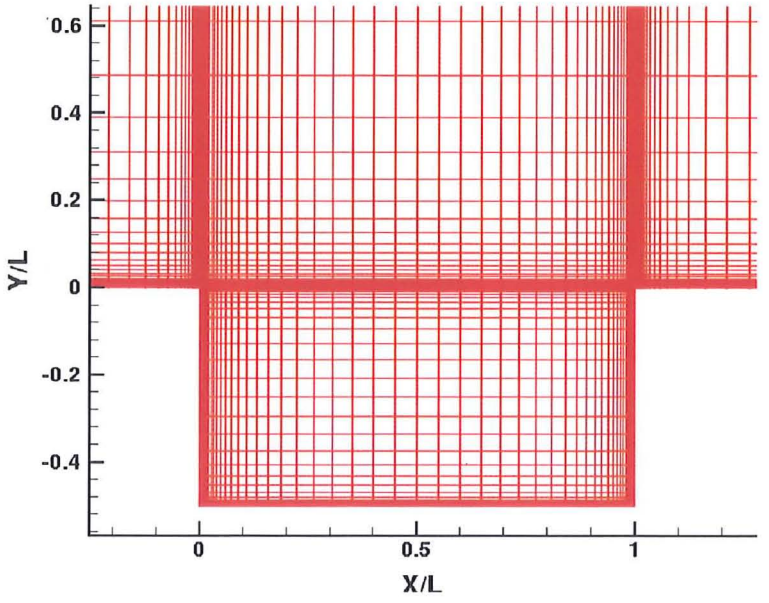

(b) L/D=2 Grid

Figure 6.1: Meshing in and near the cavity for the L/D=5 and L/D=2 coarse grids.

0.1 (units of the cavity length). As the Reynolds number is based on the cavity length, the Reynolds number used for the L/D=16 cavity was increased accordingly to 10.8528 million compared to the 6.783 million for all other cavity L/D ratios. This ensured that the L/δ ratio, which relates the cavity length to the boundary layer thickness, was held constant. The 3D grid used for the DES computations was designed in the manner described previously in Chapter 5.

To ascertain the degree of accuracy and consistency obtained with the SST turbulence model for cavities with L/D ratios of 2, 10 and 16, four computations were conducted for each geometrical configuration: coarse and fine grids with coarse ($\Delta t = 0.01 \equiv 1.814 \times$

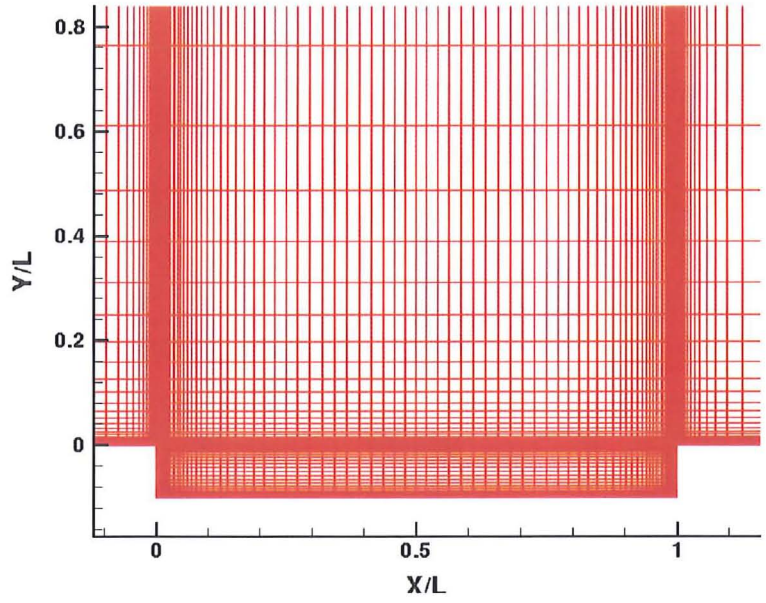

(a) L/D=10 Grid

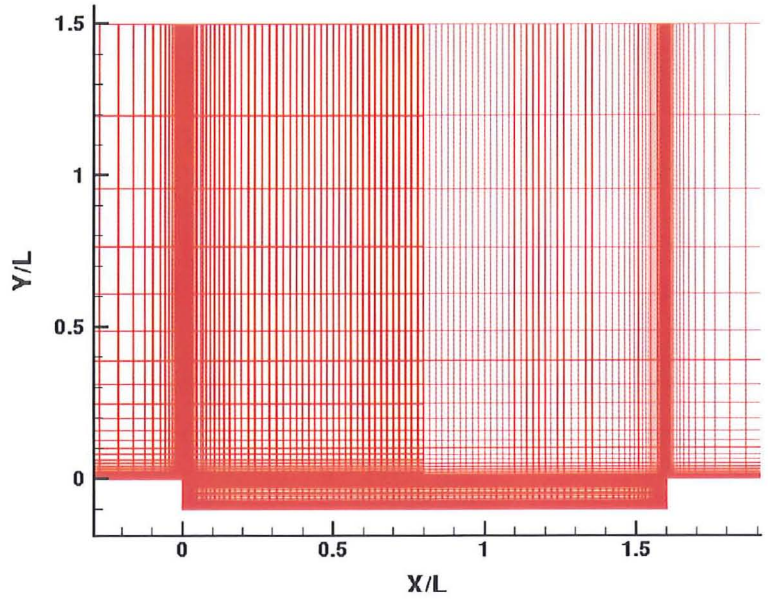

(b) L/D=16 Grid

Figure 6.2: Meshing in and near the cavity for the L/D=10 and L/D=16 coarse grids.

10^{-5}s) and fine ($\Delta t = 0.01 \equiv 9.07 \times 10^{-6}$s) time-steps. Details of the coarse and fine grids for all cases are provided in Table 6.1.

6.2 L/D=2 Open Cavity

Noise levels and spectral decomposition at three stations along the cavity floor (i.e. $x/L = 0.05$, $x/L = 0.55$ and $x/L = 0.95$) for the coarse and fine L/D=2 cavity grids with time-steps of 0.01 ($\equiv 1.814 \times 10^{-5}$s) and 0.005 ($\equiv 9.07 \times 10^{-6}$s) are shown in Figure 6.3. Comparisons

Table 6.1: Information about the 2D cavity grids with L/D ratios of 2, 10 and 16.

Grid	Overall Points	Points in Cavity	Wallspacing	Blocks in Cavity (Overall)
L/D=2 clean cavity				
SST Coarse	34,374	10,404	$y = 5 \times 10^{-6}$	2 (8)
SST Fine	137,496	41,616	$y = 5 \times 10^{-6}$	2 (8)
DES $k-\omega$	2,218,854	493,679	$y = 3.125 \times 10^{-3}$	64 (240)
L/D=10 clean cavity				
SST Coarse	46,206	16,320	$y = 5 \times 10^{-6}$	2 (8)
SST Fine	180,336	65,280	$y = 5 \times 10^{-6}$	3 (10)
DES $k-\omega$	2,218,854	493,679	$y = 3.125 \times 10^{-3}$	64 (240)
L/D=16 clean cavity				
SST Coarse	48,654	17,544	$y = 5 \times 10^{-6}$	4 (12)
SST Fine	190,128	70,176	$y = 5 \times 10^{-6}$	4 (12)

with DES results reveal good agreement with the coarse grids and for the fine grid with coarse time-step but deteriorates for the fine grid with fine time-step. As was the case with the L/D=5 cavity, the L/D=2 results demonstrate a change in the flow characteristics on refinement in space.

Analysis of the PSD plots in Figure 6.3 revealed that URANS tended to over-predict the magnitude of the second mode ($\approx 380\ Hz$) for the L/D=2 cavity. The DES calculation also indicated a strong presence of the first Rossiter mode ($\approx 160\ Hz$), which was not predicted by URANS. More scatter was also observed around the main Rossiter modes for this cavity L/D ratio with finer grids with URANS as illustrated in the spectral plots in Figure 6.3(d). Results for the L/D=2 cavity therefore still appear to show a dependency to the grid and time-step, as was the case with the L/D=5 cavity.

6.2.1 Band-Limited Frequency Analysis

Windowed frequency analysis is provided in Figure 6.4. Variation in the noise levels within the four frequency ranges that straddle the first four Rossiter modes found for this L/D ratio is illustrated in these band-limited frequency plots. The four frequency intervals used here are the same as for the L/D=5 case because the length of the cavity and the flow conditions are the same. The first Rossiter mode ($\approx 160\ Hz$) falls within the first frequency band of $50\ Hz \leq f \leq 250\ Hz$ and the second Rossiter mode ($\approx 380\ Hz$) falls in the second band of $350\ Hz \leq f \leq 450\ Hz$. The third ($\approx 600\ Hz$) and fourth ($\approx 820\ Hz$) Rossiter modes are contained within the third ($500\ Hz \leq f \leq 700\ Hz$) and fourth ($750\ Hz \leq f \leq 850\ Hz$) frequency bands, respectively.

Analysis of these windowed SPL plots revealed that variations in noise level amplitudes and SPL curve shapes differ from the coarse and fine grids, a result similar to the L/D=5 configuration. Although the fine grid (with coarse time-step) results compared reasonably well with DES for frequencies above $\approx 380\ Hz$, poor agreement was observed for the frequencies in the first frequency band (Figure 6.4(a)). Further refinement of the fine grid in time however gave different noise level amplitudes. The shape of the SPL curve

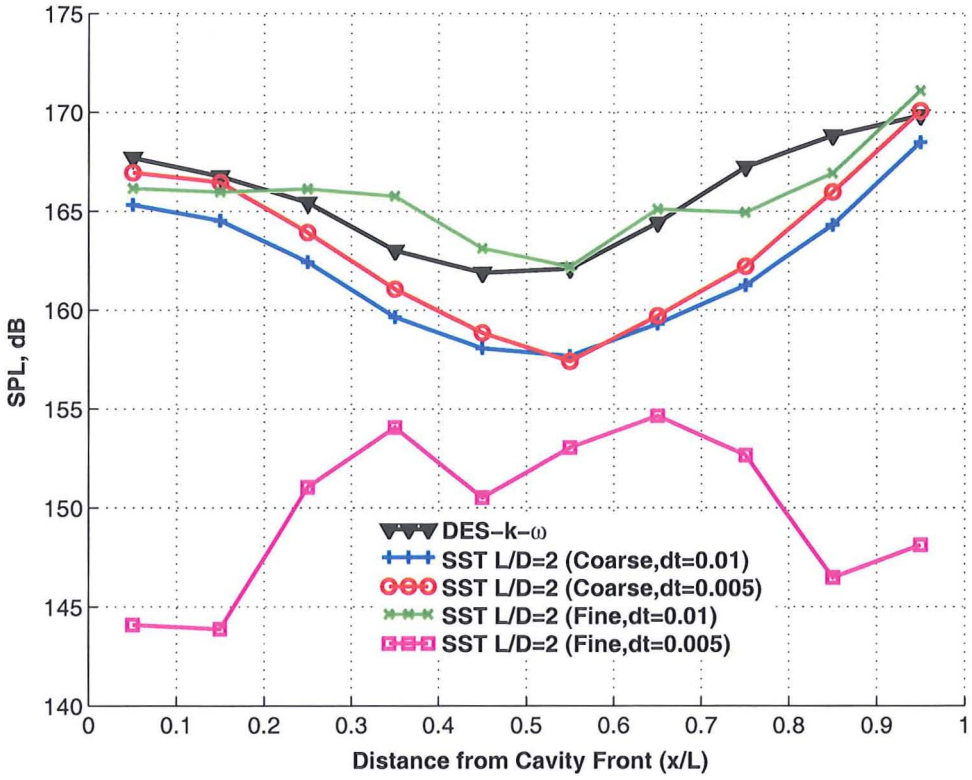

(a) SPLs

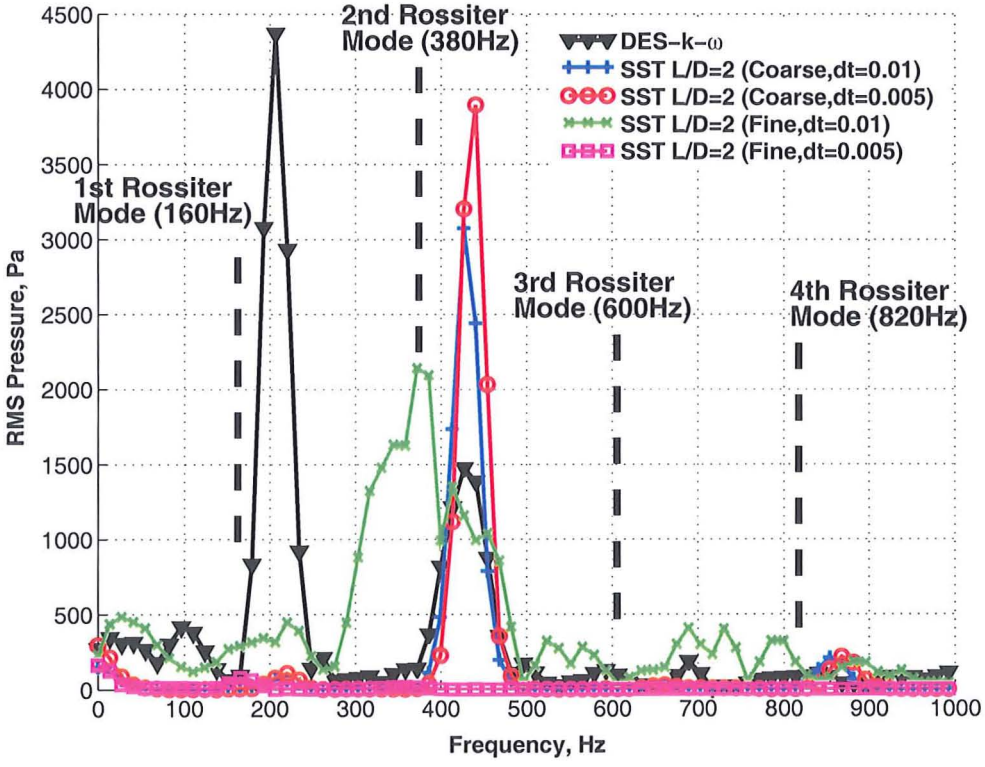

(b) PSD ($x/L = 0.05$)

Figure 6.3: (continued)

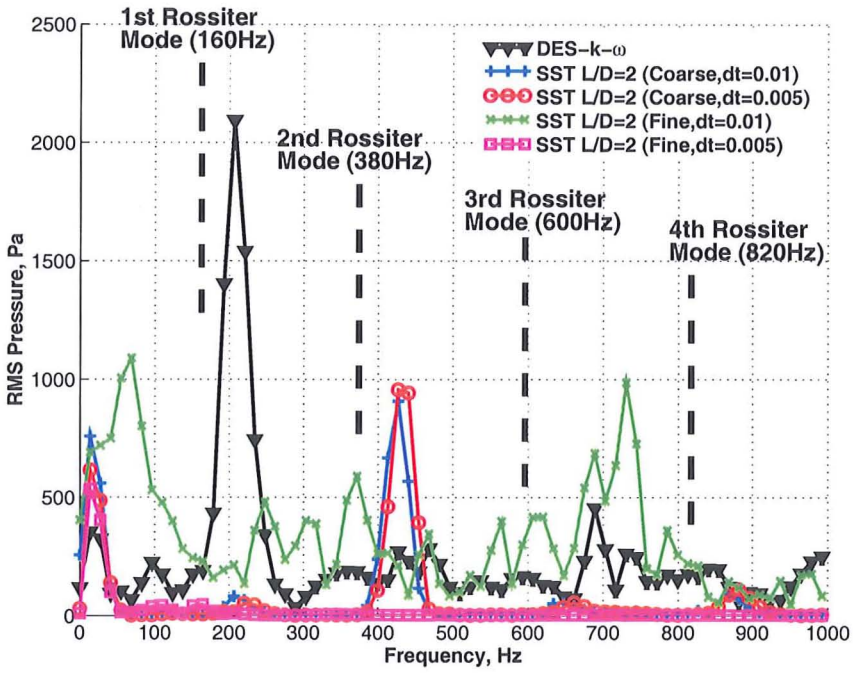

(c) PSD ($x/L = 0.55$)

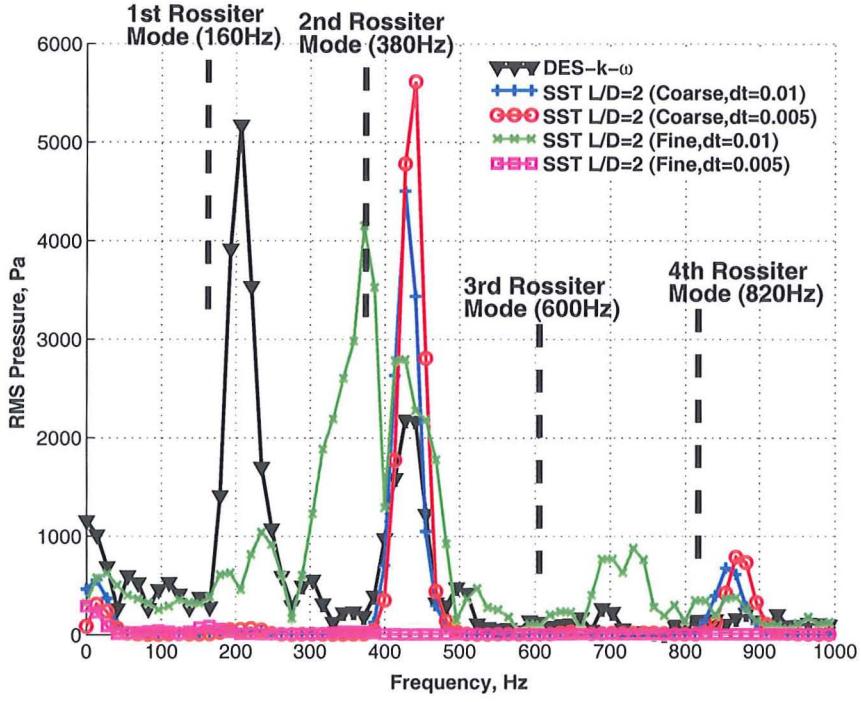

(d) PSD ($x/L = 0.95$)

Figure 6.3: SPL and PSD plots (at $x/L = 0.05$, $x/L = 0.55$ and $x/L = 0.95$) for the 2D open, rectangular L/D=2 cavity along the cavity floor using the SST turbulence model for: coarse grid, coarse time-step (solid blue with plus signs); coarse grid, fine time-step (solid red with circular markers); fine grid, coarse time-step (solid green with crosses) and fine grid, fine time-step (solid magenta with square symbols). DES results (with $k-\omega$) for the 3D L/D=2 cavity are shown in black (with triangles).

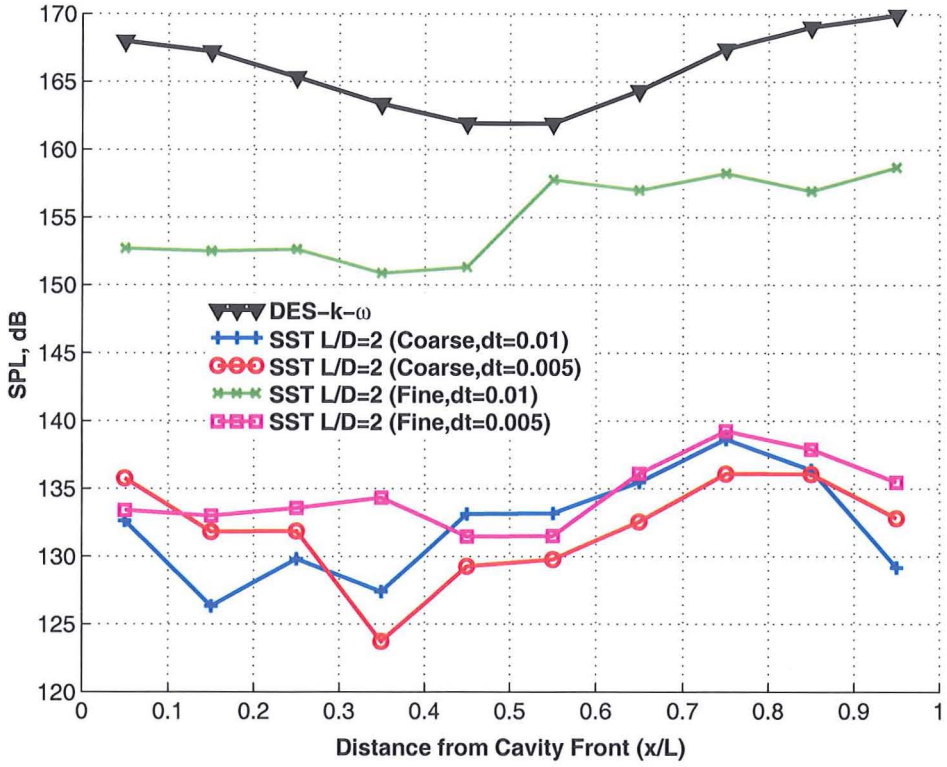

(a) $50\ Hz \leq f \leq 250\ Hz$

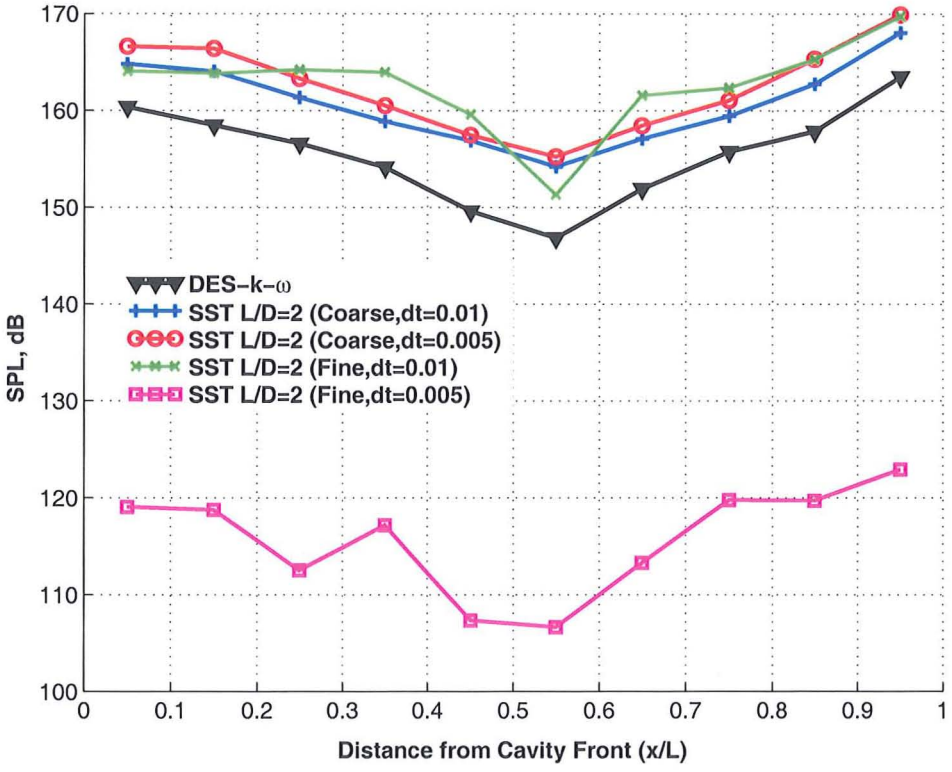

(b) $350\ Hz \leq f \leq 450\ Hz$

Figure 6.4: (continued)

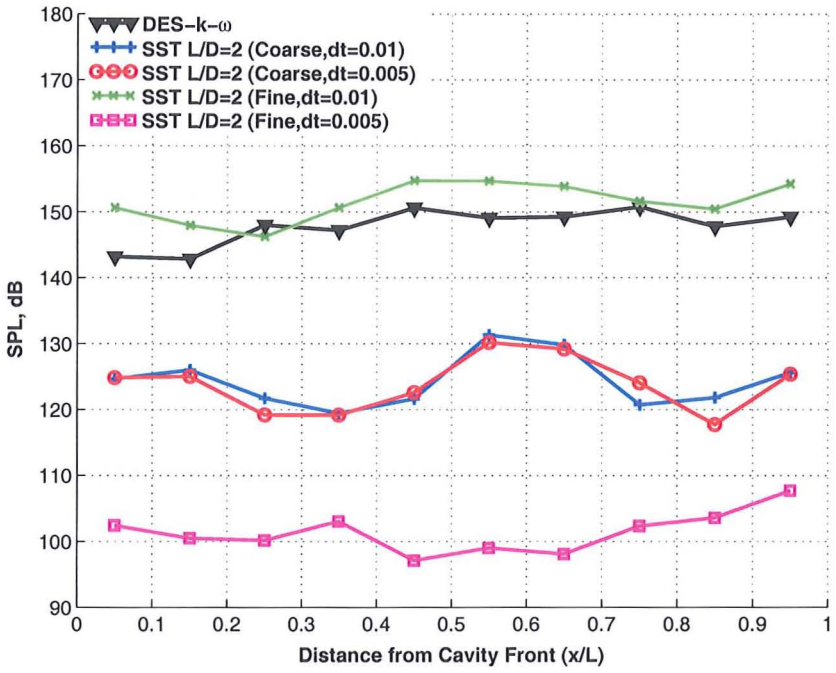

(c) $500\ Hz \leq f \leq 700\ Hz$

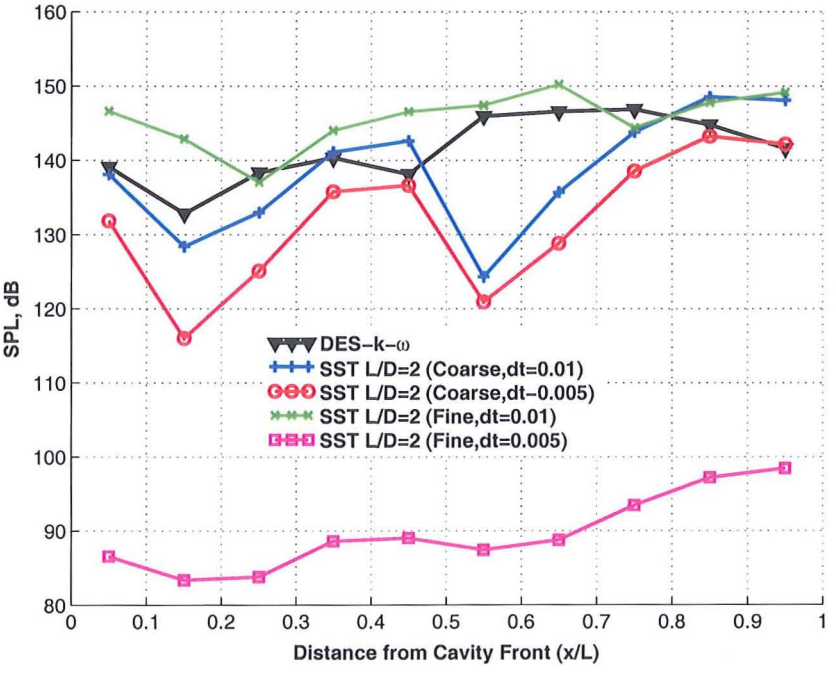

(d) $750\ Hz \leq f \leq 850\ Hz$

Figure 6.4: Band-limited SPLs for the 2D open, rectangular L/D=2 cavity along the cavity floor using the SST turbulence model for: coarse grid, coarse time-step (solid blue with plus signs); coarse grid, fine time-step (solid red with circular markers); fine grid, coarse time-step (solid green with crosses) and fine grid, fine time-step (solid magenta with square symbols). DES results (with $k-\omega$) for the 3D L/D=2 cavity are shown in black (with triangles).

also changed with the finer grids and this represented a subsequent change in the flow characteristics inside the cavity.

6.2.2 Flow-field Visualisation

Visualisation of the flow-field inside the L/D=2 cavity is indicated in Figure 6.5, which shows the time-averaged plots with Mach number contours and streamlines. The effect of time-step refinement on the noise levels and spectral decomposition was found to be less significant for the coarse grid (Figures 6.5(b) and 6.5(c)). The flow-field plots support this, which show similar contours and vortical structures inside the cavity.

The greatest difference occurred with spatial refinement, as was highlighted previously, and this is evident from the time-averaged plots in Figures 6.5(d) and 6.5(e). A large corner vortex developed at the front wall of the L/D=2 cavity with the finer grids. The primary vortex in the fine grid therefore could not span the entire length of the cavity as was the case with the coarse grids. Consequently, this primary vortex was forced to deflect upwards out of the cavity and the slightly protruded shear layer therefore tended to generate more noise. Overall, the L/D=2 cavity results with the SST turbulence model were still found to be inconsistent and sensitive to the grid employed. Consequently, turbulent simulation based on LES/DES is recommended for this L/D ratio, as was the case for the L/D=5 cavity.

6.3 L/D=10, Transitional Cavity

SPLs and PSD for the L/D=10, transitional cavity are indicated in Figure 6.6, which include plots from the coarse and fine grids with time-steps of 0.01 ($\equiv 1.814 \times 10^{-5}$s) and 0.005 ($\equiv 9.07 \times 10^{-6}$s). Comparisons with DES showed that best agreement is achieved with the coarse grid with fine time-step. The other computations predict a different shape of the SPL curve and different SPL magnitudes (Figure 6.6(a)).

Analysis of the PSD plots at the $x/L = 0.05$, $x/L = 0.55$ and $x/L = 0.95$ of the cavity in Figure 6.6 however indicate that the coarse grid with fine-step results over-predict the intensity of the second Rossiter mode ($\approx 380\ Hz$). DES results show noise distributed among many modes rather than a single mode. URANS results however do not predict this with the fine grid results and the coarse grid with coarse time-step result predicting only a first mode ($\approx 160\ Hz$). Results for the L/D=10 cavity therefore still appear to show a dependency to the grid and time-step, as was the case with the L/D=2 and L/D=5 cavities.

6.3.1 Band-Limited Frequency Analysis

A closer inspection of the spectral analysis is provided in Figure 6.7, which indicates the noise level distribution across four specific frequency bandwidths. Since the cavity length is the same for the L/D=2, 5 and 10 cavities, the first four Rossiter modes (calculated by Rossiter's formula in Equation 1.3) are also the same.

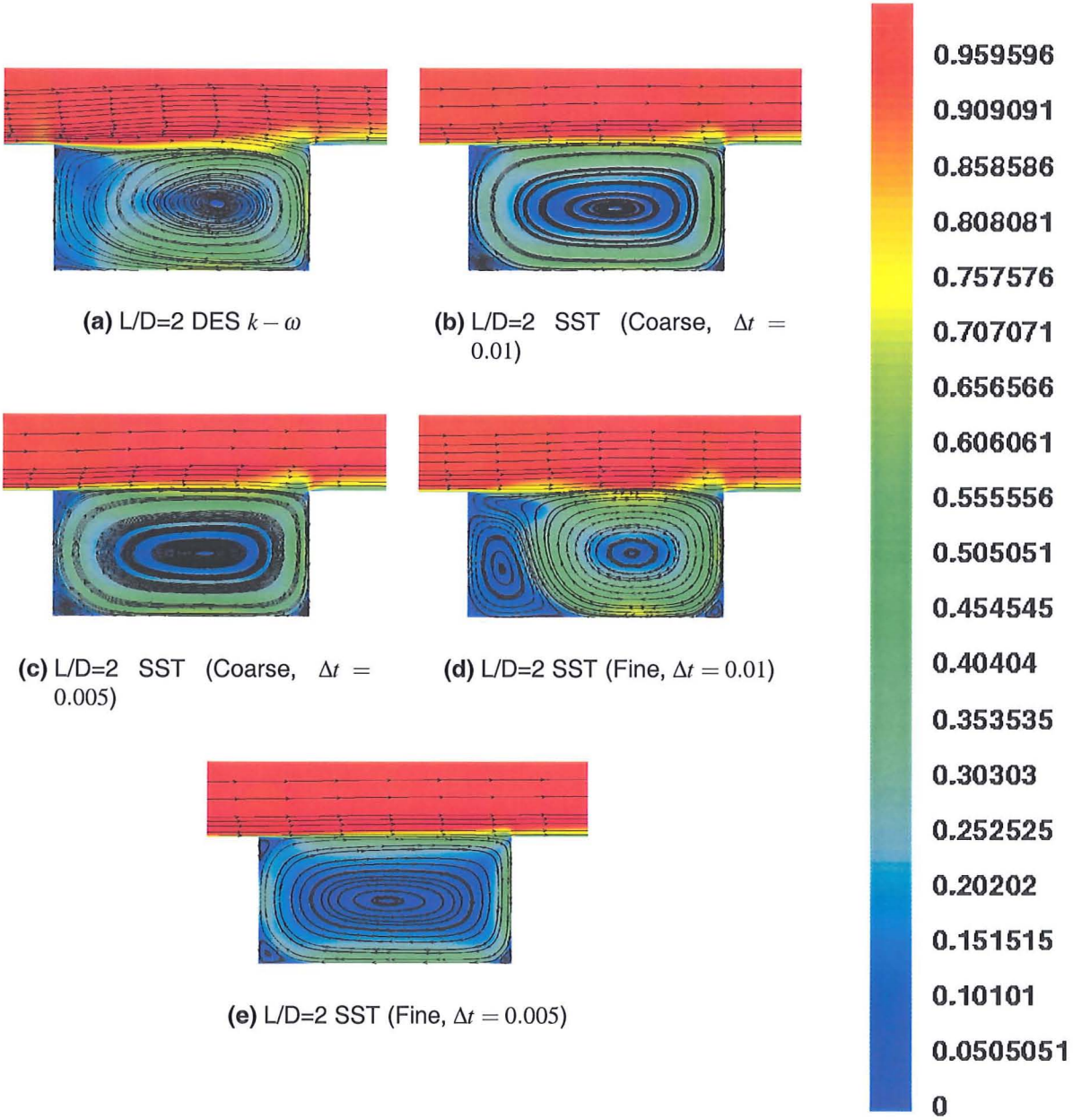

(a) L/D=2 DES $k-\omega$

(b) L/D=2 SST (Coarse, $\Delta t = 0.01$)

(c) L/D=2 SST (Coarse, $\Delta t = 0.005$)

(d) L/D=2 SST (Fine, $\Delta t = 0.01$)

(e) L/D=2 SST (Fine, $\Delta t = 0.005$)

Figure 6.5: Time-averaged Mach number contours with streamlines for the 2D L/D=2, open, deep cavity using the SST turbulence model for coarse and fine grids and time-steps and DES (with $k-\omega$) for the 3D L/D=2 cavity. Plots show Mach number normalised with respect to the free-stream Mach number, $M_\infty = 0.85$.

Variation across the four computations for the L/D=10 case was found to be more profound. Across all the four frequency intervals in Figure 6.7, it can be clearly observed that the noise levels and shape of curve are strongly influenced by the grid density and time-step used. As mentioned previously, DES results show the noise to be distributed across many frequencies. Consequently, the band-limited plots show SPL amplitudes of the same order of magnitude across all the four frequency bands analysed (Figure 6.7). URANS results do not predict this and large scatter is observed in amplitudes for all the four computations across all four frequency bands in Figure 6.7.

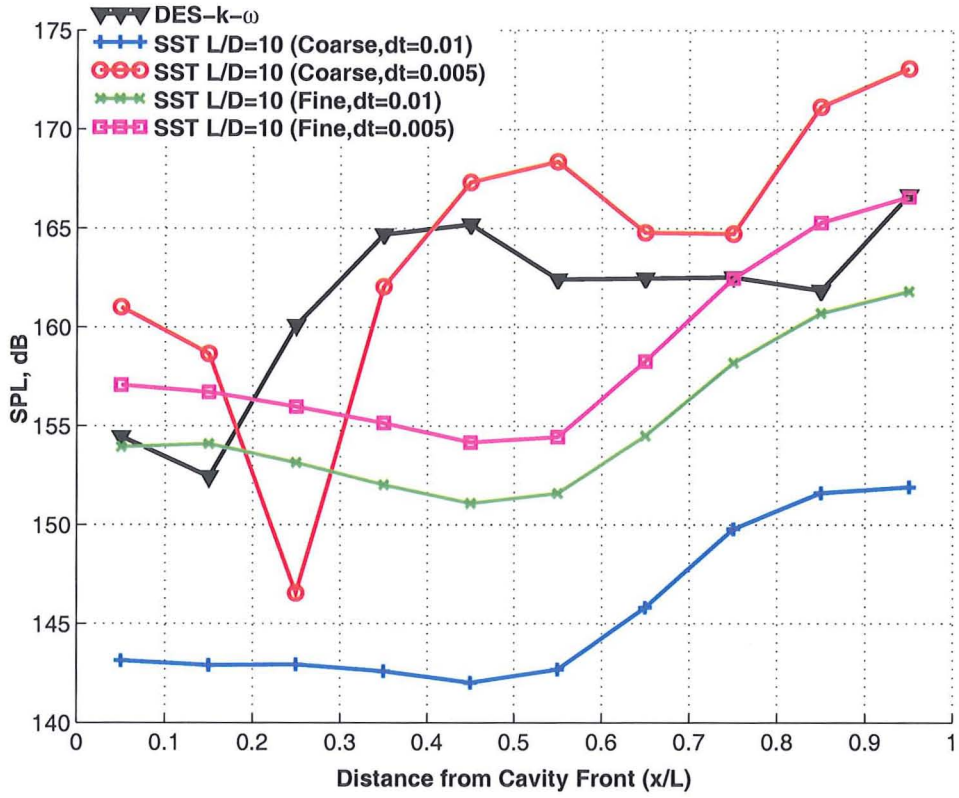

(a) SPLs

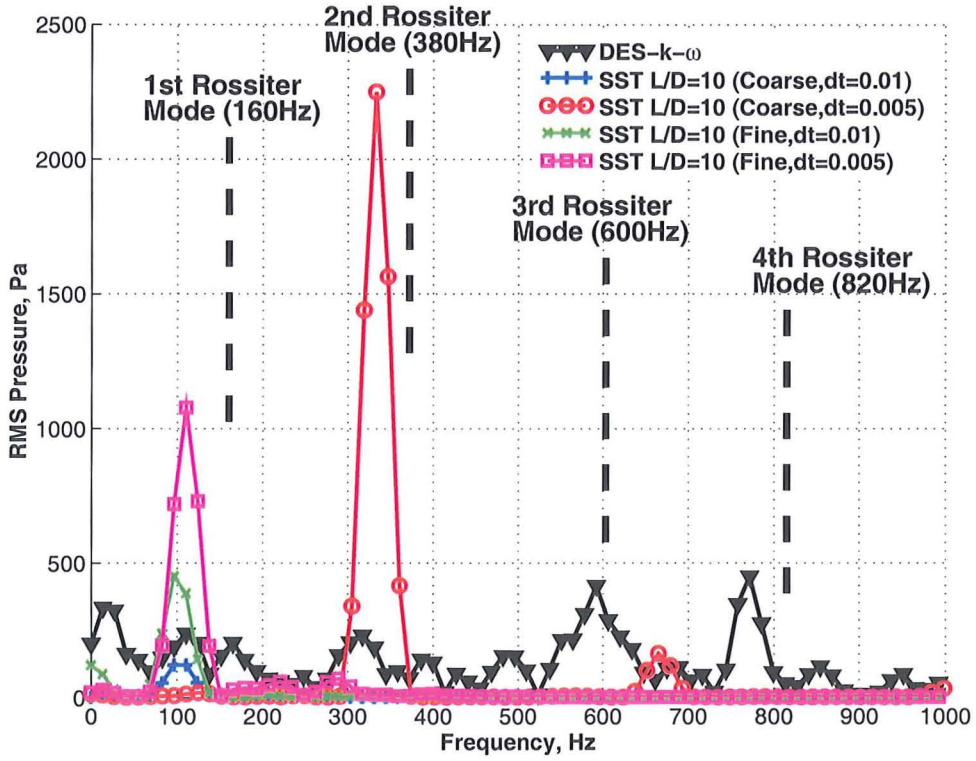

(b) PSD ($x/L = 0.05$)

Figure 6.6: (continued)

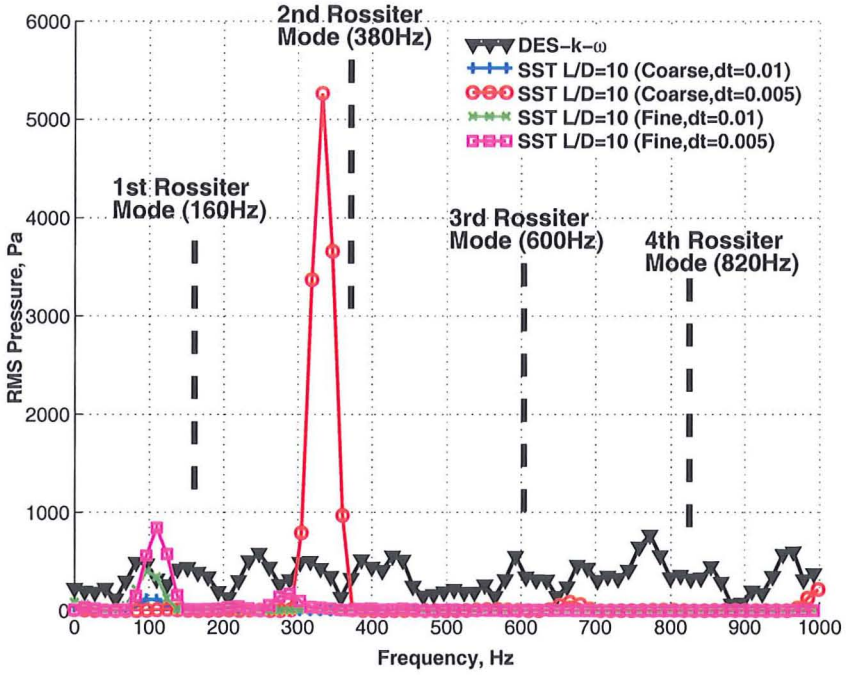

(c) PSD ($x/L = 0.55$)

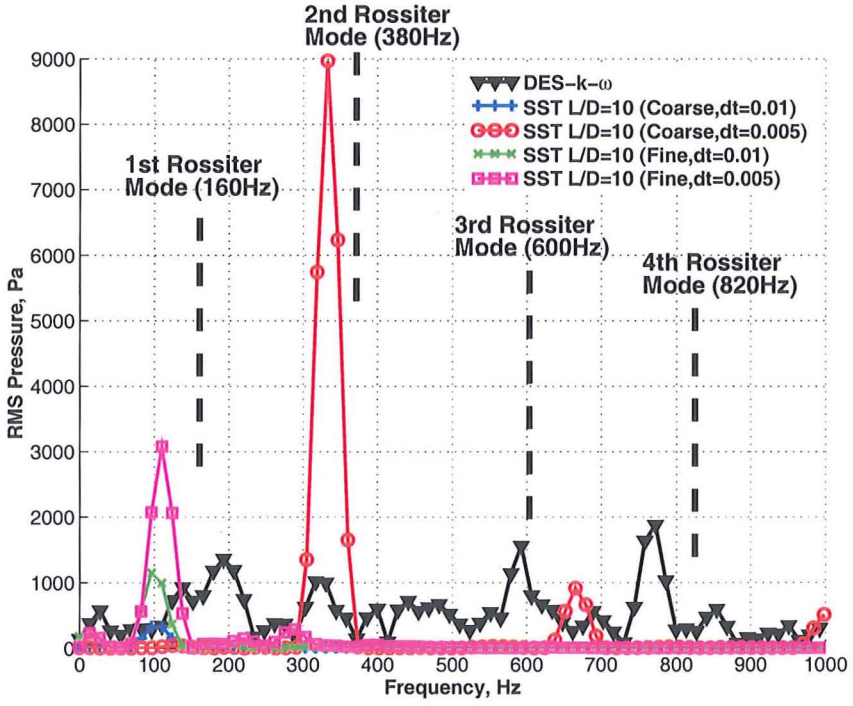

(d) PSD ($x/L = 0.95$)

Figure 6.6: SPL and PSD plots (at $x/L = 0.05$, $x/L = 0.55$ and $x/L = 0.95$) for the 2D transitional, rectangular L/D=10 cavity along the cavity floor using the SST turbulence model for: coarse grid, coarse time-step (solid blue with plus signs); coarse grid, fine time-step (solid red with circular markers); fine grid, coarse time-step (solid green with crosses) and fine grid, fine time-step (solid magenta with square symbols). DES results (with $k-\omega$) for the 3D L/D=10 cavity are shown in black (with triangles).

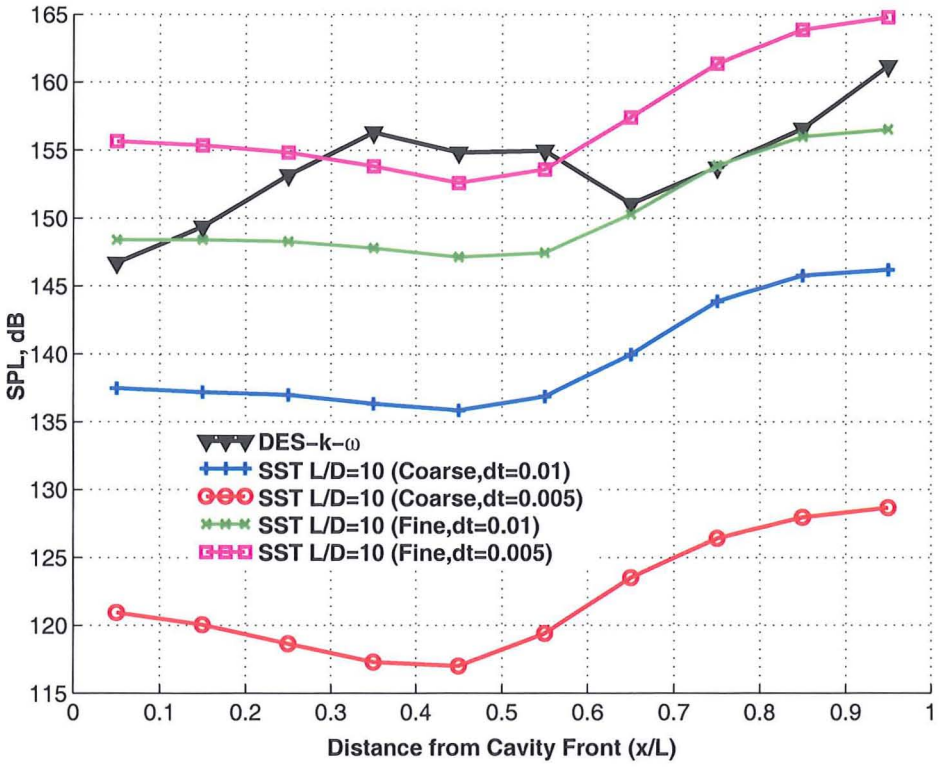

(a) $50\ Hz \leq f \leq 250\ Hz$

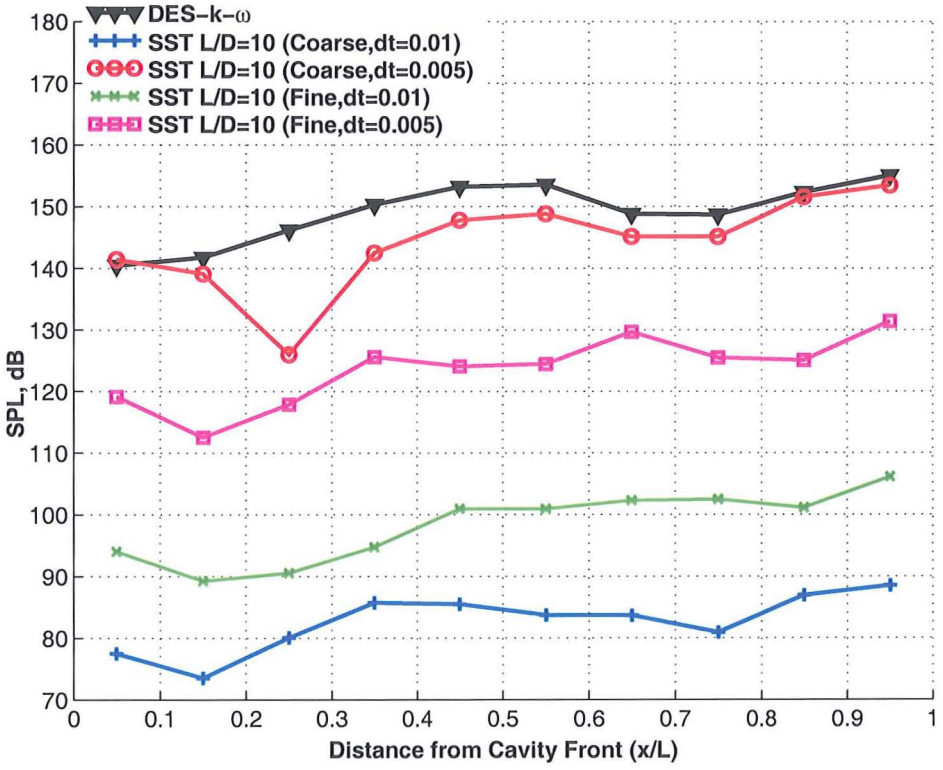

(b) $350\ Hz \leq f \leq 450\ Hz$

Figure 6.7: (continued)

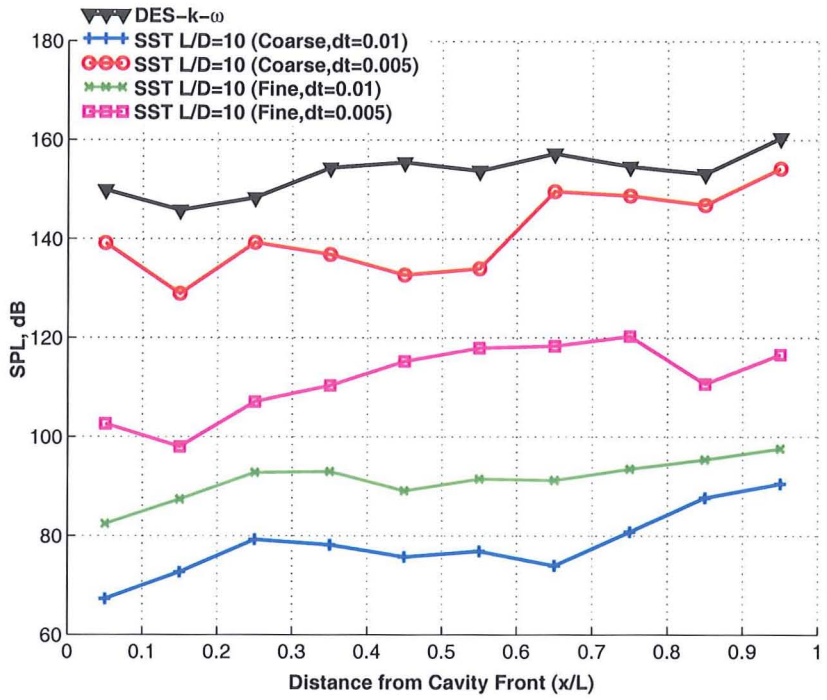

(c) $500\ Hz \leq f \leq 700\ Hz$

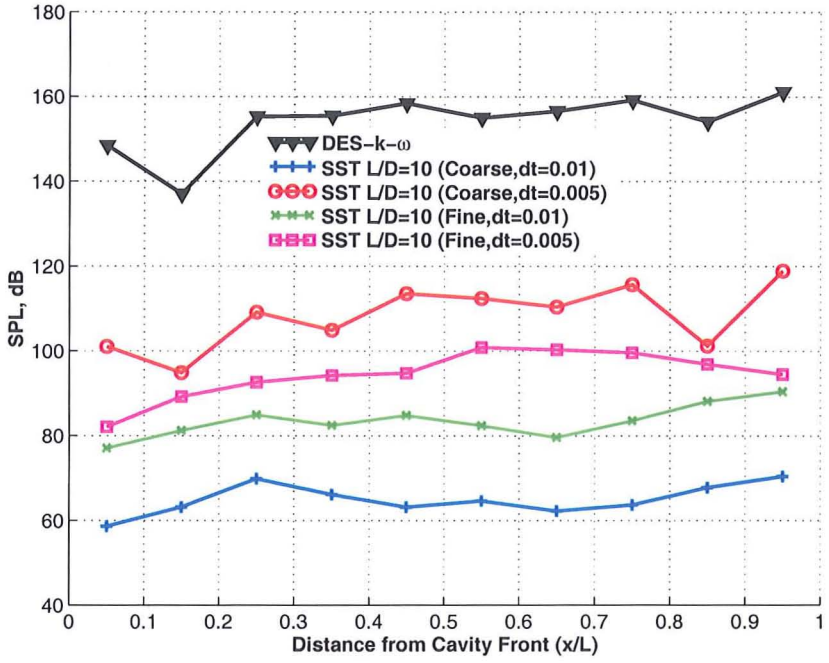

(d) $750\ Hz \leq f \leq 850\ Hz$

Figure 6.7: Band-limited SPLs for the 2D transitional, rectangular L/D=10 cavity along the cavity floor using the SST turbulence model for: coarse grid, coarse time-step (solid blue with plus signs); coarse grid, fine time-step (solid red with circular markers); fine grid, coarse time-step (solid green with crosses) and fine grid, fine time-step (solid magenta with square symbols). DES results (with $k-\omega$) for the 3D L/D=10 cavity are shown in black (with triangles).

6.3.2 Flow-field Visualisation

Flow-field plots for the L/D=10, transitional cavity are provided in Figure 6.8. Plots correspond to time-averaged flow-field data using Mach contours (normalised with respect to the free-stream Mach number of $M_\infty = 0.85$) with streamlines computed on the averaged flow superimposed.

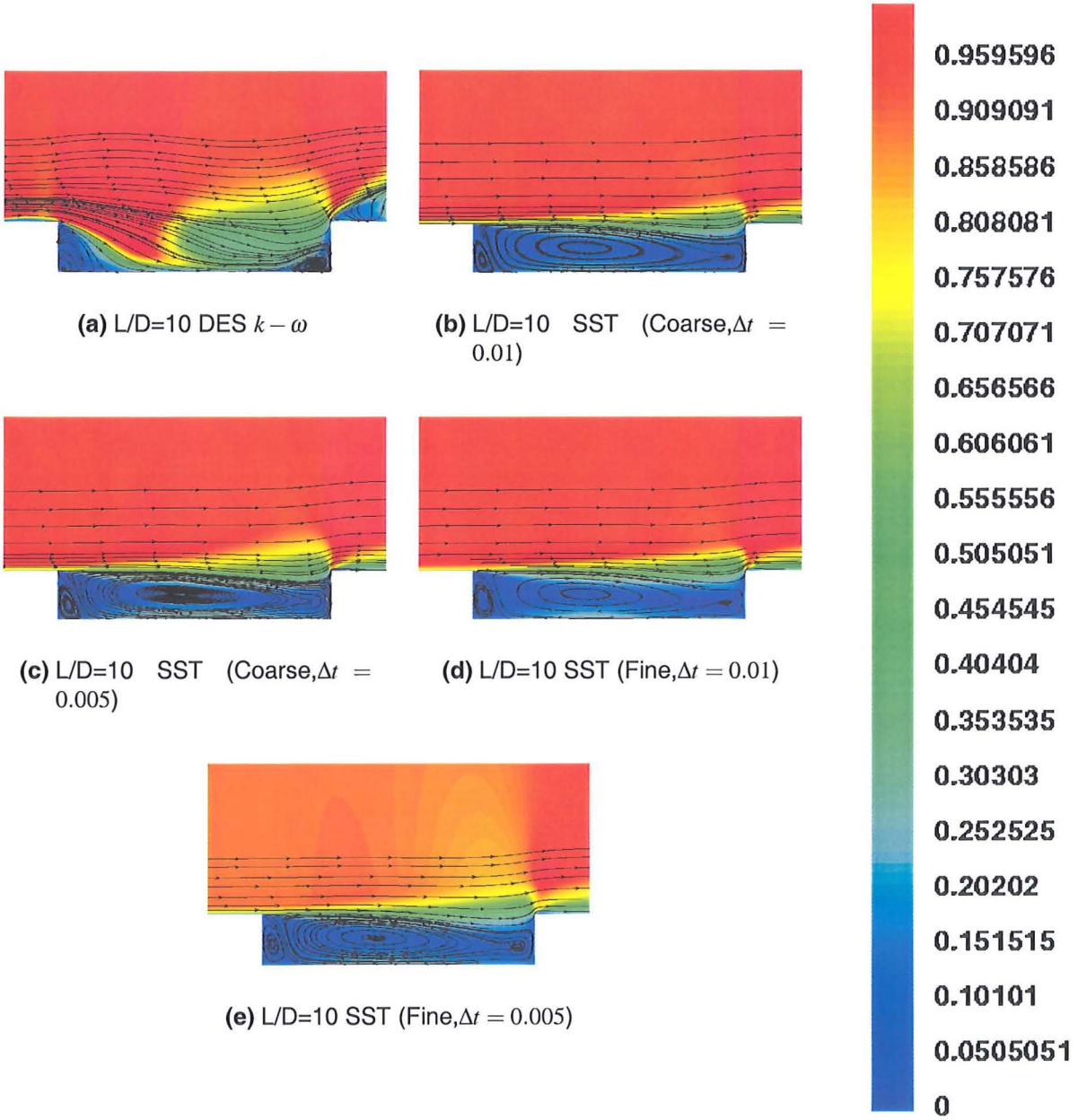

(a) L/D=10 DES $k-\omega$

(b) L/D=10 SST (Coarse,Δt = 0.01)

(c) L/D=10 SST (Coarse,Δt = 0.005)

(d) L/D=10 SST (Fine,$\Delta t = 0.01$)

(e) L/D=10 SST (Fine,$\Delta t = 0.005$)

Figure 6.8: Time-averaged Mach number contours with streamlines for the 2D L/D=10, open, deep cavity using the SST turbulence model for coarse and fine grids and time-steps and DES (with $k-\omega$) for the 3D L/D=10 cavity. Plots show Mach number normalised with respect to the free-stream Mach number, $M_\infty = 0.85$.

Comparisons between the DES and URANS results show that URANS fails to predict the correct flow features and this is reflected by the large scatter in the SPL and PSD analysis. Although, two vortices appear inside the cavity on average for both DES and

URANS computations, the position of these vortices is significantly different in the two methods. DES predicts a greater deflection of the shear layer into the cavity than URANS. Consequently, the vortices in the cavity cover a significantly smaller proportion of the cavity in the DES calculation. A region of high Mach is also observed near the middle and rear sections of the cavity with DES (Figure 6.8(a)). This corresponds to the regions where the shear layer dips into the cavity and then separates again on approaching the downstream wall. The distributed noise observed in the band-limited frequency analysis is therefore likely to be broadband rather than narrowband. In contrast, URANS still predicts a shear layer than extends across the cavity length with a vortex spanning a greater proportion of the cavity than with DES.

Although the noise levels are somewhat lower in the L/D=10 cavity, the source of noise appears to change from narrowband to broadband. It is probable that the poor agreement between URANS and DES results is due to the fact that URANS cannot predict broadband noise. Overall, the L/D=10 cavity results with the SST turbulence model were still found to be inconsistent and sensitive to the grid employed. Consequently, turbulent simulation based on LES/DES is again recommended for this L/D ratio, as was the case for the L/D=2 and L/D=5 cavities.

6.4 L/D=16 Closed Cavity

The SPLs and PSD plots for the L/D=16 cavity are presented in Figure 6.9, in which, as before, results from the the coarse and fine grids with time-steps of 0.01 ($\equiv 1.814 \times 10^{-5}$s) and 0.005 ($\equiv 9.07 \times 10^{-6}$s) are plotted. Although the fine grid produced slightly higher SPLs at the cavity front than for the coarse grid (Figure 6.9(a)), the general trend of the SPL curve and indeed the frequency content was more consistent than with shorter cavity aspect ratios. Although no DES results are presented here for validation, this level of consistency was not obtained with URANS with any of the other L/D ratios studied and so provides evidence that URANS can predict the L/D=16 closed cavity flow more accurately.

Frequencies above 500 Hz were now observed to be completely non-existent for the L/D=16 cavity. Even for frequencies between 0 Hz and 500 Hz, only the amplitudes of frequencies up to about 250Hz are significant. Consequently, only these frequencies contribute to the overall noise levels. The SPLs were also much lower for the L/D=16 cavity than was the case with the lower cavity L/D ratios, with maximum SPLs approaching approximately 155 dB at the cavity rear ($x/L = 0.95$) as highlighted in Figure 6.9(a).

6.4.1 Band-Limited Frequency Analysis

Noise level variations for four specific frequency ranges are presented in Figures 6.10. For the L/D=16 configuration, the cavity length is 1.6 times longer than for other cavity geometries analysed. Based on Rossiter's formula (Equation 1.3), which states that the frequency is inversely proportional to the cavity length, the first four Rossiter modes corresponding to this cavity L/D ratio are approximately 100 Hz, 235 Hz, 370 Hz and 505 Hz. Each of these modes is contained within the four frequency intervals illustrated in Figures 6.10.

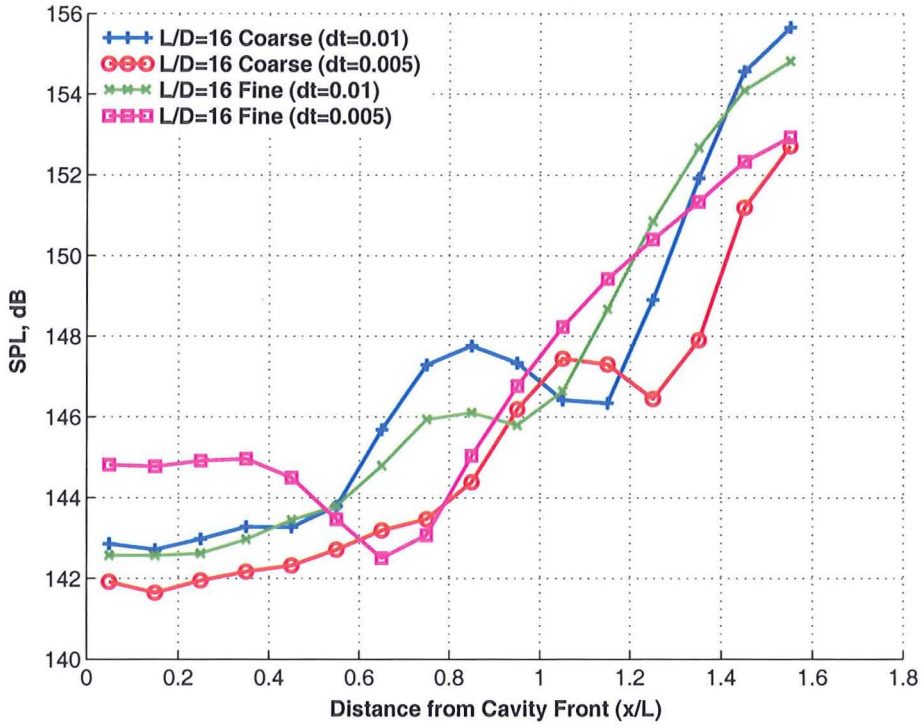

(a) SPLs

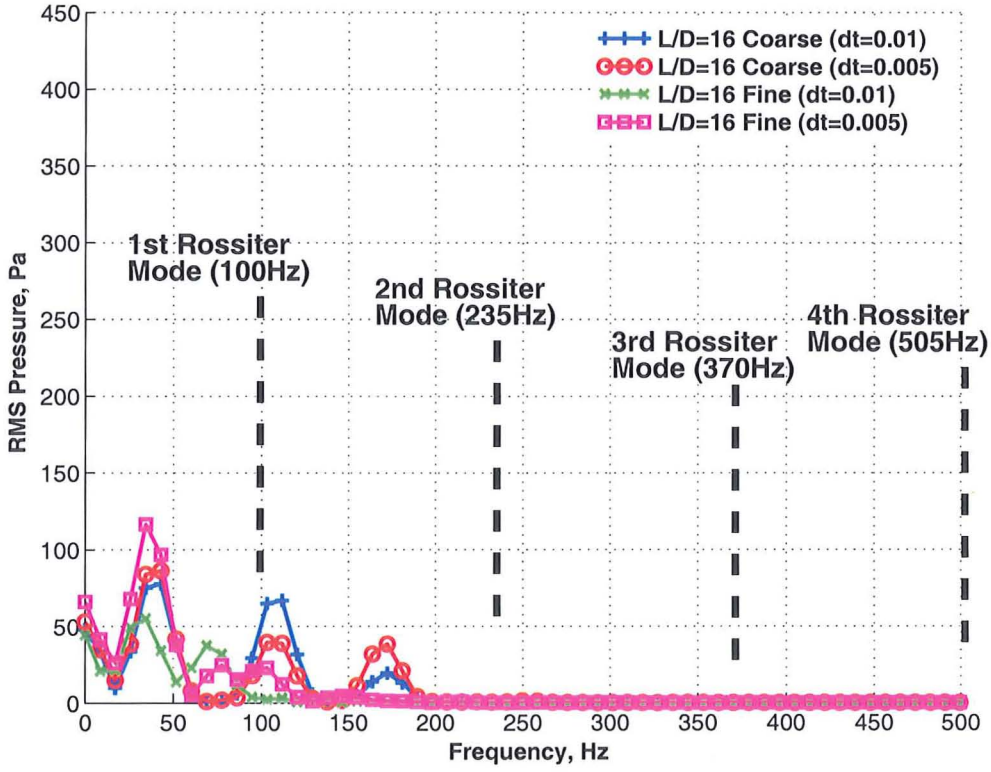

(b) PSD ($x/L = 0.05$)

Figure 6.9: (continued)

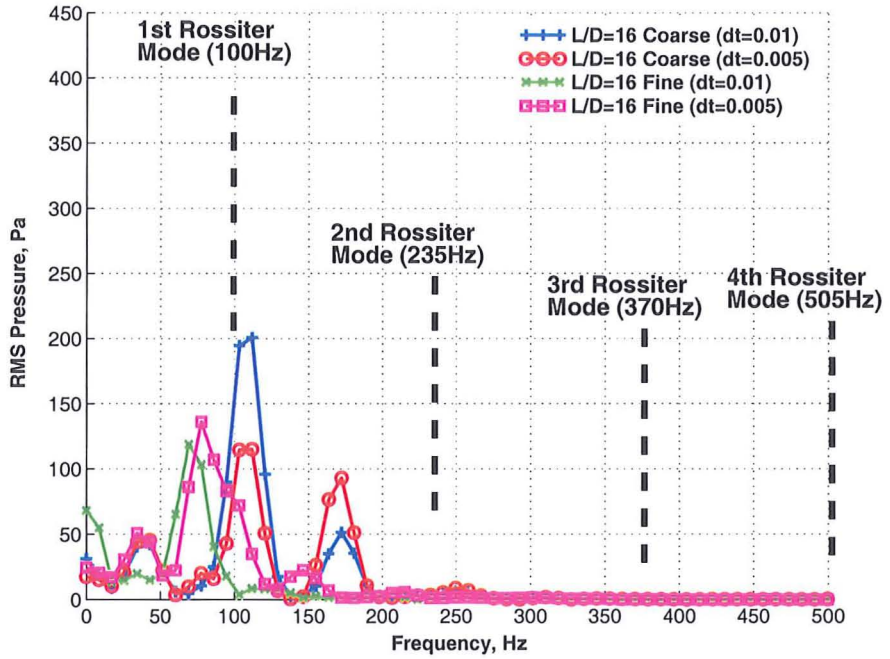

(c) PSD ($x/L = 0.55$)

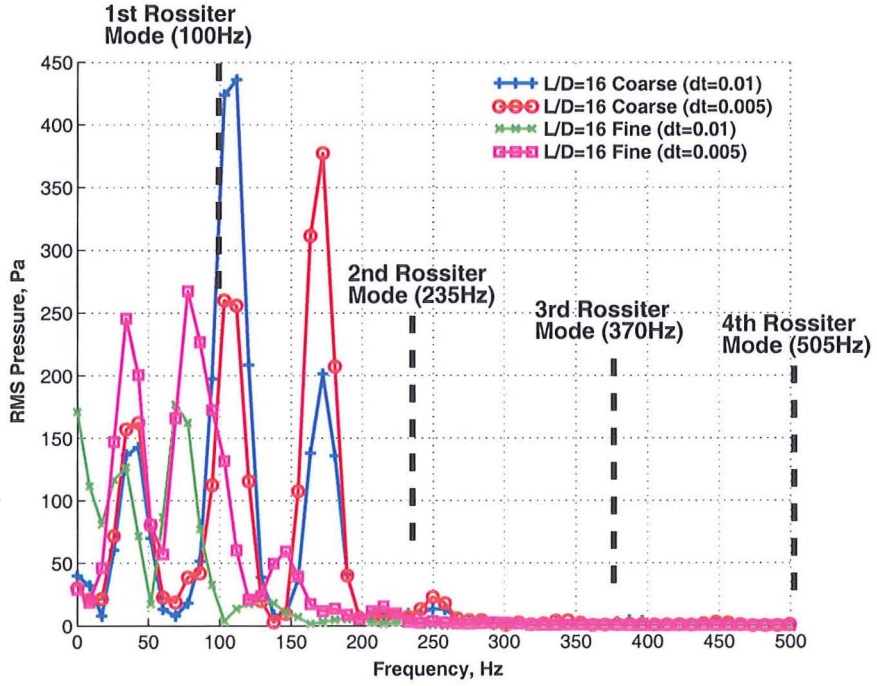

(d) PSD ($x/L = 0.95$)

Figure 6.9: SPL and PSD plots (at $x/L = 0.05$, $x/L = 0.55$ and $x/L = 0.95$) for the 2D closed, rectangular L/D=16 cavity at $x/L = 0.55$ and $x/L = 0.95$ along the cavity floor using the SST turbulence model for: coarse grid, coarse time-step (solid blue with plus signs); coarse grid, fine time-step (solid red with circular markers); fine grid, coarse time-step (solid green with crosses) and fine grid, fine time-step (solid magenta with square symbols).

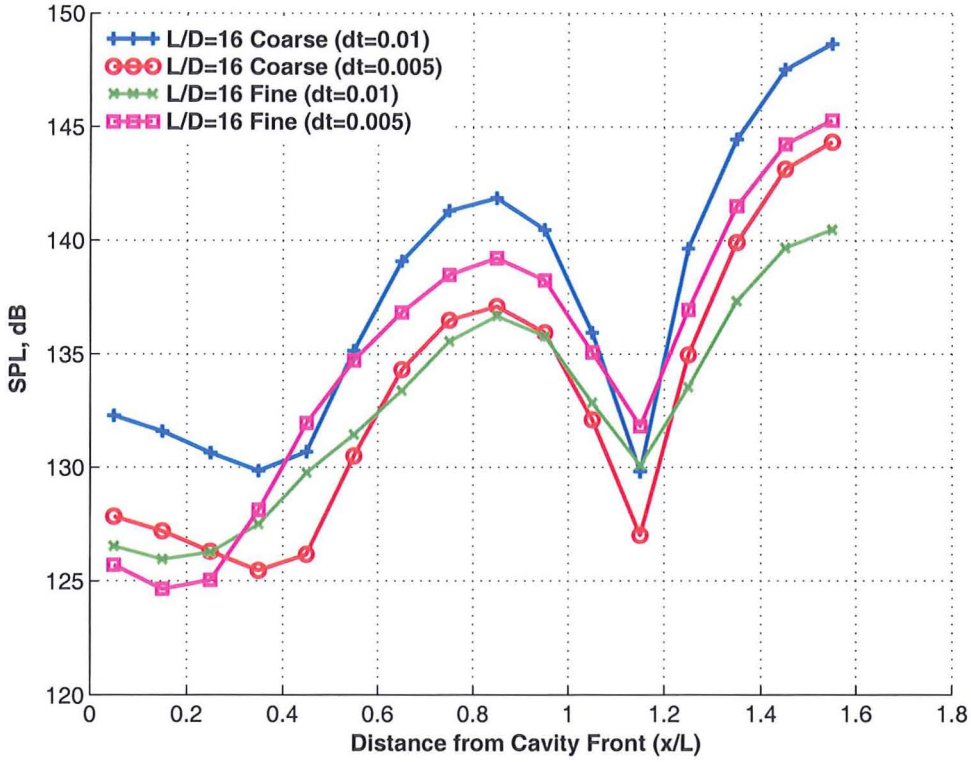

(a) $50\ Hz \leq f \leq 150\ Hz$

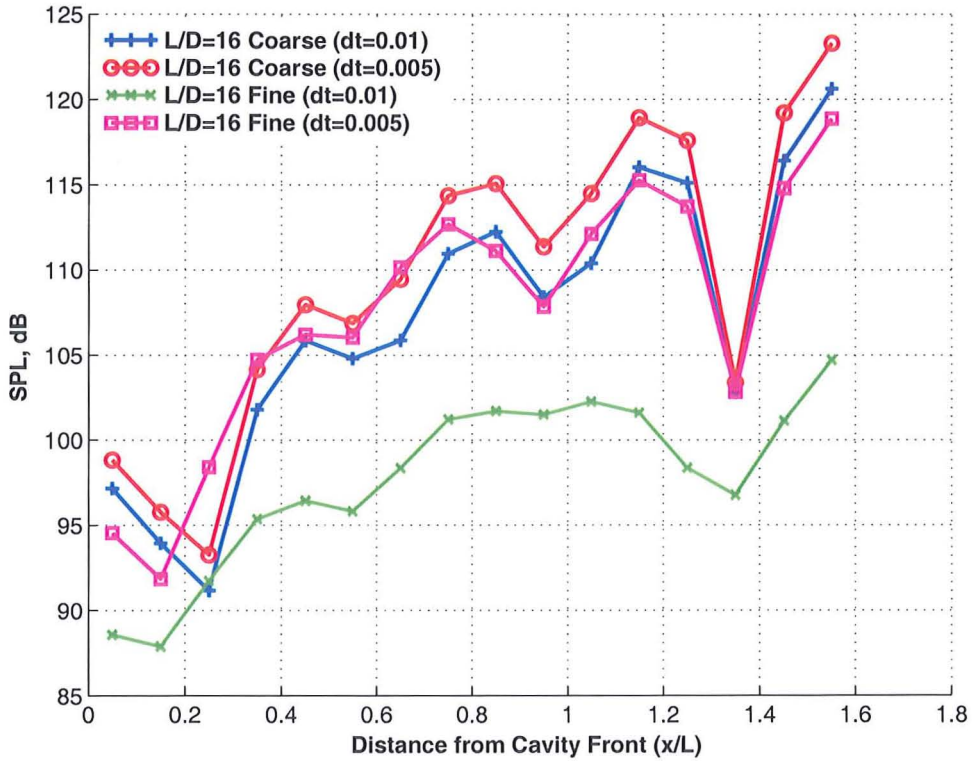

(b) $200\ Hz \leq f \leq 300\ Hz$

Figure 6.10: (continued)

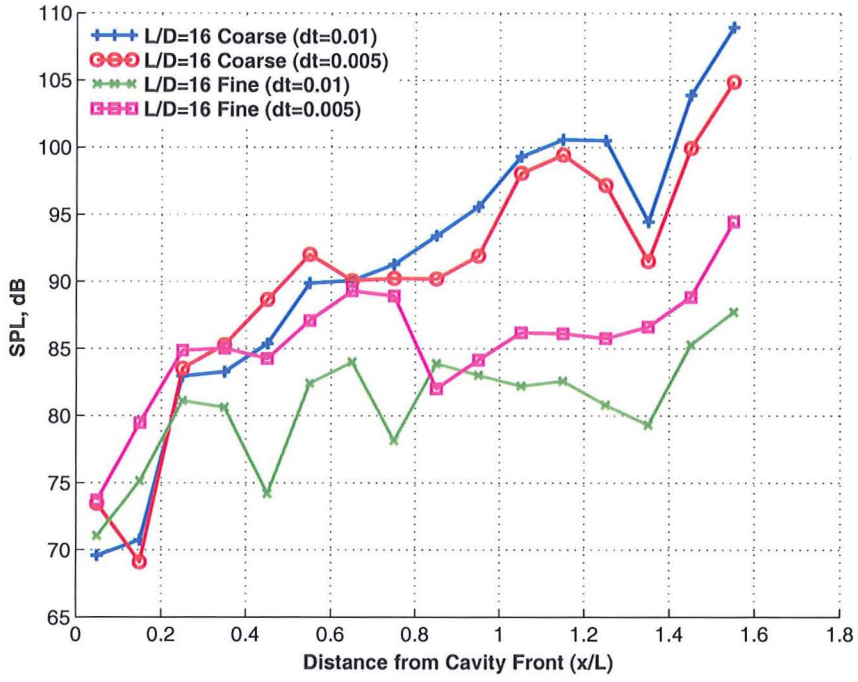

(c) $350Hz \leq f \leq 450Hz$

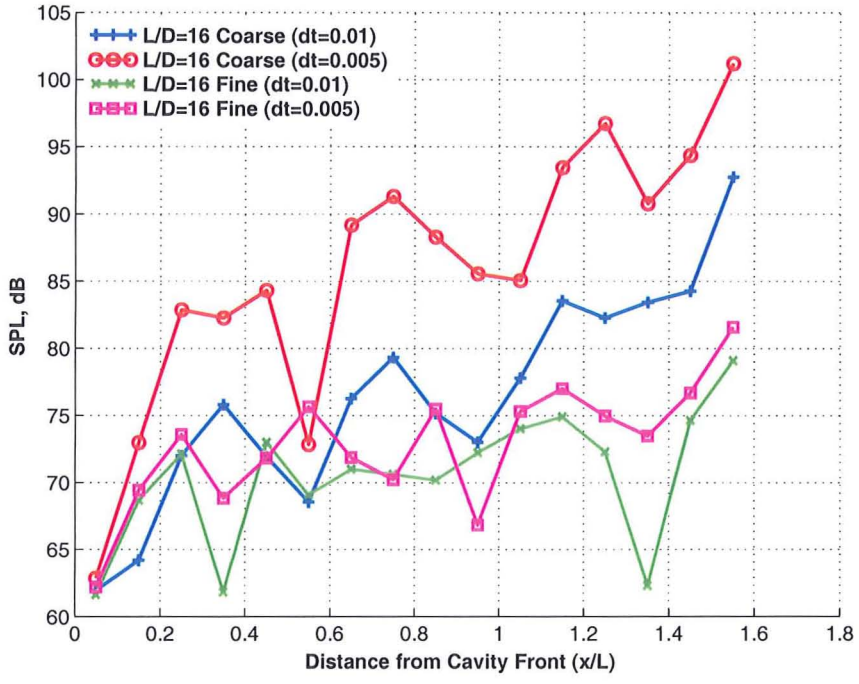

(d) $500Hz \leq f \leq 550Hz$

Figure 6.10: Band-limited SPLs for the 2D closed, rectangular L/D=16 cavity along the cavity floor using the SST turbulence model for: coarse grid, coarse time-step (solid blue with plus signs); coarse grid, fine time-step (solid red with circular markers); fine grid, coarse time-step (solid green with crosses) and fine grid, fine time-step (solid magenta with square symbols).

As mentioned previously, most of the noise was generated from frequencies up to about 250 Hz so it was anticipated that only the first two frequency bands would contribute to the overall noise levels produced inside the cavity. This was indeed reflected in Figure 6.10 where SPLs at the cavity rear fall from approximately 150 dB for the first frequency band (Figure 6.10(a)) to 125 dB for the second frequency band (Figure 6.10(b)) to around 110 dB and lower for higher frequency ranges (Figures 6.10(c) and 6.10(d)). Irrespective of frequency range, however, variations and scatter between the four computations was less pronounced for different grid sizes and time-steps for the L/D=16 cavity.

6.4.2 Flow-field Visualisation

Flow visualisation of the L/D=16 cavity for all four cases is depicted in Figure 6.11, which shows the time-averaged plots of Mach number contours and streamlines. Only a single vortex exists in the cavity on the average for the L/D=16 cavity and the flow is observed to reattach at the floor at approximately $x/L = 0.5$. For all the four computations, the time-averaged plots are very similar suggesting that grid sensitivity was less prominent for the L/D=16 cavity. Turbulence modelling based on URANS can therefore be applied for the L/D=16 cavity with good accuracy.

It would therefore seem that the longer the cavity, the less sensitive are the results to the grid employed. This issue of grid dependency may be related to the overall complexity of the flow in the cavity. An indication of how well URANS can predict the flow may, for instance, be obtained by analysing the level of unsteadiness and turbulence in the flow. In addition, the noise levels and frequencies exhibited in the cavity can be used to determine the predictive capabilities of the URANS method.

Very deep cavities such as the L/D=2 cavity, for instance, generate a shear layer that bridges the cavity opening, in a similar fashion to the L/D=5 cavity. The physical processes occurring in the L/D=2 cavity are also similar to the L/D=5 cavity with the shear layer dipping into the cavity and undergoing fluctuations. These oscillations are however not as pronounced as for the L/D=5 cavity and this is probably due to the fact that the deeper cavity restricts the movement of the large vortex that exists in the cavity. Consequently, the frequencies generated in the L/D=2 cavity are not as high as for the L/D=5 cavity. On the other hand, interactions between the larger vortex in the cavity and the shear layer and the walls still generates high noise levels. Strong coupling between the shear layer and the vortices inside the cavity therefore still exists. Since the flow is unsteady and turbulent, a slight change to the grid can cause a change in the results.

For the transitional cavity of L/D=10, the shear layer still dips further into the cavity but the movement of the shear layer is minimised. Fewer vortical structures exist in the cavity and most of the noise is broadband rather than narrowband. Although the noise levels are somewhat lower, the fact that the noise is broadband means that URANS again has difficulty in resolving the flow features consistently. As the cavity L/D ratio is increased further, i.e. closed cavity with L/D=16, the shear layer falls further into the cavity opening and reattaches at the cavity floor (at approximately $x/L = 0.35$). Only two regions of recirculation exist: a lower-pressure region between the cavity front wall and the re-attachment point and a higher-pressure region between the separation point (approximately $x/L = 0.95$) and the cavity back wall. The flow is quasi-steady and less turbulent with only lower frequencies prevailing. Combined with much lower SPLs, the flow is more quiescent and changes to the grid do not alter the flow physics inside the cavity as significantly and

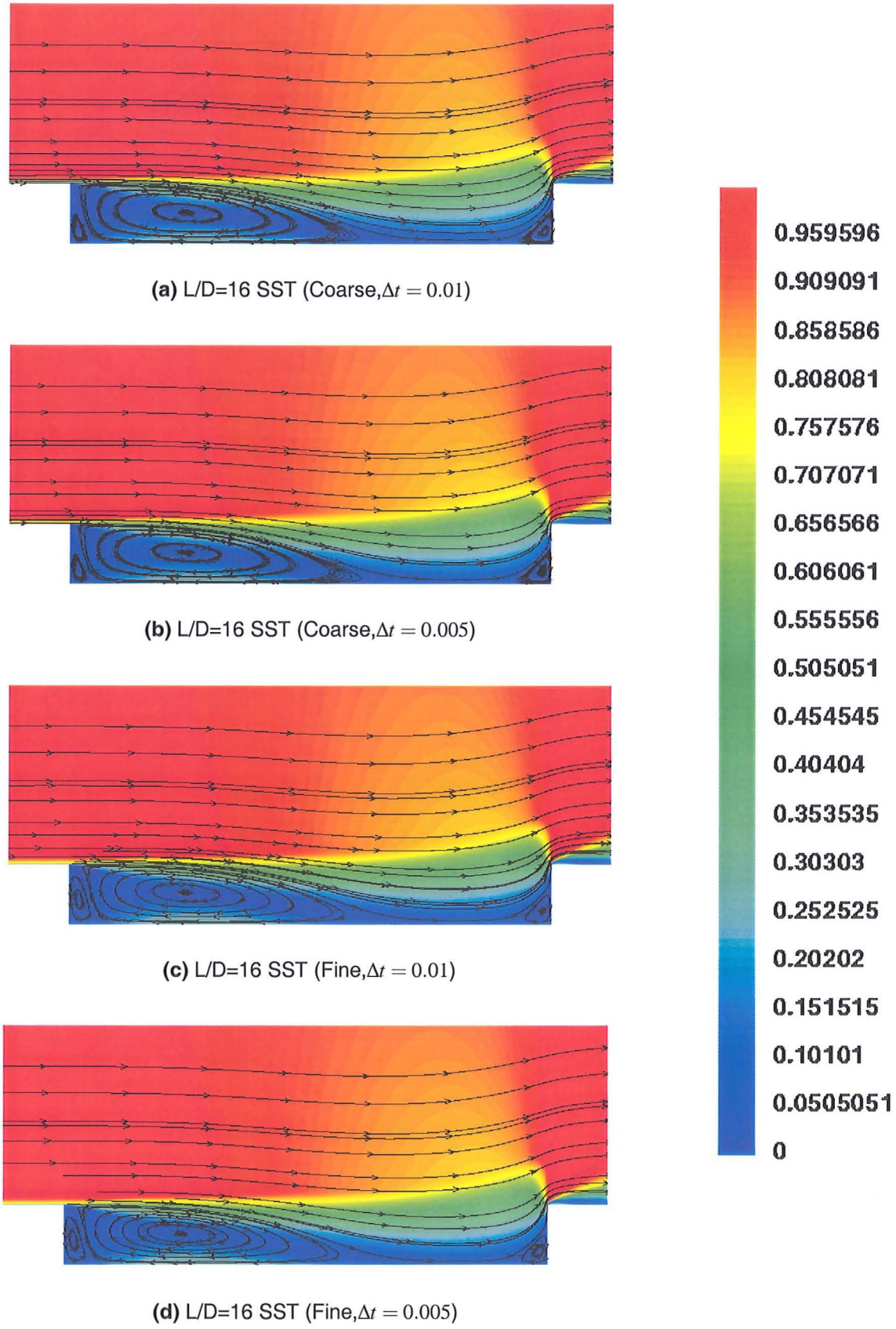

(a) L/D=16 SST (Coarse,$\Delta t = 0.01$)

(b) L/D=16 SST (Coarse,$\Delta t = 0.005$)

(c) L/D=16 SST (Fine,$\Delta t = 0.01$)

(d) L/D=16 SST (Fine,$\Delta t = 0.005$)

Figure 6.11: Time-averaged Mach number contours with streamlines for the 2D, L/D=16, closed cavity using the SST turbulence model for coarse and fine grids and time-steps. Plots show Mach number normalised with reference to the free-stream Mach number, $M_\infty = 0.85$.

statistical turbulence models provide more consistent results. In conclusion, the range of applicability of URANS can be summarised by Table 6.2. URANS can therefore be used to give reasonably accurate and consistent predictions for cavities with $L/D \geq 16$ while LES/DES would be needed for $L/D < 16$.

Table 6.2: The range of applicability of the URANS method for transonic, turbulent cavity flows ($M_\infty = 0.85$, $\mathrm{Re}_L = 6.783 \times 10^6$).

L/D ratio	Method
2	LES/DES
5	LES/DES
10	LES/DES
16	URANS

6.5 Concluding Remarks

Computations with cavities with L/D ratios of 2, 10 and 16 were conducted to assess if the grid sensitivity issue noted with the L/D=5 cavity was equally present for other cavity geometries. It was found that the SPL amplitudes, shape of the SPL curve and the frequencies were more consistently predicted with grid refinement as the cavity length-to-depth ratio was increased. Grid dependency was thought to be connected to the level of unsteadiness and turbulence in the flow, with the more unsteady and turbulent the flow, the less accurate the predictions with URANS.

With deeper cavities, the noise levels were observed to be of the same order of magnitude as for the L/D=5 cavity. High frequencies were still present and coupling between the shear layer and the vortices inside the cavity was strong. Results with URANS changed on grid refinement, as was found with the L/D=5 cavity. With transitional L/D=10 cavities, the noise levels were lower but the source of noise was more broadband than narrowband. URANS again failed to predict this accurately and more scatter was observed across all computations. With closed cavities (L/D=16), URANS provided more consistent results. This was attributed to lower frequencies and noise levels being present and with coupling between the shear layer and the flow inside the cavity to be weaker. In such circumstances, the grid dependency was less evident. It was therefore concluded that URANS could be used accurately to predict the flow in longer, closed cavities where the flow is more quiescent but LES/DES would be required for accurate resolution of the flow in cavities with $L/D < 16$.

Chapter 7

Flow Control: L/D=5 Cavity

With the flow physics inside the cavity relatively well understood, a study into suppressing the large noise levels and high frequencies generated in the open L/D=5 cavity was undertaken. Both passive and active open-loop control methods were investigated and their effects on the flow structures, noise levels and frequencies for the L/D=5 cavity demonstrated. Although cavities of higher L/D ratios may also require control, for example to ameliorate the large pitching moments that can have an adverse effect on the release characteristics of stores, the focus of the control study addressed here was to reduce the large noise levels in the open L/D=5 cavity. The weapon bay with doors-on and opened at 90^{o} is the configuration that the weapon bay will most likely be exposed to so flow control for the doors-on case is only studied here.

Effectiveness of passive and active open-loop control devices is investigated. As was mentioned in Chapter 1, passive control devices involve manipulating the existing cavity geometry or adding external physical devices to modify the flow-field in the cavity. Effects of the spoiler and slanted cavity walls were studied in this case. For active open-loop control, steady jet blowing was used, which involved blowing air into the cavity. Since this method is not time-dependent, i.e. the jet conditions do not change in time, it could be regarded as a passive device as well.

It has been mentioned before that the flow behaves two-dimensionally for the weapon bay with doors-on, so a reasonable approximation of the flow-field can be obtained by modelling the cavity as 2D. Furthermore, to conduct a proper flow control study a large number of cases need to be performed, e.g. to study the effect of different positions. In such circumstances, LES/DES becomes too expensive and URANS is more convenient. On this basis, numerical computations for the flow control study were performed on the 2D L/D=5 cavity using the SST turbulence model. In Chapter 4, it was demonstrated that the SST turbulence model gave reasonable agreement with experiment at coarse grids and provided a good qualitative prediction of the cavity flow features. Since the aim of flow control methods for the cavity is to minimise the fluctuations of the shear layer and reduce the flow unsteadiness, it can be further argued that URANS is a faster and sufficiently accurate method as it is better equipped to predict the lower frequencies that would occur in this situation.

Investigations performed with the spoiler and slanted cavity walls were based on experiments conducted by Ross and Peto [11]. On the other hand, the steady jet concept was based on Lamp and Chokani's experiments [226]. Each control device was placed at different locations (as shown in Figure 7.1) and its influence was recorded. For the spoiler,

additional computations with different heights were also performed (Figure 7.1(a)). Effects of different angles of slant for slanted cavity walls were also investigated in addition to the position of slant (Figure 7.1(b)). For the continuous mass jet, the effect of different exit jet velocities were also analysed (Figure 7.1(c)).

Details of all the results for all the configurations shown in Figure 7.1 are given in Appendix A. For the purposes of illustrating which flow control method was the best, however, only one set of results from each method is presented here (all results are given in Appendix A). For the spoiler, results with the spoiler placed in position 2 (with co-ordinates $x_{sp}/L = -0.1, y_{sp}/L = 0$) as shown in Figure 7.1(a) were used as an example. The width (w_{sp}) and height (h_{sp}) of the spoiler were 0.25 inches and 0.42 inches, respectively. The height of the spoiler was approximately equal to the height of the boundary layer, δ. The value of the boundary layer height was calculated to be the distance above the flat plate at which the velocity was equal to $0.99U_\infty$. This gave a value of 0.021L and was found to be similar to that specified in the experiments conducted by Ross & Peto [11].

To illustrate the effect of slanting cavity walls, results from the rear cavity wall slanted at 45° are used (Figure 7.1(b)). For steady jet blowing, on the other hand, results from the jet placed at the front cavity wall (Figure 7.1(c)) are used. The jet exit velocity is calculated based on a reservoir total pressure and total temperature, assuming isentropic conditions, as described by Lamp and Chokani [226]. The angle of the jet is perpendicular to the flow and the jet exit Mach number is $0.1M_\infty$. With a total reservoir pressure and temperature of 2 atmospheres and 298 K respectively, the jet exit velocity was calculated to be 29.4 m/s. The jet slot width, w_j, was 0.02L giving a value for the blowing co-efficient, C_μ, derived as the ratio of the exit jet to the free-stream mass flow rate, of 0.01. Full results for all configurations of the spoiler, slanted cavity walls and the steady jet are given in Appendix A.

The case where no control method is used are denoted as 'baseline'. Although no experimental data were available for this control study, results were compared to the computational 'baseline' case as well as to the corresponding experimental results (i.e. for the clean, 2D, L/D=5 cavity where no control method was used) to illustrate the effectiveness of the control method.

7.1 Description of Computational Domain

Figure 7.2 provides two views of the grids used for the cavity with a spoiler ahead of cavity front corner, with a slanted front cavity wall and with a jet situated on the front cavity wall. A full view of each grid is depicted on the left column whereas an illustration of the mesh distribution near the cavity corner is given on the right column of the figure. For reference, the mesh distribution for the baseline case without any control device is also illustrated.

For this control study, the original coarse L/D=5 grid was modified to include the relevant control method. For the spoiler upstream of the cavity, for instance, meshing inside the cavity remained identical to the coarse L/D=5 grid although the meshing upstream of the cavity was altered to incorporate the the spoiler (Figures 7.2(c)-7.2(d)). The front cavity corner was pushed further upstream (and the cavity length kept fixed) in the generation of the grid with the slanted front wall (Figures 7.2(e)-7.2(f)). And additional blocks were

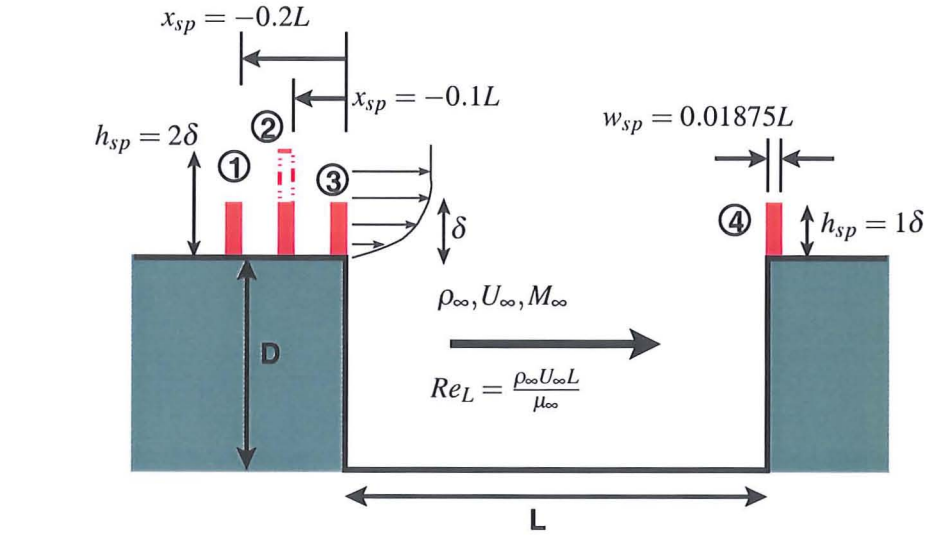

(a) Spoiler

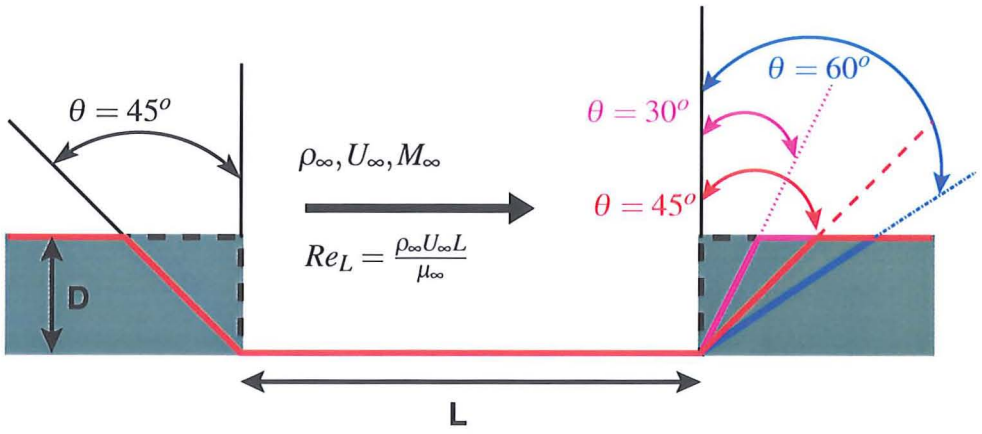

(b) Slanted Cavity Walls

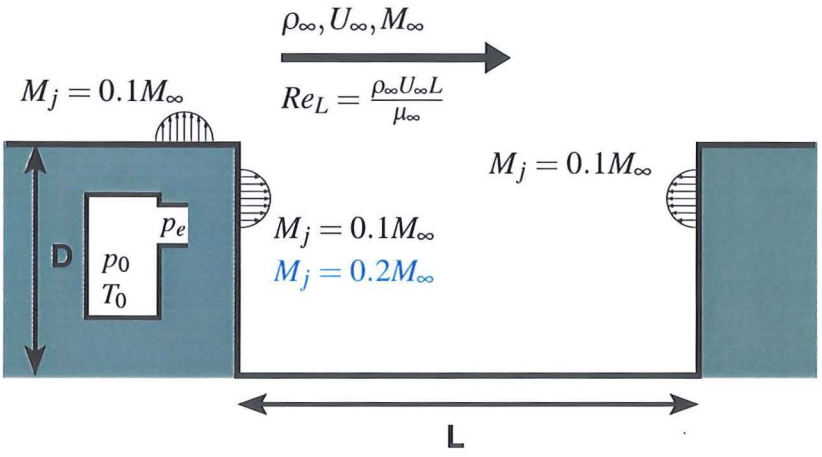

(c) Steady Jet Blowing

Figure 7.1: Schematics illustrating the different positions and heights of the spoiler, different positions and angles of slanted for shaped cavity walls and different positions and exit jet velocities investigated for the flow control study.

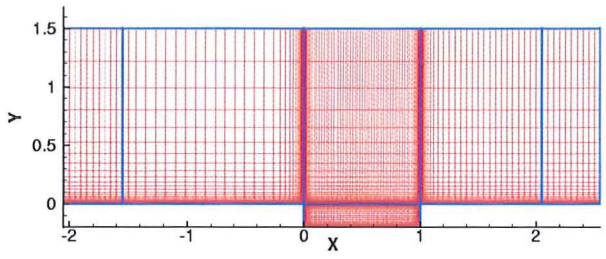

(a) Coarse L/D=5, 2D Grid

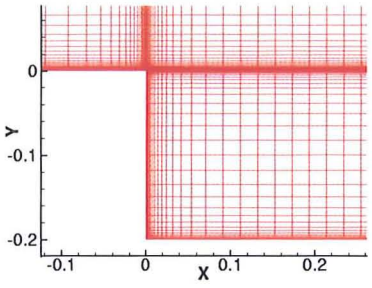

(b) Coarse L/D=5, 2D Grid (Front Corner)

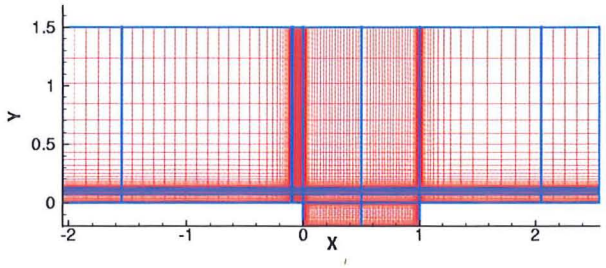

(c) Coarse Grid with LE Spoiler

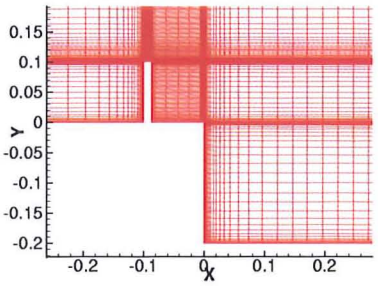

(d) Coarse Grid with LE Spoiler (Front Corner)

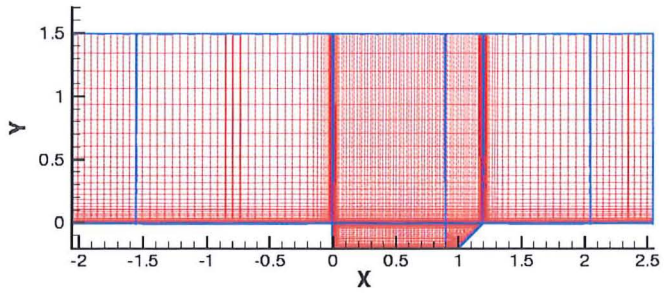

(e) Coarse Grid with Slanted TE

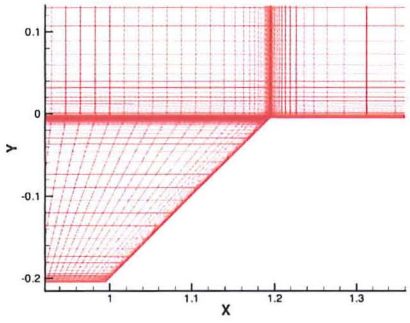

(f) Coarse Grid with Slanted TE (Rear Corner)

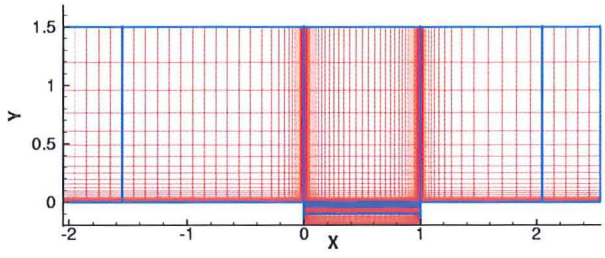

(g) Coarse Grid with Front Wall Jet

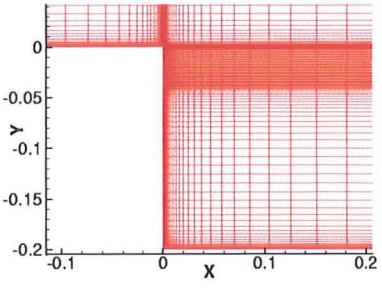

(h) Coarse Grid with Front Wall Jet (Front Corner)

Figure 7.2: Full schematics (on left column) of grids used for the coarse L/D=5 cavity (7.2(a)), LE spoiler (7.2(c)), slanted TE at 45° (7.2(e)) and jet at front cavity wall (7.2(g)). Close-up of the cavity corner for each of the grids is shown on the right column.

inserted inside the cavity for the case where a jet was fired from the front cavity wall (Figures 7.2(g)-7.2(h)).

Table 7.1 provides a description of only the grids for which results are presented here. Information on the baseline, 2D, L/D=5, coarse cavity grid is also included. Details of all the grids for all the configurations are provided in Table A.1 in Appendix A.

Table 7.1: Information about the grids used for the 2D, L/D=5, clean cavity control study.

Location	Overall Points	Points in Cavity	Wallspacing	Blocks in Cavity (Overall)
Baseline (Coarse)	33,250	10,302	$y = 1.05 \times 10^{-5}$	1 (6)
LE spoiler ($h_{sp}/L = 0.021$)	150,450	22,800	$y = 5 \times 10^{-6}$	2 (17)
Slanted Rear Wall ($\theta = 45^{o}$)	31,212	9,894	$y = 5 \times 10^{-5}$	2 (8)
Front Wall Jet ($M_j = 0.1 M_{\infty}$)	46,972	25,654	$y = 5 \times 10^{-6}$	4 (9)

7.2 Acoustic Spectrum Analysis

Pressure traces at the cavity rear ($x/L = 0.95$) and SPL variations along the cavity floor are shown in Figure 7.3. Out of the three passive control methods considered, steady jet blowing (magenta lines with square symbols) was the most effective, achieving reductions in SPLs of about 30 dB (Figure 7.3(a)). Analysis of the pressure signature in Figure 7.3(d) revealed that the jet was also effective in eliminating the higher frequencies completely leading to a steady solution. Although the spoiler (red lines with circular symbols) was also found to be effective in reducing the SPLs (as well as the higher frequencies) inside the cavity, more noise was created outside the cavity close to the position of the spoiler. As far as the slanted rear wall (green lines with crosses) is concerned, slight suppression of the pressure amplitudes was observed but it was not as pronounced as for the spoiler or the jet. However, the effectiveness of slanting the rear cavity wall is strongly dependent on the angle of slant. Analysis at additional angles of slant of 30° and 60° (refer to Appendix A) revealed that reductions of the same order of magnitude as the jet were achieved with high angles of slant and the flow became completely steady.

7.3 Band-Limited Frequency Analysis

Figure 7.4 provides a more in-depth analysis of the effectiveness of each control method by illustrating the noise level variation within four frequencies: $50\ Hz \leq f \leq 250\ Hz$, $350\ Hz \leq f \leq 450\ Hz$, $500\ Hz \leq f \leq 700\ Hz$ and $750\ Hz \leq f \leq 850\ Hz$. Each of these frequency bands contain one of the main acoustic tones (or Rossiter modes) that exist for this cavity for these flow conditions. This type of analysis assists in identifying which frequencies are

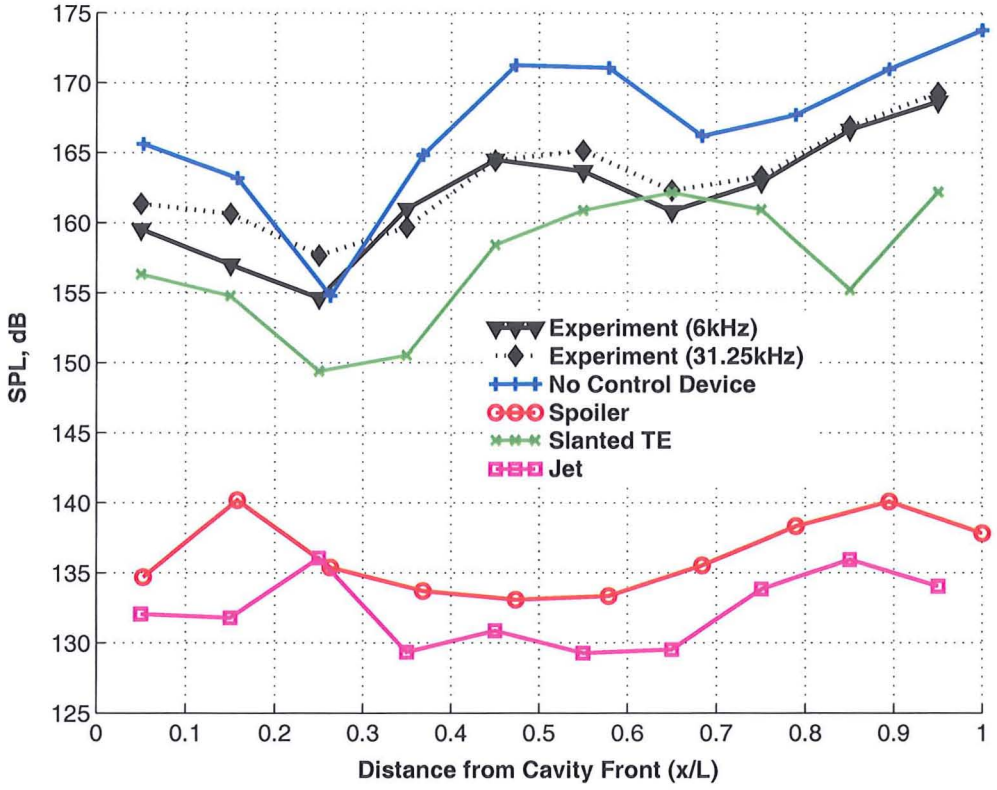

(a) SPLs

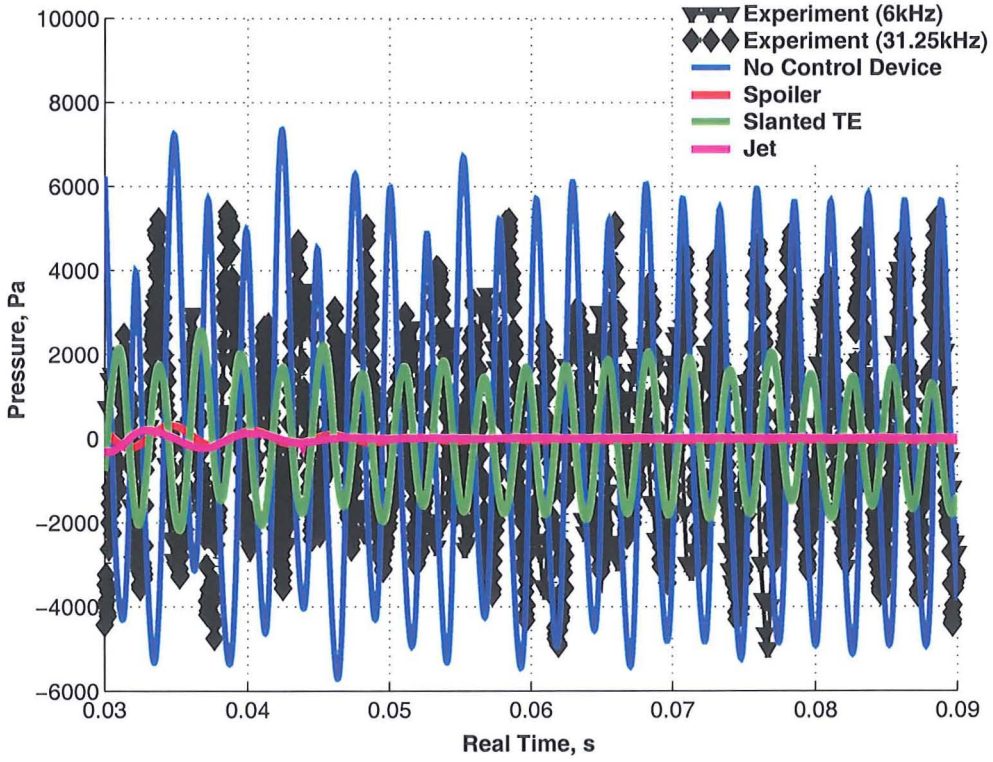

(b) Pressure Traces ($x/L = 0.05$)

Figure 7.3: (continued)

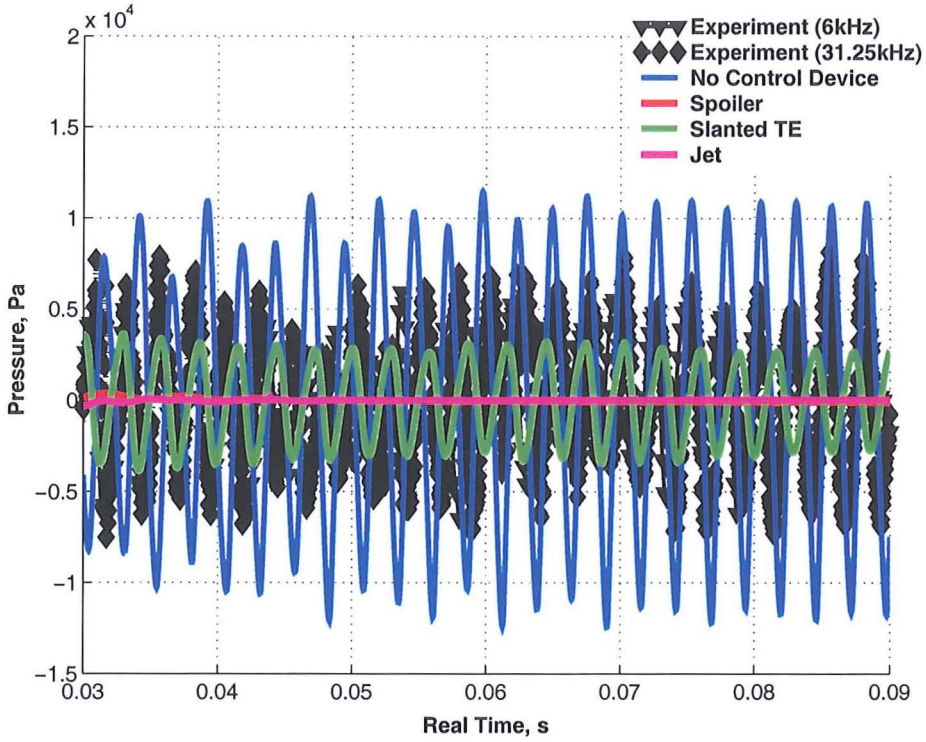

(c) Pressure Traces ($x/L = 0.55$)

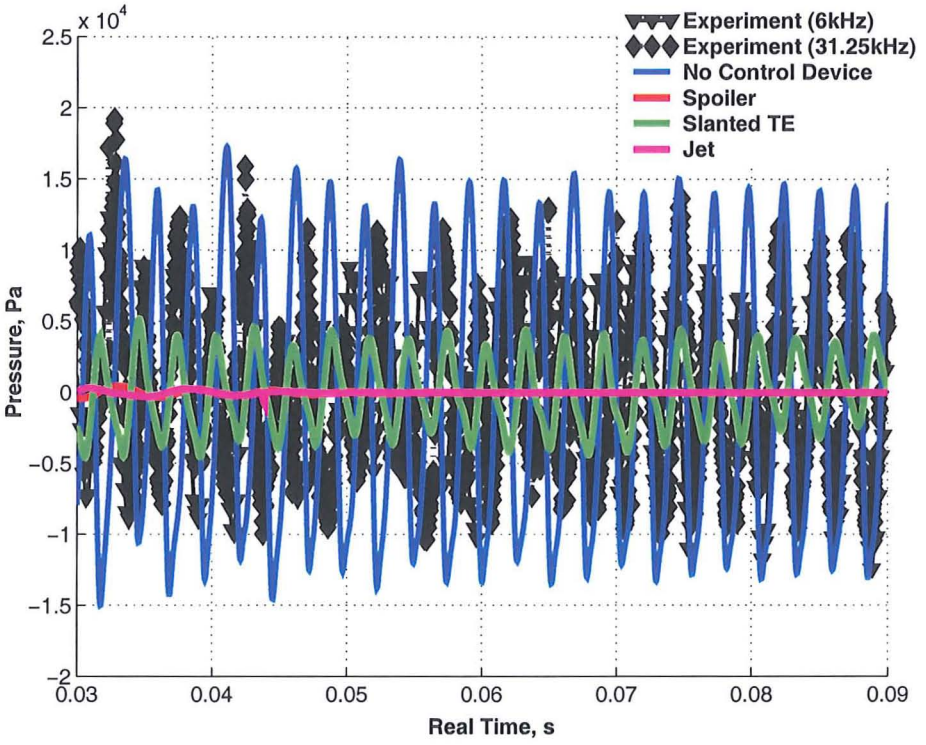

(d) Pressure Traces ($x/L = 0.95$)

Figure 7.3: SPLs and pressure traces (at $x/L = 0.05$, $x/L = 0.55$ and $x/L = 0.95$) along the cavity floor of the 2D, L/D=5 cavity using the SST turbulence model with and without control.

more dominant thereby providing more insight into the physical principles underlying the flow control of cavity flows as well as illustrating the effectiveness of each control method in more detail.

For both the spoiler and the jet, large reductions in the amplitudes are observed across all the four frequency ranges. On the other hand, for the slanted rear wall, reductions in frequency magnitudes are observed only for the first and third modes. The lower frequencies contained in the first and second frequency bands tend to contain most of the flow energy for the 2D cavity and typically correspond to the large vortical structures that exist in the cavity.

7.4 Flow-field Visualisation

Visualisation of the time-averaged flow-field inside the cavity with the upstream spoiler, slanted rear wall and the front wall jet is shown in Figure 7.5. For reference, the flow in the cavity for the baseline configuration is also shown. A dual-vortex cycle occurs for the baseline cavity where no control device was used. This typically takes the form of a strong primary vortex that spans most of the cavity length with a smaller corner vortex residing at the front wall. This front wall vortex is driven by the primary vortex situated further downstream and whose rotational sense is opposite to the primary vortex, i.e. counter-clockwise. The control devices investigated disrupt this feedback loop by primarily modifying the strength of the primary vortex and preventing this dual-vortex cycle from occurring. When a spoiler is used ahead of the cavity, a shear layer is still formed across the cavity opening but is significantly more diffused (Figure 7.5(b)). Turbulent diffusion is a key process in redistributing energy from the shear layer into the vortical structures inside the cavity. The strength of the primary vortex and hence the level of unsteadiness created inside the cavity relies on this. If the shear layer is diffused too much, however, less momentum is transferred inside the cavity. Consequently, the level of unsteadiness in the flow is reduced. Furthermore, since the spoiler offsets the shear layer from the cavity opening, the jet-edge tone interaction and hence the feedback loop is negated. The result is large reductions in the noise and frequencies as shown in Figure 7.3(a). Despite this, a compression wave was observed to form at the front corner of the spoiler, which increases the noise produced outside the cavity (although this is still much lower than the noise levels produced inside the baseline cavity as mentioned in Appendix A). Since the strength of primary vortex is reduced, the front wall corner vortex in the spoiler is also less developed (Figure 7.5(b)). Consequently, a single vortex presides and covers most of the cavity area.

For the jet, the flow was again pacified (Figure 7.3(d)) but the manner in which this is done is different from the spoiler. When the jet is fired from the front wall corner of the cavity, it adds more momentum to the shear layer. This forces the shear layer to span the cavity opening preventing it from dipping into the cavity (Figure 7.5(d)). The shear layer remains coherent and the additional momentum provided by the jet delays the onset of the diffusion process thereby preventing a redistribution of energy from the shear layer to the vortical structures inside the cavity. The strength of the primary vortex inside the cavity is again reduced so the noise levels in the cavity, produced by the interaction of the vortex with the walls, are significantly less (Figure 7.3(a)). In general, fluctuations in the shear layer are instigated by the vortex inside the cavity protruding into the shear layer. With the primary vortex not having enough energy to move the shear layer, oscillations in

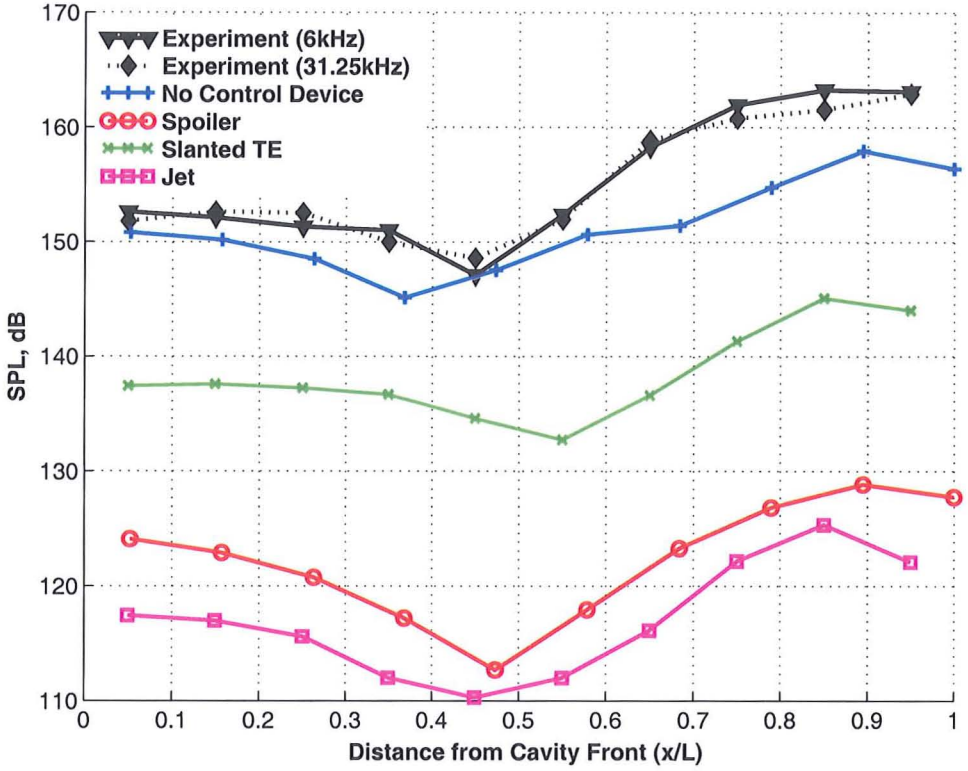

(a) $50\ Hz \leq f \leq 250\ Hz$

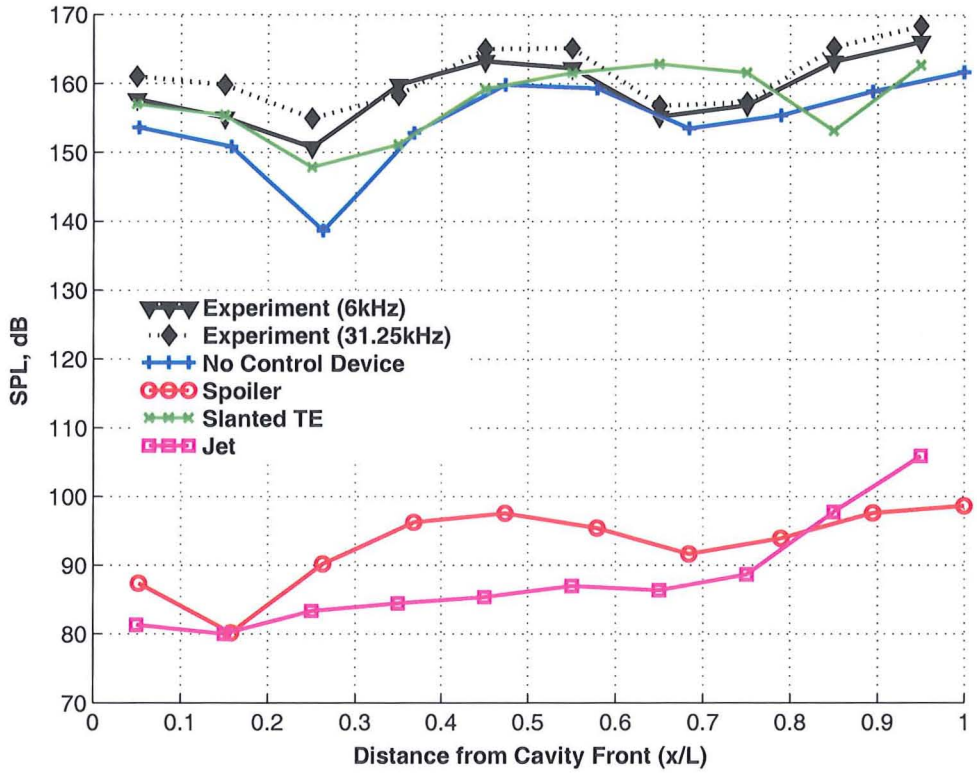

(b) $350\ Hz \leq f \leq 450\ Hz$

Figure 7.4: (continued)

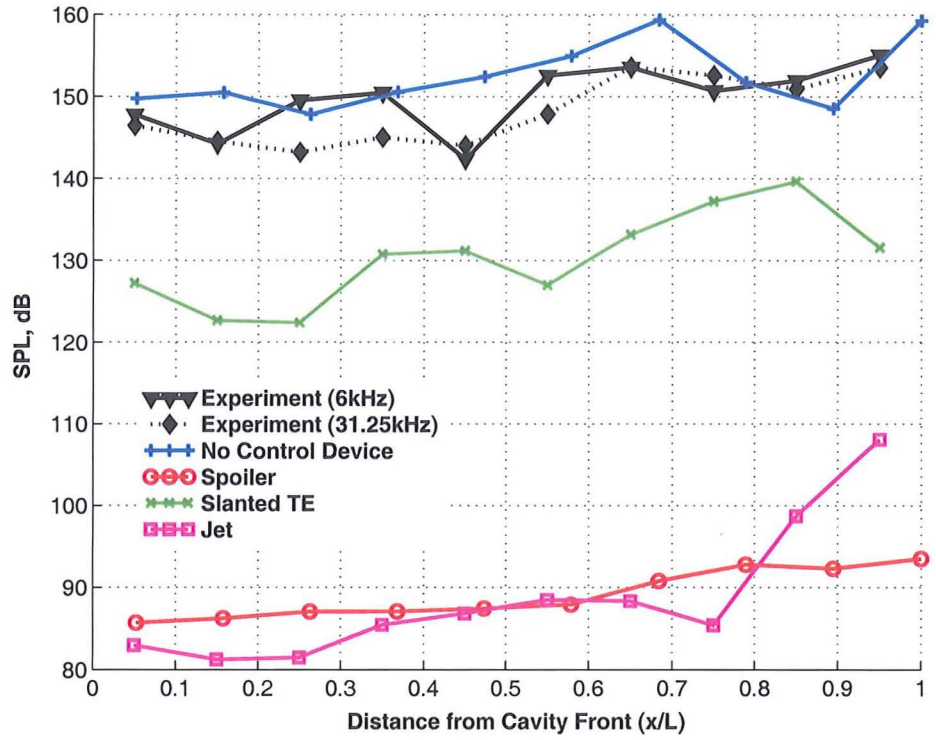

(c) $500\ Hz \leq f \leq 700\ Hz$

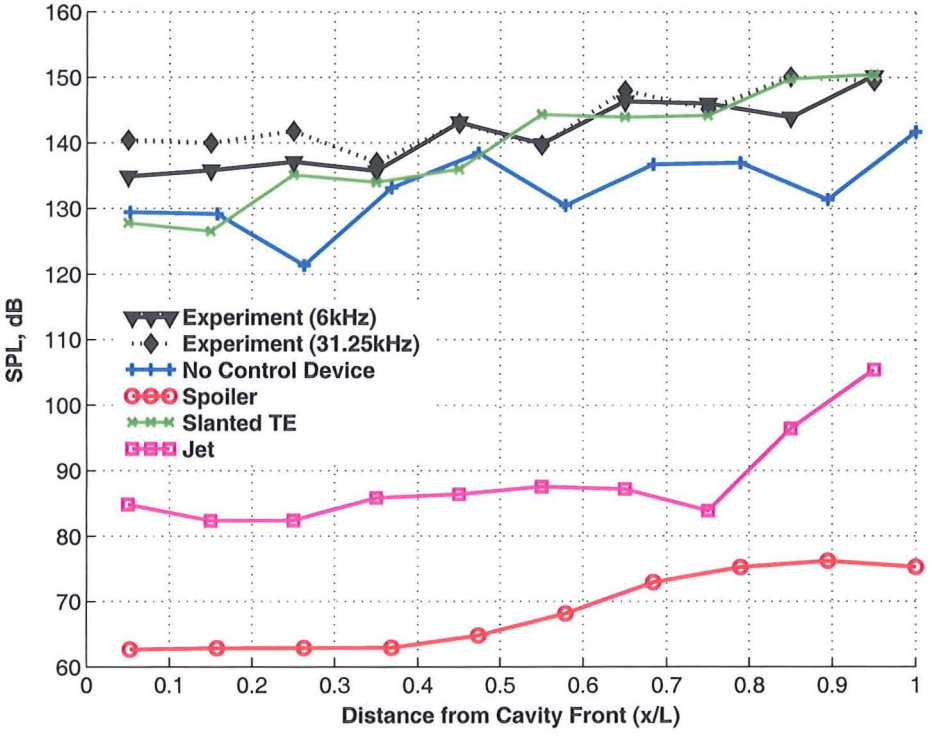

(d) $750\ Hz \leq f \leq 850\ Hz$

Figure 7.4: Band-limited SPLs within four frequency ranges along the cavity floor of the 2D, L/D=5 cavity using the SST turbulence model with and without control.

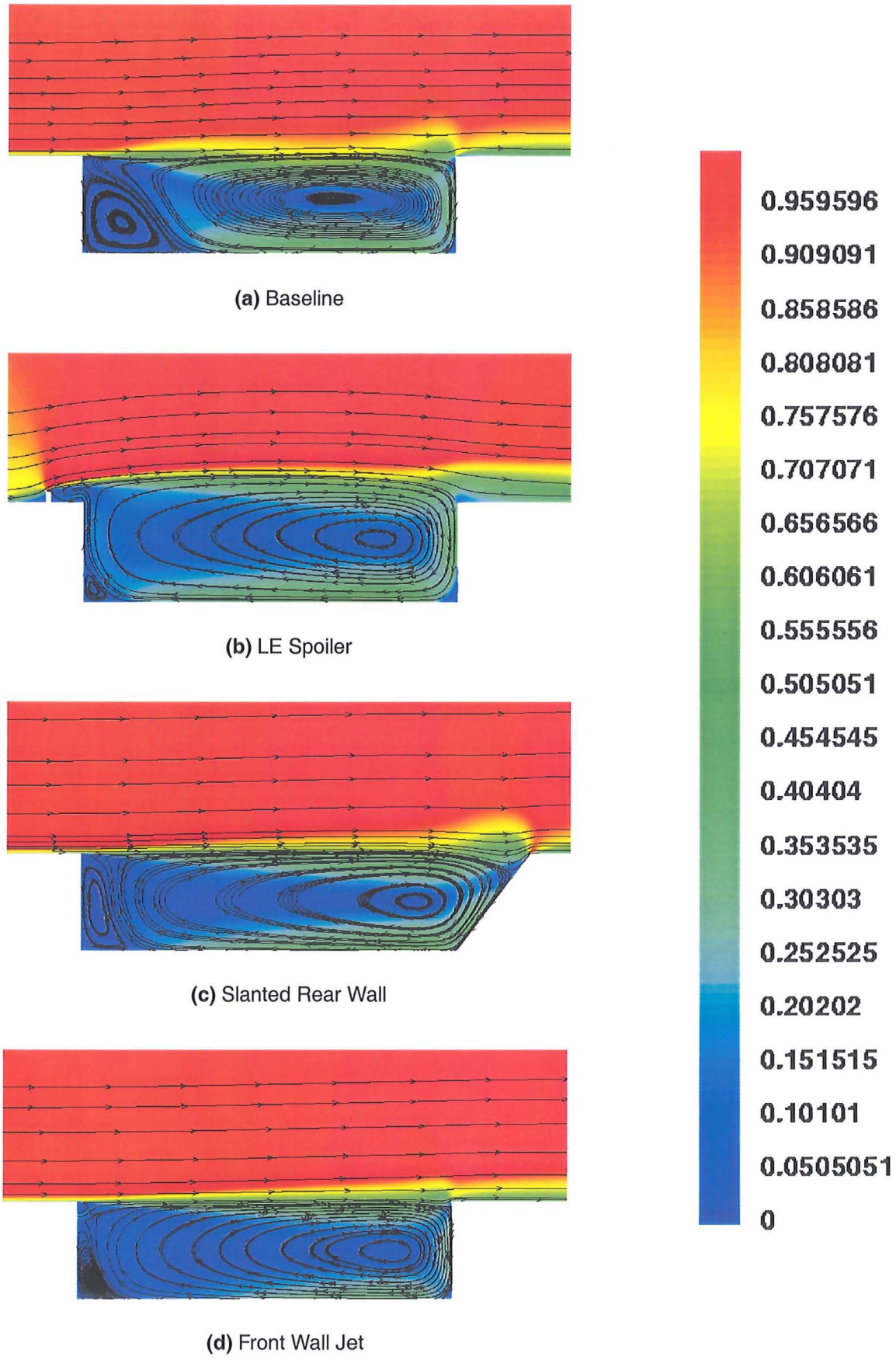

(a) Baseline

(b) LE Spoiler

(c) Slanted Rear Wall

(d) Front Wall Jet

Figure 7.5: Time-averaged Mach contours with streamlines inside the 2D, L/D=5 cavity using the SST turbulence model with and without control.

the shear layer are minimal. The mass breathing process whereby flow enters and leaves the cavity is also reduced and the higher frequencies generated by the impingement of the shear layer with the downstream wall are mitigated. The ejection of air via the jet does however add more noise at the cavity front (as is indicated by a small peak in the SPL curve at about $x/L = 0.25$), but on average this increase is still significantly lower than experimental results for the baseline cavity (Figure 7.3(a)). Although the twin-vortex cycle is again disrupted by additional blowing of air with the jet, the greater flow activity at the cavity front due to an injection of mass results in the front wall vortex becoming larger than for the spoiler.

When the cavity geometry is manipulated by slanting the rear walls, however, neither is the shear layer sufficiently diffused (as was the case with the spoiler) and nor is the shear layer prevented from dipping into the cavity (as was the case with the jet). A twin-vortex cycle is still clearly evident and the flow is more unsteady. Noise levels are nonetheless still slightly lower than the baseline experiment (Figure 7.3(a)). This is due to the fact that the force with which the vortex impacts the downstream cavity wall is spread over a larger geometric area (Figure 7.5(c)). Since the length of the cavity floor is unchanged but the length of the shear layer plane is increased (by a factor of $\sqrt{2}$), greater flow entrainment is also achieved by slanting the rear wall. Consequently, fluctuations in the shear layer are minimised somewhat but to a lesser degree to the spoiler and the jet. As was mentioned previously, however, at higher angles of slant, greater flow entrainment can be obtained and the flow becomes steady with greater reductions in SPLs being obtained (see Appendix A).

7.5 Conclusions

Calculations with different passive and active open-loop control methods with the L/D=5 cavity were conducted in the aim of reducing the high noise levels and large frequency content observed inside the cavity. The effectiveness of the spoiler and slanted cavity walls as a passive control method and continuous mass injection as an active open-loop control method was investigated.

Steady jet blowing (applied at the cavity front wall) was found to be most effective in mitigating the noise level and frequency content in the cavity. The spoiler (placed upstream of the cavity) was also effective but generated slightly more noise outside in the vicinity of the spoiler while slanting the rear wall (by 45^o) was least effective. All these methods were observed to work in fundamentally the same way: by directly reducing the intensity of the lower frequencies which originate from the energy-containing larger vortical structures, i.e. reducing the intensity of the primary vortex. With the spoiler, the shear layer was diffused and little energy was redistributed into the cavity. The jet added more momentum to the shear layer preventing it from dipping into the cavity and impinging on the rear wall thereby feeding little energy into the cavity. In contrast, the slanted rear wall increased flow entrainment in the cavity minimising the mass breathing process thereby weakening the primary vortex.

Chapter 8

Cavity with Stores

Having obtained confidence on the physics of clean cavity flows, studies of non-clean cavities, i.e. the effect of stores inside the cavity, were undertaken. Although results for a 3D, L/D=5, W/D=1 cavity (without doors) with a missile placed along the shear layer plane (i.e. y/D=0) of the cavity are only presented here, the objective is to pave the way for future research on cavity flows with stores. Since the influence of the missile is relatively unknown, the LES approach is used here, which demonstrated good accuracy and consistency for the clean cavity (Chapter 5).

The store used here corresponds approximately to the size of an air-to-air missile without fins and is sting-mounted at the rear of the cavity. The analysis was split into two parts and involved one case with a half-model cavity (with a symmetry boundary condition applied at the cavity centreline for reducing the calculation run-times) and another with a full representation of the missile and the cavity. Details of the grids used for this study are given in Table 8.1. The flow conditions specified for this study were the same as for the clean cavity study, i.e. M=0.85 and Reynolds based on the cavity length (Re_L) of 1 million.

Table 8.1: Information on grids used for the missile (without fins) placed at the shear layer plane of the L/D=5, W/D=1 cavity in the doors-off configuration.

Grid	Overall Points	Points in Cavity	Wallspacing	Blocks in Cavity (Overall)
Clean Cavity without Missile				
Clean LES (Very Fine)	8,388,608	2,097,152	$y = 5 \times 10^{-5}$	64 (256)
Cavity with Missile				
Half-Missile LES	767,250	147,500	$y = 1 \times 10^{-5}$	17 (61)
Full-Missile LES	3,876,000	976,800	$y = 1 \times 10^{-5}$	17 (61)

No experimental data were available for the cavity with the missile configuration so numerical results were compared with the experimental data with no missile to illustrate the

effect of the missile. In addition, numerical results from the 8.5 million point LES grid (with doors-off) are also included for reference. Where the cavity without any missile is referred to, it is denoted as 'baseline'.

8.1 Description of Computational Domain

The computational domain for a half-model cavity with a half-model missile placed on the cavity's shear layer plane at its half-width position (i.e. z/W=0.5) was generated. A symmetry boundary condition was then applied across the cavity half-width position. The mesh distribution on and around the missile and the surrounding symmetry plane is shown in Figure 8.1. The full-model cavity was generated simply by mirroring this grid about the symmetry axis.

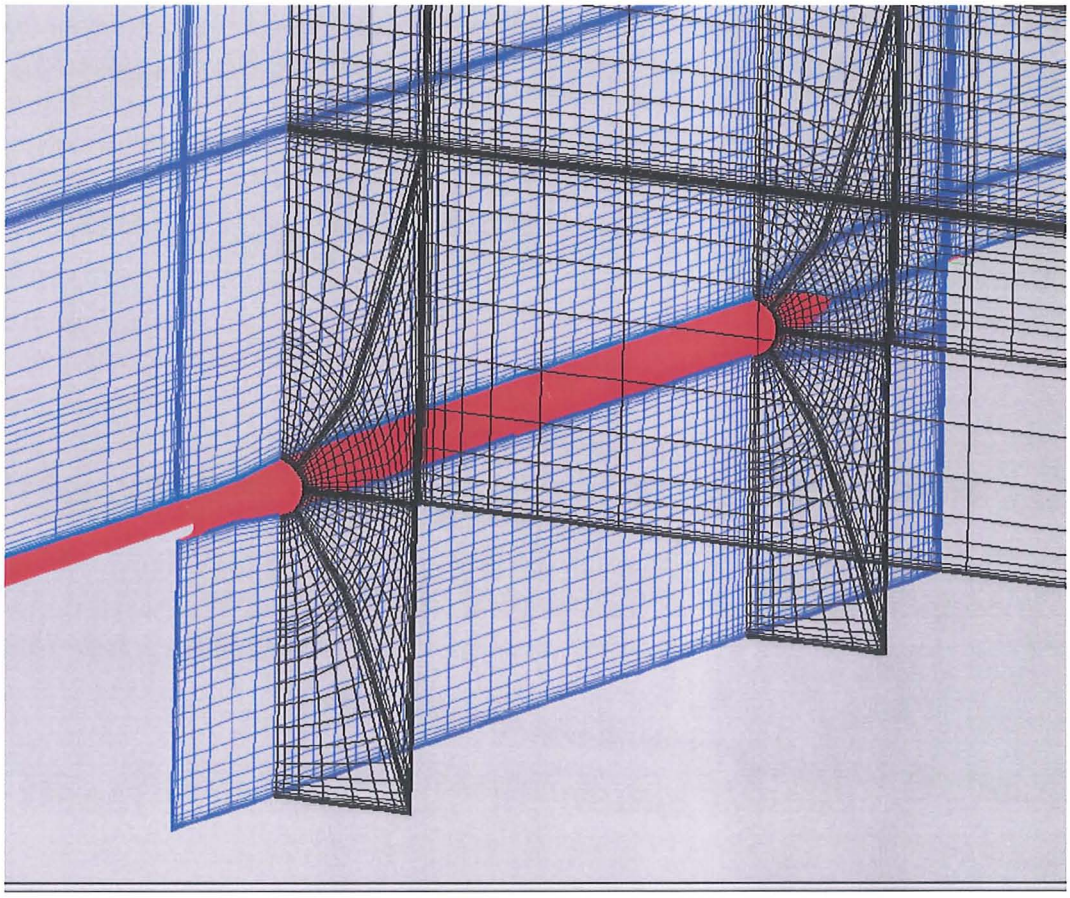

Figure 8.1: Mesh distribution on and around the half-body missile without fins.

Initial results for the half-model missile were attempted on a coarse grid (by LES standards). Although the full missile grid approached 4 million points, the resolution of these grids is admittedly low for LES computations, especially at these Reynolds numbers. However, as was demonstrated in Chapter 5, even relatively low-resolution grids for LES computations have revealed good and consistent agreement with experiment. As a first understanding of the flow inside the cavity with a store, the results presented should therefore hold reasonable merit.

8.2 Acoustic Spectrum Analysis

Analysis of the noise level content along the cavity floor is shown in Figure 8.2, which also includes the pressure signature at the cavity front ($x/L = 0.05$), middle ($x/L = 0.55$) and rear ($x/L = 0.95$). The half-body missile results are depicted by the solid red lines with circular symbols. Two sets of full-body missile results are presented: the green lines with crosses correspond to z/W=0.05, which is where the experimental results are taken, and denoted in the solid magenta lines with square symbols are the full-body missile results at z/W=0.15. The reasoning behind this is to give an indication of the acoustic content across the cavity span, where the cavity centerline is at z/W=0.1. Experimental and numerical results (indicated by the black lines with diamond symbols and blue lines with plus signs, respectively) correspond to the clean cavity with no missile. SPLs for the full-body missile are about 4 dB higher at the cavity rear than the baseline results.

The noise level produced for the half-body missile is generally lower than the full-body missile and is of the same order of magnitude as the baseline results. It would therefore seem that the symmetry boundary condition applied for the half-body missile is a reasonable assumption. For all the numerical results with the missile, the pressure signals show an increase in the wavelengths (Figure 8.2). This is indicative of the lower frequencies being more dominant. Note also that the SPLs for the full-body missile at z/W=0.05 (green line with crosses) and at z/W=0.15 (magenta line with square symbols) overlap each other. The effect of the missile placed at the shear layer plane therefore tends to reduce the spanwise variation of the acoustic content. This will therefore mean that flow features in the spanwise plane will also be more symmetric, unlike for the clean cavity case, as was illustrated in Figure 5.10 in Chapter 5.

8.2.1 Band-Limited Frequency Analysis

Band-limited SPL plots are shown in Figure 8.3, which help to identify which region of the frequency spectrum is more active thereby elucidating what type of flow-field exists in the cavity. As for the clean cavity flow analysis, noise level content across four frequency ranges (i.e. $50\ Hz \leq f \leq 250\ Hz$, $350\ Hz \leq f \leq 450\ Hz$, $500\ Hz \leq f \leq 700\ Hz$ and $750\ Hz \leq f \leq 850\ Hz$) are illustrated. These four frequency bands straddle the first four Rossiter modes typically found for the L/D=5 cavity at a free-stream Mach number of 0.85.

For both half-body and full-body missiles, SPLs are at least 15 dB lower than the baseline experimental and numerical results for frequencies above 350 Hz. For the baseline case, i.e. where no missile is used, the dominant mode is the third Rossiter mode ($\approx 600\ Hz$). When the missile is inserted at the cavity shear layer plane, the intensity of this mode has diminished by as much as 60 dB at the cavity rear (Figure 8.3(c)). The dominant mode has also shifted to the lower end of the frequency spectrum (Figure 8.3(a)) where the noise levels at the cavity rear are of the same order of magnitude as the baseline experimental and numerical results. Even with $50\ Hz \leq f \leq 250\ Hz$, however, the flow at the front of the cavity ($x/L = 0.05$) is significantly quieter than at the rear ($x/L = 0.95$). Differences between the half-body and full-body missile results are not that significant for frequencies above 350 Hz. The greatest difference occurs at the lower frequency end in $50\ Hz \leq f \leq 250\ Hz$ (Figure 8.3(a)), especially at the cavity front. In contrast, comparisons for the full-body missile at two spanwise positions reveal little differences in $50\ Hz \leq f \leq 250\ Hz$ but these become slightly more apparent for higher frequencies. On

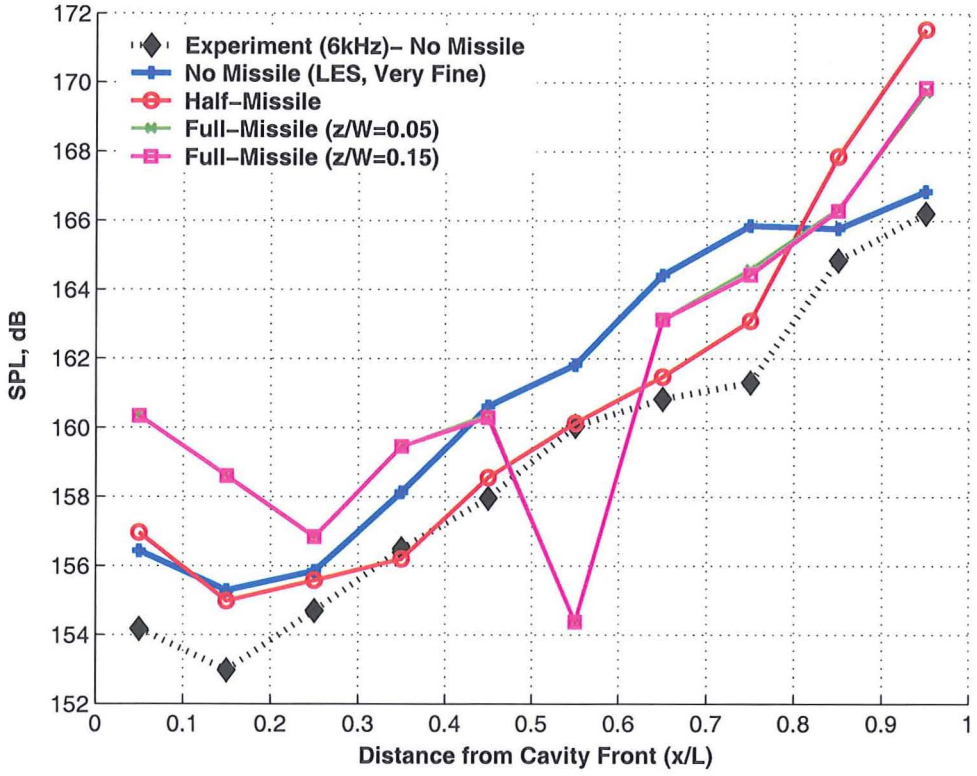

(a) SPL

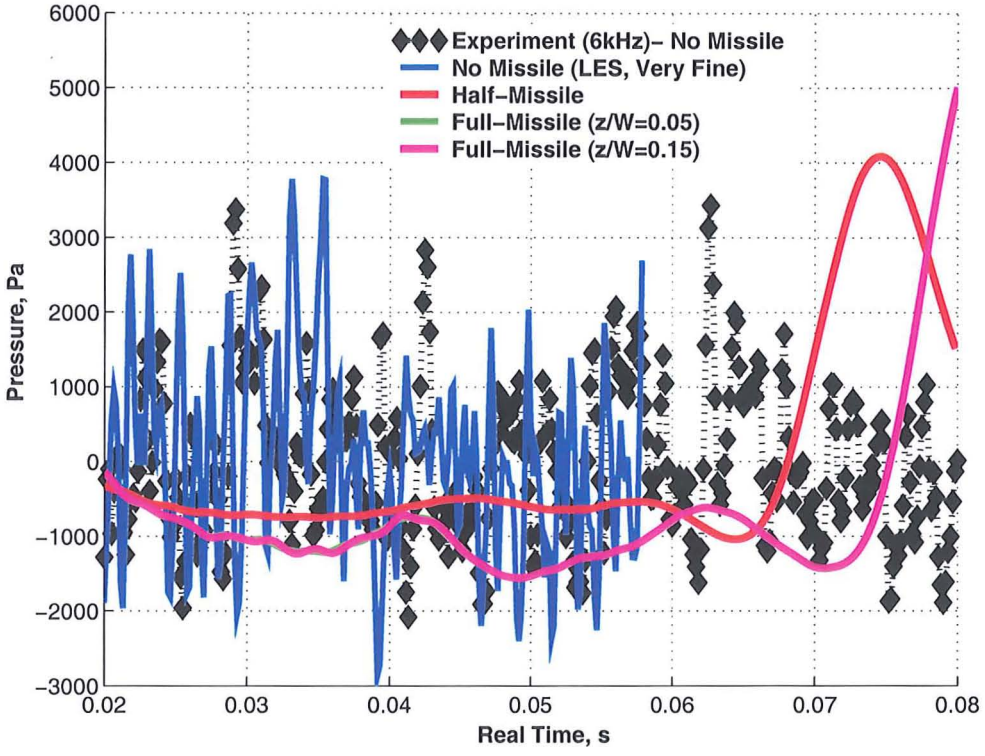

(b) Pressure Traces ($x/L = 0.05$)

Figure 8.2: (continued)

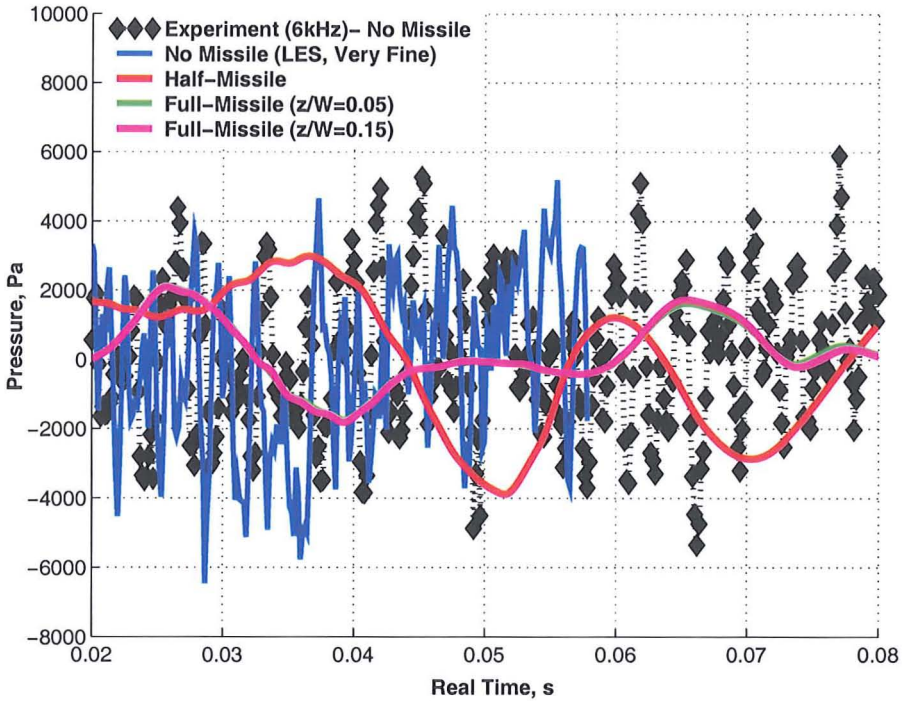

(c) Pressure Traces ($x/L = 0.55$)

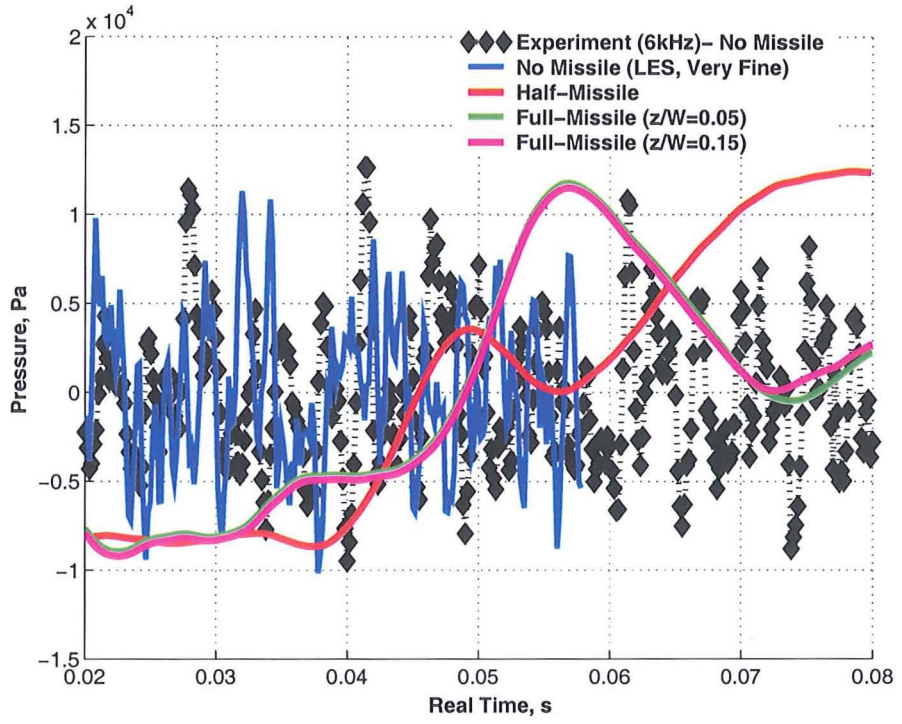

(d) Pressure Traces ($x/L = 0.95$)

Figure 8.2: SPLs and pressure traces (at $x/L = 0.05$, $x/L = 0.55$ and $x/L = 0.95$) along the cavity floor for the 3D, L/D=5, W/D=1 cavity (without doors) with missile without fins using LES for the coarse half-body missile grids and the full-body missile (at two spanwise positions).

the whole, however, the missile appears to damp out the asymmetry of the clean cavity flow.

The fact that the frequencies within the first range ($50\ Hz \leq f \leq 250\ Hz$) are dominant with the missile inserted in the cavity suggests that a wake-like mode is triggered. In the wake mode, the shear layer does not have sufficient energy to span the cavity opening and instead 'rolls up' to form vortical structures near the cavity front that convect downstream. Vortex shedding prevails in this case and the lower frequencies and their harmonics are more evident. In fact, with the missile placed inside the cavity, frequencies much lower than the first Rossiter mode ($\approx 160\ Hz$) exist and it is these that contain most of the energy. Evidence of this is provided in Figure 8.4, which illustrates the noise level content along the cavity floor for frequencies contained within the range $0\ Hz \leq f \leq 50\ Hz$. Both the half-body and full-body missile calculations produce significantly more noise in the cavity within this low frequency range. The half-body missile predicts 12 dB more noise at the rear compared to the baseline experiment results and the full body missile 20 dB more noise. The resolution of the half-body missile grid is much lower than the full-body missile grid and this may explain the discrepancies between the two sets of results.

The lower frequencies can dissipate more quickly into the surroundings and may cause less damage to the surrounding cavity structure and the store. The effect of the missile situated at the shear layer plane therefore appears to pacify the flow inside the cavity shifting the dominance from the higher frequencies to the lower ones. The influence of the missile however is likely to vary depending on where it is located in the cavity as was reported by Baysal *et al.* [139].

8.2.2 Flow-field Visualisation

Visualisation of the instantaneous flow-field inside the cavity with the missile placed in the shear layer plane is provided in Figure 8.5, which illustrates pressure contours with streamlines to show the structures developing inside the cavity. For reference, the flow-field inside the baseline clean cavity without any missile is also shown. All plots are drawn on the same scale and each plot is taken at approximately the same time-step in the flow cycle for direct comparison. Irrespective of whether a half-body or a full-body missile is used, the flow inside the cavity is observed to be more organised compared to the baseline case (Figure 8.5(a)). The flow in the baseline cavity is reasonably organised in the front of the cavity but becomes chaotic as the shear layer begins to break down. Where the missile is inserted in the cavity, typically a large region of recirculation is generated just aft of the leading edge of the missile. The lower SPLs at the cavity rear (Figure 8.2(a)) for the full-body missile may suggest that less flow is retained within the cavity causing little impingement of the flow with the downstream cavity wall. In contrast, much of the flow for the baseline cavity (Figure 8.5(a)) impinges on the cavity rear bulkhead. The high pressure that accumulates at the cavity rear manifests itself in the form of a rising SPL curve in Figure 8.2(a) for the baseline cavity.

The confining presence of the missile body prevents the vortices from moving around inside the cavity. With the missile placed along the shear layer plane, the growth of the shear layer across the cavity opening is also restricted. Consequently, the oscillatory motion of the shear layer is also limited and hence its impingement near the downstream cavity corner avoided. This prevents the creation of acoustical disturbances and high noise levels resulting in a less turbulent flow-field with lower frequencies becoming more

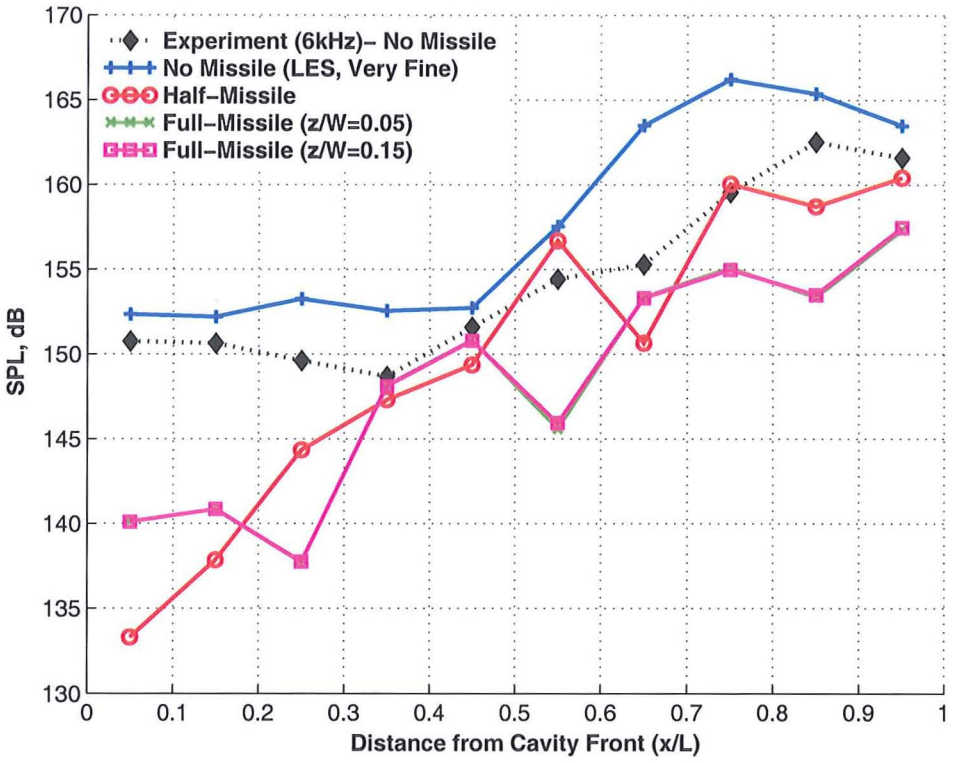

(a) $50\ Hz \leq f \leq 250\ Hz$

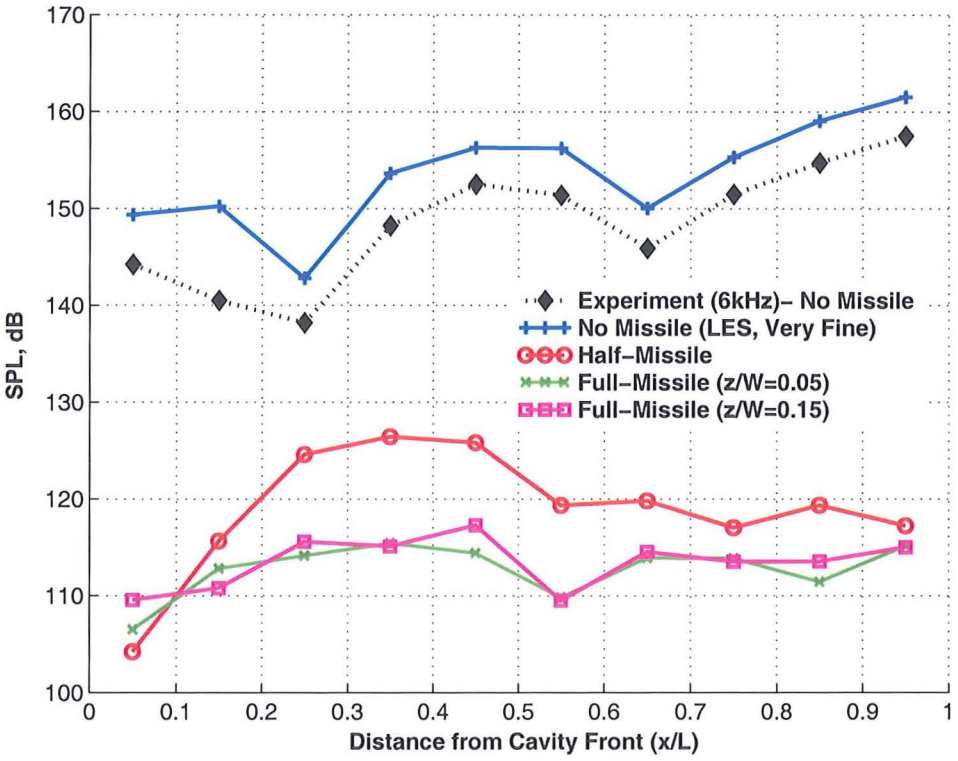

(b) $350\ Hz \leq f \leq 450\ Hz$

Figure 8.3: (continued)

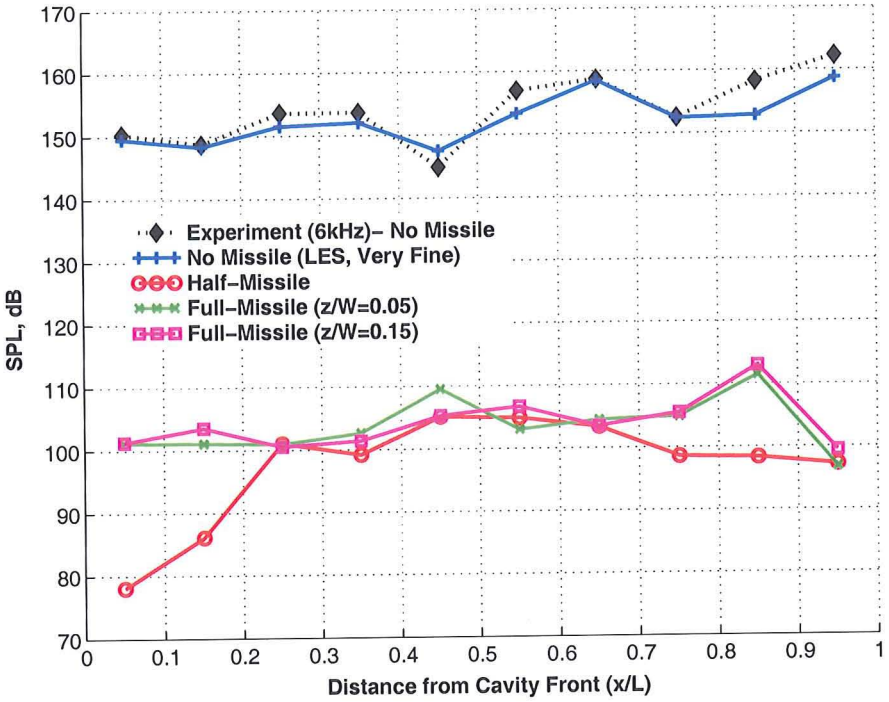

(c) $500\ Hz \leq f \leq 700\ Hz$

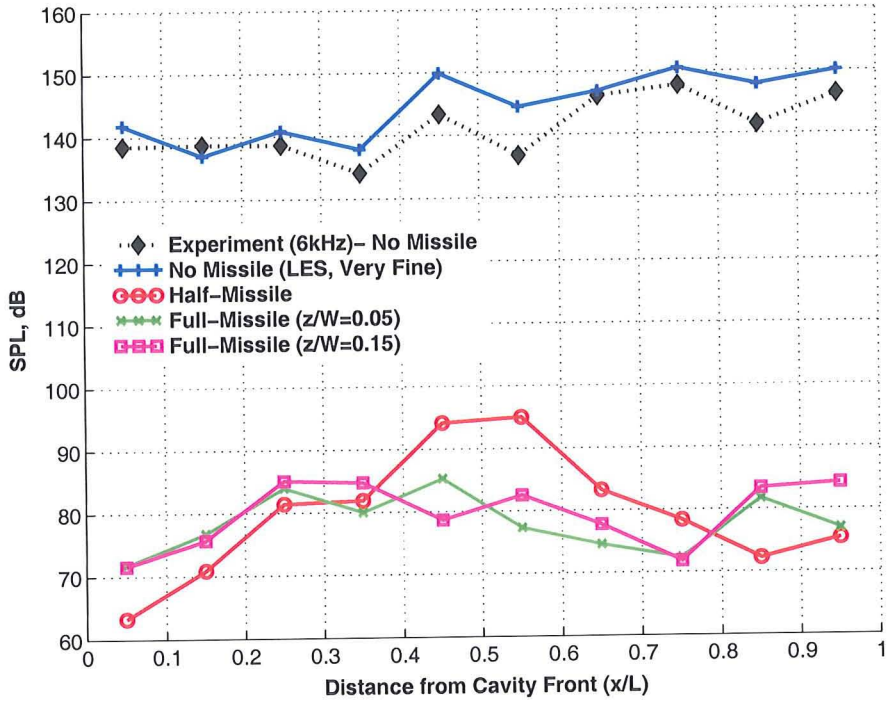

(d) $750\ Hz \leq f \leq 850\ Hz$

Figure 8.3: Band-limited SPLs along the cavity floor for the 3D, L/D=5, W/D=1 cavity (without doors) with missile without fins using LES for the half-body missile grid and the full-body missile (at two spanwise positions).

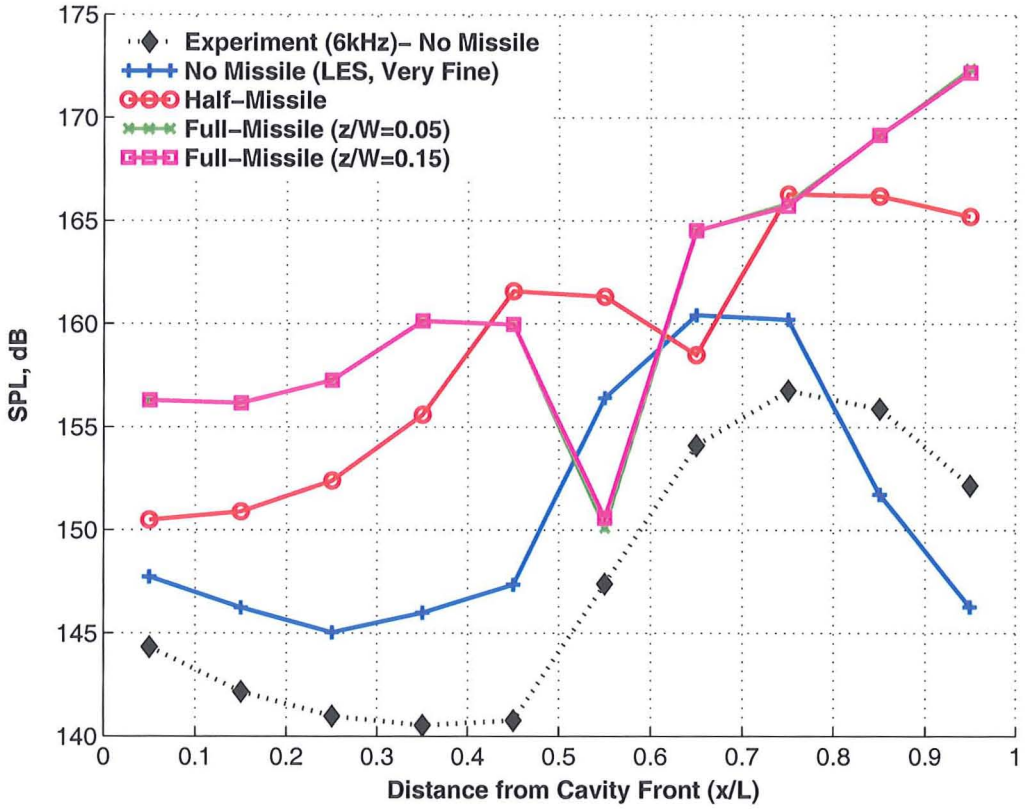

Figure 8.4: Band-limited SPLs within $0\ Hz \leq f \leq 50\ Hz$ along the cavity floor for the 3D, L/D=5, W/D=1 cavity (without doors) with a missile without fins using LES for the coarse and medium half-body missile grids and the fine full-body missile.

dominant. It is also possible that the curved nose of the missile will further promote shear layer breakdown as the flow will be forced to 'swirl' into the cavity. This results in more of the energy being redistributed from the streamwise and transverse directions into the spanwise direction. Investigations with finer grids will provide more conclusive evidence of this.

8.3 Concluding Remarks

Numerical analysis of the flow-field inside the cavity (without doors) influenced by the presence of a store placed along the shear layer plane is investigated. Comparisons were made with experiment corresponding to the cavity without missile to illustrate the effect of the missile on the flow-field.

Results for the missile without fins showed that the flow inside the cavity is more organised with lower frequencies appearing to be more dominant, which are less detrimental to the surrounding structure and dissipate quickly into the environment. The use of a symmetry plane along the cavity longitudinal axis appears to be justified when a missile has been inserted at the shear layer plane of the cavity. Comparisons of the acoustic content at two spanwise locations on the cavity floor with the full-body missile revealed little variation. This suggests that the effect of the missile (when placed at the shear layer) is to reduce the asymmetry in the flow that was previously observed in the clean cavity configuration.

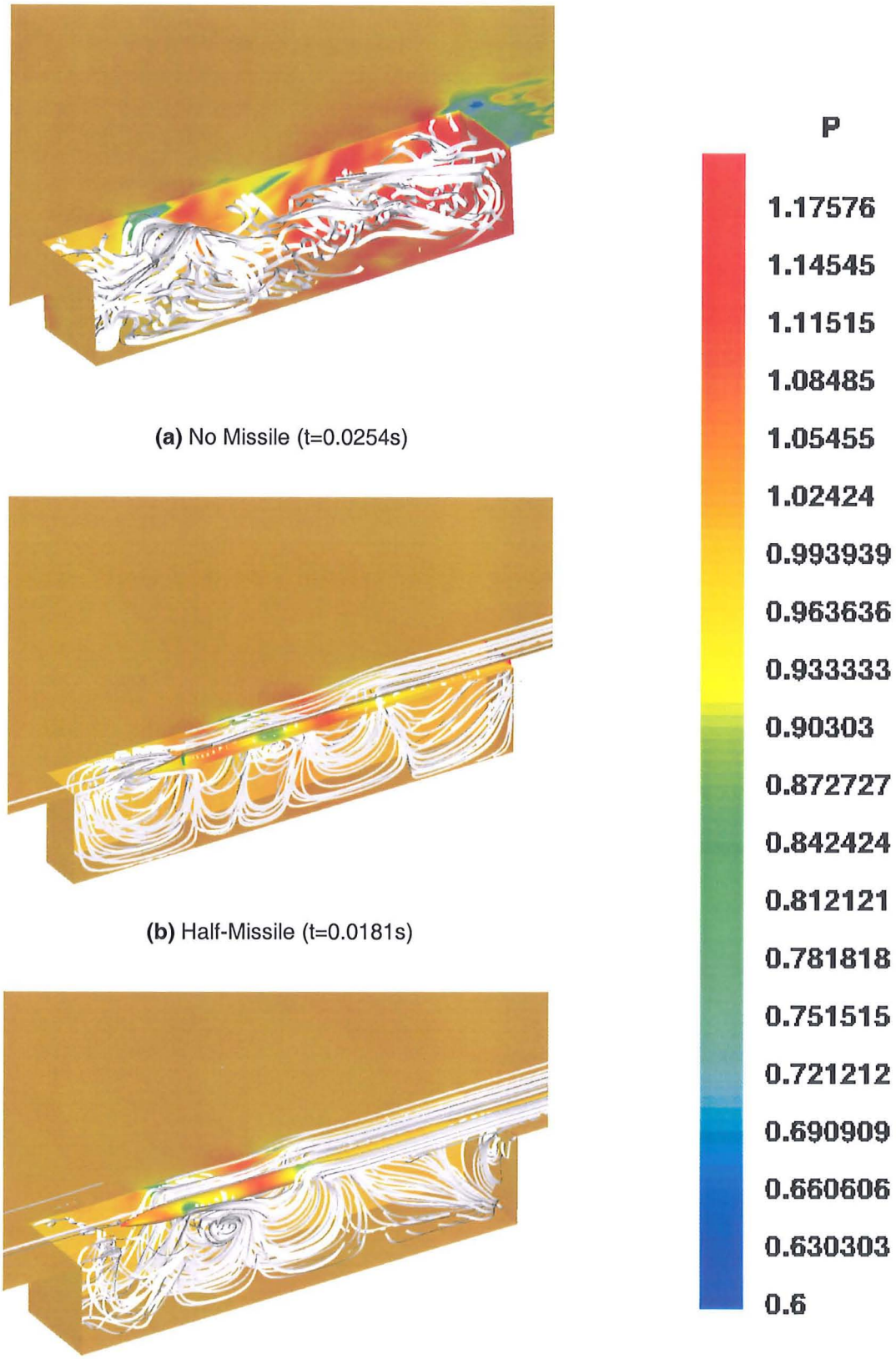

(a) No Missile (t=0.0254s)

(b) Half-Missile (t=0.0181s)

(c) Full-Missile (t=0.0181s)

Figure 8.5: Instantaneous pressure contours for the clean cavity (without doors) with and without missile (without fins), where the missile is positioned at the shear layer plane of the cavity. Clean cavity results without missile obtained using 8.5 million LES grid.

Further studies should target to analyse the flow around the missile with and without fins. The effect of doors on the cavity flow-field with a missile as well as different positions of the missile inside the cavity should also be investigated.

Chapter 9

Conclusions

The main conclusions drawn from this project are now summarised and suggestions are put forward regarding future research on cavity flows.

9.1 Conclusions from the Present Work

Numerical computations of a weapons bay modelled by 2D and 3D open rectangular cavities at a Mach number of 0.85 were performed with the PMB code developed at CFD Laboratory of Glasgow University. The upstream boundary layer was turbulent and the Reynolds number based on the cavity length was 6.783 million. The cavity with a length-to-depth ratio (L/D) of 5 (and width-to-depth ratio (W/D) of 1 for 3D cavities) was selected for the benchmark case due to the readily available experimental data. Pressure and PIV measurements were performed by Ross *et al.* [6**?** , 7] at DERA Bedford and the data used to validate the numerical results. Three different turbulence modelling techniques were applied in this project: URANS, LES and DES.

The URANS method was initially used for the 2D, L/D=5 cavity in conjunction with a variety of two-equation turbulence models to assess their capability in predicting the flow features. Effects of spatial and temporal refinement were investigated for the standard Wilcox $k-\omega$ and Menter's Baseline $k-\omega$ and SST models. Temporal refinement improved the prediction of the higher frequencies as the more intermittent scales were better resolved. Influence of grid refinement was more profound and found to be different for different turbulence models. Analysis of unsteady pressure measurements with experiment revealed that all models gave reasonable agreement with experiments on coarse grids, with the SST model providing the best prediction of the frequency and noise content. A good description of the flow-field in the cavity was also obtained with coarse grids for all turbulence models investigated. As the grid density was increased, however, the predictive capability of the models and their agreement with experiment deteriorated. For coarse grids, all models correctly predicted a shear-layer mode and a twin-vortex flow cycle governed by shear layer deflection and self-sustained oscillations. For the $k-\omega$ model, the dominant tone shifted to a lower frequency mode with grid refinement. For the Baseline $k-\omega$ model, a transition to the wake mode flow cycle (governed by vortex-shedding of large-scale structures) occurred. The SST model is similar in formulation to the Baseline $k-\omega$ model so it produced similar results. All models over-predicted the intensity of the

acoustic tones relative to experiment. With spatial refinement, the largest increase in the frequency magnitudes was associated to the first mode. As the grids were refined, the higher frequencies were suppressed for all models. The flow for the wake mode with finer grids with the Baseline $k-\omega$ and SST models was more violent and produced higher noise levels. Although the wake mode has been been identified in 2D cavities in previous experiments and numerical computations, this was at lower Reynolds numbers where the state of the upstream boundary layer was laminar. This change in the flow physics of the cavity was therefore attributed to the sensitivity of the employed turbulence models.

Comparisons of velocity and turbulent distributions inside the cavity with PIV measurements (where possible) also revealed poor agreement, especially with finer grids. However, this type of analysis did highlight the significance of the turbulent processes in driving the cavity flows. The state of the upstream boundary layer was critical in determining the flow characteristics in the cavity. The $k-\omega$ model, in particular, predicted an over-turbulent and thick boundary layer, resulting in a thick shear layer across the cavity opening. The flow was less prone to separation and fluctuations and most of the flow unsteadiness was damped out. The $k-\omega$ model therefore suppressed the higher frequencies and influenced the frequency content in the cavity. On the other hand, the Baseline $k-\omega$ and SST models limited the production of turbulence and the boundary layer for the coarse grid was thinner relative to the $k-\omega$ model. However, the Baseline $k-\omega$ and SST models over-compensated for this by adding too much momentum into the vortices making the flow more violent and unsteady. Flow separation was found to occur further upstream with the Baseline $k-\omega$ and SST models with finer grids and resulted in the formation of the wake mode.

In terms of the role turbulence has to play in cavity flows, the turbulent kinetic energy was found to control the amount of energy and momentum inserted into the cavity. The eddy viscosity levels, which identified the level of turbulence in the flow, combined with the turbulent kinetic energy both tend to have a strong influence on the shear layer thickness. High eddy viscosity (and low turbulent kinetic energy) levels led to more viscous (and slower) vortices and turbulent shear layers that were less free to move. Noise levels produced were still high due to the interaction of the vortices and shear layer with each other and cavity walls. The thicker, turbulent shear layer was however less prone to deflections and higher frequencies associated with the interaction of the shear layer with the downstream wall and the mass breathing process from the movement of the shear layer above and below the downstream corner were reduced. The effect of the turbulent stresses is difficult to isolate as it is strongly coupled with the turbulent kinetic energy. Nonetheless the turbulent shear stress was found to affect the redistribution rate of momentum from the shear layer into the cavity and therefore controls the unsteadiness in the flow. The lower shear stresses observed with the Baseline $k-\omega$ and SST models resulted in the flow inside the cavity to be more violent and unsteady, especially with finer grids. Higher shear stresses in the $k-\omega$ model appeared to minimise the fluctuations of the shear layer probably by making it less prone to movement from the vortical structures in the cavity. In contrast, normal stresses were found to stretch the vortical structures, altering their physical dimensions, and therefore may affect the breakdown of the shear layer.

Despite the difficulties with the turbulence models predicting the cavity flow features of the L/D=5 cavity with finer grids, a good qualitative description of the flow was found to be obtained with coarse grids. For better quantitative agreement with experiment, it is anticipated that non-linear turbulence models are likely to give better estimates of the level of turbulence in the cavity and therefore provide better predictions of the flow structures in the cavity.

LES (using the standard Smagorinsky SGS) and DES (with the one-equation Spalart-Allmaras turbulence model) was then applied to the 3D L/D=5, W/D=1 cavity with and without doors and compared with URANS (using Menter's Baseline $k-\omega$ model) and experiment. With doors-off, the flow is governed by intense mixing and the 3rd Rossiter mode ($\approx 600\ Hz$) was found to be the dominant mode with URANS found to predict the SPLs and the shape of the SPL curve incorrectly. Band-limited frequency analysis was adopted to illustrate the variation of noise levels within separate frequency bands and indicated that both LES and DES fared much better than URANS to predict the shapes of the SPL curves across all the four frequency bands used. URANS was found to predict the dominant 3rd Rossiter mode well but failed to provide the same level of accuracy for any of the frequencies higher or lower than this dominant mode. Analysis of flow-field plots for the doors-off cavity with Menter's Baseline $k-\omega$ model and DES revealed that DES predicted a breakdown of the shear layer while Menter's baseline $k-\omega$ model did not.

With doors-on, the flow is governed by a dual-vortex cycle and the 2nd Rossiter mode ($\approx 380\ Hz$) is dominant. Initial analysis of the doors-on results revealed that better prediction was obtained with 3D URANS than with DES and LES. Band-limited frequency analysis, however, revealed that 3D URANS predicted the dominant (2nd Rossiter) mode well but had difficulty in capturing most of the higher (and in some cases, some of the lower) frequencies as well, as was observed in the doors-off configuration. In contrast, both DES and LES fared much better in predicting correctly the shapes of the SPL curves and the intensity of the frequency tones. Furthermore, URANS was typically found to consistently over-predict the acoustic tone magnitudes in the doors-on cavity. Results for a 2D cavity were also used since the 2D cavity was assumed to be a good representation of the full 3D cavity with doors-on. These 2D results were found to over-predict the dominant 2nd Rossiter mode in the doors-on cavity by almost double the experimental values. This was attributed to a much thicker and stronger oncoming boundary layer in the 2D cavity suggesting that the 2D approximation may be a less accurate approximation for the doors-on cavity.

Analysis of the turbulent decay characteristics revealed a peak at around 4-7 kHz in the experimental and numerical results. Since this is too high to be narrowband, its source may be attributed to the Kelvin-Helmholtz instability. Since this peak was also found in the 2D cavity results, there is some merit to this hypothesis. Investigation of the broadband spectrum emphasised the inadequacy of URANS to account for broadband noise. Comparisons with PIV measurements showed consistently good agreement at the cavity front ($x/L = 0.05$) and middle ($x/L = 0.55$) using DES and LES, while URANS was found to over-predict the strength of the vortex in the cavity, especially at the middle position. At the cavity rear, however, agreement with PIV deteriorated between LES and DES and these discrepancies may be attributed to poor resolution in the PIV experiment at this position. It was concluded that high-resolution experimental data are just as much required for accurate prediction of highly unsteady and turbulent cavity flow-fields as high-resolution numerical data, i.e. simulation. Another conclusion was that it was possible to obtain good predictions of the cavity environment even with low to moderate grid resolutions for LES/DES computations.

URANS was then revisited in order to determine its range of applicability for cavity flows. This was accomplished by investigating the flow in cavities with different aspect ratios. Two-dimensional deep, open cavities (L/D=2), transitional cavities (L/D=10) and closed cavities (L/D=16) were studied using the SST turbulence model and parametric studies in time and space were conducted. Though the SST model results on the L/D=5 cavity

gave a reasonable prediction, it was found that the SPL amplitudes, shape of the SPL curve and the frequencies were more consistently predicted with grid refinement as the cavity L/D ratio was increased. With longer cavities, coupling between the shear layer and the vortical structures inside the cavity becomes less intense. The flow is less unsteady and turbulent and lower frequencies are also more dominant. Changes to grid density influenced the cavity flow physics less dramatically and the turbulence model coped better, resolving the flow features more consistently. In contrast, for deeper cavities such as the L/D=5 cavity, the flow is more unsteady and turbulent and coupling between the shear layer and acoustics is stronger. Despite a reasonable qualitative prediction of the flow-field with coarse grids, linear statistical turbulence models were however more sensitive to grid refinement in this case and the agreement with experiments deteriorated. It was further concluded that URANS was a good and accurate modelling option for closed cavities, i.e. $L/D \geq 16$, while LES/DES would be required for better prediction of open and transitional cavities, i.e. $L/D < 16$.

Calculations with different control methods with the L/D=5 cavity were then conducted in an attempt to reduce the high noise levels and large frequency content observed inside the cavity. Effectiveness of passive control methods such as the spoiler and slanted cavity walls and active open-loop control methods such as continuous mass injection were investigated. Results from the spoiler placed upstream of the cavity with its height equivalent to the height of the boundary layer, slanted cavity rear wall at 45^o and a steady jet fired from the front wall just below the cavity lip were compared. Steady jet blowing was found to be most effective in mitigating the noise level and frequency content in the cavity. The spoiler was also effective but generated slightly more noise outside in the vicinity of the spoiler while slanting the rear wall (by 45^o) was least effective. All these methods were observed to work in fundamentally the same way: by directly reducing the intensity of the lower frequencies which originate from the energy-containing larger vortical structures, i.e. reducing the intensity of the primary vortex. With the spoiler, the shear layer was diffused and little energy was redistributed into the cavity. The jet added more momentum to the shear layer preventing it from dipping into the cavity and impinging on the rear wall thereby feeding little energy into the cavity. In contrast, the slanted rear wall increased flow entrainment in the cavity minimising the mass breathing process thereby weakening the primary vortex.

Numerical analysis of the flow-field inside the cavity (without doors) influenced by the presence of a store (without fins) placed along the shear layer plane was also investigated. A half-cavity model was used to save computational run-time as well as a full-body missile with full cavity. Results for the missile without fins showed that the flow inside the cavity is more organised with lower frequencies appearing to be more dominant, which may be less detrimental to the surrounding structure as they dissipate quickly into the environment. The use of a symmetry plane along the cavity longitudinal axis appears to be justified when a missile has been inserted at the shear layer plane of the cavity since both the half-body and full-body results were similar. Comparisons of the acoustic content at two spanwise locations on the cavity floor with the full-body missile revealed little variation. This suggests that the effect of the missile (when placed at the shear layer) is to reduce the asymmetry in the flow that was previously observed in the clean cavity configuration.

9.2 Further Work

Since much of the work focused on a particular cavity geometry, one aspect of future research would be to analyse cavity flows with different dimensions, especially with different planform aspect ratios. As an extension, the effects of Mach number and Reynolds number are also addressed as possible areas of research. The most obvious areas of further work would however focus on flow control and the simulation of stores in cavities.

From the flow control perspective, implementation of pulsating and/or synthetic jets would be a natural step forward. The effect of jet frequency and angle as well as its position could be considered as parametric studies for the pulsating jet. An extension may then be to look at closed-loop control in cavities. One other area would be to extend the work performed on passive control methods over a broader spectrum of flow conditions. The spoiler has been found to be particularly efficient but has been tested only for one flow condition. Different configurations of the spoiler (such as different inclinations to the flow) might be explored to see if its efficacy can be maintained over a greater range of speeds. Since the work presented here has focused on the L/D=5 open cavity, flow control strategies on longer cavities could also be performed. Based on the success of LES/DES methodologies in cavity flows, an obvious aspect of further research would be to use LES/DES for flow control as well.

To study the flow in the cavity with stores, a natural extension would be to apply simulation strategies for the store (with and without fins) at different positions in the L/D=5 cavity with and without doors. Forces on the stores could also be calculated and compared with experiments. The effect of stores in cavities of different L/D ratios could then also be investigated. Based on the analysis of the flow in the cavity with stores, flow control methods as used for the clean cavity could then be applied to ameliorate the environment in the non-clean cavity, if required. Another area of research would be to simulate the full store separation problem with the use of Chimera overset grids or sliding planes.

One final candidate for further research is the application of acoustical analogies such as the Ffowcs Williams-Hawkings and/or Kirchoff's methods to study cavity flow aeroacoustics.

Appendix A

Flow Control: Detailed Results for the L/D=5 Cavity

The results presented here provide a more detailed account of the flow control study presented previously in Chapter 7. The effect of the spoiler at different positions and heights, slanted cavity walls at different positions and angles and continuous mass injection at different positions and exit jet velocities are highlighted here. Figure 7.1 in Chapter 7 illustrates all analyses conducted for the three control methods studied here. To reiterate, cases where no control method is used are denoted as 'baseline'. No experimental data were available for this control study so results were compared to the computational 'baseline' case as well as to the corresponding experimental results (i.e. for the clean, 2D, L/D=5 cavity where no control method was used) to illustrate the effectiveness of the control method.

Table A.1 provides a description of all the grids used for the control studies. Information on the baseline, 2D, L/D=5, coarse cavity grid is also included. For clarity, the three different spoiler configurations (detailed in the following section) are numbered. Case 1 denotes the LE spoiler whose coordinates correspond to $x_{sp}/L = -0.2, y_{sp}/L = 0$, Case 2 for the LE spoiler with coordinates $x_{sp}/L = -0.1, y_{sp}/L = 0$ and Case 3 for the TE spoiler with coordinates $x_{sp}/L = 1, y_{sp}/L = 0$. Case 2 comprises two further sub-sets: one with the spoiler height set to 1δ (Case 2a) and the other with the height doubled to 2δ (Case 2b), where δ is the height of the boundary layer. The value of the boundary layer height was calculated to be the distance above the flat plate at which the velocity was equal to $0.99U_\infty$. This gave a value of 0.021L and was found to be similar to that specified in the experiments conducted by Ross and Peto [11].

For slanted cavity walls, five different configurations were employed: three involved slanting the front wall, rear wall and both walls independently at a fixed angle of 45° with a further two configurations concentrated on the rear cavity wall slanted at 30° and 60° as well to assess the effect of slant angle. For the steady jet, three different positions of the jet were investigated: jet applied upstream of cavity, on the front and rear walls. A further test case with the jet fired from the cavity front wall was conducted at a higher exit jet Mach number (M_j). For all other steady jet blowing cases, the exit jet Mach number was fixed to 10% of the free-stream Mach number, $M_\infty = 0.85$.

Table A.1: Information about the grids used for the 2D, L/D=5, clean cavity control study.

Location	Overall Points	Points in Cavity	Wallspacing	Blocks in Cavity (Overall)
2D L/D=5 Clean Cavity				
(Coarse)	33,250	10,302	$y = 1.05 \times 10^{-5}$	1 (6)
2D L/D=5 Cavity with Spoiler				
LE (Case 1)	80,658	10,200	$y = 5 \times 10^{-6}$	2 (17)
LE (Case 2a)	150,450	22,800	$y = 5 \times 10^{-6}$	2 (17)
LE (Case 2b)	80,658	10,200	$y = 5 \times 10^{-6}$	2 (17)
TE (Case 3)	65,860	10,200	$y = 5 \times 10^{-6}$	2 (15)
2D L/D=5 Cavity with Slanted Walls				
Front Wall ($\theta = 45^o$)	35,394	11,016	$y = 5 \times 10^{-6}$	2 (8)
Rear Wall ($\theta = 30^o$)	31,212	9,894	$y = 5 \times 10^{-5}$	2 (8)
Rear Wall ($\theta = 45^o$)	31,212	9,894	$y = 5 \times 10^{-5}$	2 (8)
Rear Wall ($\theta = 60^o$)	31,212	9,894	$y = 5 \times 10^{-5}$	2 (8)
Front & Rear Walls ($\theta = 45^o$)	31,926	10,302	$y = 7 \times 10^{-5}$	1 (6)
2D L/D=5 Cavity with Steady Jet Blowing				
Front Wall ($M_j = 0.1M_\infty$)	46,972	25,654	$y = 5 \times 10^{-6}$	4 (9)
Front Wall ($M_j = 0.2M_\infty$)	46,972	25,654	$y = 5 \times 10^{-6}$	4 (9)
Rear Wall ($M_j = 0.1M_\infty$)	47,174	25,856	$y = 5 \times 10^{-6}$	4 (9)
Upstream ($M_j = 0.1M_\infty$)	103,178	30,408	$y = 5 \times 10^{-6}$	6 (24)

A.1 Passive Control: Spoiler

The spoiler's position relative to the cavity was varied to study its effect on the cavity acoustics and flow structures. The width (w_{sp}) of the spoiler was kept fixed at 0.25 inches ($= 0.0125L$). Details of the grids used in this case are provided in the previous section in Table A.1. A schematic of the different spoiler positions and corresponding dimensions are illustrated in Figure 7.1(a). Three different spoiler positions were investigated: two with the spoiler positioned ahead of the cavity front wall and one at the downstream wall. For the two LE spoilers, one was placed at a distance equal to the depth of the cavity ahead of the cavity lip ($x_{sp}/L = -0.2$, $y_{sp}/L = 0$) and another at half that distance ($x_{sp}/L = -0.1$, $y_{sp}/L = 0$). The final computation was performed with the spoiler located at the downstream cavity corner ($x_{sp}/L = 1$, $y_{sp}/L = 0$). For all positions the standard height of the spoiler (h_{sp}) was specified to 1δ. For the leading-edge spoiler (i.e. where the spoiler is located upstream of the cavity front corner) at $x_{sp}/L = -0.1$, the height of the spoiler was varied from 1δ to 2δ to assess the influence of spoiler height.

A.1.1 Effects of Spoiler Position

Pressure traces at three stations along the cavity floor ($x/L = 0.05$, $x/L = 0.55$ and $x/L = 0.95$) as well as SPLs for three different positions of the spoiler corrresponding to Cases 1, 2a and 3 (with a fixed height of δ) in Table A.1 are illustrated in Figure A.1. The first 0.03s

of the signal were discarded as transient and the remaining signal was used to calculate the SPLs. For proper comparison, the signals of the computations were sampled at the same rate of 31.25 kHz as the experiments.

Generally speaking, the further upstream the spoiler is positioned, the less is the noise produced inside the cavity. For the LE spoiler located furthest upstream (Case 1), denoted by a red line with circular symbols, pressure amplitudes are completely damped out resulting in a drop in the SPLs by as much as 30 dB from experiment. This results in a flat SPL curve (Figure A.1(a)) and is indicative of frequencies being damped out. As the spoiler is moved closer to the front corner (Case 2a), more noise is generated at the cavity front $(x/L = 0.05)$ and rear $(x/L = 0.95)$ as is indicated by the peaks in the SPL curve at about $x/L = 0.15$ and $x/L = 0.9$, respectively. Variations in the pressure signal become greater at these locations as the spoiler is moved closer to the front. These fluctuations are however much smaller than the experimental pressure oscillations and so the pressure signal appears flat for the scale drawn in Figures A.1(b)—A.1(d). Noise levels are consequently slightly higher for this case relative to the spoiler furthest upstream (Case 1) by about 5 dB but this is still about 25 dB lower than experiment at the cavity rear $(x/L = 0.95)$.

When the spoiler is placed at the downstream cavity corner (Case 3), pressure amplitudes increase significantly resulting in noise levels 6-7 dB higher at the cavity rear (Figure A.1(a)). Wavelengths of the pressure oscillations (denoted by magenta lines with square symbols) for the trailing-edge spoiler are found to be greater than experiments suggesting that lower frequencies are more dominant. This shift in the dominance from a higher acoustic tone to a lower one may suggest that the wake mode has been activated.

A.1.1.1 Band-Limited Frequency Analysis

SPL variations within four frequency ranges are provided in Figure A.2 and give a more elaborate account of the effects of spoiler position on the cavity flow processes. Although both leading-edge spoilers (Cases 1 and 2a) are effective in suppressing the large noise levels typically exhibited in the clean L/D=5 cavity, the greatest suppression occurs when the spoiler is furthest upstream from the cavity's front corner (Case 1).

With the spoiler furthest upstream (Case 1), most noise is produced from frequencies in the first band (Figure A.2(a)) with higher frequencies making negligible contributions. Reduction in noise becomes less significant as the leading-edge spoiler is moved closer to the cavity front corner (Case 2a). SPL amplitudes are generally similar to the spoiler located furthest upstream within the first frequency range $(50\ Hz \leq f \leq 250\ Hz)$. Noise levels are also significantly higher (by about 30 dB) for the first frequency band compared to the other bands (Figure A.2(a)) and this is testament to the fact that frequencies in this band contribute most to the overall noise level. Where the differences lie between the spoiler located closer to the cavity lip (Case 2a) and further upstream (Case 1) is in the higher frequency bands. For the second bandwidth $(350\ Hz \leq f \leq 450\ Hz)$, the shape of the SPL curve begins to resemble the 'W' shape observed in the no-spoiler configuration suggesting that comparatively more activity occurs along the floor as the spoiler is moved closer to the lip. For subsequent frequency ranges, noise levels are typically higher for the Case 2a spoiler than for the Case 1 spoiler.

Suppression of the higher frequencies however deteriorates as the spoiler is moved to aft of the cavity (Case 3). An increase of more than 5 dB in SPLs relative to experiment

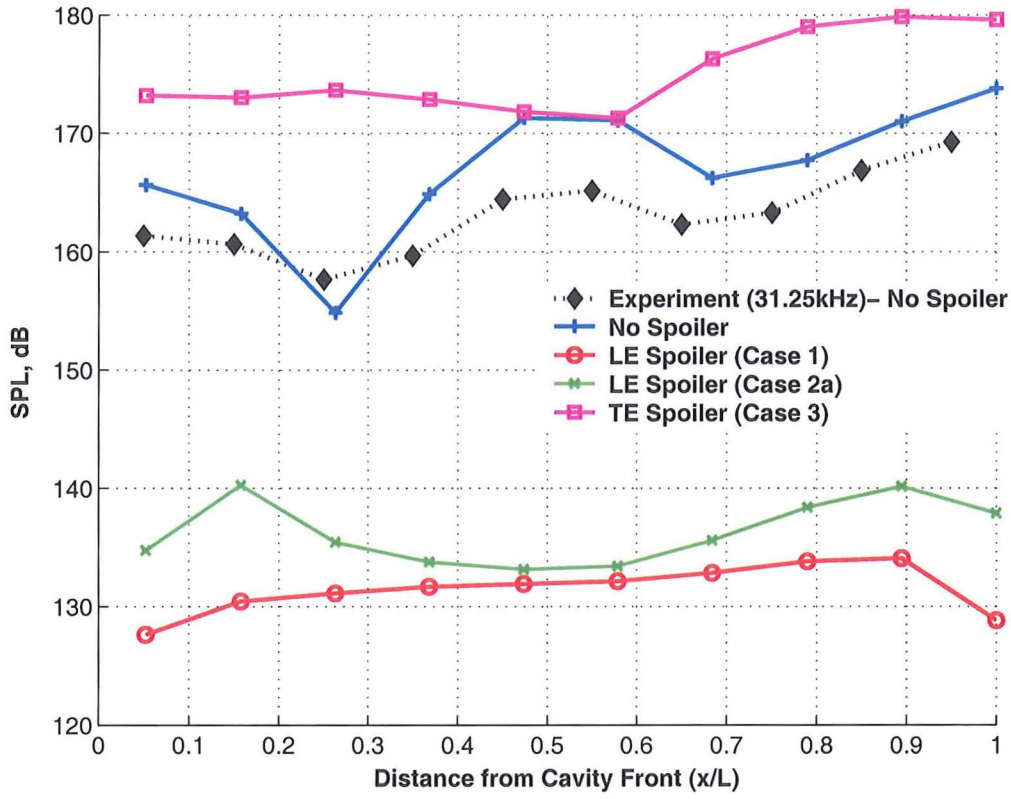

(a) SPLs

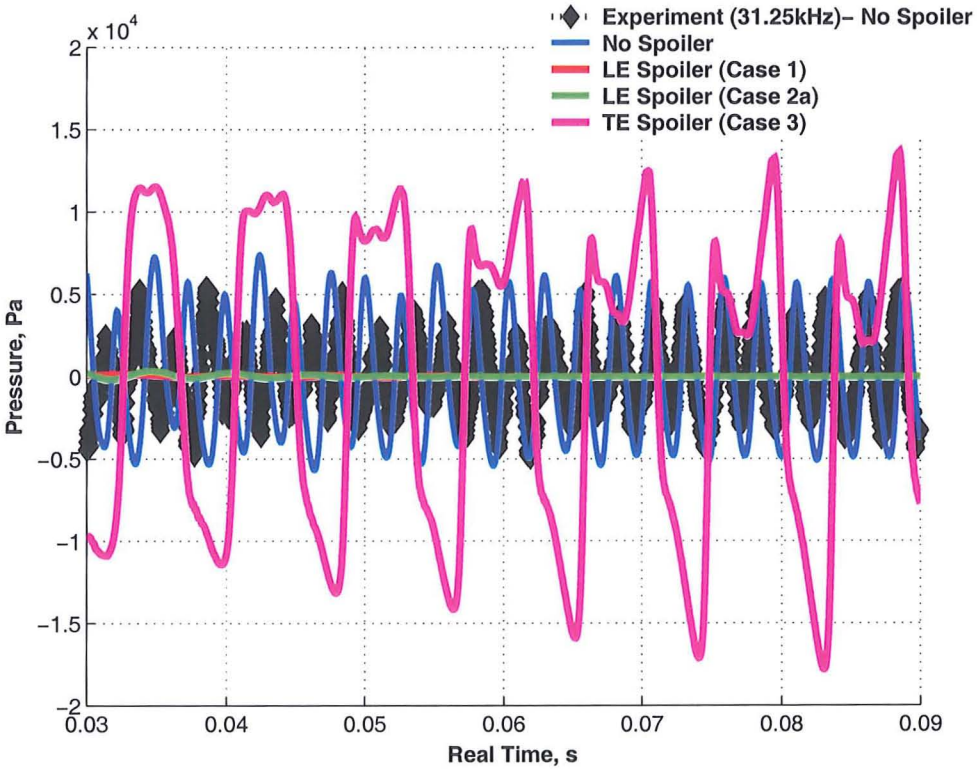

(b) Pressure Traces ($x/L = 0.05$)

Figure A.1: (continued)

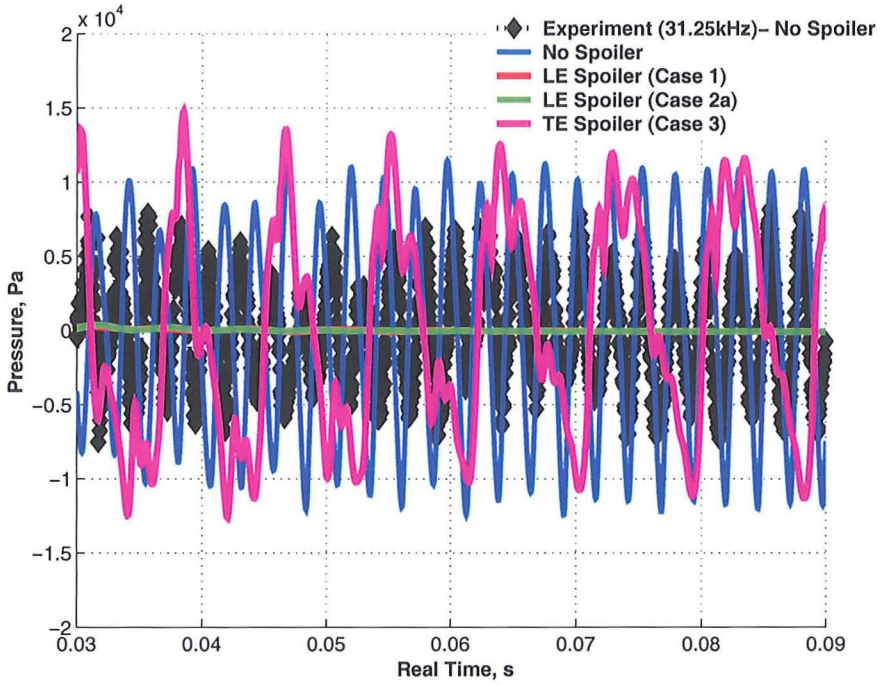

(c) Pressure Traces ($x/L = 0.55$)

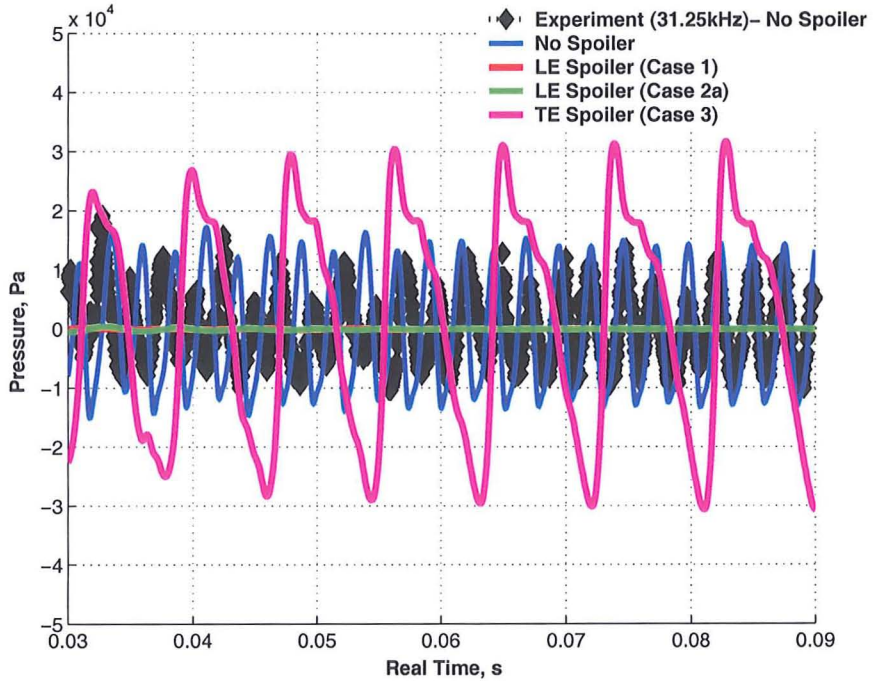

(d) Pressure Traces ($x/L = 0.95$)

Figure A.1: SPLs and pressure traces (at $x/L = 0.05$, $x/L = 0.55$ and $x/L = 0.95$) along the cavity floor of the 2D, L/D=5 cavity using the SST turbulence model with: LE Spoiler (Case 1), LE Spoiler (Case 2a), TE Spoiler (Case 3). CFD and experimental results with no spoiler also included. Case 1: $x_{sp}/L = -0.2$, $y_{sp}/L = 0$; Case 2a: $x_{sp}/L = -0.1$, $y_{sp}/L = 0$; Case 3: $x_{sp}/L = 1$, $y_{sp}/L = 0$. Height (h_{sp}) and width (w_{sp}) kept fixed to $1\delta = 0.021L$ and $0.0125L$, respectively.

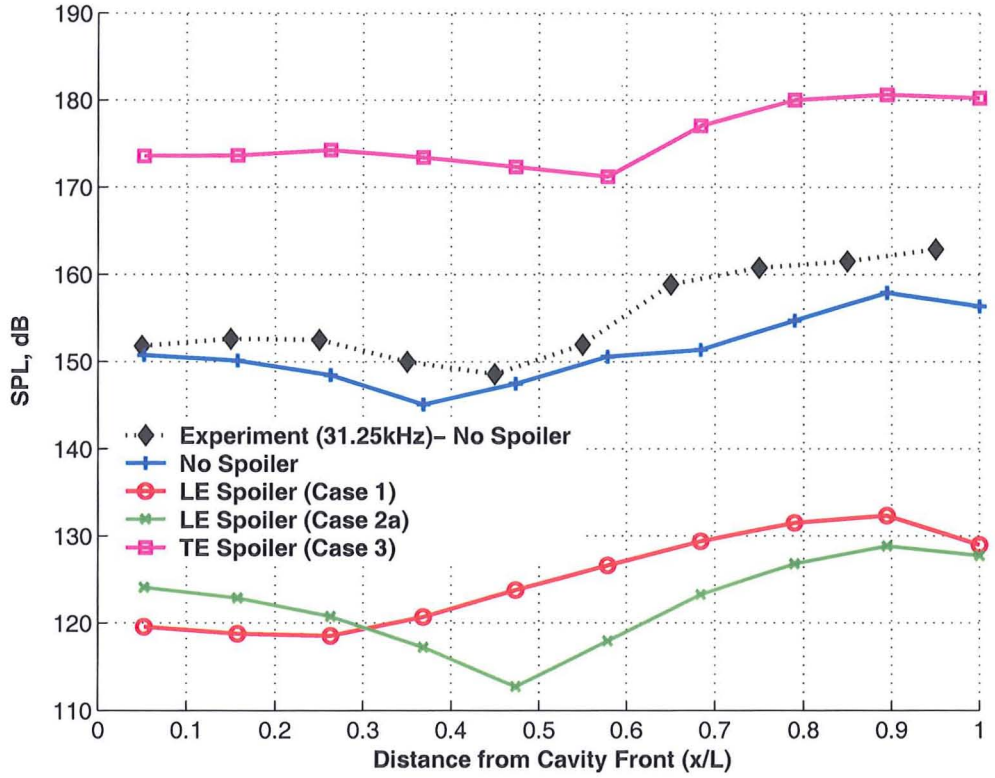

(a) $50\ Hz \leq f \leq 250\ Hz$

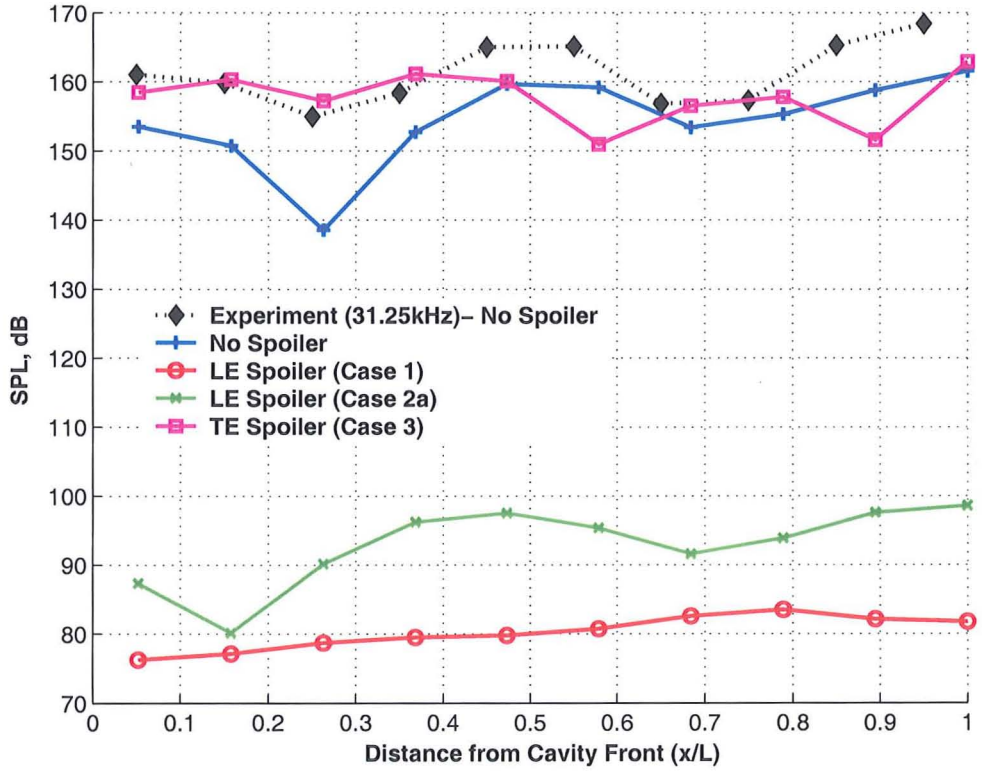

(b) $350\ Hz \leq f \leq 450\ Hz$

Figure A.2: (continued)

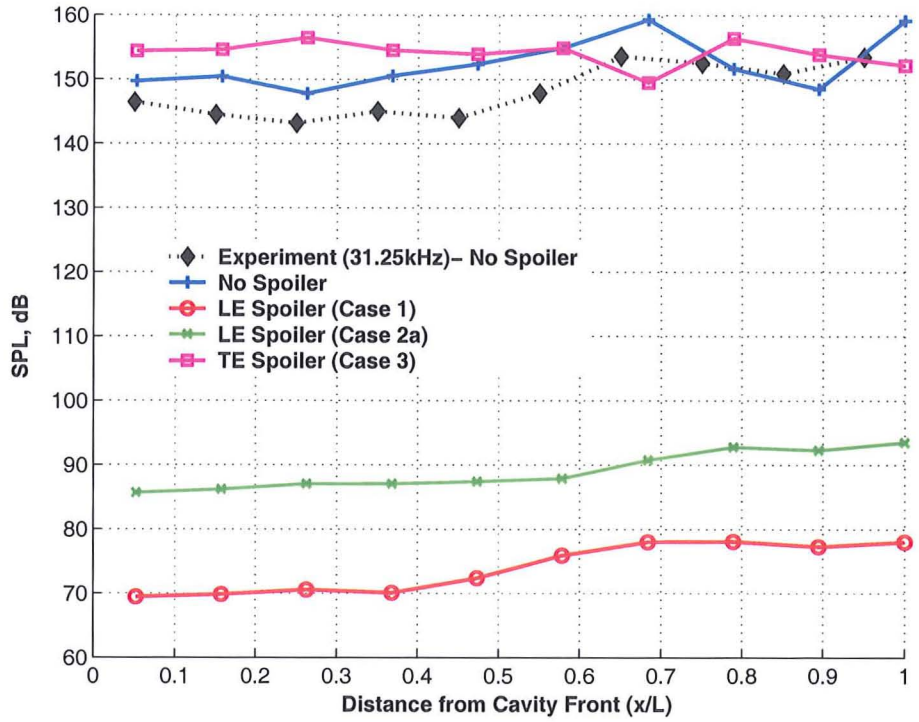

(c) $500\ Hz \leq f \leq 700\ Hz$

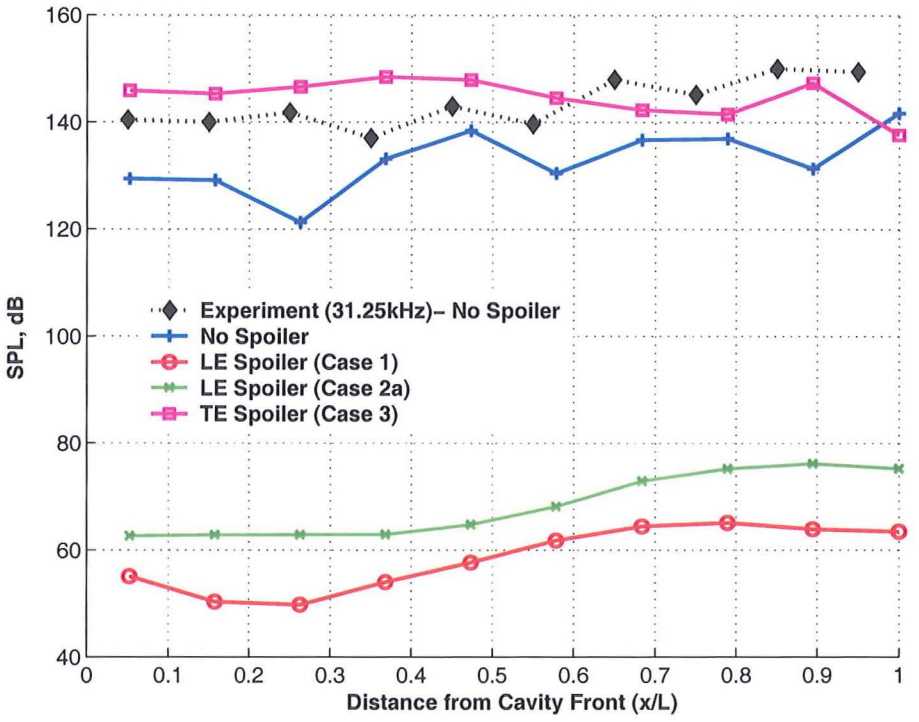

(d) $750\ Hz \leq f \leq 850\ Hz$

Figure A.2: Band-limited SPLs for the 2D, L/D=5 cavity using the SST model with: LE Spoiler (Case 1), LE Spoiler (Case 2a), TE Spoiler (Case 3). Case 1: $x_{sp}/L = -0.2$, $y_{sp}/L = 0$; Case 2a: $x_{sp}/L = -0.1$, $y_{sp}/L = 0$; Case 3: $x_{sp}/L = 1$, $y_{sp}/L = 0$. Height (h_{sp}) and width (w_{sp}) kept fixed to $1\delta = 0.021L$ and $0.0125L$, respectively.

was observed (Figure A.1(a)) associated with an increase in the amplitudes of the periodic pressure oscillations (Figures A.1(b)-A.1(d)). This increase originates from a large increase (by as much as approximately 20 dB) in the first mode ($\approx$ 160 Hz) intensity (Figure A.2(a)) while magnitudes of all other modes in subsequent frequency bands remain largely unchanged (Figures A.2(b)-A.2(d)). Since the second mode is typically dominant for the clean cavity (with no spoiler), this shift in dominance to the first mode for the trailing-edge spoiler suggests that the wake mode has been triggered.

A couple of points can be noted based on these band-limited SPL results. Firstly, even though different positions for the spoiler downstream of the cavity were not investigated, it appears that it is more beneficial to have the spoiler situated ahead of the cavity. Although the spoiler placed furthest upstream from the cavity lip was more effective out of the two LE spoilers, it cannot be definitively said that the further upstream the spoiler the more effective it is. In fact, the further the spoiler is moved upstream of the cavity lip, the greater the probability of the boundary layer reattaching before the cavity lip. In such circumstances, the flow would again separate at the lip as it did in the baseline configuration. There is therefore likely to be a specific position where the LE spoiler's effectiveness is optimum. Secondly, the greatest influence of the spoiler position occurred on the lower frequencies, evidence of which is provided by the greatest scatter in the first mode amplitudes relative to the other modes (Figure A.2). So the spoiler does not directly suppress the higher frequencies but instead does so implicitly by regulating the intensity of the lower frequencies, thereby influencing the energy cascade process.

A.1.1.2 Flow-field Visualisation

Illustration of the flow-field inside the cavity with the spoiler is shown in Figure A.3, which displays time-averaged Mach number contours and streamlines. For reference, flow-field inside the cavity without a spoiler is also included (Figure A.3(a)). Analysis of the flow-field for the LE spoilers (Cases 1 and 2a) clearly indicates that the spoiler forced the flow to separate ahead of the normal separation point at the cavity lip (see Figure A.3(a)), deflecting the flow upwards. Momentum of the free-stream then 'carried' this prematurely-separated flow further downstream. Although a shear layer still formed across the cavity opening, it is now shifted upwards and the flow re-enters the cavity tangentially to the downstream wall, i.e. vertically (Figures A.3(b) and A.3(c)). The flow was therefore observed to graze along the downstream wall rather than impinge against it. In contrast, the shear layer approaches the cavity rear for the baseline case in the streamwise direction and therefore impacts the downstream wall almost perpendicularly (Figure A.3(a)). This change in flow direction at the cavity rear was critical in the suppression of the noise levels.

By changing the position of the spoiler from upstream to downstream of the cavity, the physics of the flowfield inside the cavity changed completely. For the trailing-edge spoiler, the shear layer mode no longer existed as it did for the case without the spoiler (Figure A.3(a)). Instead, vortex shedding occurred at the cavity lip and the flow switched to the wake mode (Figure A.3(d)). The thinking behind the trailing-edge spoiler was to prevent the mass breathing process that existed for the typical open cavity. Since mass injection and expulsion is related to the deflection of the shear layer into and out of the cavity, it was thought that by inserting a spoiler at the downstream corner, it may assist in negating the frequency of shear layer vibration and hence reduce the acoustics generated inside the cavity. It was instead found that the trailing-edge spoiler decelerated a larger proportion

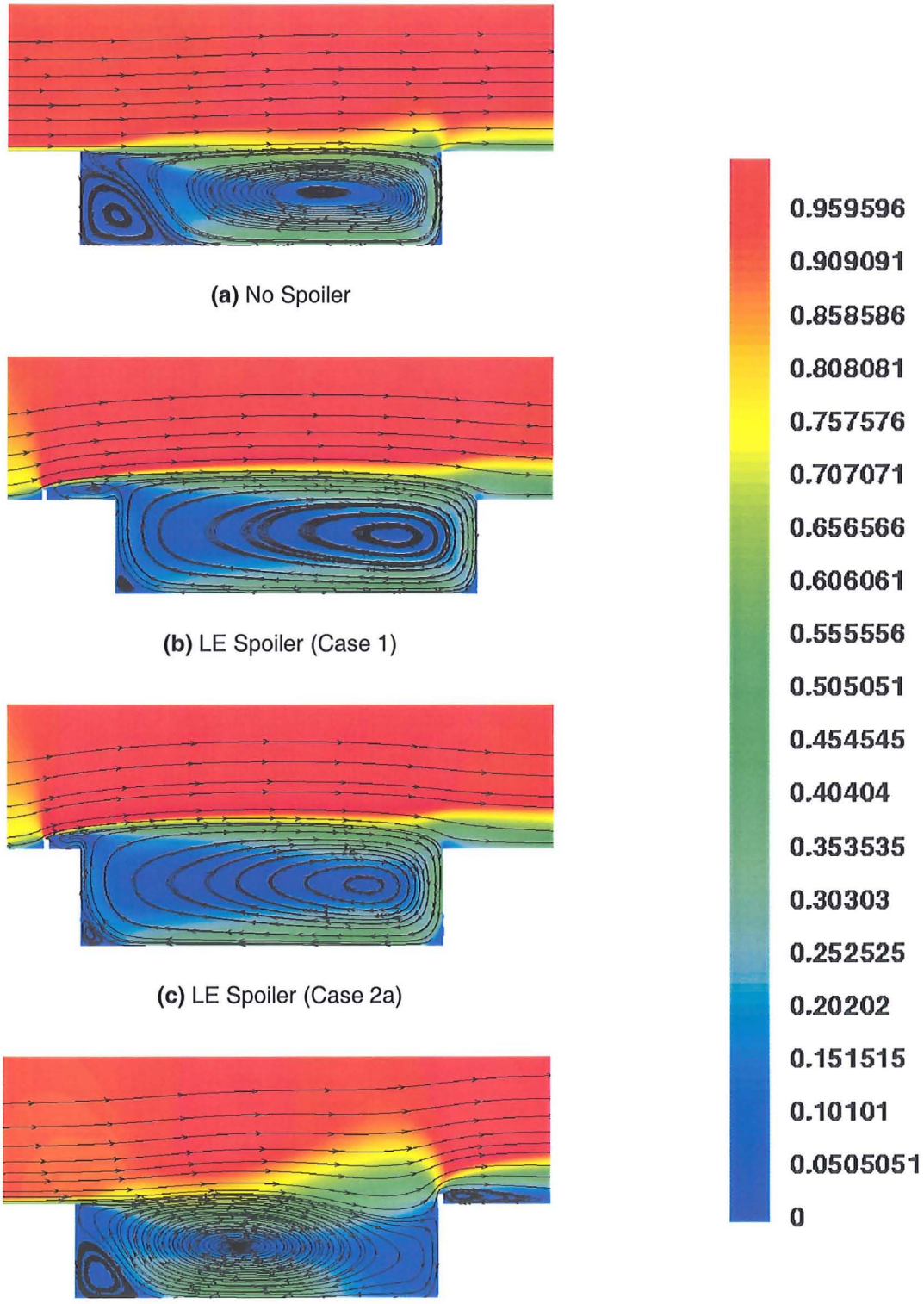

(a) No Spoiler

(b) LE Spoiler (Case 1)

(c) LE Spoiler (Case 2a)

(d) TE Spoiler (Case 3)

Figure A.3: Time-averaged Mach number contours with streamlines for the 2D, L/D=5 cavity using the SST model with: LE Spoiler (Case 1), LE Spoiler (Case 2a), TE Spoiler (Case 3). Case 1: $x_{sp}/L = -0.2$, $y_{sp}/L = 0$; Case 2a: $x_{sp}/L = -0.1$, $y_{sp}/L = 0$; Case 3: $x_{sp}/L = 1$, $y_{sp}/L = 0$. Height (h_{sp}) and width (w_{sp}) kept fixed to $1\delta = 0.021L$ and $0.0125L$, respectively. All plots are drawn to the same scale with the Mach number normalised with reference to the free-stream Mach number, $M_\infty = 0.85$.

of the oncoming free-stream air thereby creating a region of very high pressure at the cavity rear. Near the cavity front, the flow separated at the cavity lip and 'rolled' into the cavity. The high pressure region at the cavity rear, however, prevented the vortex from convecting any further downstream. As a result, the vortex was forced to expand outwards of the cavity.

The size of the vortex continued to increase and as it did so it began to deflect more of the flow around it (Figure A.3(d)). Combined with a relatively smaller region of recirculation near the cavity front wall, this large vortex induced massive separation at the cavity lip which produced another vortex that 'rolled' into the cavity. As the larger vortex approached the trailing-edge vortex, it was further decelerated. Some energy from the vortex dissipated as it hit the spoiler and some convected further downstream beyond the spoiler. It was this continuous vortex-shedding cycle that generated the large pressure oscillations inside the cavity as illustrated in Figure A.1. Large peripheral velocities of the vortices (depicted by the lighter-coloured, higher Mach regions in Figure A.3(d)) near the cavity floor indicate that the vortices are stronger. Consequently more noise was produced from the interactions of these vortices with the cavity walls (Figure A.1(a)).

Despite the similar time-averaged plots for the two different positions of the LE spoiler, slightly different flow was observed aft of the spoiler and it was this that resulted in the different SPL characteristics (Figure A.1(a)). A close-up of the flow near the spoiler is illustrated in Figure A.4. At the upstream corner of the spoiler, the flow separated and a small region of recirculation developed on the upstream side of the spoiler— a pattern similar to the forward-facing step. Flow accelerated around the corner of the spoiler and a compression wave formed. Between the spoiler and the cavity lip, a backward-facing step type flow behaviour developed. In the presence of slower-moving fluid aft of the spoiler and faster-moving fluid above the spoiler, the Kelvin-Helmholtz theory dictates that a shear layer will develop at their junction, similar to the no-spoiler cavity configuration. The natural tendency of this shear layer is to diffuse and transfer its energy to the surroundings. This is however not immediate and takes effect only after some time.

For Case 1 (Figure A.4(a)), where the spoiler is furthest from the cavity lip, there is enough distance between the spoiler and the cavity front corner for a large vortex to develop. The core of this vortex is located approximately two-thirds of the distance between the spoiler and the cavity lip and at a height equal to the spoiler height (i.e. 1δ). External regions of this vortex therefore fell within the boundary of the shear layer generated by the flow past the spoiler. Peripheral velocities of this upstream vortex were thus increased by the added energy from the shear layer and this translated to greater shearing at the wall upstream of the cavity lip as is depicted by the lighter-coloured, higher Mach regions in Figure A.4(a). This vortex was sufficiently strong to prevent early diffusion of the shear layer so the shear layer maintained its initial trajectory and transferred less energy into the cavity.

As the spoiler was moved closer to the cavity lip (Case 2a), only a smaller vortex developed in the wake of the spoiler (Figure A.3(c)). Although the core of this smaller vortex was still within the shear layer, there is less space for it to grow. The shear layer's trajectory was therefore less affected by this vortex. Higher SPLs generated at the front of the cavity for this case were therefore likely to be from the interaction of the shear layer and the flow approaching the shear layer along the front cavity wall and, to a lesser extent, the interaction of this smaller vortex with the larger, primary vortex (Figure A.1(a)).

Note also that with the shear layer offset from the original separation point at the cavity lip (Figure A.3(a)), flow at the front cavity wall is no longer restricted to within the cavity

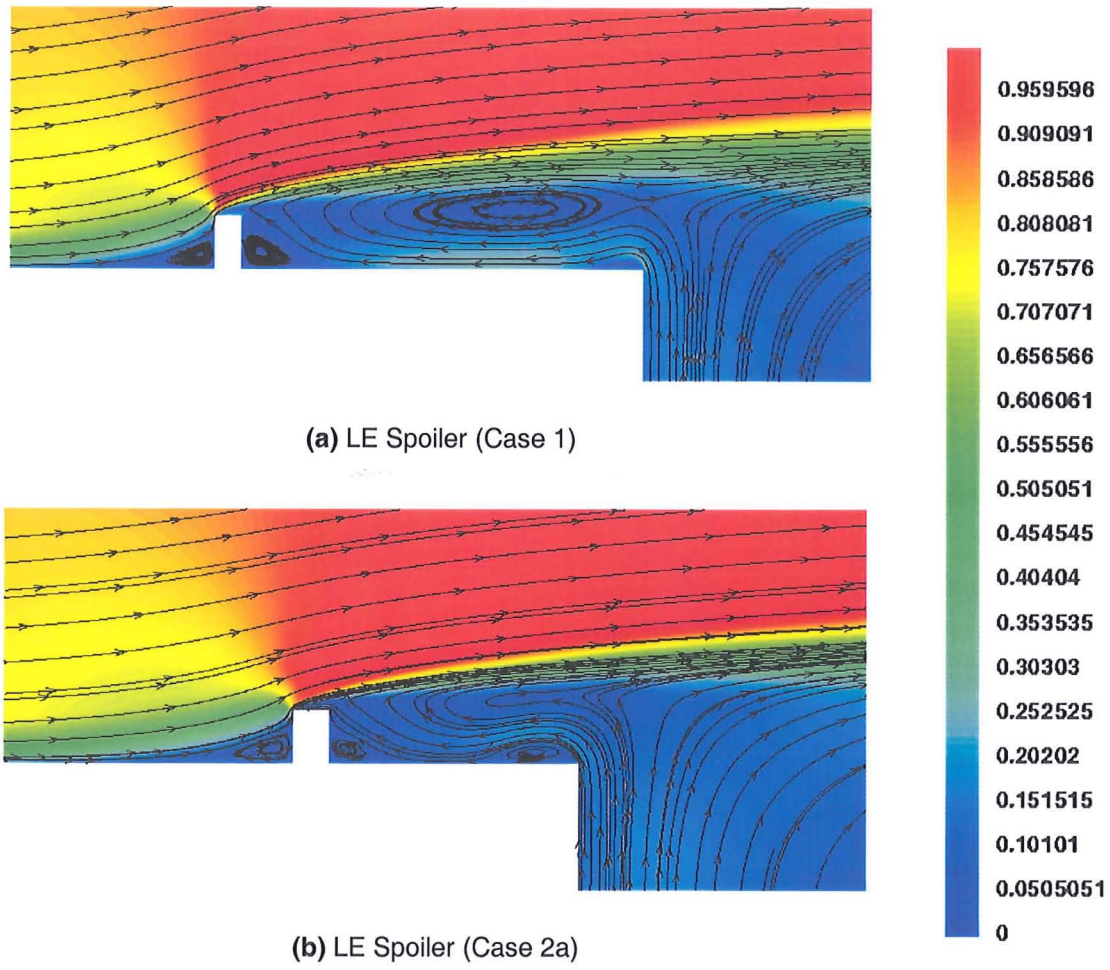

(a) LE Spoiler (Case 1)

(b) LE Spoiler (Case 2a)

Figure A.4: Close-up of the time-averaged flow-field near the vicinity of the two LE spoilers. Case 1: $x_{sp}/L = -0.2$, $y_{sp}/L = 0$; Case 2a: $x_{sp}/L = -0.1$, $y_{sp}/L = 0$. Height (h_{sp}) and width (w_{sp}) kept fixed to $1\delta = 0.021L$ and $0.0125L$, respectively. Mach number contours normalised with reference to the free-stream Mach number, $M_\infty = 0.85$.

and seeps upstream along the upstream plate toward the spoiler. Only the flow adjacent to the cavity wall enters this 'gap' between the spoiler and the actual cavity. In fact, most of the energy contained in the primary vortex existing in the cavity appears to interact little with the flow shed from the spoiler. In this scenario, the flow aft of the spoiler and before the cavity and the flow inside the actual cavity can be thought to be independent of each other giving rise to a crude assumption that the flow aft of the spoiler can equally be represented as another 'artificial' cavity. Based on this assumption, with the spoiler positioned furthest away from the cavity LE (Case 1), a scaled-down cavity with L/D ratio of about 10 (length of 0.2L and height of 0.021L) between the spoiler and the actual cavity is produced. Like for the larger-scale L/D=10 cavity discussed in Chapter 6, the flow in the gap behind the spoiler has similar characteristics. Since the flow in the cavity is driven by the shear layer, the vortex develops along the directional path of the shear layer. For this scaled-down L/D=10 cavity aft of the spoiler, flow past the spoiler is inclined therefore so is the vortex. When the spoiler is located closer to the cavity lip (Case 2a), the 'gap' between the spoiler and the actual cavity can be modelled with a L/D=5 cavity (length of 0.1L and height of 0.021L). Impingement of the shear layer with the artificial downstream wall of this scaled-down L/D=5 cavity generates more noise.

In Figure A.4, it can be clearly seen that a series of compression and expansion waves form at the front corner of the spoiler as the flow passes over it. The effect of this is to increase the acoustic content produced outside the cavity. This is illustrated in Figure A.5, which illustrates the SPLs along a plane at $y/L = 0.02$ (i.e. at a distance approximately equal to the spoiler height, $h_{sp}/L = 0.021$) above and parallel to the flat plate upstream of the cavity. Results from the Case 2a LE spoiler are presented and the dotted line represents the position of the spoiler.

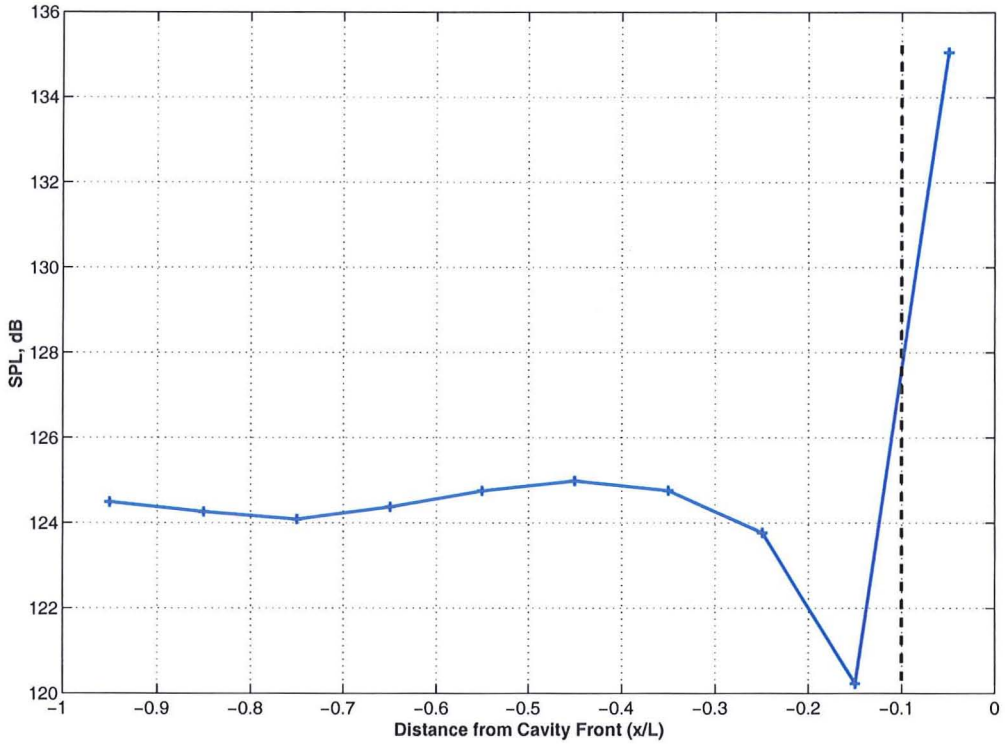

Figure A.5: SPLs upstream of cavity near the vicinity of the case 2a LE spoiler: $x_{sp}/L = -0.1$, $y_{sp}/L = 0$, $h_{sp} = 1\delta = 0.021L$, $w_{sp}/L = 0.0125$.

The increased noise levels where the spoiler is positioned is evident from Figure A.5. Despite this, the overall noise levels approach about 135 dB and this is still significantly lower than the 168 dB that is observed at the cavity rear along the cavity floor with experiment. At higher Mach numbers, where a shock wave would form near the vicinity of the spoiler, a saw-toothed spoiler would be better suited to weaken the shock strength. It is likely that this additional noise content will augment the overall broadband content produced. This however cannot justified here and LES/DES would need to be performed to verify this.

A.1.2 Effects of Spoiler Height

SPLs and pressure traces at three positions on cavity floor ($x/L = 0.05$, $x/L = 0.55$ and $x/L = 0.95$) are presented in Figure A.6. Experimental plots corresponding to the baseline (i.e. no spoiler) case are denoted in black (with diamond symbols) and the corresponding numerical results in blue (with plus signs). In this section, the position of the spoiler was kept fixed at $x/L = -0.1, y/L = 0.021$ and the height varied from 1δ (Case 2a— denoted in

red with circular symbols) to 2δ (Case 2b — denoted in green with crosses). As before, the width of the spoiler was also kept fixed to $w_{sp}/L = 0.0125$.

Noise levels were generally observed to be higher at the cavity front ($x/L = 0.05$) with a taller spoiler (Case 2b) but dropped by about 5 dB more across the remainder of the cavity (Figure A.6(a)). At the cavity rear ($x/L = 0.95$), SPLs were observed to be as low as 133 dB for Case 2b and about 138 dB for Case 2a compared to about 168 dB for experiment. Pressure signatures reveal that across all the three stations analysed, fluctuations in pressure were even less at the front of the cavity as the height of the spoiler was increased. The drop in the SPLs observed near the rear of the cavity for Case 2b was due to the lower transfer of energy and momentum from the shear layer into the cavity. With the shear layer deflected even more with the taller spoiler, the core of the vortex in the cavity was located further above the cavity floor. Interaction between the vortex and the cavity floor was therefore less intense and so the SPLs were lower.

A.1.2.1 Band-Limited Frequency Analysis

Further analysis of the effects of spoiler height is illustrated via windowed analysis of the variation in SPLs across four specific frequency ranges as presented in Figure A.7. Based on these results, the general consensus was that as the height of the spoiler was increased, the noise levels dropped by as much as 20 dB across all the four frequency bands analysed. The peak in SPLs observed for Case 2b in Figure A.6(a) resulted from frequencies even lower than the first band (i.e. $50\ Hz \leq f \leq 250\ Hz$).

A.1.2.2 Flow-field Visualisation

Confirmation of the results presented previously for different spoiler heights is now given via analysis of the flow-field inside the cavity. Figure A.8 provides two perspectives of the time-averaged flow-field for the LE spoiler with a height of 1δ (Case 2a) and the LE spoiler with a height of 2δ (Case 2b). One view gives the entire view of the cavity while the other provides a close-up of the flow-field near the spoiler.

To a large extent, the overall flow characteristics for both spoiler heights were similar (Figures A.8(a) and A.8(c)). The obvious difference is the presence of a larger vortex inside the cavity with the 2δ spoiler. This was due to the shear layer being deflected even further by the taller spoiler. The greatest difference however arose near the spoiler as is shown by Figures A.8(b) and A.8(d). With a greater spoiler height, more flow entered the region aft of the spoiler from the main vortex residing inside cavity. But up to a distance approximately equal to the height of the spoiler (i.e. 0.042 L) and as far as the distance from the spoiler to the cavity lip (i.e. 0.1 L), the flow aft of the spoiler appeared to be independent of the main cavity flow. For case 2b, the 'cavity' between the spoiler and the cavity lip had a L/D ratio of about 2.5, which falls in the very deep cavity category. As was shown for the L/D=2 cavity in Chapter 6 previously, typically one vortex forms inside the cavity. Spreading of the shear layer appeared to be less for the L/D=2 cavity as the flow from the vortex inside the main cavity played a greater role in supporting the shear layer and preventing its breakdown by providing more momentum to extend across the cavity opening.

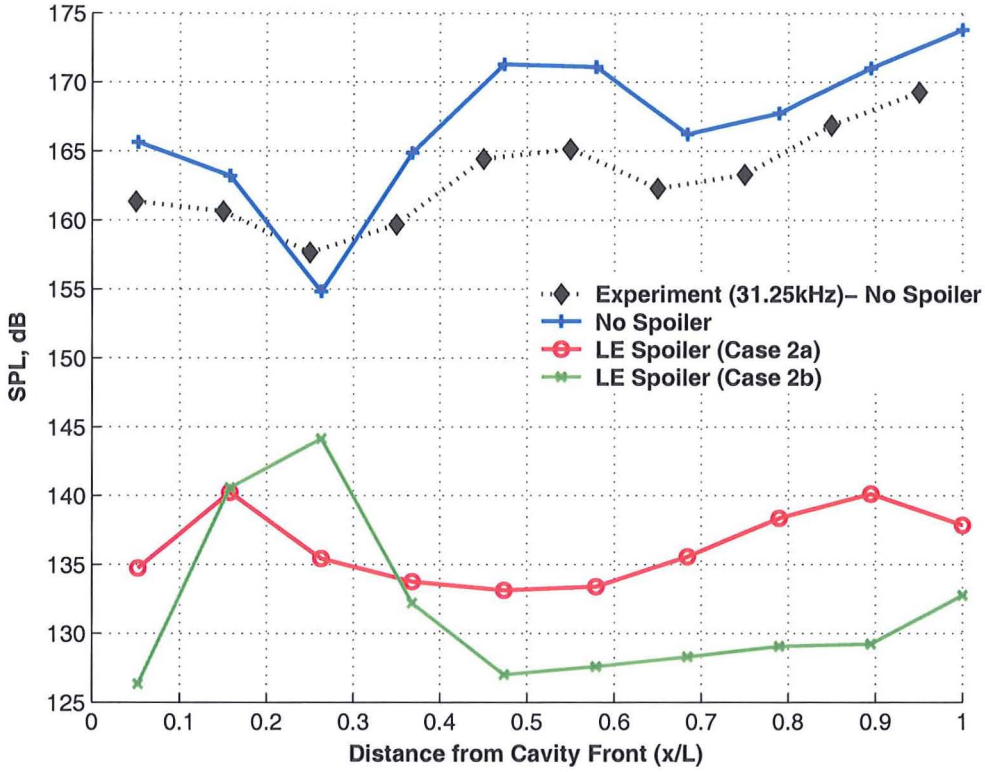

(a) SPLs

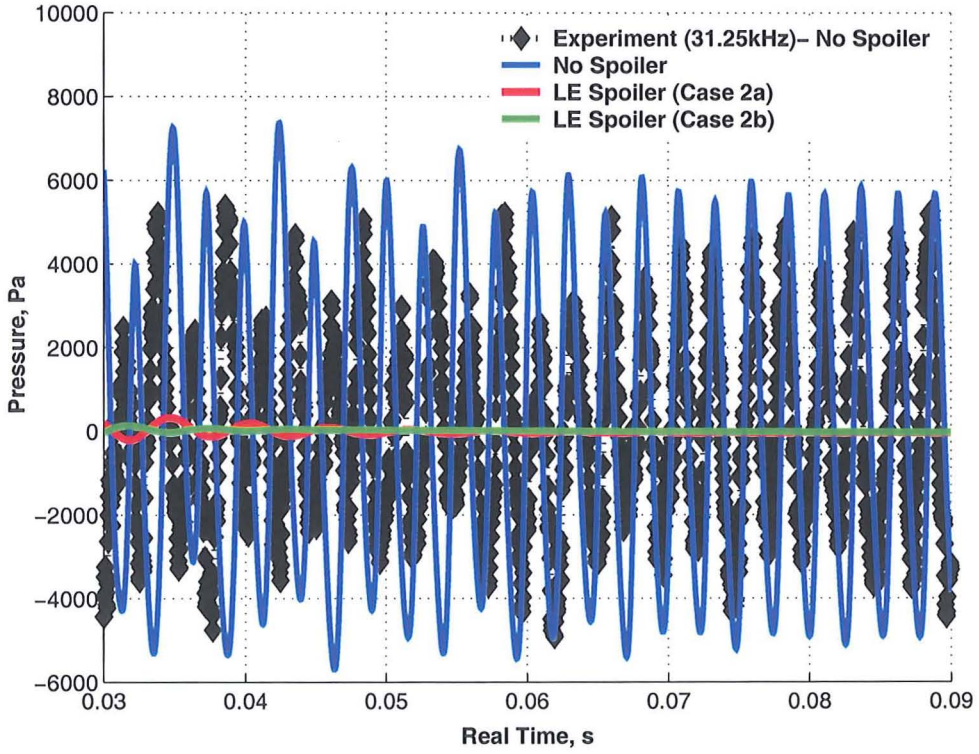

(b) Pressure Traces ($x/L = 0.05$)

Figure A.6: (continued)

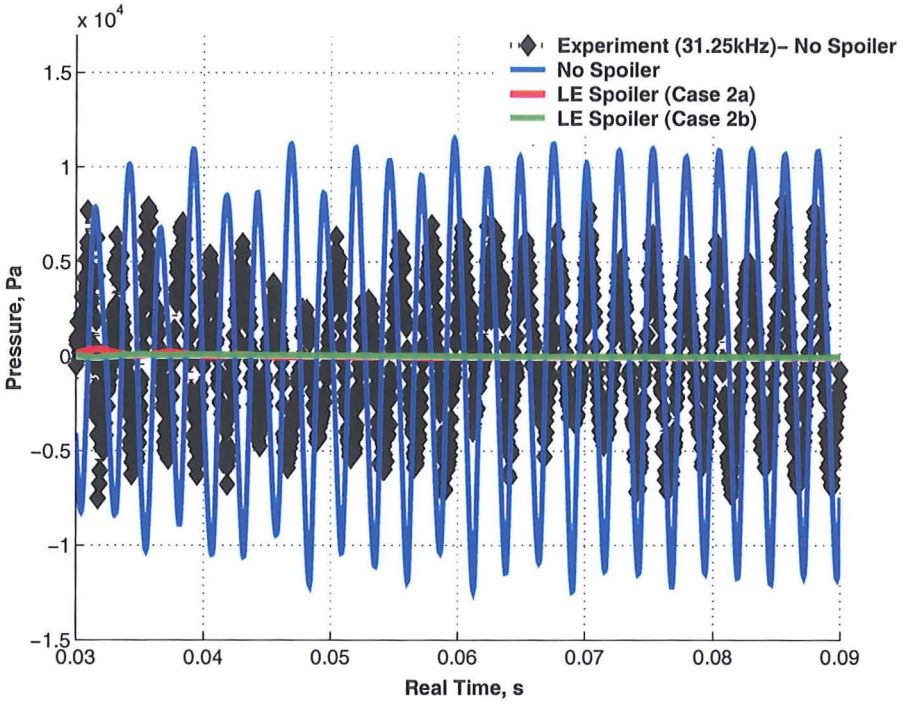

(c) Pressure Traces ($x/L = 0.55$)

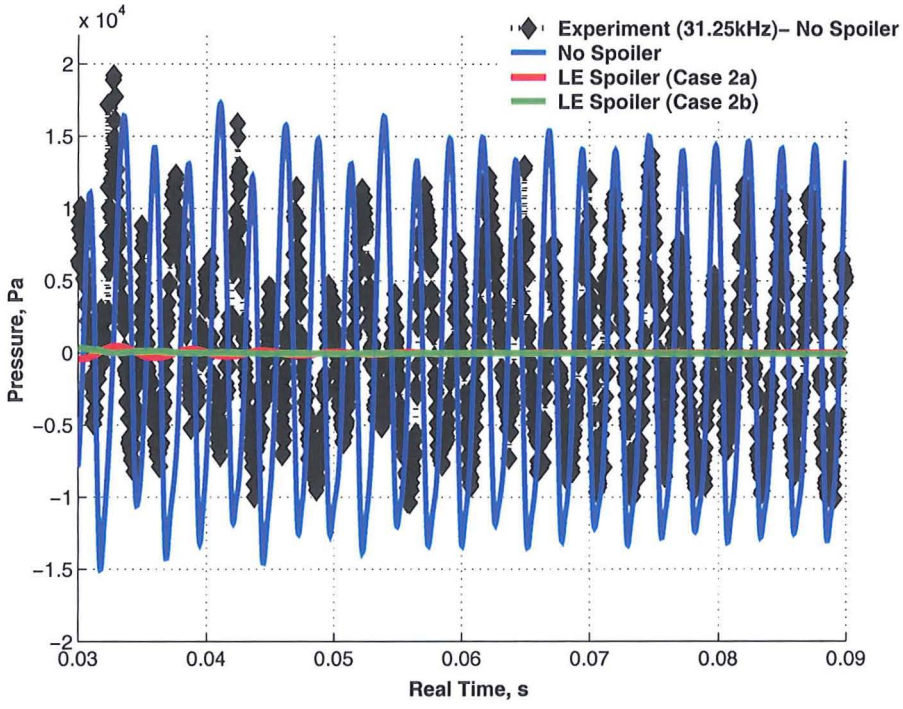

(d) Pressure Traces ($x/L = 0.95$)

Figure A.6: SPLs and pressure traces (at $x/L = 0.05$, $x/L = 0.55$ and $x/L = 0.95$) along the cavity floor of the 2D, L/D=5 cavity using the SST turbulence model with: LE Spoiler (Case 2a) and LE Spoiler (Case 2b). Case 2a: $x_{sp}/L = -0.1$, $y_{sp}/L = 0$, $h_{sp}/L = 1\delta$; Case 2b: $x_{sp}/L = -0.1$, $y_{sp}/L = 0$, $h_{sp}/L = 2\delta$. Width (w_{sp}) of spoiler kept fixed at $0.0125L$.

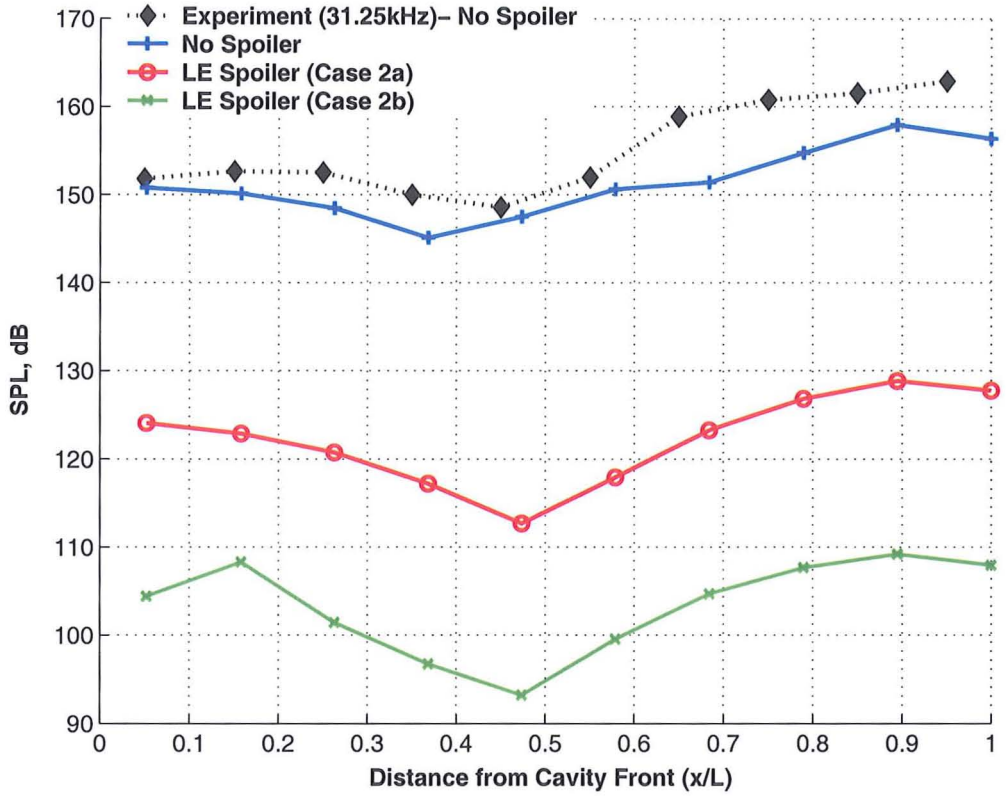

(a) $50\ Hz \leq f \leq 250\ Hz$

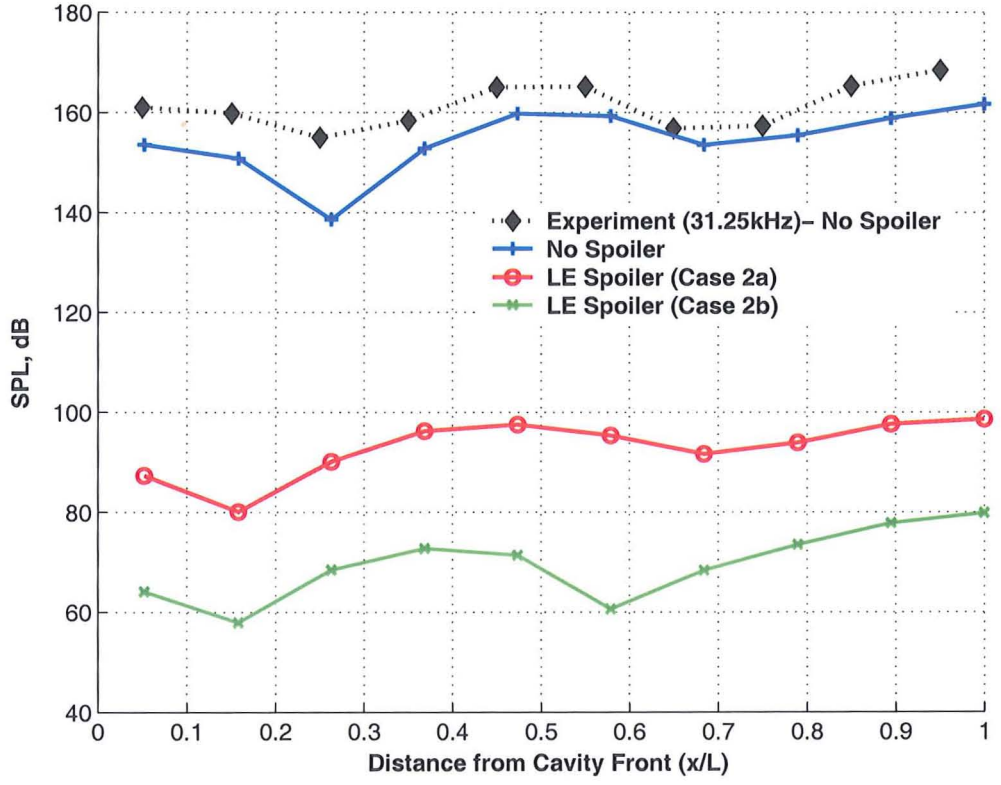

(b) $350\ Hz \leq f \leq 450\ Hz$

Figure A.7: (continued)

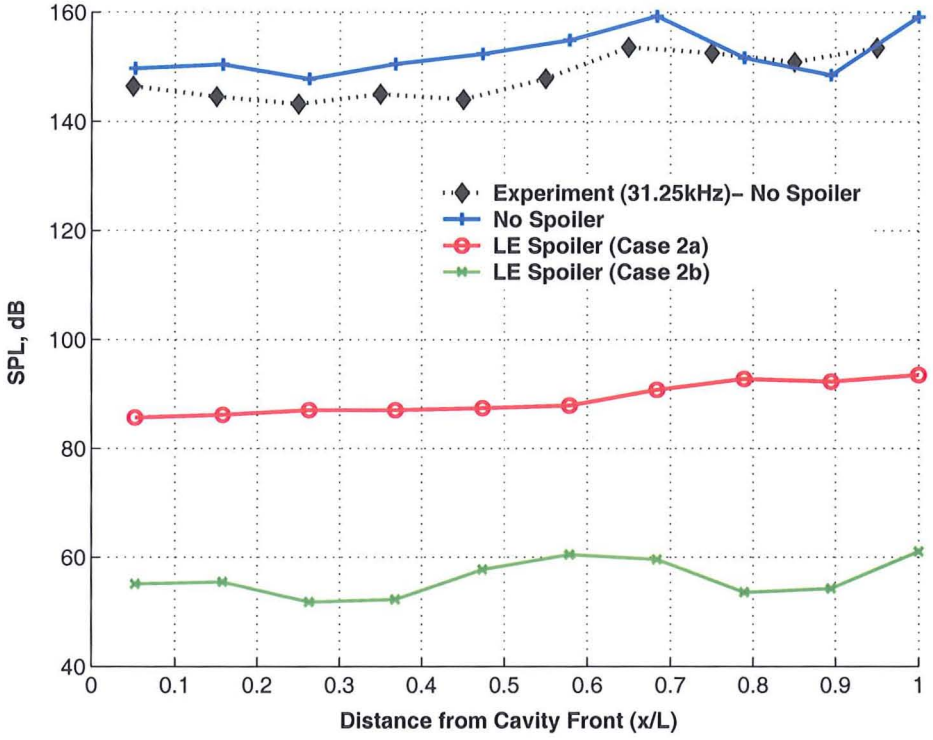

(c) $500\ Hz \leq f \leq 700\ Hz$

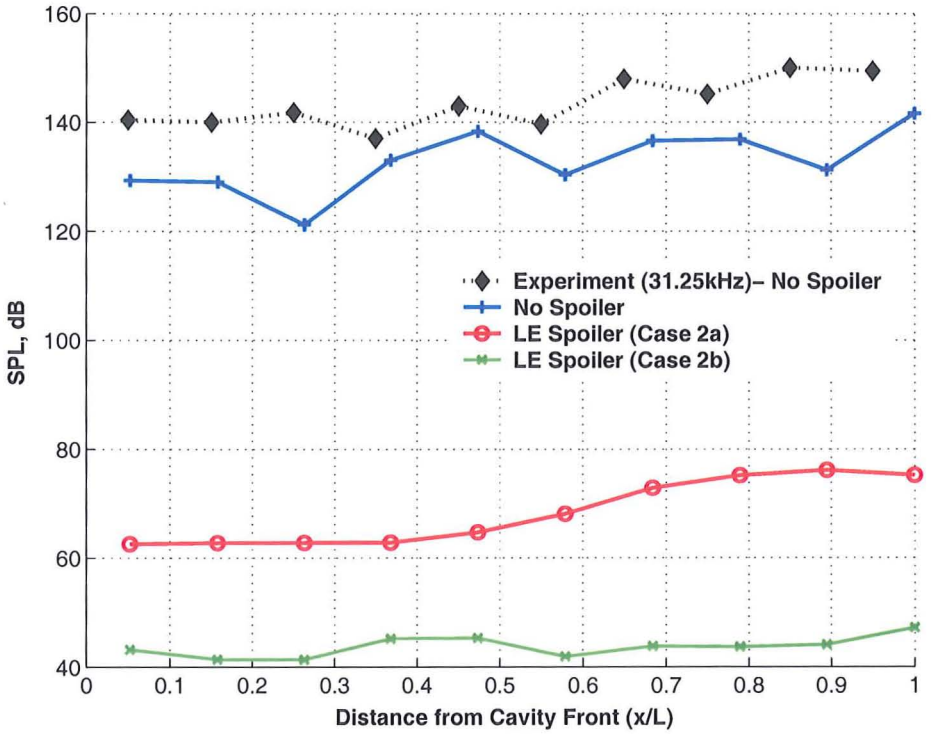

(d) $750\ Hz \leq f \leq 850\ Hz$

Figure A.7: Band-limited SPLs for the 2D, L/D=5 cavity using the SST model with: LE Spoiler (Case 2a) and LE Spoiler (Case 2b). Case 2a: $x_{sp}/L = -0.1$, $y_{sp}/L = 0$, $h_{sp}/L = 1\delta$; Case 2b: $x_{sp}/L = -0.1$, $y_{sp}/L = 0$, $h_{sp}/L = 2\delta$. Width (w_{sp}) of spoiler kept fixed at $0.0125L$.

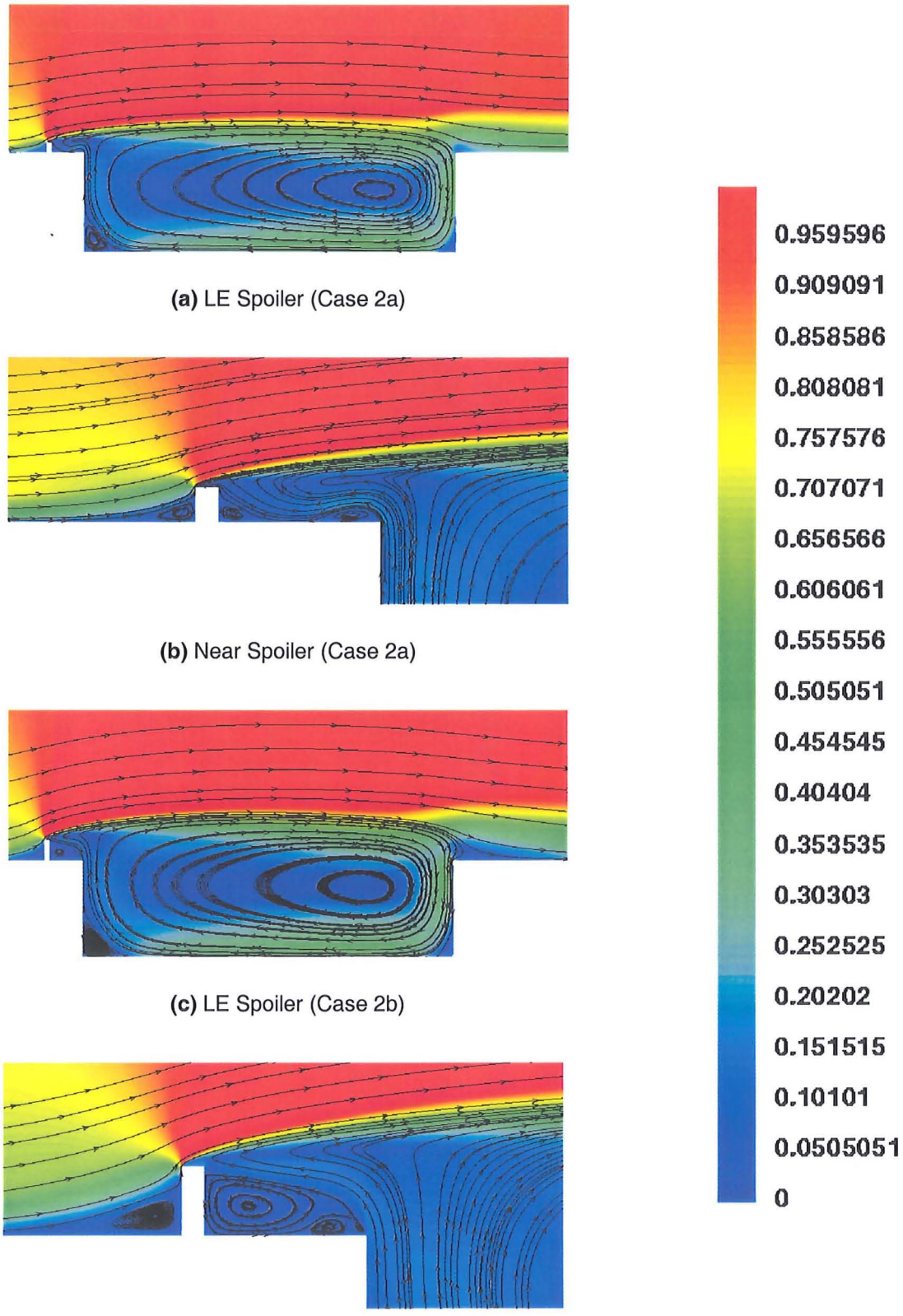

(a) LE Spoiler (Case 2a)

(b) Near Spoiler (Case 2a)

(c) LE Spoiler (Case 2b)

(d) Near Spoiler (Case 2b)

Figure A.8: Time-averaged Mach number contours with streamlines for the 2D, L/D=5 cavity using the SST model with: LE Spoiler (Case 2a) and LE Spoiler (Case 2b). Case 2a: $x_{sp}/L = -0.1$, $y_{sp}/L = 0$, $h_{sp}/L = 1\delta$; Case 2b: $x_{sp}/L = -0.1$, $y_{sp}/L = 0$, $h_{sp}/L = 2\delta$. Width (w_{sp}) of spoiler kept fixed at $0.0125L$.

A.2 Passive Control: Slanted Cavity Walls

For the slanted cavity walls, effects of the position of slant and the angle of slant were investigated for the configurations shown in Figure 7.1(b). Details of the grids used for each of these cases are provided in Table A.1. Although the idea of slanted walls was taken from the experiments performed by Ross and Peto [11], the method adopted here is different in one important way. In Ross and Peto's experiments, wedges were placed in the cavity to obtain the necessary slant of the walls. The length of the cavity floor was decreased accordingly while the length of the shear layer (i.e. y/D=0) was kept fixed. In the numerical analysis performed here, however, the length of the cavity floor has been kept fixed and the shear layer distance modified accordingly. Three different scenarios have been investigated: slanting the front cavity wall only, slanting the rear cavity wall only and slanting both front and rear walls. Initially, the angle of slant was kept fixed at 45^o in all these cases. The Influence of the angle of slant was then studied by slanting the rear wall only at additional angles of 30^o and 60^o.

A.2.1 Effects of Slant Position

Figure A.9 plot the SPLs and pressure traces (at $x/L = 0.05$, $x/L = 0.55$ and $x/L = 0.95$) for a slanted front wall (red with circular symbols), slanted rear wall (green with crosses) and both walls slanted (magenta with square symbols). Experimental (black with diamond symbols) for the clean case and numerical (blue with plus signs) results corresponding to the baseline case where no slant was implemented are also included for demonstration of the effectiveness of the control method.

As far as mitigating the intensity of noise was concerned, slanted walls, irrespective of position, appeared to be an effective method with maximum pressure amplitudes generally tending to be lower than those given by experiment. Slanting only the front wall however appeared to be the least effective of all the three cases investigated with noise levels significantly higher at around the x/L=0.25 and x/L=0.75 positions. The 'dips' in the SPL curve were also damped out (Figure A.9(a)). Slanting the downstream wall produced greatest reductions in SPLs throughout the cavity length (by $\approx$ 5-12 dB). Slanting both front and rear walls appeared to be quieter at the front ($x/L = 0.05$) and the rear ($x/L = 0.95$) while the rest of the noise level distribution resembled the slanted front wall results.

A.2.1.1 Band-Limited Frequency Analysis

Variations in the noise levels within the same four frequency bands discussed previously are highlighted in Figure A.10. The largest decrease in SPLs was observed for the slanted downstream wall across the first two frequency ranges (Figures A.10(a) and A.10(b)). In contrast, slanting only the front wall intensified the first mode by about 1–6 dBs relative to experiment for the no-slant case (Figure A.10(a)). Slanting the front wall only at 45^o generated more noise across the analysed frequency spectrum. As the frequencies approached 1 kHz, differences between all three cases became less significant. Slanting both walls generally tended to make matters worse across the analysed different frequency bands.

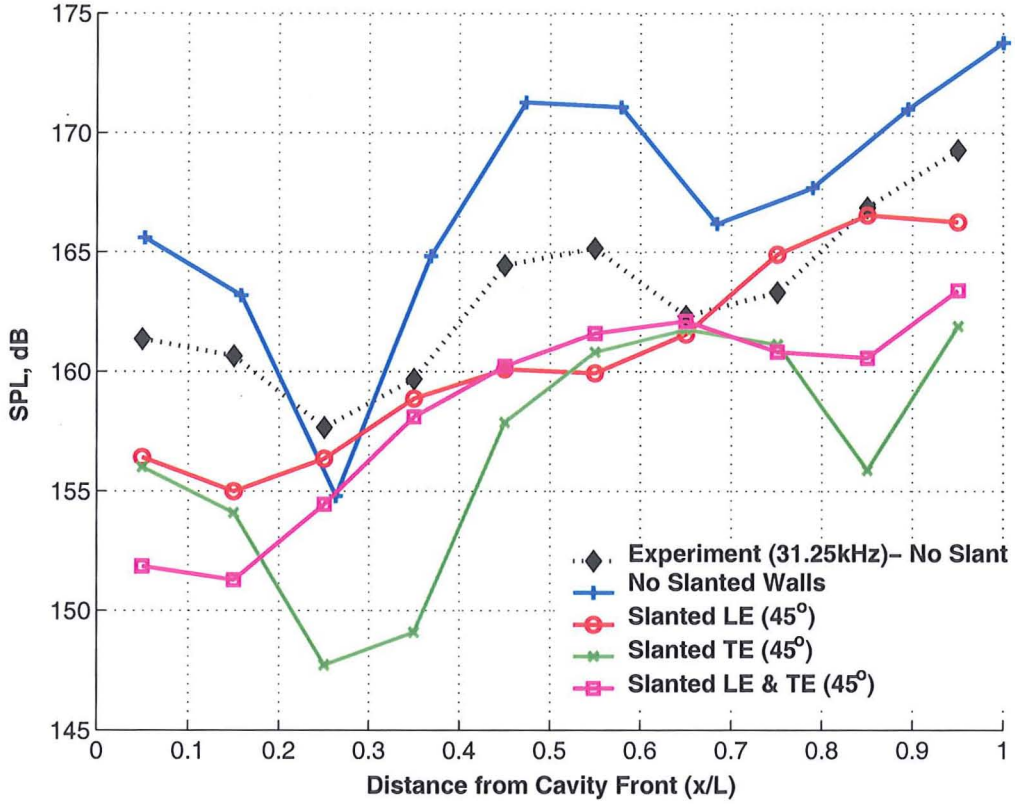

(a) SPLs

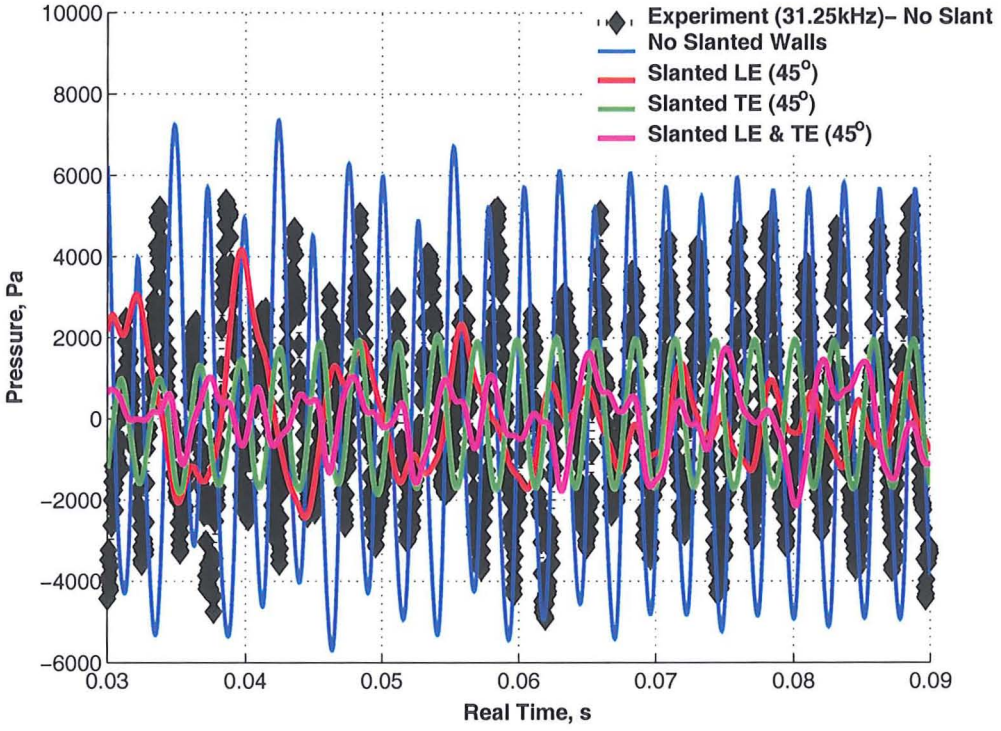

(b) Pressure Traces ($x/L = 0.05$)

Figure A.9: (continued)

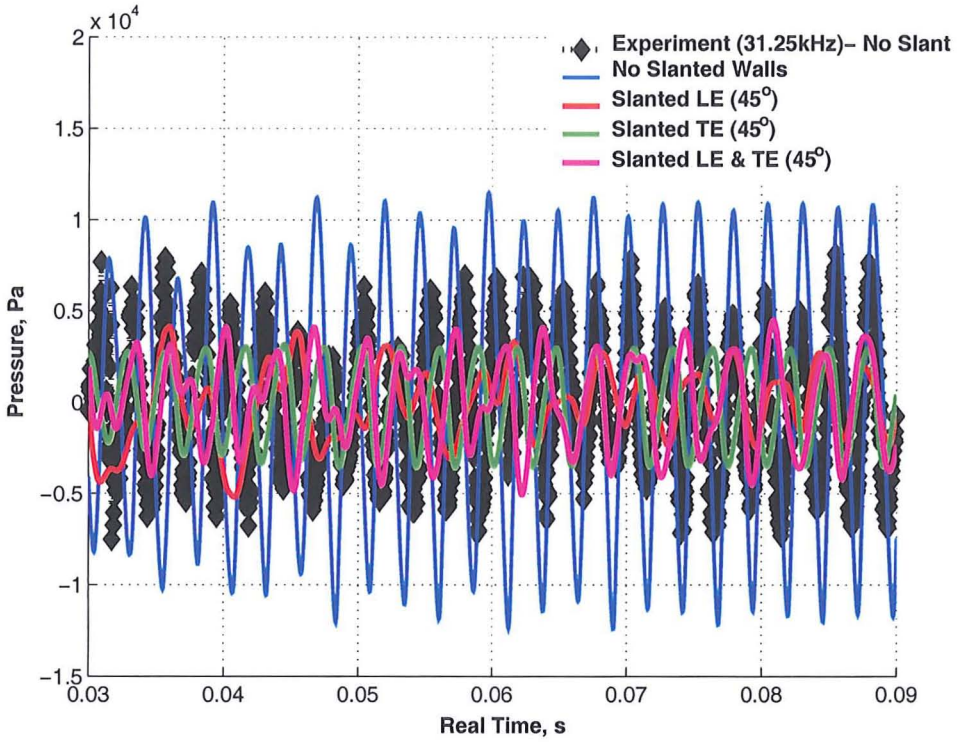

(c) Pressure Traces ($x/L = 0.55$)

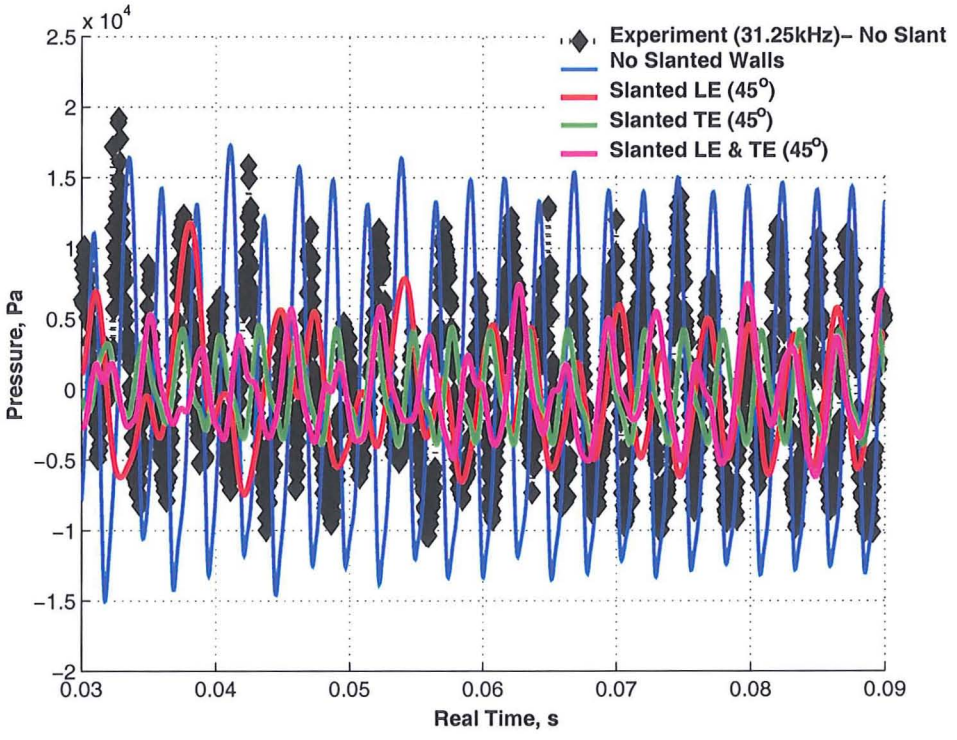

(d) Pressure Traces ($x/L = 0.95$)

Figure A.9: SPLs and pressure traces (at $x/L = 0.05$, $x/L = 0.55$ and $x/L = 0.95$) and SPLs along the cavity floor for the 2D, L/D=5 cavity using the SST turbulence model for a slanted front wall, slanted rear wall and both walls slanted. Slant angle fixed at 45°.

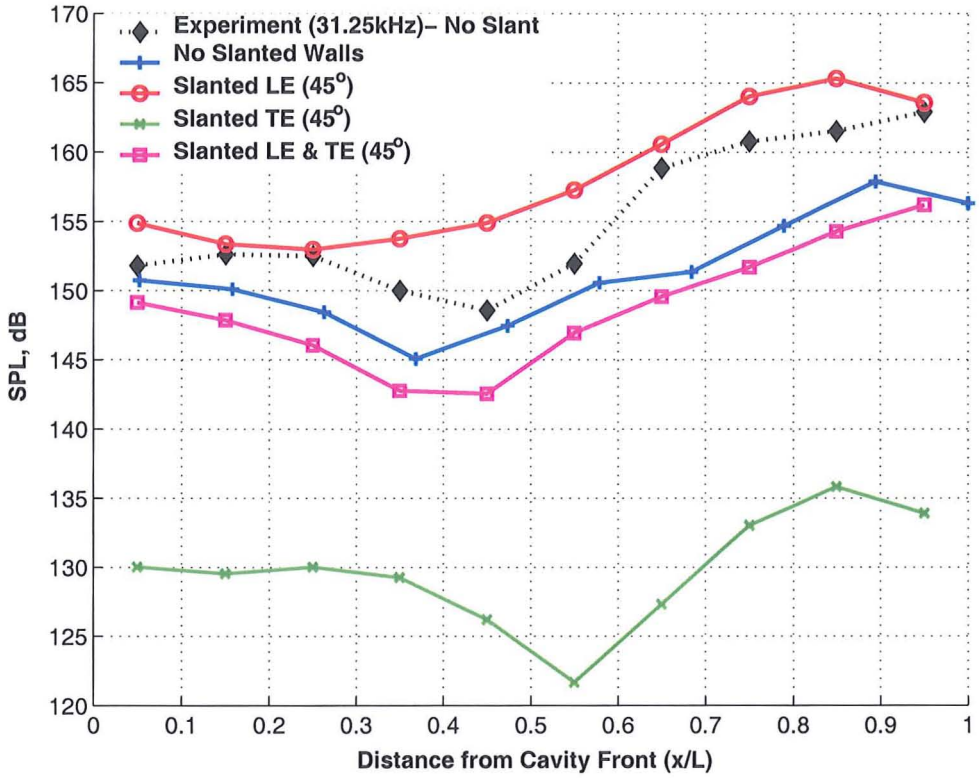

(a) $50\ Hz \leq f \leq 250\ Hz$

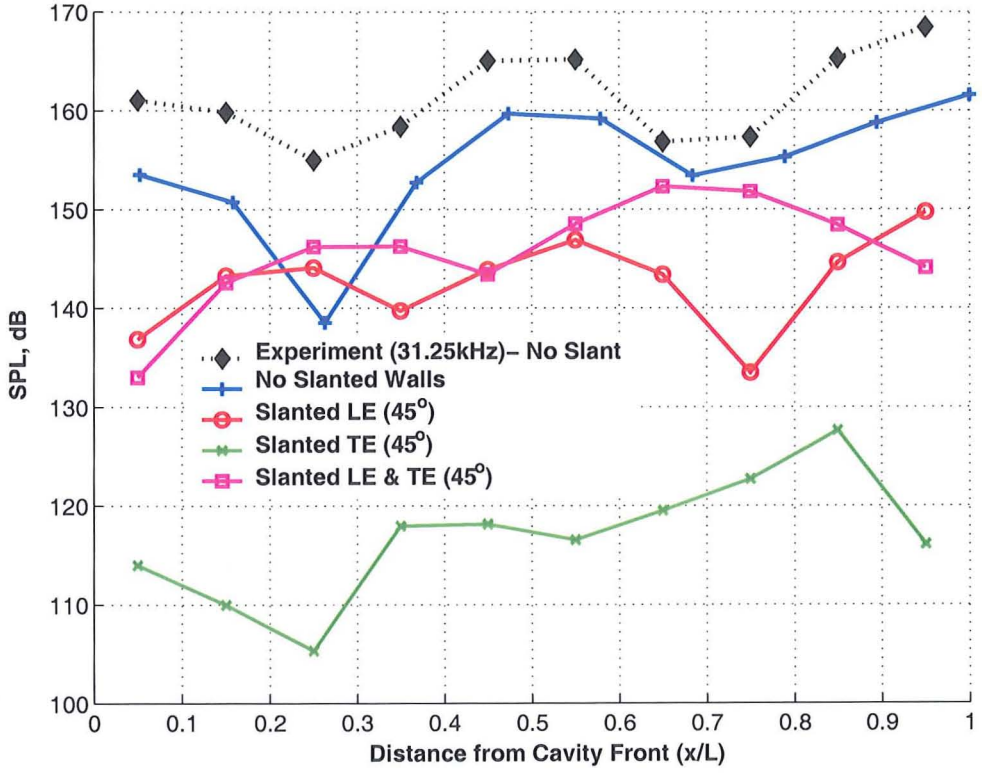

(b) $350\ Hz \leq f \leq 450\ Hz$

Figure A.10: (continued)

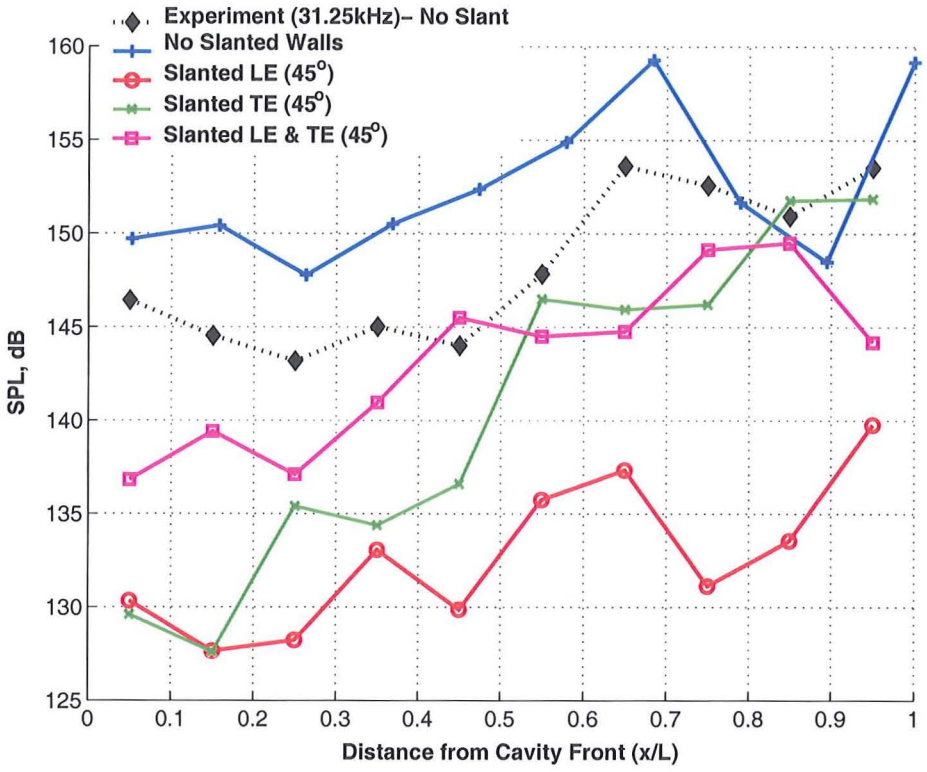

(c) $500\ Hz \leq f \leq 700\ Hz$

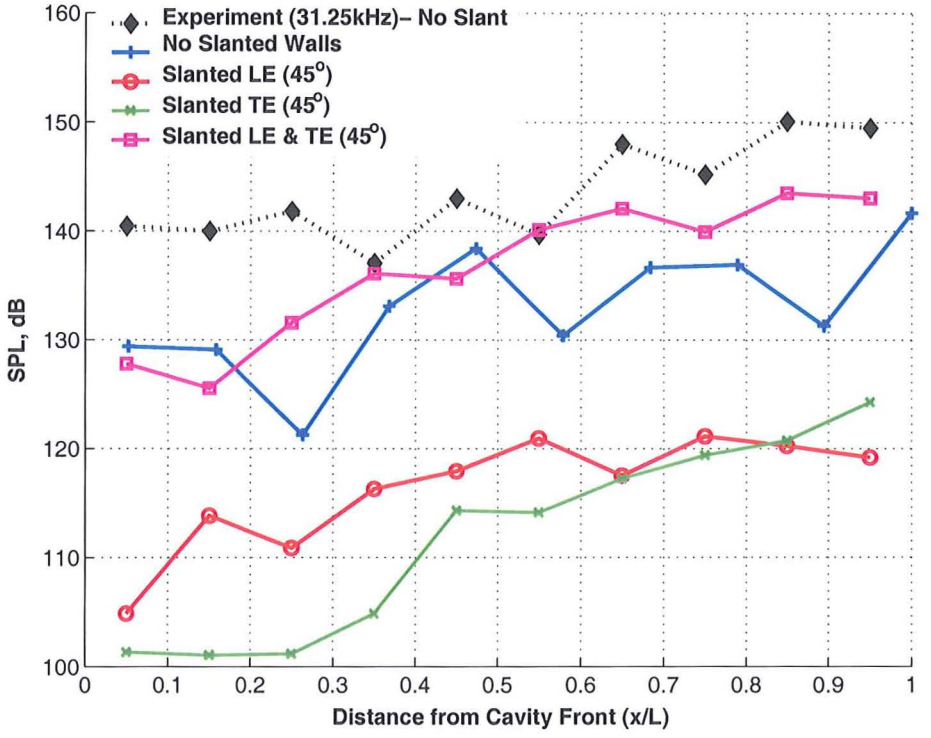

(d) $750\ Hz \leq f \leq 850\ Hz$

Figure A.10: Band-limited SPLs for the 2D, L/D=5 cavity using the SST model with a: slanted front wall, slanted rear wall and both walls slanted. Angle of slant kept fixed at 45°.

A.2.1.2 Flow-field Visualisation

Illustrations of the time-averaged flow-field inside the cavity for different slanted wall configurations are provided in Figure A.11, which show time-averaged plots of Mach number contours normalised with respect to the free-stream Mach number, $M_\infty = 0.85$, with streamlines. Boundaries and thicknesses of the shear and boundary layers are clearly defined in this manner as is the degree of flow intensity inside the cavity. For reference, the flow-field with no walls slanted is also included (Figure A.15(a)).

Irrespective of which wall is slanted, the front wall corner vortex has largely disappeared. The high Mach region along the cavity floor (distinctly evident from the lighter, green Mach number contours) extended across a greater proportion of the cavity length. Noise generated on the cavity floor due to the interaction of the vortex on it was therefore more distributed. Noise levels are significantly lower only when the rear wall was slanted (Figure A.11(c)). When the front wall was slanted (Figure A.11(b)), SPLs are at the same magnitude as the experiment and the numerical results without slant (Figure A.9(a)). This suggests that moving the position of the front corner further upstream (while keeping the L/D ratio of the cavity fixed) can cause adverse effects. Changing the angle of both walls merely combines the adverse effects of slanting the front wall and the positive effects of slanting the rear wall to give a compromised solution (Figure A.11(d)).

The downstream corner is also naturally located further downstream as a consequence of slanting the cavity back wall. This forced the shear layer and any flow structures created to remain almost completely entrained within the cavity and thus the mass breathing process is minimised. Furthermore, with the rear wall slanted at 45°, the geometrical surface area of the downstream wall has increased by a factor of $\sqrt{2}$. Consequently, the noise levels generated at the cavity rear are much lower (by $\approx$ 7 dB) compared to experiment (see Figure A.9(a)). Containment of the flow within the confinements of the cavity walls makes the flow intrinsically less unsteady. Vortical movement and shear layer deflection is minimised as a result. Evidence of this is provided in Figure A.12, which illustrates variations in the time-averaged streamwise ($\frac{U}{U_\infty}$) profiles for each of the slanted wall configurations as well as the PIV and numerical results for the baseline case at three positions along the cavity floor ($x/L = 0.05$, $x/L = 0.55$ and $x/L = 0.95$).

At the front of the cavity, the change in sign of the streamwise velocity component at y/L=-0.1 suggests that a small region of recirculation is present, where negative streamwise velocities represent upstream motion. For the baseline case, the flow moves from negative velocities near the shear layer to positive near the cavity floor, i.e. flow moves in the counter-clockwise sense, and arises as a result of the front corner vortex (Figure A.12(a)). If the rear (or even the front) wall is slanted, rotational sense of the flow changes to clockwise. The front corner vortex is absent and the flow cycle is governed entirely by a single vortex situated at the rear of the cavity. At the cavity middle ($x/L = 0.55$), flow velocities are lower ($U/U_\infty \approx -0.4$) near the cavity floor with the slanted rear wall configuration suggesting that the flow is comparatively less unsteady (Figure A.12(c)). Near the shear layer plane ($y/L = 0$), the point where $U/U_\infty \rightarrow 0.4$ marks the peripheral regions of the vortex and the lower limit of the shear layer boundary that extends into the cavity. Above the shear layer plane ($y/L > 0$), the upper limit of the shear layer extends to $y/L \approx 0.05$ (i.e. where $U/U_\infty \rightarrow 1$) with the rear wall slanted compared to $y/L \approx 0.1$ for the baseline case. Shear layer deflection is therefore much less when the rear wall is slanted by 45° implying that the vortices generated inside the cavity are less strong and the flow less unsteady. The point of zero velocity is also slightly lower for the slanted rear wall

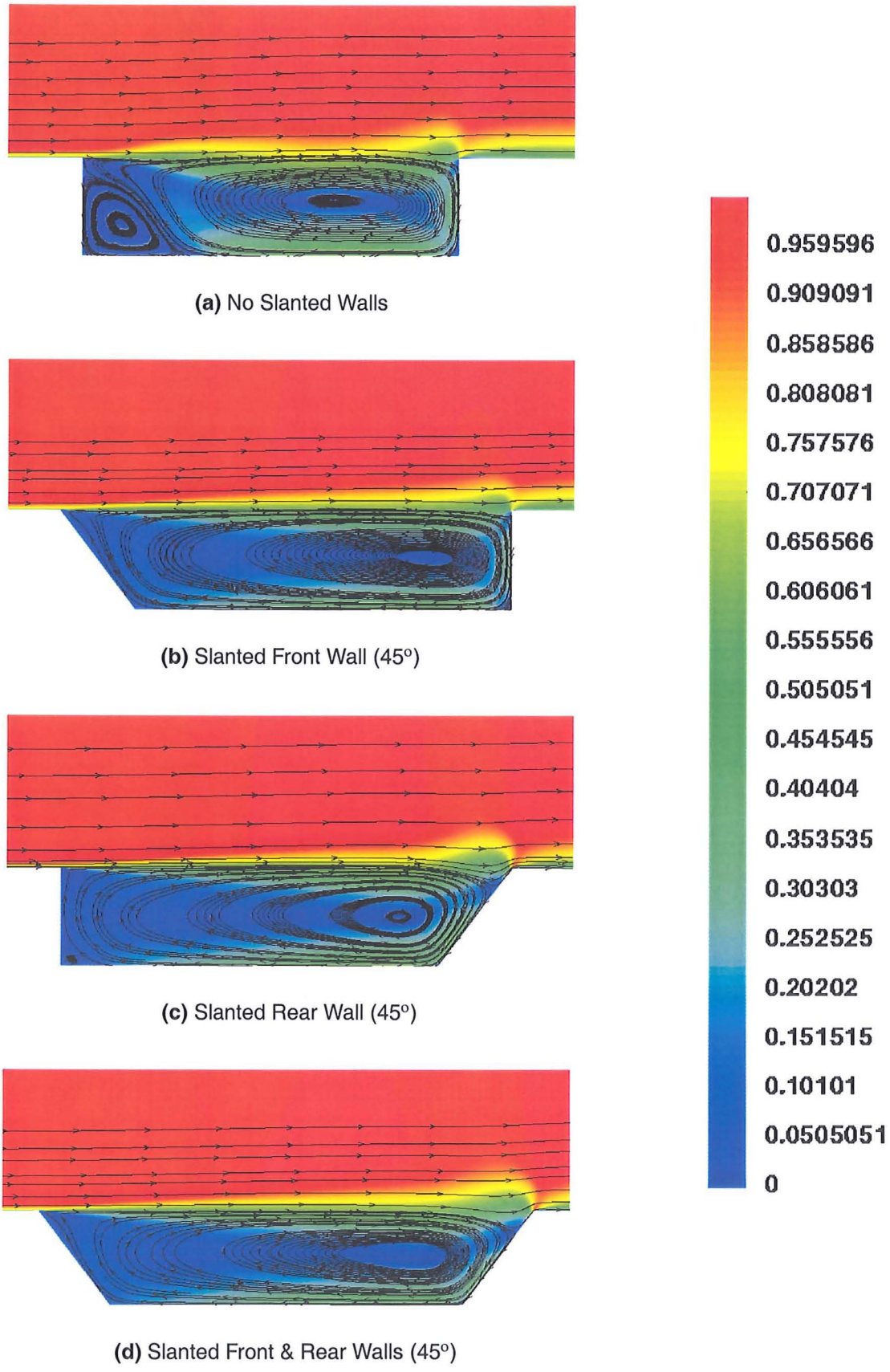

(a) No Slanted Walls

(b) Slanted Front Wall (45°)

(c) Slanted Rear Wall (45°)

(d) Slanted Front & Rear Walls (45°)

Figure A.11: Time-averaged Mach number contours with streamlines for the 2D, L/D=5 cavity using the SST model with a: slanted front wall, slanted rear wall and both walls slanted. For reference, results from no-slant case also included. Angle of slant kept fixed at 45°.

compared to the baseline case signifying that the position of the vortex core is closer to the cavity floor and the flow is more entrained in the cavity than for the baseline case.

At the cavity rear ($x/L = 0.95$), the gradient of the streamwise velocity curve (Figure A.12(e)) for the slanted rear wall is less, indicating that mass ejection and injection is not as pronounced. The streamwise velocity approaches free-stream velocity at approximately $y/L = 0.08$, which is about half of the baseline case. The mass breathing process is thus more intense for the baseline case further signifying that slanting the rear wall suppresses the higher frequencies by mitigating the shear layer deflection thereby reducing the SPLs generated inside the cavity and making the flow less unsteady.

By slanting only the front wall, a stronger vortex was shed from the front cavity corner, which now extended further upstream into the boundary layer. The larger streamwise velocity components are a testament to this (Figure A.12). This translated to greater shear layer deflection further downstream indicated by measuring the distance from the shear layer plane ($y/L = 0$) to where the streamwise flow velocity approached free-stream velocity (i.e. $U/U_\infty \rightarrow 1$). Flow is therefore more unsteady when the angle of the front wall is alterred. However, vortices still did not perturb the shear layer as much as for the baseline case and hence the SPLs generated by front wall slant are relatively lower.

When both the front and rear walls are slanted, the flow features produced in the cavity were an almagamation of the individually slanted front and rear walls. At the front, the streamwise velocity trace was therefore similar to the slanted front wall only and at the cavity rear it resembled the slanted rear wall only results.

A.2.2 Effects of Slant Angle

Investigation of the effect of the angle of slant was conducted for the slanted rear wall only. Results from 30°, 45° and 60° of slant are presented in the following sections.

Pressure traces and SPLs for the three different angles for the downstream wall are illustrated in Figure A.13 along with experimental and numerical results for the no-slant case. As the slant angle of the downstream wall increases, pressure amplitudes and frequencies decrease to such an extent that they are virtually completely damped out for the 60° case. A drop of about 30-40 dB is observed for the 60° case as indicated in Figure A.13(a).

A.2.2.1 Band-Limited Frequency Analysis

Analysis of SPL variations within four specific frequency bands was then performed and the results are presented in Figure A.14. Effectiveness of a high angle of slant (i.e. 60°) is clearly illustrated by the much lower noise levels across the entire frequency spectrum shown. At high angles of slant, both noise levels and the higher frequencies were eliminated. With the rear wall slanted by 30° from the vertical, the intensity of the noise levels for the first and third frequency bands were still comparable to the numerical results where no slant was employed. At 45°, noise levels were better suppressed especially for the first and second modes, which contributed to the most noise in the flow. The rear wall must therefore be slanted by an angle greater than 30° for the slanted rear wall to be effective as a passive control method.

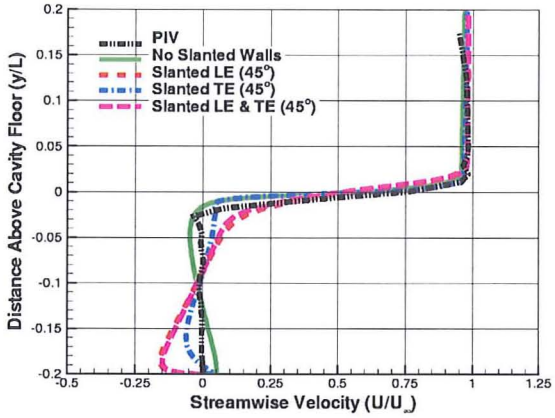

(a) Position Effects, U ($x/L = 0.05$)

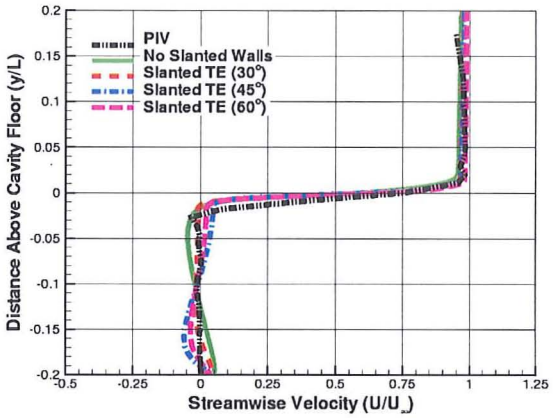

(b) Angle Effects, U ($x/L = 0.05$)

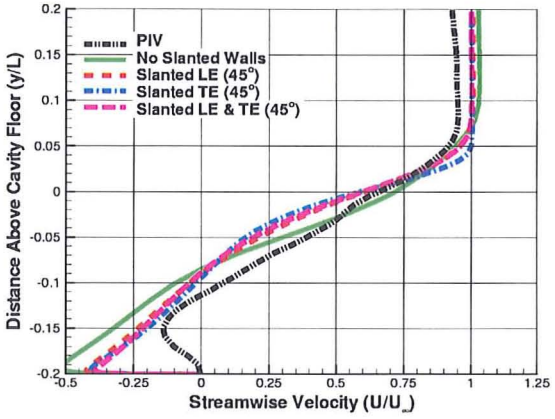

(c) Position Effects, U ($x/L = 0.55$)

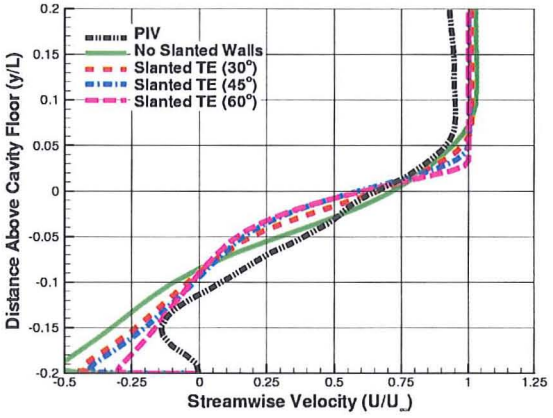

(d) Angle Effects, U ($x/L = 0.55$)

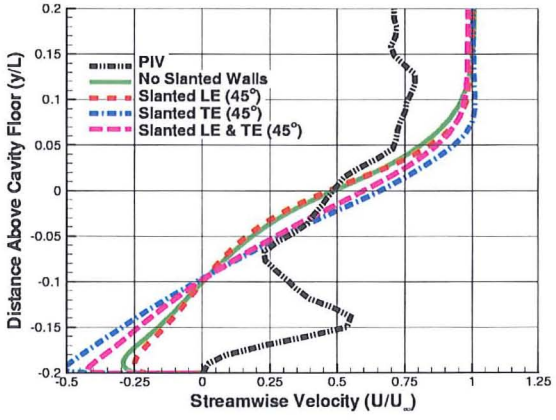

(e) Position Effects, U ($x/L = 0.95$)

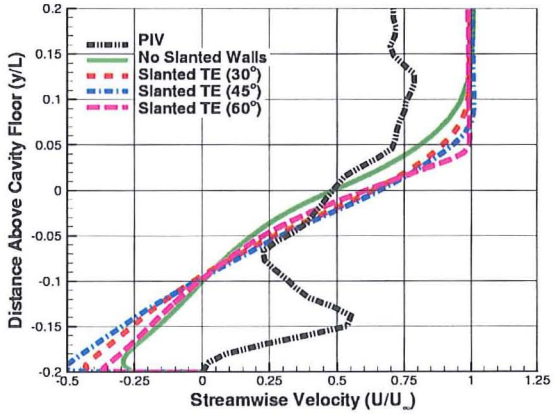

(f) Angle Effects, U ($x/L = 0.95$)

Figure A.12: Time-averaged streamwise velocity profiles ($\frac{U}{U_\infty}$) using the SST model for the 2D, L/D=5 cavity showing: effects of position with a slanted front wall, slanted rear wall and both walls slanted at 45° ; effects of angle with a rear wall slanted at 30° , 45° and 60° . For reference, numerical results and PIV measurements from no-slant case also included.

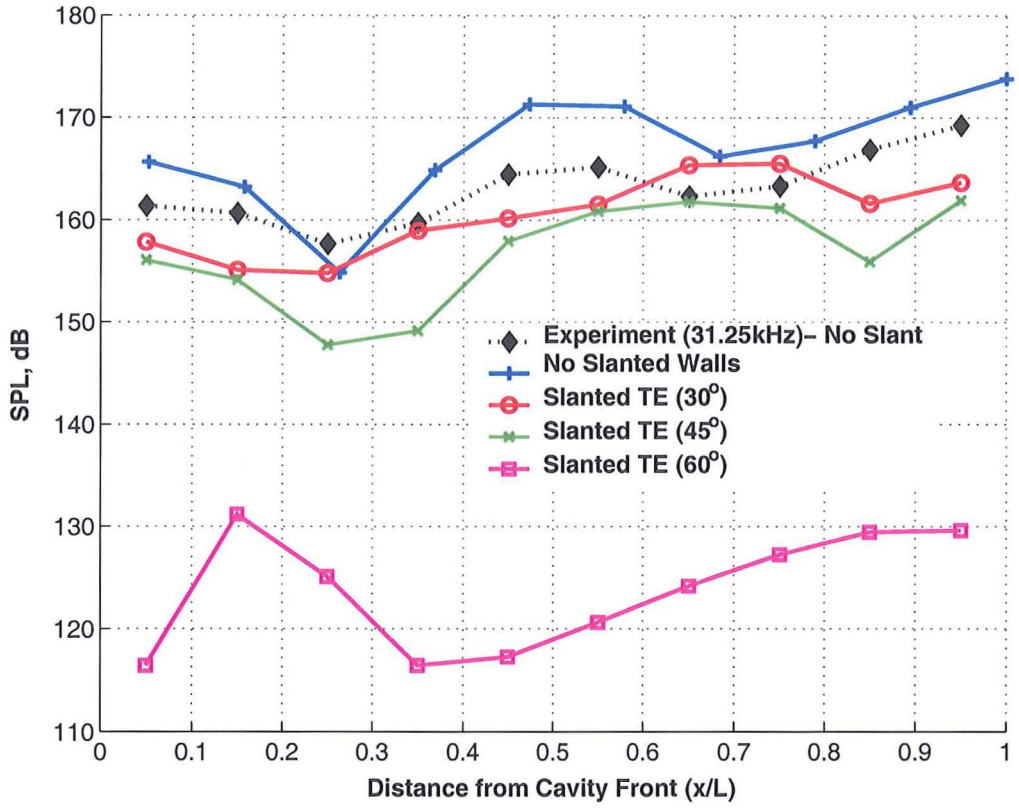

(a) SPLs

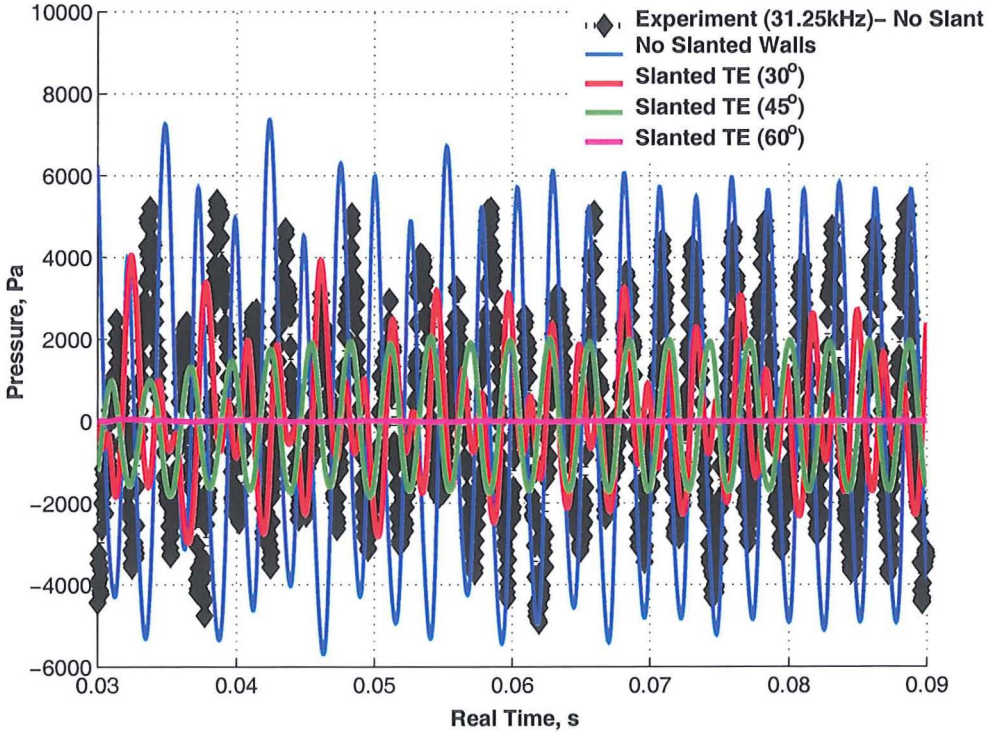

(b) Pressure Traces ($x/L = 0.05$)

Figure A.13: (continued)

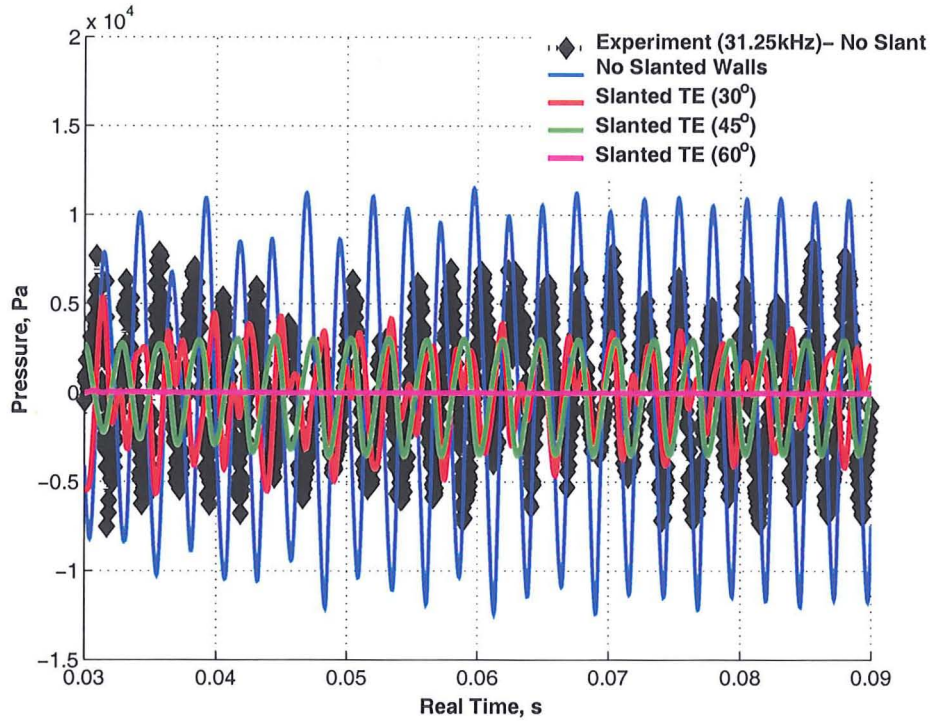

(c) Pressure Traces ($x/L = 0.55$)

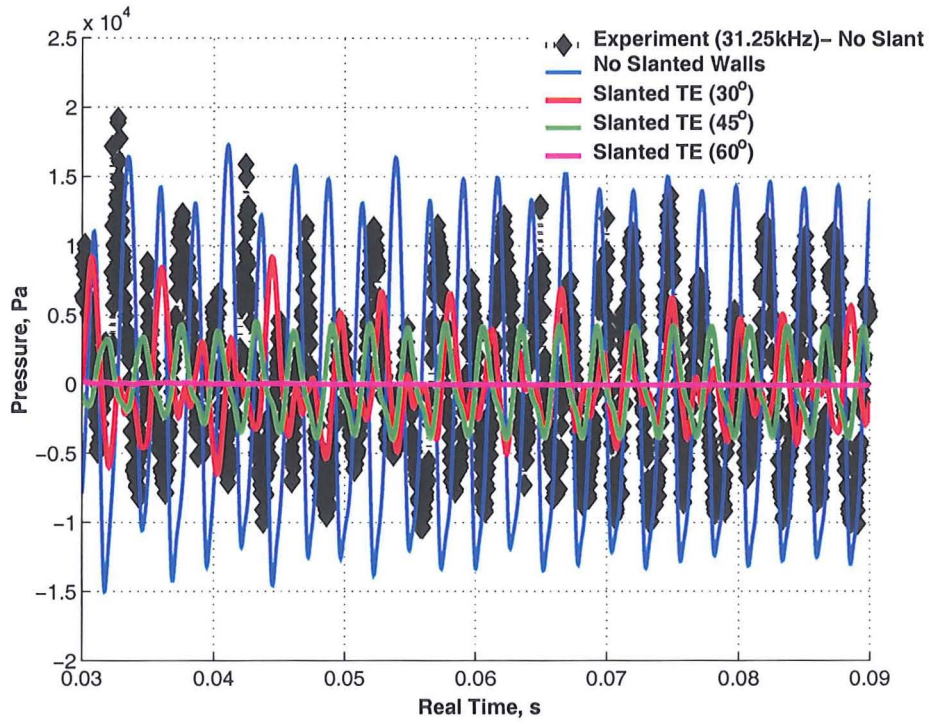

(d) Pressure Traces ($x/L = 0.95$)

Figure A.13: SPLs and pressure traces (at $x/L = 0.05$, $x/L = 0.55$ and $x/L = 0.95$) along the cavity floor for the 2D, L/D=5 cavity using the SST turbulence model for the slanted rear wall at angles of 30°, 45° and 60°.

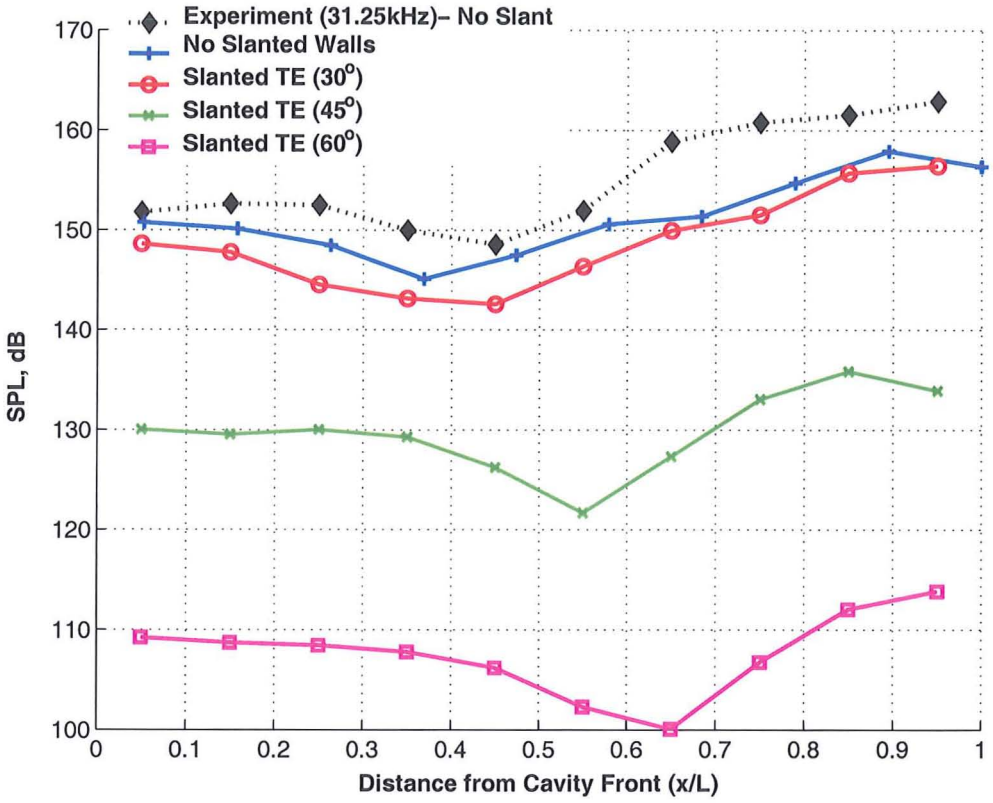

(a) $50\ Hz \leq f \leq 250\ Hz$

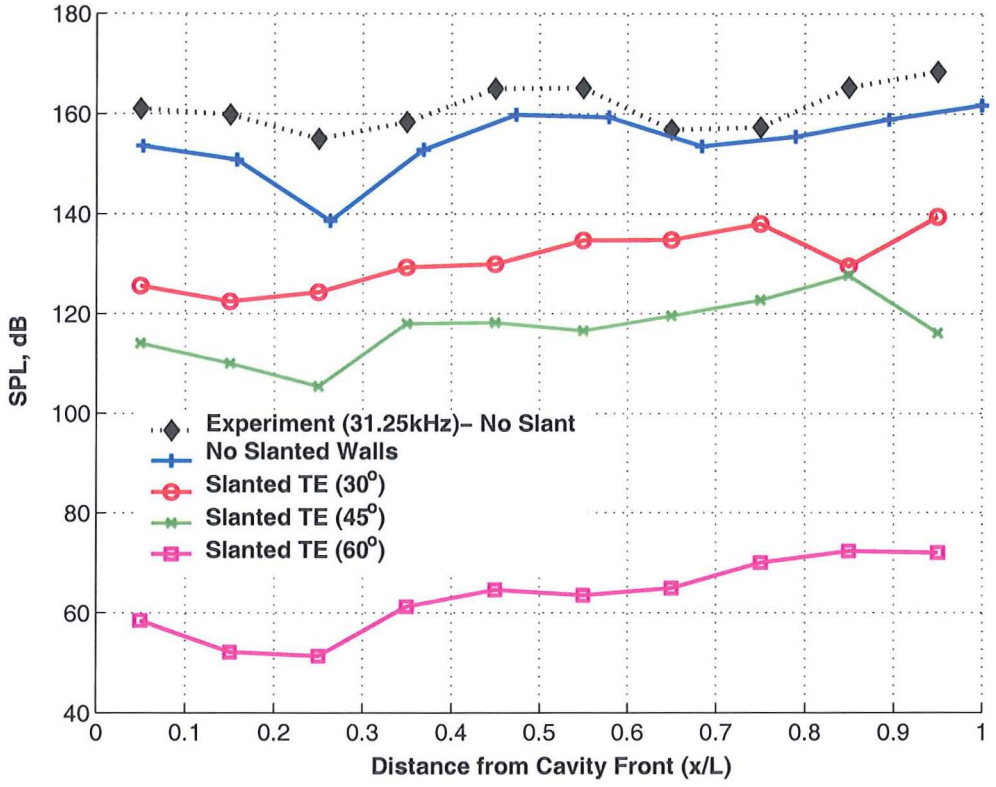

(b) $350\ Hz \leq f \leq 450\ Hz$

Figure A.14: (continued)

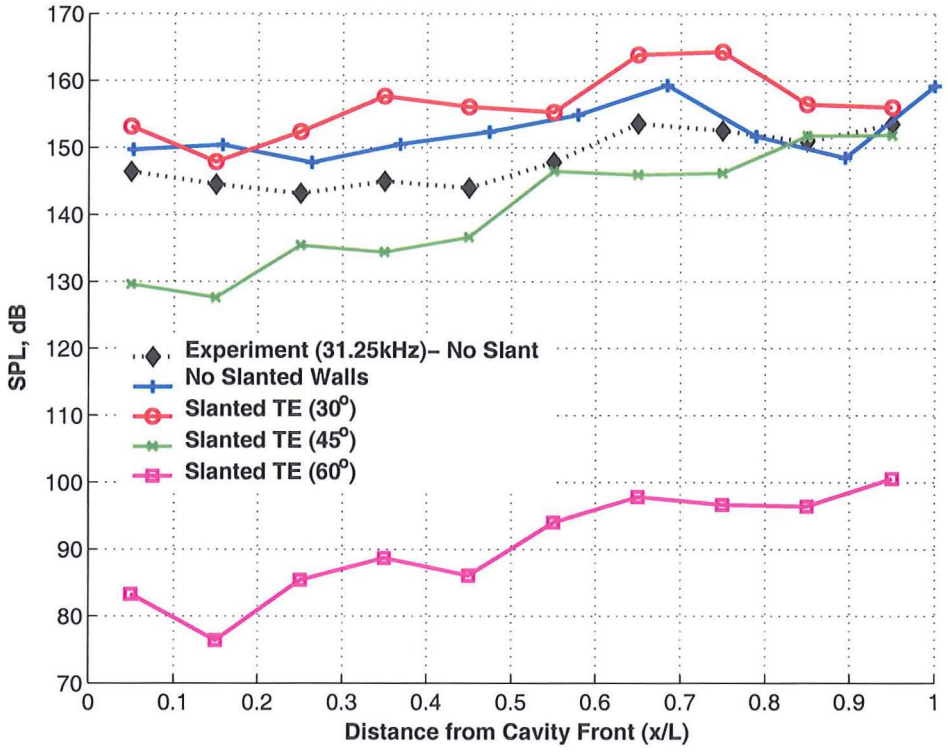

(c) $500\ Hz \leq f \leq 700\ Hz$

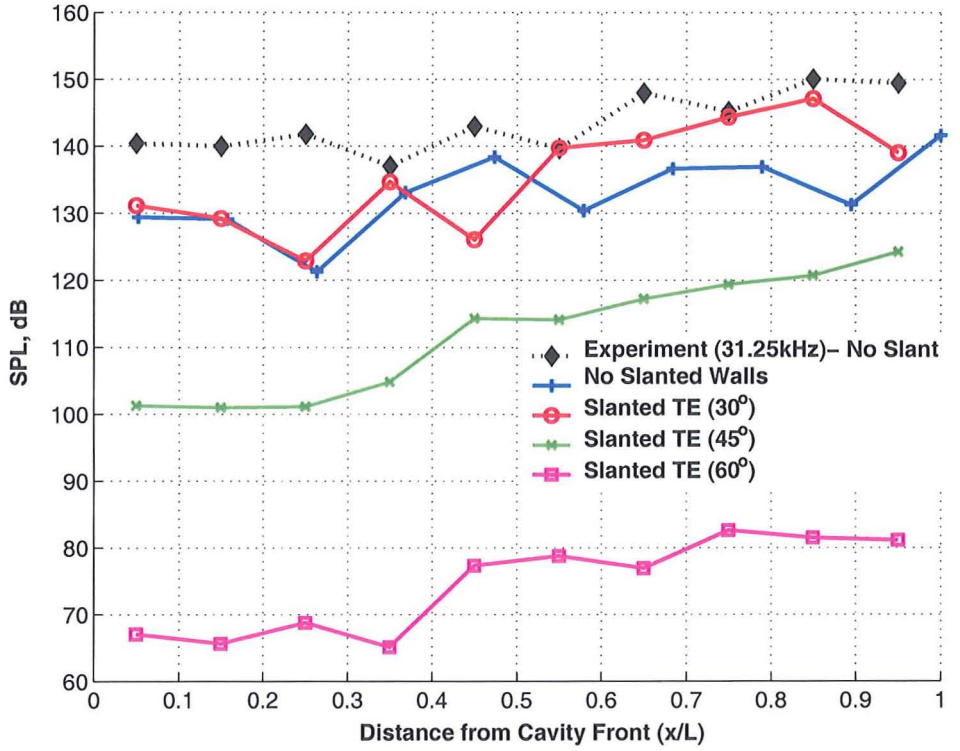

(d) $750\ Hz \leq f \leq 850\ Hz$

Figure A.14: Band-limited SPLs for the 2D, L/D=5 cavity using the SST model for the slanted rear wall at 30°, 45° and 60°.

A.2.2.2 Flow-field Visualisation

Confirmation of the steady flow generated by the 60° slant case is provided in Figure A.15, which shows time-averaged plots of the flow-field inside the cavity using Mach number contours and streamlines to illustrate the vortical structures.

At an inclination of 60°, the plane parallel to the shear layer is extended by $\sqrt{3}D$, making the effective L/D ratio at the shear layer much greater than the actual cavity L/D ratio. The distance the shear has to travel across the cavity opening is therefore much larger making it weaker as it diffuses and redistributes more energy into the surroundings. Combined with the fact that energy from the vortex is also spread over a larger geometrical surface area, the overall noise levels produced along the cavity floor were observed to be significantly reduced.

The flow was therefore found to be the least unsteady when the slant angle was at its greatest (i.e. 60°). The level of activity inside the cavity for this case was much lower and this resulted in much lower SPLs (Figure A.13(a)). Evidence of this is provided by analysing the velocity profile distribution inside the cavity, as was performed previously. Figure A.12 shows the streamwise velocities at $x/L = 0.05$, $x/L = 0.55$ and $x/L = 0.95$ for the slanted rear wall at 30°, 45° and 60°.

At the front of the cavity ($x/L = 0.05$), it was observed that a vortex existed for lower angles of slant (Figure A.12(b)). As the angle of slant was progressively increased, this vortex becomes weaker and the flow activity at this location became minimal (Figure A.15). The strength of the vortices also appeared to be less as the angle of slant was increased. The shear layer deflection was therefore reduced. This is substantiated in Figures A.12(d) and A.12(f) where the distance the shear layer extends outside of the cavity was found to be progressively less. This signifies that the mass breathing process is weaker for higher slant angles and that the flow is more entrained in the cavity leading to lower SPLs and a suppression of higher frequencies. Alternatively, as the angle of slant of the rear wall increased the stagnation point (i.e. point where the shear layer impinged on the downstream wall) fell further into the cavity (i.e. moved closer to the cavity floor) because the shear layer was forced to travel the extra distance without any further increase in its momentum. In these circumstances, a larger amount of energy is required to move the shear layer if the flow is to remain unsteady.

A.3 Active Open-Loop Control: Steady Jet Blowing

The control devices investigated thus far are classified as passive and have involved manipulating the existing cavity geometry or adding physical devices to modify the flow-field in the cavity. The final control method analysed here involves steady jet blowing and is classified as an active open-loop method, based on the discussion given in Chapter 1. Since the flow is not changing in time, steady jet blowing or continuous mass injection can be also be regarded as passive. Unlike the spoiler or slanted cavity walls, however, the jet endeavours to modify the cavity flow-field by blowing additional air into it.

The basic concept of the steady jet was taken from Lamp and Chokani [226] where the jet exit velocity is calculated based on a reservoir total pressure and total temperature, assuming isentropic conditions. The angle of the jet in this paper has been fixed to be

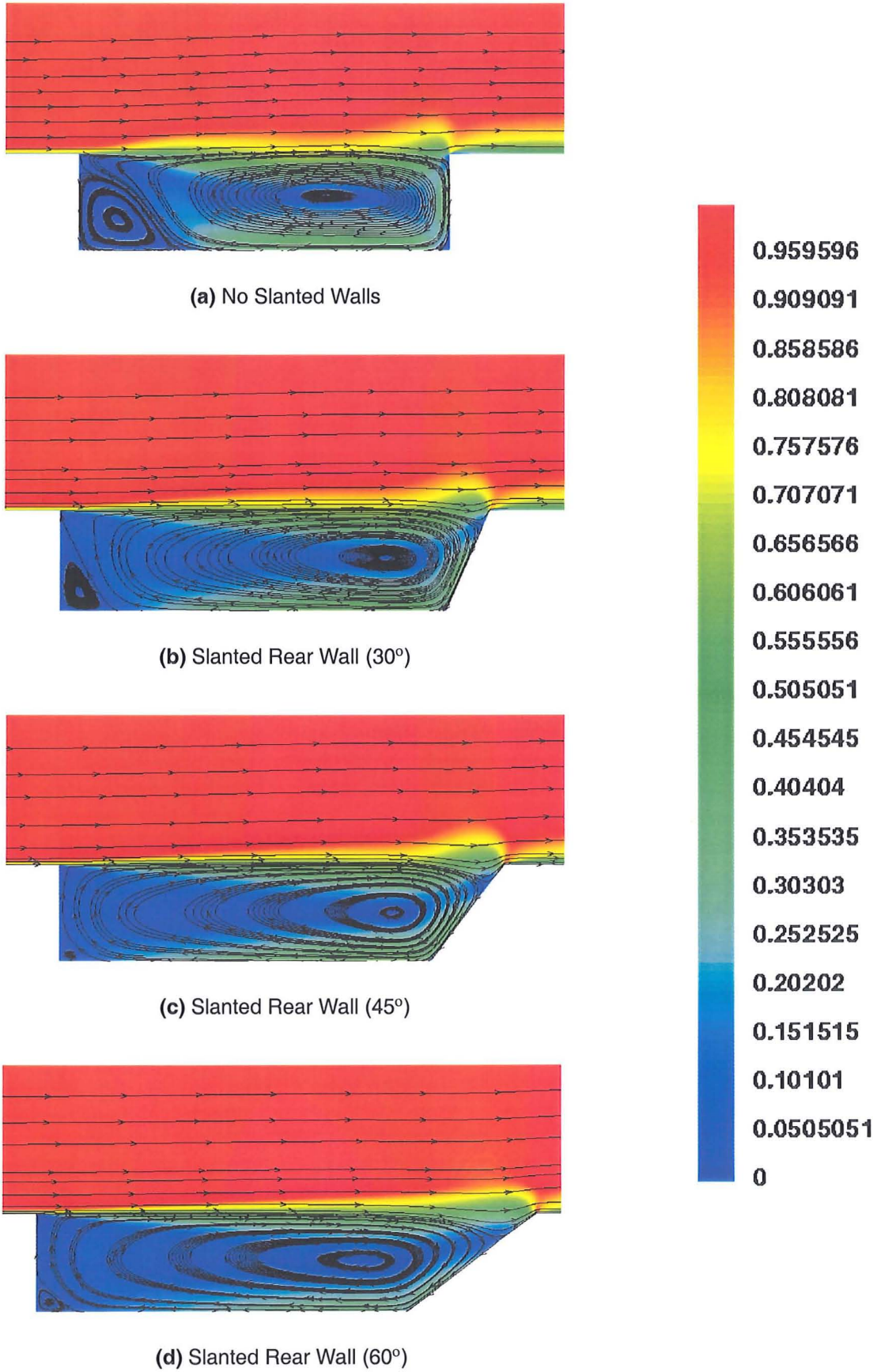

(a) No Slanted Walls

(b) Slanted Rear Wall (30°)

(c) Slanted Rear Wall (45°)

(d) Slanted Rear Wall (60°)

Figure A.15: Time-averaged Mach number contours with streamlines using the SST model for the 2D, L/D=5 cavity with the rear wall slanted at 30°, 45° and 60°.

perpendicular to the flow. For each case presented, the jet exit Mach number is set to $0.1M_\infty$. With a total reservoir pressure and temperature of 2 atmospheres and 298 K respectively, the jet exit velocity was calculated to be 29.4 m/s. The jet slot width, w_j, was kept fixed at 0.02L. For this case, the blowing coefficient, C_μ, derived as the ratio of the exit jet to the free-stream mass flow rate, comes to 0.01. With these jet configurations, computations with three different jet locations were conducted: upstream (i.e. jet located ahead of cavity front corner at $x_j/L = -0.02$, $y_j/L = 0$), front wall (i.e. jet located at $x_j/L = 0$, $y_j/L = -0.02$) and rear wall (i.e. jet located at $x_j/L = 1$, $y_j/L = -0.02$). With the jet fired from the front wall, an additional computation was performed at a higher exit jet Mach number of $0.2M_\infty$ or at an exit jet velocity of 58.8 m/s. A schematic of the jet has been depicted earlier in Figure 7.1(c), which shows all the locations of the jet that were analysed.

A.3.1 Effects of Jet Position

In all jet locations, pressure oscillations and frequencies experienced in the baseline case were damped out with steady jet blowing and the flow became steady. This is illustrated in Figure A.16, which shows the SPLs and pressure traces for the jet located upstream (red line with circular symbols), jet located at the front cavity wall (green line with crosses) and jet located at the downstream cavity wall (magenta line with square signs). For reference, experimental (black line with diamond symbols) and numerical (blue with plus signs) results corresponding to the baseline case without any jet are also included.

In terms of noise levels, positioning the jet inside the cavity was more effective than positioning it upstream of the cavity (Figure A.16(a)). At the cavity front, SPLs were reduced by as much as 20 dB for the upstream and rear wall jets and by more than 30 dB with the front wall jet. In the cavity middle and rear, in particular, the upstream jet was noisier than with the jet inside the cavity, with the former producing SPLs higher by as much as 10 dB in some places. Out of the jets applied inside the cavity, the jet applied at the front wall was most effective.

Despite the dampening of the pressure fluctuations, some flow unsteadiness and therefore acoustic content still exist in the cavity as indicated by the variations in the SPL curve. Oscillations in the pressure signature are a testament to this but are difficult to observe in Figure A.16. A close-up of the pressure trace at the rear of the cavity ($x/L = 0.95$) is thus plotted in Figure A.17 to illustrate these fluctations better. Only the results from the controlled cases with the upstream jet (solid red line with circular symbols), front wall jet (solid green line with crosses) and rear wall jet (solid magenta line with square symbols) are shown.

A.3.1.1 Band-Limited Frequency Analysis

Band-Limited SPLs are presented in Figure A.18 for four frequency ranges. Over the entire frequency spectrum, a consistent pattern was observed. Regardless of the position of the jet, a reduction in the noise levels by at least 30 dB was observed across all the frequency bands. As a control method, the jet was therefore extremely effective in suppressing the frequencies and noise levels created inside the cavity.

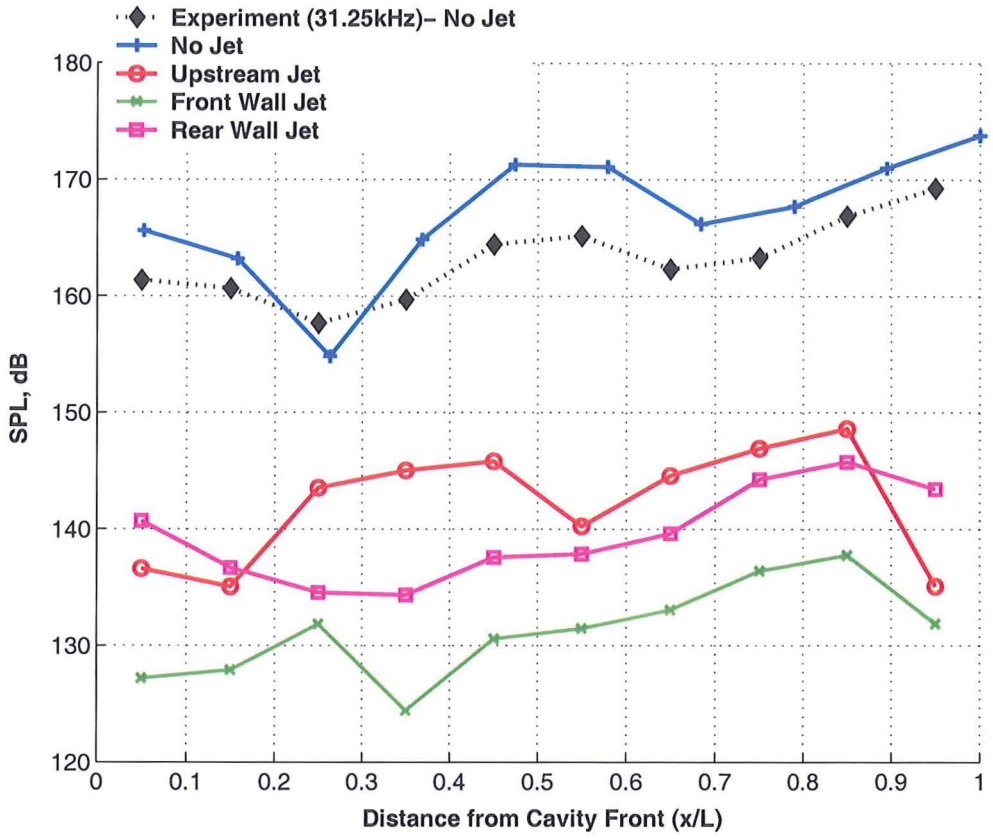

(a) SPLs

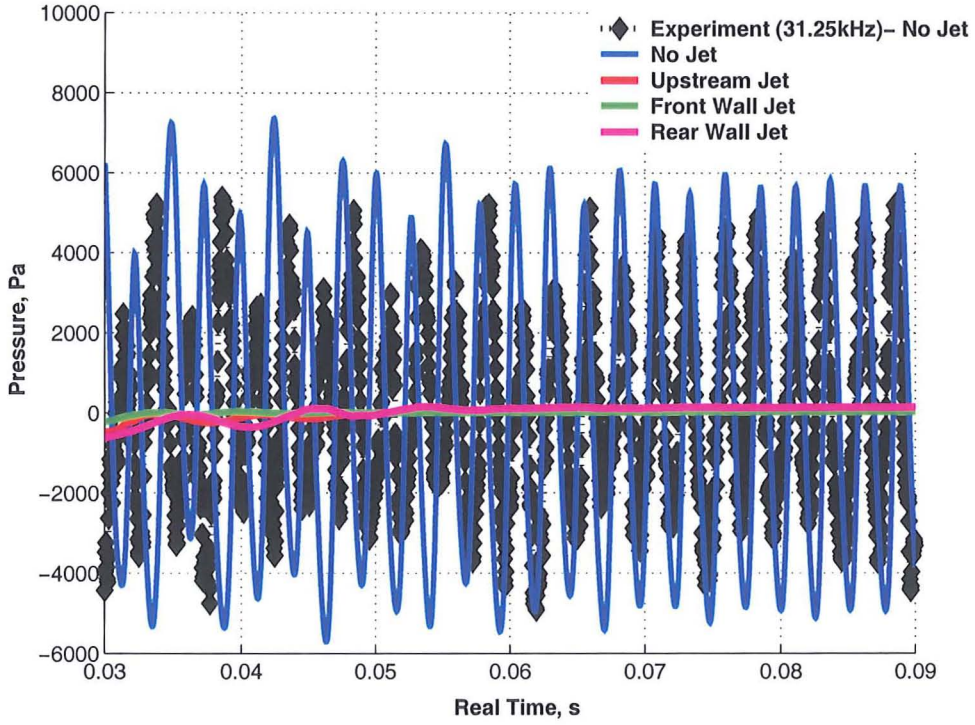

(b) Pressure Traces ($x/L = 0.05$)

Figure A.16: (continued)

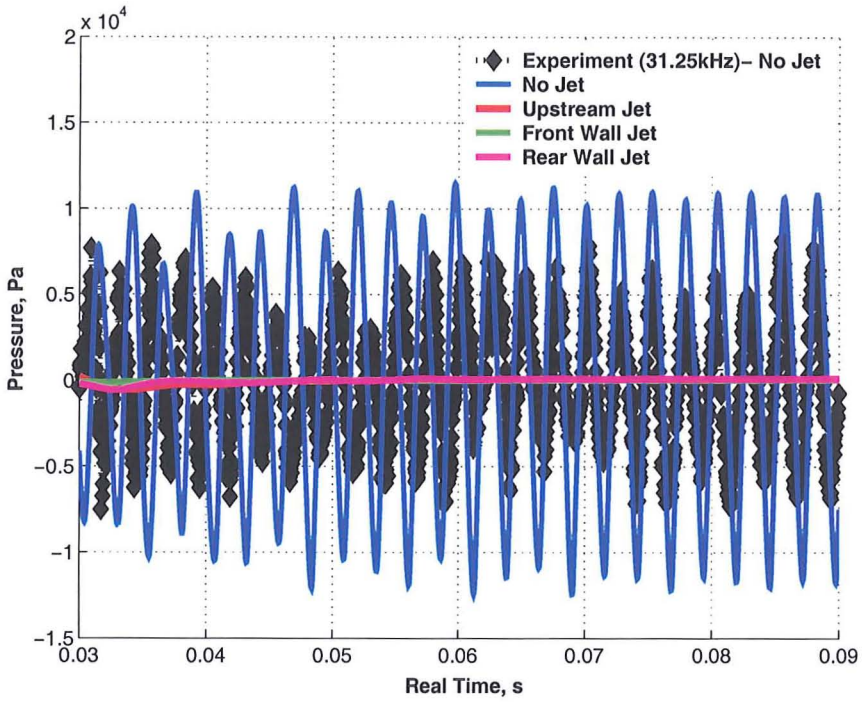

(c) Pressure Traces ($x/L = 0.55$)

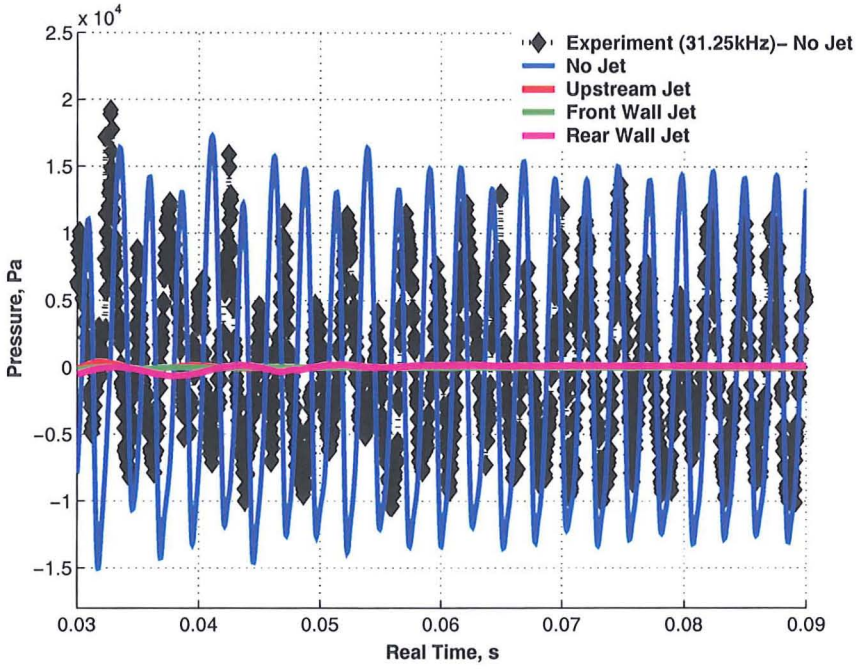

(d) Pressure Traces ($x/L = 0.95$)

Figure A.16: SPLs and pressure traces (at $x/L = 0.05$, $x/L = 0.55$ and $x/L = 0.95$) along the cavity floor for the 2D, L/D=5 cavity using the SST turbulence model with steady jet blowing applied upstream of cavity, at front wall and at rear wall. Upstream jet: $x_j/L = -0.02$, $y_j/L = 0$; front wall jet: $x_j/L = 0$, $y_j/L = -0.02$; rear wall jet: $x_j/L = 1$, $y_j/L = -0.02$. Jet exit Mach number (M_j), jet slot width (w_j) and blowing co-efficient (C_μ) kept fixed at $0.1M_\infty$, 0.02L and 0.01, respectively.

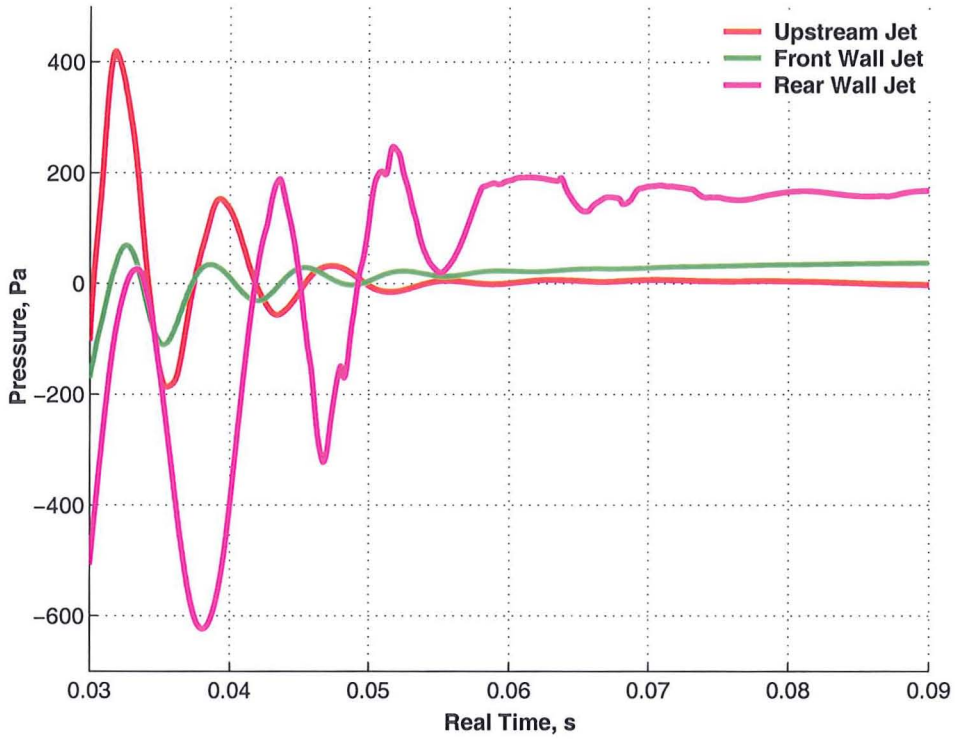

Figure A.17: A close-up of the pressure trace (at $x/L = 0.95$) along the cavity floor for the 2D, L/D=5 cavity using the SST turbulence model with steady jet blowing applied upstream of cavity, at front wall and at rear wall. Upstream jet: $x_j/L = -0.02$, $y_j/L = 0$; front wall jet: $x_j/L = 0$, $y_j/L = -0.02$; rear wall jet: $x_j/L = 1$, $y_j/L = -0.02$. Jet exit Mach number (M_j), jet slot width (w_j) and blowing co-efficient (C_μ) kept fixed at $0.1M_\infty$, 0.02L and 0.01, respectively.

From the three jet positions analysed, however, the front wall jet proved to be the most effective. When the jet is applied from the front wall of the cavity, i.e. in the downstream direction, noise levels for the lower and higher frequencies were significantly reduced. With SPLs as low as 50 dB observed for frequencies above 500 Hz (Figures A.18(c) and A.18(d)), it can be assumed that higher frequencies are completely eliminated for this jet position with an exit jet Mach of 0.1 (equivalent to 29.4 m/s of jet air flow).

When the jet was applied from the rear wall, i.e. fired upstream in the direction opposite to the shear layer motion, noise levels produced were much higher when compared to the front wall jet. Firing the jet from the rear wall therefore exacerbated the situation, especially since the effect of higher frequencies was significantly more pronounced. When the jet was applied upstream of the cavity, i.e. fired orthogonal to the oncoming free-stream, noise levels produced were higher than the front wall jet but still lower than the rear wall jet across all the four frequency domains analysed.

A.3.1.2 Flow-field Visualisation

The reason why the jet was so effective in controlling the self-sustained oscillations inside the cavity can be illustrated using the time-averaged Mach contour plots of Figure A.19. With the jet located at the front wall Figure A.22(b), the jet adds more momentum to the

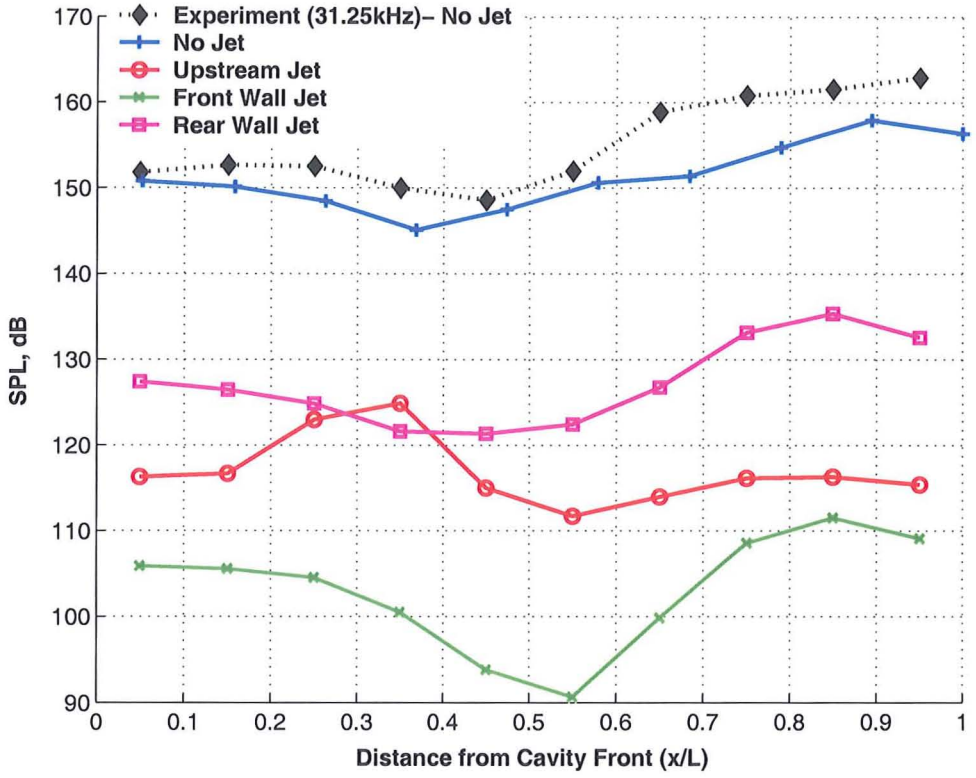

(a) $50\ Hz \leq f \leq 250\ Hz$

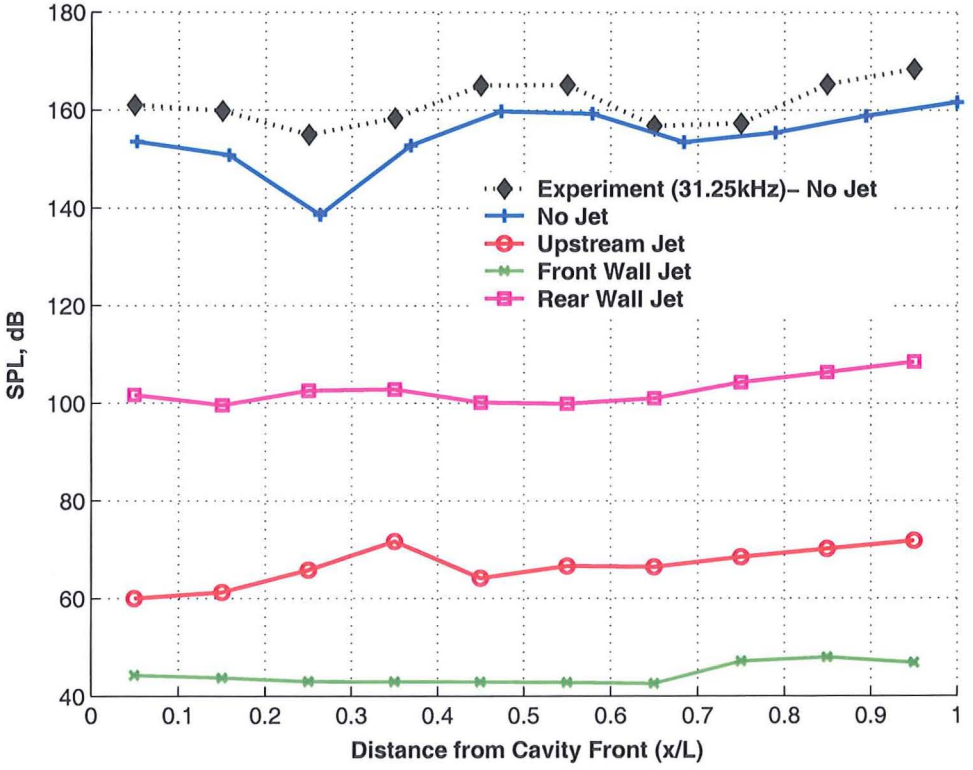

(b) $350\ Hz \leq f \leq 450\ Hz$

Figure A.18: (continued)

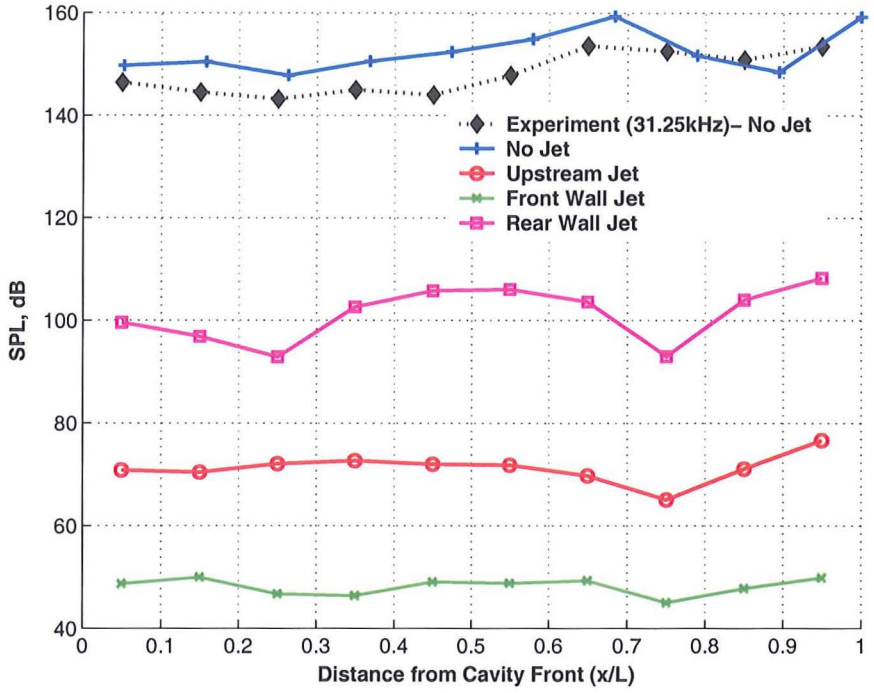

(c) $500\ Hz \leq f \leq 700\ Hz$

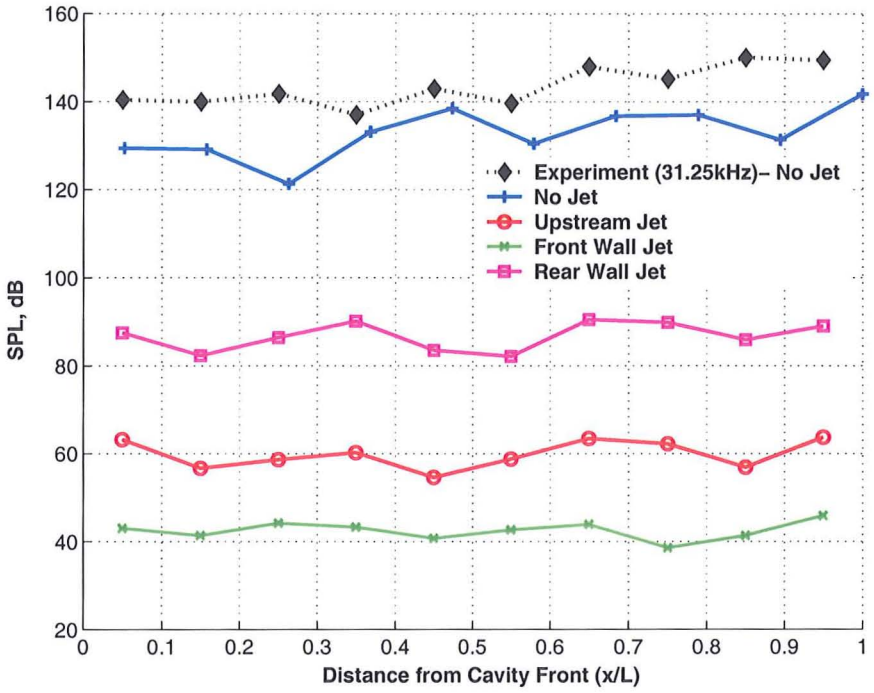

(d) $750\ Hz \leq f \leq 850\ Hz$

Figure A.18: Band-limited SPLs along the cavity floor for the 2D, L/D=5 cavity using the SST turbulence model with steady jet blowing applied upstream of cavity, at front wall and at rear wall. Upstream jet: $x_j/L = -0.02$, $y_j/L = 0$; front wall jet: $x_j/L = 0$, $y_j/L = -0.02$; rear wall jet: $x_j/L = 1$, $y_j/L = -0.02$. Jet exit Mach number (M_j), jet slot width (w_j) and blowing co-efficient (C_μ) kept fixed at $0.1M_\infty$, 0.02L and 0.01, respectively.

shear layer. The extra momentum ensures that the shear layer entirely bridges the cavity opening and minimises the extent to which energy is transferred from the shear layer to within the cavity. The acoustical disturbances caused by the impingement of the flow at the cavity downstream wall are therefore eliminated and the pressure waves and hence the self-sustained pressure oscillations maintained by the receptivity cycle is cancelled out. The flow becomes steady and the typical dual-vortex cycle with large shear layer deflection as observed in the baseline case (Figure A.22(a)) becomes a single, static vortex with no shear layer deflection with steady jet blowing (Figure A.22(b)).

With the jet positioned at the downstream wall, the steady jet fires air in the opposite direction from the oncoming flow. This aims to extract momentum from the shear layer and forces it to slow down and diffuse. Since the impingement point is typically located near the location of the jet, the relatively large jet exit velocities therefore prevent the flow from impacting the downstream wall thereby precluding the formation of acoustical disturbances. In terms of flow structures inside the cavity, the result of the rear-wall jet (Figure A.19(d)) is similar to that of the front-wall jet. The rear wall jet is therefore still effective in reducing the noise levels when compared to experiment (Figure A.16(a))

When compared with the front wall jet, however, the rear wall jet produced significantly more noise. The greater region of higher Mach numbers depicted by the lighter, green colours in Figure A.19(d) is indicative of the greater interaction between the vortices and the cavity floor and hence greater noise. Peripheral velocities of the primary vortex at the rear must therefore be larger in this configuration for this to occur. This in turn suggests that the vortex inside the cavity is stronger, which is due to the greater energy and momentum transferred into the cavity from the diffused shear layer. This diffused shear layer is clearly evident from the larger cross-sectional area of the flow shed downstream of the cavity in Figure A.19(d).

In the case of the jet located ahead of the cavity front wall, the jet is fired vertically upwards. This adds momentum to the transverse component and the shear layer deflects upwards, forcing it to detach from the surface earlier. The 'curved' shear layer creates a more favourable pressure gradient and tends to accelerate the flow over it creating a region of higher Mach (Figure A.19(b)) outside the cavity. This also translates to a region of higher Mach number flow inside the cavity as well because the inclined shear layer interacts with the free-stream, diffuses and redistributes its momentum into the cavity. Vortices of larger circulation strength are therefore created as depicted by the region of stronger Mach number at the rear of the cavity floor in Figure A.19(b) compared to other jet locations. The higher peripheral vortex velocities at the cavity floor are attributed to the higher noise levels generated inside the cavity for the upstream jet as demonstrated in Figure A.16(a). As the shear layer is redirected by the upstream jet, impingement of the shear layer with the cavity rear wall is again negated and the self-sustained pressure oscillations are attenuated. The result is therefore a steady solution (Figure A.16) and a single-vortex structure inside the cavity (Figure A.19(b)).

A.3.2 Effects of Jet Exit Velocity

The influence of the exit jet velocity is now presented. Position of the jet was fixed in this study to the front wall with the jet exit Mach number (relative to the free-stream Mach of 0.85) varied from 0.1 to 0.2, the latter resulting in a exit jet velocity of 58.8 m/s. The specifications of the jet for these two different jet velocities are given in Table A.2.

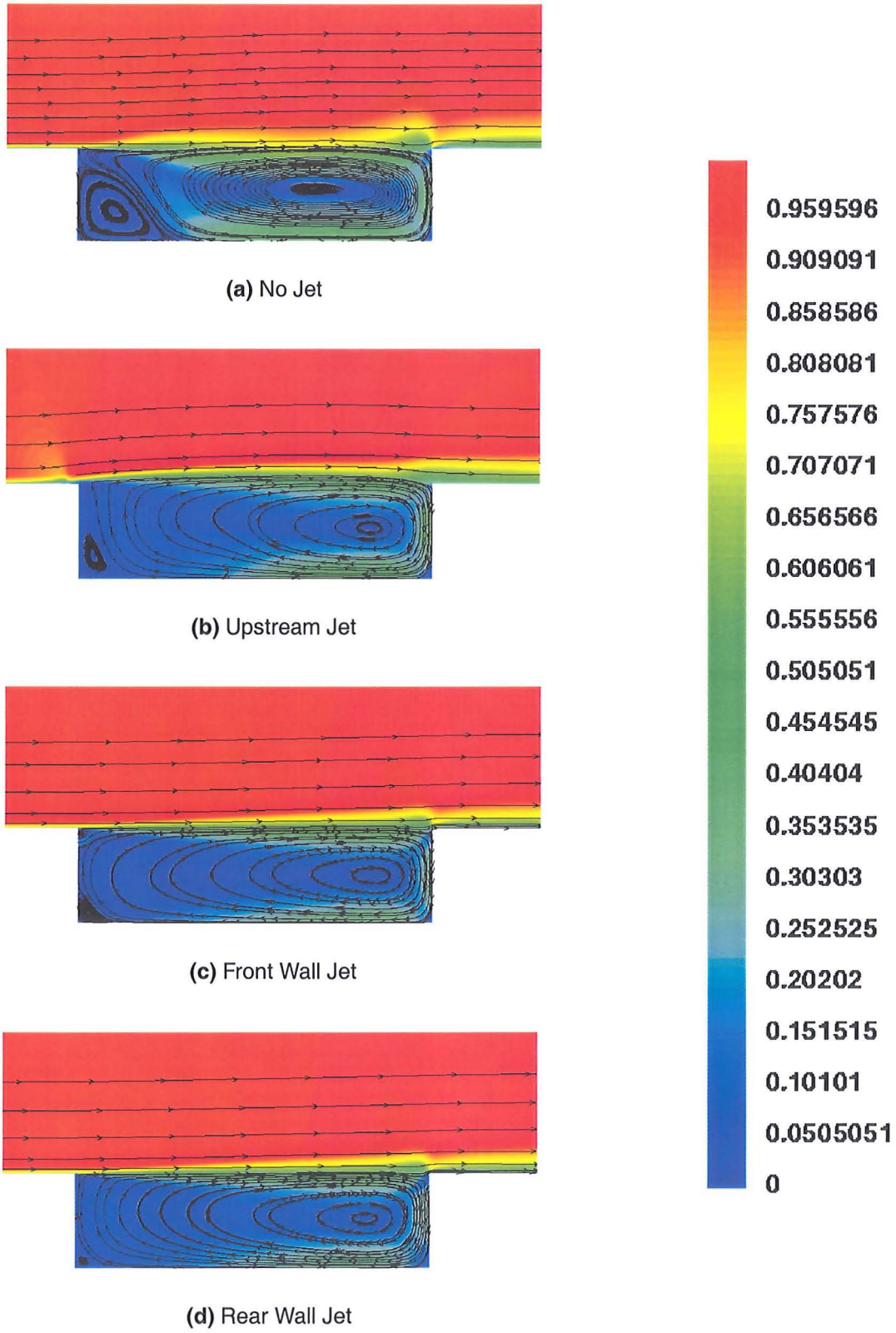

(a) No Jet

(b) Upstream Jet

(c) Front Wall Jet

(d) Rear Wall Jet

Figure A.19: Time-averaged Mach number contours with streamlines inside the 2D, L/D=5 cavity using the SST turbulence model with steady jet blowing applied upstream of cavity, at front wall and at rear wall. For reference, flow-field for the no-jet case also included. Upstream jet: $x_j/L = -0.02$, $y_j/L = 0$; front wall jet: $x_j/L = 0$, $y_j/L = -0.02$; rear wall jet: $x_j/L = 1$, $y_j/L = -0.02$. Jet exit Mach number (M_j), jet slot width (w_j) and blowing co-efficient (C_μ) kept fixed at $0.1M_\infty$, 0.02L and 0.01, respectively.

Table A.2: Jet exit conditions for the front wall jet. Values calculated using total reservoir pressure and temperature of 2 atmospheres and 298 K respectively. The jet slot width, w_j, was kept fixed at 0.02L.

Jet Location	**Front Wall**	**Front Wall**
Jet Exit Mach (M_j)	0.1	0.2
Jet Exit Velocity, m/s (U_j)	29.4	58.8
Jet Exit Pressure, Pa	201,628	198,603
Jet Exit Density, kg/m^3	2.36	2.335
Jet Mass Flow Rate, kg/s	0.35	0.7
Blowing Coefficient (C_μ)	0.01	0.02

Pressure traces and SPLs for these two exit jet velocities are illustrated in Figure A.20, in which experiment and numerical results for the baseline case are superimposed to highlight effectiveness of the control method. Although the flow still remained steady with a higher exit jet velocity, more unsteadiness is observed during the earlier stages of the pressure signal. This is likely to be the reason for the slightly higher overall SPLs observed with the higher exit jet velocity (Figure A.20(a)).

A.3.2.1 Band-Limited Frequency Analysis

SPL variations across four frequency windows are presented in Figure A.21. At higher frequencies (i.e. greater than 500 Hz), differences between the two exit jet velocities were minimal (Figures A.21(c) and A.21(d)). The higher exit jet velocity however generated more energy in the first and second Rossiter modes (Figure A.21(a)-A.21(b)). This increase was larger for the second mode (about 10 dB) compared to the first mode (about 5 dB). Frequencies above the 250 Hz were almost completely eliminated with both exit jet velocities with the first mode (although still lower than experiment by about 40-50 dB) contributing the most noise.

A.3.2.2 Flow-field Visualisation

The time-averaged flow-field inside the cavity is presented in Figure A.22. Differences between the higher and lower exit jet velocity cases were little. In both cases, the front corner vortex apparent in the baseline case (Figure A.22(a)) was reduced. This is evidence of the fact that the vortices residing in the cavity are much weaker. When a relatively strong primary vortex is forced to separate on approach to the front cavity wall, the front corner vortex forms. With a weaker primary vortex, however, the flow can remain attached along the cavity length for longer thereby preventing the formation of the front corner vortex.

In fact, with a higher exit jet velocity (Figure A.22(c)), the front corner vortex was even smaller in size than with a lower exit jet velocity (Figure A.22(b)). This suggested that the primary vortex situated at the rear of the cavity for the higher exit jet velocity case was slightly weaker than with a lower exit jet velocity. Additional momentum from the stronger jet at the cavity front into the shear layer forces the shear layer to remain more coherent across the cavity opening. The higher overall SPLs observed for the higher exit jet velocity

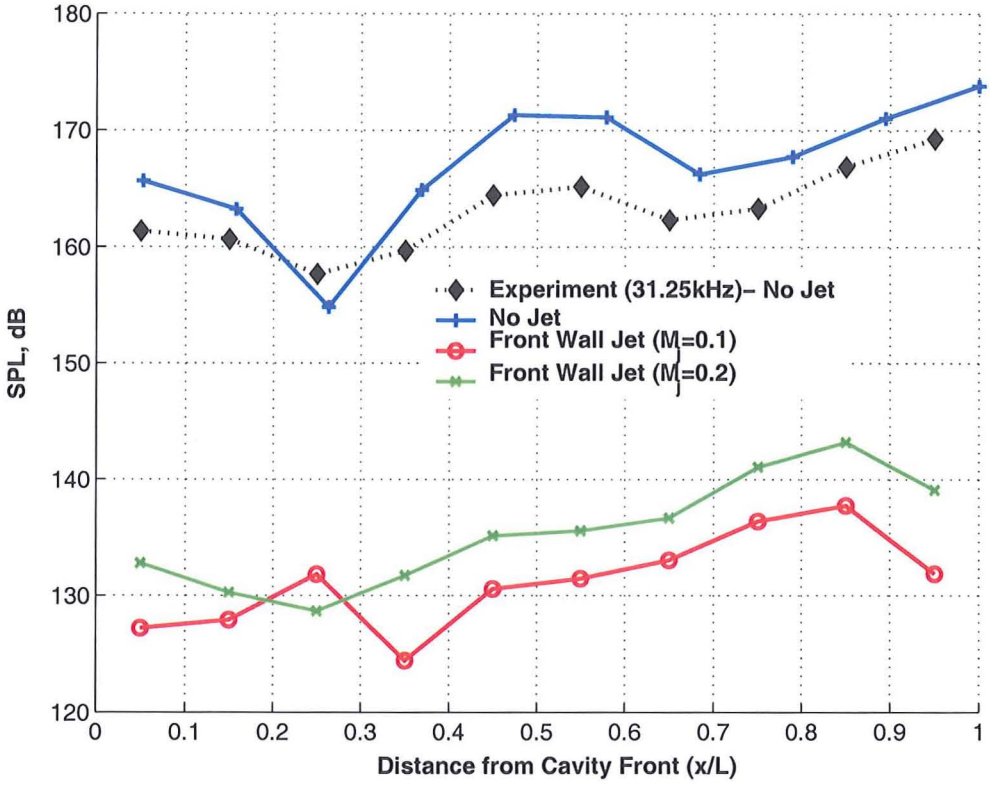

(a) SPLs

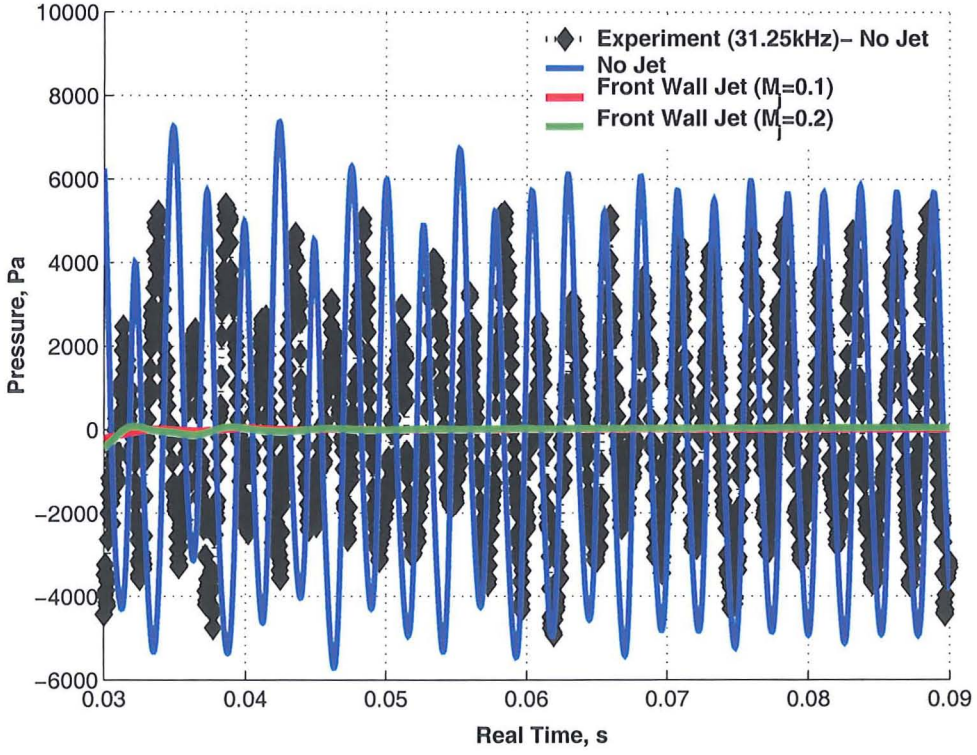

(b) Pressure Traces ($x/L = 0.05$)

Figure A.20: (continued)

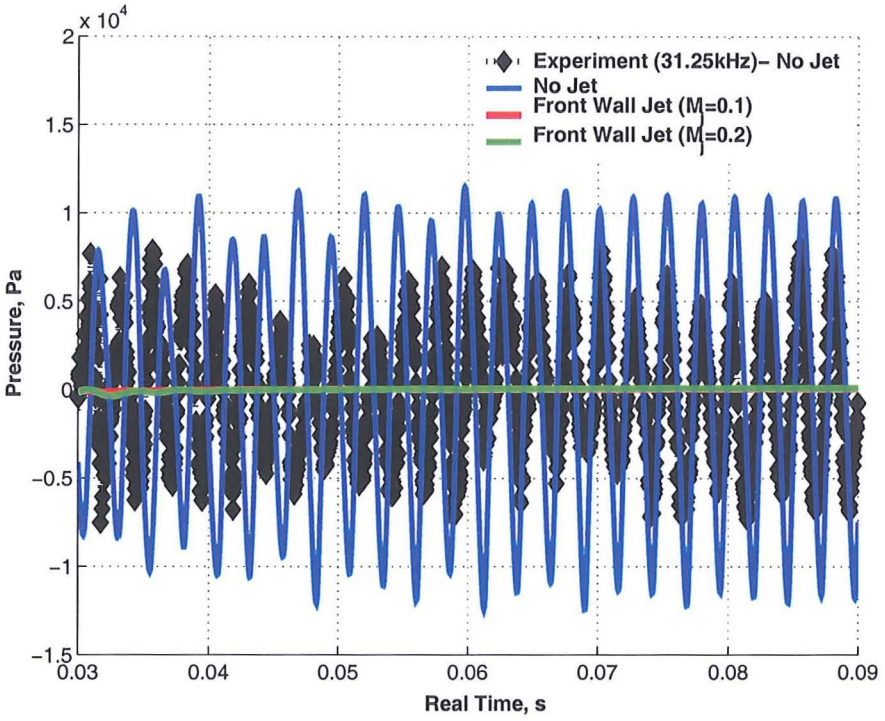

(c) Pressure Traces ($x/L = 0.55$)

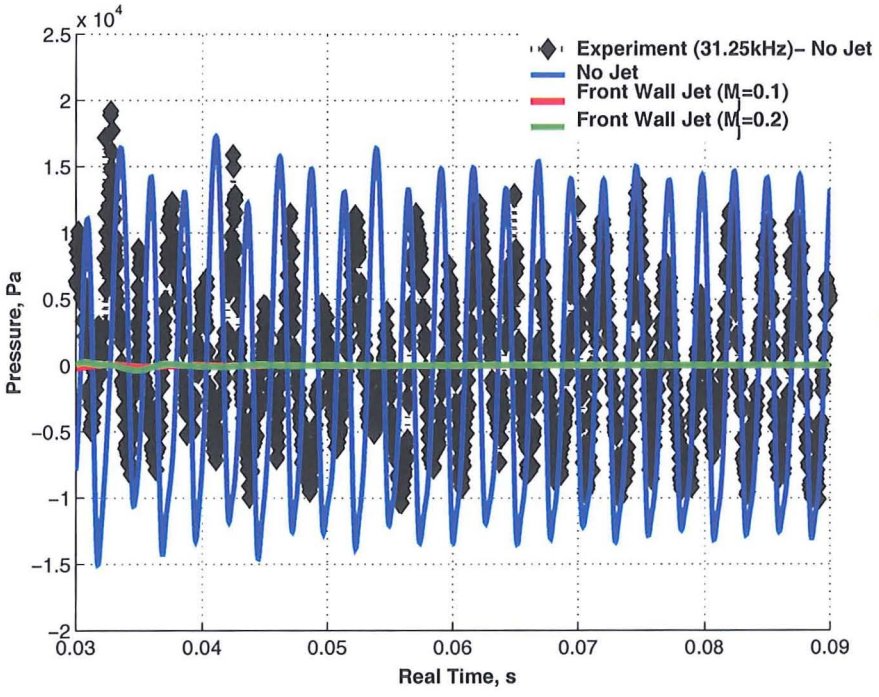

(d) Pressure Traces ($x/L = 0.95$)

Figure A.20: SPLs and pressure traces (at $x/L = 0.05$, $x/L = 0.55$ and $x/L = 0.95$) along the cavity floor for the 2D, L/D=5 cavity using the SST turbulence model with steady jet blowing applied at the front wall for an exit jet Mach of 0.1 and 0.2. Front wall jet: $x_j/L = 0$, $y_j/L = -0.02$, $w_j/L = 0.02$. Blowing co-efficient (C_μ) varied from 0.01 to 0.02.

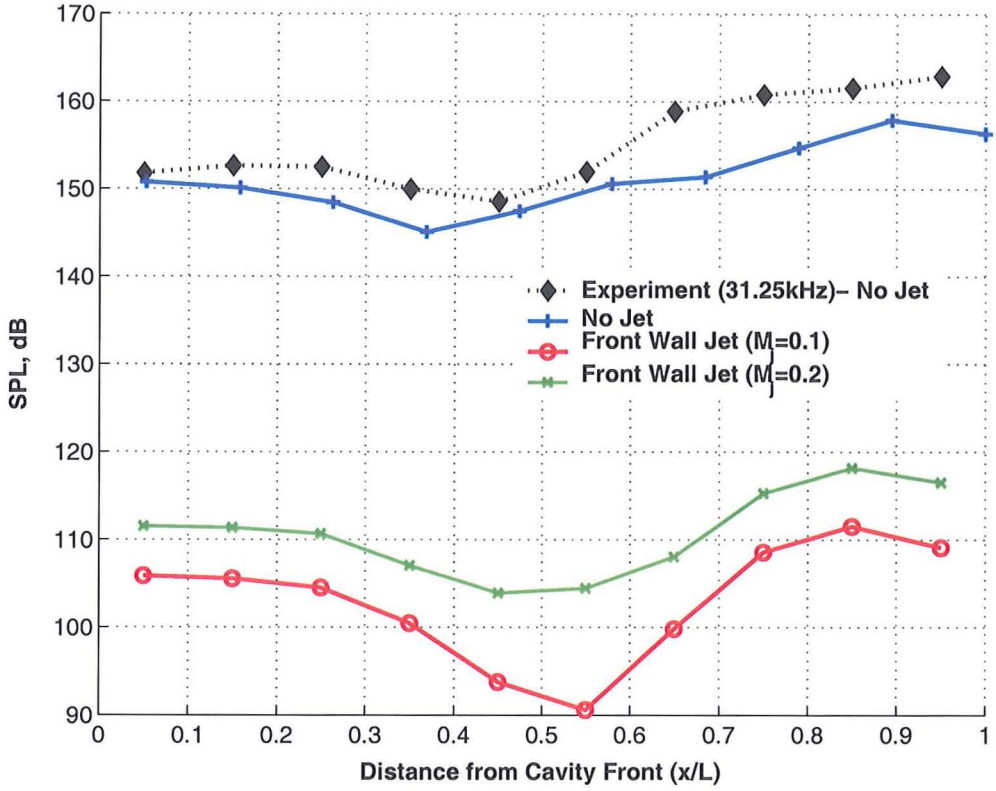

(a) $50\ Hz \leq f \leq 250\ Hz$

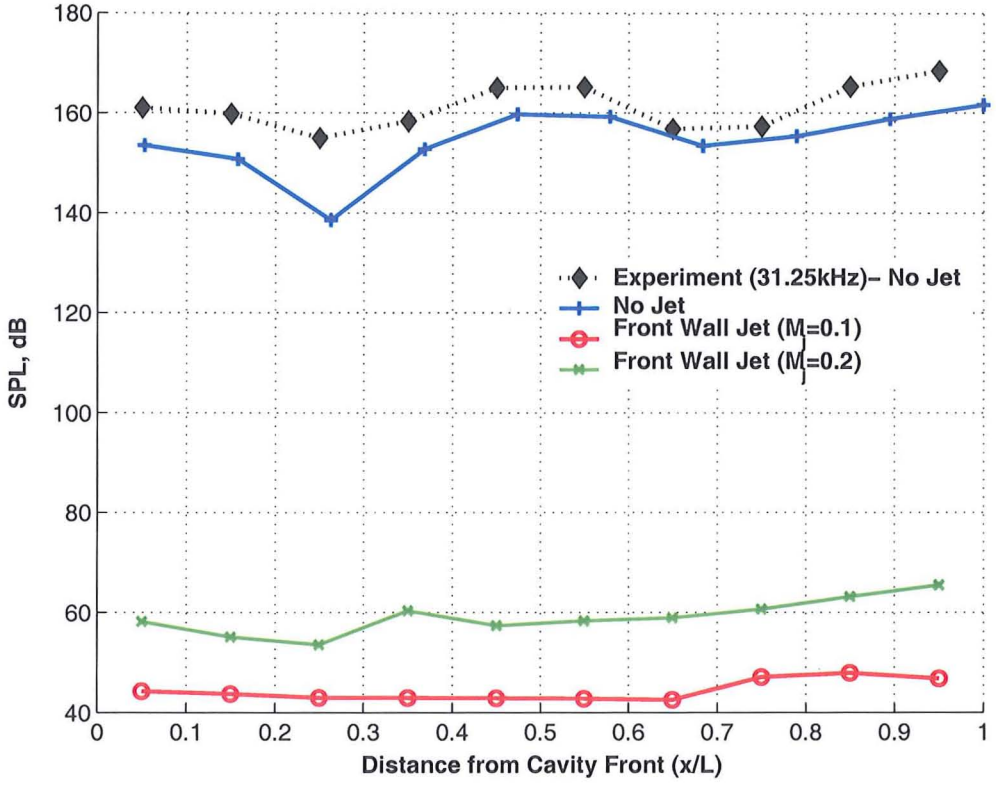

(b) $350\ Hz \leq f \leq 450\ Hz$

Figure A.21: (continued)

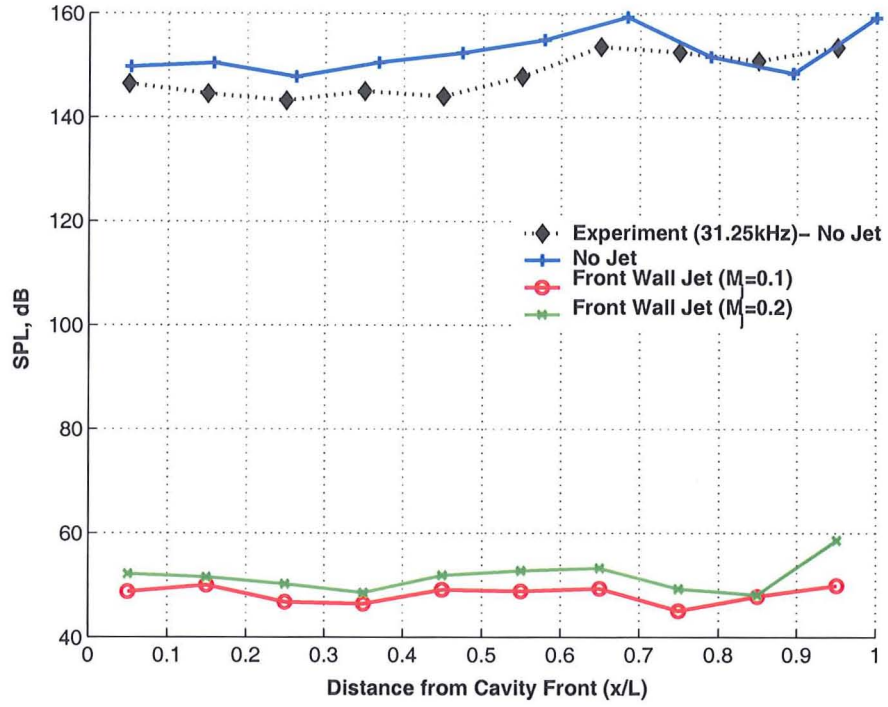

(c) $500\ Hz \leq f \leq 700\ Hz$

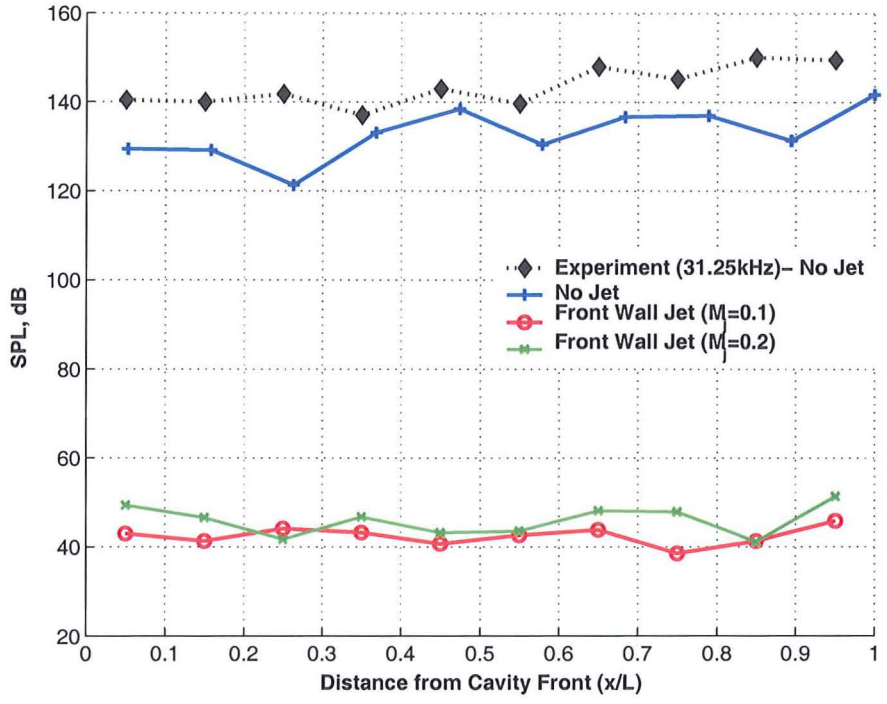

(d) $750\ Hz \leq f \leq 850\ Hz$

Figure A.21: Band-limited SPLs along the cavity floor for the 2D, L/D=5 cavity using the SST turbulence model with steady jet blowing applied at the front wall with an exit jet Mach of 0.1 and 0.2. Front wall jet: $x_j/L = 0$, $y_j/L = -0.02$, $w_j/L = 0.02$. Blowing co-efficient (C_μ) varied from 0.01 to 0.02.

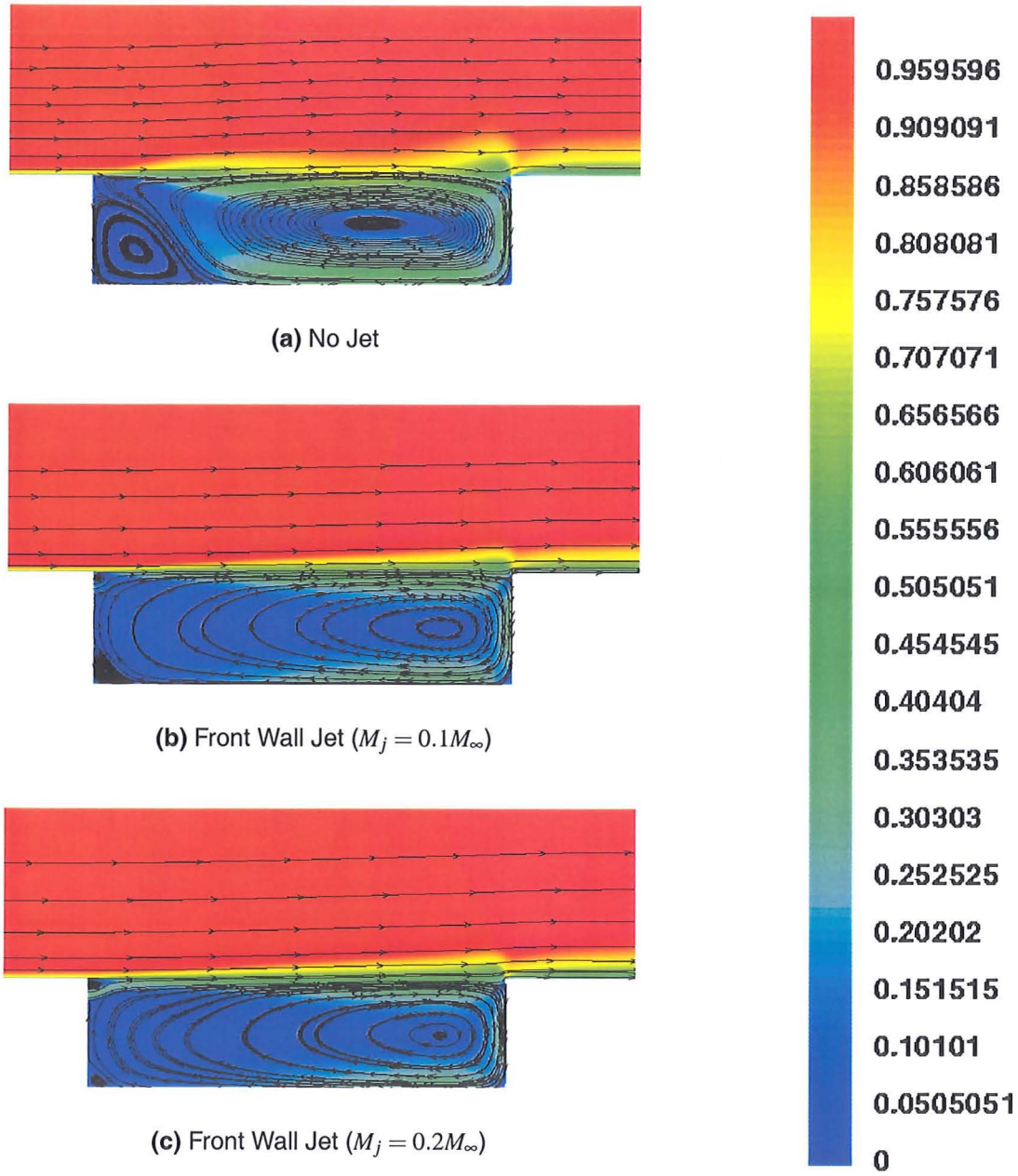

(a) No Jet

(b) Front Wall Jet ($M_j = 0.1M_\infty$)

(c) Front Wall Jet ($M_j = 0.2M_\infty$)

Figure A.22: Time-averaged Mach number contours with streamlines inside the 2D, L/D=5 cavity using the SST turbulence model with steady jet blowing applied at front wall wfor exit jet Mach numbers of 0.1 and 0.2. Front wall jet: $x_j/L = 0$, $y_j/L = -0.02$, $w_j/L = 0.02$. Blowing co-efficient (C_μ) varied from 0.01 to 0.02.

case arise predominantly from the jet itself as it fires air at higher speeds from a small slot width (i.e. $w_j = 0.02L$).

A.4 Concluding Remarks

Calculations with different passive and active open-loop control methods with the L/D=5 cavity were conducted in the aim of reducing the high noise levels and large frequency content observed inside the cavity. The effectiveness of the spoiler and slanted cavity

walls as a passive control method and continuous mass injection as an active open-loop control method was investigated.

For the spoiler, when the spoiler was placed upstream of the cavity lip, signficant noise level reduction was observed inside the cavity and the flow became steady. With the spoiler placed downstream of the cavity, however, pressure amplitudes were increased and the wake mode was instigated. When the height of the spoiler (positioned upstream of the cavity lip) was increased, greater noise reductions (by about 5 dB) was achieved at the rear of the cavity. For the LE spoiler, both the higher frequencies and overall noise levels were reduced. Reasoning behind the effectiveness of the spoiler was attributed to the premature separation of the boundary layer upstream of the cavity. The shear layer was therefore offset from the cavity opening by a distance approximately equal to the spoiler height and this prevented acoustical disturbances from being generated via the impingement of the shear layer with the downstream wall. It was noticed that the flow aft of the spoiler was typically independent of the mainstream flow inside the cavity. Based on the geometry of this 'artificial' cavity, a crude description of the flow-field in the main cavity can be estimated. When this 'artificial' cavity has a L/D ratio much lower or higher than that of the mainstream L/D=5 cavity, a further drop in the noise levels was observed.

With slanted cavity walls, slanting the downstream wall was found to be more effective. Slanting the front wall induced massive separation at the front corner. Vortices shed from the cavity front were therefore stronger and generated more unsteadiness and higher SPLs inside the cavity. When the angle of the rear wall slant was increased, SPLs and frequencies inside the cavity were significantly reduced with higher frequencies almost completely eliminated. This was attributed to the shear layer being entrained inside the cavity. The greater rear wall surface spread the energy of the shear layer and the vortices thereby minimising the mass breathing process and reducing the deflections of the shear layer. It was found that the slanted rear wall only became effective in reducing the cavity pressure oscillations if the angle of slant was greater than 30^{o}.

Steady jet blowing was found to be the most effective of all control methods. Jet fired from the front cavity competely suppressed all acoustic tones and the flow became steady. Although with jets positioned at different locations (i.e. upstream of the cavity front corner and at the rear wall) the flow also became steady, noise produced inside the cavity from these positions was much higher from the jet placed at the cavity front wall. Higher exit jet velocities reduced the strength of the vortex inside the cavity even further but added slightly more noise as the jet propelled air at a faster rate from the small slot. Additional momentum added into the shear layer by the front wall jet forced the shear layer to extend across the cavity opening. This prevented the shear layer from dipping into the cavity and avoided it from impinging at the downstream wall thereby eliminating the feedback process. Redistribution of energy from the shear layer to the vortices inside the cavity was also minimised as a result thereby reducing the unsteadiness in the flow.

References

[1] Various Authors. Aerodynamics and Aero-Acoustics of Rectangular Planform Cavities. Part I: Time-Averaged Flow. Technical Report 02008, Engineering Sciences Data Unit, April 2004.

[2] N. Taborda, D. Bray, and K. Knowles. Experimental Invesigation into Transonic Flows over Tandem Cavities. *The Aeronautical Journal*, 105(1045):119–124, March 2001.

[3] J.E. Rossiter. The Effect of Cavities on the Buffeting of Aircraft. Technical Memorandum 754, Royal Aircraft Establishment, Farnborough, UK, April 1962.

[4] C.K.W. Tam and P.J.W. Block. On the Tones and Pressure Oscillations Induced by Flow over Rectangular Cavities. *Journal of Fluid Mechanics*, 89(2):373–399, 1978.

[5] K.J. Badcock, B.E. Richards and M.A. Woodgate. Elements of Computational Fluid Dynamics on Block Structured Grids Using Implicit Solvers. *Progress in Aerospace Sciences*, 36:351–392, 2000.

[6] J.A. Ross. PIV Measurements of the Flowfields in an Aerodynamically Deep Cavity, May 2002. Private Communication.

[7] J.A. Ross, J.W. Peto. Internal Stores Carriage Research at RAE. Technical Memorandum 2233, QinetiQ, January 1992.

[8] J.A. Ross, J.W. Peto. The Unsteady Environment Within an Internal Weapons Bay or Cavity. Technical report, QinetiQ, November 1992.

[9] J. Henderson. *Investigation of Cavity Flow Aerodynamics Using Computational Fluid Dynamics*. PhD thesis, University of Glasgow, 2001.

[10] D. Lawrie. *Investigation of Cavity Flows at Low and High Reynolds Numbers Using Computational Fluid Dynamics*. PhD thesis, University of Glasgow, 2004.

[11] J.A. Ross and J.W. Peto. The Effect of Cavity Shaping, Front Spoilers and Ceiling Bleed on Loads Acting on Stores, and on the Unsteady Environment Within Weapons Bays. Technical Report DERA/AS/HWA/CR97010/1/1, QinetiQ, March 1997.

[12] J. Ross. Experimental Results: Weapons Bay Unsteady Environment. Technical Report DERA/MSS4/CR980744/1.0, QinetiQ, 1998.

[13] J.A. Ross. Cavity Acoustic Measurements at High Speeds. Technical Report DERA/MSS/MSFC2/TR000173, QinetiQ, March 2000.

[14] D. Rockwell and E.Naudascher. Review— Self-Sustaining Oscillations of Flow Past Cavities. *Journal of Fluids Engineering*, 100(2):152–165, June 1978.

[15] A.F. Charwat, J.N. Roos, F.C. Dewey Jr., and J.A. Hitz. An Investigation of Separated Flows - Part I: The Pressure Field. *Journal of Aerospace Sciences*, 28(6):457–470, June 1961.

[16] V. Sarohia. Experimental Investigation of Oscillations in Flows over Shallow Cavities. In *14th Aerospace Sciences Meeting*, Washington DC, USA, January 26–28 1976. AIAA. Paper 76-182.

[17] M.B. Tracy, E.B. Plentovich and J. Chu. Measurements of Fluctuating Pressure in a Rectangular Cavity in Transonic Flow at High Reynolds Numbers. Technical Memorandum 4363, NASA, June 1992.

[18] M. Gharib and A. Roshko. The Effect of Flow Oscillations on Cavity Drag. *Journal of Fluid Mechanics*, 177:510–530, 1987.

[19] C.-J. Tam and P.D. Orkwis. Comparison of Baldwin-Lomax Turbulence Models for Two-Dimensional Open Cavity Computations. *AIAA*, 34(3):629–631, March 1996. Also paper 95-0361.

[20] N.M. Komerath, K.K. Ahuja, and F.W. Chambers. Prediction and Measurement of Flows over Cavities - A Survey. In . AIAA, January 1987. AIAA 87-0166.

[21] D.G. Mabey. Resonance Frequencies of Ventilated Wind Tunnels. *AIAA*, 18(1):7–8, January 1980.

[22] D.B. Bliss. Aerodynamic Behaviour of a Slender Slot in a Wind Tunnel Wall. *AIAA*, 20(9):1244–1252, September 1982.

[23] D. Ricot, V. Maillard and C. Bailly. Numerical Simulation of the Unsteady Flow Past a Cavity and Application to the Sunroof Buffeting. In *Unknown*, 2001.

[24] A. Kovar-Panskus, P. Louka, J.-F. Sini, E. Savory, M. Czech, A. Abdelqari, P.G. Mestayer and N. Toy. Influence of Geometry on the Flow and Turbulence Characteristics Within Urban Street Canyons - Comparison of Wind Tunnel Experiments and Numerical Simulations. *Journal of Water, Air and Soil Pollution: Focus*, 2:365–380, 2002.

[25] Y.A. Gayev and E. Savory. Influence of Street Obstructions on Flow Processes Within Urban Canyons. *Journal of Wind Engineering and Industrial Aerodynamics*, 82:89–103, August-October 1999.

[26] A. Kovar-Panskus, L. Moulinneuf, E. Savory, A. Abdelqari, J.-F. Sini, J.-M. Rosant, A. Robins and N. Toy. A Wind Tunnel Investigation of the Influence of Solar-Induced Wall-Heating on the Flow Regime Within a Simulated Urban Street Canyon. *Journal of Water, Air and Soil Pollution: Focus*, 2:555–571, 2002.

[27] T. Loeland, L. Saetran, R. Olsen, I. Gran and R. Sakariassen. Fluid Motion in Ultrasonic Flowmeter Cavities. *Journal of Fluids Engineering*, 121:422–426, 1999.

[28] C.S. Tanner. Shuttle Cargo Bay Vent Noise and its Effect on Generic Payload Specifications and Testing Methods. In *AIAA 9th Aeroacoustics Conference*. AIAA, October 1984. Paper 84-2352.

[29] Z. Guo and D.L. Rhode. Assessment of Two- and Three-Scale k-epsilon Models for Rotating Cavity Flows. *Journal of Turbomachinery - Transactions of the ASME*, 118(4):826–834, October 1996.

[30] S.R. Wellborn, I. Tolchinsky, T.H. Okiishi. Modeling Shrouded Stator Cavity Flows in Axial-Flow Compressors. *Journal of Turbomachinery - Transactions of the ASME*, 122(1):55–61, January 2000.

[31] M.R. Gruber, R.A. Baurle, T. Mathur and K.-Y. Hsu. Fundamental Studies of Cavity-Based Flameholder Concepts for Supersonic Combustors. *Journal of Propulsion and Power*, 17(1):146–153, January-February 2001.

[32] M.R. Gruber, J.M. Donbar, C.D. Carter and K.-Y. Hsu. Mixing and Combustion Studies Using Cavity-Based Flameholders in a Supersonic Flow. *Journal of Propulsion and Power*, 20(5):769–778, September-October 2004.

[33] C-K. Kim, S.-T.J. Yu and Z-C. Zhang. Cavity Flow in Scramjet Engine by Space-Time Conservation and Solution Element Method. *AIAA*, 42(5):912–919, May 2004.

[34] R.A. Baurle, C.J. Tam, J.R. Edwards, and H.A. Hassan. Hybrid Simulation Approach for Cavity Flows: Blending, Algorithm, and Boundary Treatment Issues. *AIAA*, 41(8):1463–1480, August 2003.

[35] C.A. Atwood. Flowfield Simulation about the SOFIA Airborne Observatory. In *30th Aerospace Sciences Meeting & Exhibit*, Reno, Nevada, January 6–9 1992. AIAA. Paper 92-0656.

[36] C.A. Atwood. Selected Computations of Transonic Cavity Flows. In *1993 ASME Fluids Engineering Conference*, Forum on Computational Aero- and Hydro-Acoustics, Washington D.C., USA, June 20–24 1993. ASME.

[37] A.M. Lamp and N. Chokani. Control of Cavity Resonance Using Steady and Oscillatory Blowing. In *37th Aerospace Sciences Meeting & Exhibit*, Reno, Nevada, January 11–14 1999. AIAA. Paper 99-0999.

[38] C.M. Shieh and P.J. Morris. Parallel Numerical Simulation of Subsonic Cavity Noise. In *5th AIAA/CEAS Aeroacoustics Conference*, Bellevue, WA, USA, May 10–12 1999. AIAA. Paper 99-1891.

[39] S. Grace. An Overview of Computational Aeroacoustic Techniques Applied to Cavity Noise Prediction. In *AIAA*. AIAA, 2001. Paper 2001-0510.

[40] L.L. Shaw and R.M. Shimovetz. Weapons Bay Acoustic Environment. In *Impact of Acoustic Loads on Aircraft Structures*, Lillehammer, Norway, May 1994. RTO Symposium. Also CEAS/AIAA-95-141.

[41] T. Colonius. An Overview of Simulation, Modeling, and Active Control of Flow/Acoustic Resonance in Open Cavities. In *39th Aerospace Sciences Meeting and Exhibit*, Reno, Nevada, January 8–11 2001. AIAA. AIAA 2001-76.

[42] K. Takeda and C.M. Shieh. Cavity Tones by Computational Aeroacoustics. *International Journal of Computational Fluid Dynamics*, 18(6):439–454, August 2004.

[43] K. Wieghardt. Erhöhung des Turbulenten Reibungswiderstandes Durch Oberflächenstörungen. Technical Report 1563, ZWB Forachungsbericht, 1942.

[44] W. Tillman. Additional Measurements of the Drag of Surface Irregularities in Turbulent Boundary Layers. Technical Memorandum 1299, NACA, January 1951. Translation of ZWB Untersuchungen und Mitteilungen Nr. 6619, 1944.

[45] D.A. Norton. Investigation of B47 Bomb Bay Buffet. Technical Report D12675, Boeing Airplane Company, May 1952.

[46] R. Fail, T.B. Owen, and R.C.N. Eyre. Low Speed Wind Tunnel Tests on the Flow in Bomb Bays and its Effect on Drag and Vibration. Aero Report 2511, Royal Aircraft Establishment, May 1954. Also ARC Report 17412.

[47] K. Karamcheti. Acoustic Radiation from Two-Dimensional Rectangular Cutouts in Aerodynamic Surfaces. Technical Report 3487, California Institute of Technology, August 1955. NACA Technical Note.

[48] K. Karamcheti. *Sound Radiation from Surface Cutouts in High Speed Flow*. PhD thesis, California Institute of Technology, Pasadena, California, 1956.

[49] A. Roshko. Some Measurements of Flow in a Rectangular Cut-Out. Technical Report 3488, NACA, California Institute of Technology, August 1955.

[50] H.E. Plumblee, J.S. Gibson, and L.W. Lassiter. A Theoretical and Experimental Investigation of the Acoustic Response of Cavities in an Aerodynamic Flow. Technical Report WADD TR-61-75, AD277803, Wright-Patterson Air Force Base, Dayton, Ohio, March 1962.

[51] J.E. Rossiter. A Preliminary Investigation into Armament Bay Buffet at Subsonic and Transonic Speeds. Technical Memorandum 679, Royal Aircraft Establishment, Farnborough, UK, August 1960.

[52] J.E. Rossiter. A Note on Periodic Pressure Fluctuations in the Flow over Open Cavities. Technical Memorandum 743, Royal Aircraft Establishment, Farnborough, UK, November 1961.

[53] J.E. Rossiter and A.G. Kurn. Wind Tunnel Measurements of the Unsteady Pressures In and Behind a Bomb Bay (Canberra). Technical Note 2845, Royal Aircraft Establishment, Farnborough, UK, October 1962.

[54] J.E. Rossiter and A.G. Kurn. Wind Tunnel Measurements of the Unsteady Pressures In and Behind a Bomb Bay (T.S.R.2). Technical Note 2677, Royal Aircraft Establishment, Farnborough, UK, August 1963.

[55] J.E. Rossiter. Wind Tunnel Experiments on the Flow over Rectangular Cavities at Subsonic and Transonic Speeds. Technical Report 64037, Royal Aircraft Establishment, October 1964. Also ARC Report 3438.

[56] H.H. Heller and D.B. Bliss. Aerodynamically Induced Pressure Oscillations in Cavities— Physical Mechanisms and Suppression Concepts. Technical Report AFFDL-TR-74-133, Air Force Flight Dynamics Laboratory, February 1975.

[57] D. Rockwell and C. Knisely. The Organized Nature of Flow Impingement Upon a Corner. *Journal of Fluid Mechanics*, 93(3):413–432, 1970.

[58] R.L. Stallings Jr. Store Separation from Cavities at Supersonic Flight Speeds. *Journal of Spacecraft and Rockets*, 20(2):129–132, March-April 1983.

[59] A.B. Blair Jr and R.L. Stallings Jr. Cavity Door Effects on Aerodynamic Loads of Stores Separating from Cavities. *Journal of Aircraft*, 26(7):615–620, July 1989.

[60] F. Wilcox Jr. Tangential, Semisubmerged, and Internal Store Carriage and Separation at Supersonic Speeds. In *29th Aerospace Sciences Meeting*, Reno, Nevada, USA, January 7–10 1991. AIAA. Paper 91-0198.

[61] M. Gharib. Response of the Cavity Shear Layer Oscillations to External Forcing. *AIAA*, 25(1):43–47, January 1987.

[62] J.-C. Lin and D. Rockwell. Organized Oscillations of Initially Turbulent Flow Past a Cavity. *AIAA*, 39(6):1139–1151, June 2001.

[63] A.J. Meganathan and A.D. Vakili. An Experimental Study of Open Cavity Flows at Low Subsonic Speeds. In *40th Aerospace Sciences Meeting & Exhibit*, Reno, Nevada, USA, Janauary 14–17 2002. AIAA. Paper 2002-0280.

[64] S.A. Ritchie, N.J. Lawson, and K. Knowles. An Experimental and Numerical Investigation of an Open Transonic Cavity. In *21st Applied Aerodynamics Conference*, Orlando, Florida, June 23–26 2003. AIAA. Paper 2003-4221.

[65] G.W. Foster, J.A. Ross, and R.M. Ashworth. Weapon Bay Aerodynamics - Wind-Tunnel Trials and CFD Modelling by QinetiQ UK. In *RTO/AVT Symposium on "Flow-Induced Unsteady Loads and the Impact on Military Applications"*, Budapest, Hungary, April 25-29 2005. NATO. Paper 10.

[66] M.J. Esteve, P. Reulet and P. Millan. Flow Field Characterisation within a Rectangular Cavity. In *10th International Symposium Applications of Laser Techniques to Fluid Mechanics*, July 2000.

[67] X. Zhang. Compressible Cavity Flow Oscillation due to Shear Layer Instabilities and Pressure Feedback. *AIAA*, 33(8):1404–1411, August 1995.

[68] R.W. McDearmon. Investigation of the Flow in a Rectangular Cavity in a Flat Plate at a Mach Number of 3.55. Technical Note D523, NASA, September 1960.

[69] D. Rockwell and C. Knisely. Observations of the Three-Dimensional Nature of Instable Flow Past a Cavity. *Physics of Fluids*, 23(3):425–431, March 1980.

[70] H.H. Heller and D.B. Bliss. The Physical Mechanism of Flow-Induced Pressure Fluctations in Cavities and Concepts for their Suppression. In *2nd Aero-Acoustics Conference*, page 9, Hampton, Pennsylvania, March 24–26 1975. AIAA. AIAA 75-491.

[71] L.G. Kaufman, A. Maciulaitus, and R.L. Clark. Mach 0.6 to 3.0 Flows over Rectangular Cavities. Technical Report AFWAL-TR-82-3112, Air Force Wright Aeronautical Laboratories, May 1983.

[72] M. Gharib. *The Effect of Flow Oscillations on Cavity Drag, and a Technique for their Control.* PhD thesis, California Institute of Technology, Pasadena, California, USA, May 1983.

[73] R.L. Stallings Jr., E.B. Plentovich, M.B. Tracy, and M.J. Hemsch. Measurements of Store Forces and Moments and Cavity Pressures for a Generic Store in and near a Box Cavity at Subsonic and Transonic Speeds. Technical Memorandum 4611, NASA, May 1995.

[74] M.B. Tracy and E.B. Plentovich. Cavity Unsteady-Pressure Measurements at Subsonic and Transonic Speeds. Technical Paper 3669, NASA, Langley Research Center, Hampton, Virginia, USA, December 1997.

[75] L.C. Squire and S.H. Nasser. Cavity Drag at Transonic Speeds. *The Aeronautical Journal*, pages 247–256, August/September 1993.

[76] M.M. Rahman and J.A. Nasser. Experiment and prediction of a cavity type separated flow. *Applied Scientific Research*, 56:299–311, 1996.

[77] P.D. Orkwis and P.J. Disimile. Effect of Yaw on Pressure Oscillation Frequency Within Rectangular Cavity at Mach 2. *AIAA*, 35(7):1233–1235, July 1997.

[78] P.J. Disimile, N. Toy, and E. Savory. Effect of Planform Aspect Ratio on Flow Oscillations in Rectangular Cavities. *Journal of Fluids Engineering- Transactions of the ASME*, 122:32–38, March 2000.

[79] L.N. Cattafesta III, S. Garg, M.A. Kegerise, and G.S. Jones. Experiments on Compressible Flow-Induced Cavity Oscillations. In *AIAA*. AIAA, 1998. Paper 98-2912.

[80] S. Garg and L.N. Cattafesta III. Quantitative Schlieren Measurements of Coherent Structures in a Cavity Shear Layer. *Experiments in Fluids*, 30:123–134, 2001.

[81] X. Zhang and A. Rona and J.A. Edwards. An Observation of Pressure Waves Around a Shallow Cavity. *Journal of Sound and Vibration*, 214(4):771–778, March 1998.

[82] M.A. Kegerise, E.F. Spina and L.N. Cattafesta. An Experimental Investigation of Flow-Induced Cavity Oscillations. In *30th AIAA Fluid Dynamics Conference*. AIAA, June/July 1999. Paper 99-3705.

[83] M.A. Kegerise, E.F. Spina, S. Garg and L.N. Cattafesta III. Mode-S]witching and Nonlinear Effects in Compressible Flow Over a Cavity. *Physics of Fluids*, 16(3):678–687, March 2004.

[84] K.K. Ahuja and J. Mendoza. Effects of Cavity Dimensions, Boundary Layer, and Temperature on Cavity Noise with Emphasis on Benchmark Data to Validate Computational Aeracoustic Codes. Contractor Report 4653, NASA, Georgia Institute of Technology, Atlanta, Georgia, April 1995.

[85] M. Czech, E. Savory, N. Toy, and T. Mavrides. Aeroacoustic Phenomena Associated with Yawed Rectangular Cavities. In *6th AIAA/CEAS Aeroacoustics Cnference and Exhibit*, Lahaina, Hawaii, June 12–14 2000. AIAA. Paper 2000-1901.

[86] K.-M. Chung. Three-Dimensional Effect on Transonic Rectangular Cavity Flows. *Experiments in Fluids*, 30:531–536, 2001.

[87] K. Chung. Characteristics of Compressible Rectangular Cavity Flows. *Journal of Aircraft*, 40(1):137–142, January-February 2003.

[88] N. Taborda, D. Bray, and K. Knowles. Visualisastion of Three-Dimensional, Transonic Cavity Flows. In *5th World Conference on Experimental Heat Transfer, Fluid Mechanics and Thermodynamics*, Thessaloniki,Greece, September 24–28 2001.

[89] S.A. Ritchie, N.J. Lawson, and K.Knowles. A PIV and CFD Investigation of Cavity Flows in the Transonic Flow Regime. In *24th International Congress of the Aeronautical Sciences*, 2004.

[90] J. Martel, C. Anderson, and P. Sforza. Transonic Flow over Cavities. In *31st Fluid Dynamics Conference & Exhibit*, Anaheim, California, USA, June 11–14 2001. AIAA. Paper 2001-2997.

[91] R.C. Murray and G.S. Elliot. Characteristics of the Compressible Shear Layer over a Cavity. *AIAA*, 39(5):846–856, May 2001.

[92] Ö.H. Ünalmis, N.T. Clemens and D.S. Dolling. Experimental Study of Shear-Layer/Acoustics Coupling in Mach 5 Cavity Flow. *AIAA*, 39(2):242–252, February 2001.

[93] Ö.H. Ünalmis, N.T. Clemens, and D.S. Dolling. Cavity Oscillation Mechanisms in High-Speed Flows. *AIAA*, 42(10):2035–2041, October 2004.

[94] S. Radhakrishnan, A.J. Meghanathan, and A.D. Vakili. Open Cavity Flow at Subsonic Speeds — Comparison of Numerical Simulations with Experiments. In *40th Aerospace Sciences Meeting & Exhibit*, Reno, Nevada, January 14–17 2002. AIAA. Paper 2002-0571.

[95] G. Raman, E. Envia, and T.J. Bencic. Jet-Cavity Interaction Tones. *AIAA*, 40(8):1503–1511, August 2002. Also paper 99-0604.

[96] L. Chatellier, J. Laumonier, and Y. Gervais. Theoretical and Experimental Investigations of Low Mach Number Turbulent Cavity Flows. *Experiments in Fluids*, 36:728–740, 2004.

[97] G. Ashcroft and X. Zhang. Vortical Structures over Rectangular Cavities at Low Speed. *Physics of Fluids*, 17(1), January 2005.

[98] A.J. Bilanin and E.E. Covert. Estimation of Possible Excitation Frequencies for Shallow Rectangular Cavities. *AIAA*, 11:347–351, 1973.

[99] L.F. East. Aerodynamically Induced Resonance in Rectangular Cavities. *Journal of Sound and Vibration*, 3(3):277–287, 1966.

[100] R.C. Bauer and R.E. Dix. Engineering Model of Unsteady Flow in a Cavity. Technical Report AEDC-TR-91-17, Arnold Engineering Development Center, December 1991.

[101] E.J. Kerschen, J.O. Alvarez, and A. Tumin. A Theoretical Model for Cavity Acoustic Resonances. In *RTO/AVT Symposium on "Flow-Induced Unsteady Loads and the Impact on Military Applications"*, Budapest, Hungary, April 25-29 2005. NATO. Paper 15.

[102] O.W. McGregor and R.A. White. Drag of Rectangular Cavities in Supersonic and Transonic Flow Including the Effects of Cavity Resonance. *AIAA*, 8(11):1959–1964, November 1970.

[103] D.L. Smith and L.L. Shaw. Prediction of the Pressure Oscillation in Cavities Exposed to Aerodynamic Flow. Technical Report AFFDL-TR-75-34, Air Force Flight Dynamics Laboratory, October 1975.

[104] H.W. Bartel and J.M. McAvoy. Cavity Oscillation in Cruise Missile Carrier Aircraft. Technical Report AFWAL-TR-81-3036, Air Force Wright Aeronautical Laboratories, June 1981.

[105] K. Yu, E. Gutmark, R.A. Smith, and K.C. Schadow. Supersonic Jet Excitation Using Cavity-Actuated Forcing. In *AIAA*. AIAA, January 1994. AIAA 94-0185.

[106] J. Golliard and J.C. Bruggeman. Broadband Noise of Flow-Excited Cavities: Comparison of Prediction Models with Experimental Data. In *AIAA*, pages 1030–1037. AIAA, 1998. Paper 98-2381.

[107] T. Colonius, S.K. Lele, and P. Moin. Boundary Conditions for Direct Computation of Aerodynamic Sound. *AIAA*, 31:1574–1582, 1993.

[108] C. Bogey and C. Bailly. Three-Dimensional Non-Reflective Boundary Conditions for Acoustic Simulations: Far Field Formulation and Validation Test Cases. *Acta Acoustica*, 88:463–471, 2002.

[109] T. Colonius, A.J. Basu, and C.W. Rowley. Numerical Investigation of the Flow Past a Cavity. In *5th AIAA/CEAS Aeroacoustics Conference*, Greater Seattle, Washington, May 10–12 1999. AIAA. Paper 99-1912.

[110] T. Colonius, A.J. Basu, and C.W. Rowley. Computation of Sound Generation and Flow/Acoustic Instabilities in the Flow Past an Open Cavity. In *3rd ASME/JSME Joint Fluids Engineering Conference*, Proceedings of FEDSM99, San Francisco, California, USA, July 18–23 1999. ASME. Paper FEDSM99-7228.

[111] C.W. Rowley, T. Colonius, and A.J. Basu. On Self-Sustained Oscillations in Two-Dimensional Compressible Flow over Rectangular Cavities. *Journal of Fluid Mechanics*, 455:315–346, 2002.

[112] A. Hamed, D. Basu, A. Mohamed, and K. Das. Direct Numerical Simulations of High Speed Flow over Cavity. In *Proceedings of the 3rd AFOSR International Conference on DNS/LES (TAICDL)*, Arlington, Texas, August 5–9 2001. Air Force Office of Scientific Research.

[113] A. Hamed, D. Basu, and K. Das. Numerical Simulations of Transonic Flow Acoustic Resonance in Cavity. In *7th International Congress of Fluid Dynamics and Propulsion*, Cairo, Egypt, December 19–21 2001.

[114] S.K. Lele. Computational Aeroacoustics: A Review. In *AIAA*. AIAA, 1997. Paper 97-0018.

[115] S.K. Lele. Compact Finite Difference Schemes with Spectral-Like Resolution. *Journal of Computational Physics*, 103(1):16–42, 1992.

[116] C.K.W. Tam and J.C. Webb. Dispersion-Relation-Preserving Finite Difference Schemes for Computational Aeroacoustics. *Journal of Computational Physics*, 107:262–281, 1993.

[117] X. Gloerfelt, C. Bailly, and D. Juvé. Computation of the Noise Radiated by a Subsonic Cavity Using Direct Simulation and Acoustic Analogy. In *AIAA*. AIAA, 2001. Paper 2001-2226.

[118] X. Gloerfelt, C. Bailly, and D. Juvé. Direct Calculation of Cavity Noise and Validation of Acoustic Analogies. Technical Report RTO-MP-079(I), Research Technology Organisation/Applied Vehicle Technology Symposium, 2001. Presented at RTO AVT Symposium on "Ageing Mechanisms and Control: Part A - Developments in Computational Aero- and Hyrdro-Acoustics" in Manchester, UK, 8–11 October 2001.

[119] X. Gloerfelt, C. Bogey, C. Bailly, and D. Juvé. Aerodynamic Noise Induced by Laminar and Turbulent Boundary Layers over Rectangular Cavities. In *8th AIAA/CEAS Aeroacoustics Conference and Exhibit*, Breckenridge, Colorado, June 17–19 2002. AIAA. AIAA 2002-2476.

[120] C.J. Borland. Numerical Perdition of the Unsteady Flowfield in an Open Cavity. In *10th Fluid and Plasmadynamics Conference*, Albuquerque, New Mexico, June 27–29 1977. AIAA. AIAA 77-673.

[121] W.L. Hankey and J.S. Shang. Analysis of Pressure Oscillation in an Open Cavity. *AIAA*, 18(8):892–898, August 1980. Also paper 79-0136.

[122] T. Cebeci and A.M.O. Smith. *Analysis of Turbulent Boundary Layers*. Academic Press, New York, 1974.

[123] B.S. Baldwin and H. Lomax. Thin Layer Approximation and Algebraic Model for Separated Turbulent Flows. In *AIAA 16th Aerospace Sciences Meeting*, Huntsville, Alabama, January 16-18 1978. AIAA.

[124] O. Baysal and R. L. Stallings Jr. Computational and Experimental Investigation of Cavity Flowfields. *AIAA*, 26(1):6–7, 1988. Also Paper 87-0114.

[125] O. Baysal, S. Srinivasan and R.L. Stallings Jr. Unsteady Viscous Calculations of Supersonic Flows Past Deep and Shallow Three-Dimensional Cavities. In *AIAA 26th Aerospace Sciences Meeting*, Reno, Nevada, January 1988. AIAA. AIAA Paper 88-0101.

[126] S. Srinivasan, O. Baysal, and E.B. Plentovich. Navier-Stokes Calculations of Transonic Flows Past Open and Transitional Cavities. *Journal of Fluids Engineering*, 66:169–179, December 1988.

[127] O. Baysal and G. Yen. Implicit and Explicit Computations of Flows Past Cavities With and Without Yaw. In *28th Aerospace Sciences Meeting*, Reno, Nevada, January 8–11 1990. AIAA. Paper 90-0049.

[128] S. Srinivasan and O. Baysal. Navier-Stokes Calculations of Transonic Flows Past Cavities. *Journal of Fluids Engineering- Transactions of the ASME*, 113:368–376, September 1991.

[129] P.D. Orkwis and P.J. Disimile. Transient Shear Layer Dynamics of Two- and Three-Dimensional Open Cavities. Final F49620-93-1-0081, Air Force Office of Scientific Research, University of Cincinnati, May 1995. Also ADA 298030.

[130] C.-J. Tam, P.D. Orkwis and P.J. Disimile. Algebraic Turbulence Model Simulations of Supersonic Open-Cavity Flow Physics. *AIAA*, 34(11):2255–2260, November 1996. Also paper 96-0075.

[131] P. D. Orkwis, B. Sekar, S. Chakrawarthy, and O. Peroomian. Comparison of Three Navier-Stokes Equation Solvers for Supersonic Open Cavity Simulations. *AIAA*, 36(5):865–867, May 1998. Also Paper 97-3163.

[132] S.H. Shih, A. Hamed, and J.J. Yeuan. Unsteady Supersonic Cavity Flow Simulations Using Coupled $\kappa - \varepsilon$ and Navier-Stokes Equations. *AIAA*, pages 2015–2021, October 1994. Also paper 93-3031.

[133] W.P. Jones and B.E. Launder. The Prediction of Laminarization with a Two-Equation Model of Turbulence. *International Journal of Heat and Mass Transfer*, 15:301–314, 1972.

[134] X. Zhang and J.A. Edwards. Computational Analysis of Unsteady Cavity Flows Driven by Thick Shear Layers. *The Aeronautical Journal*, 94(940):355–364, 1988.

[135] X. Zhang and J. A. Edwards. An Investigation of Supersonic Oscillatory Cavity Flows Driven By A Thick Shear Layer. *The Aeronautical Journal*, 94(940):355–364, 1990.

[136] X. Zhang, A. Rona and J.A. Edwards. The Effect of Trailing Edge Geometry on Cavity Flow Oscillation Driven by a Supersonic Shear Layer. *The Aeronautical Journal*, March 1998.

[137] X. Zhang and J. A. Edwards. Pressure over a dual-cavity cascade at supersonic speeds. *The Aeronautical Journal*, January 1999.

[138] D.C. Wilcox. Reassessment of the scale-determining equation for advanced turbulence models. *AIAA*, 26:1299–1310, 1988.

[139] O. Baysal, K. Fouladi, R.W. Leung, and J.S. Sheftic. Interference Flows Past Cylinder-Fin-Sting-Cavity Assemblies. *Journal of Aircraft*, 29(2):194–202, March-April 1992. Also paper 90-3095.

[140] C.A. Atwood. Computation of a Controlled Store Separation from a Cavity. In *32nd Aerospace Sciences Meeting & Exhibit*, Reno, Nevada, January 10–13 1994. AIAA. Paper 94-0031.

[141] N.E. Suhs. Computational Approach to Weapons Bay Flow Field and Carriage Load Predictions. In *Symposium on Aerodynamics of Store Integration and Separation*, Ankara, Turkey, April 24–27 1995. AGARD. Published in CP-570.

[142] A. Morgenstern Jr. and N. Chokani. Hypersonic Flow Past Open Cavities. *AIAA*, 32(12):2387–2393, June 1994. Also Paper 93-2969.

[143] J. Henderson, K.J. Badcock, and B.E. Richards. Understanding Subsonic and Transonic Open Cavity Flows and Supression of Cavity Tones. In *AIAA*. AIAA, 2000. Paper 2000-0658.

[144] D. Lawrie, P. Nayyar, K.J. Badcock, G.N. Barakos, and B.E. Richards. A CFD Study of Cavity Flows. In *RAeS/CEAS Aerospace Research Conference*, London, UK, June 10–12 2003. Royal Aeronautical Society.

[145] N. Sinha, S.M. Dash, N. Chidambaram, and D. Finlay. A Perspective on the Simulation of Cavity Aeroacoustics. In *36th Aerospace Sciences Meeting & Exhibit*, Reno, Nevada, January 12–15 1998. AIAA. Paper 98-0286.

[146] J.J. Gorski, D.K. Ota and S.R. Chakravarthy. Calculation of Three-Dimensional Cavity Flowfields. In *25th Aerospace Sciences Meeting*, Reno, Nevada, January 12–15 1987. AIAA. Paper 87-0117.

[147] N.E. Suhs. Computations of Three-Dimensional Cavity Flow at Subsonic and Supersonic Mach Numbers. In *19th Fluid Dynamics, Plasma Dynamics and Laser Conference*, Honolulu, Hawaii, June 8–10 1987. AIAA. Paper 87-1208.

[148] N.E. Suhs. Transonic Flow Calculations for a Cavity with and without a Store. Technical Report AEDC-TR-92-4, USAF, September 1992.

[149] N.E. Suhs. Unsteady Flow Computations for a Three-Dimensional Cavity With and Without an Acoustic Suppression Device. In *AIAA 11th Applied Aerodynamics Conference*. AIAA, 1993. Paper 93-3402.

[150] G.W. Yen O. Baysal and K. Fouladi. Navier-Stokes Computations Of Cavity Aeroacoustics With Suppression Devices. *Journal of Vibration and Acoustics- Transactions of the ASME*, 116:105–112, January 1994.

[151] D.P. Rizzetta. Numerical Simulation of Supersonic Flow over a Three-Dimensional Cavity. *AIAA*, 26(7):799–807, July 1988. Also paper 87-1288.

[152] X. Zhang and J.A. Edwards. Analysis of Unsteady Supersonic Cavity Flow Employing an Adaptive Meshing Algorithm. *Computers & Fluids*, 25(4):373–393, 1996.

[153] N.S. Dougherty, J.B. Holt, T.E. Nesman, and R.A. Farr. Time-Accurate Navier-Stokes Computations of Self-Excited Two-Dimensional Unsteady Cavity Flows. In *AIAA*. AIAA, January 1990. Paper 90-0691.

[154] D.F. Fuglsang and A.B. Cain. Evaluation of Shear Layer Cavity Resonance Mechanisms by Numerical Simulation. In *30th Aerospace Sciences Meeting & Exhibit*, Reno, Nevada, January 6–9 1992. AIAA. Paper 92-0555.

[155] Y. Tu. Unsteady Navier Stokes Simulations of Suupersonic Flow over a Three-Dimensional Cavity. In *AIAA*, 1992. Paper 92-2632.

[156] J.L. Tracey and B.E. Richards. Navier-Stokes Solutions of Turbulent Transonic Cavity Flows. Technical report, University of Glasgow, 1996.

[157] A. Rona and W. Dieudonné. A Flow Resonant Model of Transonic Laminar Open Cavity Instability. In *6th AIAA/CEAS Aeroacoustics Conference*, Lahaina, Hawaii, June 12–14 2000. AIAA. Paper 2000-1967.

[158] J.W. Deardorff. A Numerical Study of the Three-Dimensional Turbulent channel Flow at Large Reynolds Numbers. *Journal of Fluid Mechanics*, 41:453–, 1970.

[159] U. Schumann. Subgrid Scale Model for Finite Difference Simulations of Turbulent Flows in Plane Channels and Annuli. *Journal of Computational Physics*, 18:376–, 1975.

[160] L. Larcheveque, P. Sagaut, I. Mary, O. Labbé, and P. Comte. Large-Eddy Simulation of a Compressible Flow Past a Deep Cavity. *Physics of Fluids*, 15(1):193–210, January 2003.

[161] B.R. Smith. Large Eddy Simulation of a Supersonic Cavity Flow with an Unstructured Grid Flow Solver. In C. Liu, L. Sakell, and T. Beutner, editors, *3rd AFOSR International Conference on Direct Numerical Simulation and Large Eddy Simulation (TAICDL)*, DNS/LES Progress and Challenges, pages 783–790, Arlington, Texas, USA, August 5–9 2001. Greyden.

[162] B.R. Smith, T.J. Welterlen, and N.D. Domel. Large eddy-simulation for the analysis of weapon bays flows. Technical report, Lockheed Martin Aeronautics Company, June 2001.

[163] L. Larchevêque, P. Sagaut, and T.-H. Lê. Large-Eddy Simulations of Flows in Weapon Bays. In *AIAA*. AIAA, 2003. Paper 2003-0778.

[164] D.P. Rizzetta and M.R. Visbal. Large-Eddy Simulation of Supersonic Cavity Flowfields Including Flow Control. *AIAA*, 41(8):1438–1443, August 2003. Also Paper 2002-2853.

[165] X. Gloerfelt. Large-Eddy Simulation of a High Renolds Number Flow over a Cavity Including Radiated Noise. In *10th AIAA/CEAS Aeroacoustics Conference.* AIAA, 2004. Paper 2004-2863.

[166] X. Gloerfelt, C. Bailly and D. Juvé. Direct Computation of Noise Radiated by the Flow Past a Cavity. *Acoustics, Waves, Vibrations*, 2000.

[167] X. Gloerfelt, C. Bogey, and C. Bailly. A Case of "Intermittency" in the Noise Radiated By a Turbulent Cavity Flow. In *6th CEAS-ASC Workshop "From CFD to CAA"*, Athens, Greece, November 7–8 2002.

[168] X. Gloerfelt, C. Bogey and C. Bailly. Numerical Investigation of the Coexistence of Multiple Tones in Flow-Induced Cavity Noise. In *AIAA*. AIAA, 2003. Paper 2003-3234.

[169] X. Gloerfelt, C. Bogey, and C. Bailly. Numerical Evidence of Mode Switching in the Flow-Induced Oscillations by a Cavity. *International Journal of Aeroacoustics*, 2(2):99–124, 2003.

[170] M. Lesieur and O. Métais. New Trends in Large-Eddy Simulation of Turbulence. *Annual Review of Fluid Mechanics*, 28:45–, 1995.

[171] P. Moin. Progress in Large Eddy Simulation of Turbulent Flows. In *AIAA*. AIAA, 1997. Paper 97-0749.

[172] U. Piomelli. Large-Eddy Simulation: Achievements and Challenges. *Progress in Aerospace Sciences*, 35:335–, 1999.

[173] J.P. Boris, F.F. Grinstein, E.S. Oran, and R.L. Kolbe. New Insights into Large-Eddy Simulation. *Fluid Dynamics Research*, 10:199–228, 1992.

[174] J. Larsson, L. Davidson, M. Olsson, and L.-E. Eriksson. Aeracoustic Investigation of an Open Cavity at Low Mach Number. *AIAA*, 42(12):2462–2473, December 2004.

[175] N. Sinha, S. Arunajatesan, and L.S. Ukeiley. High Fidelity Simulation of Weapons Bay Aeroacoustics and Active Flow Control. In *6th AIAA/CEAS Aeracoustics Conference*, Lahaina, Hawaii, June 12–14 2000. AIAA. Paper 2000-1968.

[176] H. Yao, R.K. Cooper, and S.R. Raghunathan. Large-Eddy Simulation of Laminar-to-Turbulent Transition in Incompressible Flow Past 3-D Rectangular Cavity. In *31st AIAA Fluid Dynamics Conference & Exhibit*, Anaheim, California, USA, June 11–14 2001. AIAA. Paper 2001-2990.

[177] X. Gloerfelt, C. Bogey, and C. Bailly. LES of the Noise Radiated by a Flow over a Rectangular Cavity. In *International Workshop on "LES for Acoustics"*, DLR Göttingen, Germany, October 7–8 2002.

[178] Y. Dubief and F. Delcayre. On Coherent-Vortex Identification in Turbulence. *Journal of Turbulence*, 1, 2000.

[179] E. Lillberg and C. Fureby. Large Eddy Simulations of Supersonic Cavity Flow. In *Fluids 2000 Conference and Exhibit*, Denver, Colorado, June 19–22 2000. AIAA. Paper 2000-2411.

[180] C.M. Shieh and P.J. Morris. Parallel Computational Aeroacoustic Simulation of Turbulent Subsonic Cavity Flow. In *6th AIAA/CEAS Aeroacoustics Conference and Exhibit*. AIAA, June 12–14 2000. Paper 2000-1914.

[181] R.H. Nichols and C.C. Nelson. Weapons Bay Acoustic Predictions Using a Multiscale Turbulence Model. Technical report, 2001.

[182] S. Arunajatesan, J.D. Shipman, and N. Sinha. Hybrid RANS-LES Simulation of Cavity Flowfields with Control. In *40th AIAA Aerospace Sciences Meeting & Exhibit*, Reno, Nevada, January 14–17 2002. AIAA. Paper 2002-1130.

[183] A. Hamed, D. Basu and K. Das. Detached Eddy Simulations of Supersonic Flow over CAvity. In *41st Aerospace Sciences Meeting and Exhibit*, Reno, Nevada, January 6-9 2003. AIAA. paper 2003-0549.

[184] A. Hamed, D. Basu, and K. Das. Effect of Reynolds Number on the Unsteady Flow and Acoustic Fields of Supersonic Cavity. In *4th ASME/JSME Joint Fluids Engineering Conference*, Proceedings of FEDSM03, Honolulu, Hawaii, USA, July 6–11 2003. ASME. Paper FEDSM2003-45473.

[185] ca F. Mendon R. Allen, J. de Charentenay, and D.A. Kirkham. CFD Prediction of Narrow and Broadband Cavity Acoustics at M=0.85. In *AIAA*. AIAA, 2003. Paper 2003-3303.

[186] A.K. Viswanathan, K.D. Squires, and J.R. Forsythe. Detached Eddy Simulation of the Flow over an Axisymmetric Cavity. In *Aerospace Sciences Meeting 2003*, Reno, Nevada, January 6–9 2003. AIAA. Paper 2003-0265.

[187] A.B. Cain, R.E. Epstein, and E.J. Kerschen. Quick Turnaround Prediction of Weapons Bay Cavity Acoustics Resonance. In *5th AIAA/CEAS Aeroacoustics Conference*, Bellevue, Washington, USA, May 10–12 1999. AIAA. Paper 99-1899.

[188] C.R. Rowley, T. Colonius, and R.M. Murray. POD-Based Models of Self-Sustained Oscillations in the Flow Past an Open Cavity. In *6th AIAA/CEAS Aeroacoustics Conference*, Lahaina, Hawaii, June 12–14 2000. AIAA. Paper 2000-1969.

[189] C.R. Rowley, T. Colonius, and A.J. Basu. Dynamical Models for Control of Cavity Oscillations. In *7th AIAA/CEAS Aeroacoustics Conference*, Maastricht, The Netherlands, May 28–30 2001. AIAA. Paper 2001-2126.

[190] D. Ricot, V. Maillard, and C. Bailly. Numerical Simulation of Unsteady Cavity Using a Lattice Boltzmann Method. In *AIAA*. AIAA, 2002. Paper 2002-2532.

[191] P.R. Spalart, W.-H. Jou, M. Strelets and S.R. Allmaras. Comments on the feasibility of LES for wings, and on a hybrid RANS/LES approach. In C. Liu and Z. Liu, editors, *First AFOSR International Conference on DNS/LES: Advances in DNS/LES*, Ruston, LA., August 1997. Greyden.

[192] P.R. Spalart and S.R. Allmaras. A One-Equation Turbulence Model for Aerodynamic Flows. In *AIAA 30th Aerospace Sciences Meeting*, Reno, NV, January 1992. AIAA. AIAA 92-0439.

[193] M. Strelets. Detached Eddy Simulation of Massively Separated Flows. In *39th AIAA Aerospace Sciences Meeting*. AIAA, January 2001. AIAA Paper 2001-0879.

[194] R.H. Bush and M. Mani. A Two Equation Large Eddy Stress Model for High Sub-Grid Shear. In *31st AIAA Computational Fluid Dynamics Conference*. AIAA, 2001. Paper 2001-2561.

[195] A. Travin, M. Shur, M. Strelets, and P. Spalart. Physical and Numerical Upgrades in the Detached-Eddy Simulation of Complex Turbulent Flows. In P. Friedrich and W. Rodi, editors, *Advances in LES of Complex Flows*, pages 239–254. Kluwer Academic, 2002.

[196] C.M. Shieh and P.J. Morris. Comparison of Two- and Three-Dimensional Turbulent Cavity Flows. In *39th AIAA Aerospace Sciences*, Reno, Nevada, January 8–11 2001. AIAA. AIAA Paper 2001-0511.

[197] J.L. Lumley. The Structure of Inhomogeneous Turbulent Flows. In Yaglom and Tatarsky, editors, *Atmospheric Turbulence and Radio Wave Propagation*, pages 166–178, Nauka, Moscow, Unknown.

[198] R. Adrian. On the Role of Conditional Averages in Turbulent Theory. In *Proceedings of the 4th Biennial Symposium on Turbulence in Liquids*. AIAA, 1977.

[199] N. Murray and L.S. Ukeiley. Estimating the Shear Layer Velocity Field Above an Open Cavity from Surface Pressure Measurements. In *AIAA*. AIAA, 2002.

[200] N. Murray. Time-Resolved, Low-Dimensional Estimation of Open Cavity Flow, May 2003. Master's Thesis.

[201] N. Murray and L.S Ukeiley. Estimation of the Flowfield from Surface Pressure Measurements in an Open Cavity. *AIAA*, 41(5):969–972, 2003. Also Paper 2002-2866.

[202] L.N. Cattafesta, D. Williams, C. Rowley and F. Alvi. Review of Active Control of Flow-Induced Cavity Resonance. In *33rd AIAA Fluid Dynamics Conference*. AIAA, June 2003. AIAA Paper 2003-3567.

[203] J.E. Grove, R.M. Birkbeck and J.M. Kreher. Acoustic and Separation Characteristics with Bay Leading Edge Blowing. In *AIAA*. AIAA, 2000. Paper 2000-1904.

[204] P.J. Zoccola Jr. *Experimental Investigation of Flow-Induced Cavity Resonance*. PhD thesis, School of Engineering of the Catholic University of America, Washington DC, USA, June 2000.

[205] R.M. Forristal and R.K. Cooper. Computation of Unsteady Airflow over a 2-Dimensional Rectangular Cavity. In *Proceedings of the ASME FEDSM'00*, ASME 2000 Fluids Engineering Division Summer Meeting, Boston, Massachusetts, USA, June 11–15. AIAA. Paper FEDSM2000-11202.

[206] R.A. Smith, E. Gutmark, and K.C. Schadow. Mitigation of Pressure Oscillations Induced by Supersonic Flow over Slender Cavities. *Journal of Aircraft*, 29(6):999–1004, November-December 1992.

[207] F.J. Wilcox Jr. Experimental Measurements of Internal Store Separation Characteristics at Supersonic Speeds. NASA Technical Report.

[208] R.L. Stallings Jr., E.B. Plentovich, M.B. Tracy, and M.J. Hemsch. Effect of Passive Venting on Static Pressure Distributions in Cavities at Subsonic and Transonic Speeds. Technical Memorandum 4549, NASA, June 1994.

[209] Y.N. Jeng and U.J. Payne. Numerical Study of a Supersonic Open Cavity Flow and Pressure Oscillation Control. *AIAA*, 32(2):363–369, March-April 1995.

[210] S.W. Perng and D.S. Dolling. Suppression of Pressure Oscillations in High-Mach-Number Turbulent, Cavity Flow. *Journal of Aircraft*, 38(2):248–256, March-April 2001.

[211] R. Clark. Evaluation of F-111 Weapon Bay Aero-Acoustic and Weapon Separation Improvement Studies. Technical Report AFFDL-TR-79-3003, Air Force Flight Dynamics Laboratory, Wright-Patterson Air Force Base, Ohio, USA, February 1979. Also ADA070253.

[212] J.C.F. Pereira and J.M.M. Sousa. Influence of Impingement Edge Geometry on Cavity Flow Oscillations. *AIAA*, 32(8):1737–1740, 1993. Technical Note.

[213] D.S. Dolling, S.W. Perng, and Y.L. Leu. An Experimental Study of Passive Control of Hypersonic Cavity Flow Oscillations. Final Report F49620-95-1-0001, Air Force Office of Scientific Research, Austin, Texas, USA, March 1998. Also ADA339335.

[214] R.L. Sarno and M.E. Franke. Suppression of Flow-Induced Pressure Oscillations in Cavities. *Journal of Aircraft*, 31(1):90–96, February 1994. Also AIAA Paper 90-4018.

[215] L.S. Ukeiley, M.K. Ponton, J.M. Seiner, and B. Jansen. Suppression of Pressure Loads in Cavity Flows. *AIAA*, 42(1):70–79, January 2004. Also AIAA paper 2002-0661.

[216] M.J. Stanek, G. Raman, V. Kibens, J.A. Ross, J. Odedra, and J.W. Peto. Control of Cavity Resonance Through Very High Frequency Forcing. In *6th AIAA/CEAS Aeroacoustics Conference*, Lahaina, Hawaii, June 12–14 2000. AIAA. Paper 2000-1905.

[217] B.R. Smith, T.J. Welterlen, B.H. Maines, L.L. Shaw, M.J. Stanek, and J.E. Grove. Weapons Bay Acoustic Suppression from Rod Spoilers. In *40th AIAA Aerospace Sciences Meeting and Exhibit*, Reno, Nevada, January 14–17 2002. AIAA. Paper 2002-0662.

[218] L.N. Cattafesta III, D. Shukla, S. Garg, and J.A. Ross. Development of an Adaptive Weapons-Bay Suppression System. In *AIAA*, pages 676–682. AIAA, 1999. Paper 99-1901.

[219] B.R. Smith, J.K. Jordan, E.E. Bender, S.N. Rizk, and L.L. Shaw. Computational Simulation of Active Control of Cavity Acoustics. In *6th AIAA/CEAS Aeroacoustics Conference*, Lahaina, Hawaii, June 12–14 2000. AIAA. Paper 2000-1927.

[220] L. Shaw. Active Control of Cavity Acoustics. In *AIAA*. AIAA, 1998. Paper 98-2347.

[221] G. Raman, S. Raghu, and T.J. Bencic. Cavity Resonance Suppression Using Miniature Fluidic Oscillators. In *AIAA*, pages 653–663. AIAA, 1999. Paper 99-1900.

[222] L. Mongeau, H. Kook, and M.A. Franchek. Active Control of Flow-Induced Cavity Resonance. In *AIAA/CEAS*. AIAA/CEAS, 1998. Paper 98-2349.

[223] L.N. Cattafesta III, S. Garg, M. Choudhari, and F. Li. Active Control of Flow-Induced Cavity Resonance. In *28th AIAA Fluid Dynamics Conference/4th AIAA Shear Flow Control Conference*, Showmass Village, Colorado, USA, June 29- July 2 1997. AIAA. Paper 97-1804.

[224] M.A. Kegerise, L.N. Cattafesta III, and C. Ha. Adaptive Identification and Control of Flow-Induced Cavity Oscillations. In *1st AIAA Flow Control Conference*, St. Louis, MO, USA, June 24–27 2002. AIAA. Paper 2002-3158.

[225] M.A. Kegerise, R.H. Cabell, and L.N. Cattafesta III. Real-Time Adaptive Control of Flow-Induced Cavity Tones. In *AIAA*. AIAA, 2004. Paper 2004-0572.

[226] A.M. Lamp and N. Chokani. Computation of Cavity Flows with Suppression Using Jet Blowing. *Journal of Aircraft*, 34(4):545–551, July-August 1997.

[227] L. Shaw. High Speed Application of Active Flow Control for Cavity Acoustics. In *6th AIAA/CEAS Aeroacoustics Conference and Exhibit*, Lahaina, Hawaii, June 12–14 2000. AIAA. Paper 2000-1926.

[228] P.C. Bueno, Ö.H. Ünalmis, N.T. Clemens, and D.S. Dolling. The Effects of Upstream Mass Injection on a Mach 2 Cavity Flow. In *40th Aerospace Sciences Meeting and Exhibit*, Reno, Nevada, January 14–17 2002. AIAA. Paper 2002-0663.

[229] A.D. Vakili, R.C. Wolfe, and P.A. Nagle. Active Control of Cavity Aeroacoustics. In *Proceedings of the 1st Joint CEAS/AIAA Aeroacoustics Conference*, pages 1199–1206, Munich, Germany, June 12–15 1995.

[230] D. Festzy, K.J. Badcock and B.E. Richards. Cavity Control by Unsteady Jet Blowing - Modelling Study. Final report, University of Glasgow, July 2000.

[231] R.H. Cabell, M.A. Kegerise, D.E. Cox, and G.P. Gibbs. Experimental Feedback Control of Flow Induced Cavity Tones. In *AIAA*, 2002. Paper 2002-2497.

[232] D.R. Williams and D. Fabris. Experiments on Controlling Multiple Acoustic Modes in Cavities. In *6th AIAA/CEAS Aeroacoustics Conference*, Lahaina, Hawaii, June 12–14 2000. AIAA. Paper 2000-1903.

[233] D.R. Williams, C. Rowley, T. Colonius, R. Murray, D. MacMartin, D. Fabris, and J. Albertson. Model-Based Control of Cavity Oscillations — Part 1: Experiments. In *40th AIAA Aerospace Sciences Meeting and Exhibit*, Reno, Nevada, January 14–17 2002. AIAA. Paper 2002-0971.

[234] C.W. Rowley, D.R. Williams, T. Colonius, R.M. Murray, D.G. MacMartin, and D. Fabris. Model-Based Control of Cavity Oscillations. Part II: System Identification and Analysis. In *40th AIAA Aerospace Sciences Meeting & Exhibit*, Reno, Nevada, January 14–17 2002. AIAA. Paper 2002-0972.

[235] D.R. Williams. Closed-Loop Control of Acoustic Tones in Aircraft Cavities. Final F49620-98-1-0276, Fluid Dynamics Research Center, Illinois Institute Technology, Chicago, Illinois, USA, February 2002.

[236] C.W. Rowley and D.R. Williams. Control of Forced and Self-Sustained Oscillations in the Flow Past a Cavity. In *AIAA*. AIAA, 2003. Paper 2003-0008.

[237] M. Samimy, M. Debiasi, E. Caraballo, J. Malone, J. Little, H. Özbay, M.Ö. Efe, P. Yan, X. Yuan, J. DeBonis, J.H. Myatt, and R.C. Camphouse. Exploring Strategies for Closed-Loop Flow Control. In *42nd AIAA Aerospace Science Meeting*, Reno, Nevada, January 5–8 2004. AIAA. Paper 2004-0576.

[238] A. Jameson. Time Dependent Calculations Using Multigrid with Applications to Unsteady Flows Past Airfoils and Wings. In *Proceedings of the AIAA*, Honolulu, HI, June 1991. Paper 91-1596.

[239] S. Osher and S. Chakravarthy. Upwind Schemes and Boundary Conditions with Applications to Euler Equations in General Geometries. *Journal of Computational Physics*, 50:447–481, 1983.

[240] P.L. Roe. Approximate Rieman Solver, Parameters Vectors and Difference Schemes. *Journal of Computational Physics*, 43:357–372, 1981.

[241] M. Woodgate, K.J. Badcock, B.E. Richards and R. Gatiganti. A Parallel 3D Fully Implicit Unsteady Multiblock CFD Code Implemented on a Beowulf Cluster. In *Parallel CFD Conference*, Williamsburg, USA, 1999.

[242] Computer Services for Academic Research (CSAR). http://www.csar.cfs.ac.uk/.

[243] HPCX Capability Computing. http://www.hpcx.ac.uk/.

[244] P. Nayyar and G. Barakos. A Summary of Turbulence Modelling Approaches in CFD. Aero Report 0206, University of Glasgow, Aerospace Engineering Dept., September 2002.

[245] F.R. Menter. Two-Equation Eddy-Viscosity Turbulence Models for Engineering Applications. *AIAA*, 32(8):1598–1605, 1994.

[246] M.V. Morkovin. Effects of Compressibility on Turbulent Flows. In A. Favre, editor, *Méchanique de la Turbulence*, pages 367–380. CNRS, 1962.

[247] B.S. Baldwin and T.J. Barth. A One-Equation Turbulence Transport Model for High-Reynolds Number Wall-Bounded Flows. Technical Memorandum 102847, NASA, August 1990. Also as AIAA Paper 91-0610.

[248] S. Moir and A. Gould. VoTMATA - British Aerospace Default Model. Technical report, BAE SYSTEMS, 1998.

[249] K. Hanjalic and B. E. Launder. A Reynolds Stress Model of Turbulence and its Application to Thin Shear Flows. *Journal of Fluid Mechanics*, 52:609–644, 1972.

[250] P.A. Durbin. Near-Wall Turbulence Closure Modelling Without Damping Functions. *Theoretical Computational Fluid Dynamics*, 3:1–13, 1991.

[251] T.J. Craft, B.E. Launder, and K. Suga. Development and Application of a Cubic Eddy-Viscosity Model of Turbulence. *International Journal of Heat and Fluid Flow*, 17(2):108–115, April 1996.

[252] T.P. Sommer, R.M.C. So, and H.S. Zhang. A Near-Wall Four-Equation Turbulence Model for Compressible Boundary Layers. Contractor Report 4436, NASA, April 1992.

[253] P. Malecki and R.Houdeville. Etude de modèles de turbulence pour les couches limites tridimensionnelles. In *29ième Colloque d'Aérodynamique Appliqué*, Bislarosse, September 21–23 1992. Association Aéronautique et Astronautique de France.

[254] P. Malecki. *Etude de modèles de turbulence pour les couches limites tridimensionnelles*. PhD thesis, L'Ecole National Supérieure de l'Aéronautique et de l'Espace (Supaéro), Toulouse, France, November 1994.

[255] K. Hanjalic, B.E. Launder, and R. Schiestel. Multiple-Time-Scale Concepts in Turbulent Shear Flows. In L.J.S. Bradbury, F. Durst, B.E. Launder, F.W. Schmidt, and J.H. Whitelaw, editors, *Turbulent Shear Flows*, volume 2, pages 36–49, New York, 1980. Springer-Verlag.

[256] S.-W. Kim. Numerical Investigation of Separated Transonic Turbulent Flows with a Multiple-Time-Scale Turbulence Model. Technical Memorandum 102499, NASA, January 90.

[257] C.P. Chen. A Non-Isotropic Multiple-Scale Turbulence Model. Contractor Report 184217, NASA, 1990.

[258] S. Deck, P. Duveau, P. d'Espiney, and P. Guillen. Development and Application of Spalart-Allmaras One-Equation Turbulence Model to Three-Dimensional Supersonic Complex Configurations. *Aerospace Science and Technology*, 6:171–183, 2002.

[259] P.R. Spalart and M. Shur. On the Sensitization of Turbulence Models to Rotation and Curvature. *Aerospace Science and Technology*, 1(5):297–302, July 1997.

[260] A.N. Kolmogorov. Equations of turbulent motion of an incompressible fluid. *Izvestiya Akademii Nauk. Seriya Fizicheskaya*, 6:55–58, 1942.

[261] F.H. Harlow and P.I. Nakayama. Transport of Turbulence Energy Decay Rate. Technical Report LA-3854, Los Alamos Sci. Lab., 1968.

[262] D.B. Spalding. The Prediction of Two-Dimensional Steady Turbulent Flows. Heat Transfer Section Report EF/TN/A/16, Imperial College, 1969.

[263] C.G. Speziale, R. Abid, and E.C. Anderson. Critical Evaluation of Two-Equation Models for Near-Wall Turbulence. *AIAA*, 30:324–331, 1992.

[264] D.A. Johnson and L.S. King. A Mathematically Simple Turbulence Closure Model for Attached and Separated Turbulent Boundary Layers. *AIAA*, 23(11):1684–1692, 1985.

[265] D.C. Wilcox. Simulation of transition with a two-equation turbulence model. *AIAA*, 32:247–255, 1994.

[266] C.C. Chieng and B.E. Launder. On the Calculation of Turbulent Heat Transport Downstream from an Abrupt Pipe Expansion. *Numerical Heat Transfer*, 3:189–207, 1980.

[267] A. Favre. Equations des Gaz Turbulents Compressibles. *Journal de Méchanique*, 4(3):361–390, 1965.

[268] P. Batten, U. Goldberg and S. Chakravarthy. Sub-Grid Turbulence Modeling for Unsteady Flow with Acoustic Resonance. In *38th AIAA Aerospace Sciences*. AIAA, January 2000. Paper 00-0473.

[269] G.W. Foster, J.A. Ross and I. Wrisdale. Weapon Bay Aerodynamics - Wind-Tunnel Trials and CFD Modelling by DERA UK. In *Aircraft-Store Compatibility Symposium*, March 2001.

[270] J. Odedra, J.A. Ross and G.W. Foster. *Cavity Unsteady Pressure Measurements - Examples from Wind-Tunnel Tests*. QinetiQ, 2001.

[271] J. Smagorinsky. General Circulation Experiments with the Primitive Equations: I. the Basic Experiment. *Monthly Weather Review*, 91:99–163, 1963.

[272] L. Larcheveque, P. Sagaut, T.-H. Lê, and P. Comte. Large-Eddy Simulation of a Compressible Flow in a Three-Dimensional Open Cavity at High Reynolds Number. *Journal of Fluid Mechanics*, 516:265–301, October 2004.